University of Sheffield

SCALING-UP THE TRIBOLOGICAL ASSESSMENT OF LASER CLAD RAIL TO BUILD THE CASE FOR FIELD IMPLEMENTATION

KAZIM YILDIRIMLI

Thesis submitted for the degree of Doctor of Philosophy

THE UNIVERSITY OF SHEFFIELD
FACULTY OF ENGINEERING
DEPARTMENT OF MECHANICAL ENGINEERING

July 2024

Abstract

The wheel/rail contact in railways is one of the most examined parts and from the beginning of railway travel new solutions were needed to optimise its performance. Wear and rolling contact fatigue (RCF) are the two biggest problems. Those problems directly affect the rail and wheel life in the railway industry. When rails have high deformation (taking the rail profile outside of acceptable geometrical thresholds defined by standards) or damage, they need to be taken out and replaced and that causes many delays and problems. This would be longer in lighter traffic lines, but in heavy and mostly used traffic lines the rail life is 2-3 years. Surface treatment methods increase the lifetime of rails and coating over rail surface have given good solution for those problems.

Laser cladding is an additive manufacturing coating method. It allows the same or a different type of material to be coated over a rail or wheel substrate. Laser cladding process parameters and material selections are important factors for achieving this purpose.

In this thesis work showed that laser clad coated rail specimens tested under different test scales: small-scale tests, full-scale tests in laboratory conditions and field tests with actual environmental conditions. Material selection of laser clad specimens was based on previous tests for improved wear and RCF resistance. They were compared with standard grade rails and premium rails. The clad materials were martensitic stainless steel (MSS), Stellite 6, R260, and T400. The substrate rail material used was R260 grade rail. Also, some premium rail tests were conducted for comparison: Manganese (Mn), Chromium (Cr) and R400 HT.

Small-scale twin disc tests were conducted to find the full lifespan of MSS clad and some repair solutions with MSS clad, Stellite 6 clad and R260 clad over R260 rail specimen “damage”. The premium rail specimens were analysed and compared with R260 rail specimen and MSS clad specimens. Also, laser cladding process parameters were changed with MSS clad over R260 rail and tested to find how clad “quality” affects the performance of clad specimens and how defects change or cause problems when optimal clad parameters changed. Full-scale tests were conducted to see how clad specimens and repair specimens perform under actual loading conditions. MSS clad, Stellite 6 clad and R260 un-clad pocket specimens were analysed and compared with small scale tests. A T400 rail specimen was tested for repair analysis. The results of small-scale tests were reflected in the full-scale test outcomes. In all tests the clad layers performed well in terms of wear and RCF resistance which gave the confidence needed to initiate field tests. MSS clad twin-disc experiments showed that the clad disc did not fail over

400,000 cycles. However, experiments with R260 standard grade rail discs observed failures occurring around 15,000 cycles in the literature. It is evident that the MSS clad disc exhibited at least 20-25 times higher wear and rolling contact fatigue (RCF) resistance than the standard grade rail disc. These were started, and data collection undertaken for R260 rails, HP 335 premium rails, MSS clad rails with different clad thickness, Stellite 6 clad rails, and insulated block joint (IBJ) components.

Acknowledgments

When coming to the end of this PhD journey, I would like to express my deepest gratitude to my supervisor Professor Roger Lewis for his expertise, support, guidance, and encouragements. I want to thank to my advisory supervisor Professor David Fletcher for his valuable contribution, and support to my research.

I would like to express my gratitude technical and academic staff in the University of Sheffield for their helps and advice.

Big thanks also to PhD students and post doctorate friends in the E201 PhD office for their advice and continuous support with friendship, presence, and valuable discussions.

I would like to extend my heartful thanks to the Turkish Ministry of National Education for supporting as my sponsor during this study.

Furthermore, I am deeply appreciative of the friendships I have cultivated both in Sheffield, across the UK, and in other countries with fellow scholarship recipients. The shared experiences and support have been invaluable to me.

Finally, I am so grateful to my family. Their encouragement and understanding have been so big support during my academic journey. My father, my mother, my two sisters and brother always showed their heartful support.

Declaration

I, KAZIM YILDIRIMLI, confirm that the Thesis is my own work. I am aware of the University's Guidance on the Use of Unfair Means (*www.sheffield.ac.uk/ssid/unfair-means*). This work has not been previously been presented for an award at this, or any other, university.

Publications Arising from This Thesis

1. Journal Paper

K. Yildirimli, H. Boschetti Pereira, H.Goldenstein, D.I. Fletcher, Z.S. Lee, R. Lewis, "Scaling-Up Laser Cladding of Rails", Wear, Vol. 540-541, 205227, https://doi.org/10.1016/j.wear.2023.205227

2. Conference Paper

K. Yildirimli, K. Tomlinson, D. Fletcher, and R. Lewis, "Small-scale testing of rail laser cladding longevity, parameter tolerance and in-situ repairs in preparation for field implementation", presented at the 12th International Conference on Contact Mechanics and Wear of Rail/Wheel Systems, Melbourne, Australia, 2022.

Contents

Figures List

Tables List

Nomenclature

μ_d	Dynamic or sliding friction coefficient	
μ_s	Static friction coefficient	
E_s	Energy density of the laser beam	J/m^3
P	Laser power	W
D	Spot diameter	mm
V_b	Laser scanning speed	$mm\ s^{-1}$
AR	Aspect ratio	
G	Temperature gradient	K/m
R	Solidification rate	$m.s^{-1}$
μ	Friction coefficient	
η	Lubricant velocity	$N.s.m^{-2}$
P	Average pressure	Pa
ω	Rotational speed	$rad\ s^{-1}$
r	Rolling radius of discs	mm
Ra	Average roughness of profile	μm
Tγ/A	T-gamma over area	N/mm^2

Chapter 1

1 Introduction

1.1 Overview of the Problem

Rail travel is getting more popular day by day. The increasing population of the passengers who are using rail travel is leading to more trains with greater loads and increasing train speeds which is leading to more severe wheel/rail contact conditions. Maintenance of the train lines is expensive and railway schedule progress is going to aim for 24/7 operation. For that reason, different ways should be used to reduce damage and effect repairs to rail.

Increasing train speeds and loads affects the safety of trains so the wheel/rail interface is very important to consider. These features of trains have led to increase in stresses in the wheel/rail interface. Increased stresses drive rail and wheel damage. This damage is mainly wear and rolling contact fatigue (RCF) (Lewis et al., 2019). The wheel/rail contact is very complicated. Understanding, modelling, and optimization needs more interdisciplinary work (Lewis & Olofsson, 2009).

Wear and RCF can cause rail failures and necessitate rail replacement. The need for increased rail life is becoming more important because rail replacement has quite a high cost. These replacements are the same for all rail components including insulated block joints (IBJ) or switches and crossings (Lewis et al., 2017). Cost is the main problem for the replacement and there is material wastage too. A large length of rail could need replacing because of a small failure (Lewis et al., 2015).

RCF is the one of the main limitations of railway infrastructure systems. RCF causes periodic replacement of damaged track. Tangential stresses and high normal load combinations between the wheel and rail cause the RCF faults. As a result of these loads and stresses, plastic deformation (ratcheting) occurs on the surface layer of the rail material and the ductility of the material decreases. RCF can be seen in various forms such as: shelling, head checks, corner-gauge crack and flaking. These defects are caused by initiation of cracks and their propagation in the rail material. Also, switches and crossings (S&C) suffer from head checks particularly. S&C's have flange contact at the gauge corner because of the decreased wheel and rail contact area and increased slip. These cracks that are surface initiated might cause failure of rail and

even derailment if the cracks eventually grow to form a rail break (Franklin et al., 2005; Clare et al., 2011).

New materials are being developed and new processing techniques used to increase the wheel and rail life. There are many methods for reducing the wear and RCF problems which are related to surface treatments. These surface treatments are case hardening, peening and surface coatings. They increase the wear and RCF performance of rail materials. Also, there is another method for surface improvement and repairing that is Laser Cladding (LC), a large-scale additive manufacturing technique. LC is used for adding premium materials to a standard grade substrate material. LC of rail materials could enhance the rail durability and it allows a decrease in wear and increase in RCF resistance.

In the laser cladding process, different or the same material is cladded on top of the base material. Laser cladding of different types of materials gives more beneficial opportunities for rail improvements (Lewis et al., 2015; Narayanan et al., 2019). Laser cladding has many advantages over other surface treatments, and it gives better tribological and mechanical properties when it is processed on the original substrate material. It is also able to repair small defects in a cost-effective way for the railway industry (Guo et al., 2015).

In the past, there have been many research projects and tests related to rail and wheel materials. These tests are divided into small-scale and full-scale based tests. Small-scale tests have been used initially and then research continued with full-scale tests. These laser cladded rail tests results showed that it provides a significant increase in rail surface quality, wear performance and RCF reduction. The results were used to provide confidence that field tests were worthwhile.

1.2 Novelty and Impact

As a new technology there are many aspects to laser cladding of rail that need investigating. The key novelty in this work was the:

1) Study of the life of a clad layer as previous tests have not run more than around 50,000 cycles
2) Scaling up of the testing to study clad layer behaviour on actual rail using an actual wheel to roll over the rail
3) Investigation of laser cladding as a repair technology and study like-on-like cladding which has not been done before

4) Study of the impact of changing cladding parameters to see what can happen if they are non-optimal and how this may affect damage propagation
5) Comparison of the performance of clad layers with premium rail materials including those used for S&C applications

After these small scales and full-scale tests, it was important to know how these materials can be used in the field and to move forward to implementation on the railway network which is one of the key end goals of this study.

For implementation on Network Rail track for testing, the cladding process will need to go through the Network Rail approvals process. While small-scale and full-scale testing helps with this, real confidence in the technology can only come from field tests. The impact of this work is that wear and RCF performance has been shown to improve and now further rollout can be explored on how to make benefit of the wear and RCF performance increases that cladding gives and the subsequent reduction in maintenance costs.

1.3 Aims and Objectives

In this research, the aim was to study the potential for rail component life extension through the cladding of premium material on the rail surface and develop the process to allow field implementation. To achieve this aim five objectives were set:

1-Experimental work to establish wear and RCF life extension

2-Investigation of laser cladding for Insulated Block Joints (IBJs) and Switch and Crossings (S&C)

3-Studying the possibility of using cladding as a repair tool through a mix of small-scale tests, full-scale tests and field testing.

4-The impact of changing laser cladding parameters to analyse how different conditions affect the clad performance has been investigated.

5- Different premium rails and laser clad coated standard rail wear and RCF comparisons.

1.4 Overview of the Thesis

Figure 1.1 shows the flow of the chapters and the test approaches used. The thesis structure is divided into 10 chapters. A more detailed overview of each chapter is given below:

2-Literature Review: this gives an overview of the wheel/rail interface, the cladding process and cladding used as a tribological “coating” as well as specific examples of work on railway applications in the past. Limitations and gaps are highlighted.

3-Experimental Methodology for Laser Cladding at Multiple Scales: this chapter shows the difference between the test scales and why these test scales are chosen for the research. Then, the starting point of the project is shown related to materials and the tests. Also, the differences and limitations of the test scales will be analysed in this chapter with complexity and control outlined. Following that the test scales are analysed within different chapters. Also test rig details, test methods and further machine information is presented in this chapter.

4-Tribological Characterisation of Rails Cladded with MSS Laser Cladding: this chapter includes test rig details, test specimens, and sectioning information. Surface, friction data, wear data, subsurface, microstructural changes, and hardness value analyses of MSS clad over R260 substrate rail twin disc specimen showed in the chapter. It is finished with a discussion and conclusion.

5-Tribological Assessment of the Use of Laser Cladding for Repair: this chapter includes test specimen information with different clads that are MSS, Stellite 6 and R260 over R260 substrate rail twin disc specimens. For small-scale tests surface evaluations, roughness, mass loss, friction, subsurface images and hardness values were evaluated.

6-Rail Laser Cladding with MSS and Stellite 6 and Standard R260 Grade Rail Full Scale Tests and T400 Repair Tests: this chapter covers the test rig explanation, test specimens that are MSS clad, Stellite 6 clad and R260 pocket specimens, test conditions, results that are surface, wear data with profiles, wear debris, subsurface, microstructural changes, and the hardness value analysis. The chapter ends with a discussion and conclusion. Also, T400 clad over R260 rail substrate was analysed in a full-scale test.

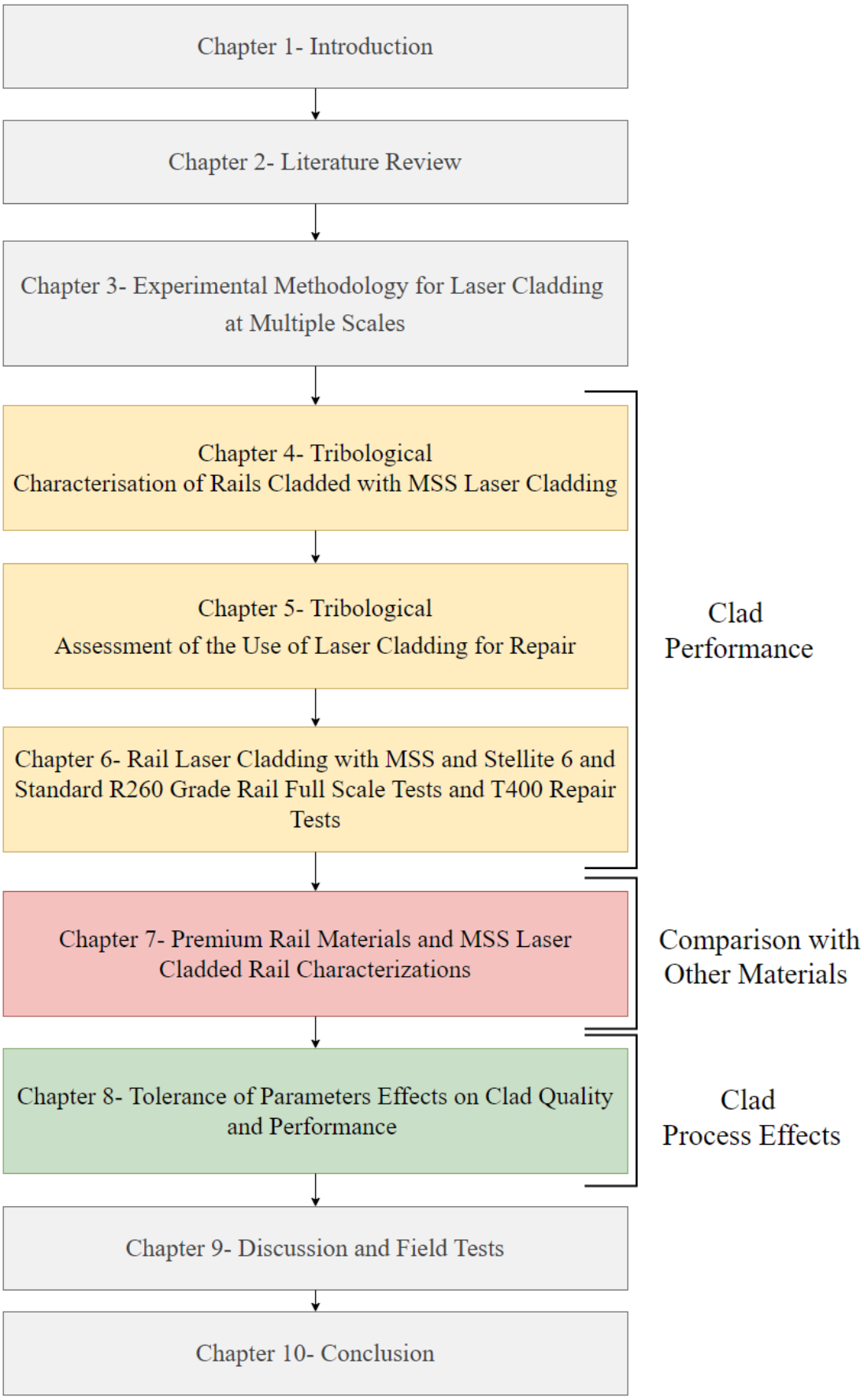

Figure 1.1: Schematic of the thesis chapters

7-Premium Rail Materials and MSS Laser Cladded Rail Characterizations: this chapterinclude different premium rails that are Manganese [Mn], Chromium [Cr], R400 premium rail twin-disc tests and MSS clad over R260 substrate assessed using twin-disc tests. Measurements, test conditions, and test specimens were described. Surface evaluations, wear debris, roughness, wear rates, friction, subsurface images, and hardness values are analysed. The chapter is finished with a discussion and conclusions.

8-Tolerance of Parameters Effects on Clad Quality and Performance: the chapter includes different laser clad parameter changes and their effects on MSS clad over R260 substrate. Clad quality changes were analysed with X-ray images before and after the tests. Test apparatus, specimens, measurements and test conditions are shown. Surface evaluations, wear rates, subsurface images and hardness values are analysed. The chapter finished with a discussion and conclusion.

9-Discussion: the thesis structure continues with a high-level discussion chapter. In this chapter, all results are compared and discussed between all scales ad results because all chapters were including discussion parts on each chapter. Also, there were field tests analysed including test site apparatus, properties of test specimens, test conditions and results that are surface, wear data, and hardness analysis.

10-Conclusions: the conclusions chapter brings the key findings together and further work is identified.

Chapter 2

2 Literature Review

2.1 Introduction

The aim of the literature review was to give an overview of wheel/rail contact tribology and then the use of laser cladding to improve the tribological performance. Gaps in the knowledge are identified, test methods identified, and data collected for comparison.

This research focuses on the potential for rail component life extension through cladding of premium material on the rail surface. Rail life extension is significant because solutions to problems in the rail industry are expensive. It should be used in a more cost-effective way as rail travel is getting more popular these days. These problems occur generally from rail and wheel contact issues. The rail and wheel contact is very complicated due to the constantly varying position. Load and slip within the contact and the open nature of the contact. Understanding modelling and optimization needs more interdisciplinary work and the contact is crucial for the efficient and safe operation of a railway network. The main damage forms are wear and rolling contact fatigue (RCF). These issues are the most important factors for rail and wheel contact problems. Rail and wheel surfaces include these damage forms. The wheel and rail interface is one of the most crucial mechanism in operating safety and service performance of railways (Lewis & Olofsson, 2009; Zhu et al., 2019) .

Table 2.1 shows the rail and wheel steels. These steels are used in Europe (E) and consist of R260 which is the stock rail material. Also, R350 HT and R400 HT are heat-treated (head-hardened) materials (EN 13674-1). Furthermore, Bainitic rail steels improved the maximum hardness available by heat-treating pearlitic rail, but there were necessities for enough higher levels from different microstructures. The requirement is seen in the Japanese (J) CrB1400 Bainitic steel. Also, ER8 is a wheel material and it is frequently used on multiple units, on freight cars, ER7 is used and on high-speed vehicles, Japanese CM64 wheel materials are used (Lewis et al., 2019; Tyfour et al., 1995) .

Table 2.1: European and Japanese rail and wheel steels (adapted from Heyder & Maedler (2015)

	Rail Steels				**Wheel Steels**		
	R260 (E)	**R350HT (E)**	**R400HT (E)**	**CrB1400 (J)**	**ER7 (E)**	**ER8 (E)**	**C64M (J)**
Tensile Strength "MPa"	≥880	≥1175	≥1280	≥1400	820-940	860-980	940-1100

Rail failures and replacements are caused by wear and RCF. Cost is the main issue for rail replacements and the aim of increasing rail life is important because of that reason. All rail components including insulated block joints (IBJ) or switches and crossings (S&C) replacements have cost issues and need to increase lifespan for them. The railway industry has tried to develop some solutions for this kind of surface-related problems. These methods are case hardening, peening and surface coatings. They increase the wear and RCF performance of rail materials. Also, there is another method of surface protection or repair that is laser cladding.

Laser cladding could also be used for repairing small defects in a cost-effective way for the railway industry. The cladding process is laser-based, and laser energy is used for different surface treatments because it can be concentrated in the small beam area and it shows high power. Wear resistance can be developed with rising hardness and strength of wheel and rail materials. Also, high hardness of cladding increases the wear resistance of heavy-haul wheel and rail rollers. The hardness decreases close to substrate hardness with rise of depth in the cladded region (Wang et al., 2014).

The advantage of the laser cladding is that premium materials can be clad onto the top of the substrate material for better tribological and mechanical features. Laser cladding allows to lower cost instead of using full premium rails because it can allow deposition of a layer on a standard rail grades to keep costs down. In this chapter there will be information about wheel/rail interface. Also, it will show information on track components. Moreover, it will introduce some problems and defects related to wear and RCF. Laser cladding is one of the potential methods for improving them so it is important to lay down a benchmark for current rail performance..

2.2 Wheel/Rail Interface

2.2.1 Track and Main Components

Laser cladding can be applied to standard track where it could offer life extension, but this may not be of cost benefit. Cladding of high value track components may offer greater advantages. One example of these is an insulated block joint (IBJ) as shown in Figure 2.1. It is a key component of railway track and it includes two insulated fishplates. These fishplates are bolted through the web of both rails to form a double lap joint. A gap is present between these two adjoining rails. The gap is filled with an endpost that is made from insulating material. They are as part of the railway signalling system. Location of trains is determined by use of track circuits that IBJs help create. If the IBJs fail or the endpost gap is closed (for example by flow of rail material) then the circuit fails and trains have to be halted which results in a lot of costly delay (Mandal & Peach, 2010; Beaty et al., 2015).

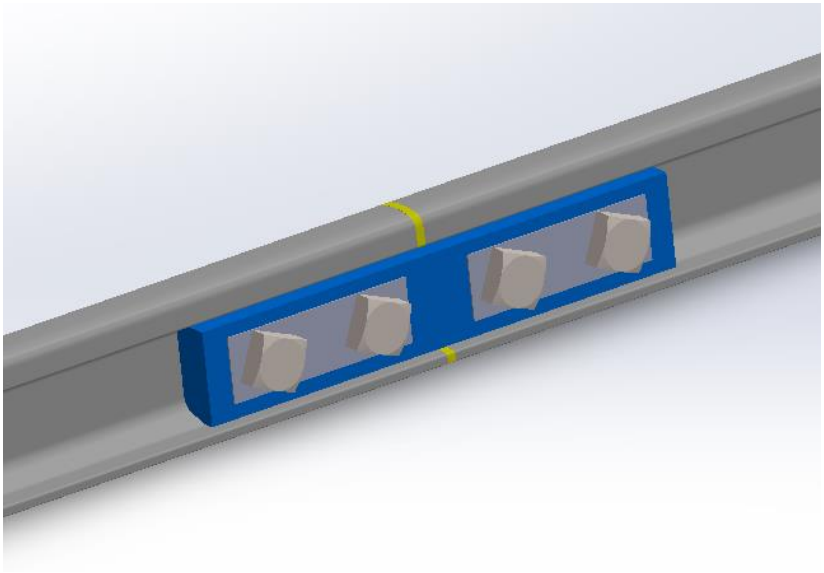

Figure 2.1: Insulated Block Joint (IBJ)

Mechanical and electrical failures mainly occur on IBJs. Mechanical failures do not cause a breakdown of the system; however electrical failures cause problems for the signalling systems because electrical insulation is lost between two adjoining rails. These electrical failures could be because of contamination over the endpost, de-bonding of the glue layer in a joint or lipping.

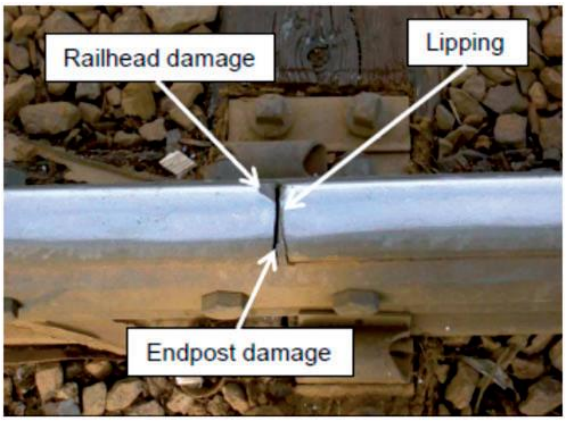

Figure 2.2: Lipping as a material deformation of the rail head (adapted from Beaty et al. (2015))

Figure 2.2 shows the lipping on the IBJs. It can be seen that IBJs have a problem with the plastic flow of rail. This plastic flow occurs in rails either side of IBJ because of the cyclic loading from passing wheels. The name of the failure is lipping, and it causes failure of the signalling systems.

2.2.2 Contact Mechanics

The wheel/rail interface mainly focuses on the contact mechanism. The position of the contact is important for wear rate. The contact is in generally 1 cm^2 in size and it depends on the wheel and rail profile. The degree of track curvature and the wheelset and bogie designs could also affect it. Normally, in tangent of track the railhead and wheel tread is in contact and in the curved track, there is wheel flange and rail gauge corner contact (Lewis & Olofsson, 2009).

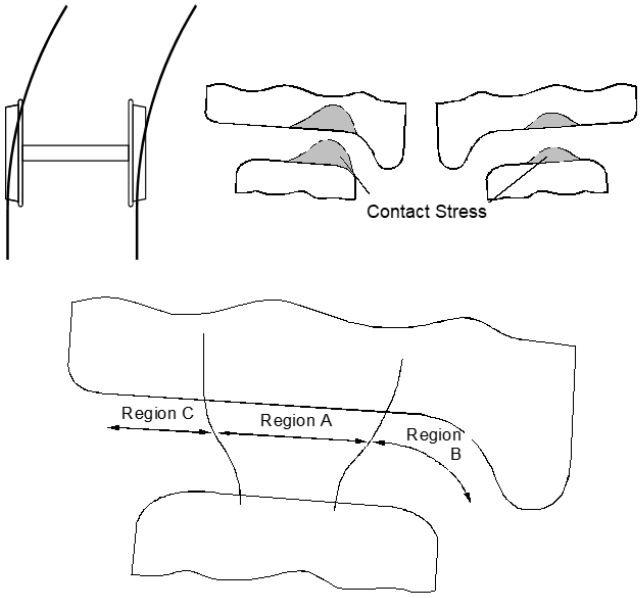

Figure 2.3: Wheel–rail contact zones. (Adapted from Tournay (2001))

Figure 2.3 shows the regions of contact in wheel-rail system. Region A shows the wheel tread and railhead contact and it is the region where the contact mainly occurs with the lowest contact stresses and lateral forces. Region B shows the wheel flange and rail gauge corner contact. This contact is more intense than region A and the contact size is smaller. Also, the wear rates and contact stresses are higher. If there is two-point contact, that is tread and flange, there could be high wear and material flow. Region C shows the field sides of wheel and rail contact and the contact occurs with the lowest probability. If the contact occurs in region C, contact stress would be so high and it could cause adverse wear features (Lewis & Olofsson, 2009).

Rail side wear damage happens mainly in Region B. Damage in region A is typically corrugation, surface fatigue and head checks. Field work on heavy-haul wheel/rail systems showed the wear of the rail side and wheel flange have a crucial effect on service life (Wang et al., 2014). Laser cladding could be used over the whole contact zone on the rail surface for within the field. In curves it might be best used on the gauge corner. In straight track it could be on the railhead, but in some instance the gauge corner/side as well.

2.2.3 Creep Force Relationships.

Friction forces are named as creep forces. Friction coefficients could be divided into dynamic or sliding and static ($\mu_d < \mu_s$). Generally, static friction coefficients are higher than dynamic or sliding ones. Commonly, the friction coefficient depends on the sliding velocity that is decreasing while the velocity increase. Therefore, when creepage rises beyond the saturation point, the creep force decreases after that. This is shown in Figure 2.4 (Thompson, 2009).

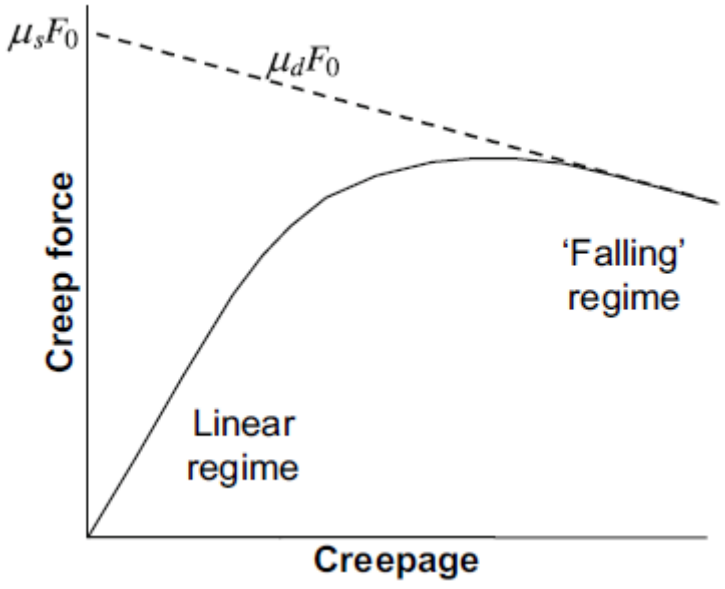

Figure 2.4: Creep force-creep relationship (adapted from Thompson (2009))

The tractive force increases from zero to a steady state as the level of slip in the contact changes (Lewis et al., 2017). Wear rates can be evaluated with creepage situations, both wear rates of wheel and rail rise as creepage is increased (Hu et al., 2020). The rolling friction coefficient shows differences with laser cladding of wheel or rail. The single-layer treated wheel or rail friction coefficient is smaller than that of the wheel/rail rollers without laser cladding because mild wear occurs on the single-treated wheel or rail specimens. Friction coefficients show differences due to the wear debris in the contact interface of the wheel/rail on single-layer treated or untreated specimens (Guo et al., 2015).

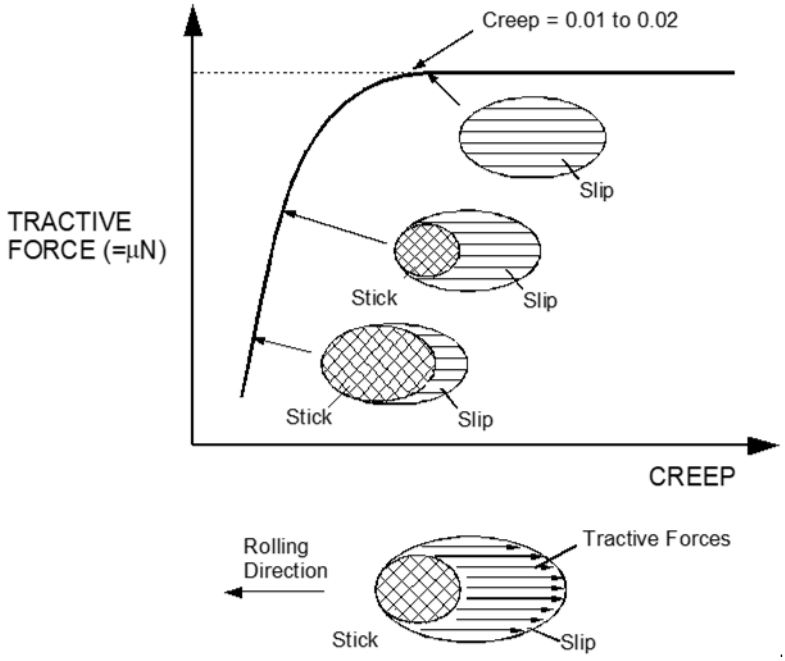

Figure 2.5: Tractive force and creep relationship by creep curve (adapted from (Olofsson et al. (2013))

The creep and tractive force (adhesion) relationship in wheel-rail contact is shown on Figure 2.5. It shows the stick and slip contact patch between wheel and rail. Slip is happening on the rear region of the contact patch and slips cause tangential forces and longitudinal creep. The slip region rises, and stick region decreases because of rising tangential forces and rolling and sliding contact occur. Also, a sliding situation occurs when the tangential forces go to its saturation point as a result of that the stick region is lost (Olofsson et al., 2013).

2.2.4 Wear/RCF and Railway Components

Characterisation of possible wear situations are dependent on the contact conditions (load and slip) and the number of contact cycles. Sliding and rolling are the two features of the wheel and rail contact. Micro sliding occurs dependent on the slip and stick regions present in the

wheel and rail contact. Furthermore, different wear mechanisms could result from sliding. These mechanisms are oxidative wear that happens in mild contact conditions with low load and sliding velocity. Rail head and wheel tread contact typically exhibit this wear mechanism. Also, adhesive or galling wear occurs in more severe conditions. It probably occurs in curves in the contact of rail gauge corner and wheel flange. Abrasive wear can occur, if particles are existing in the contact (Lewis & Olofsson, 2009).

As load or contact severity increases, wear mechanisms evolve in a predictable sequence. Initially, adhesive wear occurs as surfaces bond and transfer material. With heightened contact severity, abrasive wear becomes prominent, characterized by the scratching away of material by hard particles. Under conditions of high temperature and pressure, oxidative wear weakens surfaces due to exposure to oxygen. Delamination wear may then develop as layers separate and cause progressive damage, particularly under increased load. Finally, plastic ratcheting, or creep wear, becomes pronounced under sustained stress or cyclic loading, leading to gradual material deformation and eventual failure. Understanding this progression is crucial for effectively managing wear and ensuring the durability of components subjected to varying levels of load and contact severity.

The wear mechanisms with more detail are defined. Adhesive wear is when wheel and rail asperities bond together it causes Adhesive wear especially on the same materials used for wheel rail contact. Movement of a wheel over a rail causes asperities to break and new asperities occur then loose asperities start to break off and became wear debris. If there are some grooves and scratching over the surface because of the sharp asperities or another particle between the wheel and rail it is called abrasive wear.

Delamination could take place within rails. Repeated rolling contact cause accumulation of plastic shear strain then the formation of thin layers occur at the surface and become loose and turns to wear debris as shown first by Suh (1977). Oxidation also causes wear because the sliding contact defects the protective oxide layer after cycle and then reformed through a cycle.

Damage on rail occurs because of wear and RCF. Wear situations can be divided into sliding, rolling, impact, and single or repeated cycle mechanisms. First, some of the wear mechanisms created because of sliding. These wear mechanisms are abrasive wear that occur if particles are shown in contact, oxidative wear happen if there is mild contact condition, adhesive wear in severe contacts, seizure which occur in high sliding conditions, and fretting wear occur from reciprocating motion. Second, rolling cause some other damage mechanisms. Fatigue is the

main damage mechanism from rolling. Also, this causes material to be lost from surface and subsurface cracks occur and grow. Third, impact is another damage situation. Single or repeated cycle cause the deformation on the material. Impact has erosive and percussive effects on materials (Williams, 2005).

Figure 2.6 shows an image of a sectioned rail steel disc. It was rolled against a wheel disc in a twin-disc test to illustrate the rolling-sliding conditions in an actual wheel-rail contact. Fatigue is the main mechanism for the wear behaviour with rolling motion. Ratchetting leads to a process of loss of wear particles from the surfaces of materials. Surface fatigue is based on repeated cycle deformation mechanisms. Crack formation and propagation comes from surface fatigue. Cracks are typically initiated from the surface to grow downwards from the surface and extend with contact cycles. When significant traction is applied, cracks occur on the surface. A rolling contact produces traction. When rolling is happening, sliding is occurring at the same time. When the two components are moving at different velocities, slip can occur. Rolling and sliding behaviours can be seen on wheel and rail contact situations (Lewis & Olofsson, 2009). Also, when contact happens there are wear debris occurring during RCF wear tests and surface delamination happens during the rolling-sliding contact for pure sliding contact and it confirms flake-like particle generation (Athukorala et al., 2017).

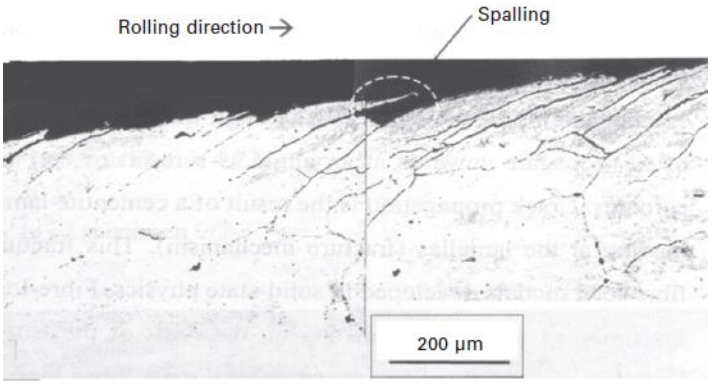

Figure 2.6: Material removing and cracking caused by a rolling/sliding wear situation (adapted from Lewis & Olofsson (2009))

Numerous load cycles cause some failures and RCF is one of the failures more for rails after initiation and propagation of cracks. Head-hardened and modern rails can have RCF cracks as well. Residual stress and material properties affect RCF failure (Garnham & Beynon, 1991; Schmid et al., 2010). Sometimes wear at the surface can act to remove the crack initiation sites and protect against the propagation of the cracks, but some water or lubricant might propagate and increase the chance of RCF cracks (Magel et al., 2016).

RCF has different forms, for example, squats, head checks and shelling. RCF is one of the main problems for switches and crossings (S&C) and the contact is near the gauge corner on the S&C. Flange contact takes place there. In this kind of case, the slip ratio is high and the contact area is reduced. As a result, increased crack formation and wear occurs due to the severe contact stresses. The RCF resistance should be increased because with this kind of problem rails need to be ground often to remove cracks. They all add to cost problems and reduces rail traffic flow (Franklin et al., 2005). Repairing switches and crossings is difficult because they are geometrically complex components (Xin et al., 2018). Welding repair and grinding is the cost-efficient way. Avoiding the formation of martensite on welds needs preheating and cooling rate considerations. In welding such as flash-but welding or aluminothermic welding, if the material is different to the substrate rail it may cause a different wear rate at the joint and cause higher impact loads (Gao et al., 2018).

2.2.5 Wear and RCF Reduction Methods

Wear and RCF are the main two damage mechanisms in wheel/rail contact and some methods are used to improve the wear and RCF resistance. New premium materials can be used, or a material that is more durable and harder can be coated onto the wheel and rail, or material can be heat treated. There were four different premium rail were used for reduce wear and RCF and compared with MSS clad and R260 grade rail in the previous tests. They have tested for different slip values and found premium rails and MSS clad showed wear resistance (Christoforou et al., 2019). Hardness and microstructural features on wear are significant. Work by Vasic (2013) showed wheel wear decreased with water in the contact compared to dry case. It can be seen that wheel wear rate is affected positively with decreasing wear debris. Wear debris decreased with the usage of water (Lewis et al., 2019).

The amount of wear is significant in curved tracks. Wear occurs between wheel flange and rail gauge corner in curved tracks. Friction is the key parameter and lubrication is used there to decrease friction. Also, heat-treated rails can be used for the reduction of wear. Heat treatment causes the increase of hardness (Seo et al., 2019). It is used in heavy-haul and curved tracks to improve wear or fatigue resistance. Heat treatment on rails decreases the lamellar spacing in the pearlite structure (SF HT, 2017). As a premium rail, HP335 rail is a hypereutectoid steel that is introduced first in 2012 by British Steel as a high-performance premium rail. With increasing carbon content of about 0.87% this rail increased rail life span by 66% (HP335, 2020). Also, another study showed that laser cladding on the railhead improved RCF and decreased the noise emissions in a narrow-radius curved rail. A twin disc test was used for the

research and they used UIC (260 grade) 900 A base material and selected two new surface materials for the project (InfraStar). They studied the effect of lubrication with distilled water, applied load and coating thickness. The water lubricated twin disc test showed no cracks in both materials after 200,000 cycles, however, the base material showed severe cracking just after 4,000 cycles. As a result of the cladding, RCF resistance was increased significantly (Franklin et al., 2005). An Fe-based alloy coating has been used for examining of microstructure of laser cladding (Fu et al., 2015). They found that wear resistance and hardness of wheel and rail materials are increased. Also, wear mechanisms changed from severe spalling and delamination wear on untreated specimens to slight peeling on treated specimens.

2.3 Laser Cladding

In the 1960's, the use of lasers was a breakthrough in science. After decades from the start of using lasers, laser welding, hardening, and cutting was possible with improvement of high-power gas lasers, such as CO_2 lasers. The material processing technologies allowed the use of laser cladding in late 1970's. Powder injection laser cladding was developed in the late 1980's in academia. Then this technology started to be used in industry because laser cladding has more advantages than conventional processes. Laser cladding was a very useful process for the management of wear and corrosion resistance (Kaierle et al., 2012; Toyserkani et al., 2017; Pawlowski, 1999; Zanzarin, 2015).

2.3.1 Overview of Laser Cladding

Laser energy is used for different surface treatments because it can be concentrated in the small beam area, and it shows high power. Laser hardening or alloying of different powders are used for improving wear and corrosion resistance of materials. Laser cladding is the method for bonding materials or alloys onto a base material and it has similarities to welding. However, a laser beam is used as a heat source and it creates a melt pool with a heat-affected zone (HAZ) because of the controlling parameters of heating (Vilar, 2001).

Laser cladding can be used with many different methods. These methods are shown in Figure 2.7. One-step laser cladding by powder injection is the most ideal method. This method has many advantages over the two-step method (preplacing powder method) and wire feed method. A rough surface and porosity occur because of decomposition or evaporation of binder residues in the two-step method. Also, it is hard to manufacture complex geometries in the two-step method. The wire feed method also has some drawbacks. The main drawback in cladding by

feeding a wire is material selection to the melt pool. If there is low energy absorption, it can be overcome by heating the wire which causes increase the dilution (Vilar, 2001).

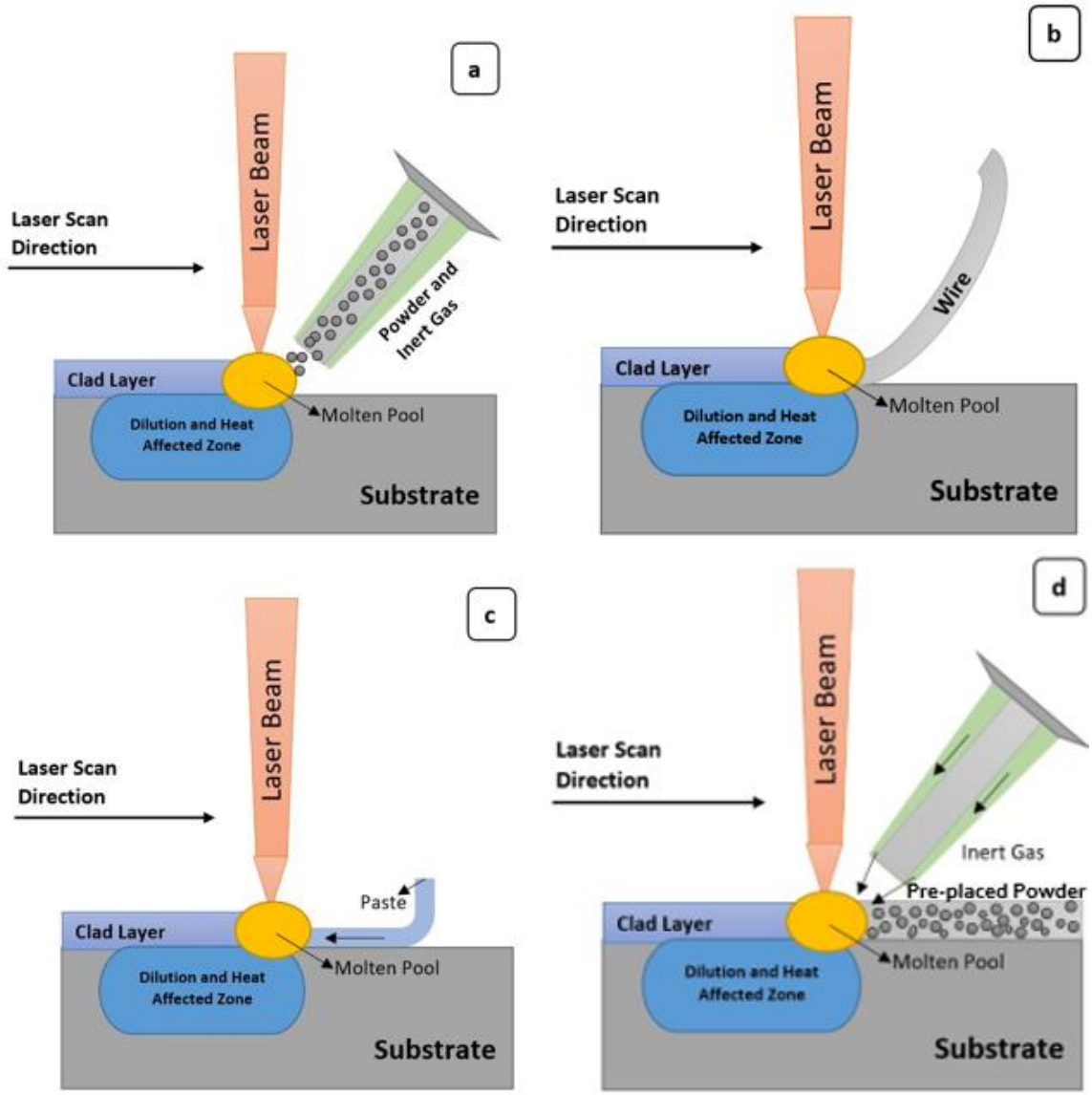

Figure 2.7: Methods of Laser Cladding: a) powder injection; b) wire feeding; c) paste feeding;

d) preplaced powder

In the one-step laser cladding process, while a cladding material added on the surface of the substrate, a high energy laser is passed over that surface. The laser melts the surface of the substrate material and the coating material successively and welds them together. When the laser beam creates a melt pool, powder is injected into the pool and the particles melt and a single track of the clad is created. This process can be repeated for a second layer over the first layer of clad (Vilar, 2001; Lewis et al., 2015; Niederhauser & Karlsson, 2005).

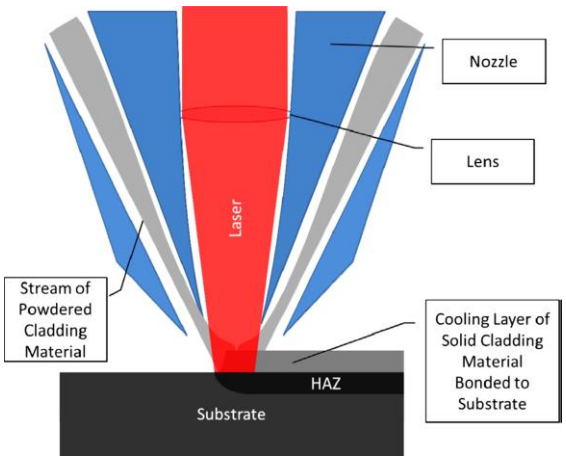

Figure 2.8: Schematic of one-step laser cladding process (Lewis et al., 2015).

Figure 2.8 shows a one-step laser cladding process. On the surface of the substrate material, a thin melt pool is created by the high heat input of the laser. Then, metal powder is fired into this melt pool. The powder is melted when it passes through the laser and fuses with the melt pool on the substrate material surface. The clad occurs by single tracks. The powder is delivered to the substrate surface by an inert gas that prevents degradation of the powder particles at high temperatures. These inert gas functions carry the powder to the melt pool with high speed and to protect the particles because they could react with the atmosphere. Inert gas is utilized to maintain a clean environment, preventing contamination of the metal powder and facilitating improved adherence to the surface. Also, a heat-affected zone (HAZ) is created because the high thermal energy input of the laser heats the substrate material and melts the powder. When the laser passes over the substrate, the substrate starts to cool at a fast rate. The substrate has greater volume that cladding, and this high rate of cooling occurs because of that. Also, a fine microstructure occurs in the clad because of the volume differences. The microstructure of the bulk material changes with heating and rapid cooling. Heating, cooling rates and material types affect the microstructure changes depend on them. The layer of modified microstructure is between the cladding and substrate. The layer is known as a heat-affected zone (HAZ). Residual stresses also occur in clad layer and the substrate. Residual stresses occur mainly because of three factors. Different thermal expansion coefficient is the first factor affecting residual stress in the clad and substrate material. The second one is thermal gradient from clad to substrate because of the process and the third one is phase transformations, and they are related with a linear expansion or contraction (Vilar, 2001; Lewis et al., 2015; Niederhauser & Karlsson, 2005).

2.3.2 Clad Materials

Laser cladding applications can be divided in three different ways. Figure 2.9 shows these methods. They are clad with the same material as the substrate, clad with a different material that has different chemical composition from the substrate, and the last way is using hard particles such as cobalt, carbides or tungsten in the layer of coating as a composite. Cladding with the same material has many advantages that are harder surface, controlling microstructure. Using hard particles as a composite cladding can reach high hardness values, but it can be changed depending on the particle location. Hardness can be lower in the location of particles than in the area surrounding the particles (Pawlowski, 1999). Also, a multiple powder feeder can be used, and it has many advantages depending on the different particle properties (Kaierle et al., 2012).

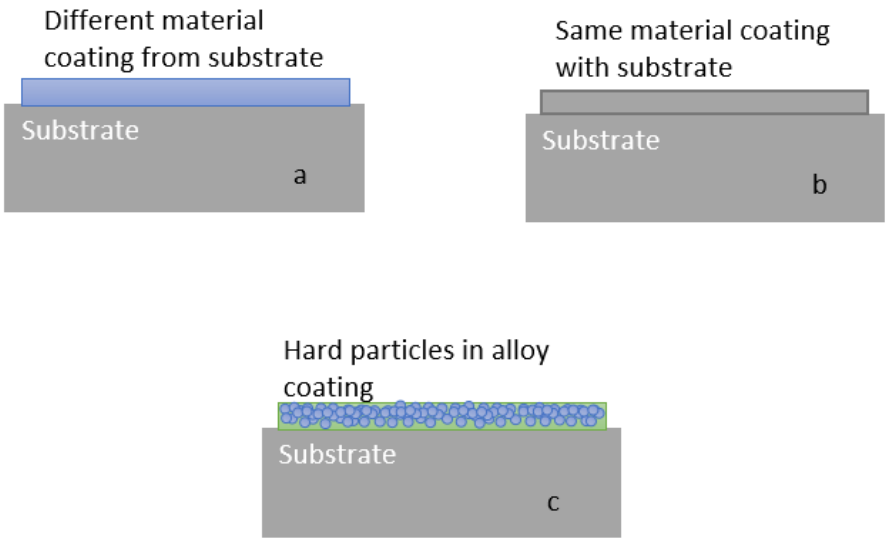

Figure 2.9: Coating types a) different material coating from substrate b) same material coating as substrate c) hard particles in alloy coating

Laser cladding is a potential method for rail and wheel, and it increases the performance of them positively. The cladded rail contains the rail base material, the heat affected zone (HAZ), and laser cladding. The advantage of laser cladding is that premium materials can be clad onto the top of the substrate material for better tribological and mechanical properties. Premium rail materials could be used for longer rail life, but the cost is the biggest problem with that. Instead of using premium rail material, laser cladding of rail shows efficient RCF performance of standard grade rail. Also, cost of the rail replacement and repair can get lower with laser cladding of rail with flexibility. On engineering structures and components, laser cladding is

used as a hard facing process and it gives an opportunity to coating certain areas of the surfaces of engineering materials (Lewis et al., 2016; Seo et al., 2019; Zhu et al., 2019).

Material selection for laser cladding can change depending on the desired performance or where the clad specimens will be used. The same clad material as the substrate can be used. There can be different features on clad part because of the cladding process. Hardness can be expected to be higher than the substrate and mechanical properties, but there can be good bonding and compatibility. Different materials can be used depending on the purpose of the test. Wear resistance or other kind of purposes affect the metal alloy selections (Christoforou, 2020). Heavy-haul railway mainly use hypereutectoid rails which were chosen as a substrate in research and they were tried with different laser clad combinations using 410L, 420SS, Stellite 6 and Stellite 21 materials. Co-based Stellite 6 and Stellite 21 materials showed some cracks when they used a combination of preheating and post weld heat treatment methods (Lai et al., 2019). In another research they used high carbon martensitic 415SS steel over a hypereutectoid rail substrate and examined residual stresses and microstructure changes for different post processing methods and they found that high temperature post processed clad 415SS showed good results about microstructure and other stress measurements (Kendall et al., 2022).

When using the same material as a cladding powder as the substrate, material properties change due to the cladding process. These differences can be seen in mechanical properties and other characterisation properties. With the same clad and substrate material there is good compatibility and bonding in the melt pool because they have the same bonding properties and melting point. In other cladding options, the cladding is used for a target that could be corrosion protection or wear resistance. The key point is that there is good material compatibility for example, melting point differences might be a problem in some combinations and many polymers could be compatible with ceramics or other polymers (Ayrault et al., 1996). Ceramic is appropriate for metal alloys, and it has satisfactory properties (Zeng et al., 1996). Ceramic-metal composites (cermets) are the most common research topic nowadays about intermetallic compounds that are being used in laser cladding. Furthermore, bio-compatible materials have been cladded with titanium alloys. These materials are Fluorapatite and Hydroxyapatite. These bio-materials are very popular in research nowadays (Weng et al., 2014).

Laser cladding gives the opportunity to use different materials on the surface of substrate materials. Different regions and countries use different rail and wheel materials. The most common rail material is pearlitic steel.

In laser cladding of rail, several hard-facing materials have been for improving hardness of the substrate materials. Stellite 6, nickel alloy, maraging steel, and Hadfield steel have been used on tests for rail, and these materials showed they are all suitable for cladding. Their hardness and work hardening behaviours are satisfactory when used on R260 grade rail (Singh, Kumar, Mishra & Tiwari, 2014; Clare et al., 2011).

R260 grade rail is used in many research projects as a baseline. Premium clad materials have been cladded onto R260 grade rail. Lewis et al. (2016) tested six of the rail samples in twin-disc machine. They used Martensitic stainless steel (MSS), TWIP Steel, Stellite 6, Stellite 12, NiCrBSi, and a multi-phase manganese steel variant (MMV). These materials were tested for wear and RCF performance. The MSS, Stellite 12 and Stellite 6 samples showed decreased wear rates compared to standard R260 grade rail material (Lewis et al., 2016). They also did some full-scale tests with Stellite 6 and a grade of martensitic stainless steel because, in the earlier small-scale tests, they showed desirable wear and RCF features during the twin disc tests. These two clad materials also reduced the wear rates significantly and improved insulated block joints compared to standard R260 grade rail (Lewis et al., 2017). In other research about residual stress in laser cladded rail, they used MSS and Stellite 6 for the clad material on R260 grade rail because these two clad materials showed better performances in previous works for wheel/rail contact conditions (Narayanan et al., 2019).

In another study, four different clad materials were tested on rail discs. These materials are Hadfield, Stellite6, Maraging and 316 Stainless Steel with 1- and 2-mm clad layers of both. Wear rates were measured and RCF cracks were detected. They found that wear is not reduced with all clad samples and some of the materials need more cycles for the test. They showed RCF of rail life increase with laser cladding (Lewis et al., 2015). A common materials list has been prepared (Christoforou, 2020). These materials are listed in Table 2.2.

Table 2.2: Common materials in laser cladding (adapted from (Christoforou 2020)

Name/Category	Clad Material	Nominal Composition
MetcoClad™	316L-SI	Fe 12Ni 17Cr 2.5Mo 2.3Si 1Mn 0.03C
	C276	Ni 15Cr 16Mo 5Fe 4W
	625(F)	Ni 21.5Cr 8.5Mo 3.5Nb 3Fe
	718	Ni 19Cr 18Fe 3Mo 0.5Al 5Nb 1Ti 0.05C
	6(F)	Co 28Cr 4W 3Ni 3Fe 1.5Si 1C 1Mo
	21	Co 27Cr 5.5Mo 3Ni 0.25C
	23	Co 25Cr 5Mo 2.5W 2Ni
	52001	W 3.5C
	52052	WC 40(NiCrBSi)
Spherotene®	40S-400	60% Spherotene® (WC) / 40% Matrix (Ni/Cr) (3000 HV ± 500 HV)
Hardfacing Alloys Cobalt alloys (Co,C,Cr,W)	Stellite 6	Co 27-32Cr 4-6W 2.5Ni 0.9-1.4C Ni Fe Si Mn (380-490 HV)
	Stellite 12	Co 27-32Cr 7.5-9.5W 1.4-1.7C Ni Fe Si Mn (435-590 HV)
	Stellite 21	Co 26-29Cr 4.5-6Mo 0.2-0.35C 2-3Ni Fe Si Mn (290-430 HV)
	Stellite X40	Co 26.5Cr 8W 0.55C 11.5Ni 2Fe 1Si 1Mn
	Triballoy T800	50Co 18.5Cr 3NiFe 30Mo 3.8Si 0.08C N O P S (700 HV)
	Crystalloy™	Numerous super alloys and carbide-free
	Tungstrong™ /	Varying percentages of a WC and metal material matrix
	Toughstrike™	Applications needing superior impact resistance with high toughness
	DuctileArmor™	Laser remelting to increase hardness of austempered ductile iron (ADI)
	Tungsten Carbide	WC 10Ni 5Cr, 50%, 60%, 70% WC
	Eatonite®	39Ni 29Cr 1Si 8Fe 2.4C (42HRc)
Nickel Based (Ni-Cr-B-Si)	Inconel® 625	Ni 20-23Cr 9Mo 4Fe 3.5Co+Ta 0.3Ti 0.3Al 0.3Mn 0.25Si
	Inconel® 718	Ni 17-21Cr3.3Mo Fe 5.5Co+Ta 1.15Ti 0.8Al 0.3Mn 0.25Si 0.3Cu
	Hastalloy® C276	Ni 2.5Co 16Cr 16Mo 5Fe 4W 1Mn 0.35V Si C Cu
	Hastalloy® X	Ni 1.5Co 22Cr 9Mo 18Fe 0.6W 1Mn 0.15Ti 1Si 0.1C 0.5Al 0.5Nb
	Wall Colmonoy 69	Ni 16.5Cr 3.6B 4.8Si 0.55C 3Fe 3.5Mo 2.1Cu
	Wall Colmonoy 88	Ni 17.3W 15Cr 4Si 3.5Fe 3B 0.8C (750 HV)
	Deloro 60®	Ni 17.3W 14-15Cr 2-4.5Si 4Fe 3-3.5B 0.7C (56 Rock "C")
Steel Based (Fe, Cr, Ni)	304 Stainless Steel	Fe 12Ni 20Cr 0.75Si 2Mn 0.08C
	308 Stainless Steel	Fe 9.5Ni 19.9Cr 0.58Si 2Mn 0.024C
	316 Stainless Steel	Fe 12Ni 17Cr 2.5Mo 1Si 2Mn 0.08C
	420 Stainless Steel	Fe 1Ni 14Cr 1Si 1.3Mn 0.036C
	431 Stainless Steel	Fe 3Ni 18Cr 1Si 2Mn 0.2C
	4140 Steel	Fe Ni 1.2Cr 0.35Mo 0.4Si 1.1Mn 0.44C
	Maraging Steel	Fe 19Ni 9Co 5Mo 1Ti 0.15Al
Tool Steel (Fe, C, Cr, V)	REX 20	10.5Mo 6.25W 3.75Cr 2V 1.3C 0.35Mn 0.25Si (300 HV)
	CPM 9V	1.3Mo 5.55Cr 9.1V 1.9C
Titanium Based	CP Titanium	Ti 0.18-0.4O 0.2-0.5Fe 0.08C 0.03-0.05N
	Ti6Al-4V	Ti 5.5-6.5Al 3.5-4.5 V0.13O 0.25Fe 0.08C 0.05N
Ceramic Coatings	….....	VC Cr7 C3 (1050 HV)
Super Alloys	(Ni, Co, Mo, Cr, Si)	….....
Aluminum Alloys	(e.g. Al-(Mg)-Si)	….....
Copper Alloys	Copper-Silver	….....
Biocompatible Alloys	Hydroxyapatite (HA) Fluorapatite (FA) 45S5/S520 bioactive glass	…..... …..... …..

2.3.3 Processing Parameters

In laser cladding, process parameters have great effects on the clad layer quality. Clad quality is the most important issue for the wheel/rail interface improvements by laser cladding. In laser cladding, process parameters are important for the clad quality. The energy density of a laser beam is consisting of different parameters such as; laser power scanning speed, spot size and feed rate. The energy density of the laser beam, E_s is given by;

$$E_s = \frac{P}{D\,V_b} \tag{2.1.}$$

where, P is the laser power, D is the spot diameter and V_b is the scanning speed of the laser (Fu et al., 2016). Depending on the surface and application requirements, the parameters can be changed easily in laser cladding. There are more parameters that might be evaluated in laser cladding. These parameters are temperature, laser wavelength, melt pool intensity, size, laser focal point, laser distance to substrate and when powder and material feeder examined, some more parameters are inert gas supply, material selection, scanning speed, number of layers, powder feed rate and powder particle size and shape. These parameters can be extended with type of laser clad equipment (Christoforou 2020; Wang et al., 2021). Temperature of cladding, thermal gradient, profile of spot and cooling rate was detected during clad process by infrared camera for process parameters and their effects on clad quality and they found that process conditions, molten pool spot and temperature of clad had strong relationships each other. At the end of the analysis, they found that microstructure and micro-hardness were projected successfully. Also, it allowed to detect instability and found the geometry and microstructure of the cladded substrate (Srisungsitthisunti et al., 2022).

Laser clad thickness is another key parameter, and it is are generally from 0.5 mm to 2 mm on applications If a thicker clad layer is needed, it can be achieved as well depending on the different set-up (Christoforou, 2020). Powder feed rate and process speed determine the clad height and laser beam diameter determine the clad width generally, but that clad size can be changed by gas supply as well. Gas supply and powder feed rate show a big effect on the clad depth (Chryssolouris et al., 2002). Multi-layer laser cladding on rail curvatures were examined and there were not many changes in the hardness or microstructure (Kendall et al., 2023).

2.3.4 Cladding Problems

In the literature, it could be seen that laser cladding is a valuable surface treatment method. However, clad quality might not be successful in all applications. On that point, the energy density equation could be examined with the parameter changes. When equation 2.1 is evaluated, values of *D* and *Vb* can be kept unchanged and *P* could increase, and the energy density of the laser beam will increase. As a result of this, cracks are going to decrease, layer depth of cladding increases, and air pores in the cladding layer gradually disappear. In another way, *P* and *Vb* values can be kept unchanged and energy density decreased with an increase of *D*. Decreasing energy density leads to improved quality of the surface because of the hardness of the clad layer increases, however, the number of cracks increases, and cladding layer dilution rate decreases gradually. Also, the depth of dilution is another parameter, and it can be decreased by increasing level of the gas supply. Depth of dilution can increase with increase of powder feed rate. For the best cladding quality and decrease in the number of cracks, these parameters should be selected suitably (Fu et al., 2016; Chryssolouris et al., 2002). Furthermore, clad geometry is affected by the processing parameters. An ideal clad should be achieved by adjusting these parameters effectively. Minimum melting should be on the substrate and metallic bonding should be good. Uniform and continuous clad tracks should be produced in the laser cladding process and these tracks should be as wide as the laser spot size. Also, clad geometry affects the post machining time (Ya, 2015).

Laser cladding can be evaluated as laser based on plate welding. A metallic bond occurs between substrate and coating material without a high amount of penetration and mixing. The mixing should be controlled between 2 to 8% to maintain the integrity of clad track. This mixing ratio is defined as a dilution. Dilution is the ratio of the mixing between substrate and the coating materials in the melt that is solidified (Ya, 2015.).

Quality of clad track/layers includes many parameters. Aspect ratio (AR) is one of the most important parameters. The AR is found by Equation 2.2:

$$AR = \frac{W_c}{h_c} \qquad \text{Eq 2.2.}$$

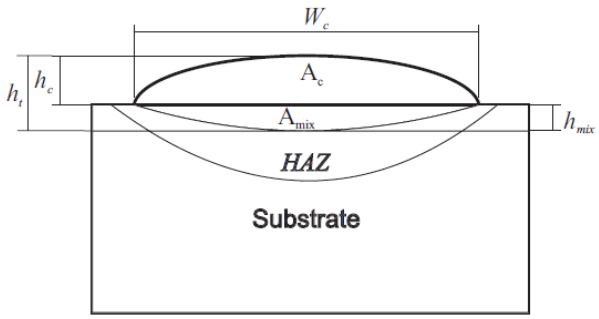

Figure 2.10: Schematic view of the cross section of a clad track (adapted from (Ya, 2015))

The diagram in Figure 2.10 illustrates a cross-section of a track with a cladding bonded to a base material. It shows features like cladding height (h_c), cladding width (W_c), the area of cladding above the substrate (A_c), the mixed area below the substrate (A_{mix}), melt depth (h_{mix}), and the heat-affected zone (HAZ).

Also, after the cladding, the clad layer and clad/substrate material interface should be examined for the quality of the clad. Inclusions can be seen in the clad layer and clad/substrate material interface because of the cladding process. Fatigue crack initiation might start at these inclusions. The HAZ is the weak point in cladded materials, and it should be evaluated for the better-clad samples (Lewis et al., 2017).

In a study of nickel-based alloy clad, overlapping clads showed surface cracks. In these multilayer experiments, crack initiation was from the top of the clad. It was evaluated that high cooling rates caused these cracks that they are a result of thermally induced stresses. For the clad/substrate quality, cooling rate might be decreased on the substrate and quality of cladding could be better (Clare et al., 2011). Microstructure is one of the most crucial parts of laser cladding and it generally depends on the temperature gradient (G) and solidification rate (R) during the laser cladding process. The G/R value comes from solidification theory. It has an important effect on the microstructure morphology of cladding. Columnar crystal is shown in early stage on laser cladding because of large G/R value. When the laser cladding continues, the dendrite crystal occurs because of the decrease of G/R value (Fu et al., 2015).

2.4 Tribological Performance of Clad Layers

2.4.1 Laser Cladding for Damage Protection

In the laser cladded materials, three different parts are shown in a surface layer. They have the clad layer, heat affected zone (HAZ) parts and substrate parts. There can be seen a good

metallurgical bond between cladding and substrate. When microstructures are observed, cellular and columnar dendrites are seen frequently (Guo et al., 2015).

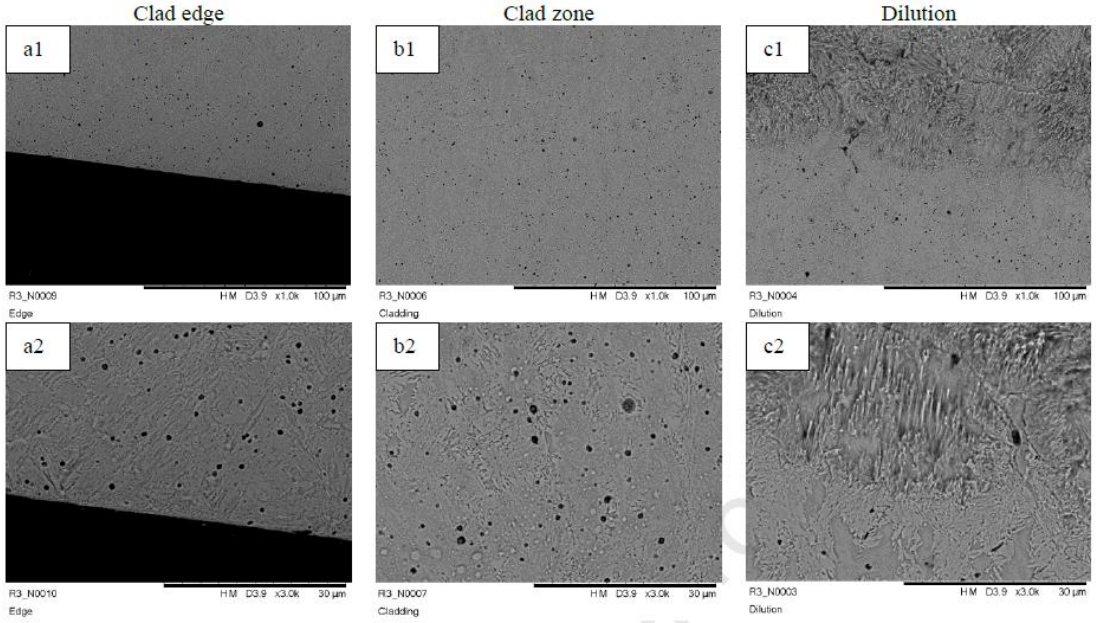

Figure 2.11: Microstructure of clad zone in untested MMS on R260 (4.76% Nitric, 47.62% hydrochloric and 47.62% water etched): (a1), (a2) are for the clad edge; (b1), (b2) are for the clad zone; (c1), (c2) are for the dilution zone (adapted from(Lu et al., 2018))

Figure 2.11 shows the microstructure of a clad zone in untested MMS on R260. A mixture of martensite retained austenite and delta ferrite deposit on microstructure of MMS within the clad zone. Higher amount of carbon in the rail grade causing decrease in the amount of delta ferrite and a rise in the amount of austenite within the microstructure. When deformation depth was checked on the study, it showed 10 and 20 µm. There was no cracking and only a small amount of MSS clad layer showed material flow. The rest of the clad layer had a similar structure to that in Figure 2.11. These low amount of plastic deformation on clad rail defined why there was no cracking on all rail samples (Lu et al., 2018).

Laser cladding is used for repairing surfaces in a number of different applications. It is used in different areas depending on the requirements of surface properties and how they are different from bulk materials. It is used various fields from power generation, transportation, healthcare, security, mining, nuclear, aerospace applications, oil, and gas industries. In these industries, mining industry components work under very harsh conditions and there are high wear rates. For example, drilling equipment and excavator's teeth were repaired using laser cladding. In the oil industry, cladding of drill bits is used for oil prospecting. Instead of replacing these

components, repairing them with laser cladding are the most cost-effective way. (Lewis et al., 2015; Narayanan et al., 2019).

Turbine blades are high-value components. Laser cladding is used for turbine blades refurbishment and repairs. Turbine blades have significant amount of mechanical and thermal stresses such as; thermal gradient and centrifugal force. The blades suffer from life cycle fatigue, hot corrosion, creep and much more damage mechanisms therefore, manufacturing problems, maintenance and costs play vital roles. Also, laser cladding has low heat input property and this is significant for jet engine components repair applications that includes metal depositions in superalloys (Toyserkani et al., 2004).

(Guo et al., 2015) studied single wheel or rail material treated by laser cladding. They compared the untreated and treated systems by laser cladding, and they found that the untreated wheel or rail specimens have severe wear and surface damage. However, laser cladded wheel or rail materials show mild wear damage. Also, they found that laser cladding improves wear resistance and decrease the rolling friction coefficient. Figure 2.12 shows the untreated, single treated wheel or rail fatigue damage.

Also, when cladding is used on the rail, residual stress must be well understood and characterised for the material selection and thermal processing parameters. It could cause the delamination or damage. When cladded layers are examined, this maybe reduce the damage with multiple layers, but tensile residual stress might result in delamination (Narayanan et al., 2019). 410L and Stellite 6 laser clad materials over heavy-haul rails were tested for residual stress investigation by neutron-diffraction and they found that residual stress mainly occurred near to top surfaces. Heat treatment after laser cladding process showed it was an efficient method for decreasing residual stresses (Roy et al., 2020).

Residual stress measurement methods were widely examined by Kendall et al. (2023) for railway components, joints, repair structures. Residual stresses mainly occur during those processes where heat affected zones and plastic deformation are generated and correct measurement types also have more importance to find out crucial aspects of the manufacturing and repairing processes. These showed pros and cons of destructive and non-destructive methods for measuring that stress measurement methods.

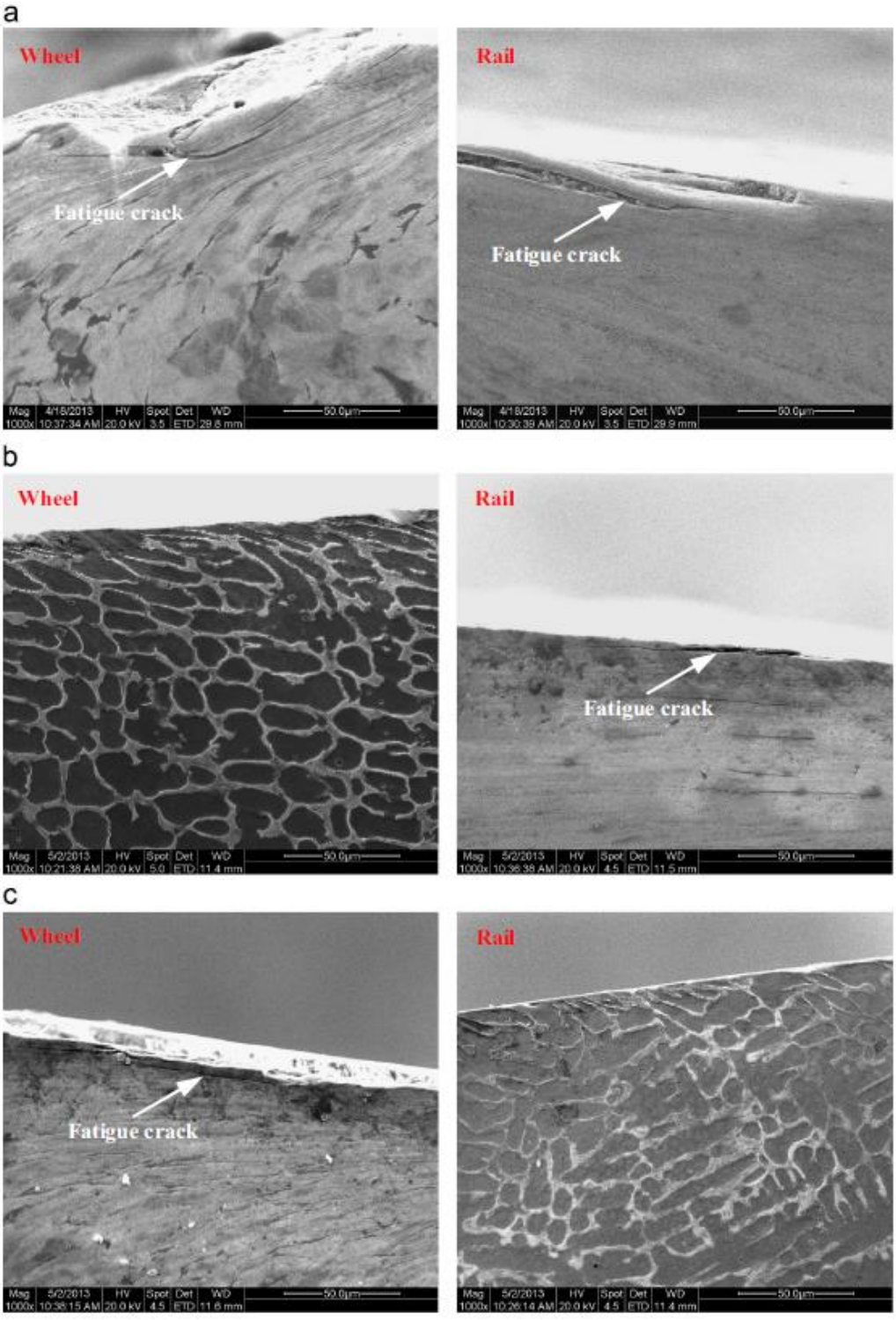

Figure 2.12: Fatigue damage of wheel/rail specimens: (a) untreated wheel/rail specimens; (b) single-treated wheel specimen; (c) single-treated rail specimen (Adapted from Guo et al. (2015)).

2.4.2 Cladding for new components/repairs

High-value components have high costs and many design and machining processes. These high-value components might have some design errors or machining errors. Repair technology is one of the most significant process. Laser cladding is one of the best repairing technology to

the repair of these components. Laser cladding has many advantages over the traditional methods. This process has small heat zone, lower dilution, increased controllability over the depth of HAZ, rapid solidification, and increased cleanness. Also, in traditional methods, welding is used to protect these damaged parts but, these methods are damaging because of the wide temperature distribution over the repair area. For example, metal inert gas, tungsten inert gas, electron beam welding and plasma cause a large amount of heating during the deposition and this lead big temperature rise in the component. This situation causes crack, short life of component, a low mechanical quality, and porosity. Laser cladding can be used in some parts that are considered unweldable by traditional methods because of advantages of laser cladding over traditional methods (Toyserkani et al., 2004).

Improving rail life also an aim for the laser cladding and when need a repair on rail it is repairing the local damage and it is increasing the rail life noticeably and increase the mechanical features for wheel/rail contact (Wang et al., 2021). Twin-disc tests with laser cladding specimens were conducted and they used Stellite 21, Inconel 625 and Hastalloy C. Wear rate was proportional with hardness and Stellite 21 had the highest wear rate and highest hardness among the materials (Seo et al., 2019). Stellite 6 clad material was used over the R350 HT rail for examining laser cladding as a repair method. HAZ showed higher hardness than surface clad and substrate because of the martensite formation. A ball on disc tribometer used for tests and wear volume decreased for clad rail specimen almost two times lower than unclad rail (Nellian et al., 2019).

Laser cladding is used in another research to repair within a small part over rolling/sliding disc with 5 different clad materials which are 304, 314, 2Cr13, 316L, and 434L over U75V rail substrate. Xie et al. (2021) found that wear rates of the rail disc get lower and damage behaviours of the clad part showed differences in front and rear edge of the clad part (Xie et al., 2021). In another research they used laser cladding and tested under the roller-on disc. The chosen clad materials were Stellite 6 and Martensitic stainless steel (MSS) and compared with laser cladded hypereutectoid rail type. Depending on the experiments they found that laser cladding was efficient on tribological performance with the chosen suitable alloy (Fasihi et al., 2022). AirMet100 was used for clad material for repairing bainitic steel railway and they found that wear resistance, mechanical properties and microstructure performance showed suitability of repair performance highly with 28% decrease in mass loss (Zhang et al., 2022).

2.4.3 Key parameters for tribological performance

Hardness is one of the key parameters for material selection in the railway industry. Hardness of wheel/rail components are significant for the wear and RCF issues. In the past, less studies about wear of rail and wheel focused on changing hardness effects. Hardness and wear relation on rail is coming from some reviews that show if hardness of rail increase, rail wear rate will be decreased and it will cause an increase in wheel wear, but it is not commonly justified. In a twin disc study on pearlitic rail steels, wheel wear was independent of rail hardness, but a full-scale test showed when rail hardness increased, wheel wear decreased. In general, when overall system wear was considered, increasing rail hardness decreased system wear (Lewis et al., 2019). The tests showed that when wheel hardness increased, wheel wear decreased and rail wear increased also, overall wear behaviour was independent of wheel hardness. (Markov, 1995). Also, another project showed that rail steel (R260, R350HT, and R400T) hardness increased, rail wear decreased. Also wheel steels (ER7 and ER8) showed that wheel wear rate increased when running against harder rails after 5,000 cycles but, then it decreased after 150,000 cycles (Vasic, 2013).

Laser cladding is also good for rolling friction coefficient which is one of the most significant parameters in contact tests. When the wheel/rail is untreated, the friction coefficient increases highly and arrives at a steady state up to the end of the test. If laser cladding of the single rail or wheel is in the test, the rolling friction coefficient decreases noticeably and becomes stable after about 2000 cycles. Single treated wheel roller friction coefficient is smaller than other rollers. Wear debris differences in the wheel/rail contact interface can cause different friction coefficients (Guo et al., 2015).

The failure of lipping in IBJs, untreated and treated rails by laser cladding have been compared for the improvement of the signalling quality in full-scale tests. Stellite 6 and MSS were used for cladding material on baseline R260 grade rail. Lipping resistance is significantly improved with cladding either side of IBJs when it is compared to a non-clad standard R260 baseline. Also, Stellite 6 and MSS clads on rail showed similar performances for plastic flow resistance. Furthermore, wear/RCF tests showed that RCF is not seen the full-scale test specimens. Standard R260 baseline rail showed some plastic deformation that is a precursor of RCF. Delamination was not seen on any clad rails and wear rates of stellite 6 and MSS cladding were 22% and 11% of the wear rate of standard R260 grade rail respectively (Lewis et al., 2017). Furthermore, Beaty et al. (2015) found the thickness of endpost does not affect the lipping rate. However, when the material selection of the endpost is changed, the effect of lipping is

changed. Harder rail steel and an endpost that has higher compressive strength enhanced the performance. They changed the materials of the endpost from PA6 to epoxy-glass composite which has a better performance. In another test they used laser cladding on the running surface and these cladded discs showed better performance. Stellite 6 was used for the clad material (Beaty et al., 2015).

Lewis et al. (2017) worked on laser cladding of rail in full-scale tests. Also, they worked on lipping of insulated block joints (IBJs) and bending fatigue of clad samples. R260 rail grade was used for the test and two different clad materials were chosen that are Stellite 6 and a grade of martensitic stainless steel. Both two clad materials improved the wear rate of rail and there was no visible RCF in these tests. Lipping resistance increased with both cladded rails.

2.5 Summary

Rail replacement causes high costs and more wasted time in the railway industry. These replacements take place because of wear and RCF damage types mainly. Other rail components also have the same problems such as insulated block joints (IBJ)s and switches and crossings (S&C). Rail and wheel life extension play vital role in the rail industry. Laser cladding is a method of improving surface quality of the materials. This method allows the add premium materials to a standard grade substrate material. Laser cladding has beneficial effects on wheel/rail contact problems.

In the literature, there were many studies related to wheel/rail contact. The literature can be divided into small-scale, full-scale, and field based tests and research. Mainly tests have been done for small scale test and then continued to full-scale tests and field tests. Use of laser cladding on rail, tests are giving satisfactory results for the improvement of rail quality.

Furthermore, laser cladding has significant effects on damage and wear properties, but it would be good to know when the clad layers will fail. It is known that laser cladding of rail discs showed very small deformation and low wear properties. Long RCF tests would show that point. Small scale tests will show the life of clad layer and the failure model. The tests will go with full scale tests that are going to be carried out to show how layers will perform under representative conditions and it is aimed to examine how the layers will cope with actual loading conditions on clad insulated block joints in field tests.

While there are many parameters that need optimising to make laser cladding perform well, there is no work on what happens to layers when they are not optimised and what impact this has on component failure. Examining those non optimal clad quality failures show how clad

specimens perform under the small-scale tests and it can lead the have more analyse with adding different parameters. There are also new methods to examine how those failures change with image analysis.

The key aspects of research are using laser cladding for rail component life extension, insulated block joints (IBJs) and switch and crossings (S&C), also there will be work to establish wear and RCF life extension experimentally. Laser cladding will be used as repair tool and the impact of a “bad” cladding process of rolling contact failures will be assessed. Laser cladding and premium rail specimens will be analysed to how they perform under similar conditions and compare with standard grade rail specimens. In another point these plans will be carried out for clad layers in small scale, full scale, and field tests. Full scale tests will be showing how the clad and un-clad pocket specimens perform under actual load conditions. At the end field tests will be conducted to see how clad, premium and standard rails perform under real conditions.

Chapter 3

3 Experimental Methodology for Laser Cladding at Multiple Scales

3.1 Test Scales

In this study, three types of experiments were used. These tests were chosen to show how laser cladding can improve the quality of rails. Laser cladding is considered to be one of the best surface treatment methods for rail based on the research reviewed in previous sections. Laser cladding on rail aims to improve wear resistance and extend the life of rail. The types of test were divided into: a small-scale tests and a full scale test (laboratory and field).

These three test scales have different purposes in the investigation to improve the understanding of clad layers and the potential for using cladding for repairs. Small-scale tests will be used for understanding life of a clad layer and ultimate failure mode. Furthermore, premium material, laser cladding as a repair method and tolerance of clad quality over disc experiments were used in small scale tests. Then, full-scale tests will be used to show layer performance under more representative conditions. Full scale tests were used in the laser clad pocket specimen tests and repair tests. Field tests were conducted for comparison of clad rails, premium rails and standard quality rails.

3.2 Chosen Approach

The tests were chosen specifically for understanding the clad layer performance in each condition. These test methods have some benefits and drawbacks. These features can be explained by the complexity versus control relationship. The approaches of tests can be evaluated with these two parameters. Long-term tests were planned for a small-scale test rig because it would take too long on the full-scale test rig. Also the benefit of good control of test parameters and easier measurements means that a better characterisation of the progression of wear and ultimate failure mode could be made. Repair tests were also planned for the small-scale approach. This is an area that has not been explored well, so testing with better control and repeatability meant that a good understanding could be gained before tests were scaled up to the full-scale situation where control of conditions in the wheel/rail interface is harder to achieve. The same clad materials were used on full-scale tests for comparison with the new and

previous small scale test results. Tests on other premium materials (such as those used for crossing noses) were also carried out as a benchmark.

Table 3.1 shows the test types for experiments and the basic description of these tests. Complexity and control relationships can be seen in the table and the complexity of these tests increases in going down the list. When all the test types are compared for control and complexity relationships, small scale tests have good control over specimens (Materials and geometry, roughness etc.). Loads, speed, and slip can also be controlled very well and measurements can be taken more easily. However, this changes for full-scale and field tests. Full-scale is a better representation of the actual conditions and complexity increases from small scale to full-scale and field testing has the highest complexity between them because it has real wheel/rail contacts and environmental conditions, but control is very low because contact load, contact stress and environmental conditions change considerably. Measurements also are harder under these conditions.

Table 3.1 Categories of tests

Test Type	**Description**
Small-scale (Twin-disc) Tests	High control capability on the test specimens, easier measurements (wear, friction etc.). The contact geometry is simplified though so “complexity” is low.
Full-scale tests	More representative contact conditions over small-scale tests as the actual wheel and rail components are used. As the rig is laboratory-based measurements are possible, but harder to realise than those on small specimens.

3.3 Starting Point for Laser Cladding Experiments and Material Selection

Small scale twin disc tests had been established in previous projects and were continued in this work with long term wear/RCF tests to learn more about the ultimate failure mechanism of a clad layer. Laser cladding on rails has been tested many times and these tests were examined with different analysis, as outlined in the literature review.

3.3.1 Laser Cladding

Additive manufacturing with laser clad coatings can be used for adding premium materials to a standard grade substrate material. Laser cladding can enhance rail durability; the process can

be used with a choice of rail materials dependent on required properties or position on the track providing beneficial opportunities for rail improvements (Lewis et al., 2015; Narayanan et al., 2019).

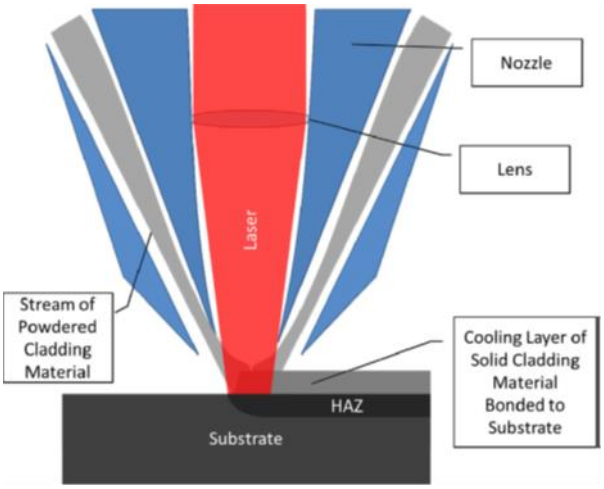

Figure 3.1: One-step laser cladding scheme (Lewis et al., 2015).

In the one-step laser cladding process (see Fig. 3.1), while a cladding material is added to the surface of the substrate, a high-energy laser is passed over the surface. The laser melts the surface of the substrate material and the coating material (in powder form) successively and welds them together. When the laser beam creates a melt pool, the powder is injected into the pool and the particles melt and a single track of the clad is created. This process can be repeated for further layers over the first layer of clad to build-up the thickness (Clare et al., 2011; Lewis et al., 2015, 2016; Lu et al., 2018; Xie et al., 2021). In this research, laser cladding was performed by an external company.

Table 3.2: Clad materials and substrate material list that were used in the thesis.

Clad Material	**Substrate Material**
Martensitic Stainless Steel (MSS)	R260
Stellite 6	R260
R260	R260
T400	R260

Table 3.2 shows the clad materials and substrate materials which were used in the different chapters of the thesis. It can be seen that MSS clad, Stellite 6 clad, R260 clad and T400

materials were used over R260 substrate materials. MSS clad, Stellite 6 clad, and R260 clads were used in the small-scale tests and full scale tests. T400 clad was used in a full-scale test.

3.4 Test Apparatus

3.4.1 SUROS 1 Twin Disc Test Rig

Twin disc testing was the small-scale test method used for the wear and RCF experiments. These were carried out using the Sheffield University Rolling Sliding (SUROS 1) twin-disc test machine. A line contact is used between the twin-disc test specimens on this machine to simulate the contact stress and rolling-sliding performance at the wheel/rail interface.

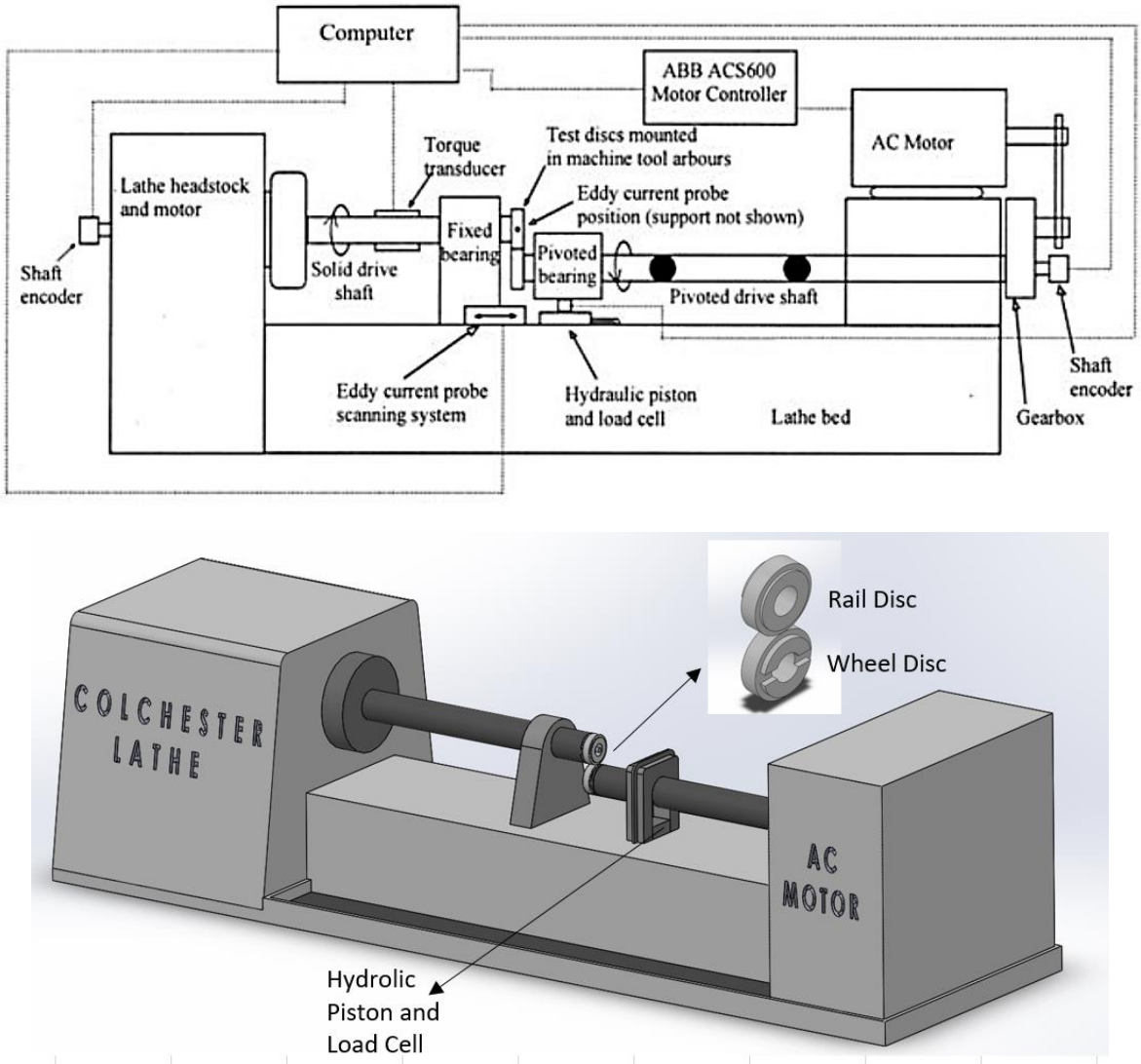

Figure 3.2: Schematic of SUROS 1 twin-disc test machine (Fletcher & Beynon, 2000)

Figure 3.2 shows the SUROS 1 twin-disc test machine schematic. This machine was originally developed by (Fletcher & Beynon, 2000). It uses two discs, one made of rail material and the other of wheel steel. The discs have a diameter of 47 mm and a contact width of 10 mm. As

can be seen on the schematic, the rail disc is mounted on the Colchester Lathe upper shaft run at a speed of 400 rpm and the wheel disc on the lower shaft of the test machine that is controlled by an AC motor. This allows a full range of slip values to be used and closely controlled using a feedback control loop. The slip ratio calculation is shown in Equation 3.1, where ω is rotational speed and r is the rolling radius of discs:

$$\text{slip} = \frac{\omega_{\text{wheel}} \cdot r_{\text{wheel}} - \omega_{\text{rail}} \cdot r_{\text{rail}}}{\omega_{\text{wheel}} \cdot r_{\text{wheel}} + \omega_{\text{rail}} \cdot r_{\text{rail}}} \tag{3.1}$$

The load on the rig is applied to the wheel disc shaft bearing housing via a hydraulic piston and measured by a load cell.

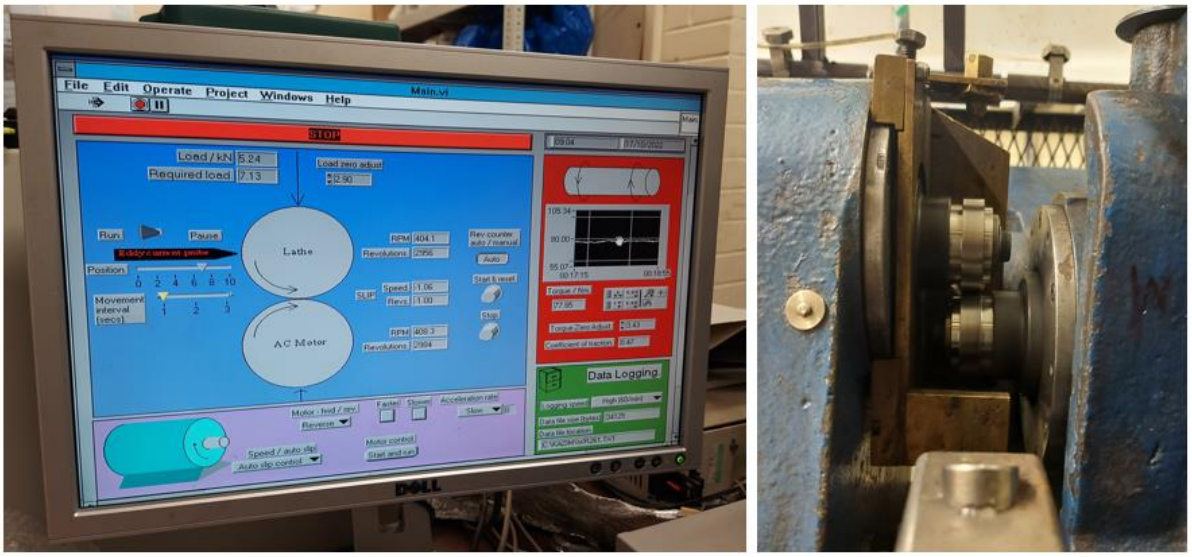

Figure 3.3: Computer Labview screen during a SUROS 1 test and discs mounted on the test rig

After setting up the parameters for an experiment in the computer and the required measurements were recorded, the rail and wheel discs are inserted into the test rig. The discs are tightened with a torque wrench with 60 Nm. The discs are then lined up together and the security guard is closed. The required contact pressure and slip value are entered into the control software and then a test can be started. An example software page can be seen in Figure 3.3. At the start of a test the disc shaft rotation is started first. In the Labview software the torque is then adjusted to zero. The slip value is checked to see if it is at the correct value. Once the desired slip is achieved, the discs are brought into contact by application of the load. The load is adjusted to the correct value. The test is then run until the desired number of cycles are achieved.

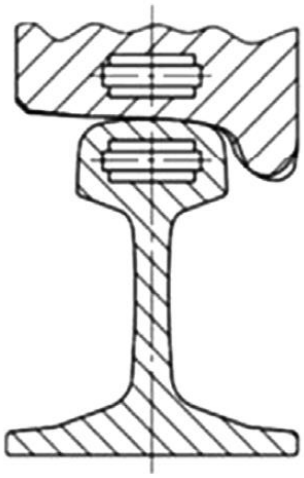

a)

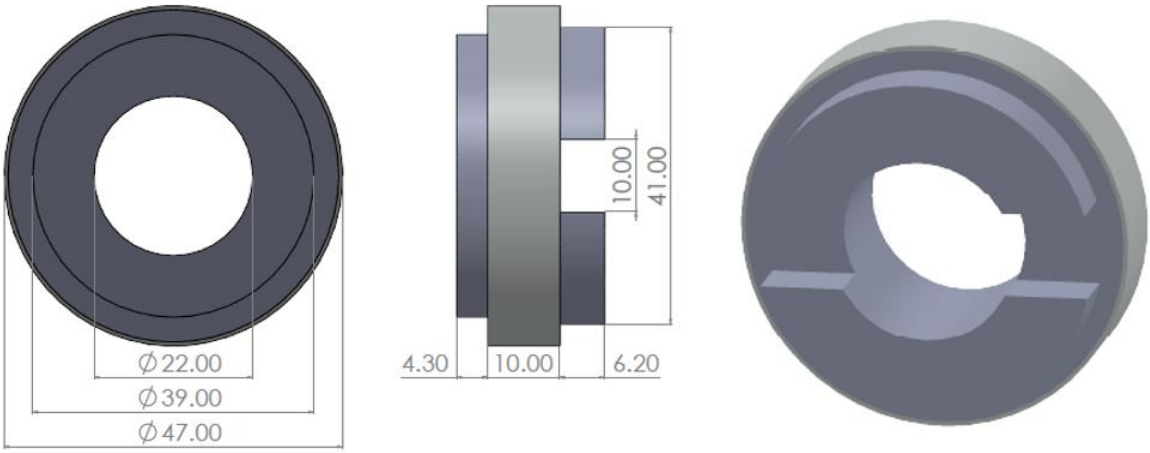

b)

Figure 3.4: (a) Twin disc rail and wheel sample extraction locations from actual rail and wheel (Lewis et al., 2014): (b) Clad rail disc dimensions

Twin-disc tests need two small-scale discs, and those were cut from actual rail and wheel material. A SUROS disc is shown in Figure 3.4 with dimensions. Rail discs are cut parallel to the top rail surface, and wheel discs are parallel to the wheel tread surface. This is to ensure that as far as possible discs have properties representative of those of material contacting in an actual wheel/rail interface.

3.4.2 Full-Scale Test Rig

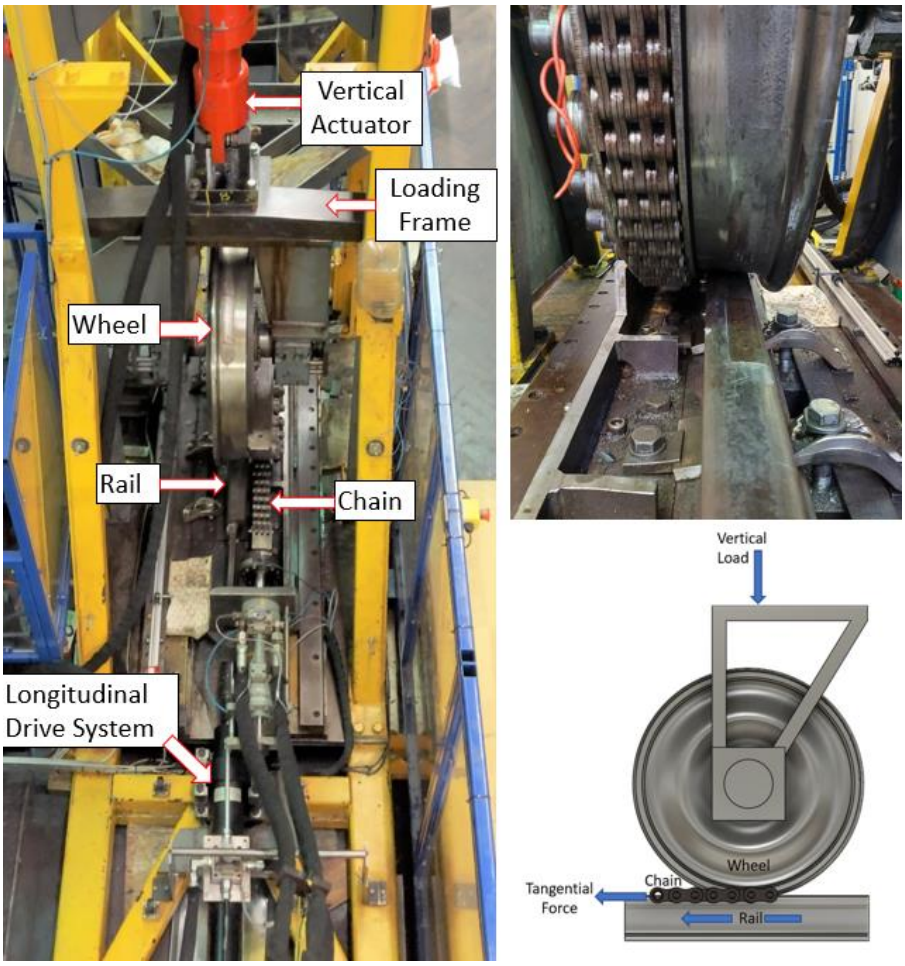

Figure 3.5: Full-scale wheel/rail test-rig

The full-scale test rig is shown in Figure 3.5. This test rig is used for simulating actual wheel/rail contact conditions in the laboratory. This hydraulically driven test rig may apply up to 200 kN in vertical load. The rig is assembled from the following parts: wheel, vertical actuator, rail, loading frame, and longitudinal drive system. The wheel is supported on an axle and can rotate freely, and this axle rotates on two journal bearings positioned in a loading frame. A hydraulic actuator is used to pull the rail under the wheel. The rail is clamped and fitted into a sliding bed with a cant (angle of tilt) of 1 in 20. The rail moves and it creates friction as the wheel rotates. A further actuator pulls a chain attached to the wheel which allows slip to be imparted in the wheel/rail interface.

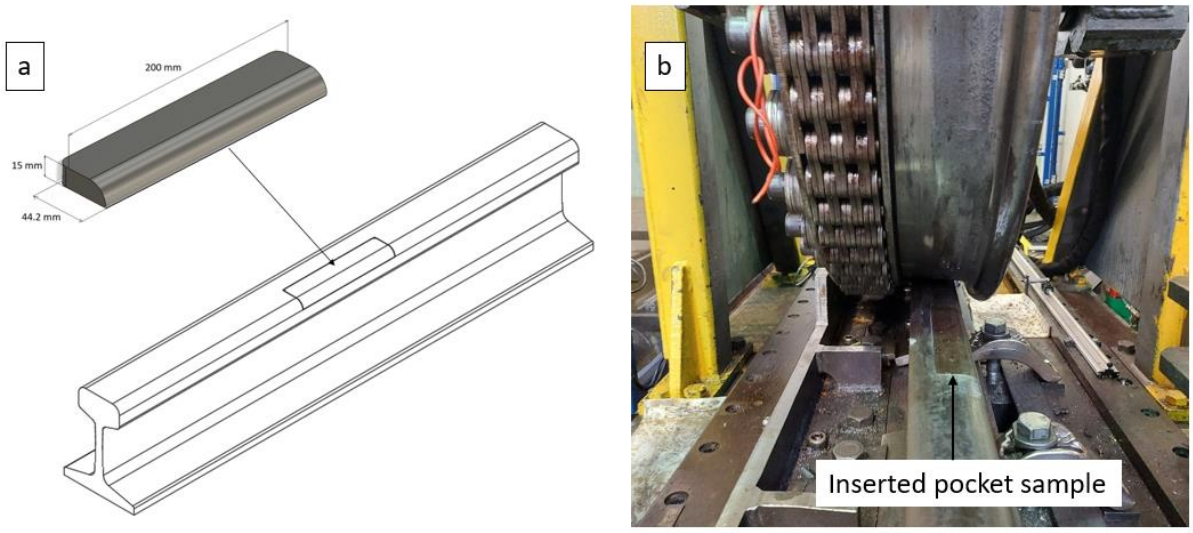

Figure 3.6: Pocket sample test material preparation and insertion in the full-scale test rig for an experiment

Pockets cut from the rail head were used for the tests. The pocket dimension is shown in Figure 3.6(a) These pockets were assembled into a base rail fitted onto the rig as shown in Figure 3.6(a). Before inserting the pockets, the rail and pocket insertion points were cleaned to ensure a good fit was achieved. After that the pocket profile, surface measurements and mass were recorded before the pocket was inserted into the rail and tightened with 3 bolts. Before starting the tests, the surface of the pocket was cleaned with acetone.

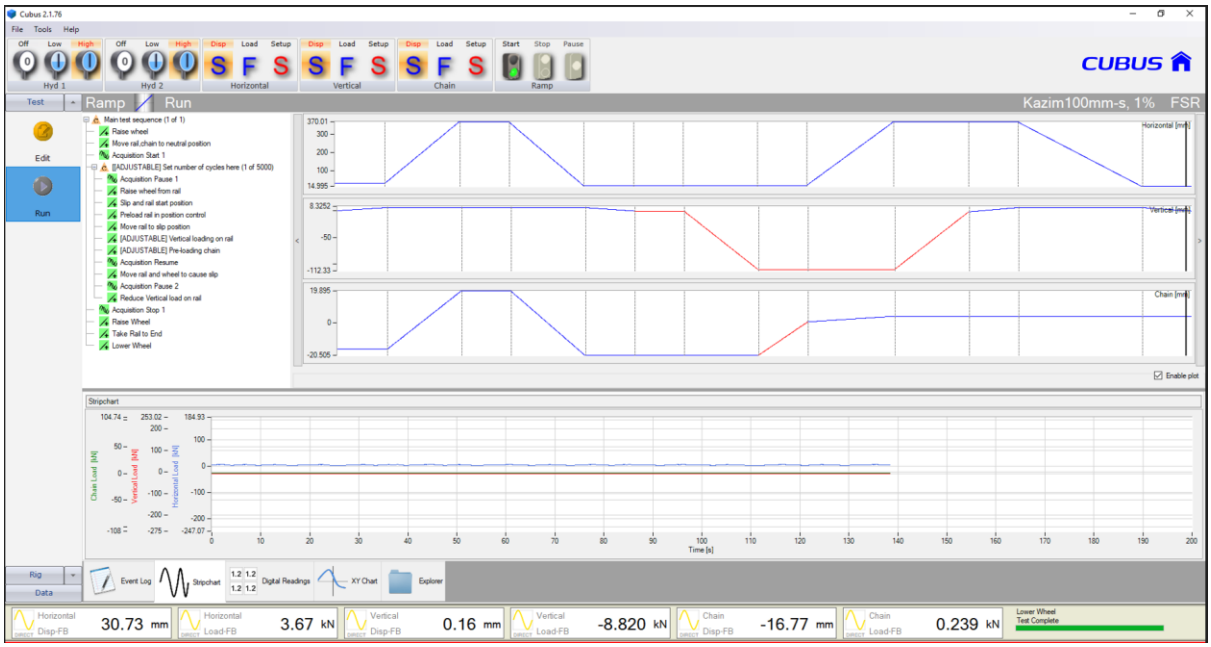

Figure 3.7: Full-scale test rig computer set-up screen and Cubus software screen (Cubus, n.d.)

Figure 3.7 shows the Cubus software screen for the full-scale tests. Slip values and velocity were set-up before the start of the test, the number of cycles was entered and vertical load and pre-loading on the chain was adjusted. Hydraulic pressures were then turned on for the

hydraulic actuators. Then in the run section, the test was started. When all cycles were finished the test rig was stopped and after turning off the hydraulic actuators the cage of the test rig was ready to be opened. The data was then extracted from the computer and analysed.

3.4.3 Surface Measurements

3.4.3.1 Alicona Infinite Focus SL

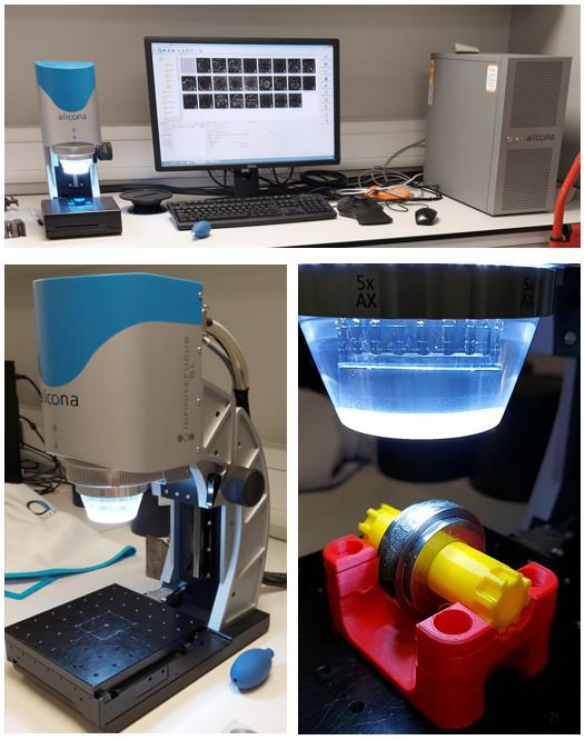

Figure 3.8: Alicona surface roughness measurements tool

The Alicona (see Fig. 3.8) is a three-dimensional optical measurement system (InfiniteFocusSL Alicona, n.d.). This was used for measuring surface roughness values. The machine has 3 types of lenses. They are 5 times, 10 times and 20 times zoom lens magnifications. In this research the 5 times AX zoom lens magnification was mainly chosen due to its fast and bigger scan capacity with 3.61 mm x 3.61 mm for one image. It was a non-contact system and the stage under the lens allowed the measured maximum of 50x50 mm. Samples were put on the stage and the focusing was arranged over the desired measurement area. Desired image brightness and contrast were then set up.

The Alicona has two types of measurement, single and multi-image. Single measurement allows only a small part of the area and multiple image more collates number of single images into one image with bigger dimensions. Mainly the multiple images option was chosen. Multiple image option points from the desired surface are added depending on the desired measurement area. After that height points are added to bring the lens closer to the surface and

far from the surface. The height point addition allows the creation of a 3D surface to be created of the desired area. When all the points are added and the resolution is set-up, the image capture starts. When a 3D image is created it allows measurement of surface roughness.

Surface roughness was measured by creating a line over the surface. Surface roughness parameters over that distance are then calculated.

3.4.3.2 Calipri

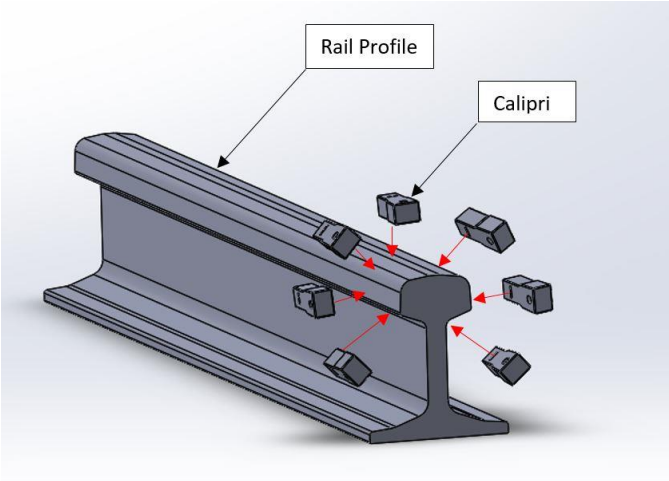

Figure 3.9: Use of Calipri for profile measurements (Nextsense, n.d.)

The Calipri is a 2D profilometer (see Fig. 3.9) used for rail profiles and pocket specimen profiles in the full-scale experiments. It was used to get 2D profiles of worn samples for comparison with reference profiles. The Calipri is portable equipment and one tablet and portable laser scanner were used to scan samples.

First, the Calipri software was opened and the required parameters entered. If scanning a rail profile, the reference had to be chosen, such as; 54E1 or any profile other standard profile depending on the sample. After setting-up the portable Calipri laser tool over the sample at an appropriate distance, the start button is pushed. When the measurement is finished it shows the profile on the screen. Also, there is another software for analysing, comparisons between two profiles.

3.4.3.3 Laser 3D Scanner

A laser scanner by Creaform was used for profile measurements (see Fig.3.10). It allows 3D and 2D profile measurements. Magnetic bands were put near the desired area around the sample for surface measurements and those bands were put over the sample except the desired surface region. When all magnetic parts were put around the area, the laser scanner was ready to measure and the software was opened on the laptop.

In the software, the surface scan was chosen first then surface magnetic bands were chosen on the software for the start point of the scan. After that sample scans were chosen and the sample scan started. When finishing the part scan all connected parts were chosen on the surface and other scans were deleted and the good parts were saved. After finishing all steps 2D and 3D analyses were made with the same software and the results were saved.

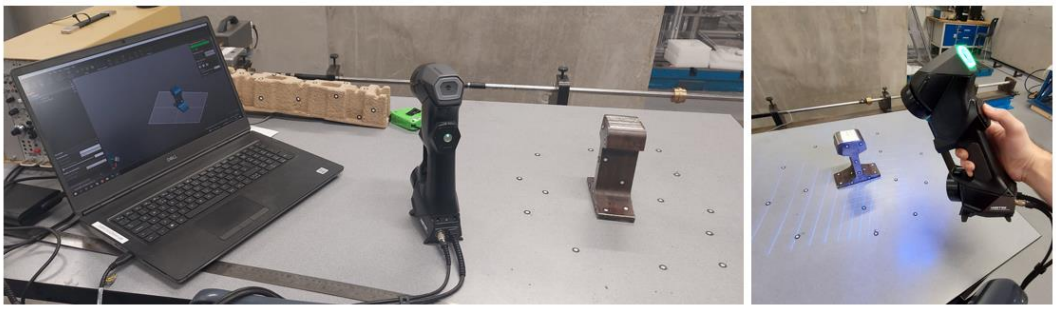

Figure 3.10: HandScan Creaform laser 3D scanner for profiles (Creaform3D, n.d.)

3.4.3.4 Replicating the Surface Roughness Properties

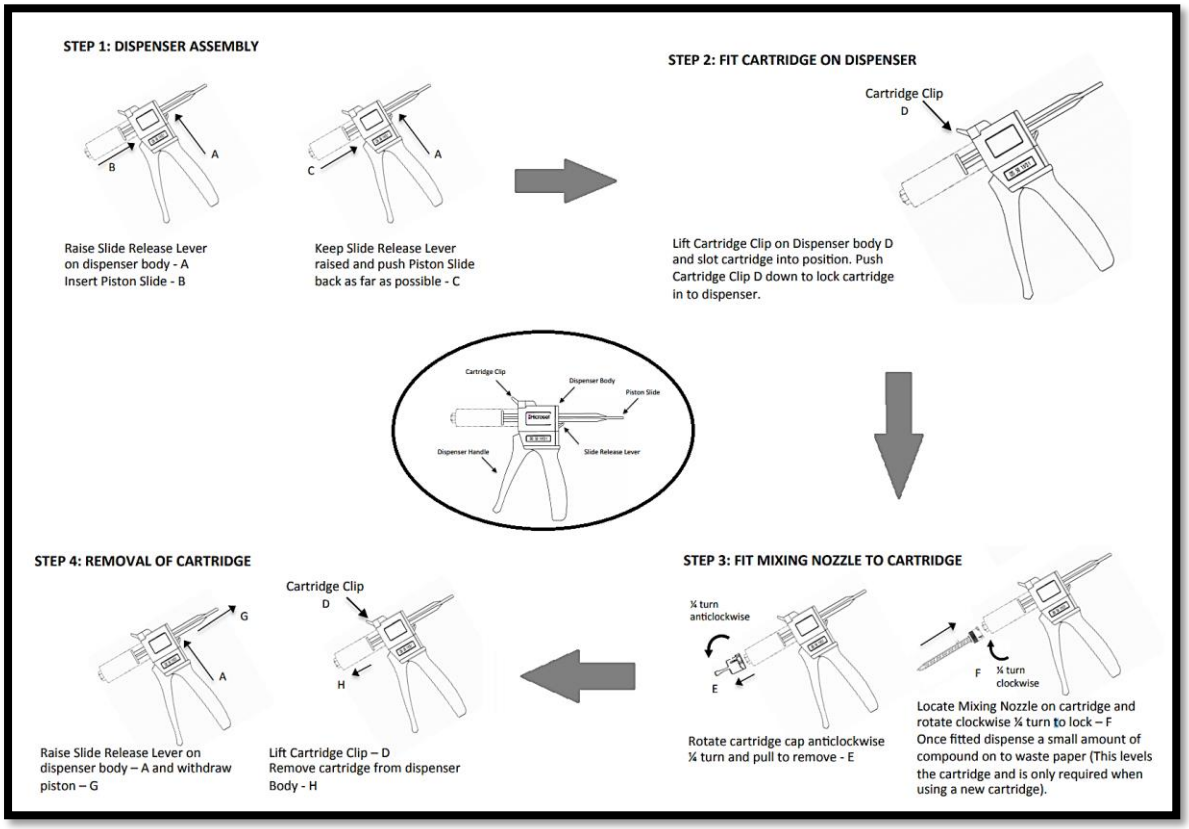

Figure 3.11: Use of replica steps (Microset, n.d.)

Replicas were used on the sample surface when they were bigger than the Alicona stage sizes. Figure 3.11 shows how the replica compound fits in a replica gun (Microset, n.d.). Replica compound was spread over a surface and then cure paper was placed over it. Then there was a

wait of 3-5 mins for curing. When it was cured, the compound was slowly peeled away from the surface and put in a sealed bag for surface measurements using the Alicona.

3.4.4 Microstructure Analysis

3.4.4.1 Sectioning

An Abrasimet is a sectioning machine for samples (see Fig. 3.12) (AbrasiMet 250). The blade was chosen depending on the hardness of the steel. The blade was attached to the machine by using a screw and flange. Then samples were inserted by using clamps. After ensuring the blade screw was tightened, the light was turned on, the cooling water worked properly, and the cage was closed machine could be started. The sectioning process starts with adding cooling water over the blade. The machine was controlled by hand and the sample was sectioned.

Figure 3.12: Abrasimet sectioning machine

3.4.4.2 Mounting

Sectioned samples were mounted by using a Simplimet 1000 machine (see Fig. 3.13) (SimpliMet 1000). Samples were sectioned depending on the size of the mounting surface. Mounting samples were chosen for allowing use in the SEM machine. When the mounting space was lowered down, the sample mounting powders were poured over the sample and the sample was lowered down all the way through and the cap was closed to allow pressurization. The machine starts with preheating and then it starts to mount the sample. When the mounting

was finished, the machine stops and the cap can be opened and the sample was ready to grind and polish.

Figure 3.13: Simplimet 1000 mounting machine

3.4.4.3 Grinding and Polishing

Figure 3.14: Automet 250 Pro grinding and polishing machine

Grinding and polishing were carried out using the Buehler Automet 250 Pro machine in the micro preparation lab (EcoMet 250) (see Fig.3.14). After mounting the samples grinding was done first with 400 µm, 800 µm and 1200 µm grinding papers respectively. Those numbers means that when there is a higher sandpaper number the paper has a finer abrasive and it creates smoother surface finish, but when the number is lower, it represents coarser abrasives which

scrape off materials much quicker. Each of the grinding papers was used once and the time was chosen as 1 minute per grinding paper.

Polishing was carried out with different polishing consumables. Generally, it was done with 9 µm, 3 µm and 1 µm polishing papers. Depending on the end polishing, Silica was used in some of the samples as well. For the polishing duration, it was longer than grinding as it took almost 10 minutes total time for all polishing steps.

3.4.4.4 Micro Hardness

Figure 3.15: DuraScan micro-hardness machine

Micro-hardness measurements were made using a microhardness tester (DuraScan) (see Fig. 3.15). The Vickers hardness method was used. After finishing the 1 µm or silica polishing stage on the sample, it was put under the indentation stage. When the machine was turned on and the set-up load was chosen as HV 1, the location was then chosen over the steel part from the surface to the bulk part. Depending on the desired measurement area indent numbers and distance between two indentation points was set-up. The machine started and micro-indent hardness measurements were taken. At the end, all indentation points were checked and if it did not choose the correct points, a measurement was made manually at that point. When finished and the results were all clear, they were saved as an Excel file and hardness data were saved.

3.4.4.5 Nano Hardness

Nano-hardness measurements were taken using a Bruker nano-hardness machine (see Fig. 3.16) and it was mainly used for examining the surface point hardness values on the samples (Hysitron.). After the micro-hardness measurements were finished, if the surface needed examining more closely, the nano-indenter was used.

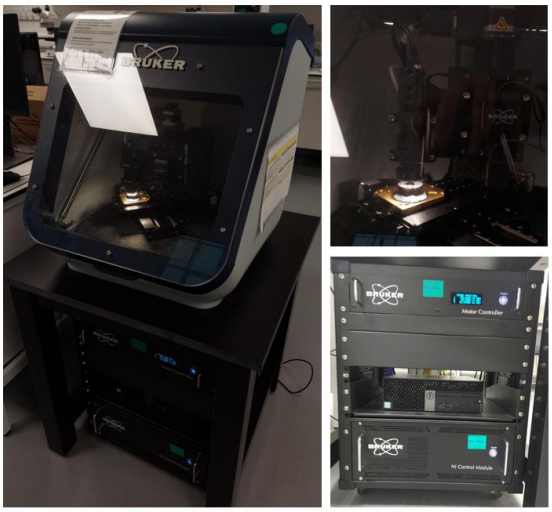

Figure 3.16: Bruker nano-hardness machine

Measurements were done in 10 × 10 matrix of indentation points on a sample and the load was chosen depending on the material. The loads that were mainly used 5000 µN or 3000 µN depending on the hardness of the sample. Before starting measurements, a calibration was made. After that indentation numbers were chosen with load and then desired measurement areas were chosen. Then the start indentation points were chosen and the machine was started with auto focus. After the machine analysed the height of the sample, the desired hardness area was chosen and measurements started. At the end of the test, the data were collected as a nano-hardness map and csv files.

3.4.4.6 Etching

Etching was made in the micro preparation lab at the University of Sheffield (see Fig. 3.17). Most of the experiment materials were possible to etch by %2 Nital solution (nitric acid and ethanol), for example, R260 grade materials and Stellite 6 materials. Vilella reagent etchants were used for MSS Clad parts. It is made by mixing 1 g picric acid, 5 ml Hydrochloric acid (HCL), and 100 ml IMS.

Figure 3.17: Etching preparation table

Etching was made after polishing and if needed the last step of polishing was made again just before etching to help etch more easily. The sample was submerged in the etchant and if etched it is cleaned with water and isopropanol if not the etchant was used by a wipe of cotton over the sample to etch.

3.4.4.7 Microscope

Figure 3.18: Nikon Eclipse LV 150 optical Microscope

A Nikon Eclipse LV 150 optical microscope (see Fig. 3.18) was used for the microstructure analysis (Nikon) . After preparation, the sample was put on the stage in the microscope and software was opened on the computer. When the software was opened, required settings were chosen for the best image quality and magnification was chosen. Images were collected with higher magnifications and images were saved.

3.4.4.8 SEM

SEM images were taken using a tabletop Hitachi TM3030 SEM machine (see Fig. 3.19) (Hitachi). The table-top SEM allowed imaging of the microstructure with higher magnifications. First the machine and the computer were turned on and the machine vacuum was released to insert the sample inside. After that the software was opened and the sample was prepared depending on the height of the machine. The sample was inserted inside and the vacuum was turned on again. After the vacuum finished, the software allowed visualisation of microstructure. Brightness, contrast, and focus were set-up and images were taken with different magnifications. When all images were saved, the machine vacuum was released again and the sample was taken off.

Figure 3.19: TM3030 tabletop SEM machine

3.4.4.9 LIBS Analyzer

LIBS (Laser Induced Breakdown Spectroscopy) is a hand held portable chemical analyses tool (see Fig. 3.20) (SciAps, n.d.). It was used in the laser cladding repair tests. It was expected to measure the chemical compositions of the clad parts and they were compared with other similar materials.

Figure 3.20: LIBS chemical analyses portable tool (SciAps, n.d.)

3.4.5 X-Ray Scanning Machine

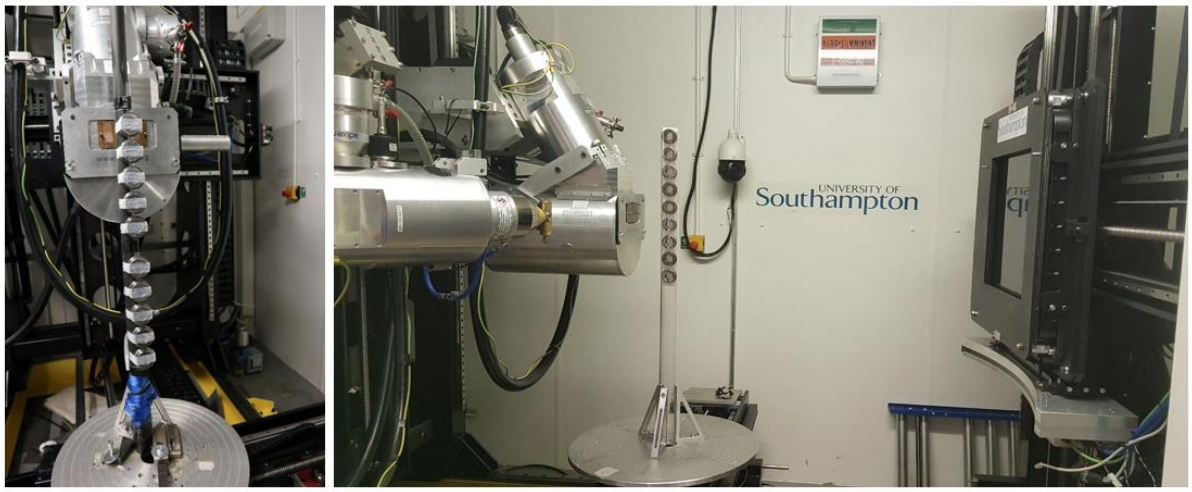

Figure 3.21: University of Southampton X-Ray laboratory facilities (University of Southampton, n.d.)

An X-Ray scanning machine allows specimens to be scannned before and after the experiments to check for changes in internal flaws/damage. The discs were X-Ray scanned prior to the small-scale twin disc tests to determine the extent of porosity using ‘custom 450 kVp/225 kVp hutch’ CT system at the University of Southampton (see Fig. 3.21).

Chapter 4

4 Tribological Characterisation of Rails Cladded with MSS Laser Cladding

An outstanding question from previous work is related to when the clad layer would fail and how it would do so. Previous small-scale twin disc testing has been limited to around 50,000 contact cycles, to this point wear has been low, little deformation has been generated in the clad material and no cracks have been initiated. The longevity test was developed to push the coating to its limit, therefore an RCF test was selected. In this test, R260 grade standard rail steel was used as the base rail material with 1 mm of MSS cladding material deposited on the rail disc.

The SUROS 1 test apparatus was used for the experiments as described in Section of 3.4.1.1.

4.1 Test Conditions and Measurements

The test conditions were set at 1500 MPa contact stress and 1 % slip ratio. The first 500 cycles were run unlubricated (dry) to generate roughness and initiate cracks (this is a standard approach used on standard rail grades (Fletcher et al., 2000)). Followed by blocks of 20,000 cycles with distilled water dripped on to the surface of the wheel disc at a rate of 1 drop per second.

The MSS clad rail disc and wheel disc were weighed, and their diameters measured before the start of the test and recorded. Then for the first test cycle block 500 dry cycles were run and then 20,000 cycles with distilled water addition at 1 drip per second. All the following cycles were continued with distilled water addition. After each of the 20,000 cycle blocks the test rig was stopped and discs were taken off the rig and then cleaned with acetone.

Following that, discs were weighed again and measured with callipers. Room temperature and humidity were recorded as well and their dimensions between all block of cycles. After that, rail surfaces were examined using an optical (non-contact) Alicona Infinite-Focus SL profilometer. The profilometer gives the chance to obtain high-resolution images and 3D surface profiles measurements with a vertical resolution of up to 10 nm. Surface roughness' were recorded from the Alicona scans. This process was followed for all blocks of cycles.

4.2 Test Specimens

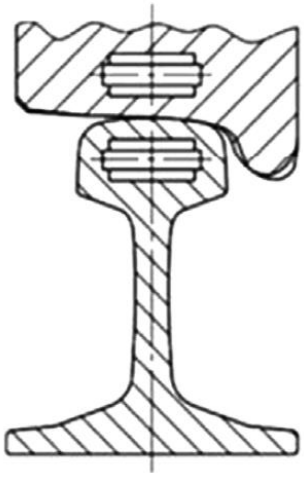

(a)

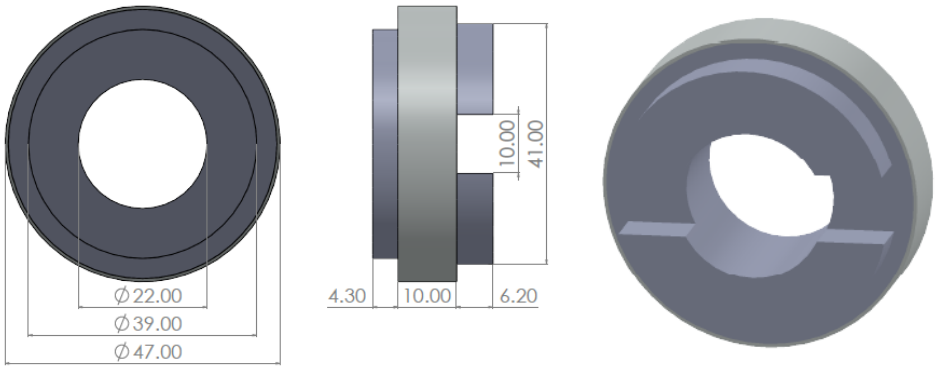

(b)

Figure 4.1: (a) Actual twin disc rail and wheel sample extraction locations from actual rail and wheel (Lewis et al., 2014). (b) Clad rail disc dimensions

Twin-disc tests need two small scale discs, and those were cut from actual rail and wheel material. A SUROS disc is shown in Figure 4.1 with dimensions. Rail discs are cut parallel to the top rail surface, and wheel discs parallel to the wheel tread surface. This is to ensure that as far as possible discs have properties representative of those of material contacting in an actual wheel/rail interface.

Table 4.1: Rail and wheel materials used in samples in the MSS Clad tests

Sample	**Substrate Material**	**Clad Material**
Rail Sample [CS414]	R260 grade rail	Martensitic Stainless Steel [MSS]
Wheel Sample	ER8	-

Table 4.2: The chemical composition of the martensitic stainless steel (Christoforou et al., 2019).

C [%]	Si [%]	Mn [%]	S [%]	P [%]	Cu [%]	Ni [%]	Cr [%]	Mo [%]	V [%]	Co [%]	W [%]	Balance [%]
0.22	0.18	0.87	< 0.003	0.011	< 0.01	2.25	9.53	0.24	0.27	1.22	0.46	84.75

Table 4.1 shows the materials that were used in the tests and Table 4.2 shows the chemical composition of clad material which is martensitic stainless steel. In this test, R260 grade standard rail was used as a base material and Martensitic Stainless Steel (MSS) was used as a cladding material on the rail with 1 mm thickness over rail material. The wheel disc was made from ER8 material. Before the tests, the discs were cleaned in acetone. An ultrasonic bath was used for the cleaning. Disc weight was recorded with the aim of determining mass before and after tests. During the test 13 different wheel discs were used in some periods because of the deformation and flaking of the wheel material as it reached its rolling contact fatigue limit. Wheel discs were changed depending on their condition after 20,000 cycle blocks were completed. If the condition of wheel was good enough to finish second block of 20,000 cycles they were used again but if wheel disc deformed more, new wheel discs were used after 20,000 cycles too. Most of the wheel discs were changed after 40,000 cycles.

4.3 Results

4.3.1 Surface Evolutions

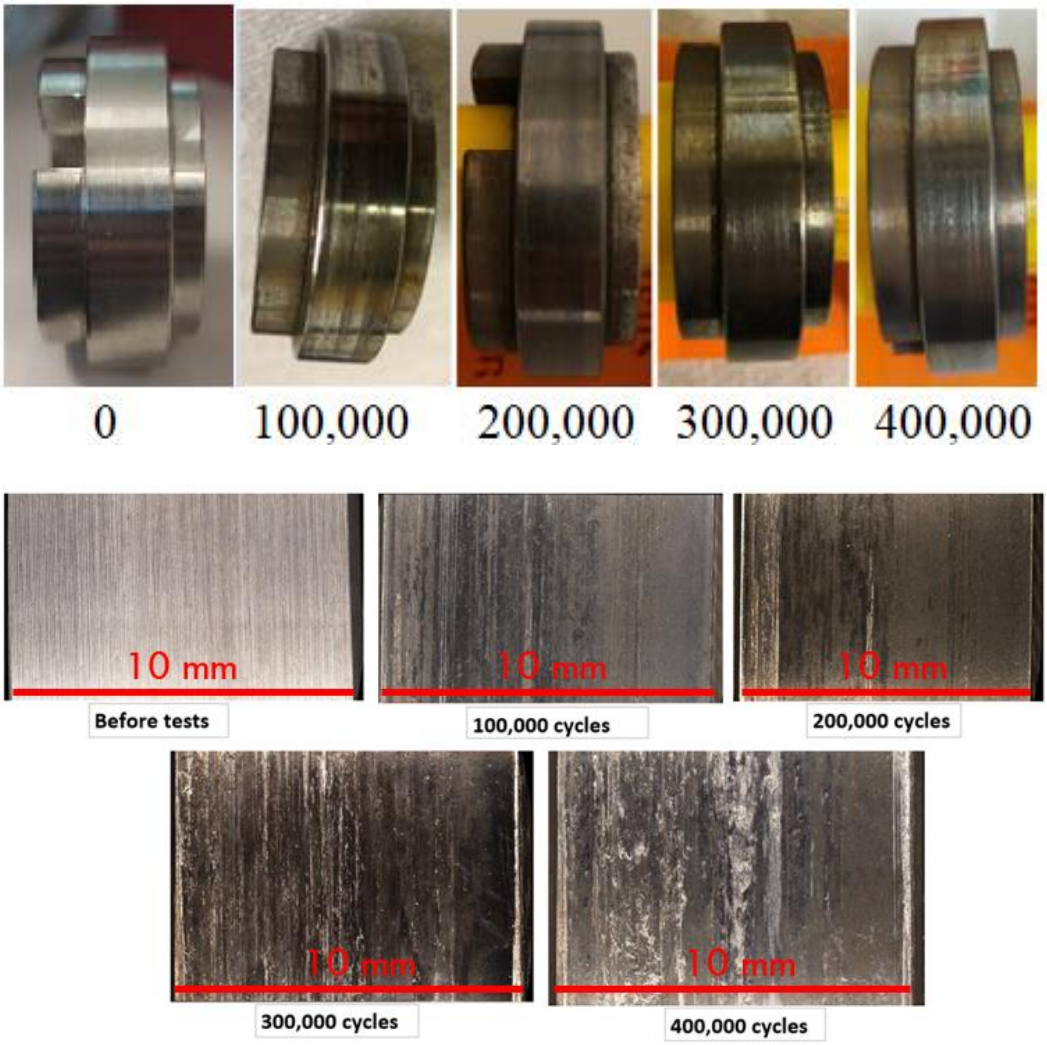

Figure 4.2: Laser clad disc surface images during longevity test

Images of the laser clad disc surface are presented in Figure 4.2 at intervals of 100,000 contact cycles, up to the end of the test at 400,000 cycles, at which point the test was stopped, but the laser clad coating had not failed at this point. After 400,000 cycles the clad layer was still intact and there were no visible signs of cracking or flaking. This implies that the surface material is not deforming and reaching its ratchetting strain limit. It can be seen, however, that there are some scratches over the surface of disc with increasing test cycles. Abrasive wear was observed, perhaps promoted by the wheel wear debris trapped in the contact. To put this into context, R260 grade rail material tested under the same conditions would show significant damage after 15-30,000 cycles (Franklin et al., 2005; Lewis et al., 2015, 2016). This also explains why the wheel discs needed replacing often during the test.

4.3.2 Roughness

Roughness was measured after each block of cycles and the value of roughness was recorded and the data extracted from the profilometer. The whole length of the lateral roughness in disc was measured with around 10 mm. The longitudinal part of the disc was measured around 6-10 mm for roughness. The surface roughness was monitored with the Alicona throughout the longevity tests in both the longitudinal and lateral directions on the rail disc, as shown in Figure 4.3(a).

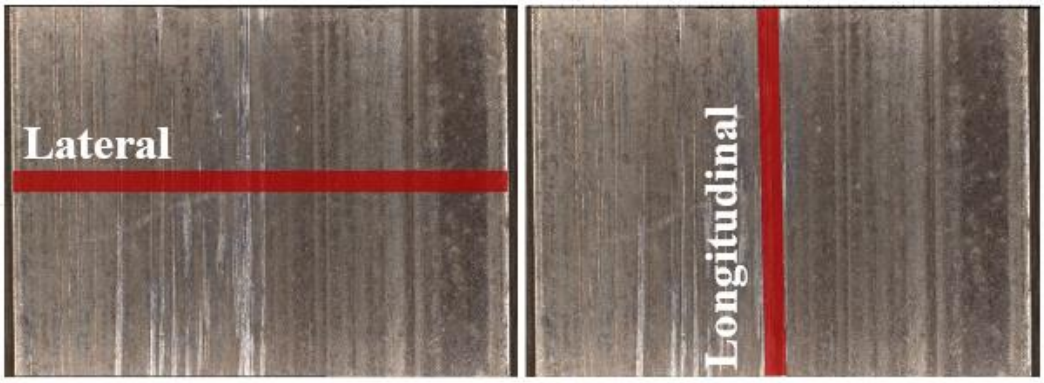

(a)

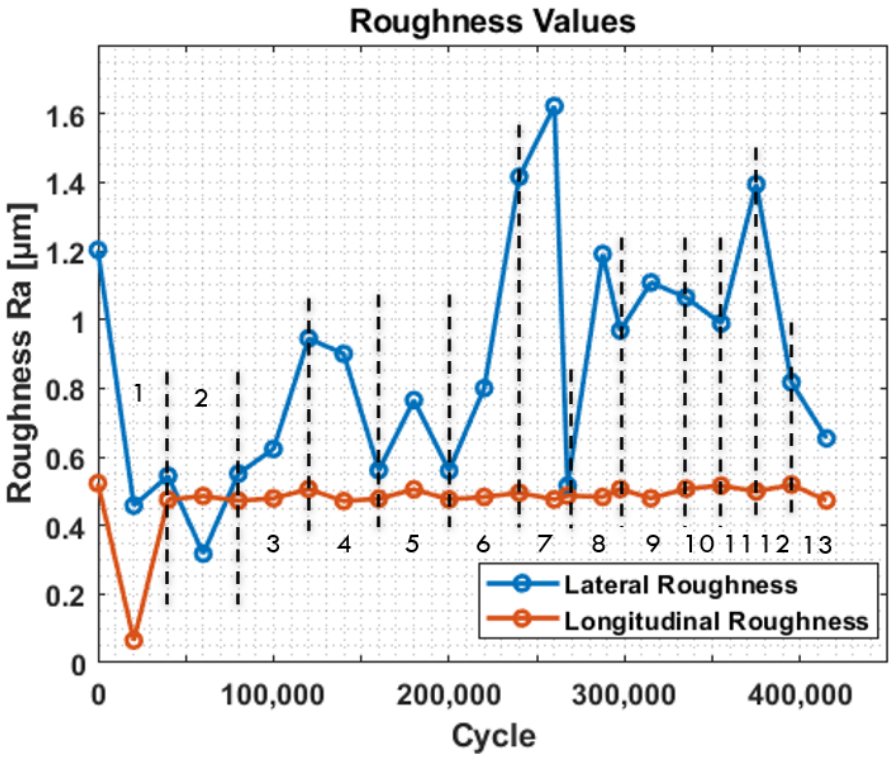

(b)

Figure 4.3: Roughness measurements of the laser clad coating during the longevity tests: (a) direction of measurements; (b) Ra roughness values.

The arithmetic average roughness (Ra) measurements in Figure 4.3(b) show that after an initial reduction after 20,000 cycles the longitudinal roughness remains at a steady state. The lateral roughness shows variation throughout testing with the evolution of the surface. The Ra roughness value increases between 200,000 and 260,000 cycles peaking at 1.65 µm. It can be also from previous wear scratch images in Figure 4.3, after 200,000 cycles wear scratches are seen more on the images of the surface. 13 different sections are shown and they were the wheel change points Lu et al. (2018) shows that unclad R260 roughness values are higher than 6 µm after 30,000 cycles of a test so these values are relatively very low.

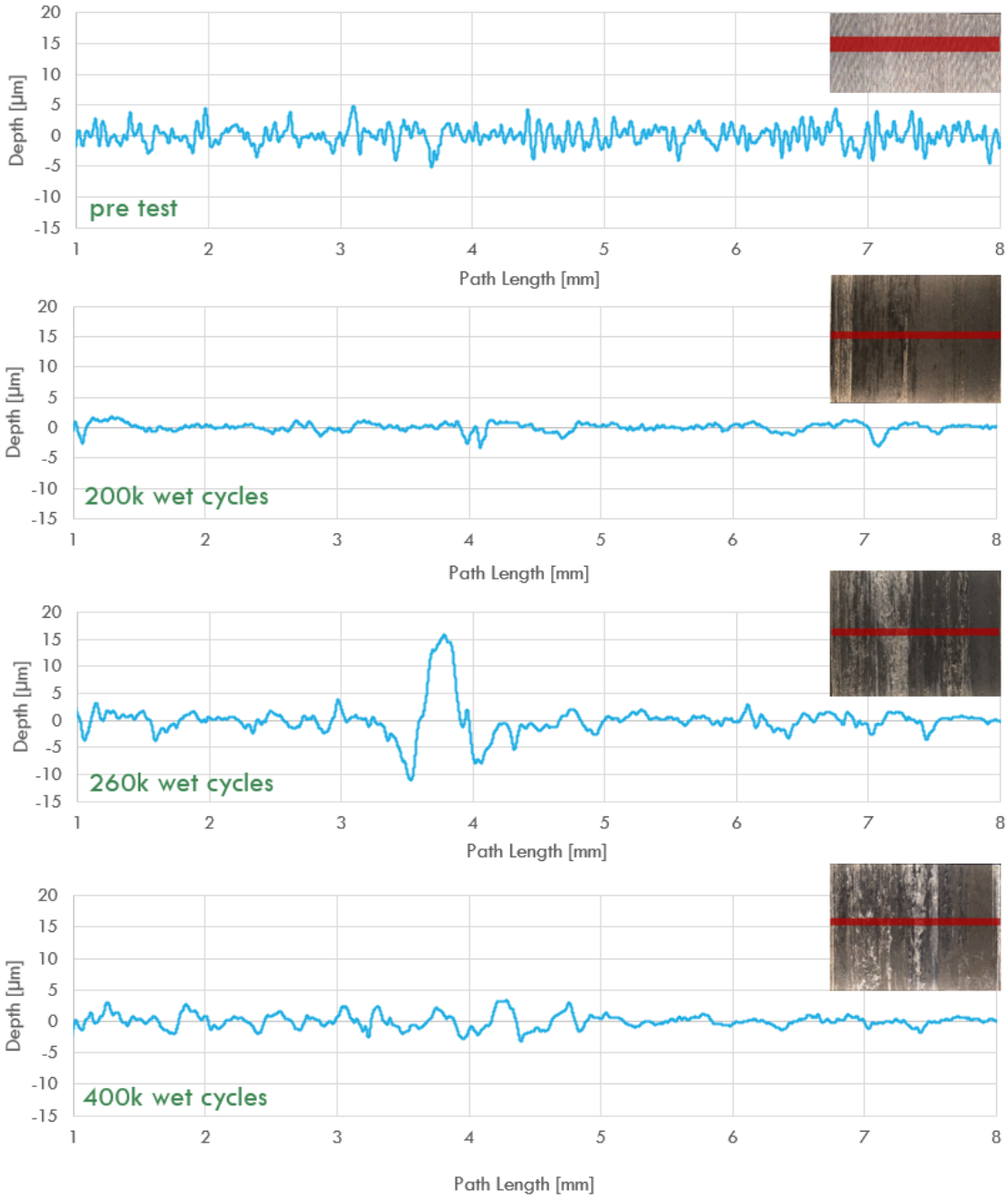

Fig. 4.4 (a)

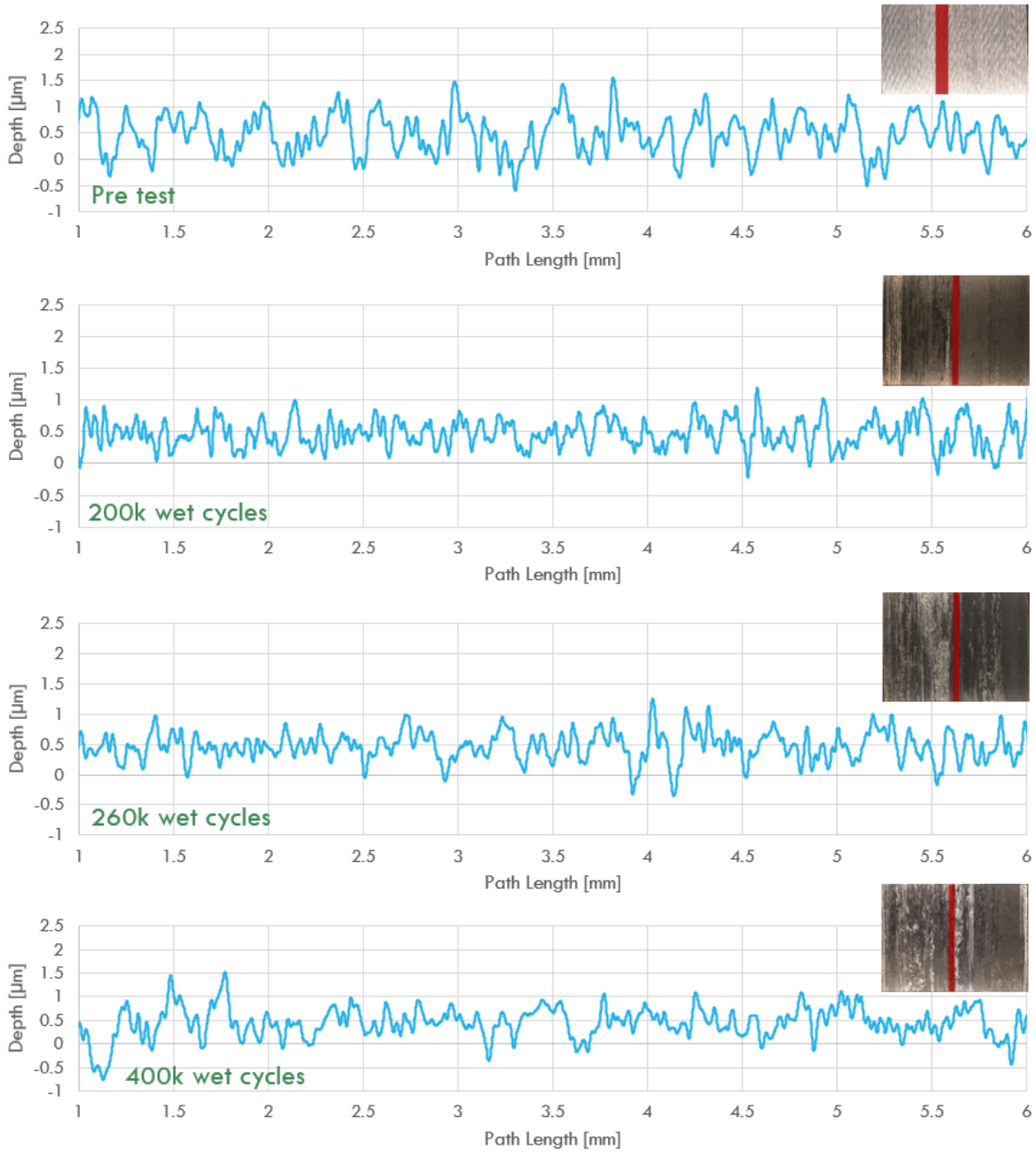

Fig. 4.4. (b)

Figure 4.4: MSS lateral and longitudinal sides of rail disc roughness graphs: (a) lateral; (b) longitudinal

Figure 4.4 shows the MSS clad rail disc lateral and longitudinal roughness profiles after each block of tests. Figure 4.4 a shows the roughness in the lateral direction and Figure 4.4 b shows the longitudinal roughness. For the lateral direction, the values show a similar trend between pre-tests values and the values at the end of the test and the depth of the profiles stay between -5 to 5 µm values in all graphs, however, there are some depth differences between some of the

cycle blocks, especially around the point of peak roughness shown in Figure 4.3(b) with 260,000 cycles. The longitudinal roughness values show a similar trend for each block of cycles. The roughness profiles show a difference after 260,000 cycles in Figure 4.4.a which is probably because the wheel disc in this instance was run for too long and degraded more than the others. However, while the peak looks significant, 2.5µg/cycle is still a low wear rate.

4.3.3 Mass Loss

Rail disc and wheel disc wear rates can be seen on the graphs shown in Figures 4.5a and 4.5b.

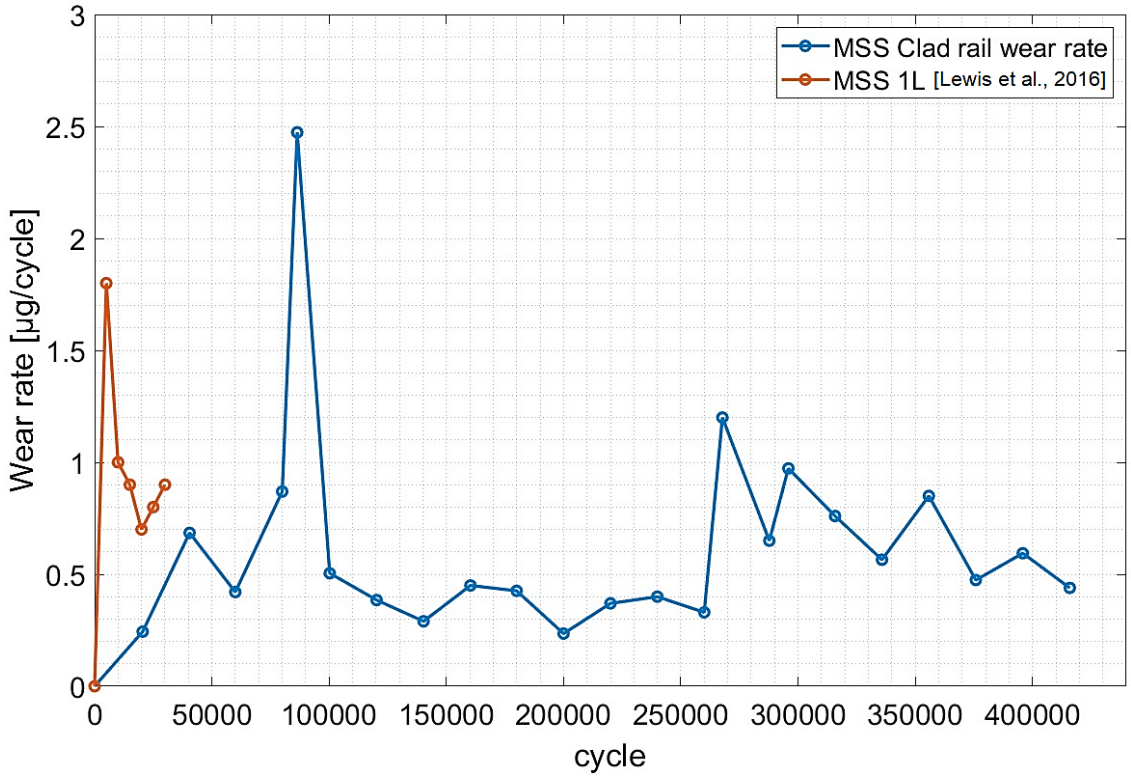

Fig. 4.5. (a)

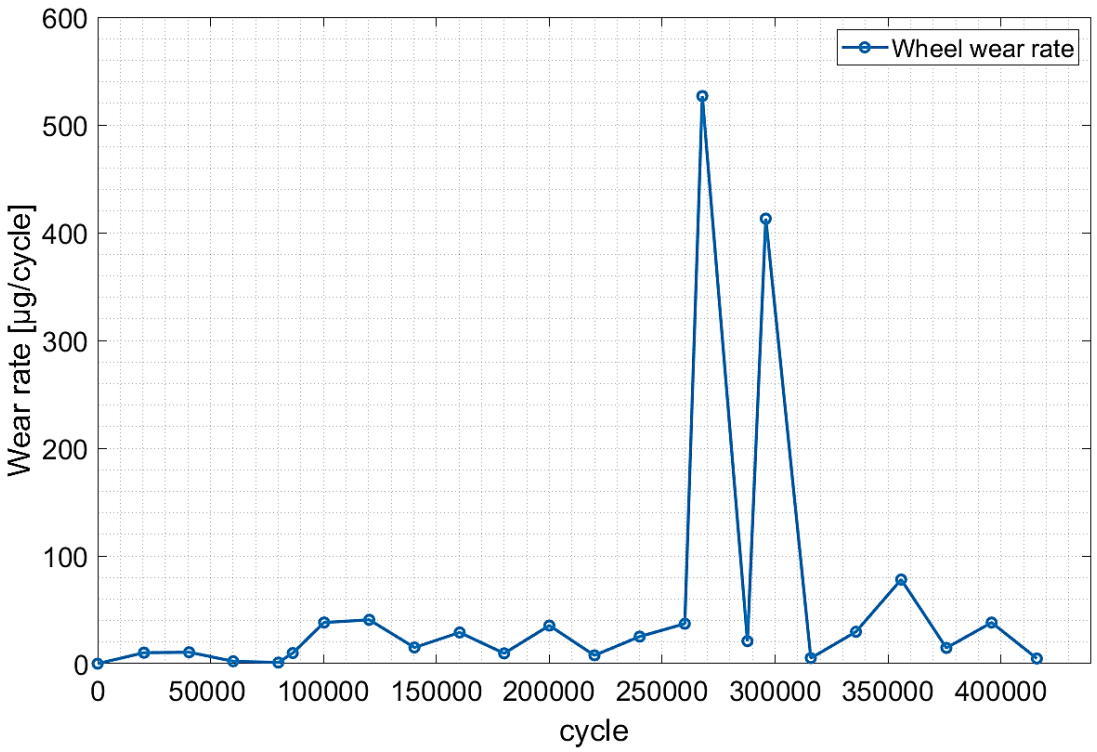

Fig. 4.5. (b)

Figure 4.5: Wear rate during the longevity test: (a) Laser clad rail disc; (b) R8 wheel disc

The laser clad rail disc experienced a peak in wear rate of almost 2.5 µg/cycle after 80,000 cycles before settling below 0.5 µg/cycle until a second lower maintained rise occurred at 280,000 cycles. This coincides with visible wear appearing on the rail disc surface around 300,000 cycles. The peak points also occurred because of the worn wheel discs and needed change the wheel discs. It is because wheel disc dimensions change after long number of cycles. This could be because the clad layer is starting to break down more, but the wear rate is still much lower than would be seen in unclad materials where wear rates of 13 µg/cycle would be expected for R260 after 30,000 cycles (Lewis et al., 2016).The exceptional peak at 80,000 cycles could have been due to an effect from the wheel disc deterioration.

To put this data into context, in a shorter test for an MSS clad layer on R260 rail for another project, the wear rate experienced a similar peak at 5,000 cycles and then the wear rate reached a steady state during the rest of the test until the end at 30,000 cycles, as can be seen in Figure 4.5(a) (Lewis et al., 2016).

The wear rate of the wheel disc similarly peaked after 280,000 cycles, reaching 520 µg/cycle having remained below 50 µg/cycle up to that point. The peaks occurred as the fatigue life of the wheel material was exhausted and gross flaking occurred.

4.3.4 Friction

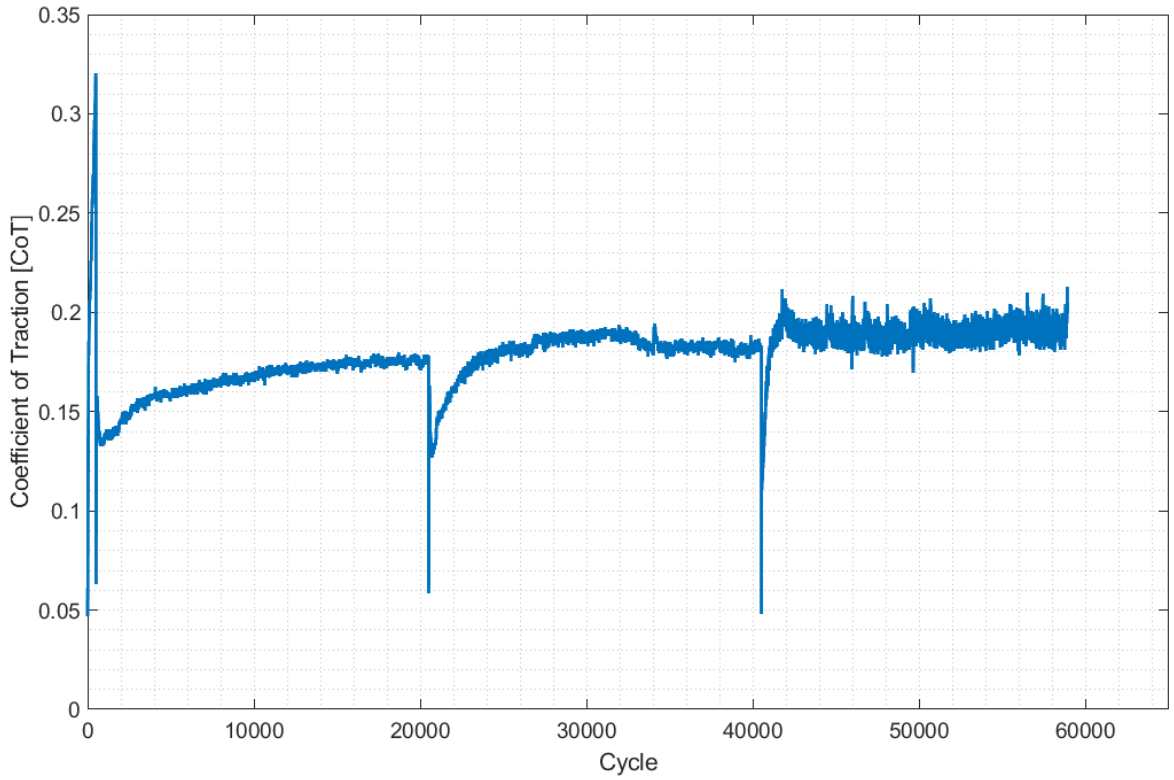

Figure 4.6: Coefficient of traction versus cycles on MSS clad long cycle tests

Figure 4.6 shows the coefficient of traction (CoT) versus cycles. The graph created covers the first 60,000 cycles, but it was the same data profile during the rest of the test. The test first started with 500 dry cycles and it can be seen that for this period there was higher friction than for the following blocks of cycles as they continued with water lubrication. The CoT value is around 0.2 during the water lubricated tests. Every 20,000 block of cycles experiment finished and mass loss and surface measurements were taken. That's why the data goes down suddenly between the 20,000 block of cycles due to the machine stopping and restarting.

4.3.5 Sub-surface

4.3.5.1 Subsurface Images

a) Before Etching

SEM images were taken to analyse the microstructure of the cladding and substrate parts. Figure 4.7a, shows the 1 mm MSS clad and the findings indicate that there is no deformation on the surface of the clad and the substrate material shows good bonding (Figure 4.7b and c) except for some very small inclusions in the clad and substrate region.

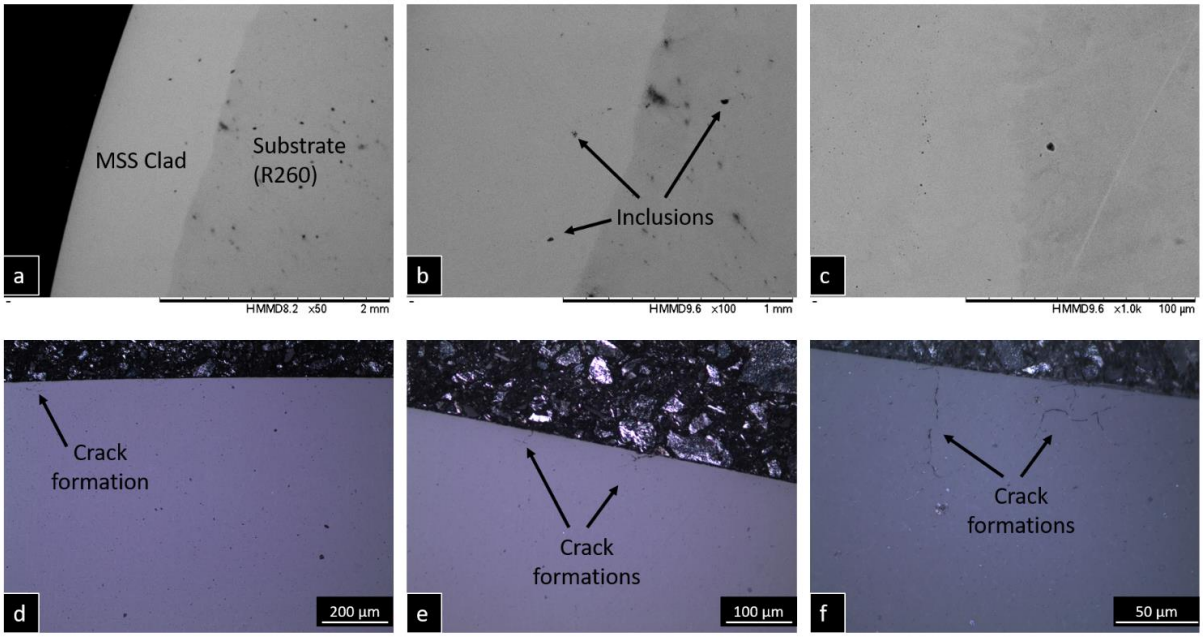

Figure 4.7: SEM and microscope images of MSS Clad rail discs:(a) MSS Clad and R260 Substrate; (b) Clad and substrate bonding; (c) Clad and substrate bonding with diffusion zone; (d) Microscope image showing some small cracks; (e) Microscope image of some small cracks in surface with higher magnification; (f) Microscope image of crack growth from surface with higher magnification

Figures 4.7 d, e and f show the MSS clad rail disc with different magnifications from microscope. In the image in Figure 4.7c, the full clad and substrate regions can be seen, and it shows that there is small deformation on the surface. Furthermore, other images (e and f) show small cracks on the surface of the clad rail from surface to the clad with higher magnifications. On image f, intergranular shapes of the crack from the surface can be seen.

b) After Etching

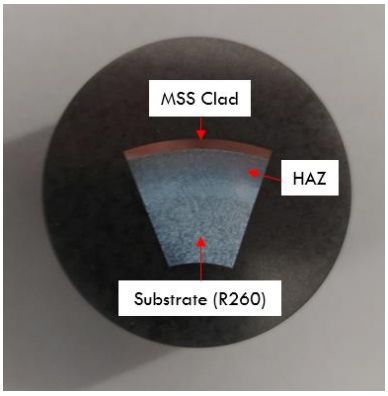

Figure 4.8: Disc surface after etching with clad part

Figure 4.8 shows the clad sample after etching the substrate part. The shiny part of the sample is the MSS clad. It needed to be etched with a different etchant, so nothing is visible of its microstructure here. For exposing the substrate microstructure, a 2% Nital solution was used.

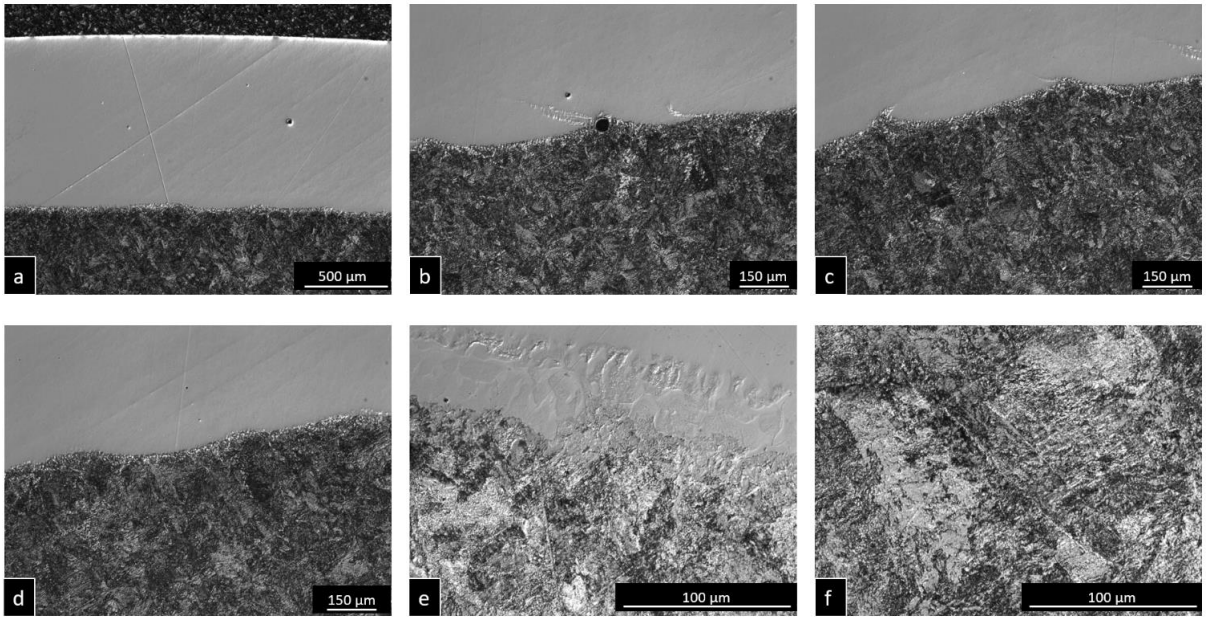

Figure 4.9: Clad rail substrate microstructure after etching with Nital solution at different magnifications of the microscope images.

In Figure 4.9 clad samples after etching of the substrate part are shown at different magnifications. Images b, c and d show the bond between the clad and substrate. Only in image b an inclusion can be seen. It shows good bonding though. Image e shows bonding and diffusion zone with higher magnification.

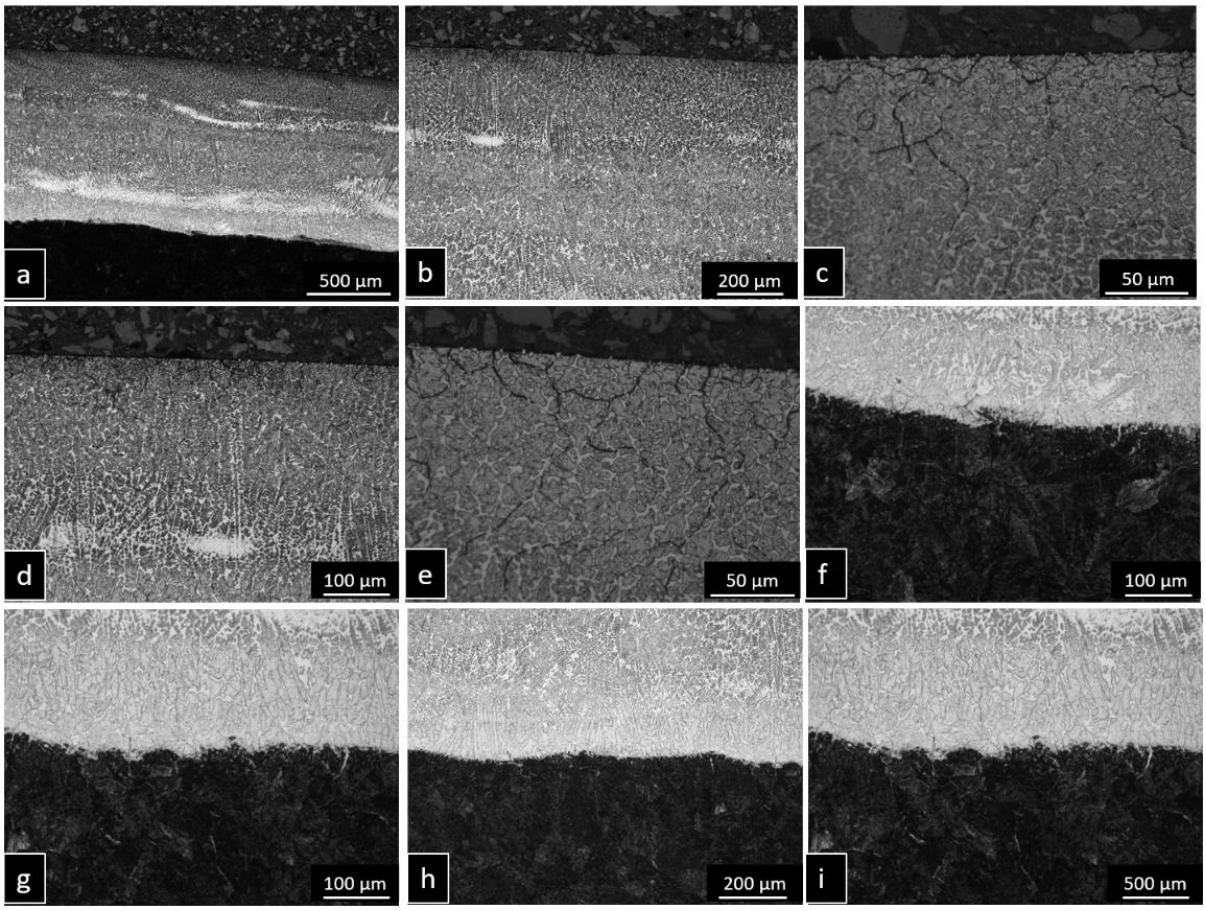

Figure 4.10: Martensitic Stainless Steel [MSS] clad microstructure after etching.

Figure 4.10 shows the MSS clad microstructure, and some small cracks can be seen on the surface. Also, in the images the bonding can be seen. The substrate part is now over etched because of the clad part etchant is stronger that the Nital used for this area.

4.3.5.2 Micro Hardness

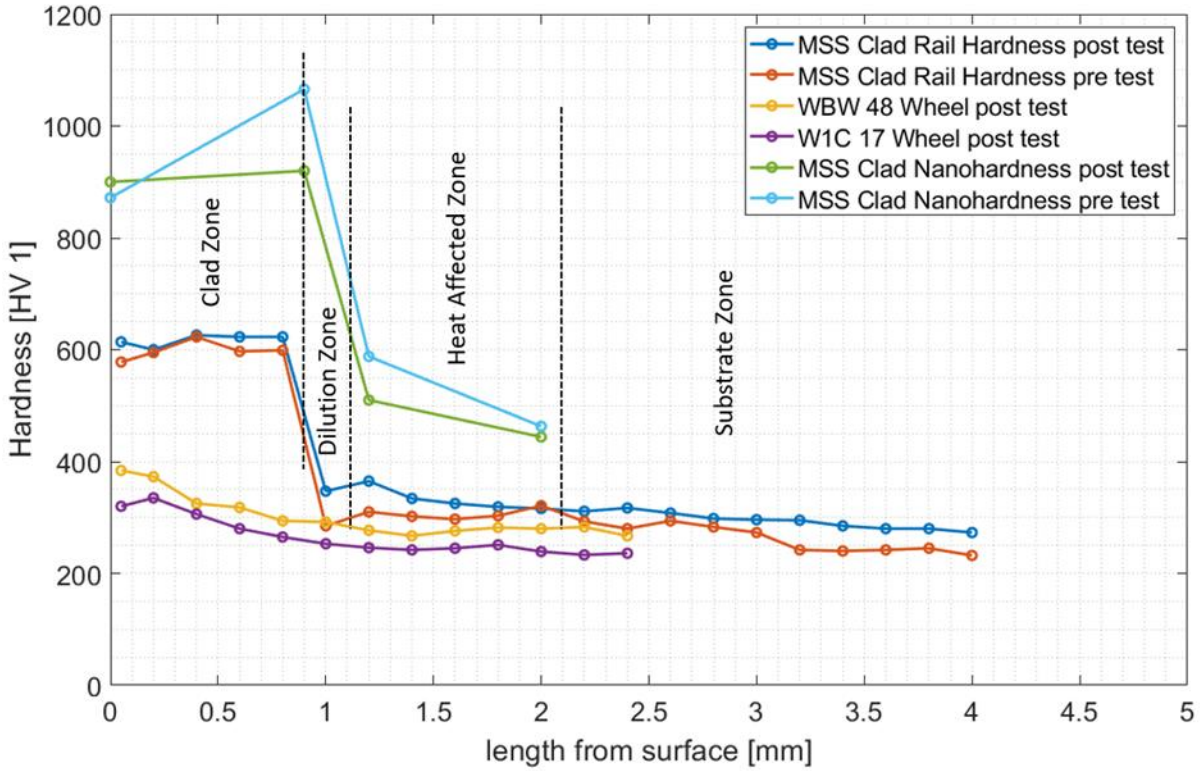

Figure 4.11: MSS clad tests hardness graphs of MSS clad disc, WBW 48 and W1C 17 wheel discs

Hardness values shown in Figure 4.11 have been plotted from the surface of the clad rail disc and two (out of the total) wheel discs after testing. The graph shows the nano-hardness and micro-hardness values from clad disc and wheel discs were measured by micro-hardness tester. Nano-hardness values are higher than micro-hardness data. The first surface first point was measured by nano-indenter because the micro-hardness tester does not allow measurements close the surface. The surface hardness is 1020 HV depending on the nano-hardness tester and micro-hardness value is the 630 HV close the surface point. Care must be taken with interpreting the nano-hardness value as typically values from nano-indentation are higher than the micro-hardness values by about 30% (Qian et al., 2005). They explain that the main reason for that is nano-indentations use the projected contact area at peak load, however, micro-hardness uses residual projected area.

After the 1 mm clad zone, hardness decreased sharply as the heat affected zone in the substrate material is softer and it decreases to around 350 Hv. Then it continues to decrease gradually to 300 Hv into the bulk. In those parts of the disc shows 20%-30% higher values depending on the nano-hardness data.

The wheel disc WBW 48 hardness decreases gradually from 380 Hv to 300 Hv and the W1C 17 hardness decreases from around 350 Hv to 240 Hv. Typically, the surfaces of the wheel material would work-harden to a higher value in dry conditions (580Hv), but the shear stress is lower in the predominantly wet test here so the work hardening effect was diminished (Lewis et al., 2019).

4.3.5.3 Nano Hardness

MSS Clad Surface

Figure 4.12 shows MSS clad surface nano-hardness data. The left-hand image shows 10x10 nanoindentation points. The centre image shows the nano-hardness plot and the right plot shows the reduced modulus data points. The average hardness at the surface of the MSS clad is around 8.84 GPa and approximately 900 HV and reduced modulus is 220 GPa. However the closest point of the surface indentation shows the hardness values to be10GPa.

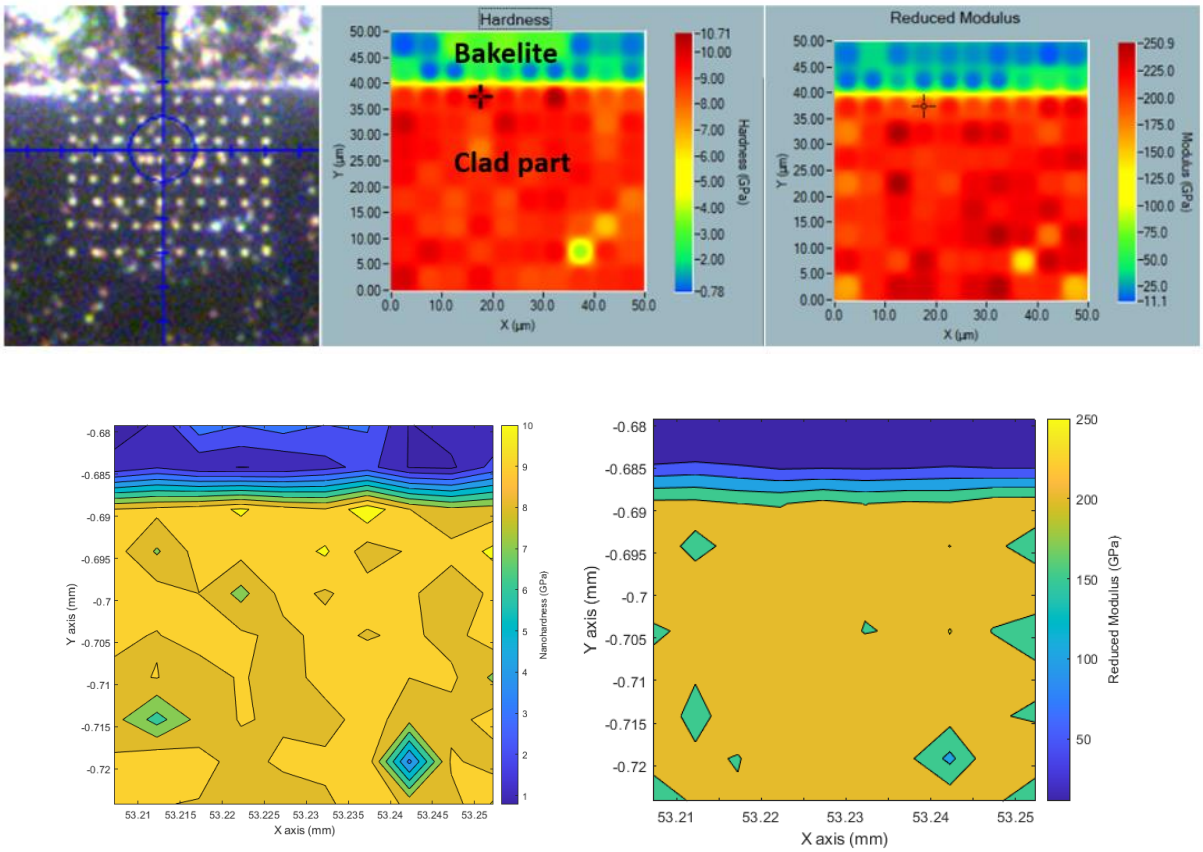

Fig. 4.12. (a)

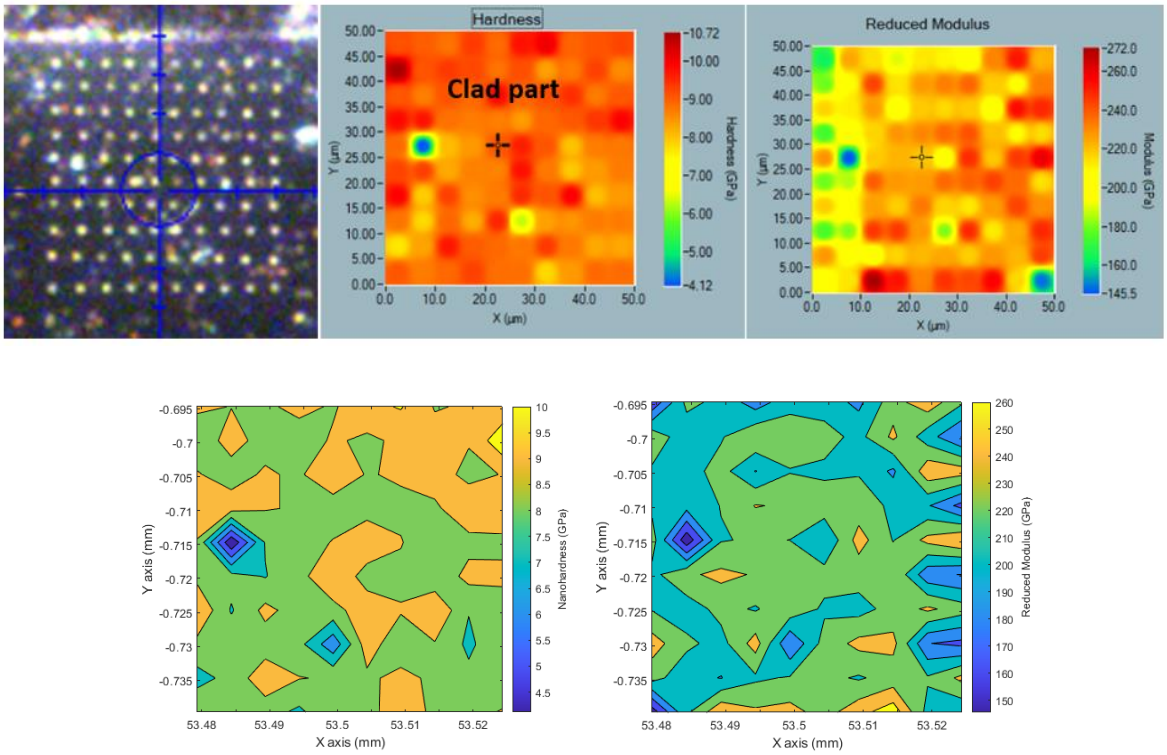

Fig. 4.12. (b)

Figure 4.12: Nano-hardness measurements of the clad rail disc surface zone: (a) Clad surface to Bakelite mounted part indentation; (b) Only clad zone under the surface.

Clad to Substrate Transition Zone (Dilution Zone)

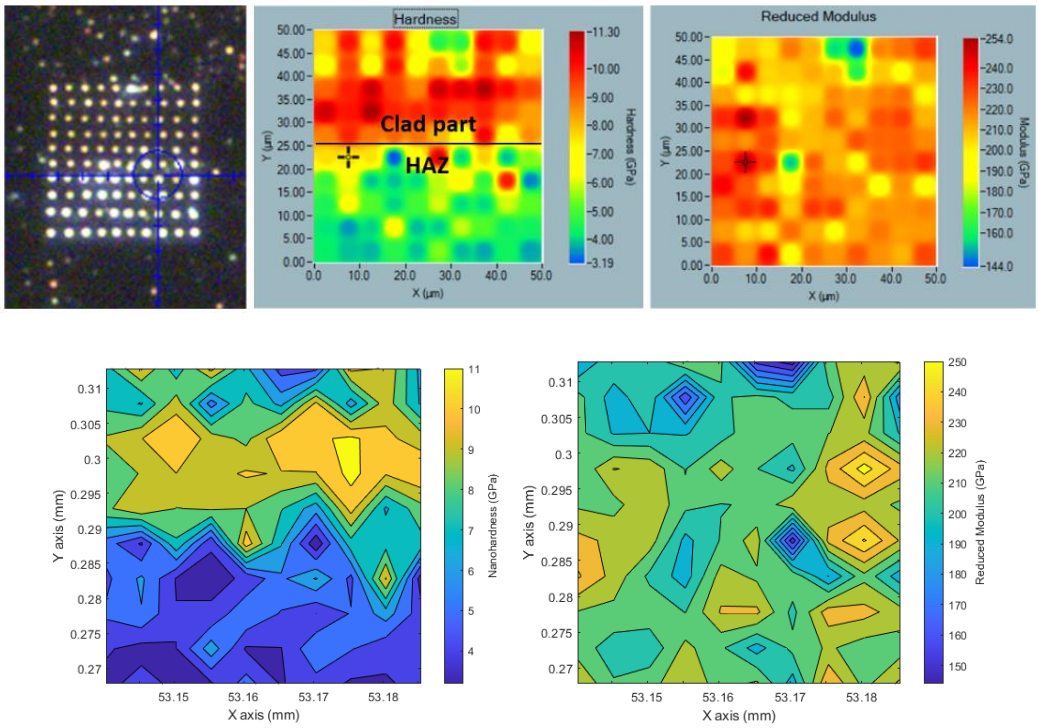

Figure 4.13: Nano-hardness measurements of the clad rail disc clad zone substrate transition zone

Figure 4.13 shows MSS clad to heat affected zone (HAZ) data. On the left-hand side the 10x10 nano-indentation points can be seen. The middle plot shows nano-hardness data and the right hand plot the reduced modulus data. The hardness is around 9 GPa and approximately 920 HV on the transition edge and HAZ hardness is around 5 GPa and approximately 510 HV. The reduced modulus is similar both clad and substrate zone and it is around 215 GPa.

Substrate (HAZ)

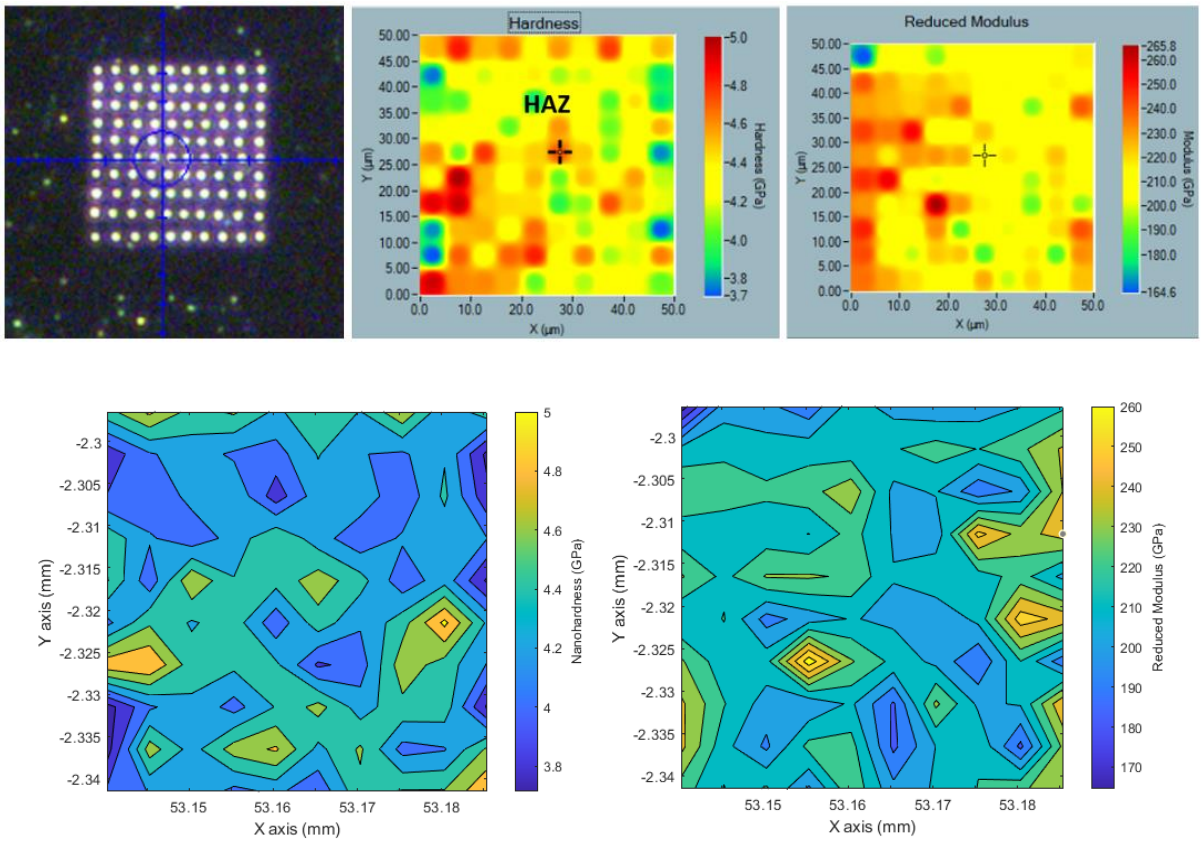

Figure 4.14: Nano-hardness measurements of the clad rail disc substrate zone.

Figure 4.14 shows the nano-hardness data for the substrate part of the disc. The left hand image shows 10x10 nano-indentation points and in the middle the nano-hardness plot can be seen and on the right hand side the reduced modulus data points can be seen. Substrate nano-hardness average is around 4.35 GPa and approximately 444 HV. Average reduced modulus is around 217 GPa.

4.4 Discussions

The long RCF MSS clad rail disc tests showed good performances after 400,000 cycles of loading. Typically, R260 rail would fail at 20,000 to 30,000 cycles (Lewis et al., 2015). The wheel material failure was at around this point which is why so many wheel discs were used. The test was expected to identify a clad layer failure point, but the tests showed it still needs more cycles. Wear rate and roughness values showed MSS clad rail disc has high capabilities and less damage by many times over unclad material.

The roughness and wear measurements in the longevity tests indicate a change in performance after around 260,000 cycles. Visually the surface change was observed after 400,000 cycles. This could be due to the clad layer starting to degrade, but the level of wear is still below what would be expected for an unclad material. It could also be related to changes in wheel material behaviour. Also, in Figure 4.3 shows that the surface material is not deforming and reaching its ratchetting strain limit after the surface evaluations. Clearly there is some abrasive wear occurring, perhaps promoted by the wheel wear debris trapped in the contact. To put this into context, R260 grade rail material tested under the same conditions would show significant damage after 15-30,000 cycles (Franklin et al., 2005; Lewis et al., 2015, 2016). This also explains why the wheel discs needed replacing often during the test.

Figure 4.4 shows higher Ra values after 200,000 cycles and it could also be from previous wear scratch images in Figure 4.3, after 200,000 cycles wear scratches are seen more on the images of the surface. Lu et al. (2018) shows that unclad R260 roughness values are higher than 6 µm after 30,000 cycles of a test so these values are relatively very low.

Wear rates in Figure 4.6 a) shows higher peak after 280,000 cycles and this could be because the clad layer is starting to break down more, but the wear rate is still much lower than would be seen in unclad materials where wear rates of 13 µg/cycle would be expected for R260 after 30,000 cycles (Lewis et al., 2016b).The exceptional peak at 80,000 cycles could have been due to an effect from the wheel disc deterioration.

To put this data into context, in a shorter test for an MSS clad layer on R260 rail for another project, the wear rate experienced a similar peak at 5,000 cycles and then the wear rate reached a steady state during the rest of the test until the end at 30,000 cycles, as can be seen in Figure 4.6(a) (Lewis et al., 2015).

The lighter bands in Figure 4.11(a) could be either a microsegregation or a HAZ in the molten metal originating from the heat of the next clad pass. Another hypothesis is that only the HAZ

exists in the molten zone: this may be because the interface region has the highest cooling rate of the HAZ. Thus, there may be a region with less mobility of solutes by diffusion and a more uniform martensite chemical composition, which needed more time to develop the partitions.

Figure 4.11 (b) and (d) shows interdentritic phases and these may indicate that: either there is a diffusion of some elements (mainly the carbon) into the molten metal, or the cooling rate did not let another phase form, or both.

Figure 4.12 shows the hardness measurements and first point of the clad surface hardness measured by the nano harness tester. It shows high hardness values after the experiments, and it is around 1020HV and then clad surface shows the hardness values around 600HV and between clad and substrate zone there are dilution and HAZ. In the HAZ, hardness goes around between 350-450 HV values when compared to nano and micro hardness data. At the substrate part of the disc shows around 280-300 HV values depending on the micro-hardness values.

Subsurface images show no more damages on the microstructure of the clad disc. Figure 4.11 shows, there are some small crack initiation points on the microscope images, but no plastic deformation on the surface and microstructure of the disc.

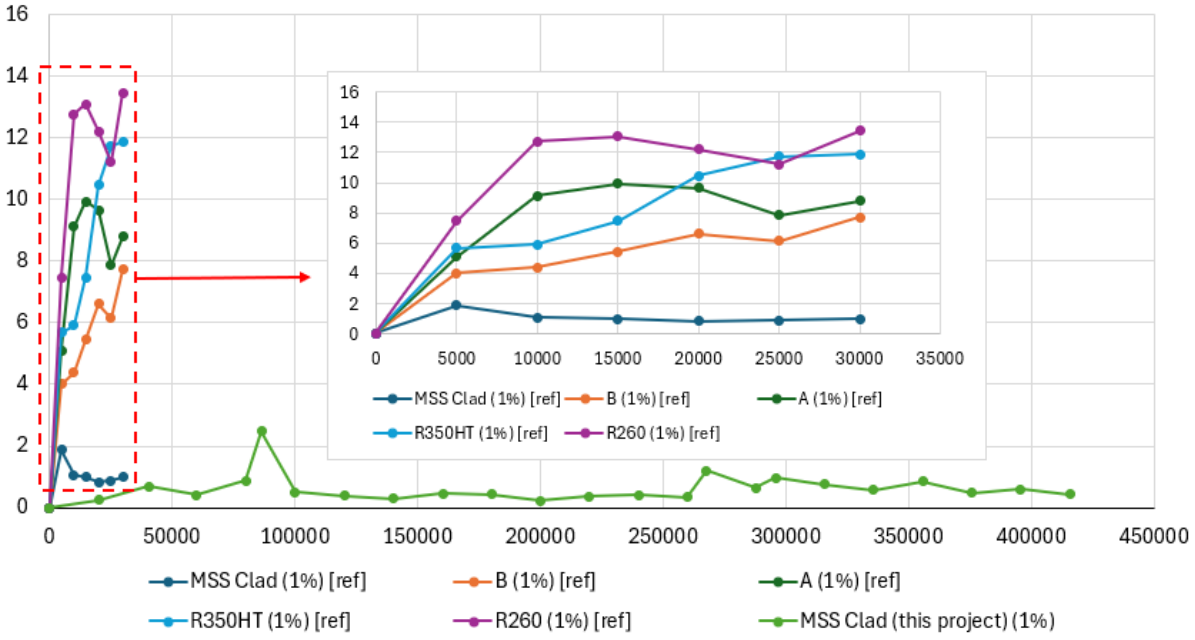

Figure 4.15: Rail wear rate per cycle at 1% 1500 MPa contact pressure and 400 rpm primary rotational speed dry condition (Christoforou et al., 2019).

The clad rail showed relatively lower wear rates when compared to the R260 rail wear rate, shown in Figure 4.15. The highest wear rate of the R260 is around 13 µg/cycle and MSS clad

test wear rate is around 1 µg/cycle. On this research it is found around 0.5 µg/cycle and the maximum wear rate was 2.5 µg/cycle there see (Fig 4.5(a)). When compared to the two data points, it showed a bigger difference on wear rates for R260 and MSS clad rail. MSS clad showed better wear resistance.

4.5 Conclusion

MSS clad rail twin disc experiments were carried out for more than 400,000 cycles and the clad layer did not fail. After the testing it still showed good wear resistance.

The clad sample were analysed after extensive testing. Wear rates of the MSS clad test showed much lower values than R260 normal grade rail wear rate.

When the test was reaching its end after 420,000 cycles some wear scratches occurred, but it did not show high roughness on the rail surfaces.

MSS clad layers and substrate part showed good bonding from laser cladding. After the test it did not show any failure signs on the bonding parts. Microstructural images showed some small crack initiation or flake formation points from the contact surface of the rail.

Chapter 5

5 Tribological Assessment of the Use of Laser Cladding for Repair

5.1 Test Apparatus

Repair tests were applied on the twin disc the Sheffield University Rolling Sliding (SUROS) test rig as described in section 3.4.1.1. Wear and RCF experiments were carried out on twin disc specimens with simulated repairs. A line contact is used between twin-disc test specimens on this machine to simulate the normal load and rolling-sliding performance at the wheel/rail interface.

5.2 Measurement of the Repair Discs Cladded with MSS, Stellite 6 and R260

The clad repair rail discs and wheel discs were weighed, and their diameters were measured before the start of the test and recorded. Before and after the measurements discs were cleaned with acetone.

For dry tests, the test was paused after 1,000, 5,000, 10,000 cycles, and then after further blocks of 10,000 cycles until the end of the test. Between each block of cycles, the test rig was stopped and the discs were weighed, and diameters and surface properties were measured.

For the water lubricated tests, the first test cycle block was 500 dry cycles were run and then 15,000 cycles were run with distilled water addition at 1 drip per second in blocks of 5,000 cycles. Again between blocks of cycles, the test rig was stopped and the disc was weighed, and diameters and surface properties were measured.

Room temperature and humidity were recorded as well for all blocks of cycles. After that, rail surfaces were examined using an optical (non-contact) Alicona Infinite-Focus SL profilometer. The profilometer gives the chance to obtain high-resolution images and 3D surface profile measurements with a vertical resolution of up to 10 nm. Surface roughness' was recorded from the Alicona scans. This process was followed for all blocks of cycles.

Microstructure of the samples were examined at the end of each test after sectioning, mounting, grinding, polishing and etching. Also, hardness was measured by using a micro-hardness tester.

5.3 Test Conditions

Table 5.1: Repair small scale twin disc test conditions

Test Type	Total Number of Cycles	Contact Pressure	Slip
All dry contact	50,000	900 MPa	0.5%
500 dry cycles + water lubricated contact until end	15,500	900 MPa	0.5%
All dry contact	50,000	1500 MPa	1%
500 dry cycles + water lubricated contact until end	15,500	1500 MPa	1%
All dry contact	20,000	1500 MPa	3%
All dry contact	20,000	1800 MPa	1%

Test conditions were varied to simulate different wheel/rail contact scenarios. 900 MPa and 0.5% slip were used to represent top-of-rail/wheel tread conditions. 1500 MPa and 1 or 3% slip and 1800 MPa and 1% slip were used to represent rail gauge corner/wheel flange conditions. Dry tests were started with 1000 cycles first then a further 4,000 cycles, following this, 5,000 cycles and then 10,000 cycles in each test were carried out until 50,000 cycles were achieved for the dry tests at 900 MPa. Higher stress tests were run for 20,000 cycles.

Wet tests were conducted with distilled water. 1500 MPa contact stress and 1% slip values were used with water lubrication. These tests were started with 500 non-lubricated cycles to initiate cracks as used in previous RCF tests on the disc (Lewis et al., 2016). Then distilled water was added to accelerate crack growth (through crack pressurisation and reduction of crack face friction) until tests reached 15,000 cycles (in 5,000 cycles blocks).

5.4 Test Specimens

5.4.1 Materials

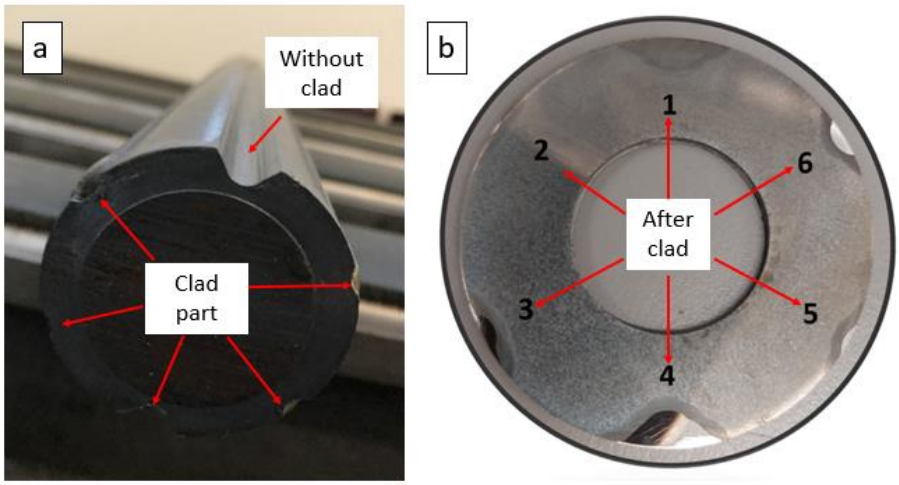

Figure 5.1: a) Repair bar before cladded all parts and sectioned; b) repair clad disc after etching to show clad parts

Figure 5.1 shows the repair bar with clad and one empty slot without clad. After the clad process, all slots filled with clad materials as can be seen in the Figure 5.1 with numbers of clad. Six slots with different widths and depths were cut on a cylinder of R260 rail head material for the cladding process (as shown in Figure 5.1 a) depending on aim of the deep, moderate and shallow repairs.

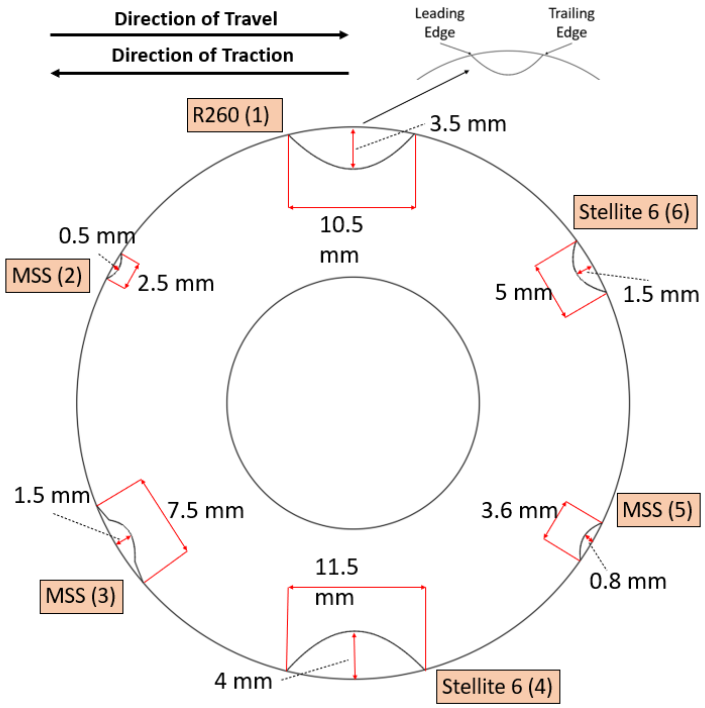

Figure 5.2: Repair bar showing laser-clad slots and schematic of the repair disc.

Figure 5.2 shows the schematic of the cladded repair disc.The repair bar specimen slots were filled with 3 different materials: Stellite 6 (2 slots), MSS (3 slots) and R260 grade material (1 slot) (the same material as the substrate) by laser cladding. One step laser cladding by powder injection were used to fill repair slots on the repair bar. Table 5.2 gives details chemical compositions of the materials used. The "repairs" were evaluated with pre and post-test measurements. The aim was to assess the potential for in-situ repair with laser cladding.

Table 5.2: Chemical compositions (%by mass) of E8 wheel, R260 rail, MSS, and Stellite 6 and T400 clad materials

	C	Mn	Si	Cr	Ni	Mo	Co	V	W	N	Al	S	P
R260	0.74	1.08	0.31	0.040	-	-	-	0.004	-	-	0.003	0.018	0.013
MSS	0.06	1.22	0.46	14.64	3.31	0.42	2.01	0.51	0.62	0.04	0.01	0.005	0.009
St. 6	1.0	<0.1	0.9	27.0	-	-	Bal	-	4	-	-	-	-
E8	0.542	0.734	0.253	0.141	0.120	0.048	-	0.006	-	-	-	0.006	0.011

5.5 Results

5.5.1 Surface Evaluations

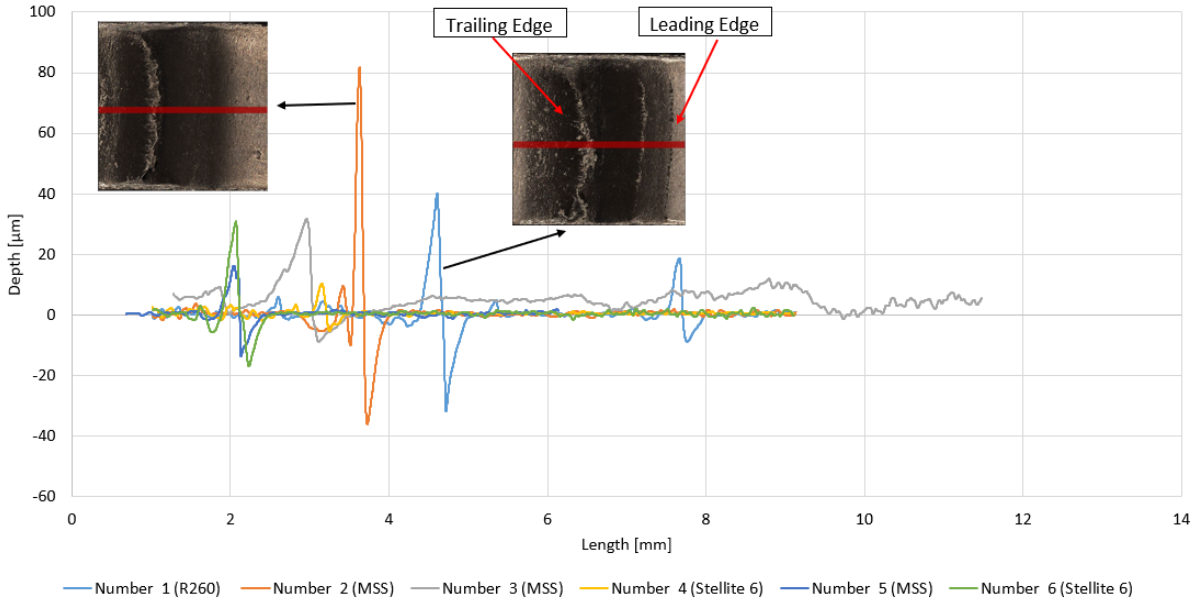

Figure 5.3: Roughness profile comparisons between different transition points for 900MPa, 0.5% slip dry test after 40,000 cycles

Figure 5.3 shows the 900 MPa, 0.5% slip dry repair test roughness profile comparisons for transitions when material flow over clad part after 40,000 cycles with supporting images added for number 1 (R260 clad) and number 2 (MSS clad) showing where and why the roughness profile peaks occured. The peak points of the graphs are where the R260 material flows over

the clad region. Number 2 showed the highest point at around 80 µm. The peak points and clad parts changed depending on the clad widths on the discs. Other roughness profile image matches can be seen in Appendix 5.B. These peaks on the graph occurred because of the substrate material flowed over the clad repair parts. The peaks that occurred were higher in the trailing edges of clad parts than the leading edges.

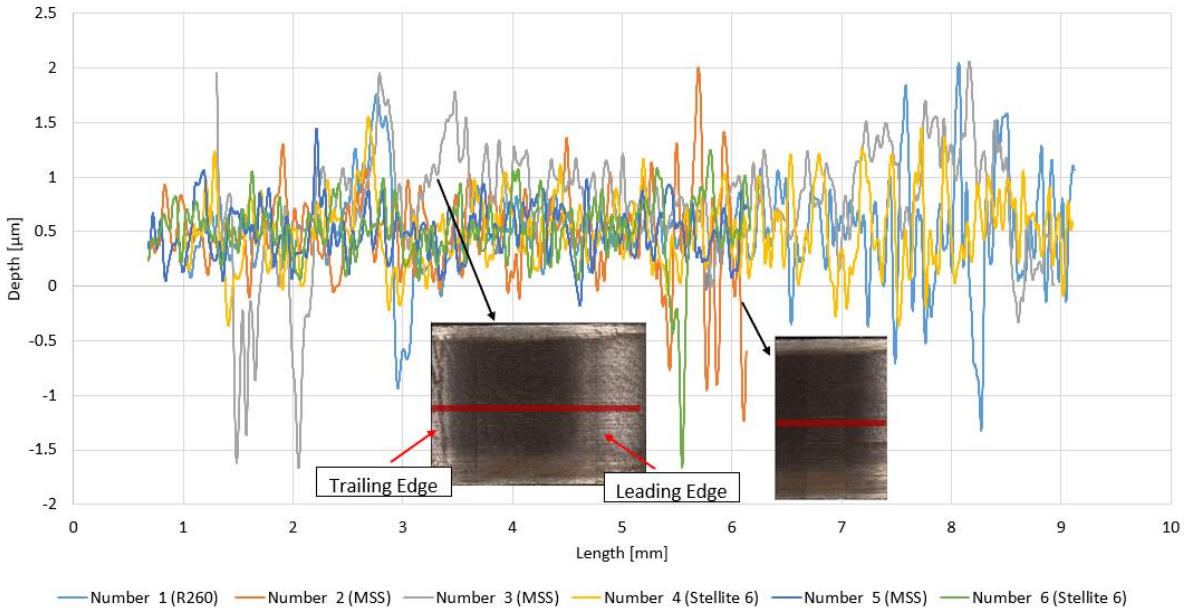

Figure 5.4: Roughness profile comparisons between different transition points for the 900MPa, 0.5% slip water lubricated test after 10,000 cycles

Figure 5.4 shows the 900 MPa, 0.5% slip water lubricated repair test roughness profile comparisons after 10,000 cycles and supporting images of the number 2 (MSS clad) and number 3 (MSS clad) transitions. Roughness profiles were smoother and did not have big peak points because of the lower friction, which led to less deformation/flow of material, when using water which acted as a lubricant. Number 3 profile shows different limits than other and it can be due to the shape of the repair slot and also that profile seems higher than other profiles because of the height difference of disc holder. Figure 5.1 shows all repair slots and only number 3 has different shape than others.

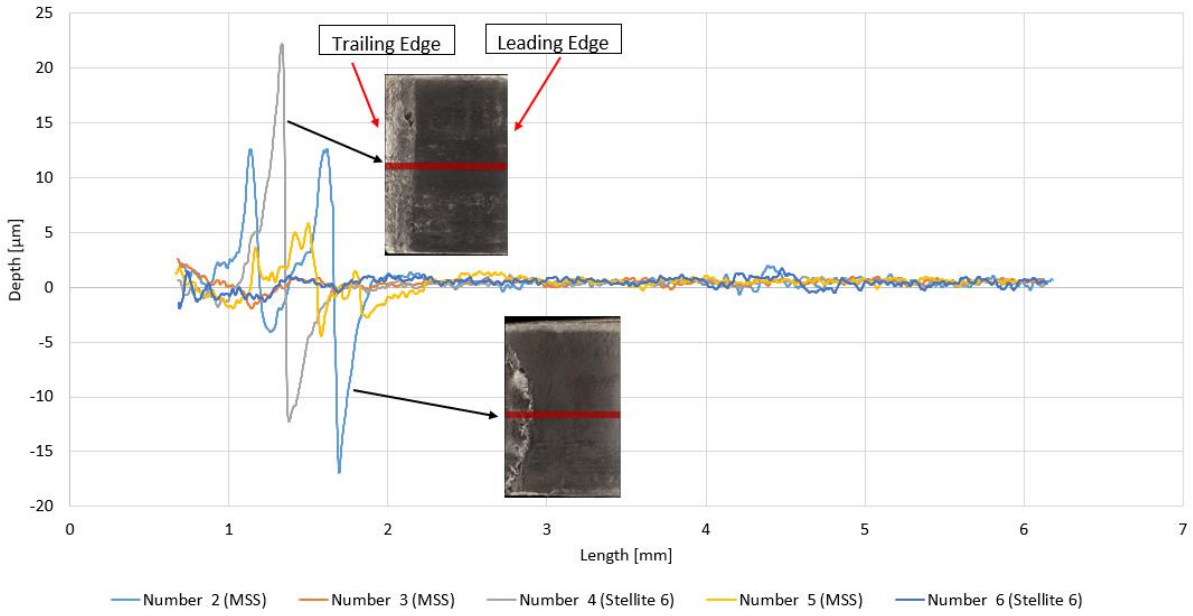

Figure 5.5: Roughness profile comparisons between different transition points for the 1500 MPa, 1% slip dry test after 10,000 cycles

Figure 5.5 shows the 1500 MPa, 1% slip dry repair test roughness profile comparisons after 50,000 cycles and supporting images for the number 2 (MSS clad) and number 4 (Stellite 6 clad) at roughness profile peaks. The peak points of the graphs show the R260 material flow over clad parts. Number 2 showed the lowest point at around -16 µm and number 4 showed the highest peak point at 22 µm.

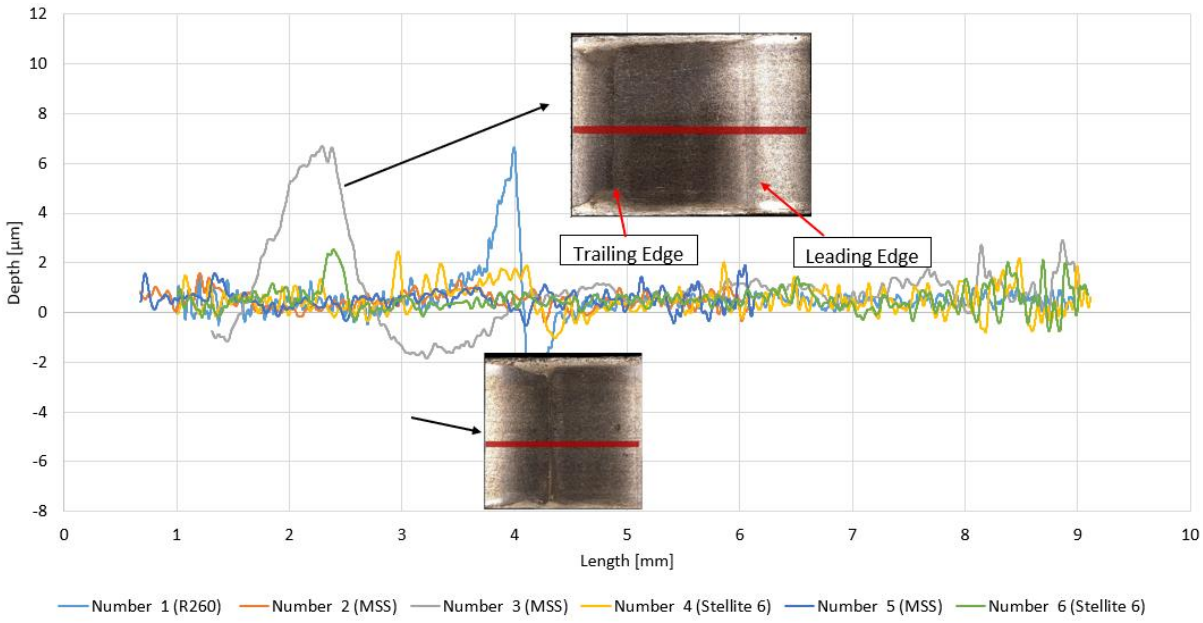

Figure 5.6: Roughness profile comparisons between different transition points for the 1500MPa, 1% slip water lubricated test after 10,000 cycles

Figure 5.6 shows the 1500 MPa, 1% slip water lubricated repair test roughness profile comparisons after 10,000 cycles and supporting images for the number 1 (R260 clad) and number 3 (MSS clad). Roughness profiles did not have big peak points because using water reduce the shear and therefore the material flow. Number 1 and number 3 though were an exception. Number 1 had the lowest point with -6 µm. Number 3 profile shows different limits than other and it can be due to the shape of the repair slot and also that profile seems higher than other profiles because of the height difference of disc holder. Figure 5.1 shows all repair slots and only number 3 has different shape than others.

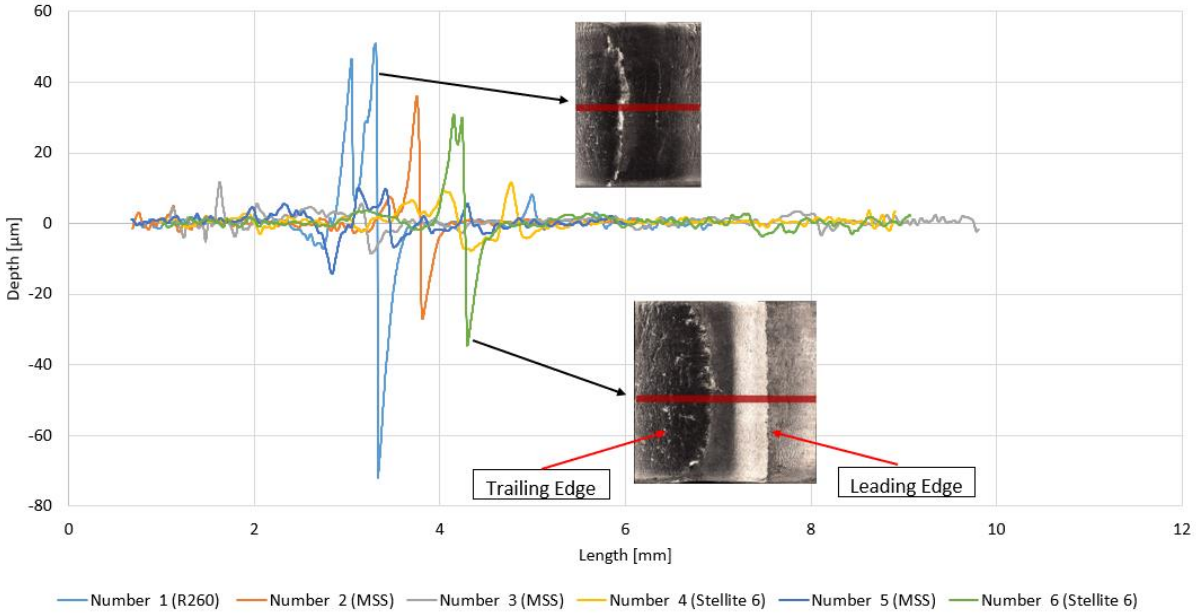

Figure 5.7: Roughness profile comparisons between different transition points for the 1500 MPa, 3% slip dry test after 20,000 cycles

Figure 5.7 shows the 1500 MPa 3% slip dry repair test roughness profile comparisons after 20,000 cycles and supporting images for the number 1 (R260 clad) and number 6 (Stellite 6 clad). The peak points of the graphs show R260 the material flow points over the clad parts. Number 1 showed the lowest and highest points with around -70 µm and 50 µm respectively. Number 2 and number 6 showed signs of material flow with the peak points.

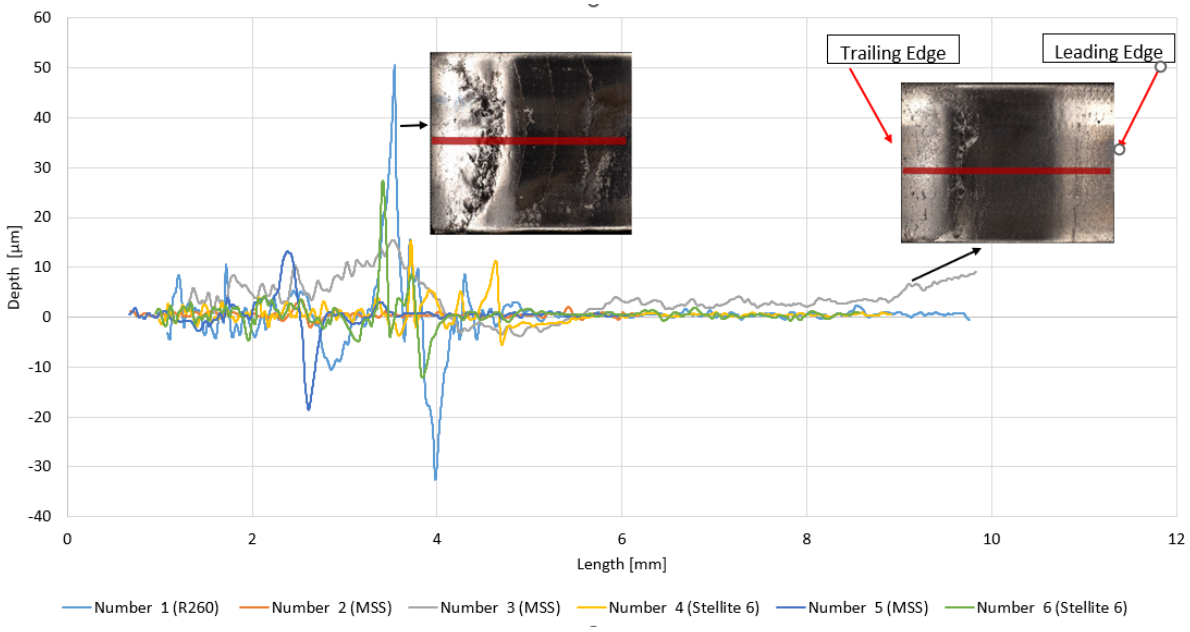

Figure 5.8: Roughness profile comparisons between different transition points for the 1800 MPa, 1% slip dry test after 20,000 cycles

Figure 5.8 shows the 1800 MPa, 1% slip dry repair test roughness profile comparisons after 20,000 cycles and supporting images for the number 1 (R260 clad) and number 3 (MSS clad). The peak points of the graphs show the R260 material flow points over the clad parts. Number 1 showed the lowest and highest points with around -30 µm and 50 µm respectively. Number 3 showed signs of material flow with peak points.

5.5.2 Roughness

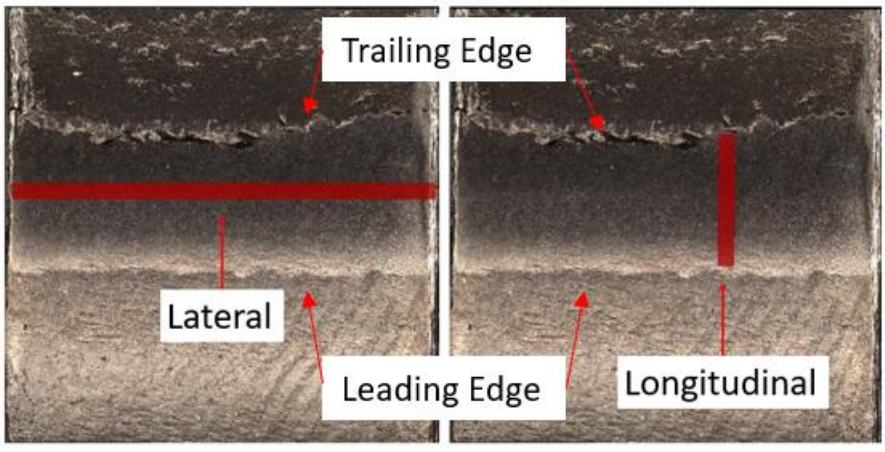

Figure 5.9: Roughness measurements directions for the clad parts of the discs (example from number 6 clad) .

Figure 5.9 shows the measurement direction of the clad discs in lateral (across the disc contact surface) and longitudinal (along the surface in the rolling direction) directions. All

measurements were taken from the clad regions and values of the most typically used parameter, Ra, were recorded. Corresponding wheel disc roughness values are also shown.

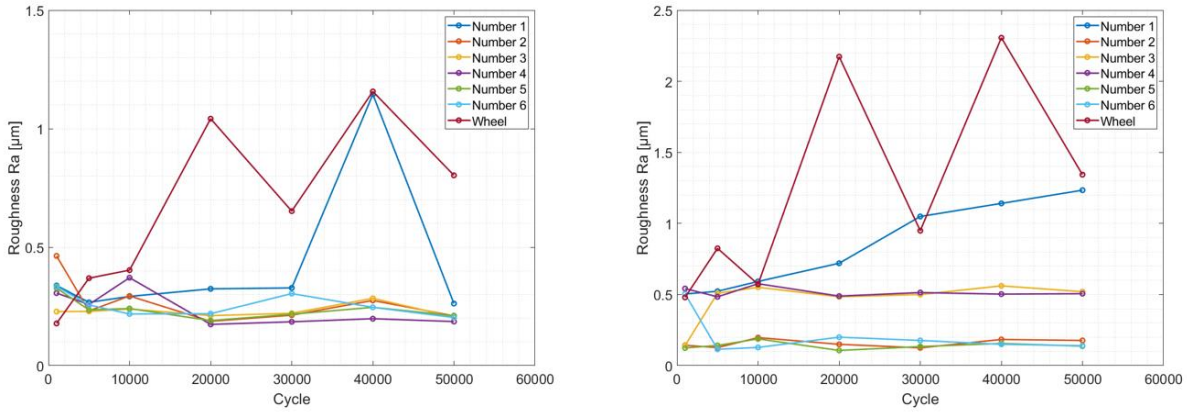

Figure 5.10: 900 MPa, 0.5% slip dry test roughness values in: (a) lateral and (b)longitudinal directions

Figure 5.10 shows 900 MPa, 0.5% slip dry test roughness graphs in lateral and longitudinal directions against number of cycles. Lateral roughness values show wheel roughness was the highest and number 1 (R260 clad) roughness showed the highest point after 40,000 cycles. Other clad materials showed values between 0.2 to 0.4 µm. Longitudinal roughness values show number 1 had the highest value between clad materials with a value of around 1 µm after 50,000 cycles. The wheel showed the highest value between all.

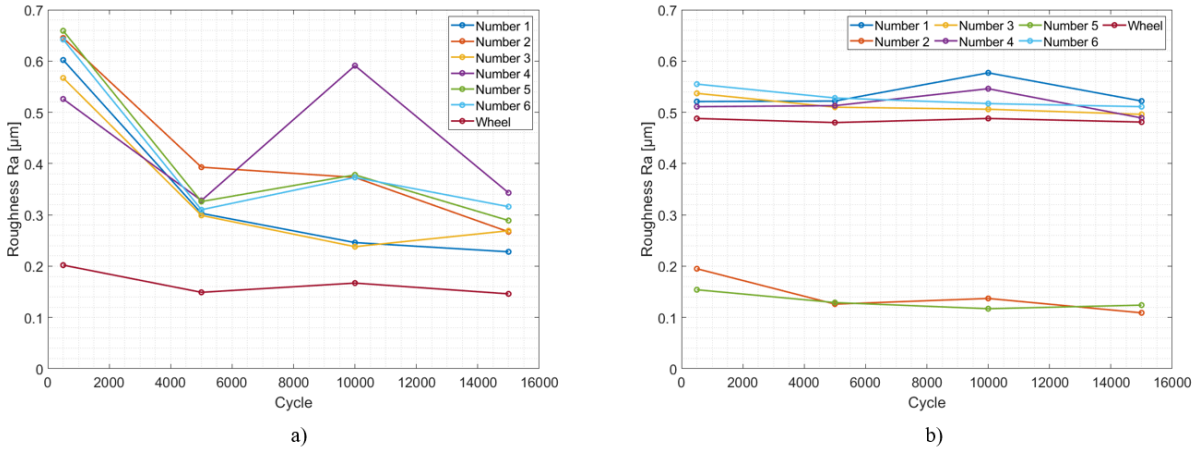

Figure 5.11: 900 MPa 0.5% slip test (wet) roughness values in: (a) lateral and (b) longitudinal directions

Figure 5.11 shows 900 MPa, 0.5% slip water lubricated test roughness graphs in lateral and longitudinal directions against number of cycles. Lateral roughness values show a decrease from 1,000 cycles with 0.5-0.7 µm values to 15,000 cycles with 0.2-0.4 µm values except for number 4 at 10,000 cycles with a value of 0.6 µm. The wheel lateral roughness value was the

lowest between 0.1-0.2 µm during the test. The longitudinal direction of measurements showed 2 groups. Number 2 (MSS clad) and number 5 (MSS clad) parts showed the lowest values around 0.1 µm while others all showed values between 0.5-0.6 µm.

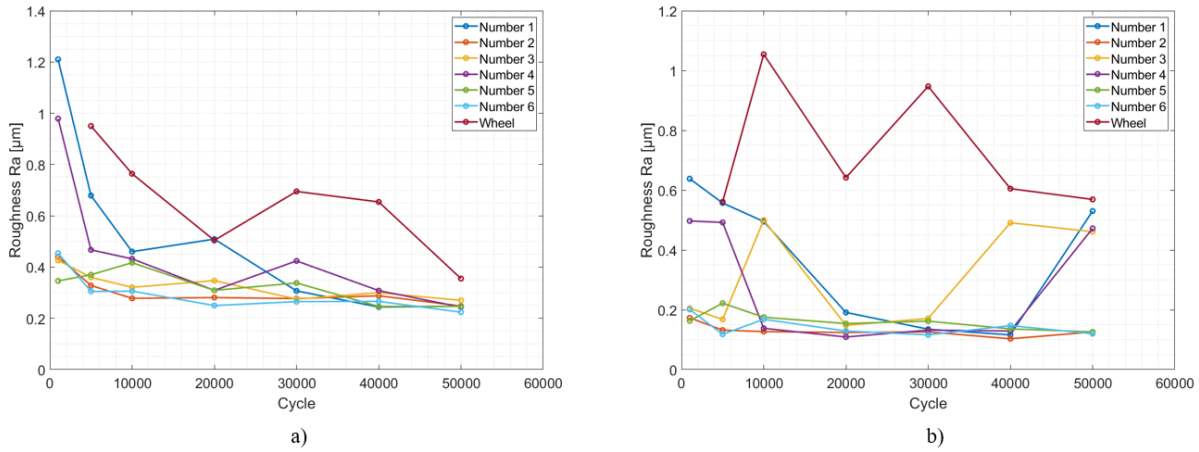

Figure 5.12: 1500 MPa, 1% slip dry test roughness values in: (a) lateral and (b) longitudinal directions

Figure 5.12 shows 1500 MPa, 1% slip dry test roughness graphs in the lateral and longitudinal directions against number of cycles. Lateral roughness values show a decrease until the end of the test and the highest decrease happens in number 1 (R260 clad) which goes from 1.2 to 0.3 µm. Number 4 (Stellite 6 clad) showed a similar decrease from 1 µm to 0.3 µm from 1000 cycles to 50,000 cycles. Other clad materials showed values around 0.4 µm. Wheel roughness also decreased except at 30,000 cycles and 40,000 cycles, to around 0.7 µm. Longitudinal roughness values show number 1 had the highest value between clad materials reaching around 0.6 µm after 1,000 cycles. At the end of the tests, number 2 (MSS clad) and number 6 (Stellite 6 clad) showed the lowest Ra values at around 0.1 µm. The wheel showed the highest value with 1 µm after 10,000 cycles.

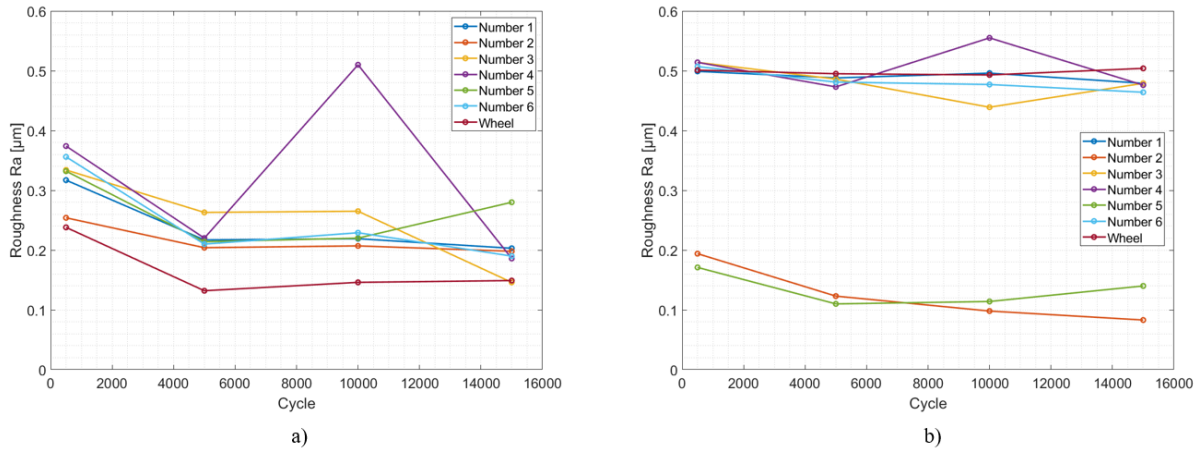

Figure 5.13: 1500 MPa, 1% slip test (wet) roughness values in: (a) lateral and (b) longitudinal directions

Figure 5.13 shows 1500MPa, 1% slip water lubricated test roughness graphs in lateral and longitudinal directions against number of cycles. Lateral roughness values show a decrease from 1,000 cycles to 15,000 cycles except for number 4 at 10,000 cycles which rose to 0.5 µm. Number 1 (R260 clad) and wheel roughness values showed a slight increase from 10,000 cycles to 15,000 cycles. Wheel lateral roughness values were the lowest at 0.1-0.25 µm during the test. The longitudinal direction of measurements showed 2 groups. Number 2 (MSS clad) and Number 5 (MSS clad) parts showed the lowest values at around 0.1-0.2 µm, while others all show values between 0.45-0.55 µm.

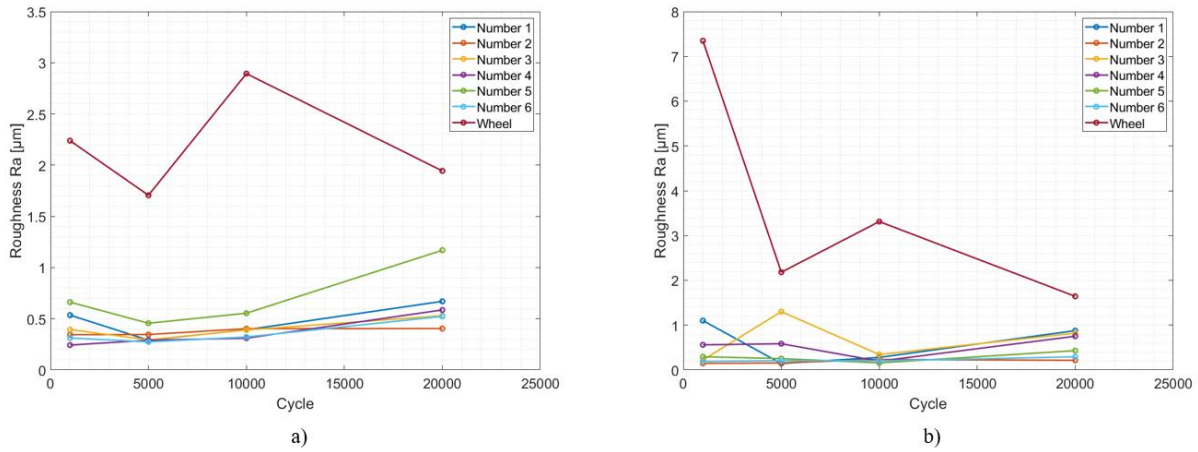

Figure 5.14: 1500 MPa 3% slip dry test roughness values in: (a) lateral and (b) longitudinal directions

Figure 5.14 shows 1500MPa, 3% slip dry test roughness graphs in lateral and longitudinal directions against number of cycles. Lateral roughness values of clad materials showed an increase until the end of the test and the highest decrease happened in Number 1 (R260 clad) from 0.6 to 1.2 µm. Other clad materials showed values around 0.4 µm to 0.6 µm. Wheel roughness showed unstable data and it was the highest Ra value among all the parts. Ra values were between 1.5 µm and 3 µm. Longitudinal roughness values showed values between 0.1 to 1 µm in the clad parts. Number 3 had the highest value among the clad materials going to around 1.1 µm after 5,000 cycles. The wheel showed the highest value with 7.5 µm after 1,000 cycles, but by the end of the test, it had decreased to 1.8 µm.

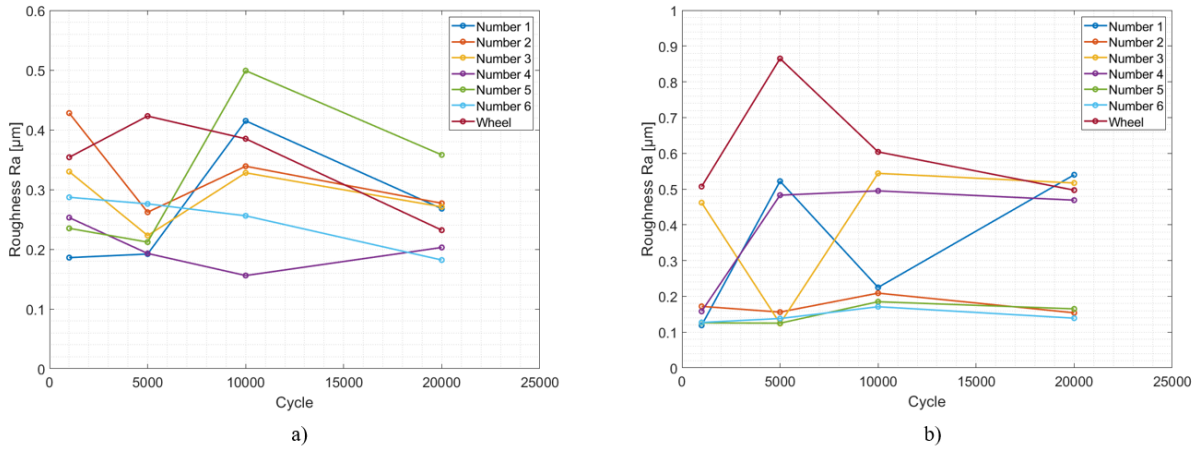

Figure 5.15: 1800 MPa 1% slip dry test roughness values in: (a) lateral and (b) longitudinal directions

Figure 5.15 shows 1800MPa, 1% slip dry test roughness graphs in lateral and longitudinal directions against number of cycles. Lateral roughness values of clad materials showed number 5 (MSS clad) had the highest Ra value with 0.5 µm after 10,000 cycles. The number 4 (Stellite 6 clad) Ra value was the lowest Ra with 0.15 µm. Longitudinal roughness values showed wheel had the highest value after 5,000 cycles with 0.85 µm. Number 1 (R260 clad), number 4(Stellite 6 clad) and number 3(MSS clad) showed the highest increase at the end of the tests.

5.5.3 Mass Loss

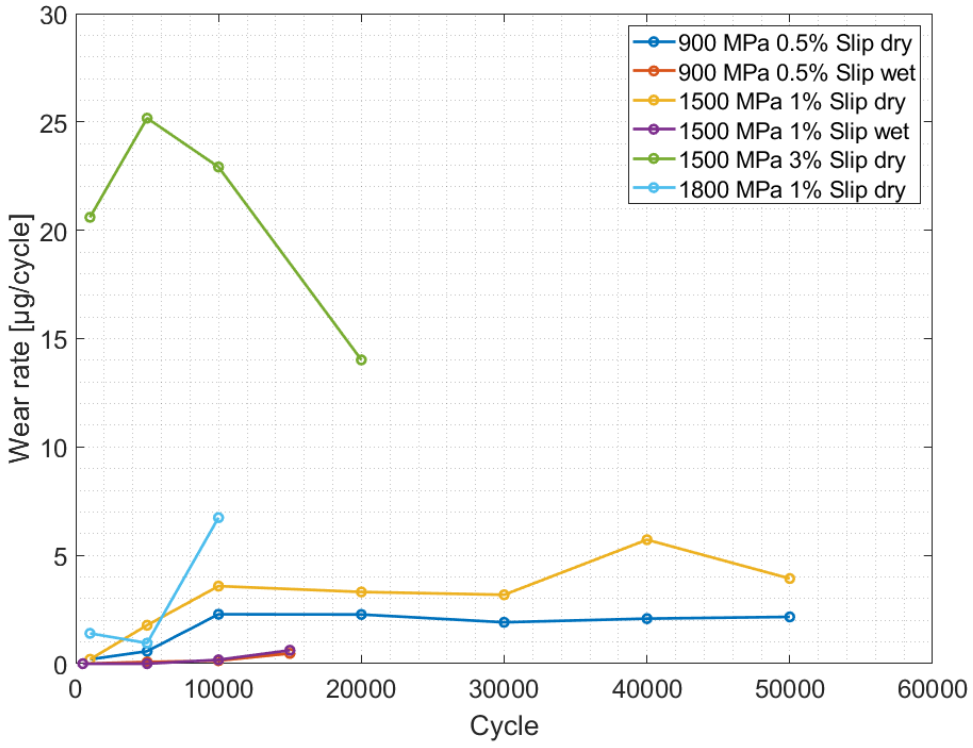

Fig. 5.16. (a)

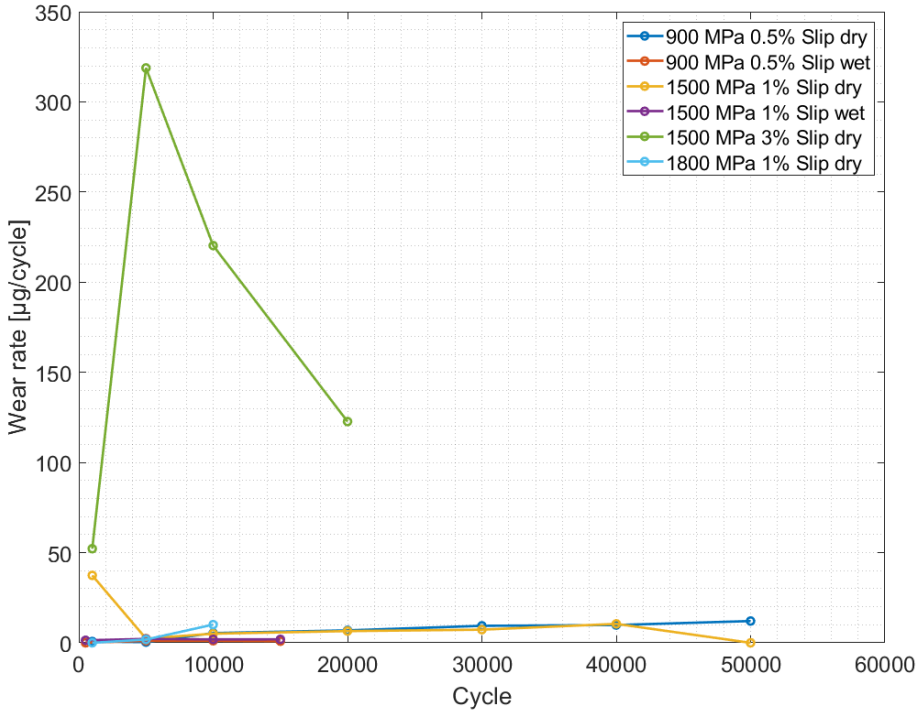

Fig. 5.16. (b)

Figure 5.16: Repair tests wear rates for different test conditions: (a) rail disc wear rates; (b) wheel disc wear rates

Mass loss was measured to calculate wear rates for the tests, as shown in Figure 5.16. This is the combined wear of all the different clad layers and the R260 between the clad regions. The number itself is therefore hard to use in anyway, but differences between the test conditions can be checked.

The 1500 MPa, 3% slip test had the highest wear rate on the rail and wheel disc. The slip value is the highest slip value of all the test conditions and it leads to the greater wear. Figure 5.16 (a) shows rail wear rates and following the 1500 MPa, 3% slip tests, the 1800 MPa, 1% slip test, 1500 MPa, 1% slip test and 900 MPa, 0.5% slip test had the next highest wear rates respectively. They were all dry cycle tests and it was expected they would have higher wear rates than water-lubricated tests. Water-lubricated tests showed similar wear rates, but the 1500 MPa, 1% slip water-lubricated test wear rate was slightly higher than the 900 MPa, 0.5% slip wear rate at 20,000 cycles. Figure 5.16 (b) shows the wheel wear rates and similar to rail wear rates, dry contact tests gave higher wear rates than water-lubricated contact wear rates.

5.5.4 Friction

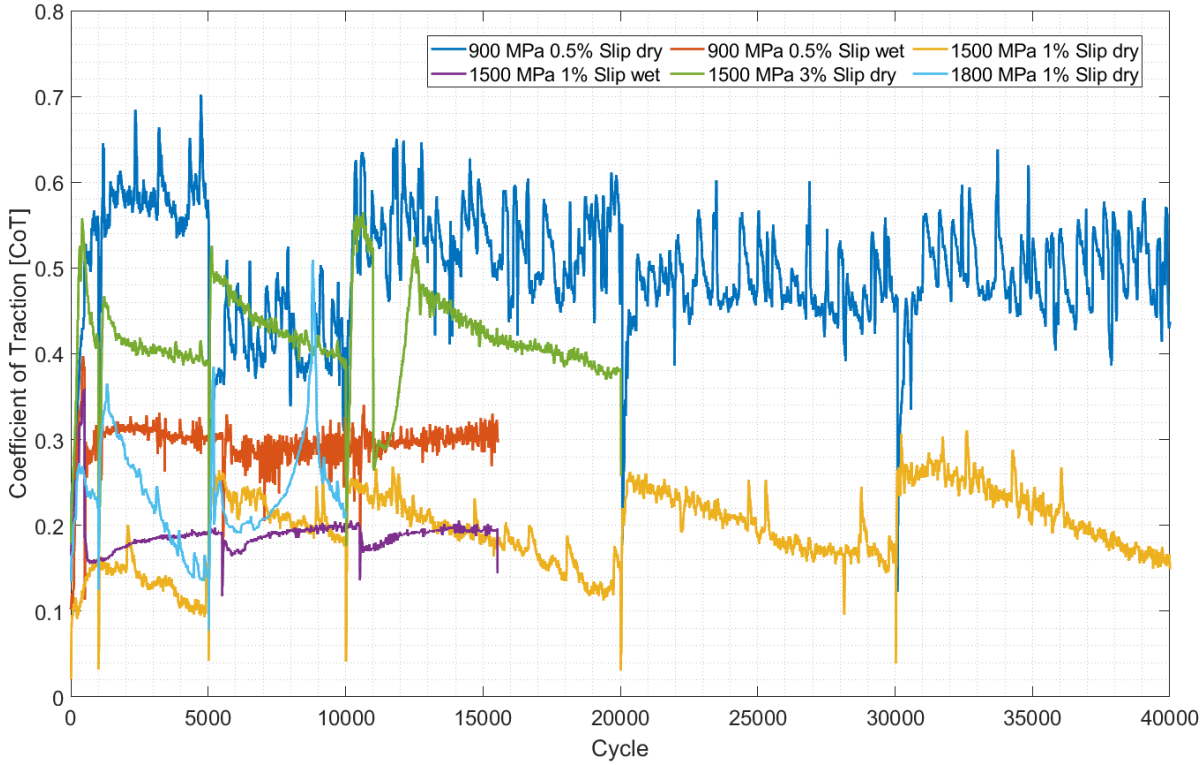

Figure 5.17: Repair tests friction data for all test conditions

Figure 5.17 shows friction data versus cycles for all repair tests. As with wear this data is hard to interpret as the surface conditions vary around the disc surfaces. The highest friction value occurred for 900 MPa, 0.5% slip dry tests at 0.5. Water lubricated tests showed friction of around 0.3 for the 900 MPa, 0.5% slip tests. It can be seen that the 1500 MPa, 1 % slip water lubricated and dry tests have similar average values. Water lubricated tests showed a smoother pattern though than the dry data. 1500 MPa 3% slip tests friction values were around 0.4 value. 1800 MPa, 1% slip dry tests friction values showed unstable data values were between 0.1 and 0.5. This was probably due to the changing surface conditions and uneven wear.

5.5.5 Cross-section Analysis

5.5.5.1 Cross-section Images

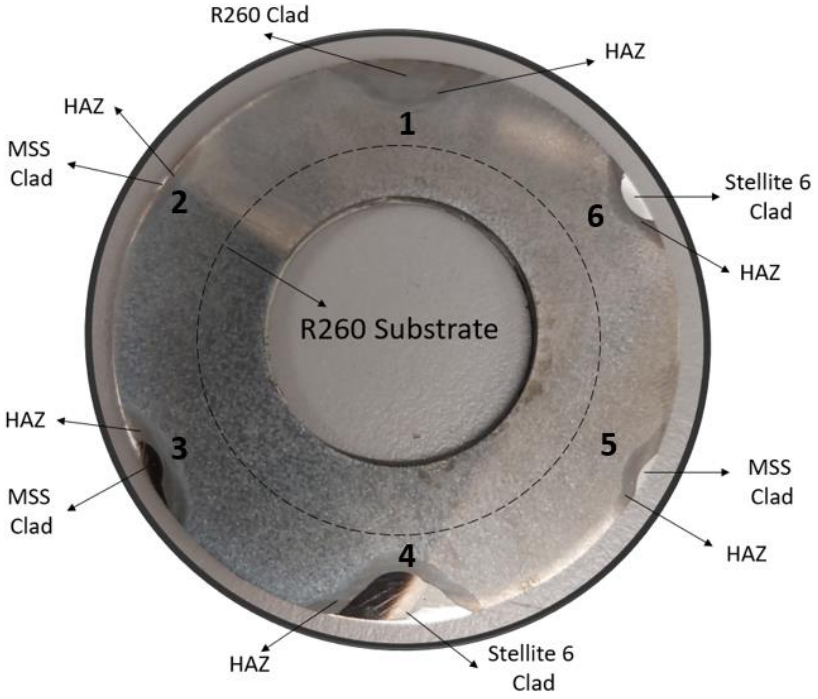

Figure 5.18: 2% Nital etched rail disc pre-test with clad and HAZ parts

R260 Clad

R260 clad over R260 substrate is shown in Figure 5.18 as “slot” number 1. After all the 6 different tests, the R260 clad showed good bonding on the substrate part of the disc. R260 clad samples were etched with 2% Nital etchant (see Fig. 5.19). In the dry tests, the microstructure showed material flow over the clad part, as would be expected in normal R260 disc tests. Over clad part, some flake formation was seen on the surface as well. This is similar to what has been seen in previous testing on R260 and is typical of the ratchetting wear mechanism.

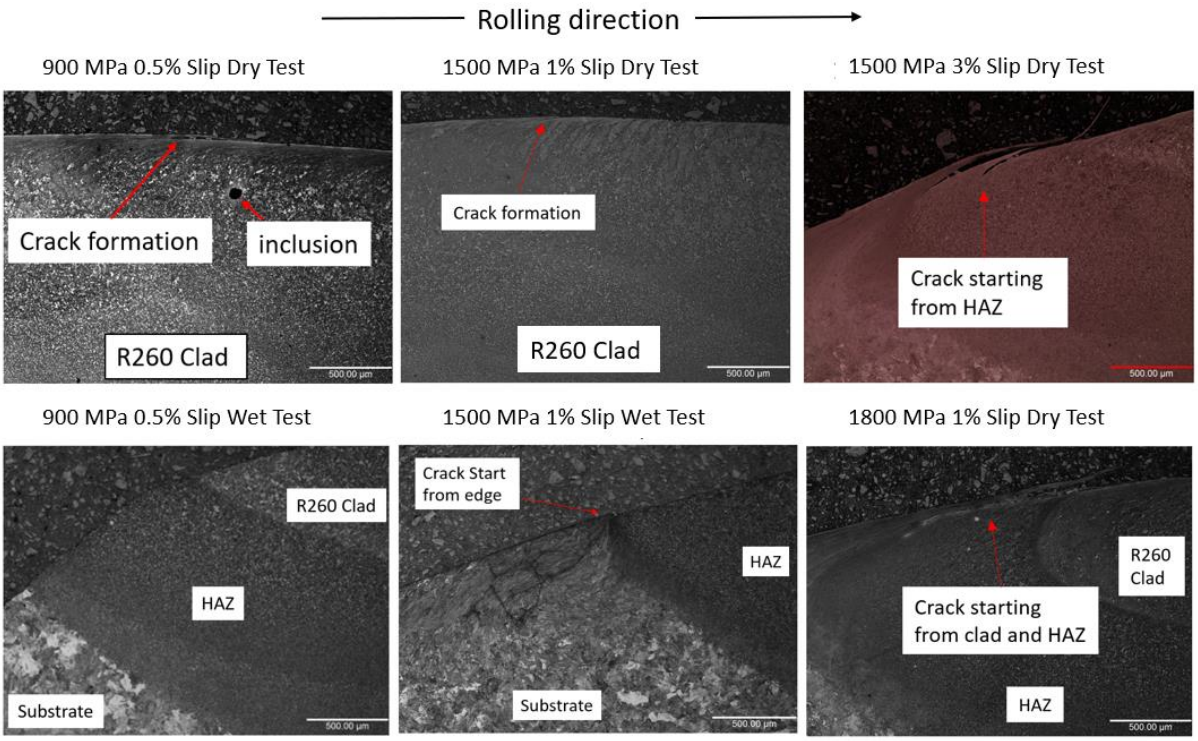

Figure 5.19: R260 Clad sub-surface microscope images from different test conditions

The water-lubricated RCF tests showed some material deformation as well. Cracks generally started from the edges and it is because of the different hardness of the substrate and clad materials. The 1500MPa, 1% slip water lubricated test microstructure image showed some cracks between the HAZ and substrate (see Appendix 5.C, Figure 12.9).

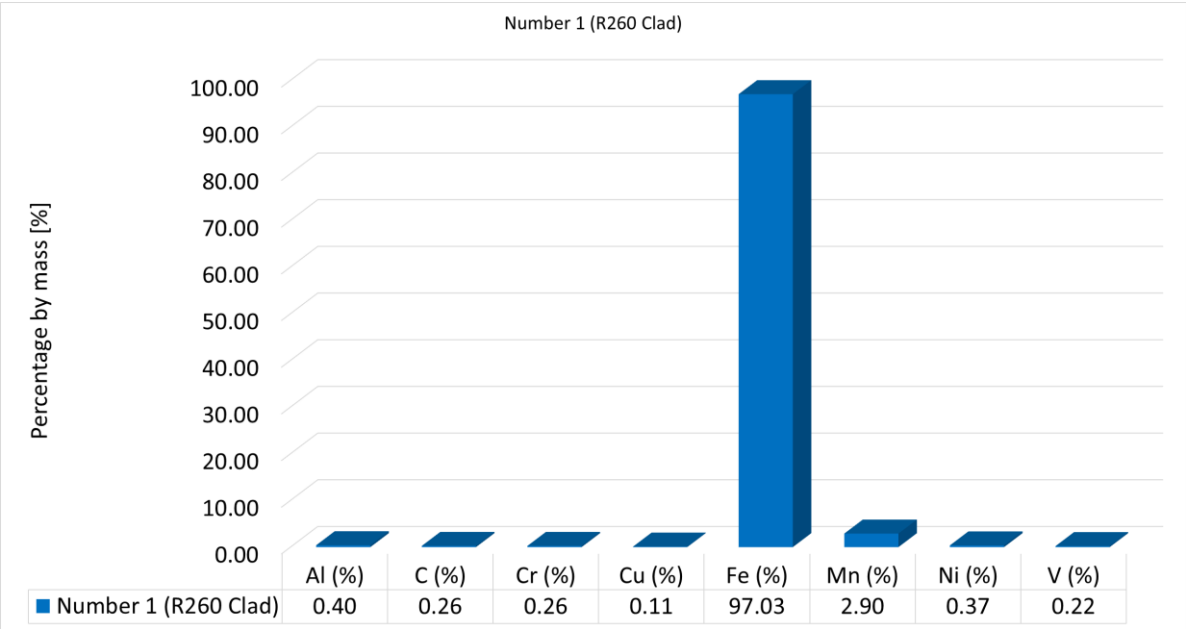

Figure 5.20: R260 clad chemical composition LIBS analysis

Figure 5.20 shows the LIBS analysis of the R260 clad repair part. Values shown are percentage by mass. Unsurprisingly, iron had the highest percentage with 97.03 wt%. Mn is followed that with 2.9 wt%. All other elements in the figure were lower than 0.41 wt% and the lowest amount was seen in Cu with 0.10 wt%. Table 5.1 shows the chemical composition of the R260 rails as well and when it is compared with LIBS data of R260, LIBS data in Figure 5.20 showed Al, Cr, Mn, and V showed lower percentage than industrial data. C showed higher percentage value than the table 5.2 value.

MSS Clad

MSS clad over R260 substrate is shown in Figure 5.18 with 3 slots over the disc, numbers 2, 3 and 5. MSS clad samples were etched with %2 Nital etchant first to see the substrate and HAZ on the discs. Bigger slots of the MSS clad were etched with Vilella etchant to see clad microstructure as well. In dry tests, material flows (of R260) were seen over the clad part caused by wear due to the tractive force and some cracks and big flakes were seen in some microstructure images.

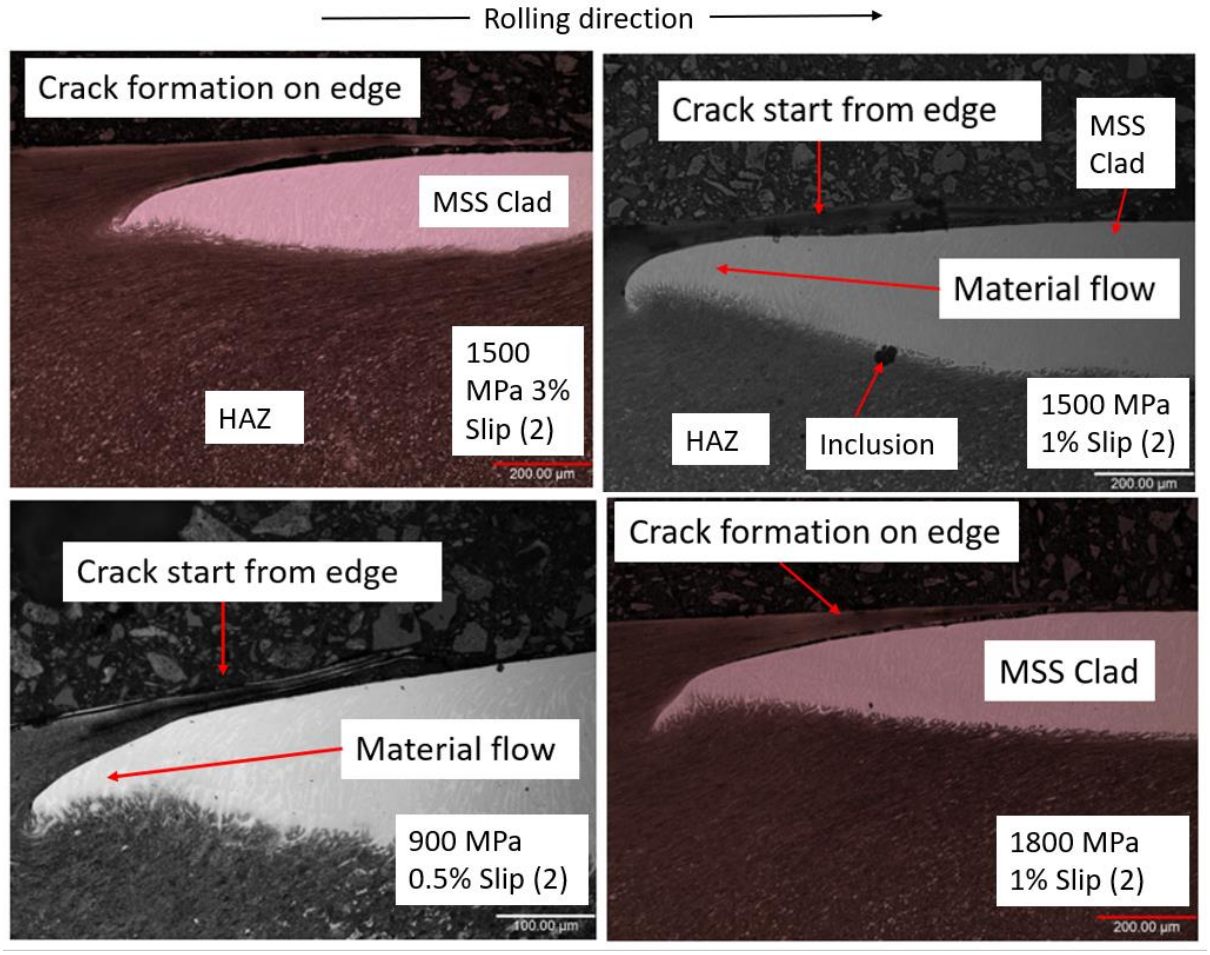

Figure 5.21: MSS clad dry test number 2 MSS clad microstructure images

MSS clad number 2 can be seen in Figure 5.21 for all dry test conditions. Both images show crack formation from the trailing edge of the clad on dry tests. When all images were evaluated (see Appendix 5.C Figure 12.10) cracks mainly occurred from flake formation and material flow was seen on the leading edge of the clad parts Number 2 is one of the smallest shallow clad and it also caused some material flow on the edges more and below the clad part. It could be seen that the clad part slightly moved on the surface. Some small inclusions between the cladding and HAZ transition points can be seen.

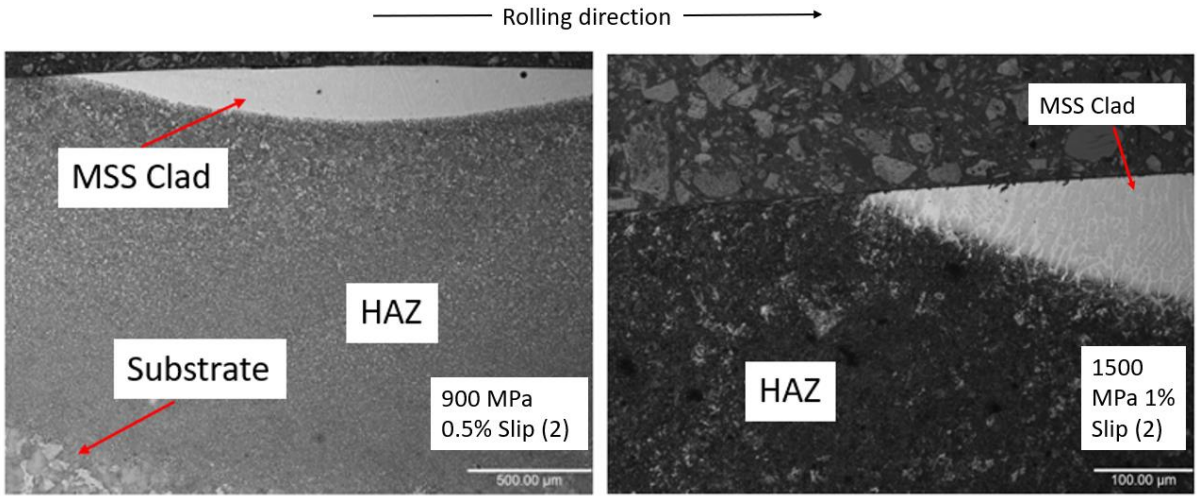

Figure 5.22: MSS Clad water lubricated tests number 2 MSS clad microstructure images

In the water-lubricated RCF tests, MSS clad parts showed good performance and there was no visible deformation (see Fig. 5.22). The leading and trailing edges of the clad showed no visible cracks or big material deformations. Some small inclusions inside the clad part can be seen (see Appendix 5.C, Figure 12.10).

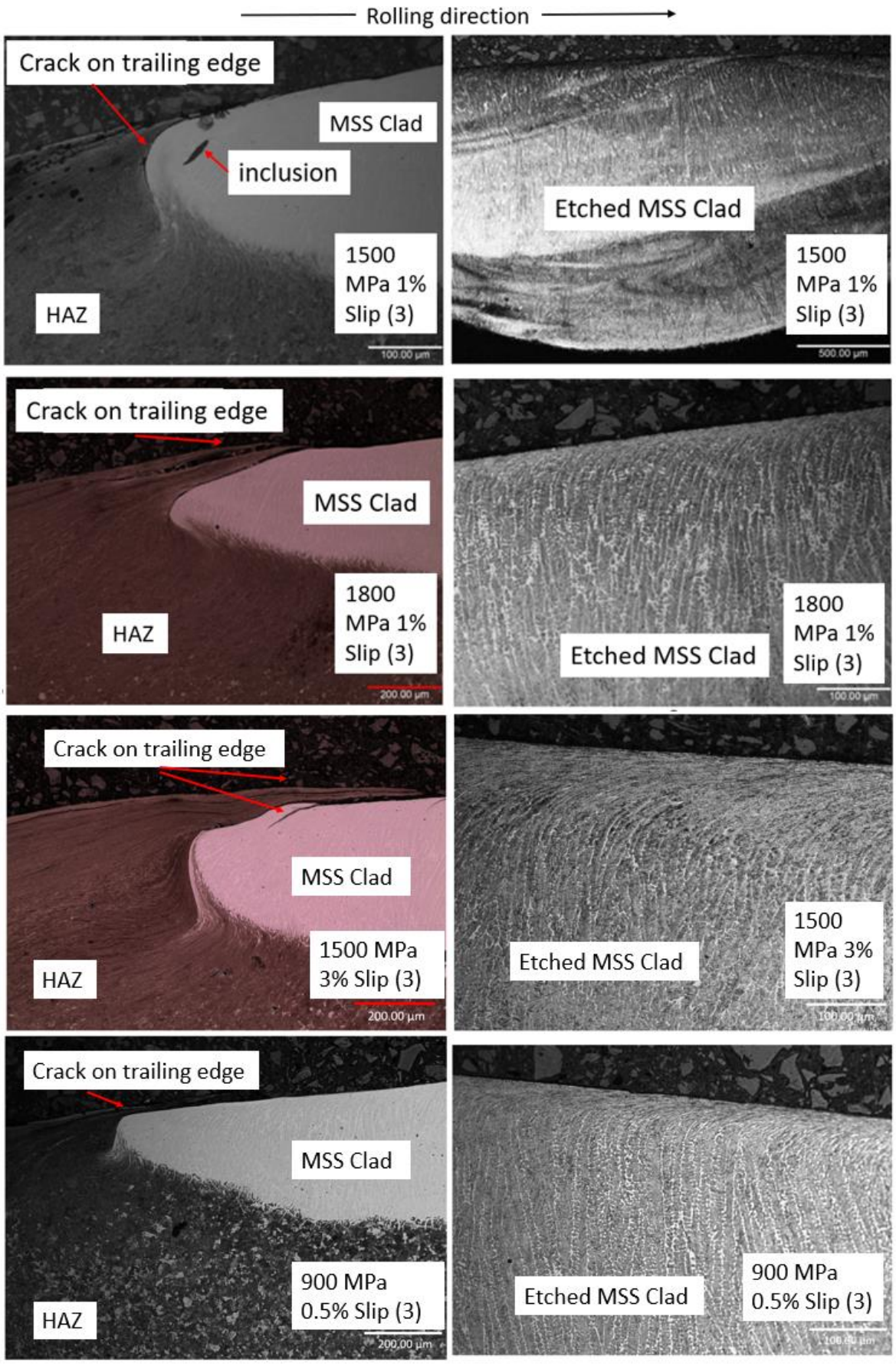

Figure 5.23: MSS clad dry tests number 3 MSS clad microstructure images

Figure 5.23 shows clad number 3 images after tests for dry tests. Material flow on the trailing edges of the 1500 MPa, 1% slip dry test and 1800 MPa, 1% slip dry test can be seen with a crack starting from the same area. Other test conditions showed similar deformation and some small inclusions on the clad and HAZ parts in number 3 clad on discs (see Appendix 5.C, Figure 12.11). Also, the etched clad part can be seen with more layers on repair number 3. The clad surface shows no more deformation on the dry tests.

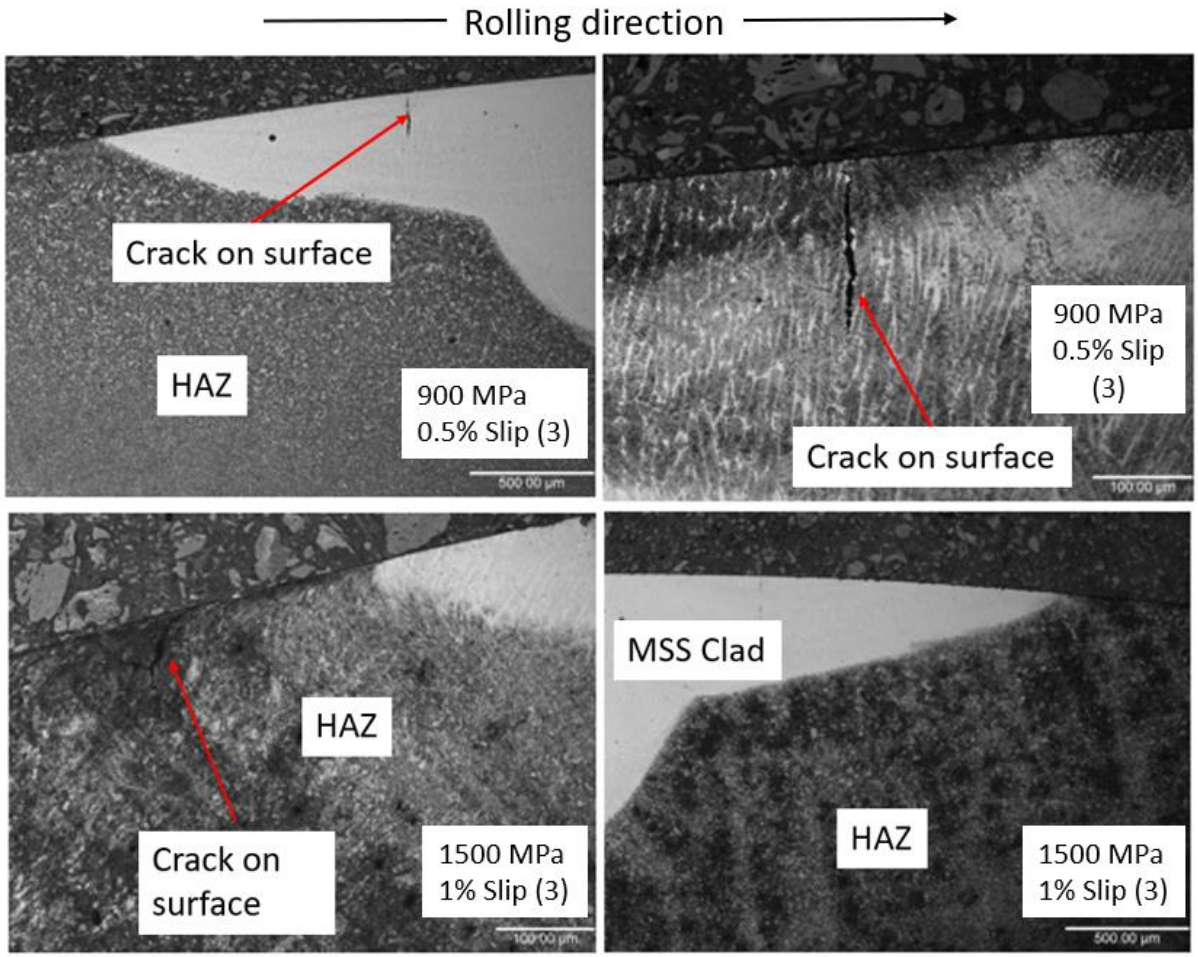

Figure 5.24: MSS clad water lubricated tests number 3 MSS clad microstructure images

Figure 5.24 shows the water-lubricated tests microstructure images. A crack can be seen from the clad surface on the 900 MPa, 0.5% tests it is visible on the unetched and etched part of the images. The crack behaviour could be related to the clad repair depth, but this would need further testing to establish. Also, other images from 1500 MPa, 1% slip tests showed a crack in the HAZ part. Some small signs of material flow on the trailing edge of the clad region can be seen. More images can be seen in Appendix 5.C, Figure 12.11.

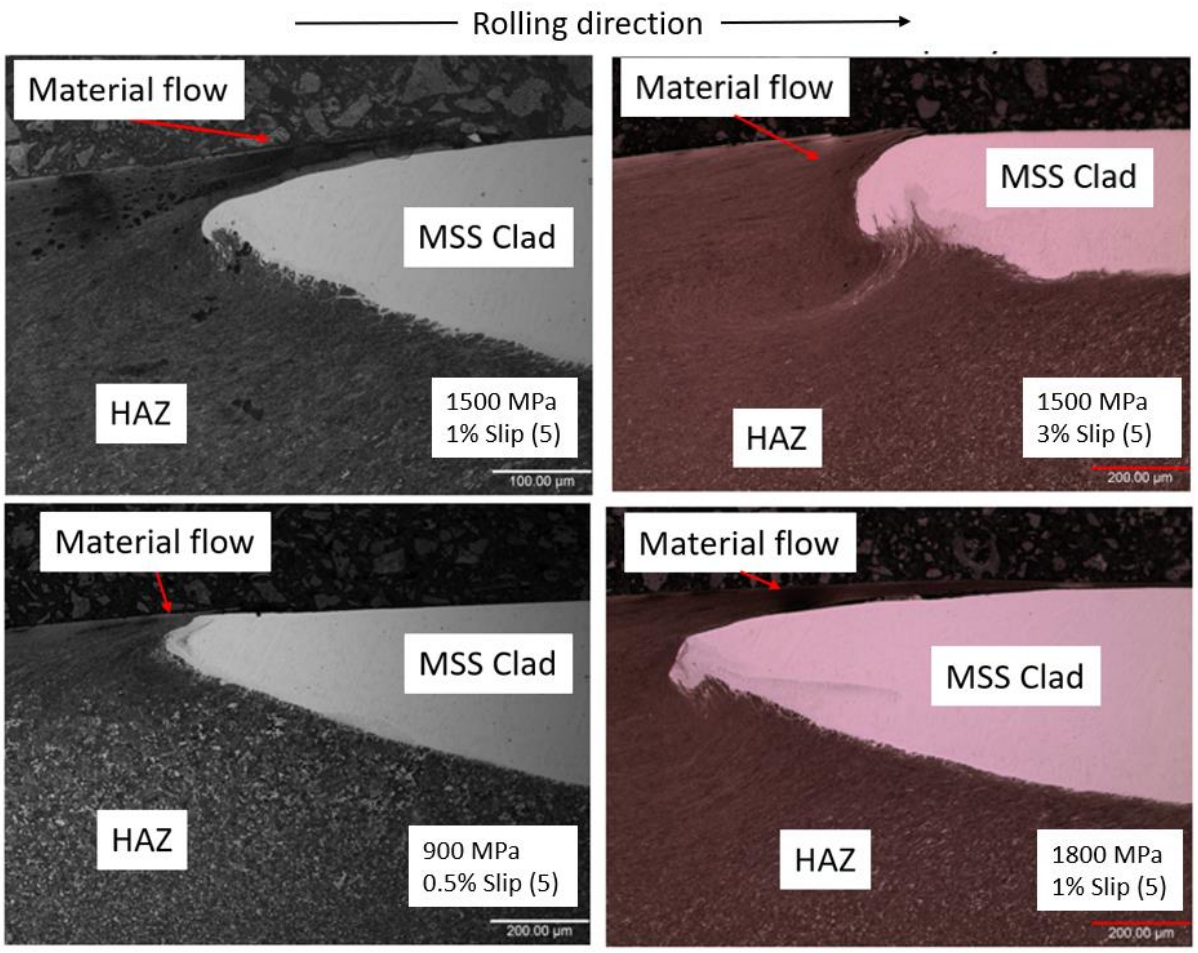

Figure 5.25: MSS clad dry tests number 5 MSS clad microstructure images

Figure 5.25 shows number 5 MSS clad microstructure images. The images show material flows on the trailing edges with other test conditions as well (see Appendix 5.C, Figure 12.12). Also, flake formations were seen on the trailing edge with the material flow on the leading edge.

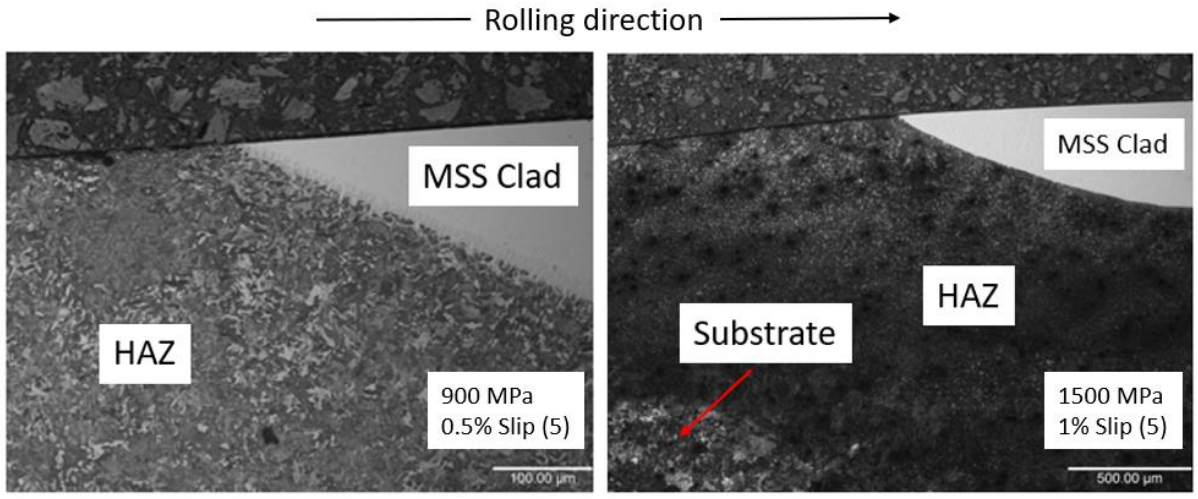

Figure 5.26: MSS clad water lubricated tests number 5 MSS clad microstructure images

Figure 5.26 shows the water-lubricated tests microstructure images. In the images, there are no signs of any cracks. The leading and trailing edges of the discs do not show a high amount of material flow. More images can be seen in Appendix 5.C, Figure 12.12.

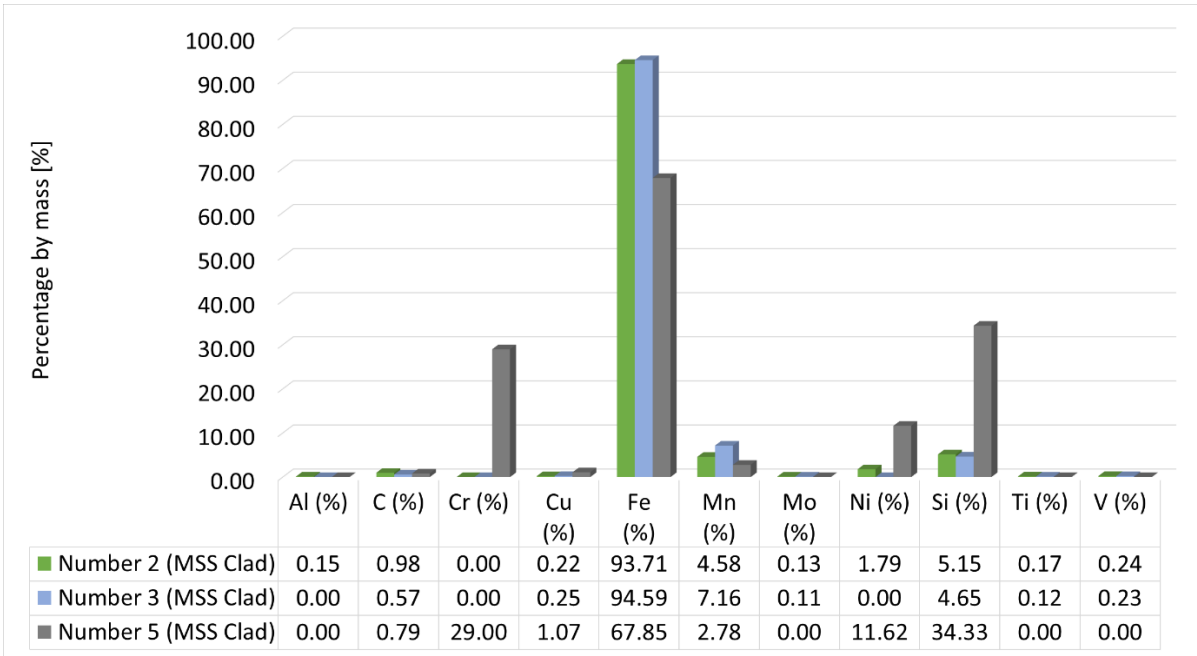

	Al (%)	C (%)	Cr (%)	Cu (%)	Fe (%)	Mn (%)	Mo (%)	Ni (%)	Si (%)	Ti (%)	V (%)
Number 2 (MSS Clad)	0.15	0.98	0.00	0.22	93.71	4.58	0.13	1.79	5.15	0.17	0.24
Number 3 (MSS Clad)	0.00	0.57	0.00	0.25	94.59	7.16	0.11	0.00	4.65	0.12	0.23
Number 5 (MSS Clad)	0.00	0.79	29.00	1.07	67.85	2.78	0.00	11.62	34.33	0.00	0.00

Figure 5.27: MSS clad chemical composition LIBS analysis

Figure 5.27 shows the LIBS analysis of the MSS clads repair part with number 2, 3 and 5. Values are percentage by mass and iron has the highest percentage with 94.58 wt% in number 3 and number 2 had with 93.70 wt% while number 5 had 67.85 wt%. Number 2 and number 3 showed similar values and Mn, and Si followed iron with around 5-7 wt%. However, number 5 had higher Si, Cr and Ni than other two clads. While Si was 34.3 in number 5, the other two numbers were around 5 wt%. Different numbers of compositions due to material flow and size of the clad parts can be seen. Also HAZ sizes are different in the clad parts. The indent point for LIBS analysis show some differences because of the size and material flows.

Stellite 6 Clad

Stellite clad over R260 substrate is shown in Figure 5.18 with 2 slots over the disc with the numbers 4 and 6 (see Fig 5.2). Stellite 6 clad samples were etched with 2% Nital etchant to analyse the microstructure and it showed material flow caused by the direction of traction over clad parts in dry tests.

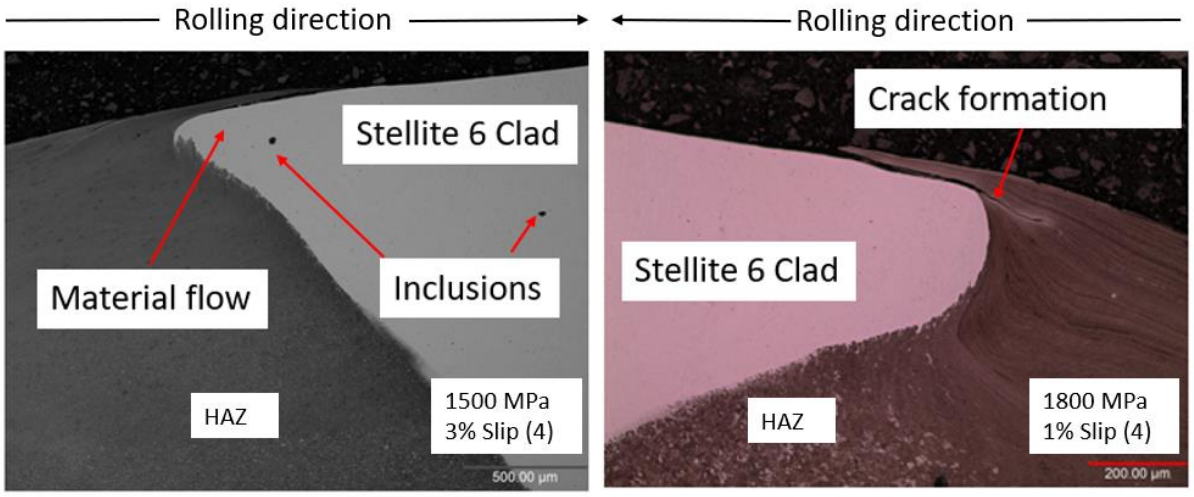

Figure 5.28: Stellite 6 clad dry tests number 4 Stellite 6 clad microstructure images

Figure 5.28 shows 1500 MPa, 3% slip and 1800 MPa, 1% slip dry contact microstructure images. The trailing edge of the images showed some proof of crack formation from the flake starting point and some inclusions were shown in the 1500 MPa, 3% slip clad part. All other conditions were examined and material flow behaviour was a bit different than other dry test conditions in the 900 MPa 0.5% slip tests (see Appendix 5A, Figure 12.13)

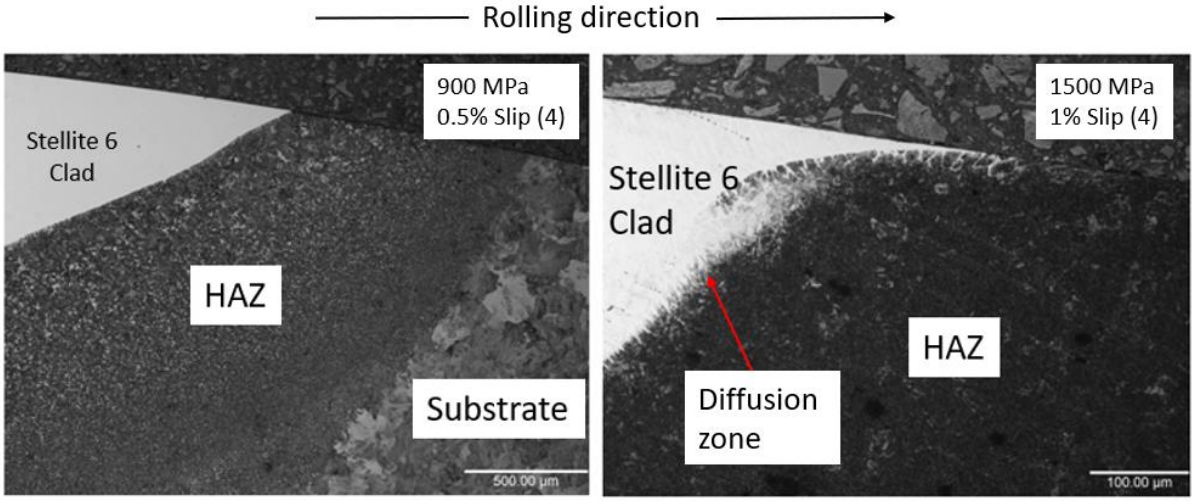

Figure 5.29: Stellite 6 clad water lubricated tests number 4 Stellite 6 microstructure images

Figure 5.29 shows 900 MPa, 0.5% slip and 1500 MPa, 1% slip water lubricated contact microstructure images. In the water-lubricated RCF tests, good performance is shown and there is no deformation over the clad part. The 1500 MPa, 1% water lubricated test clad part had a diffusion zone visible. Trailing and leading edge photos are shown in Appendix 5.C, Figure 12.13.

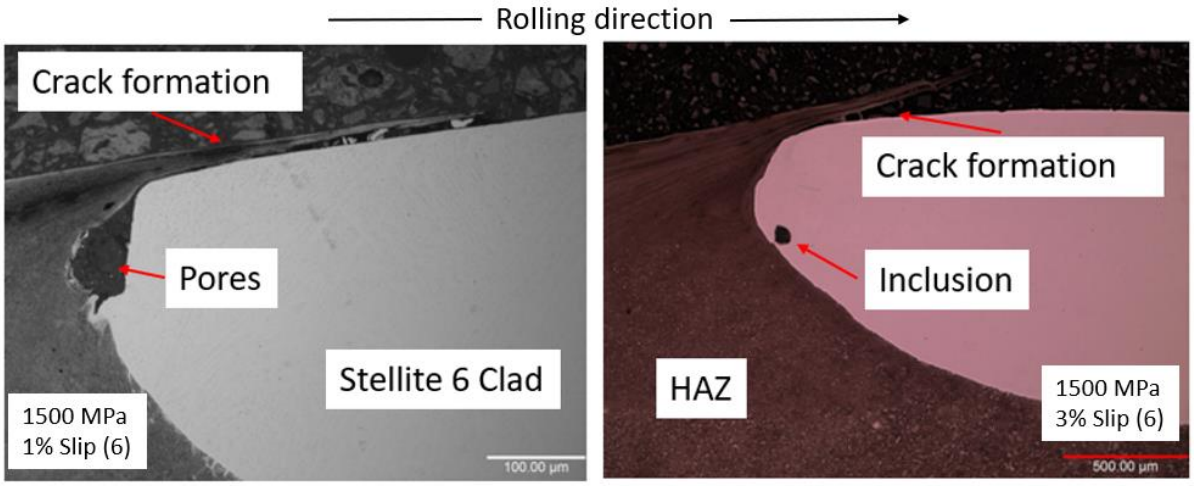

Figure 5.30: Stellite 6 clad dry tests number 6 Stellite 6 microstructure images

Figure 5.30 shows the number 6 Stellite 6 clad microstructure images from 1500 MPa 1% and 3% slip conditions. The trailing edge of the clad parts showed crack formation with all other test conditions (see Appendix 5.C, Figure 12.14). Also, the 1500 MPa, 1% slip dry test showed a pore in the trailing edge. The pore in the clad repair, indicating that the process parameters were not right for the Stellite 6 powder. The 1500 MPa, 3% slip test showed small inclusions in the trailing edge.

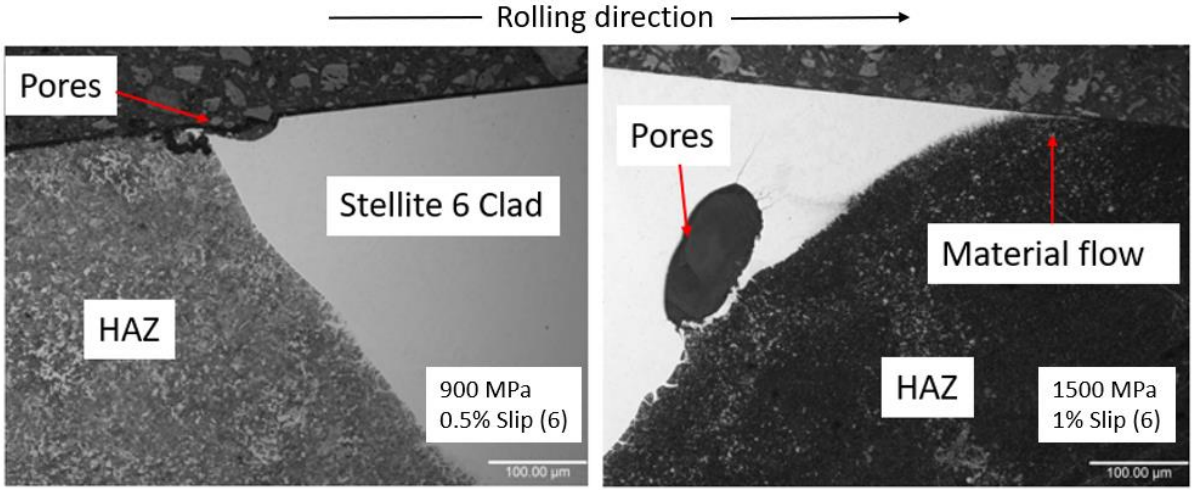

Figure 5.31: Stellite 6 clad water lubricated tests number 6 Stellite 6 microstructure images

Figure 5.31 shows number 6 water-lubricated tests microstructure images. Both test conditions had some pores in the clad part. The 1500 MPa, 1% water lubricated test showed some cracks around the pore. The 900 MPa, 0.5% water lubricated test showed some small signs of cracks in the trailing edge of the clad (see Appendix 5.C, Figure 12.14). Also, both clad parts showed a small amount of material flow on the leading edge.

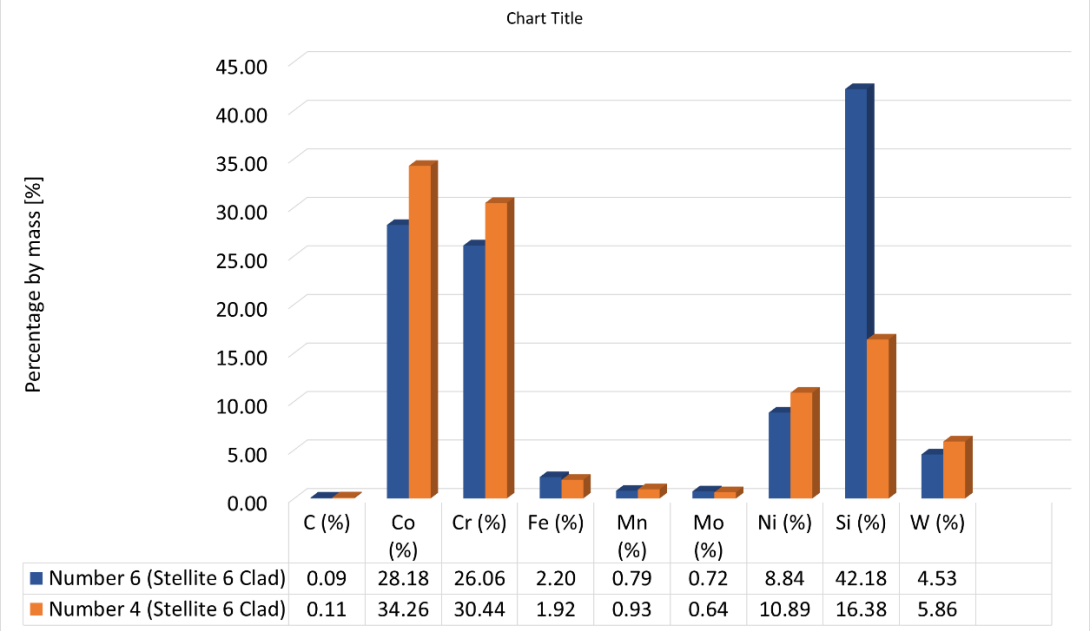

Figure 5.32: Stellite 6 clads chemical composition LIBS analysis

Figure 5.32 shows the LIBS analysis of the Stellite 6 clads repair parts. Values are percentage by mass and Si had the highest percentage with 42.18 wt%. in number 6 while number 4 was 16.37 wt%. Co and Cr had also higher amounts with more than 25 wt% on both clad parts. Ni and W followed them respectively. Stellite 6 is a cobalt based alloy with carbide phase and Co and Cr are expected to be high.

5.5.5.2 Micro Hardness

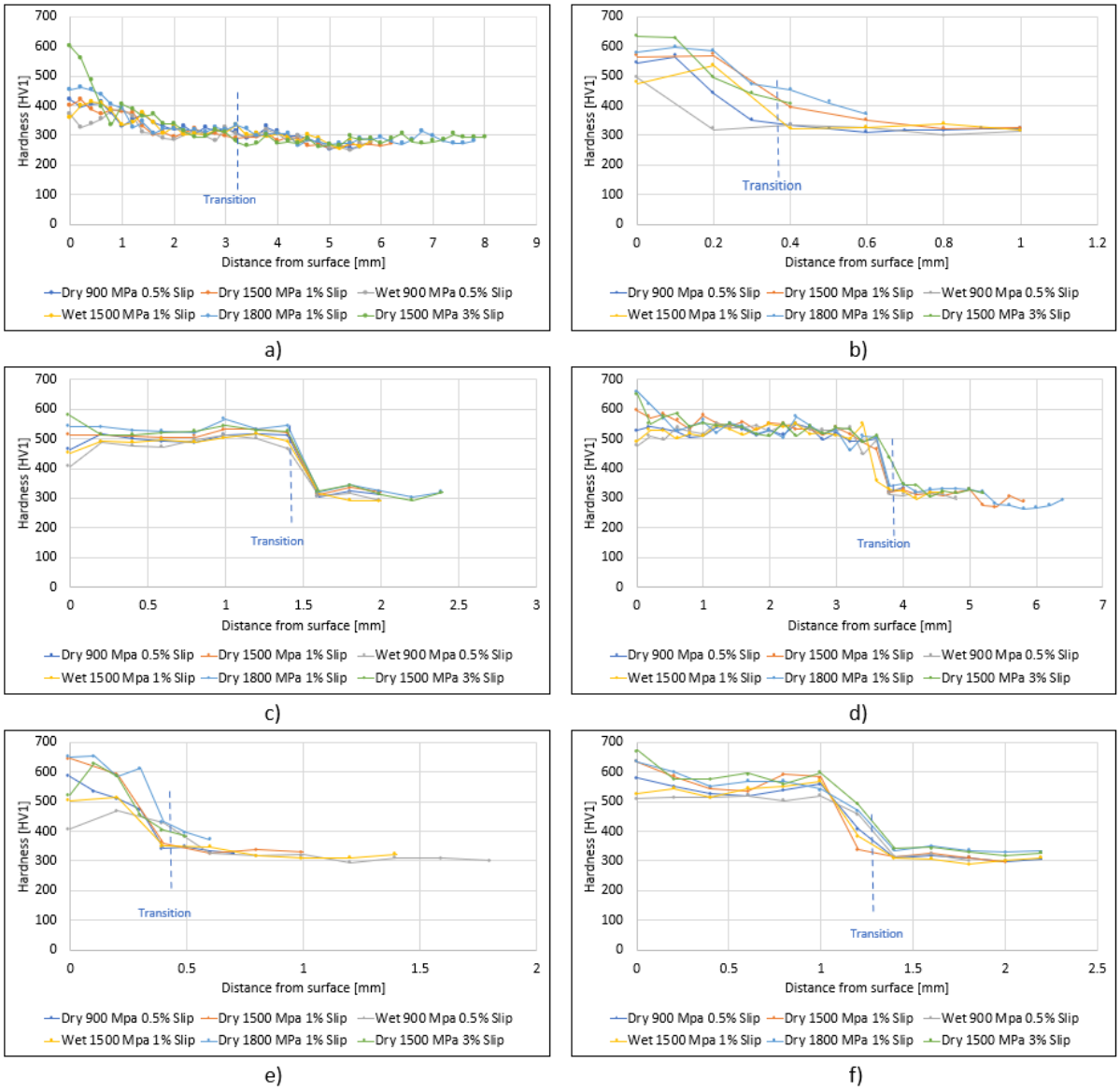

Figure 5.33: Twin-disc repair clad parts hardness measurements: (a) Number 1 (R260 Clad); (b) Number 2 (MSS Clad); (c) Number 3 (MSS Clad); (d) Number 4 (Stellite 6 Clad); (e) Number 5(MSS Clad); (f) Number 6 (Stellite 6 Clad)

Figure 5.33 shows the hardness measurements of the repair test samples through the clad layer and HAZ into the substrate material. It can be seen on the graphs that, as expected, R260 is most linked with substrate materials. MSS (Slots 2, 3 and 5) clad material hardness values are between 400 and 600 HV1. Stellite 6 (Slots 4 and 6) hardness values are between 500 and 600Hv. Slot 1 (R260) hardness values are around 400 HV1. The substrate material is R260, and that part of the materials is around 300 HV1.It can be seen when hardness difference is high, that cracks formed more in the trailing or leading edges or material flow behaved differently. However, R260 hardness showed there good bonding and a gradual decrease of

hardness from the clad part to the substrate part. It allowed crack shapes different to clad materials. Also material flows over R260 clad showed better flow.

5.6 Discussions

In the twin-disc tests, MSS clad, Stellite 6 clad and R260 clad materials were used over R260 substrate material. MSS clad and Stellite 6 clad materials had higher hardness values than R260 rail hardness values (see Fig. 5.33). Those hard materials had cladding with different depths over the disc substrate and they all showed similar behaviour after the tests. Material flows on the edge of the discs cause some crack initiations and some bonding issues with those hard clad materials such as Figure 5.23 and Figure 5.28. Similar behaviours also can be seen in white etching layers (WEL) as well. They are also hard materials that appear is isolated spots surrounded by softer rail substrate, and they also have some issues with cracks at the leading and trailing edges. However, R260 clad over R260 substrate materials showed the best performance in the wear tests. It had harder material than normal R260 after cladding due to the higher temperatures, but it had a nice bond between the clad and substrate at the edge of the clad (see Fig. 5.19).

R260 clad repair (number 1) showed more material flow and deformation over the clad part than MSS clad repairs (number 2, 3 and 5) and Stellite 6 clad repairs (number 4 and 6). Roughness profiles also show difference in the Section 5.5.1 and Appendix 5.B in the lateral and longitudinal directions. Hardness and microstructure images showed that R260 is well bonded and it allows better material flow. Also the hardness difference from the HAZ in the R260 gradually decreases which is why it gave some more bonding quality. Plastic shear strain can be seen on that repair clad part and HAZ more than other MSS clad and Stellite 6 clad repairs.

Figure 5.30 and Figure 5.31 showed some big pore defects in the Stellite 6 clad repair, and it is due to the cladding process parameters. Also, other clad materials showed pores and some inclusions, but they were not as big as those in Stellite 6. Shape of the clad repairs affected the clad quality as well as repairs with shallow depth or low angles had more pores and inclusions (see Appendix 5.C).

Repair clad tests wear rates are shown in Figure 5.16. When they are compared with unclad R260 rail wear rates most of the test conditions showed lower wear rates. Lewis et al. (2016) found that the unclad R260 rail wear rate was around 14 µg/cycle after 30,000 cycles in 1500MPa, 1% slip twin-disc tests. For the rail wear rates in Figure 5.16 (a) only the 1500 MPa,

3% slip dry test wear rate was higher than the un-clad R260 rail wear rate because of the higher slip value. For the same condition (1500MPa, 1% slip), the clad repair test stayed mostly below or around 5 µg/cycle during the tests. On the wheel wear rate, the same trend was seen between tests. Lewis et al. (2016) showed a wheel wear rate of 22 µg/cycle. Similarly, for the 1500 MPa, 3% slip test the wear was much higher than the value in Figure 5.16 (b). Other test conditions were mostly lower than that except the 1500 MPa, 1%slip dry test after 1000 cycles. It can be seen that at the start of the tests the repair clad parts caused higher wear rate, but during the tests it went down lower than 12 µg/cycle.

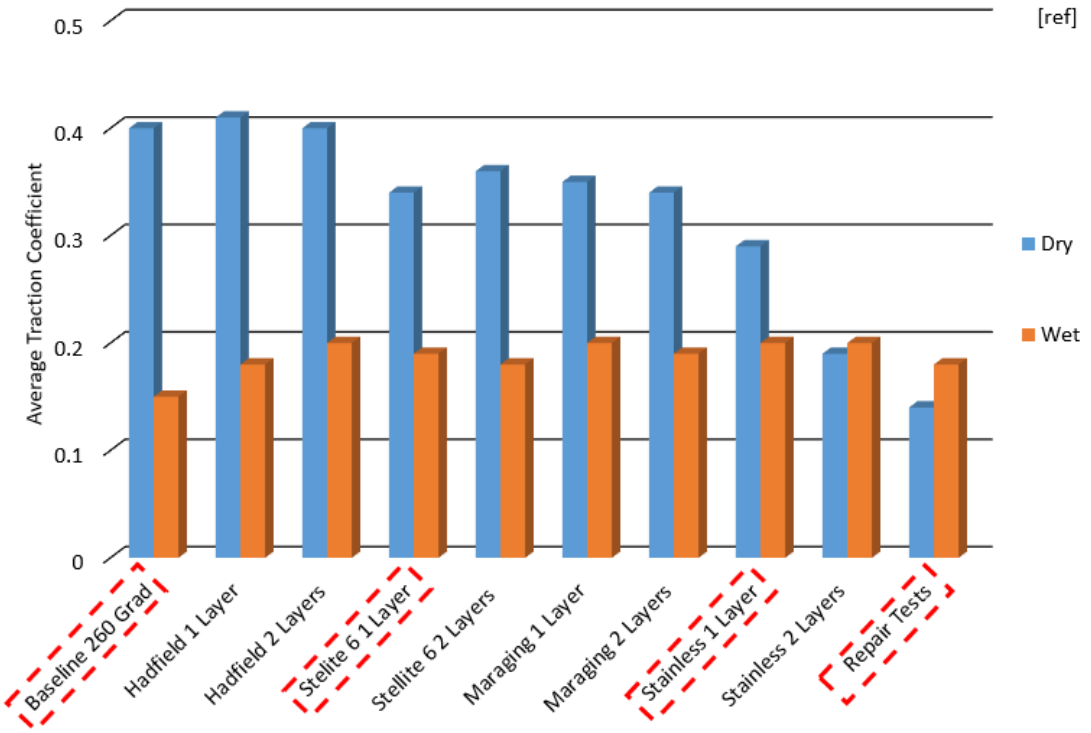

Figure 5.34: Average traction coefficients from 1500 MPa, 1% slip tests by (Lewis et al., 2015) and repair test data for 1500 MPa and 1% slip test

In the Figure 5.17 CoT values are shown for different test conditions for repair tests with dry and water lubrication. It shows that the 900 MPa, 0.5% slip dry test had the highest CoT values with an average of 0.49. It can be seen when contact stress and slip were lower, the friction tends to get higher, but when contact stress and slip are higher, friction tends to lower values in dry and water lubricated tests.

Figure 5.34 shows twin-disc CoT values from previous research and 1500 MPa 1% slip test data in repair test for comparison. In the graph, the baseline R260 CoT value is around 0.4 in dry condition and 0.15 in water lubricated condition for 1500 MPa, 1% slip tests. Stellite 6 1 layer is around 0.33 in dry and 0.19 in wet tests. Stainless 1 layer is around 0.29 in dry and

0.20 in wet tests (Lewis et al., 2015). In the Figure, 1500 MPa and 1% slip dry and wet tests average CoT values are 0.14 and 0.18 respectively. However,baseline R260 grade is 0.4 in dry condition and 0.15 in water lubricated condition as mentioned previous paragraph. Repair test twin disc specimen had 6 different clad slots over the R260 baseline (see Fig. 5.1). That clad parts affected friction as well because of harder clad specimens. Also, in dry repair tests friction values gradually decrease on each 10,000 block of cycles but water lubricated repair tests showed stable values during the tests. Also, in Chapter 4, the MSS clad tests friction value was around 0.18 in water lubricated tests as well (see Fig. 4.6).

Roughness of the clad part surfaces with Ra values showed in section 5.5.2 and graphs showed all roughness values with lateral and longitudinal directions. The highest rail surface roughness Ra value is around 1.3 in longitudinal direction on 900 MPa, 0.5% slip test from number 1 (R260) clad part. On the R260 rail roughness after 1500 MPa 1% slip tests Lu et al., (2018) found Ra value 6.0614 after 30,000 cycles. It shows that non-clad R260 roughness value is much higher than the repair clad region surface roughness values. It can be because of the higher hardness in R260 clad over R260 substate material. When clad the same material clad parts shows higher hardness than base material.

In the microstructure analysis it showed that R260 clad section showed best material flow integrity with parent rail which is same material but other clad materials had some more cracks on the edges of the clad parts.

5.7 Conclusions

In the small-scale twin disc tests 3 different materials were tested in 6 different slots on an R260 disc with different sizes of slots. R260 clad, MSS clad, and Stellite 6 clad materials were used over an R260 substrate material. After the tests disc surfaces, clad and substrate bonding issues, and material flows were evaluated.

Chosen laser clad parameters showed R260 clad over R260 substrate had bonded better than MSS clad and Stellite 6 clad materials. Inclusions and pores were seen more in the MSS clad and Stellite 6 clad parts on the disc.

In the dry test conditions and water lubricated test conditions R260 clad rail showed the best tribological performance with good clad and substrate integrity and also with deeper HAZ than the others. Tests showed that same clad material with parent material had better option for repair options in in-situ applications.

In the microstructure analysis, MSS clad and Stellite 6 clad parts over R260 rails had some crack issues mainly on the trailing and leading edges of the clad parts, but R260 showed material flow continued over R260 clad part successfully and not many cracks happened in the leading and trailing edges of that clad.

Chapter 6

6 Full-Scale Laser Cladding Tests – Fully Clad and Repaired Rail

Full scale tests were planned to assess clad rail specimens at realistic condition. Pocket rail specimens were clad with 1.8 mm layers of Stellite 6, and 3 mm layers of martensitic stainless steel (MSS) materials over R260 base material. These materials were chosen because they showed a good performance in small-scale cladding tests using a twin disc approach (Lewis et al., 2017; Lu et al., 2018). The data from full-scale tests was evaluated and compared against the small-scale test data. These comparisons were made using the Ty/A approach. T is tractive force, y is amount of slip in the contact, and A is contact area. This approach can be used for evaluation of wear results from test rigs at different scales (Buckley-Johnstone et al., 2019). This approach was used first by Bolton & Clayton (1984) in twin-disc testing and then for full scale tests.

Furthermore, T400 clad over standard grade R 260 rail were clad to examine repair performance of the laser cladding under the full scale test condition.

6.1 Test Apparatus and Measurements

The full-scale test rig is shown in section 3.4.2. This test rig is used for simulating actual wheel/rail contact conditions in the laboratory. A full-scale repair test was also conducted on the full-scale test rig. A different test set was used from the pocket specimen tests. A machined down short rail section was repaired with multiple clad layers. It was then mounted between two sections of standard grade R260 rail to create the full length of rail needed for the test.

The pocket specimens were weighed, and their profiles measured before the start of the test and recorded. Then the pocket specimen surfaces were cleaned with acetone and 5,000 dry cycles were run. After each of the 5,000 cycle blocks the test rig was stopped and wear debris from the pocket specimens was collected and then the pocket specimens were taken out from the rail.

Following that, pocket specimens were cleaned with acetone and weighed again. Lab temperature and humidity were recorded before and after the test. After that, the rail surfaces were examined using an optical (non-contact) Alicona Infinite-Focus SL profilometer by using

replicas of the pocket specimen surfaces. Rather than taking roughness measurements, a replica process was used which allows a copy of the surface to be created. Microset 101 fluid replicating compound was used for making the copies of surface. This compound is a silicon polymer which is spread over the rail surface. A stiff backing Is applied and then the compound Is left to dry, for 3-5 minutes. After it is fully cured, the replica is peeled off the rail surface for measurement of roughness. The profilometer gives the chance to obtain high-resolution images and 3D surface profiles measurements with a vertical resolution of up to 10 nm. Surface roughness' were recorded from the Alicona scans.

After that, pocket specimen profiles were measured by Calipri profilometer and a 3D laser scanner. Then pocket specimens were sectioned, mounted, ground, polished. Hardness measurements were carried out and then the pocket specimens were etched for microstructure analysis.

The full-scale repair test sample was analysed with a Calipri 2D and laser 3D scanner to assess profile differences. Tests were conducted until visible wear occurred over the clad part. The test finished around 5,000 cycles. The same measurements were then done for the full-scale samples as were done the twin-disc specimens, roughness and microstructure analysis.

6.2 Test Conditions

It was planned to do some tests on the full-scale test rig to study wear and understand how the small-scale tests reflect what happens in a more representative wheel/rail interface. The vertical load was 110 kN that equal to contact stress used was 1500 MPa as it is the most common pressure used in small-scale twin disc tests and the slip ratio was 1%. The desired speed was 100mm/s.

Full-Scale repair tests also were conducted with a load of 110 kN, which is equal to 1500 MPa and 1% slip in the full-scale test rig with dry contact conditions (Brunskill et al., 2012). The tests were started with a small number of cycles as it was uncertain how the clad layer would respond. When 1,000 cycles were reached the test was run on until 5,000 cycles had been achieved.

6.3 Test Specimens

Pockets cut from rail head were used for the tests. These had been clad with MSS and Stellite 6 except for an un-clad R260 pocket specimen. The MSS clad was made up of two layers with a 3 mm total thickness over an R260 substrate and the Stellite 6 clad was 1.8 mm thick, again over an R260 substrate. The thickness difference arose as the layers have to ground after

application to return the rail to profile and one had more grinding. The clad surface Initially looks like weld beads. These pockets were assembled into a base rail fitted onto the rig as shown in Figure 6.2.

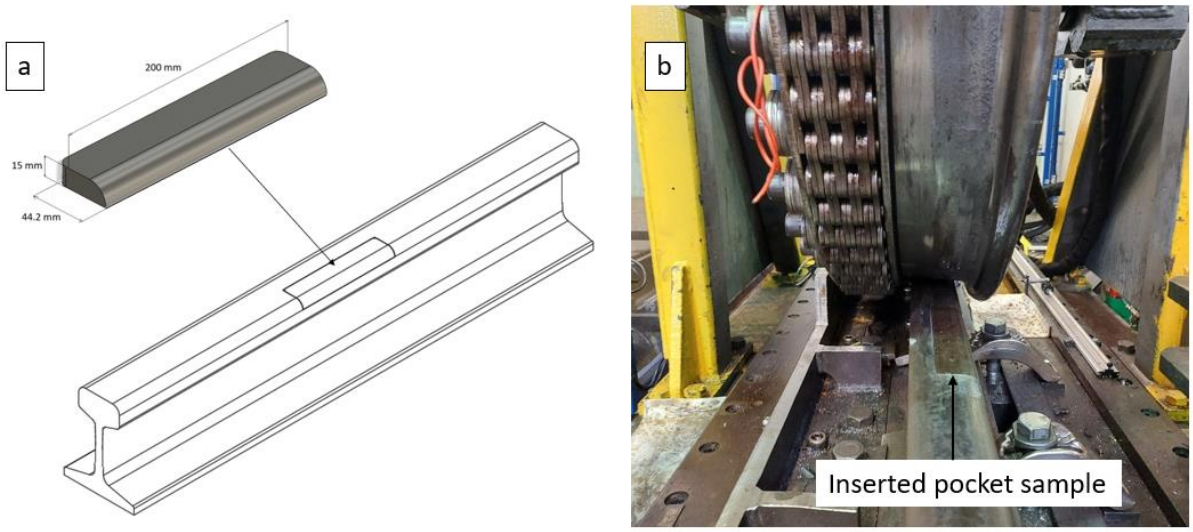

Figure 6.1: Pocket sample test material preparation and insertion in the full-scale test rig for an experiment

Figure 6.2(a) shows the rail and pocket sample with the pocket sample dimensions. Figure 6.2(b) shows how the pocket sample is inserted in the rail. The pocket samples were inserted into the rail with three bolts from the back face of the pocket sample and one from underneath the pocket sample. Figure 6.3 shows the pocket specimen images from before the experiments.

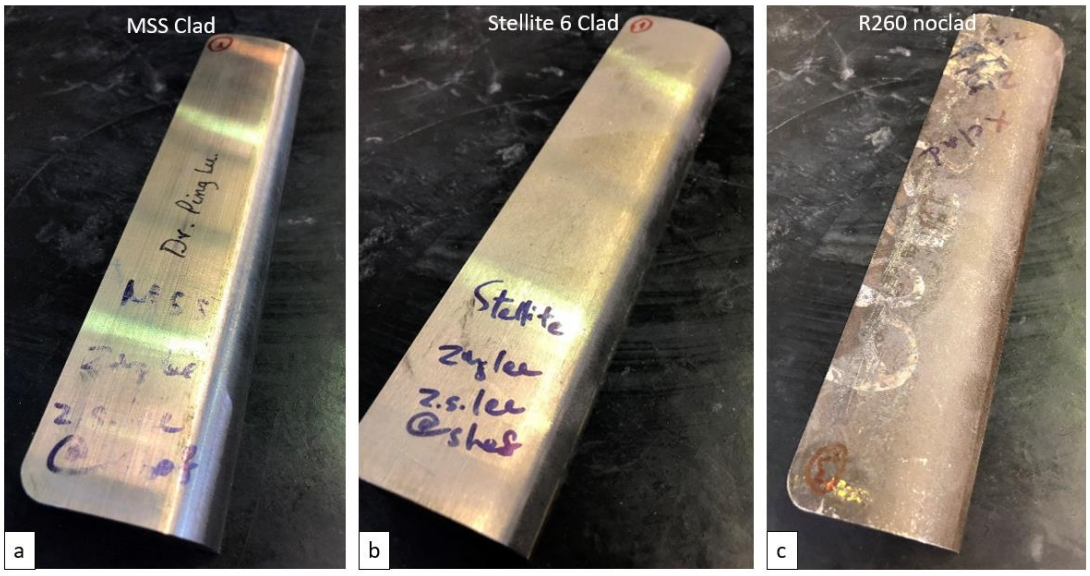

Figure 6.2: Full scale test pockets before tests: a) MSS Clad; b) Stellite 6; c) un-clad R260 un-clad

Table 6.1: Chemical compositions (%by mass) of E8 wheel, R260 rail, MSS, and Stellite 6 clad materials (Martensitic Stainless Steels; Santa et al., 2019; Stellite)

	C	Mn	Si	Cr	Ni	Mo	Co	V	W	N	Al	S	P
R260	0.74	1.08	0.31	0.040	-	-	-	0.004	-	-	0.003	0.018	0.013
MSS	0.06	1.22	0.46	14.64	3.31	0.42	2.01	0.51	0.62	0.04	0.01	0.005	0.009
St. 6	1.0	<0.1	0.9	27.0	-	-	Bal	-	4	-	-	-	-
T400	<0.1	-	2.6	8.5	Bal.	28.5	Bal.	-	-	-	-	-	-
E8	0.542	0.734	0.253	0.141	0.120	0.048	-	0.006	-	-	-	0.006	0.011

Chemical compositions of the R260, MSS clad material and Stellite 6 clad materials shown in the Table 6.1. R260 is rail steel that is a standard rail commonly used in the UK and Europe. Martensitic stainless Steel (MSS) and Co based Stellite 6 cladding was used because of their higher wear and RCF resistance properties shown in previous twin-disc tests (Lewis et al., 2017; Lu et al. 2018).

For the full-scale test repair specimen, post machining, the rail section was rebuilt to its original shape using many layers of T400 clad over standard R260 grade rail (see Figure 6.3). T400 has high wear and corrosion resistance and it is cobalt based alloys. In the other tests, the clad repair surfaces were ground to give a smoother surface, but here beading texture were used directly without any grinding step. Some cracks can be seen already over surface of the clad part.

Figure 6.3: T400 Clad over R260 full scale rail with many clad layers

6.4 Results

6.4.1 Surface Evolution

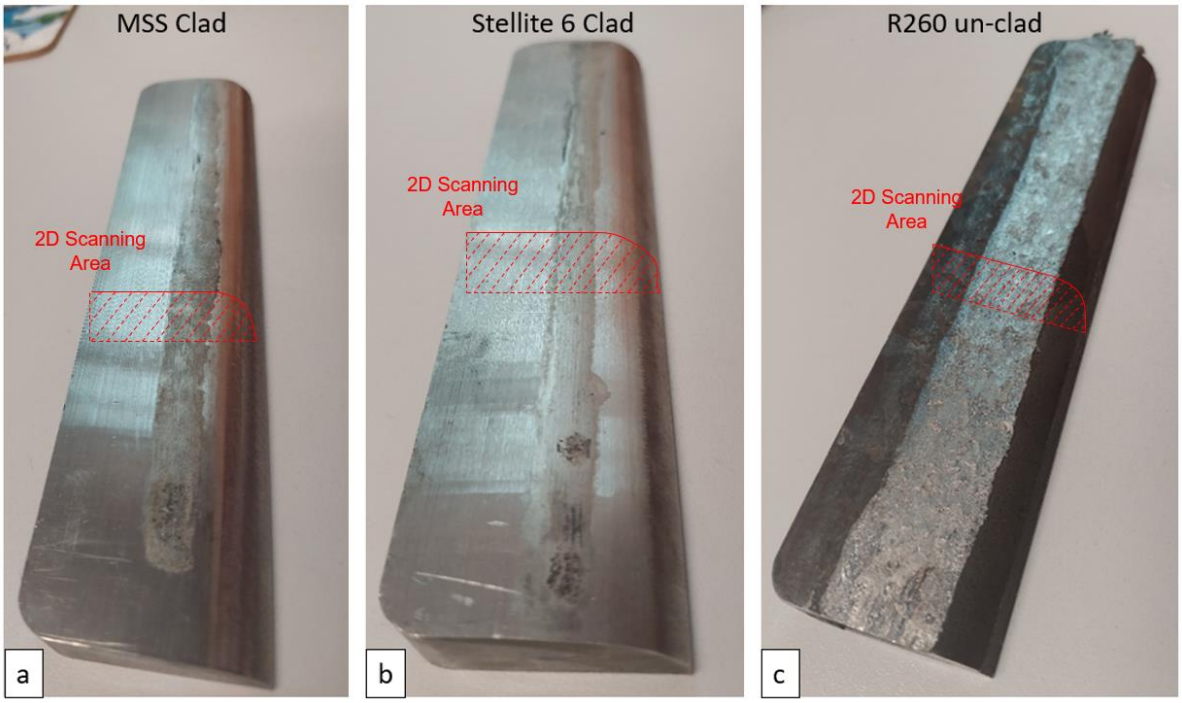

Figure 6.4: Full scale test pockets after tests: a) MSS Clad pocket specimen; b) Stellite 6 pocket specimen; c) un-clad R260 pocket specimen

Figure 6.4 shows the pocket images after the 5,000 cycles of the full-scale tests. Figure 6.4a shows the MSS clad pocket, Figure 6.4b shows the Stellite 6 clad pocket and Figure 6.4c shows the un-clad R260 pocket. Wear bands can be seen in the images. The R260 pocket sample has the widest wear band. The MSS clad pocket sample and Stellite 6 clad pocket sample show a similar size of wear band.

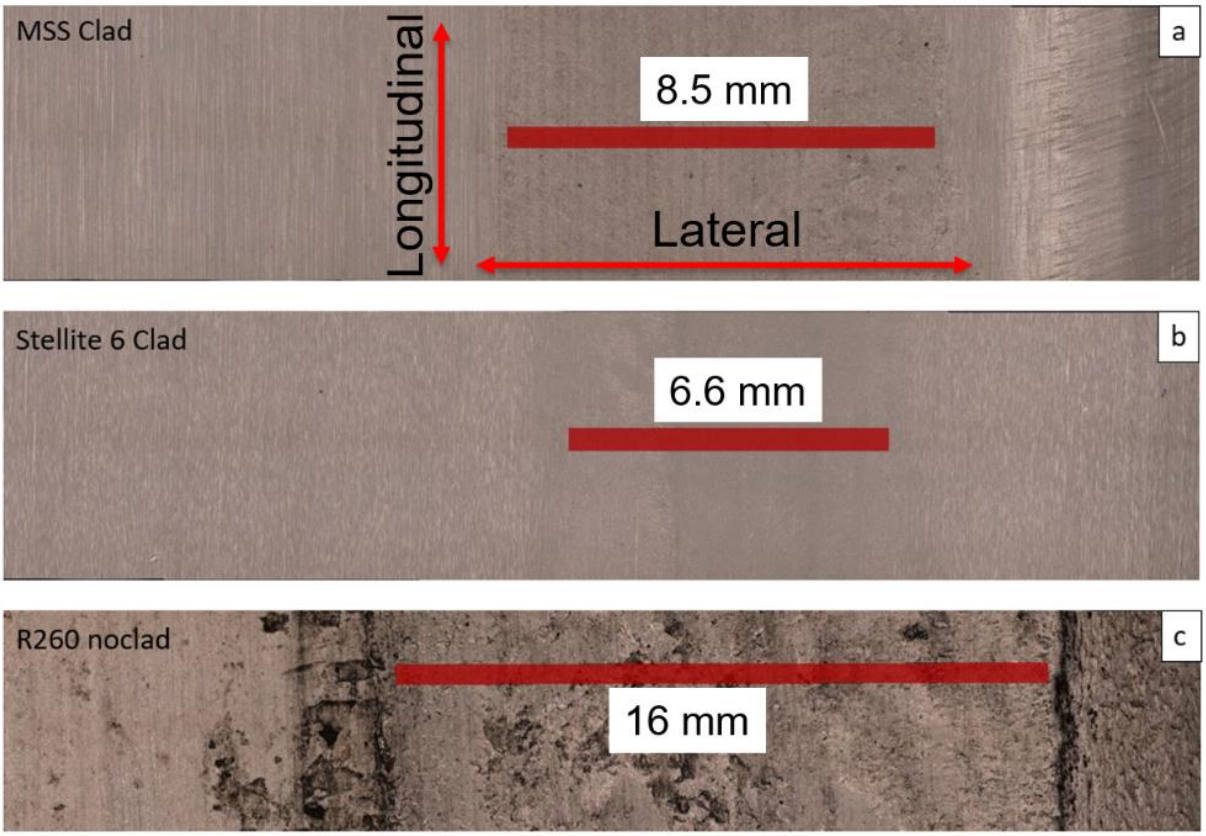

Figure 6.5: Full scale test pockets surface images after from the Alicona measurements: a) MSS Clad pocket specimen; b) Stellite 6 pocket specimen; c) R260 no clad pocket specimen

Images of the specimen surfaces are presented in Figure 6.5. The MSS clad, Stellite 6 clad and un-clad R260 surface images show how pockets deformed/wore and how wear tracks formed after the 5,000 full-scale cycles. It can be seen that the unclad R260 was damaged more, and the contact patch exhibits far more severe wear than the other clad pocket specimens. Local deformation and flake formation are visible. The MSS and Stellite 6 pockets show similar contact patches after the completed cycles. These wear scars appear smoother than the original surface but have some visible abrasive scratches.

6.4.2 Surface Profiles

Rail profiles were measured on the pocket specimens before and after the tests. These profiles were measured using a Calipri profilometer before and after the tests and a 3D laser scanner after the tests.

MSS Clad

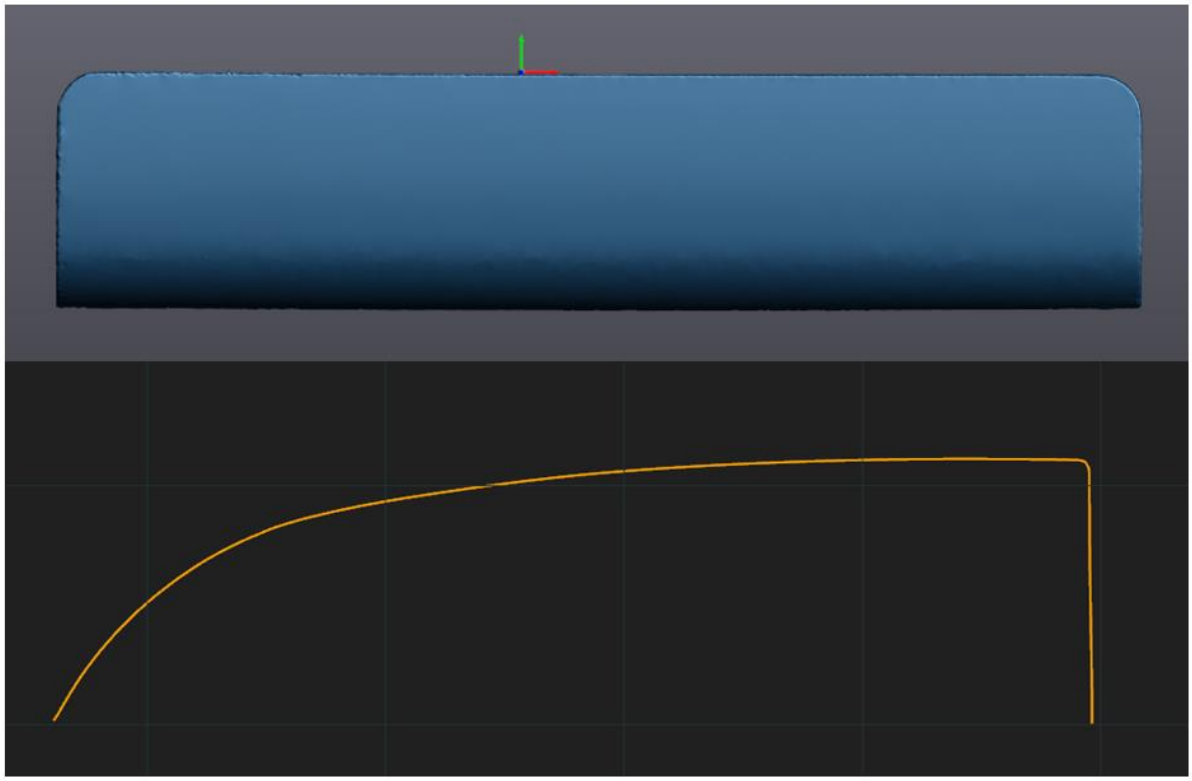

a)

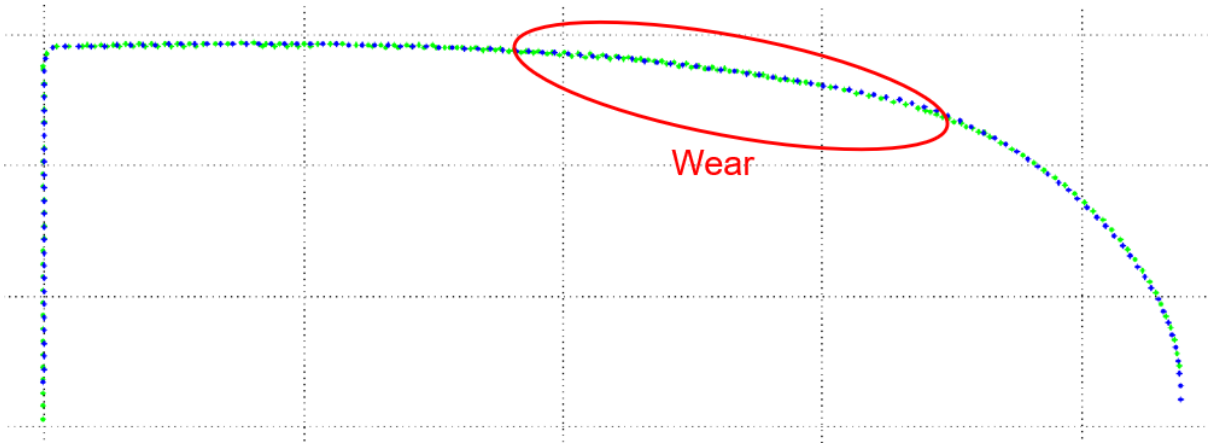

b)

Figure 6.6: MSS clad pocket surface profile measurements: a) profile measurements by 3D laser scanner; b) profile measurement by Calipri before and after 5,000 cycles (green line refers to before test and blue colour to after test).

2D profiles of the MSS clad pocket specimen were taken close to the middle part of the specimens. The location of the section is shown Figure 6.4(a). The MSS clad pocket specimen

profile showed there was no obvious deformation after 5,000 cycles. A wear region can be seen on Figure 6.6(b), but not much plastically deformation.

Stellite 6 Clad

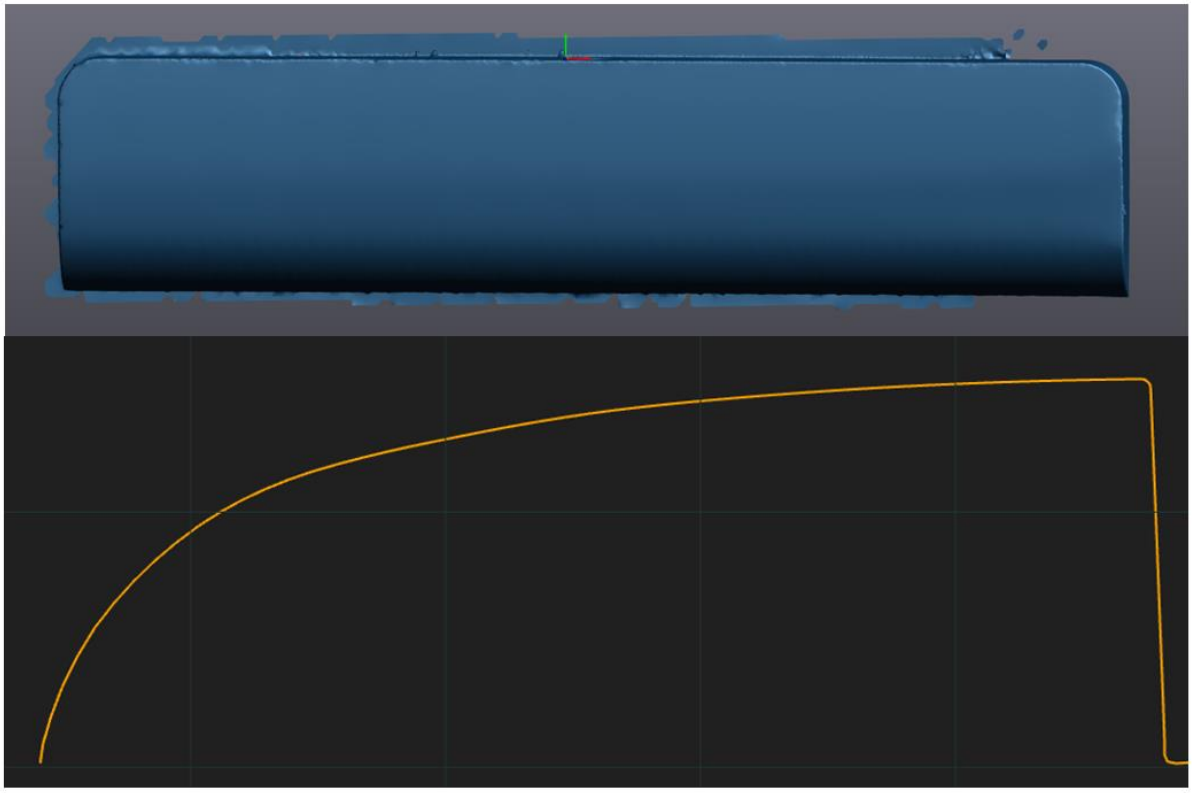

a)

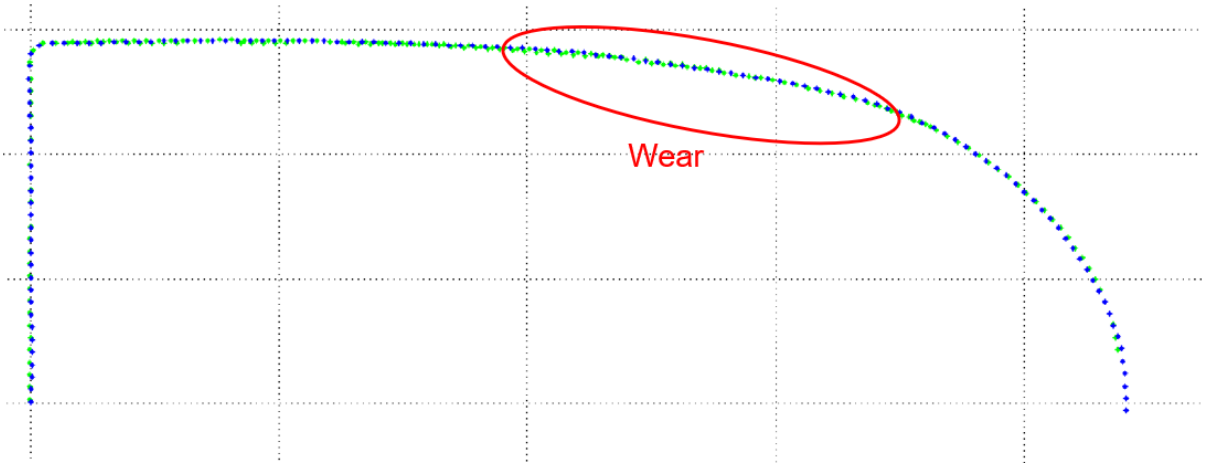

b)

Figure 6.7: Stellite 6 clad pocket surface profile measurements: a) profile measurements by 3D laser scanner; b) profile measurement by Calipri before and after 5,000 cycles (green line refers to before test and blue colour to after test).

2D profiles of the Stellite 6 clad pocket specimen were taken close to the middle part of the specimen. The location of the section is shown Figure 6.4(b). The Stellite 6 clad pocket specimen profile measurements also showed there was no obvious deformation after 5,000 cycles. A wear region can be seen in Figure 6.7(b) but it is not plastically deformed. The wear zone inside the red circle part is shown.

Un-Clad R260

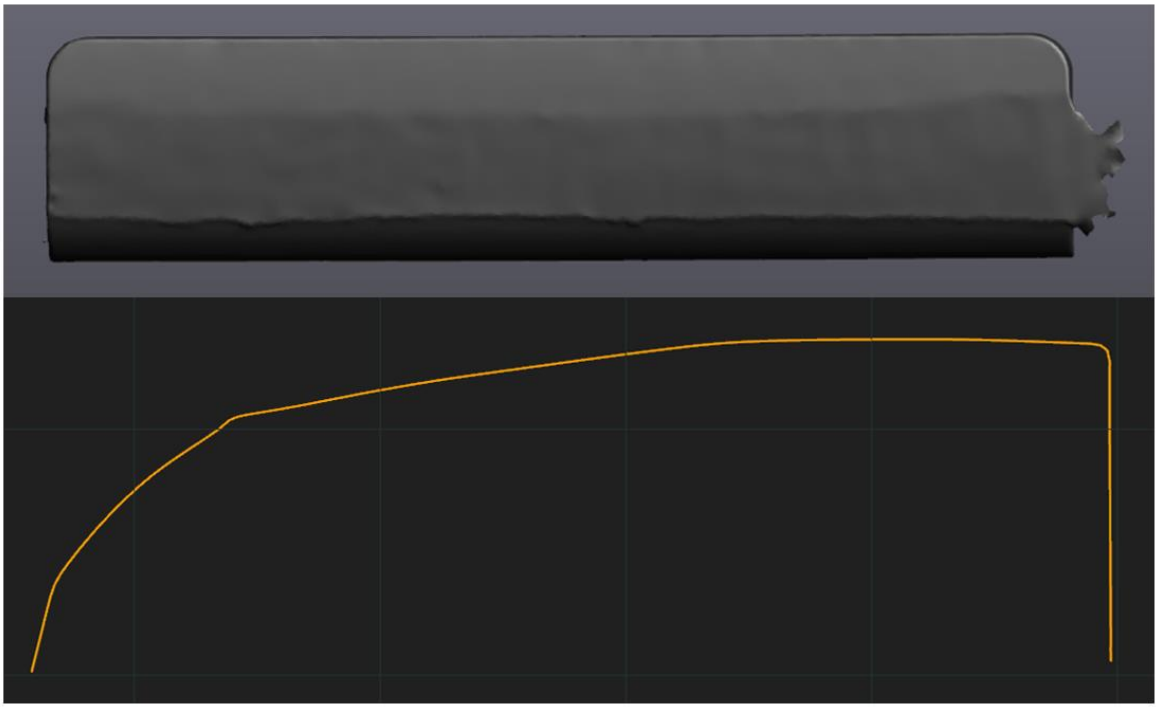

a)

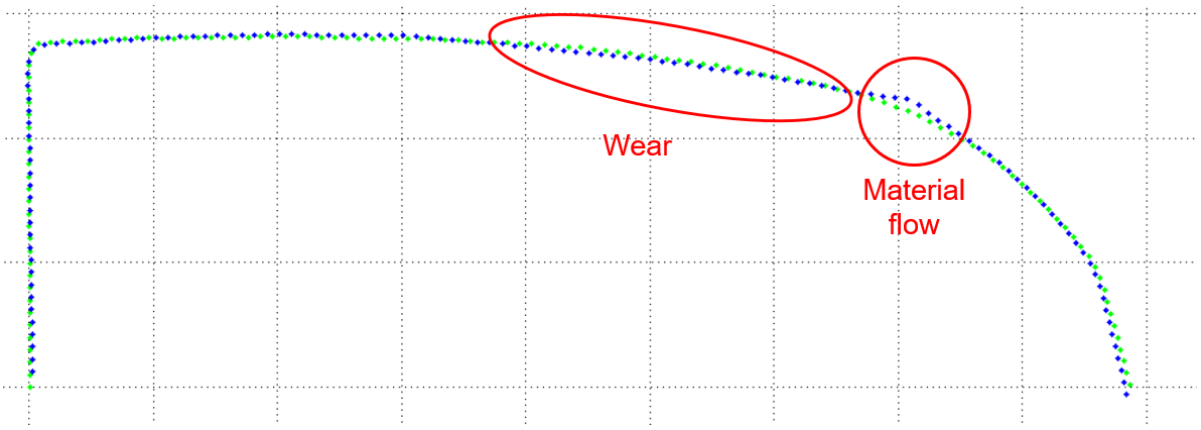

b)

Figure 6.8: Un-clad R260 pocket surface profile measurements: a) profile measurements by 3D laser scanner; b) profile measurement by Calipri before and after 5,000 cycles (green line refers to before test and blue colour to after test).

2D profiles of the un-clad R260 pocket specimen were taken close to the middle part of the specimens. The location of the section is shown Figure 6.4(c). The un-clad R260 pocket specimen profiles showed far more deformation than the clad materials after 5,000 cycles. Wear region can be seen in Figure 6.8(b) with material flow.

T400 Repair Specimen

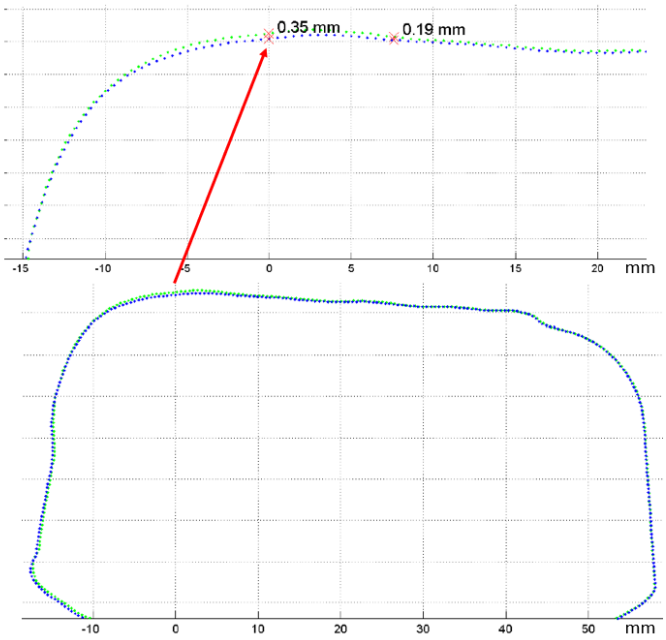

a)

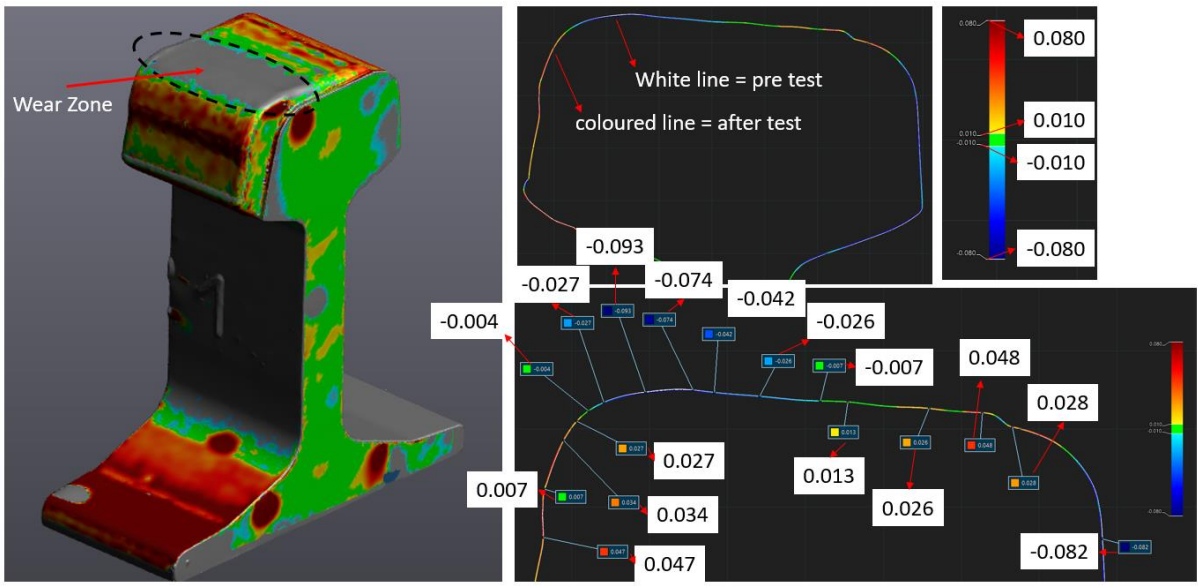

b)

Figure 6.9: Clad rail profile comparisons between pre and post-test condition: a) comparison by Calipri tool; b) comparison by HandyScan laser tool

Figure 6.9 shows the clad rail profile comparisons between the pre-test and after 5,000 cycles using the Calipri and HandyScan laser scanner tools. Figure 6.9 (a) shows the blue colour as an after the test profile while green shows pre-test. In the wear zone it showed around a 0.35 mm difference in height. However, the laser scanner tool output shown in Figure 5.9 (b) is different. When comparing all parts, the clad part, it deformed/wore with different amounts. In the wear zone it changed around -0.074 mm on the 2D image. The accuracy of the HandyScan laser tool is around 0.025 mm so the change is higher than the measurement resolution.

6.4.3 Comparisons between Laser Clad Pocket Profiles

MSS and Stellite 6

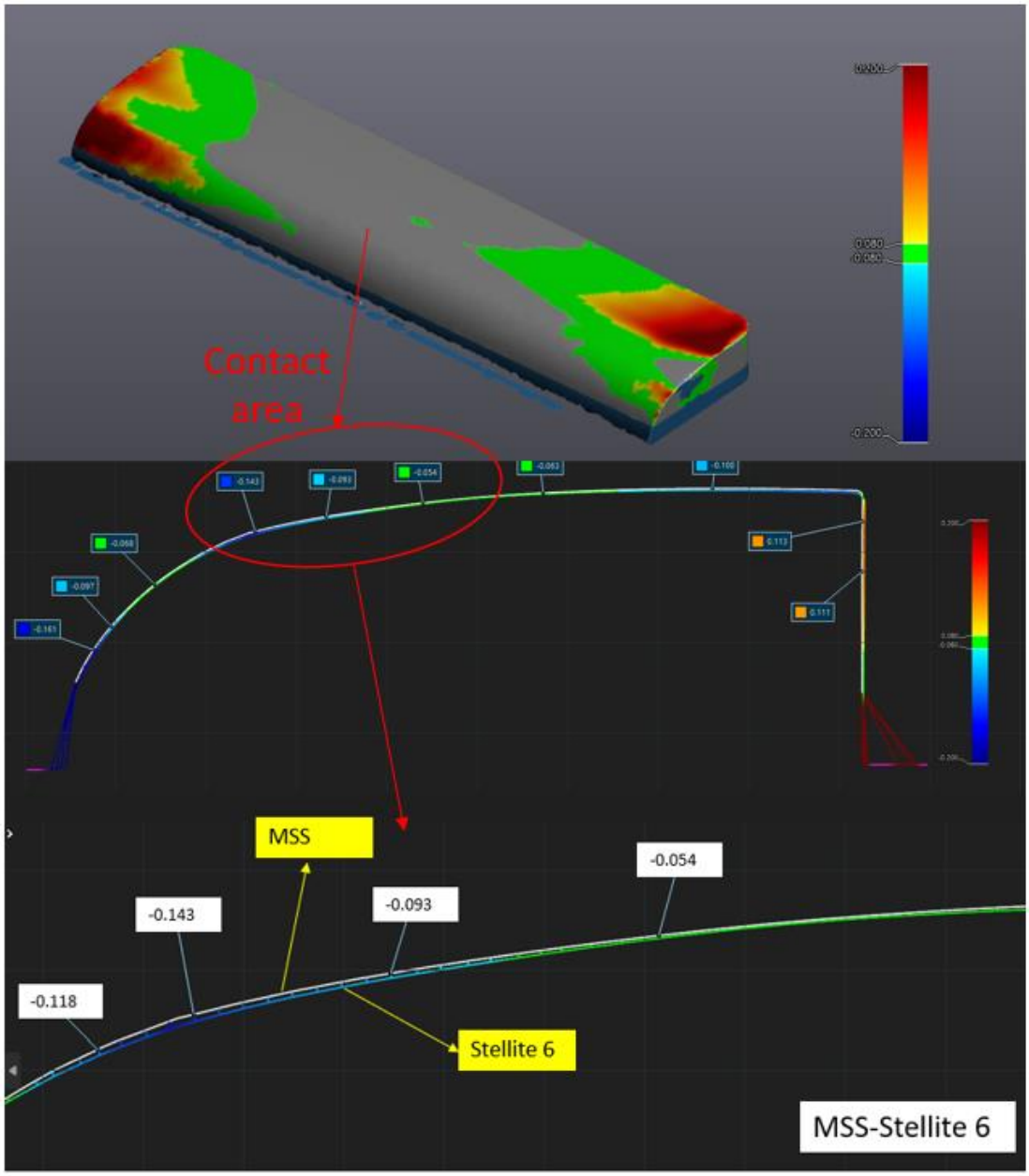

Figure 6.10: MSS clad and Stellite 6 clad pockets comparison after tests with 3D view of pockets and 2D profiles from laser scanner.

Figure 6.10 shows the MSS clad pocket specimen and Stellite 6 clad pocket specimen comparison after the tests. Images show the relationship between MSS clad pocket and Stellite 6 pocket profiles and how the contact happens during the tests. The contact patch can be seen in Figure 6.9 and the software from Creaform 3D laser scanner allowed matching of the scans. The MSS profile has worn slightly less than that of the Stellite 6.

MSS and R260

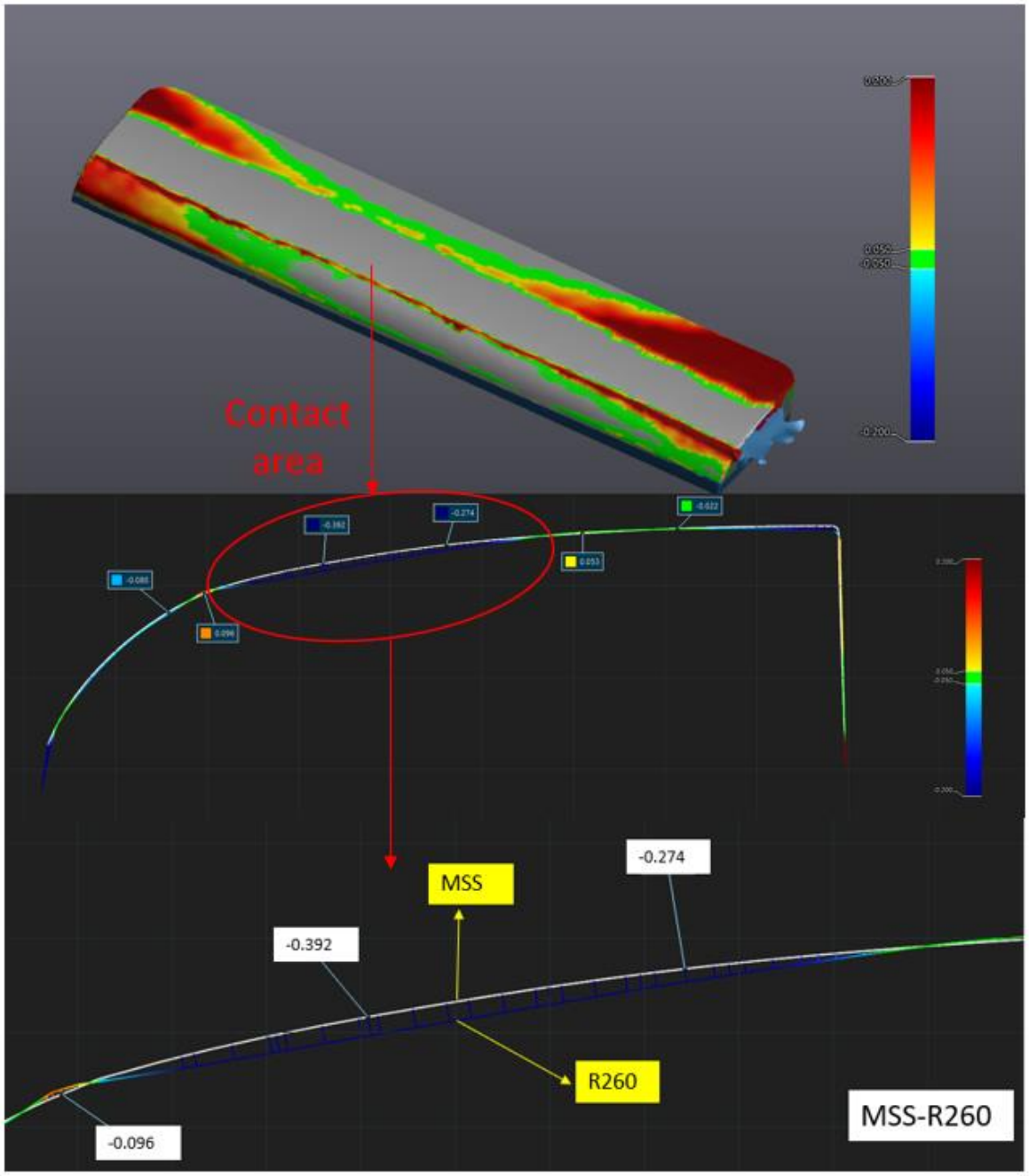

Figure 6.11: MSS clad and R260 no clad pockets comparison after tests with 3D view of pockets and 2D profiles from laser scanner

Figure 6.11 shows the MSS and unclad R260 pocket specimen comparison. These show the contact difference after 5,000 cycles of tests and the contact patch can be seen to have a big size difference. The R260 pocket specimen deformation is higher as its shape changed through plastic deformation and wear. The contact patch can be seen in Figure 6.11 and the software from Creaform 3D laser scanner allowed matching of the two specimens. From the 2D profiles,

it can be seen that the un-clad R260 pocket specimen profile wear is much greater than MSS clad pocket specimen profile wear. The contact area showed that R260 profile plastically deformed and the highest deformation can be seen at -0.392 mm from MSS clad pocket profile.

Stellite 6 and R260

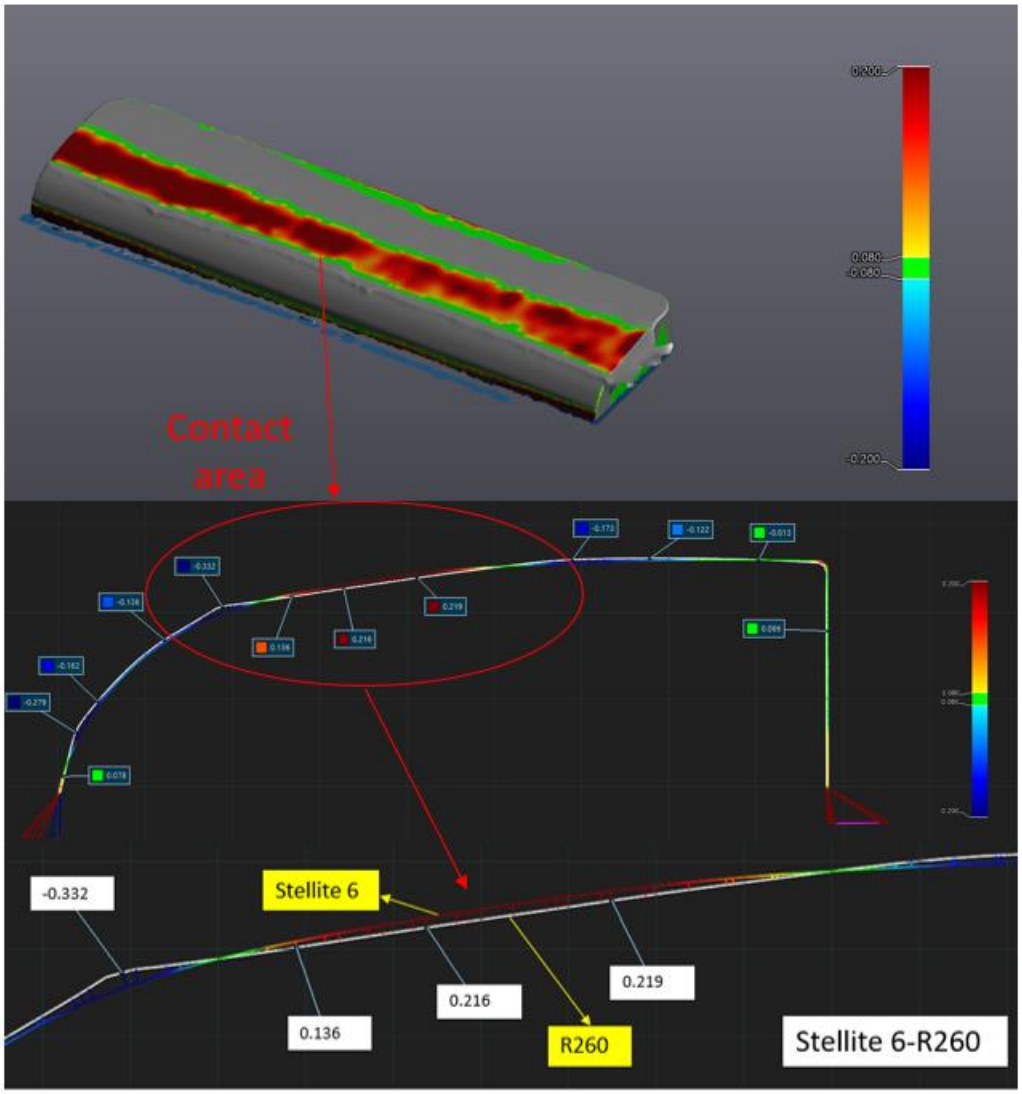

Figure 6.12: Stellite 6 clad and R260 no clad pockets comparison after tests with 3D view of pockets and 2D profiles from laser scanner

Stellite 6 and the un-clad R260 pocket specimen comparisons in Figure 6.12 show how the R260 is deformed more than the Stellite 6 clad. The contact patch can be seen in Figure 6.12 and the software from Creaform 3D laser scanner allowed matching of the scans. From the 2D profiles, it can be seen that the Stellite 6 wear is much lower than the un-clad R260. Material flow is visible on the edge on the un-clad R260.

6.4.4 Roughness

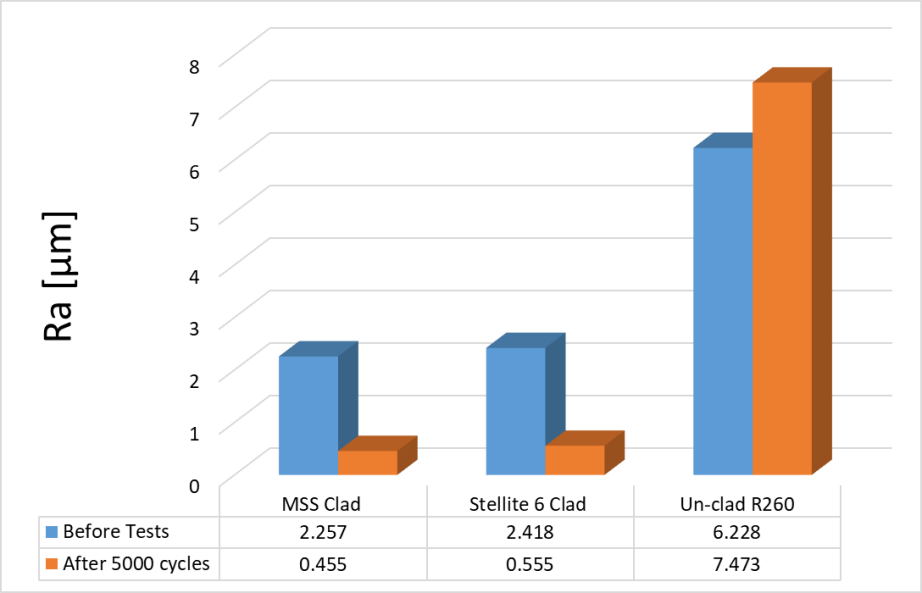

a)

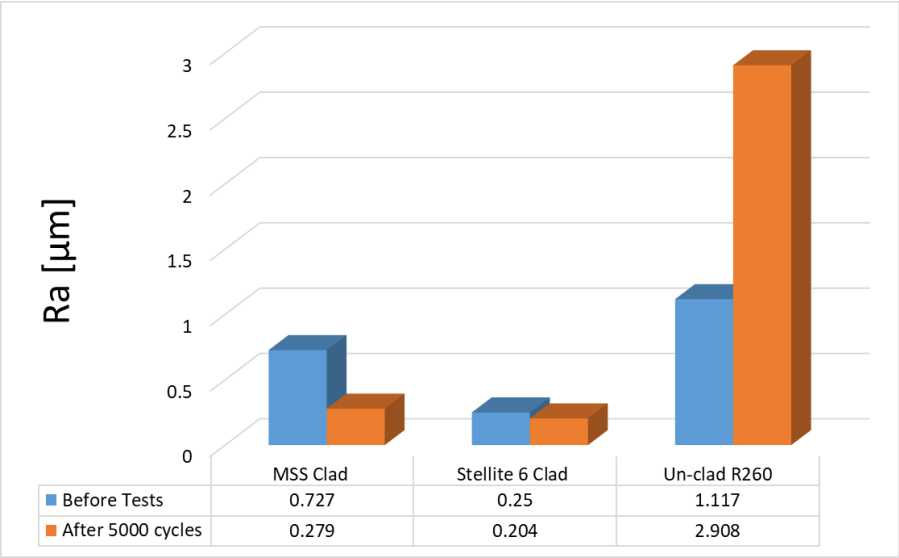

b)

Figure 6.13: Pocket tests roughness values on wear zone before and after 5,000 cycles. a) lateral roughness graph of pockets b) longitudinal roughness graph of pockets

Figure 6.13 shows the Ra roughness values for MSS clad, Stellite 6 clad and R260 pocket specimens. The lateral and longitudinal roughness measurements in the wear scars showed that the clad layers became smoother during the test, backing-up the observation of "polishing" made earlier. The un-clad R260 became rougher due to the local deformation and flake formation.

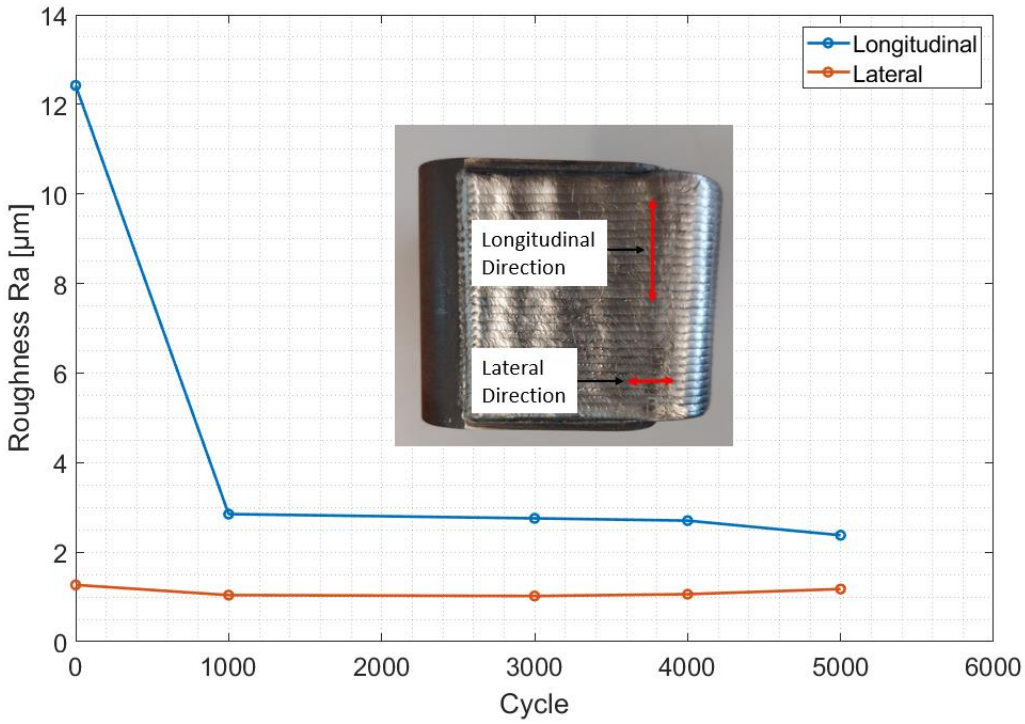

Figure 6.14: Full Scale clad rail roughness values in lateral and longitudinal directions

Figure 6.14 shows full-scale repair clad rail roughness values in lateral and longitudinal roughness directions. The figure shows a sharp decrease in the longitudinal direction from around 12 µm to 3 µm from the beginning to 1,000 cycles. This was initially very high because of the beading of the clad material across the railhead. It continued around that range until the end of the tests. Lateral direction roughness values showed a similar range from the beginning to the end of the cycles with around 1 µm.

6.4.5 Mass Loss

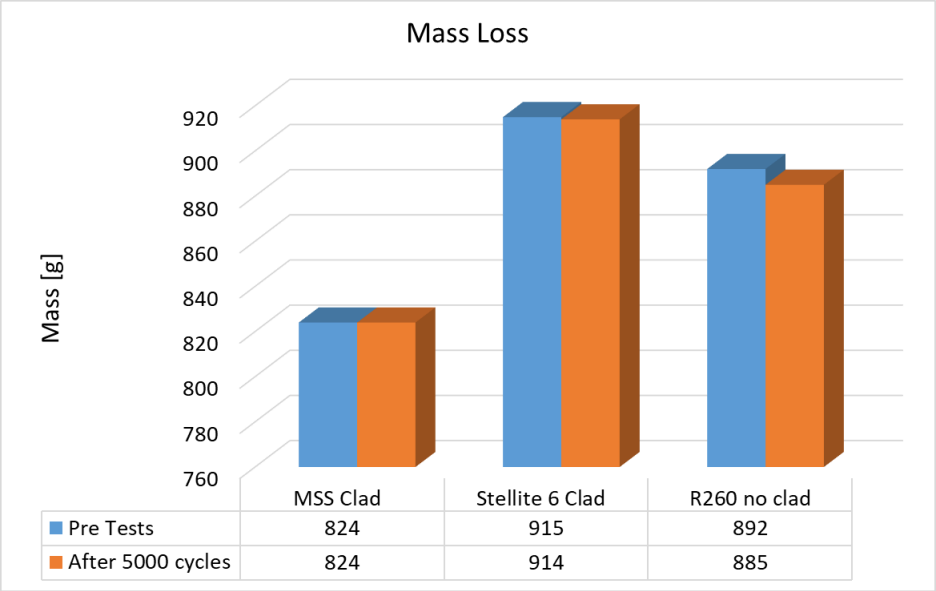

Figure 6.15: Pocket tests mass loss after 5000 cycles of full-scale tests

Mass of the pockets was measured before and after the tests and is shown in Figure 6.15. The R260 pocket had the highest mass difference, followed by the Stellite 6 and then MSS specimens. The level of mass loss will be put into context when the wear rates are compared with twin disc data in the discussion section.

6.4.6 Wear Debris

MSS Clad

Wear debris form the MSS clad pocket test was collected from the wear band after the test. Note that this would be made up of rail and wheel material. There Is no way of separating the two. Figure 6.16 shows the wear debris with different magnifications. It can be seen that the wear debris is flake like which would be characteristic of a ratchetting/delamination process. It seems more likely that the large flakes are from wheel, which would undergo the same process and the smaller particles (perhaps the lighter ones In the images) are from the MSS.

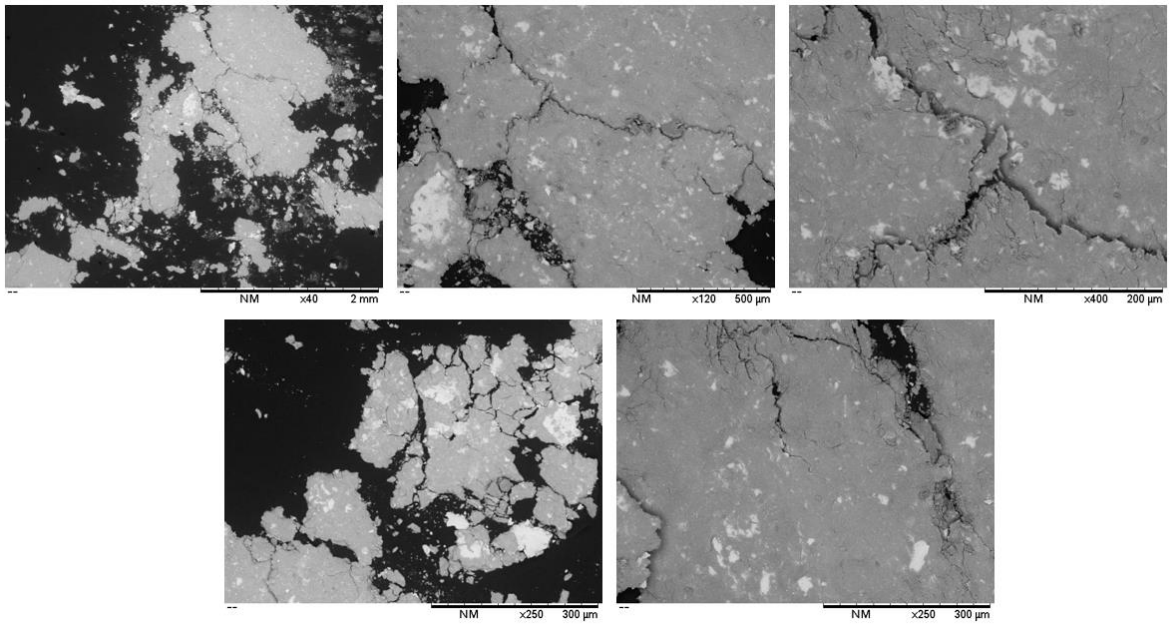

Figure 6.16: MSS Clad pocket test wear debris after 5000 cycles

Stellite 6 Clad

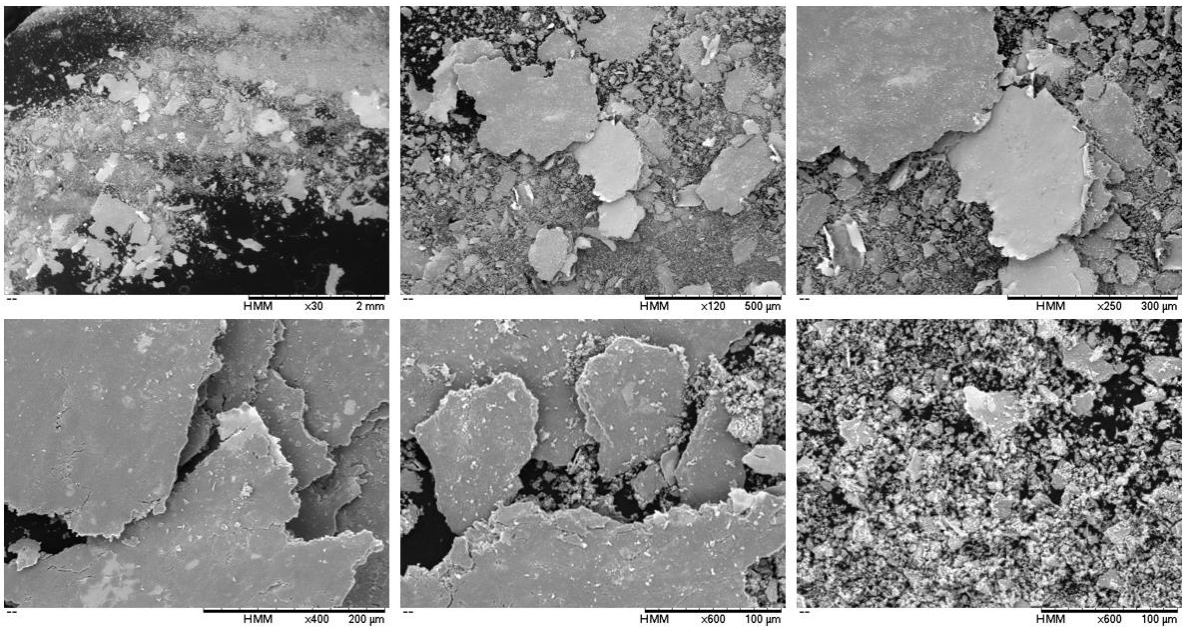

Figure 6.17: Stellite 6 Clad pocket test wear debris after 5000 cycles

Wear debris form the Stellite 6 clad pocket was collected from the wear band after the test. Figure 6.17 shows the wear debris with different magnifications. It can be seen that again there are large flakes present as well as some much finer debris. It is likely that the large debris is from the wheel and the smaller, fine particles are from Stellite 6.

R260 Un-clad

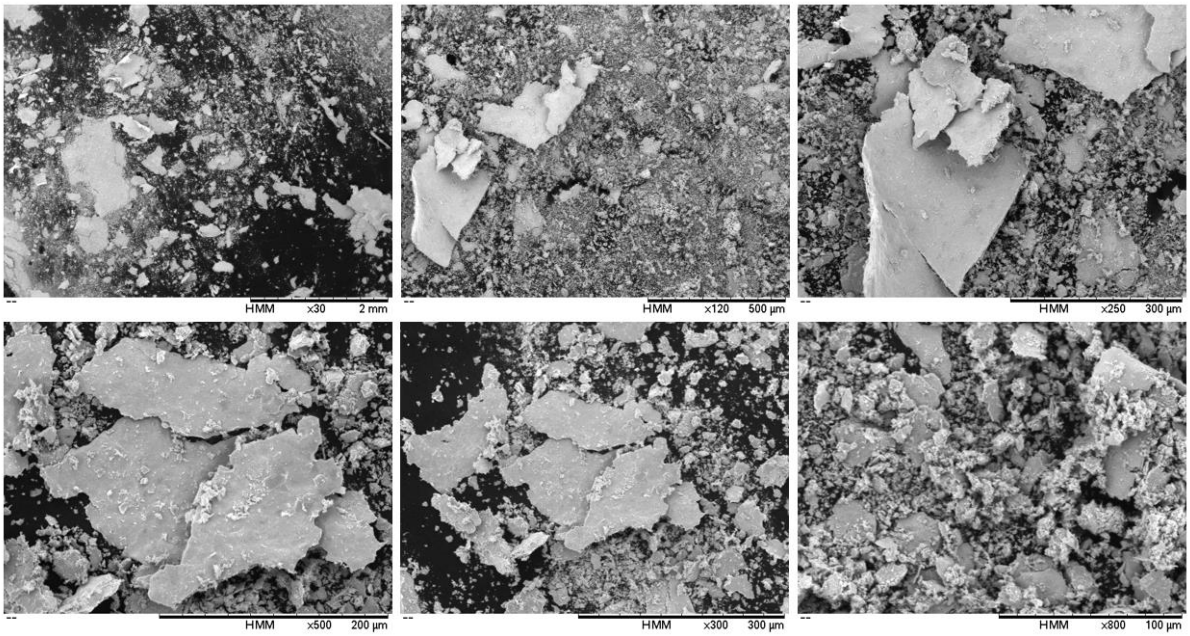

Figure 6.18: Un-clad R260 pocket test wear debris after 5000 cycles

Wear debris form the un-clad R260 pocket was collected from the wear band after the test. Figure 6.18 shows the wear debris with different magnifications. It can be seen that the wear debris is generally smaller than that from clad tests. Again, for the R260, the wheel will probably wear less so it is not surprising that the debris is generally smaller.

6.4.7 Sub-surface Analysis

6.4.7.1 Subsurface Images

After the full-scale rolling/sliding tests on the pocket samples were completed and all other measurements and images taken, they were sectioned and prepared for microstructural analysis. After mounting, grinding and polishing the samples were etched to expose the microstructural features. When etching the samples first, 2% Nital solution was used. This was able to expose the microstructure of the un-clad R260 pocket sample and the Stellite 6 pocket sample (clad layer and R260 substrate). However, to show the microstructure of the MSS clad layer it had to be etched with Vilella etchant as well.

MSS Clad

Figure 6.19 shows the sub-surface of the MSS clad. From the surface to the HAZ, there are two microstructure regions occurring in clad part. First starting from the surface until the second layer and then microstructure form changes until to the HAZ. It can be seen that some flake

formations occurred on the clad surface after the 5,000 cycles, indicating that some sub-surface deformation has occurred, although much lower than that experienced by the un-clad R260. The deformation depth is around 25 µm.

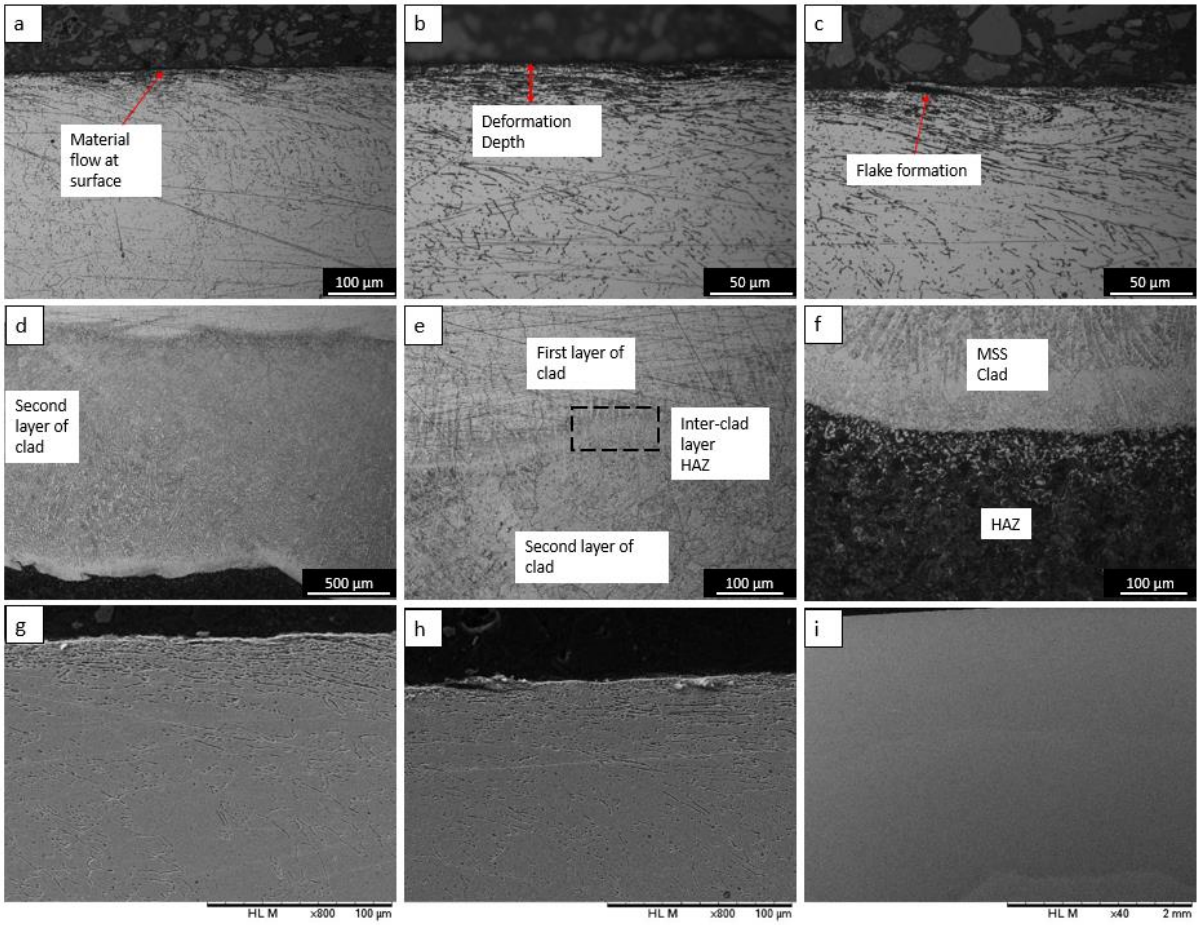

Figure 6.19: MSS Clad pocket test sub-surface microstructure images from optical microscopy (a-f) and SEM (g-i)

In Figure 6.20 the MSS clad and R260 substrate zone bonding region is shown. The images show that the bonding is good. The diffusion zone is approximately 50 µm thick. Lu et al., (2018) found the diffusion zone around 10 µm after the twin-disc experiments. It shows in the pocket specimen diffusion zone is bigger that the twin-disc specimen. Also clad thickness is bigger than the twin-disc specimen clad.

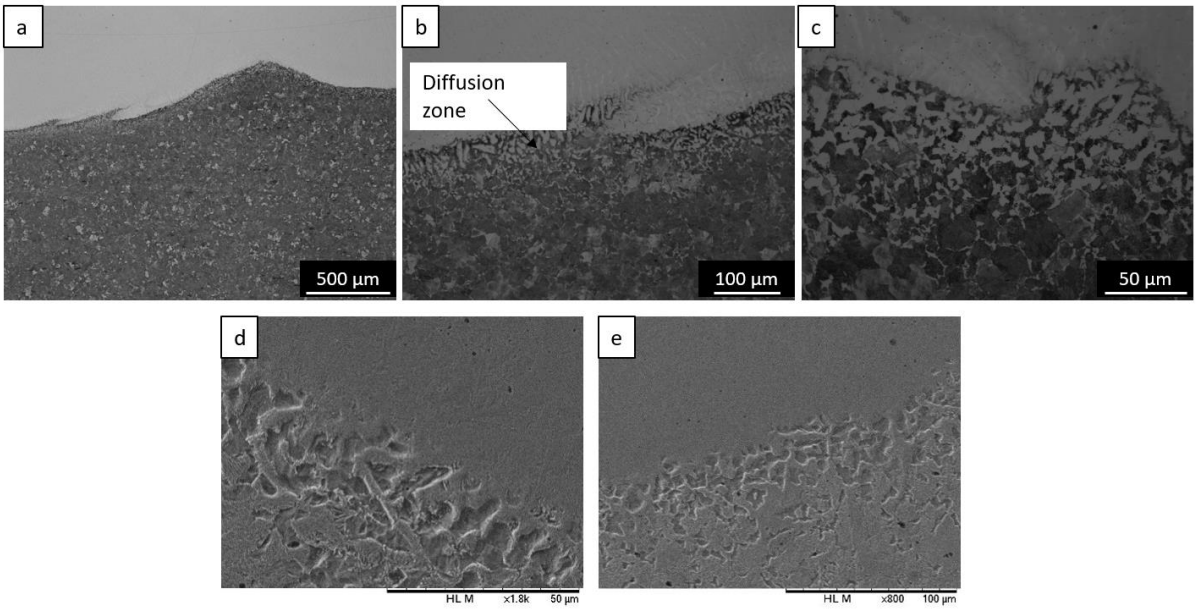

Figure 6.20: MSS clad pocket test clad and substrate part bonding microstructure images from optical microscopy (a-c) and SEM (d-e)

Stellite 6 Clad

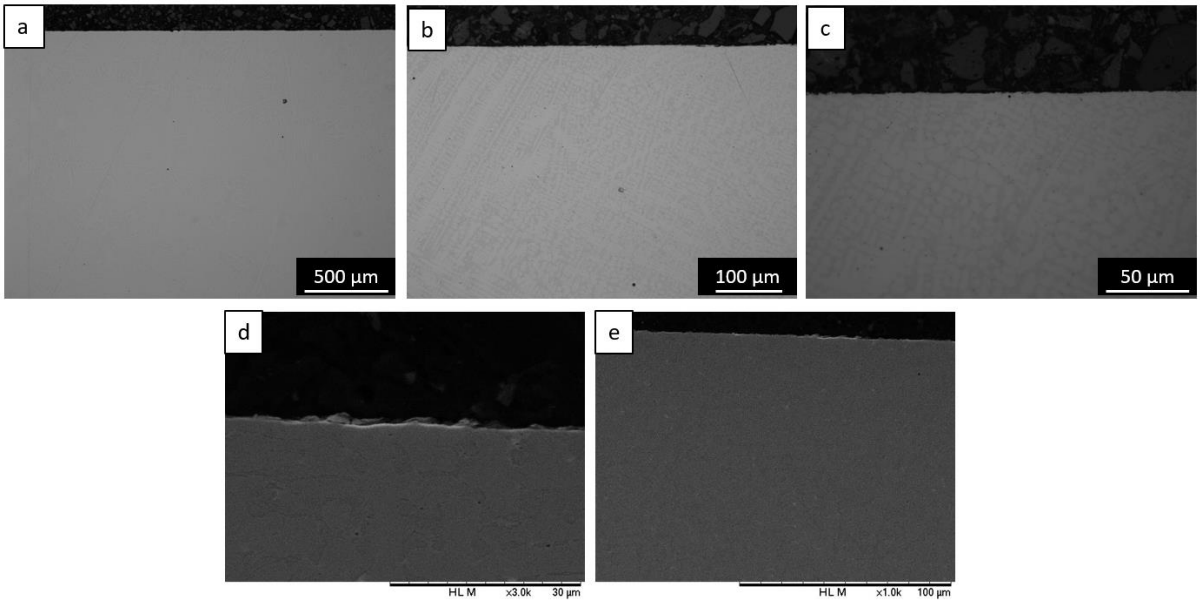

Figure 6.21: Stellite 6 Clad pocket test sub-surface microstructure images from optical microscopy (a-c) and SEM (d-e)

Figure 6.21 shows the sub-surface of the Stellite 6 clad and it looks as if it is undeformed after the 5,000 cycles. The microstructure of the Stellite 6 coating shows both inter-dentritic and dentrite structure on the images. The inter-dentritic structure is the darker colour of the structure on clad part and the dentritic structure is bright colour structure in the clad part in Figure 6.21

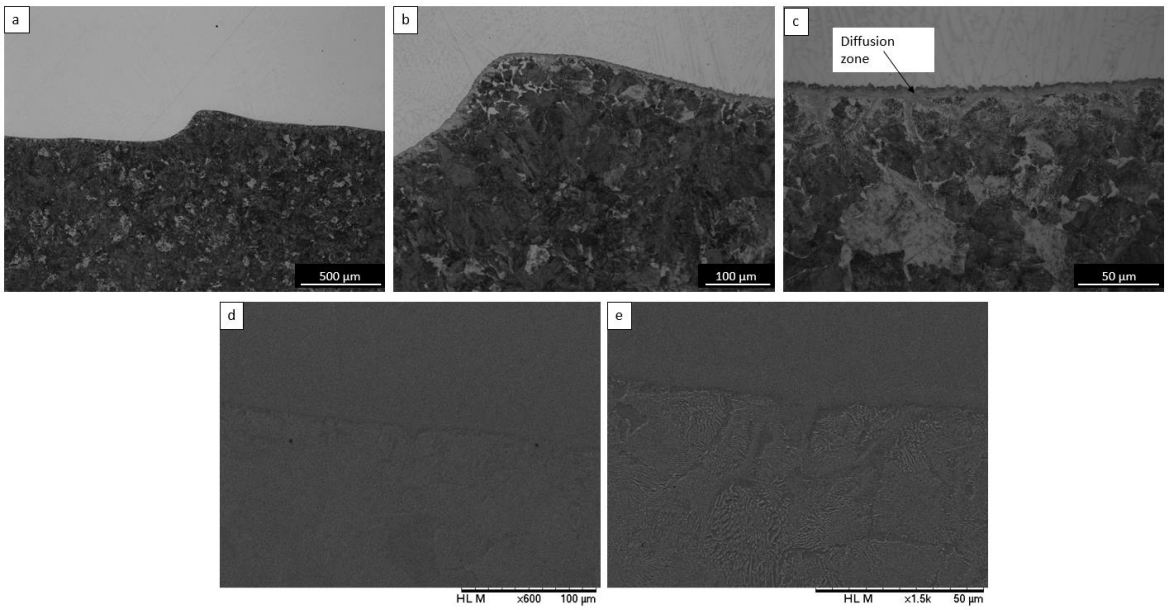

Figure 6.22: Stellite 6 Clad pocket tests clad and substrate part bonding microstructure images from microscope and SEM

Figure 6.22 shows the Stellite 6 clad and R260 substrate zone bonding. It shows good bonding was achieved between the two materials. The images show the HAZ in the substrate part as well as a small diffusion zone between under the clad approximately 10 µm deep.

Un-clad R260

Figure 6.23 shows the un-clad R260 pocket sample after etching. There is more deformation on the R260 pocket sample than the two clad pocket samples. The deformation depth is around 500 µm. The optical microscopy images show the extensive plastic deformation because of the rolling/sliding. At one point an interest "swirling" feature can be seen. Figure 6.23 d, e and f show the "swirling" shapes under the surface. Flakes are also visible on the surface which can be the initiation point of RCF cracks. In some places cracks have grown a little deeper into the material.

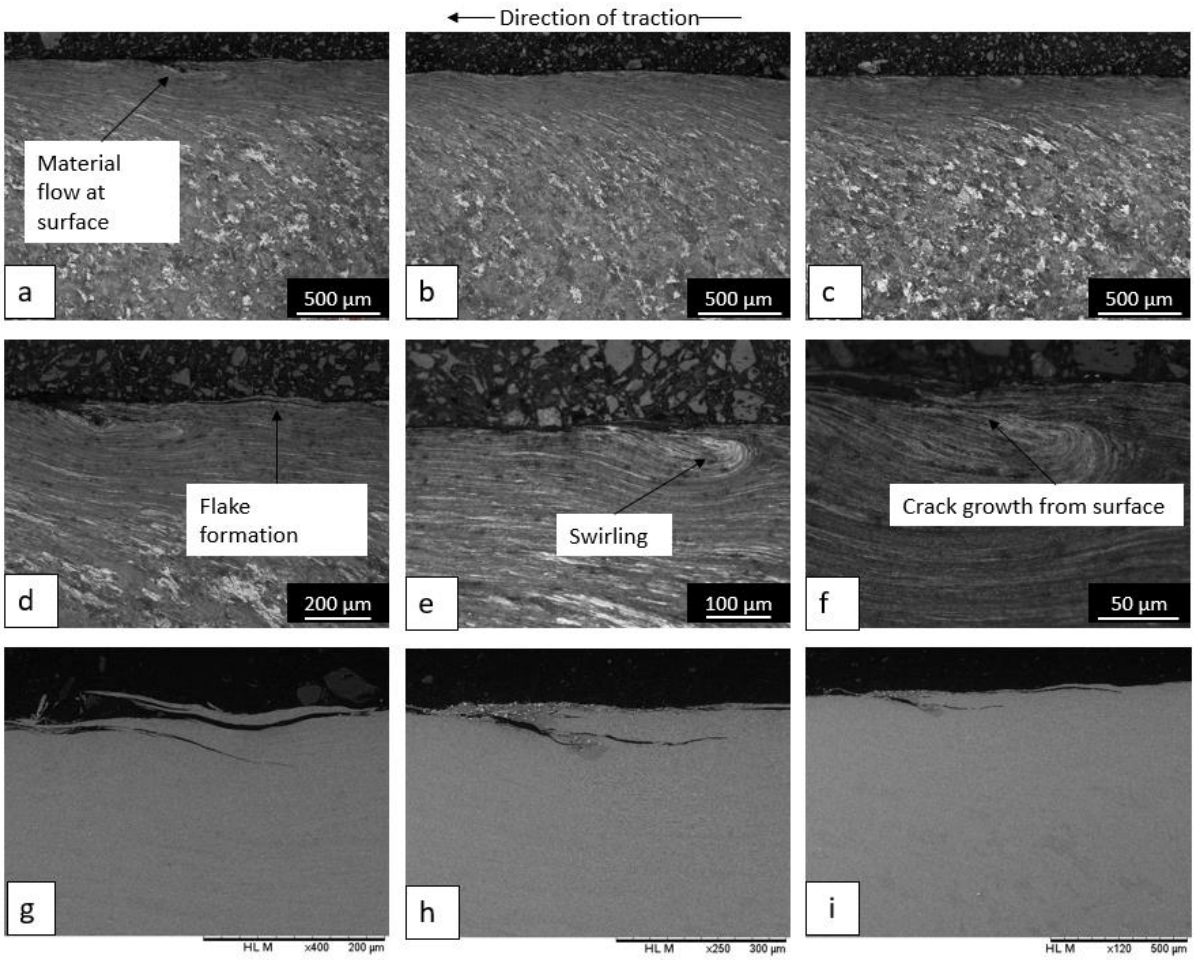

Figure 6.23: R260 un-clad pocket test microstructure images from optical microscopy (a-f) and SEM (g-i)

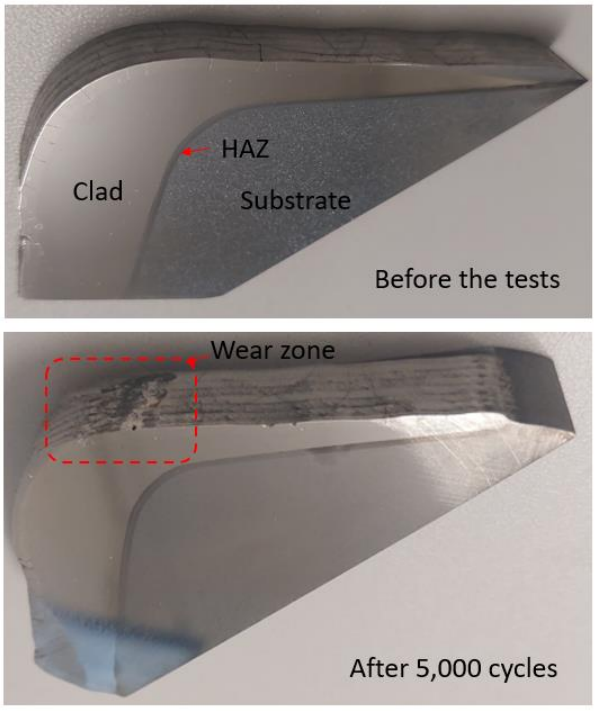

Figure 6.24: Full-scale rail-clad sample before and after tests images

Figure 6.24 shows before and after images of the sectioned full-scale samples. The substrate part was etched with 2% Nital solution to reveal the microstructure. The shiny part over the etched part is the T400 clad part. In total there were 35 layers of T400 clad over the substrate rail.

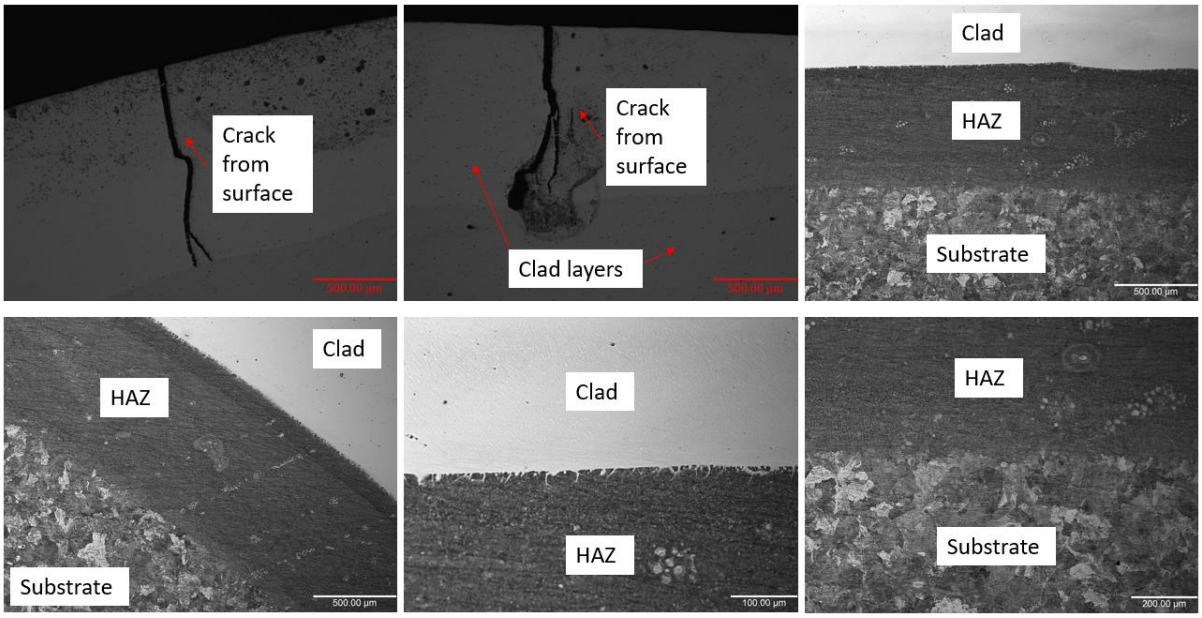

a)

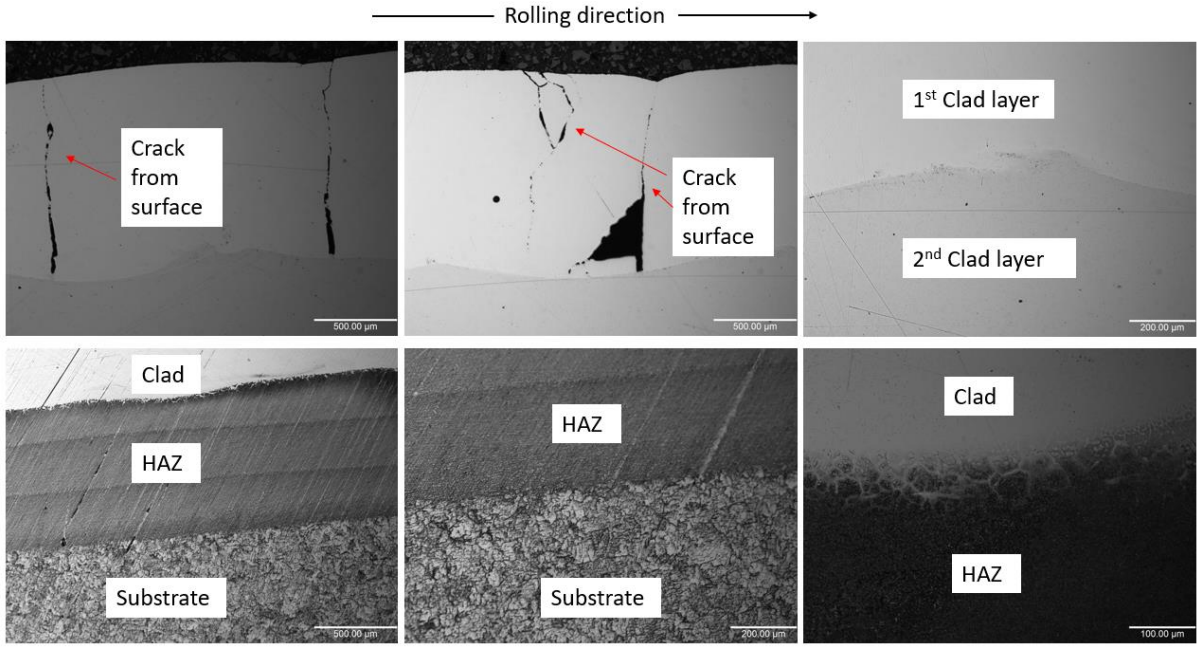

b)

Figure 6.25: Microstructure images of clad rail: (a) before the tests and (b) after the tests

Figure 6.25 shows the microstructure images of the full-scale rail clad section Images were captured from wheel and rail contact zone that is shown in Figure 6.24a. There were a few cracks in the top layer of clad applied, but the lower layers were fine. Figure 6.25a showed there were still some cracks before starting any experiment. Figure 6.25b shows microstructure images after 5,000 cycles and cracks were seen on the surface layers but they had not grown into the lower layers.

6.4.7.2 Micro Hardness

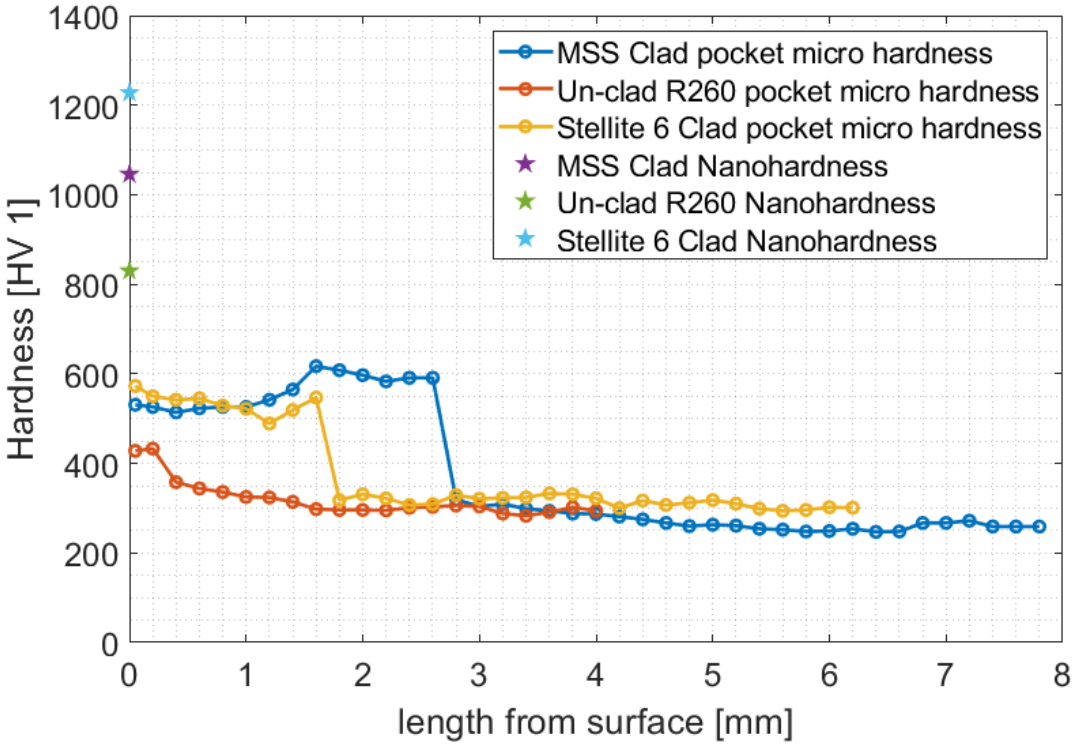

Figure 6.26: Full scale test specimen micro-hardness and nano-hardness measurements after tests

Figure 6.26 shows the hardness of the full-scale pockets after tests. It shows both nano-hardness and micro-hardness data. Nano-hardness data shows higher values than micro-hardness. Nano-hardness measurements were carried out as they could be achieved closer to the specimen contact surfaces. The surface hardness is 1046 HV for MSS, 1228 HV for Stellite 6, 830 HV for the un-clad R260. Nano-hardness values show a big difference from micro-hardness values so care must be taken with interpreting the nano-hardness value as typically values from nano-indentation are higher than the micro-hardness values by about 30% (Qian et al., 2005). They explain that the main reason for that is nano-indentations use the projected contact area at peak load, however, micro-hardness uses residual projected area.

The micro-hardness data covers the clad layer through to the bulk material. R260 pocket was non-clad pocket, and it has lowest hardness data between micro-hardness data. Stellite 6 clad zone has higher data than MSS clad zone until 1mm of the surface then MSS clad zone continue with higher values than Stellite 6 clad. When the clad zone finishes it continued with the HAZ and substrate parts and hardness decreases sharply after the clad zones. On the substrate part both clad specimens showed similar values to the un-clad R260.

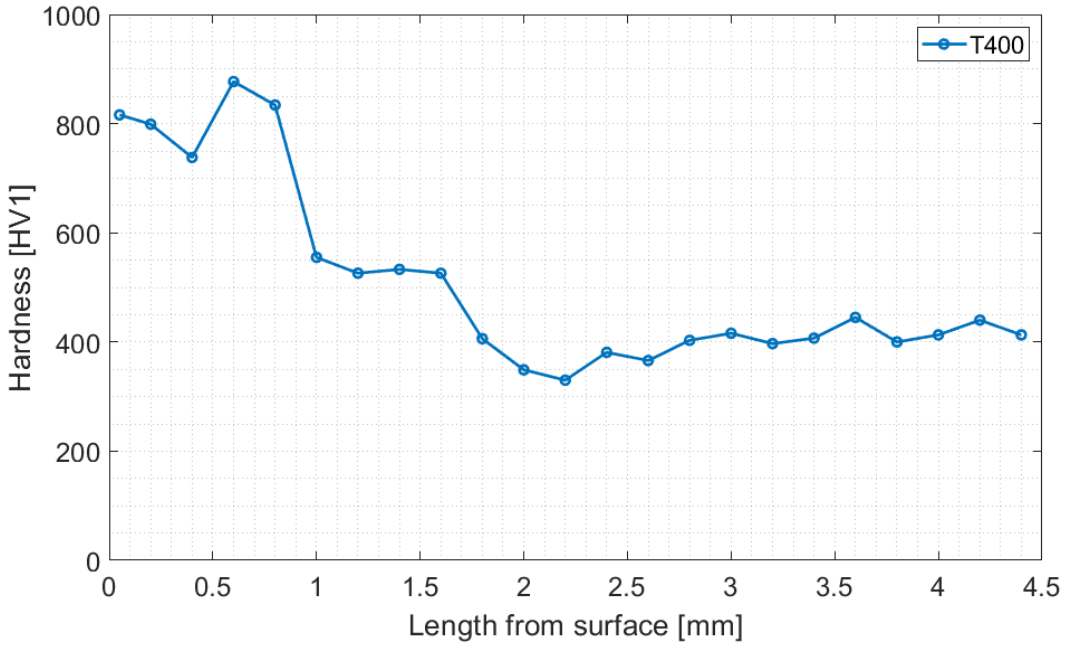

Figure 6.27: Repair T400 full scale sample hardness measurements

Figure 6.27 shows the hardness measurements of the repair full-scale sample. In the clad part from the surface to a depth of a few mm, hardness value shows around 800-1000 HV1 and in the HAZ part of the rail specimen it decreases until 500 HV1 and in the substrate part it shows hardness around 400 HV1.

6.4.7.3 Nano Hardness

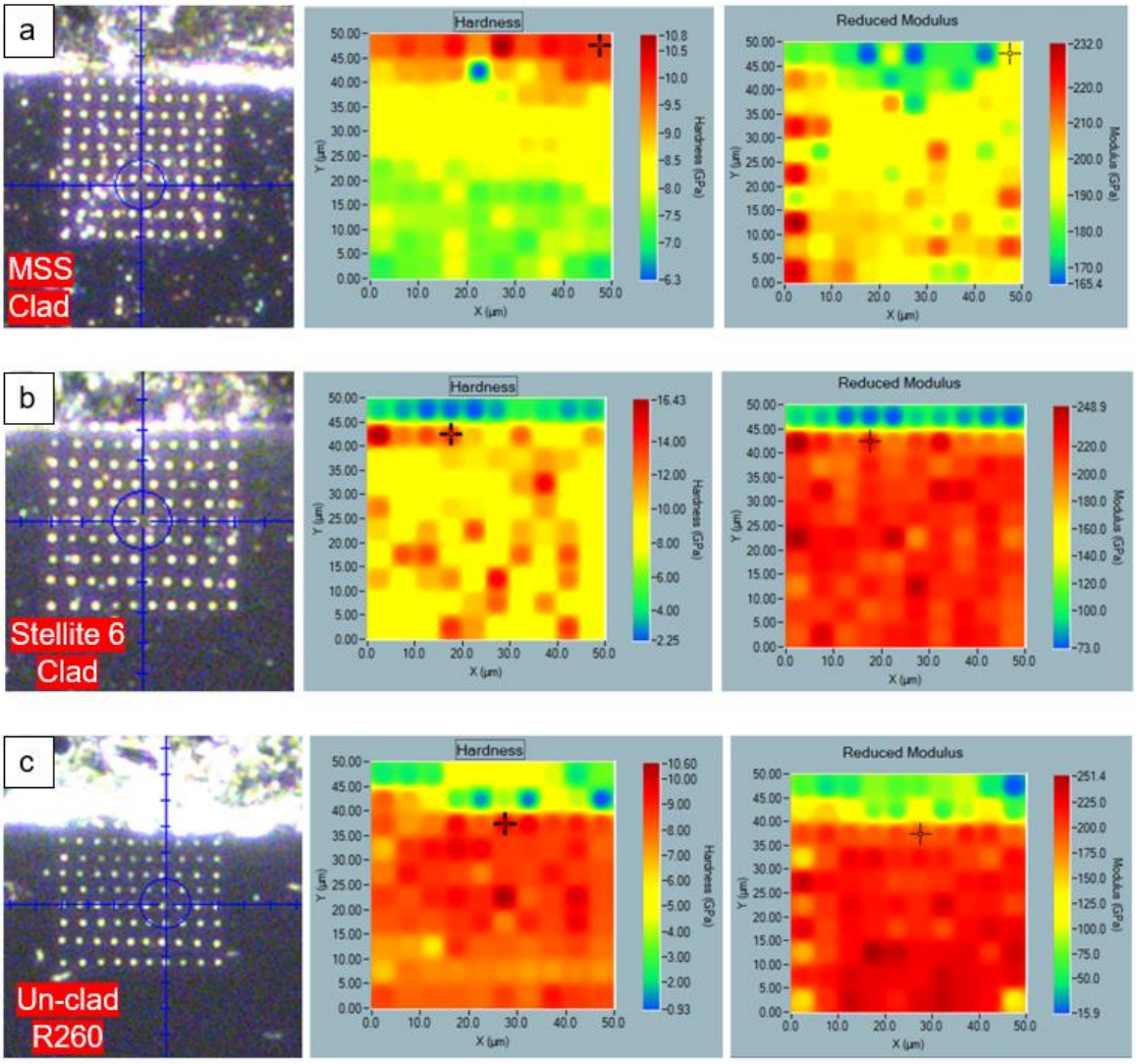

Figure 6.28: Full scale tests pocket specimen nano-hardness maps after tests: a) MSS clad; b) Stellite 6 clad; c) Un-clad R260

Figure 6.28 shows the pocket specimen nano-indentation maps. Each has a matrix of 10x10 nano-indentation points The MSS clad surface nano-hardness map in Figure 6.24 a shows the average nano-hardness value is 8.26 GPa and the reduced modulus is 195.93 GPa. On the surface the nano-hardness is 9.95 GPa and reduced modulus is 192.59 GPa. The Stellite 6 clad surface nano-hardness map in Figure 6.24 b shows the average nano-hardness value is 9.94 GPa and the reduced modulus is 226.56 GPa. At the surface the nano-hardness is 13.65GPa and reduced modulus is 223.58 GPa. The un-clad R260 surface nano-hardness map in Figure 6.28 c shows The average nano-hardness value is 8.23 GPa and the reduced modulus is 220.33 GPa. At the surface the nano-hardness is 9.48 GPa and reduced modulus is 198.33 GPa.

6.5 Discussion

6.5.1 Wear Mechanisms

The un-clad R260 shows evidence of higher wear and deformation than the clad layers through all the measurements. The surface flakes (which caused the surface roughness to increase) and the sub-surface deformation Indicate that a ratchetting mechanism dominates as has been seen in many other studies of rail material wear.

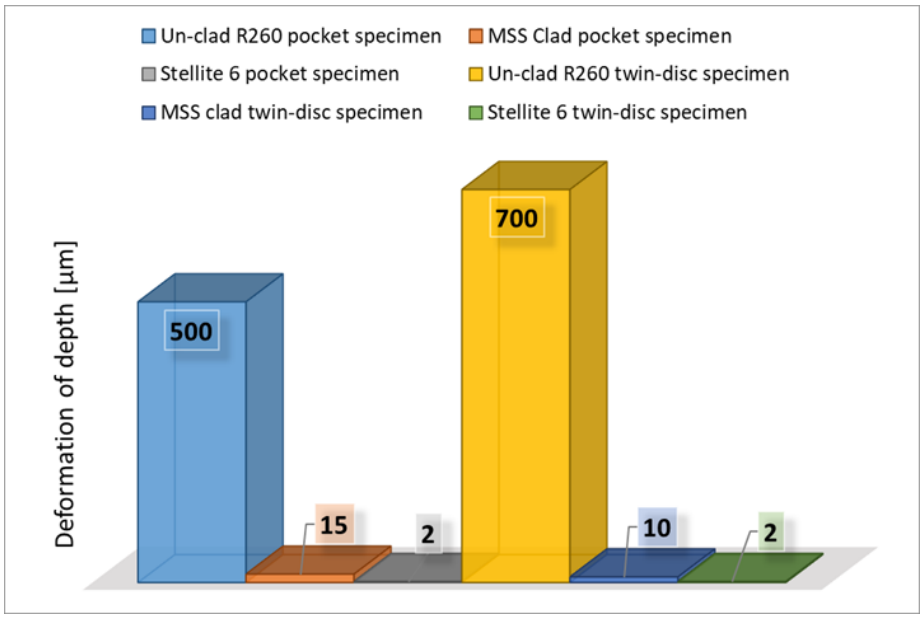

Figure 6.29: Deformation of depths after the experiments from twin-disc tests by (Lu et al., 2018) and full-scale tests comparison

The clad layers experienced much less wear. The surfaces also became smoother during the tests. There was some indication of deformation in the sub-surface images, but this was an order of magnitude lower than that seen on the un-clad R260 (see Figure 6.29). This matches observations from twin disc testing (see Figure 6.29 and Figure 6.30). In both twin-disc and full-scale testing the deformation was higher in the MSS than Stellite 6 which was probably due to the higher hardness of the Stellite 6 (see Figure 6.26). The evidence suggests that ratchetting is not the dominant wear mechanism in the case of the clad layers and perhaps that mild abrasion was observed which would explain the polishing effect that led to the lower post-test roughness. The lowering of roughness was also seen in twin disc testing of these materials (see Table 6.2) (while unpublished, the data is from tests carried out in Lewis et al. (2016)).

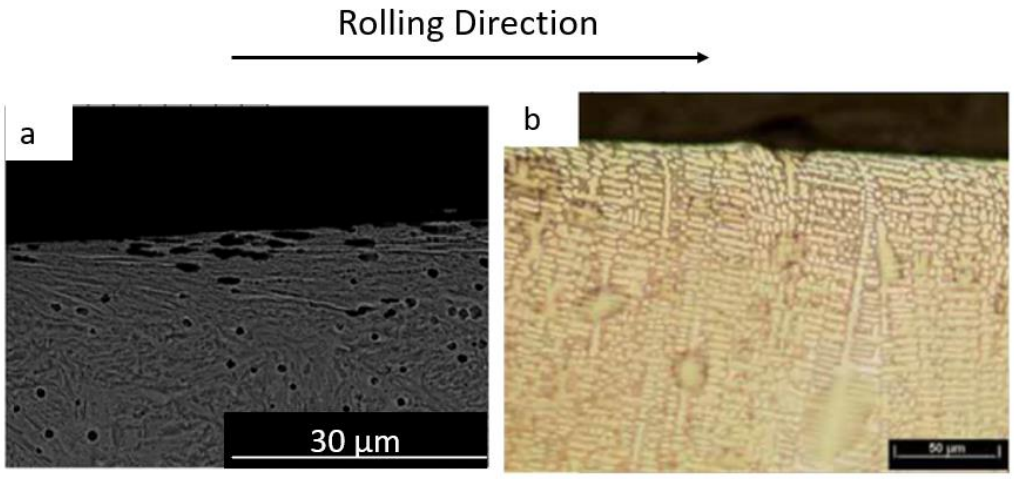

Figure 6.30: Microstructures images after tests a) MSS clad twin disc sample after 30,000 cycles (Lu et al., 2018); b) Stellite 6 clad twin-disc sample after 30,000 cycles (Lewis et al., 2016)

Table 6.2: Comparison of roughness Ra [µm] between test scales and materials

Reference	Test	Material	Initial Roughness (Ra [µm])	Final Roughness (Ra [µm])	Percentage Roughness Change (((final/initial roughness) ×100)-100)
Lewis, et al. (2016)	Twin disc	MSS	1.66	1.09	-33%
Lewis, et al. (2016)	Twin disc	Stellite 6	1.70	1.00	-41%
Lewis, et al. (2016)	Twin disc	R260	0.84	5.16	514%
Current study	Full-scale	MSS	2.257	0.455	-80%
Current study	Full-scale	Stellite 6	2.418	0.555	-77%
Current study	Full-scale	R260	6.228	7.473	20%

The biggest roughness change can be seen in R260 twin-disc sample with 514% in table 6.2. MSS and Stellite 6 clad specimen roughness's were decreased from initial roughness to final roughness values. R260 pocket specimen roughness shows increase with 20% but the final roughness value still highest between final roughness values. The percentage difference low due to the grinding on twin-disc R260 sample.

6.5.2 Wear Rates

One approach that can be used to compare wear for different test scales is the Tγ method. Tγ (where T is the tractive force (friction coefficient × normal force) and γ is the slip in the contact) is an indication of energy dissipated in the interface. This can be normalised by dividing by area (A) allowing different contacts to be compared. It has been shown in the mild wear regime, that wear rate is proportional to Tγ /A (Lewis & Dwyer-Joyce, 2004). Figure 6.26 shows twin disc wear data for un-clad R260 and MSS and Stellite 6 clad layers from previous studies (Lewis & Dwyer-Joyce, 2004; Lewis et al., 2015b; Lu et al., 2018) along with the full-scale wear data from these tests. It can be seen that the wear rates fit the same linear relationship against Tγ/A Indicating that the full-scale results are In line with the twin-disc results. This shows it is valid to use twin-disc testing wear rates as a means to predict full scale wear through the Tγ method. The full-scale results also confirm that the clad layers perform well.

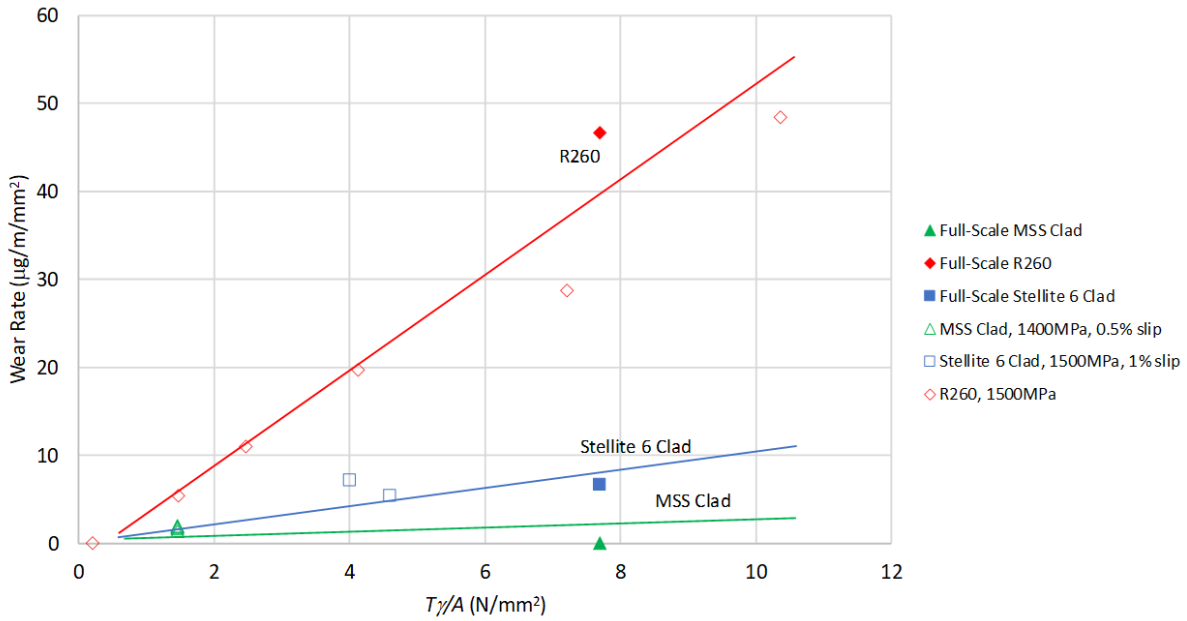

Figure 6.31: Wear rates of full-scale rail pocket specimens and twin-disc specimens against Tɣ/A approach

6.5.3 Hardness Evolution

Final hardness values for the MSS clad and Stellite 6 compare well with those from twin disc testing as shown in Figures 6.27 and 6.28 and Table 6.3.

Work hardening trends between the small and full scale specimens are similar. This is quite promising as the thermal processing between the two is different due to the size difference between the two and some hardness values may not be accurately comparable as they will have been taken at different depths.

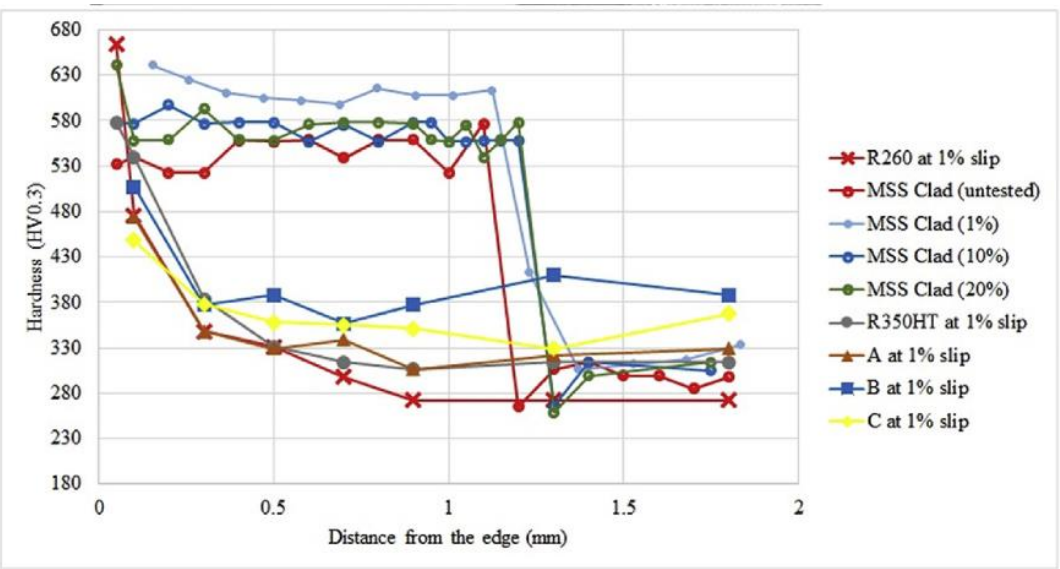

Figure 6.32: Hardness data for a range of clad and un-clad materials after twin disc testing (Christoforou et al., 2019)

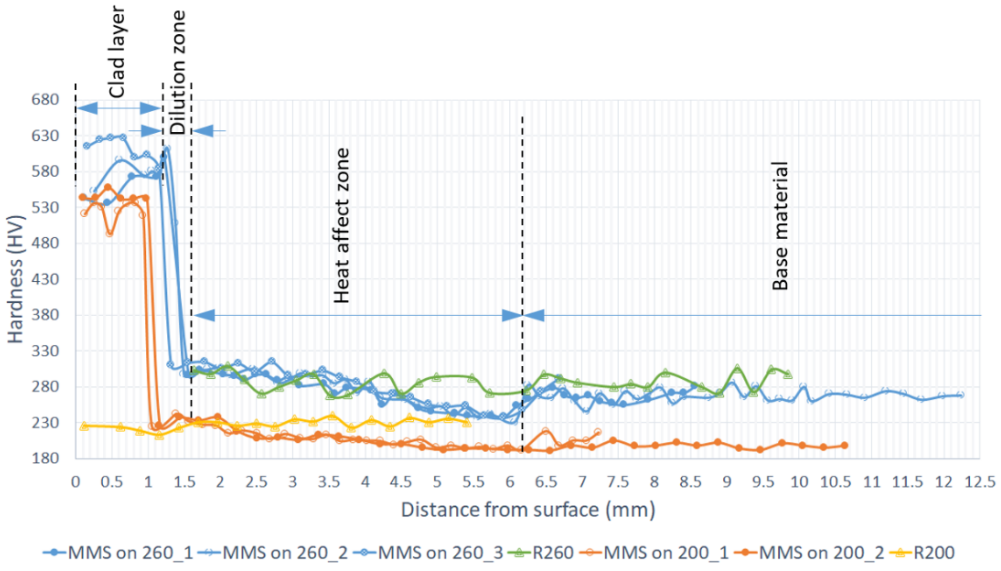

Figure 6.33: Hardness data for clad layers from previous twin disc testing (Lu et al., 2018)

Table 6.3: Comparison of clad layer micro-hardness between current full-scale tests and previous twin disc testing

Reference	Test	Material	Initial Hardness [Hv]	Final Hardness [Hv]	Percentage Work Hardening (((final/initial hardness) ×100)-100)
Lu et al. (2018)	Twin disc	MSS	-	630	-
Christoforou et al., (2019)	Twin disc	MSS	-	640	-
Lewis, et al. (2016)	Twin disc	MSS	607	805	+33%
Lewis, et al. (2016)	Twin disc	Stellite 6	647	786	+22%
Lewis, et al. (2016)	Twin disc	R260	308	784	+154%
Current study	Full-scale	MSS	600	804*	+34%
Current study	Full-scale	Stellite 6	550	944*	+71%
Current study	Full-scale	R260	300	638*	+113%

* Micro-hardness value estimated by dividing nano-hardness value by 1.3 (based on (Qian et al., 2005))

Percentage of work hardening was shown in table 6.3 and un-clad R260 showed highest values with %154 In twin disc group of tests and %113 in full scale group of tests. When work hardening percentage increase from twin-disc tests to full scale tests in MSS and Stellite 6 clad,

R260 percentage decreased from %154 to %113. Also, Stellite 6 samples were showed the highest difference with increasing from %22 to %71 from small-scale test to full-scale test.

6.5.4 Microstructure Observations

Some interesting features were seen in the microstructure images of the clad layers that will be discussed here.

In Figure 6.19(a-c,g,h), the MSS clad shows two phases with dentritic solidification morphology, the black phase is clearly visible together with the white phase due to etching. The second phase may correspond to retained delta ferrite due to an incomplete peritectic transformation or a $M_{23}C_6$ carbide or both according to the pseudo-binary phase diagram in Figure 6.34. The matrix has deformed on the surface and aligned these black phases to the runout of the deformation.

Figure 6.19(e) shows a fascinating phenomenon. A heat-affected zone (HAZ) is formed within the melt zone of the first MSS clad pass. Thus, we have an aligned dendritic morphology in the region with higher heat input at the interface of the first and second pass, which austenitizes and returns to room temperature in a way that has less of a rough casting texture. The regions with lower heat input may undergo recrystallization and recovery but tend to change morphology less. This phenomenon is known as “temper bead” (Vishnu, 2018). For steels, that have a greater tendency to form untampered martensite during the weld, this temper bead helps to increase the toughness in these HAZ regions. However, martensitic steels will soften locally in this region.

Figure 6.20(b) reveals some important information. In the region described as the diffusion zone, phases similar to the pro-eutectoid morphology can be seen. To analyse this microstructure, the phase diagram in Figure 6.34 is useful. Assuming that most of the substitutional alloying elements cannot get enough mobility and the fact the carbon, an interstitial alloying element, level in the MSS is considerably smaller than the rail (see Table 6.1), the carbon will be the one to migrate by diffusion toward the molten metal, generating this diffusion zone (Bhadeshia & Honeycombe, 2006). As shown in Figure 6.34, when increasing the amount of carbon at high temperature, there may be a tendency to enter the liquid, delta ferrite (BCC), or austenite (FCC) at higher temperature and the precipitate in the form of carbide $M_{23}C_6$ region.

The Stellite 6 clad layer microstructure in Figure 6.21(b,c) clearly shows the dendritic morphology of the molten zone, including the main direction tending towards heat extraction

(pointing towards the surface). The dendritic morphology occurs due to the heat extraction/micro-segregation and is very characteristic of the molten zone.

In Figures 6.22(b) and 6.22(e) it can be seen that at the rail adjacent to the clad metal, the microstructure presents pro-eutectoid ferrite decorating the former austenite grain boundaries with pearlite inside the grains. Diffusion leads to a local decrease of carbon concentration at the interface and tends to form pro-eutectoid ferrite. Pro-eutectid ferrite found in rail welding also follows the prior austenitic grain boundary (Nishikawa & Goldenstein, 2019). The same feature is observed in Figure 6.20. The diffusion region causes the rail carbon (with higher concentration) to diffuse toward the molten metal (MSS – lower concentration) and deplete it locally. The lower amount of carbon leads the rail to have a composition less than that of the eutectoid (see table 6.1) and consequently forms pro-eutectoid ferrite on cooling.

Throughout the images where the HAZ below the clad layer is visible an evolution is visible as the depth increases towards the bulk R260 microstructure (for example Figure 6.19(f)). This was also described in detail in twin-disc testing of MSS clad layers (Lu et al., 2018). It follows the observations made by, others (Mansouri & Monshi, 2004) and is similar to that seen in rail welds.

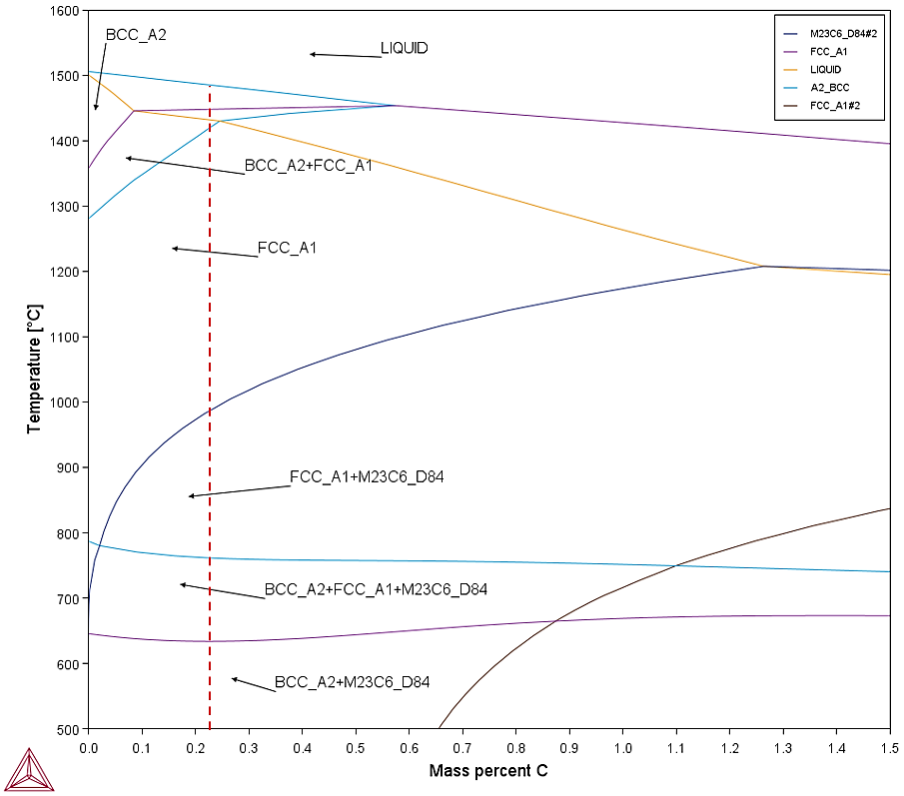

Figure 6.34: Pseudo-binary diagram of steel with similar chemical composition to MSS clad deposited layer calculated by Thermocalc® software.

6.5.5 Full-scale Clad Repair Behaviour

In the full-scale repair test, the T400 clad specimen was a harder material and after many clad layers it showed some cracks in the surface (outer) layers before the tests and they went down until the top surface layer over the substrate in Figure 6.25 (a). Those cracks could be because of the laser cladding parameters or material choice. Some materials give tensile residual stress that means it is more likely to crack or not be good for multiple layers (Narayanan et al., 2019).

After the tests it could be seen that surface layer cracks did not go further than the outer layer, so they had not propagated. That first layers of clad were not deformed much and the T400 clad specimen did not fail under full-scale test conditions. In the field, such deep layers of clad repair are not expected, but it showed that this kind of the repair can stay in place without any big failure. As long as the clad repair part and rails are at the same height, the rail can survive.

A limitation in both the small scale and full-scale tests is that they do not have any bending effect in the experiments. It can be good to check how bending affects the clad performance in three or four point bend tests, such as those carried out previously by Lewis et al. (2017).

6.6 Conclusions

Full-scale tests have been carried out of clad rail samples and an un-clad R260 reference sample. All samples were analysed using a range of measurements to allow a comparison between the clad and un-clad rail behaviour as well as comparisons with previous twin disc testing of the same materials.

The MSS and Stellite 6 clad layers performed very well in the tests exhibiting far less wear, plastic flow and crack formation than the un-clad R260 material. This confirms what was seen in previous twin disc testing. The clad materials stayed well bonded and are clearly a good solution for assessment in field trials.

The good correlation between the twin-disc testing and full-scale testing across wear rates, mechanisms, work hardening, and roughness evolution shows that the outcomes of small-scale tests are good indicators of full-scale behaviour for reducing the amount of full-scale testing needed in assessing future potential clad materials.

The observations of the microstructures, particularly around the differences seen in different layers when multiple layers were applied will be very useful in designing approaches for cladding in the future to create specific microstructures in the clad layers.

In the full-scale repair tests, it was seen that the T400 material did not fail under actual load conditions, but there were some issues with the chosen laser clad parameters and clad layer thickness. It is not expected that such deep clad layers will be used in the field, but it showed that it can survive with a high number of layers.

Chapter 7

7 Premium Rail Materials and MSS Laser Cladded Rail Characterizations

Premium rail materials can be used in the railways, and they have had some good effects on the durability of the rails (Christoforou et al., 2019). In this testing, wear and RCF performance of some premium materials used in crossing-nose applications were evaluated using twin disc tests to compare with the laser cladding tests. Wear tests showed good results and comparisons between premium rails and clad rails. In the tests, Mn, Cr and R400 rail discs were used as premium rail and MSS clad was used as a clad material over the R260 substrate rail. ERT 7 was used for wheel discs in the tests.

7.1 Test Apparatus

Premium rails wear tests were carried out on the Sheffield University Rolling Sliding (SUROS 1) twin-disc test rig, as can be seen in Figure 4.1. Line contact is used between twin-disc test specimens on this machine to simulate the normal load and rolling-sliding performance at the wheel/rail interface.

7.2 Measurements

Measurements were divided into those taken before, during and after the tests. Before starting the experiments, surface roughness was measured using an Alicona non-contact surface measurement tool. Images were taken and discs were cleaned with Acetone. After cleaning, mass and diameter of the discs were recorded at room temperature and humidity in the SUROS 1 laboratory.

During the tests, after each block of cycles, the tests were stopped and the mass and diameter of discs were recorded again. Surface roughness values were measured, and tests were continued with recording the temperature and humidity of the laboratory. The same was done between all blocks of the tests.

After all the blocks of cycles in each test were finished, the mass, diameter of the discs, and roughness measurements were recorded. Laboratory temperature and humidity were recorded, and discs were sectioned for further analysis. Sectioned discs were mounted, ground and

polished. Micro and nano hardness measurements were done and after that, premium rail samples, and the substrate part of the MSS clad disc and wheel discs were etched with %2 Nital solution for microstructure analysis. Vilella etchant was used for the MSS clad disc to expose the microstructure of the clad layer on the disc. Microstructure images were collected for further analysis.

7.3 Test Conditions and Test Specimens

The conditions of the wear tests were 1400 MPa and 1800 MPa contact pressure and 0.5% slip. Table 7.1 shows the all-test conditions for the wear tests. Mn, Cr, and R400 premium rail discs were tested in both 1400 MPa 0.5% slip and 1800 MPa with 0.5% slip test conditions. The MSS-clad disc was tested with 1400 MPa and 0.5% slip only.

Table 7.1: Premium rails and MSS Clad test conditions

Test No.	Rail Material	Wheel Material	Contact Pressure [MPa]	Slip [%]	Disc Speed [rpm]
1	Mn-13	ERT 7	1400	0.5	400
2	Cr	ERT 7	1400	0.5	400
3	R400	ERT 7	1400	0.5	400
4	Mn-13	ERT 7	1800	0.5	400
5	Cr	ERT 7	1800	0.5	400
6	R400	ERT 7	1800	0.5	400
7	MSS Clad	ERT 7	1400	0.5	400

Rail and wheel discs were used in that experiments and the specimen features and images were shown in the chapter 3. The premium rail specimens were Manganese (Mn), Chromium (Cr) and R400 rail materials. ERT7 material was used as the wheel disc material in the tests. An MSS-clad rail disc was used to compare with the premium rails in wear tests using ERT 7 wheel discs. The chemical compositions of the premium rails, MSS clad and ERT7 wheel discs are shown in Table 7.2.

Table 7.2: Premium rails (Cr, Mn, R400), MSS clad and wheel (ERT 7) chemical compositions

	C [%]	Mn [%]	Si [%]	Cr [%]	Ni [%]	Mo [%]	Co [%]	V [%]	W [%]	N [%]	Al [%]	S [%]	P [%]	Fe [%]	Cu [%]	H [ppm]
Cr-Bainit	0.34-0.37	0.65-0.75	0.8-0.88	2.65-2.75	-	0.30-0.35	-	-	-	-	-	<0.007	<0.01	-	-	-
Mn 13	1.90	12.00	0.40	-	-	-	-	-	-	-	-	-	-	Bal.	-	
R400 HT	0.90-1.05	1.00-1.30	0.20-0.60	<0.30	-	-	-	-	-	-	-	Max. 0.020	Max. 0.020	Bal.	-	Max. 1.5
MSS	0.06	1.22	0.46	14.64	3.31	0.42	2.01	0.51	0.62	0.04	0.01	0.005	0.009	-	-	-
ERT 7	0.52	0.80	0.40	0.30	0.30	0.08	-	0.06	-	-	-	0.015	0.020	-	0.3	-

These premium rail materials were commonly used in rail and crossing applications. Cr rail steel grade has bainitic microstructure with 420-480 HBW hardness, higher than 1050 MPa tensile strength. Mn 13 is high manganese steel with 13% Mn. It has 450 HBW hardness and 420 MPa tensile strength. The R400 HT rail grade is a fine-pearlitic heat-treated rail grade and it is mainly used in tracks with extreme loading conditions. It has 440 HBW hardness, higher than 1280 MPa tensile strength. MSS is martensitic stainless steel and it has tensile strength up to 1700 MPa ERT7 has 245 HBW hardness, higher than 520 MPa tensile strength.

7.4 Results

7.4.1 Surface Evolutions

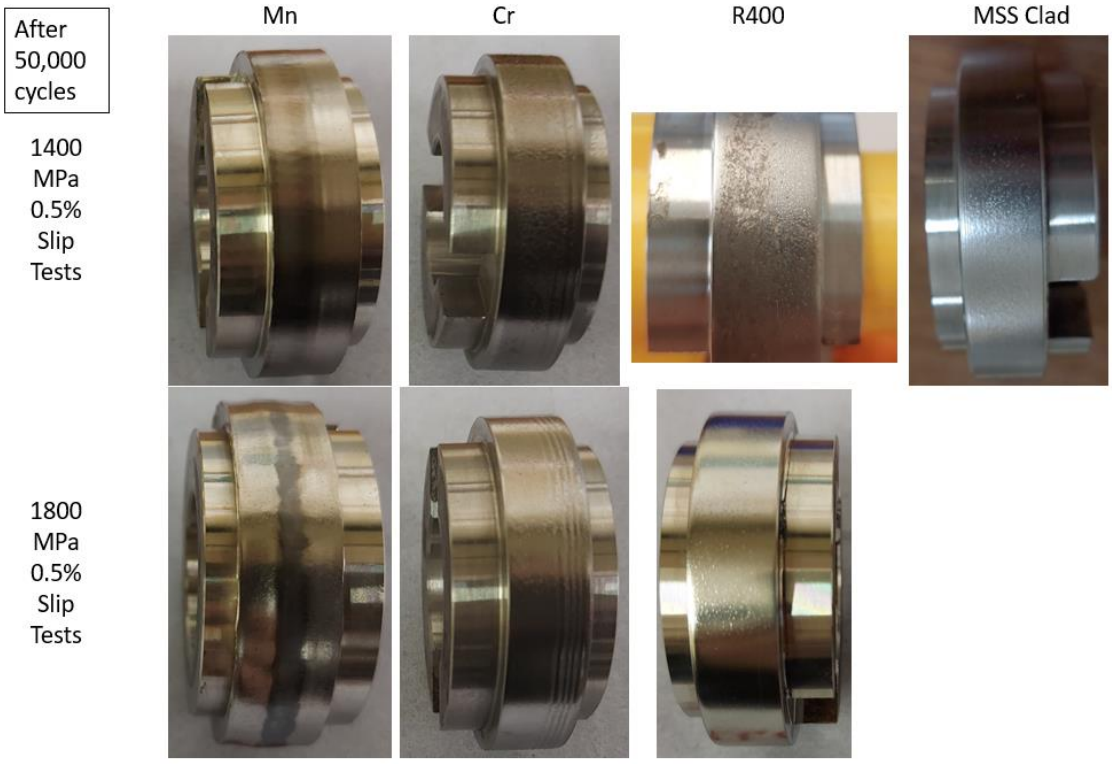

Figure 7.1: Premium rail discs and MSS clad rail disc surface images after 50,000 cycles with 1400 MPa, 0.5% slip and 1800, MPa 0.5% slip test conditions.

Figure 7.1 shows the surface images of the premium and clad discs after 50,000 cycles. The Mn disc showed a different pattern over the disc surface, and it can be easily seen for the 1800 MPa test condition, in the middle of the surface it shows a band of dark colour in the contact area. Cr disc showed some lines close to the edge of the contact surface and other discs showed some flake formation starting over the surface. In Appendix 7.A, Figure 12.15 and Figure 12.16, surface images can be seen for all cycles.Mn disc experiments showed that the wheel disc showed more deformation after the experiments. Also the Mn disc showed a dark colour band in the middle of the contact surface. That dark part caused partial contact over the disc and it caused the wheel disc to plastically deform more than other materials as can be seen in Appendix 7.A. The Mn rail disc was sectioned from middle of the surface in the dark region. It can be seen in the microstructure images Section 7.4.5..

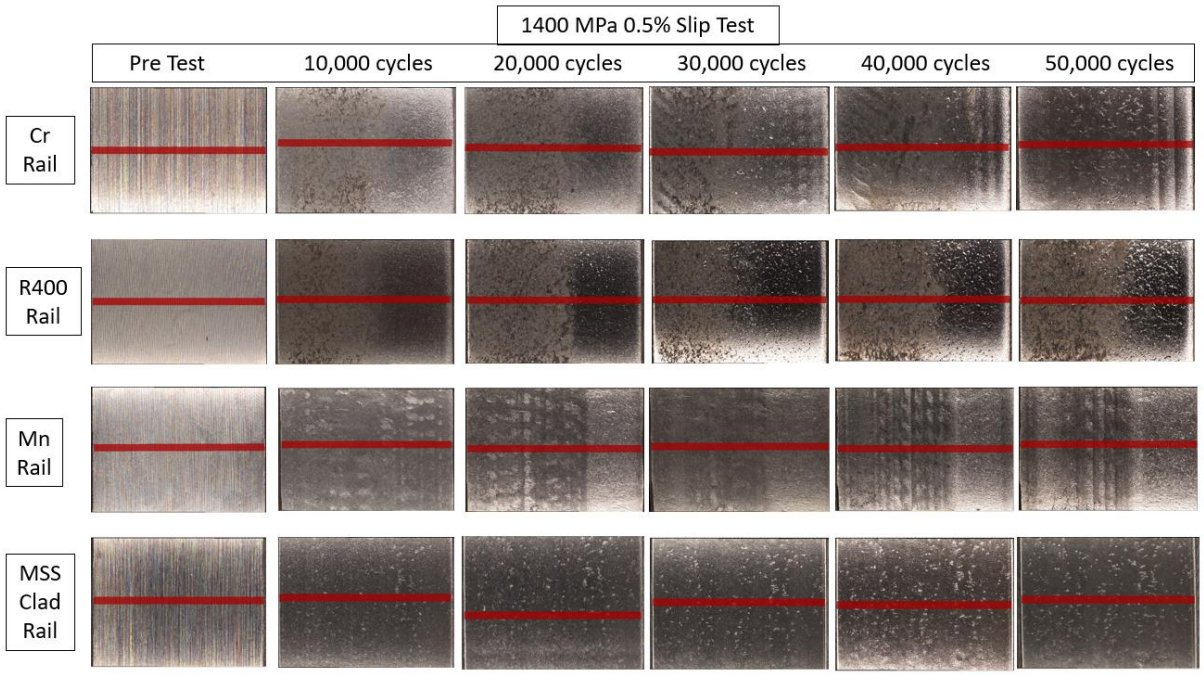

a)

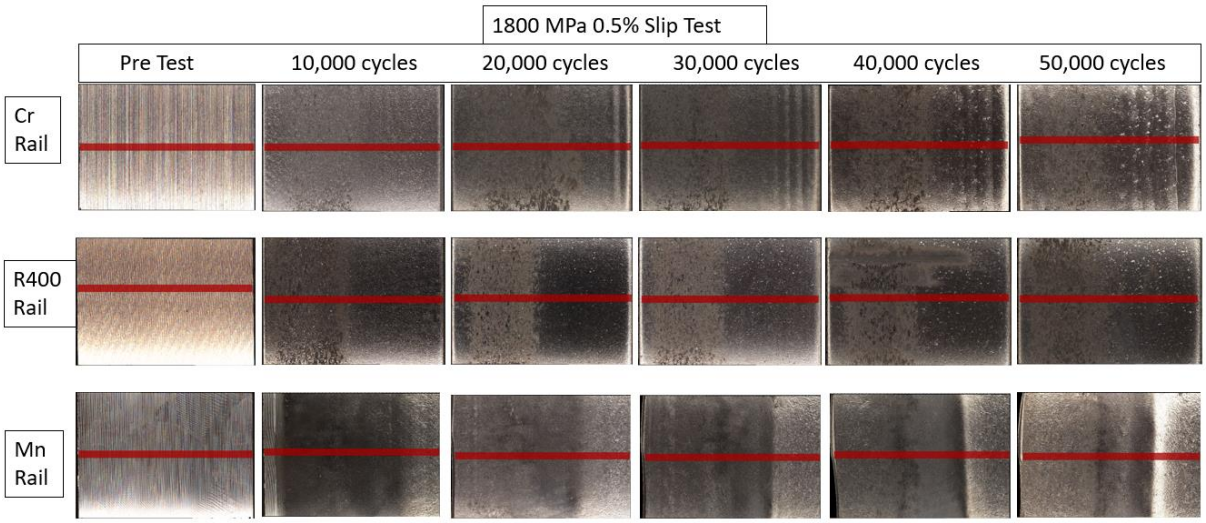

b)

Figure 7.2: Premium rail and MSS clad rail surface evaluations during the tests with images from Alicona (a) 1400 MPa, 0.5% slip tests; (b) 1800 MPa, 0.5% slip tests

Figure 7.2 shows the surface images of the rail discs during the tests. Before starting the experiment, machined surfaces can be seen on pre-test sections and then after starting experiments surface images were taken every 10,000 cycles. When analysed post-test it could be seen that on the Cr rail disc at 1400 MPa, flake formation starts from 30,000 cycles while it starts at 40,000 cycles in the 1800 MPa test. R400 rail samples show flake formation started at 20,000 cycles in the 1400 MPa test and 1800 MPa test, but the number of flakes were lower

in the 1800 MPa test. Mn rail samples showed different wear mechanisms and no flake formation occurred during the tests. The MSS clad sample was only tested at 1400 MPa and flake formation was seen after 10,000 cycles.

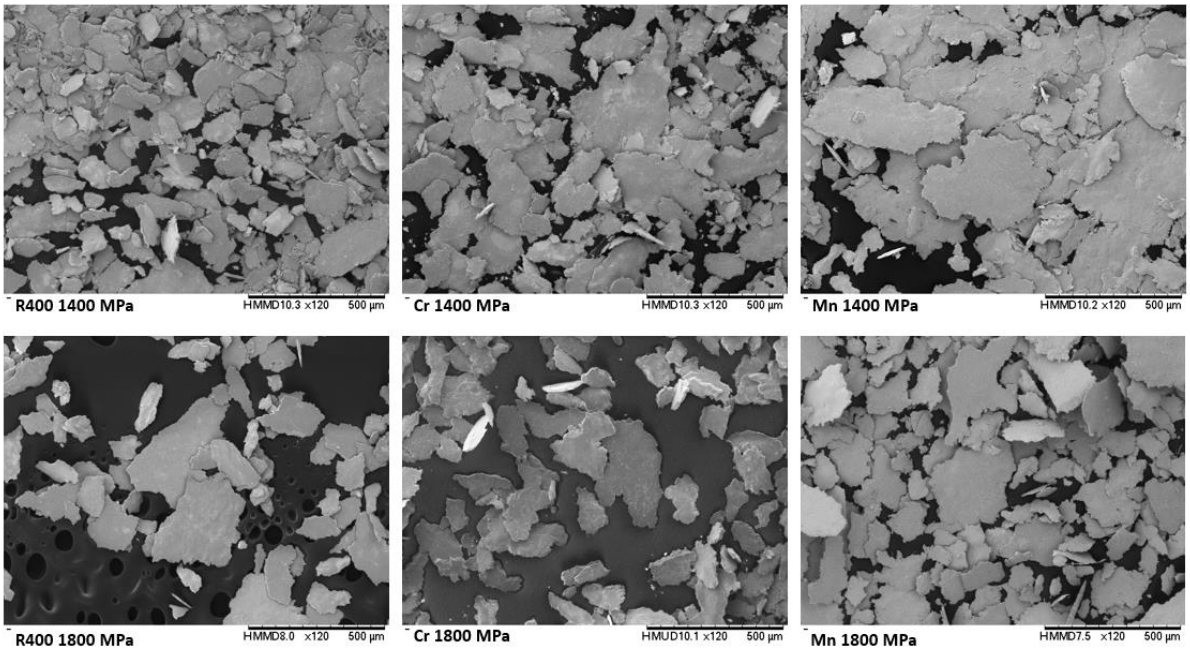

Figure 7.3: Premium rail twin-disc tests wear debris after 50,000 cycles

Wear debris were collected to analyse the wear behaviours of the discs during the tests. The debris collected via round shaped sticky bands after the experiments. Those sticky band surfaces with wear debris analysed under SEM machine. Wear debris came from both rail and wheel discs. The debris SEM images are shown in Figure 7.3 for premium rails in two different test conditions. It can be seen that R400, and Cr tests wear debris amounts are lower when the test condition is 1800 MPa, but Mn has different properties and different wear mechanisms. All tests had large-size wear debris and it shows there are severe wear conditions due to the dry contact. More wear debris comparisons are shown in Appendix 7.B.

7.4.2 Roughness

Figure 7.4 shows lateral and longitudinal direction roughness (Ra) values on premium and clad rail discs. In Figure 7.4 (a), lateral roughness values show pre-test measurements are higher than after the tests. From 10,000 cycles to 50,000 cycles most of the discs showed a gradual increase in Ra values. At the end of the tests, Mn discs showed the roughest surfaces. MSS Clad lateral roughness measurement settled in the mid-lines between all discs. In Figure 7.4 (b), longitudinal roughness showed a similar range for all cycles with Ra between 0.4 to 0.6, except for Mn and Cr 1400 MPa tests. After 10, 000 cycles the The value for Mn disc surface

roughness increased and then decreased, but for the Cr 1400 MPa disc Ra value decreased after 10,000 cycles and then started to increase slowly in the following cycles.

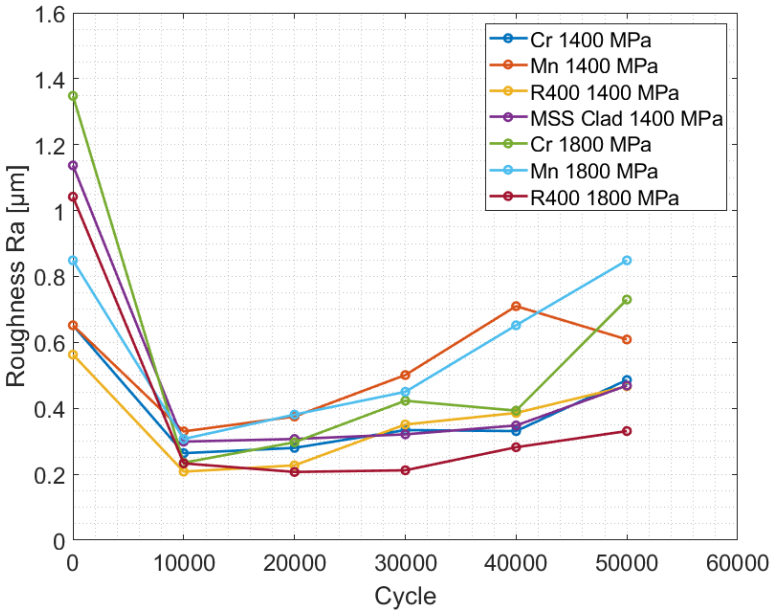

a)

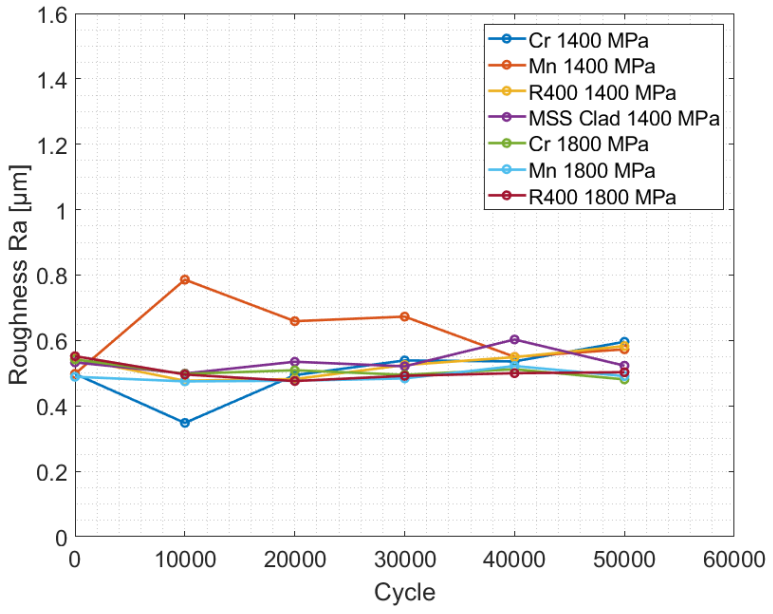

b)

Figure 7.4: Premium material and MSS clad rail disc roughness values: (a) lateral direction; (b)longitudinal direction

Wheel roughness Ra values are shown in Figure 7.5 for lateral and longitudinal directions of the disc surfaces. In the lateral direction, it can be seen that 1400 MPa and 1800 MPa tests were

divided into their groups, and they show similar values. However, the MSS clad test wheel sample showed a different value to the others. The longitudinal direction of Ra values showed MSS clad test wheel had the highest Ra values during the test and only after 50,000 cycles Mn passes that value and then had the highest value. Furthermore, Mn disc surface hardness values increased sharply after the 50,000 cycles. It is because of the plastically deformed wheel discs. Wheel disc surface width increase was higher than other wheel disc surface widths and it caused higher wheel disc surface roughness increases. The Mn surface width increase can be seen in Appendix 7.A.

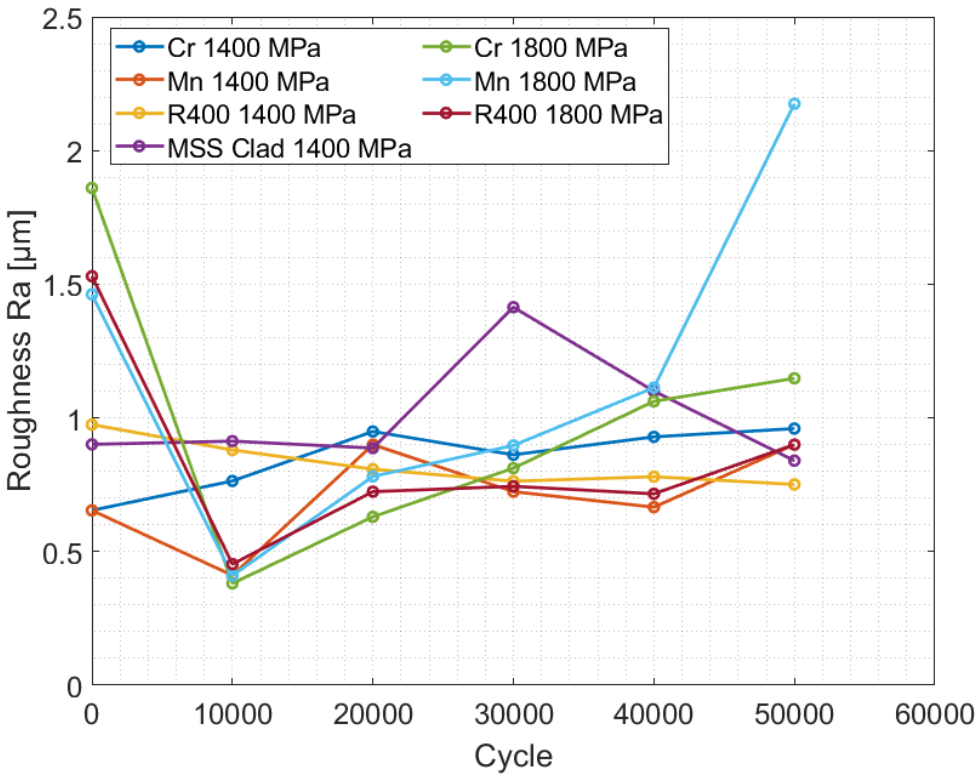

Fig. 7.5. (a)

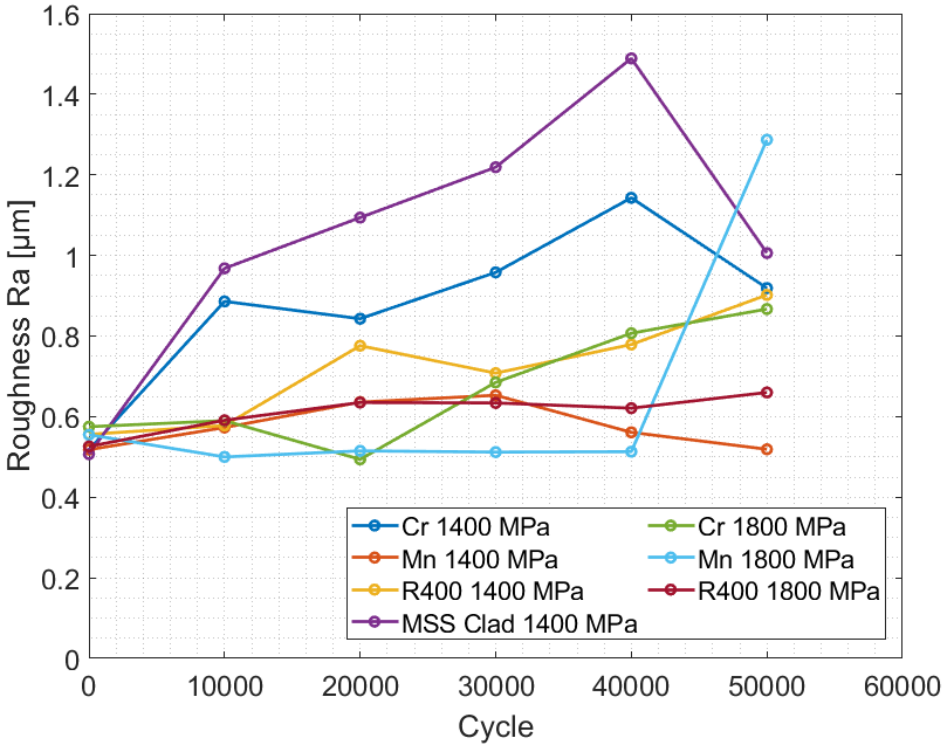

Fig. 7.5. (b)

Figure 7.5: Premium material and MSS clad tests wheel disc roughness values: (a) Lateral direction; (b) Longitudinal direction

7.4.3 Mass Loss

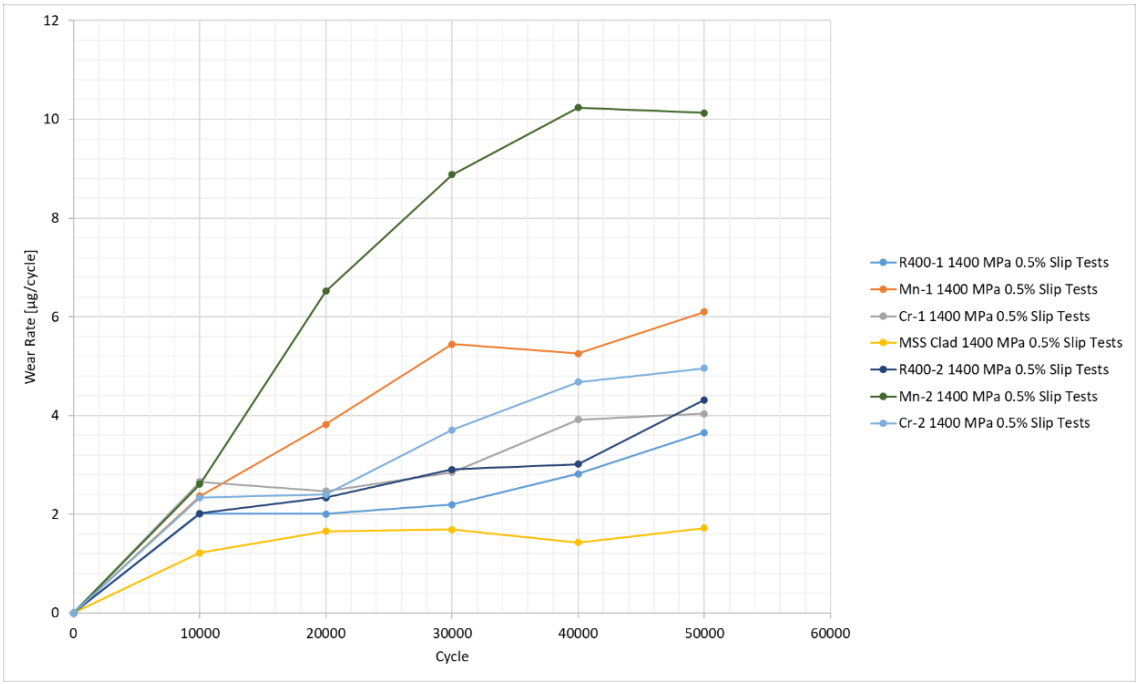

Fig. 7.6. (a)

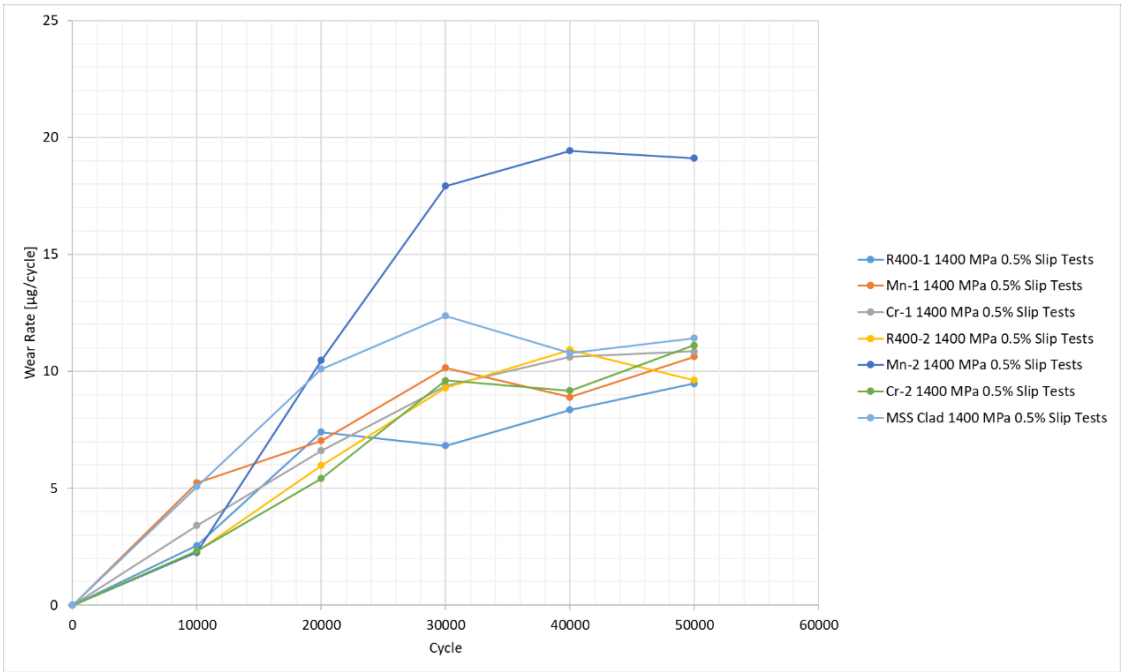

Fig. 7.6. (b)

Figure 7.6: Wear rate of the premium rail and MSS clad tests of 1400 MPa, 0.5% slip: (a) rail wear rate; (b) wheel wear rate

Figure 7.6 (a) shows rail wear rates of the premium rail and clad disc, and Figure 7.6 (b) shows wheel disc wear rates of the tests. Mn data showed the highest wear rates among all tests while the MSS clad rail disc wear rate was lowest on rail discs. 1800 MPa, 0.5% slip tests for Mn showed the highest wear rates in both Mn-1 and Mn-2 tests. 1400 MPa, 0.5% slip tests for Mn also showed higher wear rates than other material tests for all conditions. Cr, R400 and MSS clad wear rates stayed below 5 µg/cycle. MSS clad had the lowest value with 2 µg/cycle after 50,000 cycles between all tests after that cycle. For the wheel wear rates, Mn tests wheel wear rates were the highest. Other tests showed similar wear rates at the end of the tests.

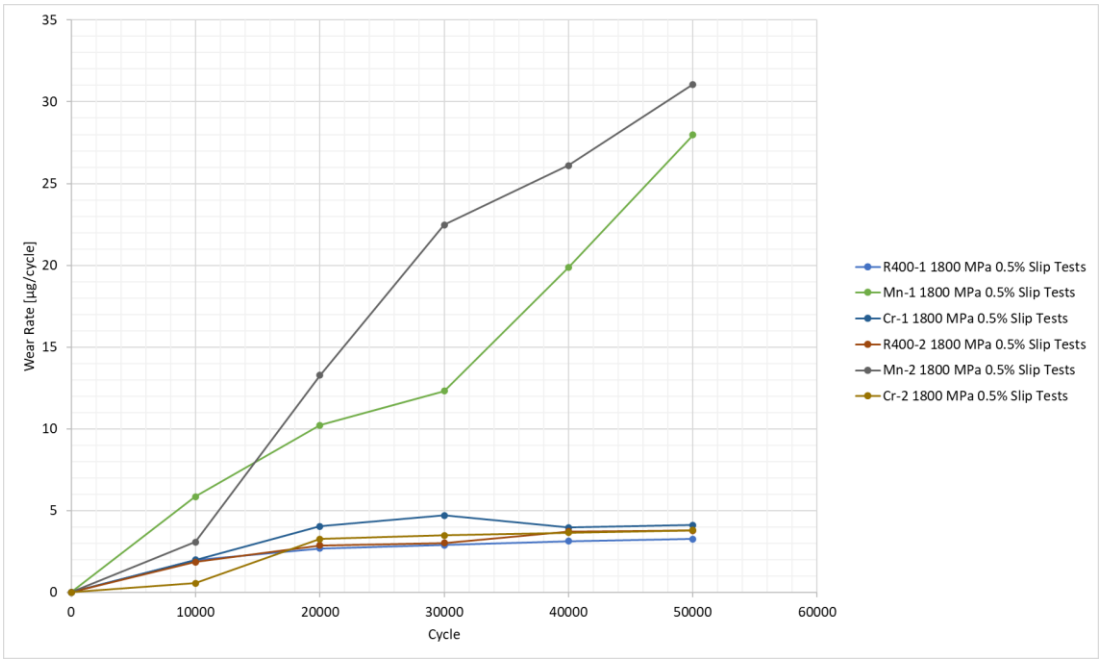

a)

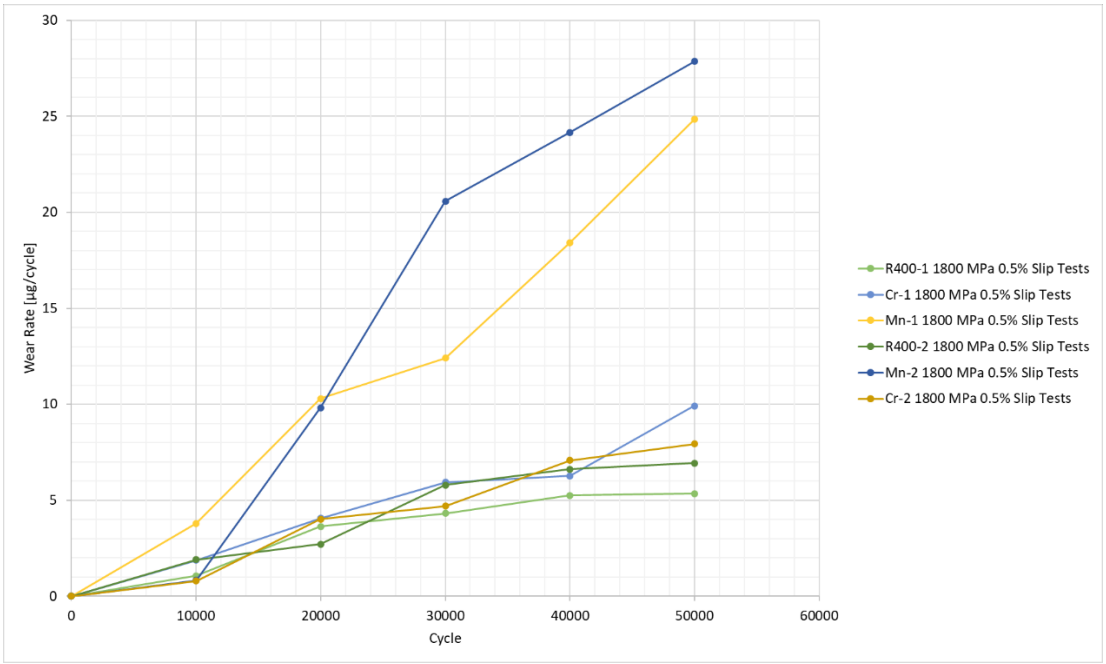

b)

Figure 7.7: Wear rate of the premium rail tests 1800 MPa, 0.5% slip tests: (a) rail wear rate; (b) wheel wear rate

Figure 7.7 (a) shows rail wear rates of the premium rail materials and Figure 7.7 (b) shows wheel disc wear rates of the 1800 MPa, 0.5% slip tests. Mn data showed the highest wear rates similar to the 1400 MPa tests. Cr and R400 wear rates stayed below 5 µg/cycle. In the tests with the Mn rail disc, wheel wear rates were the highest between all materials and the other two test wheel wear rates stayed below 10 µg/cycle.

7.4.4 Friction

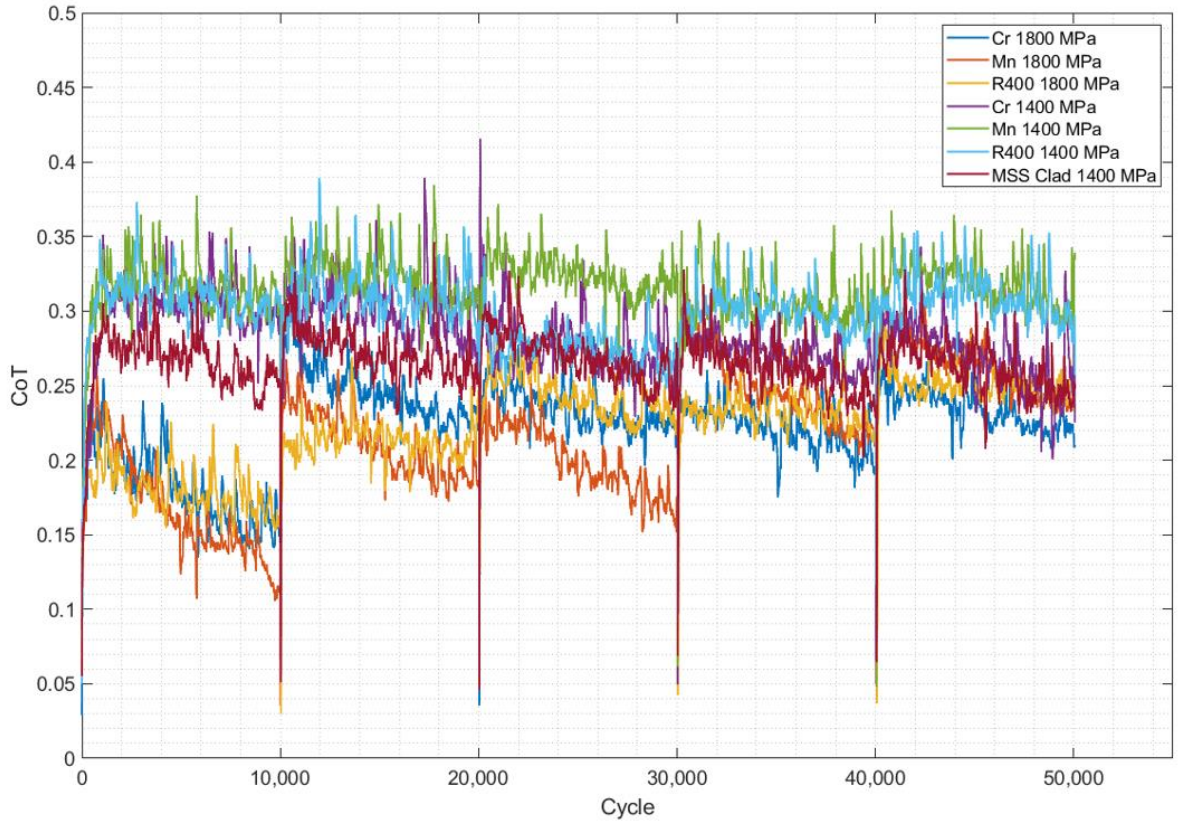

Figure 7.8: Premium rail tests and MSS clad rail test coefficient of traction (CoT) values

Figure 7.8 shows the coefficient of traction (CoT) versus cycle data. The figure shows 1800 MPa tests friction data were the lowest and compared to 1400 MPa data it was more unstable. However, MSS clad test friction data showed a CoT about 0.25-0.30 and it was stable. The highest friction occurred in the Mn 1400 MPa, 0.5% slip tests and other 1400 MPa tests followed that. When it comes to 1800 MPa tests they showed similar values and when it goes to the end of each block of tests CoT decreased a bit. MSS-clad CoT values stayed between 1400 MPa and 1800 MPa test values.

7.4.5 Sub-Surface

7.4.5.1 Subsurface Images

Figure 7.9 shows the Cr sub-surface microstructure images. It shows the material flow and depth of deformation from the surface and some cracks and flake formation on the surface with some small shallow cracks. The deformation layer was seen with crack formation.

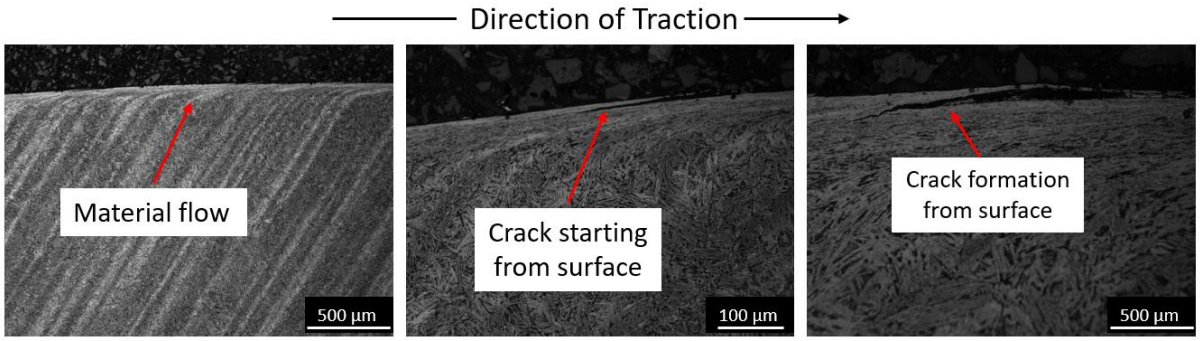

Figure 7.9: Cr 1400 MPa, 0.5 % slip microstructure images

Figure 7.10 shows the Mn sub-surface microstructure images. It shows the material flow and intergranular shapes on microscope images and some evidence of a twinning mechanism. Twinning mechanism occur due to the stress or deformation creates new crystal lattice structure similar to other crystal lattice structure, and it increase through a mirror effect on the structure as can be seen on image in Figure 7.10. A high rate of work hardening can be seen in the steels due to that structure. On the surface point, there is a low amount of deformation depth.

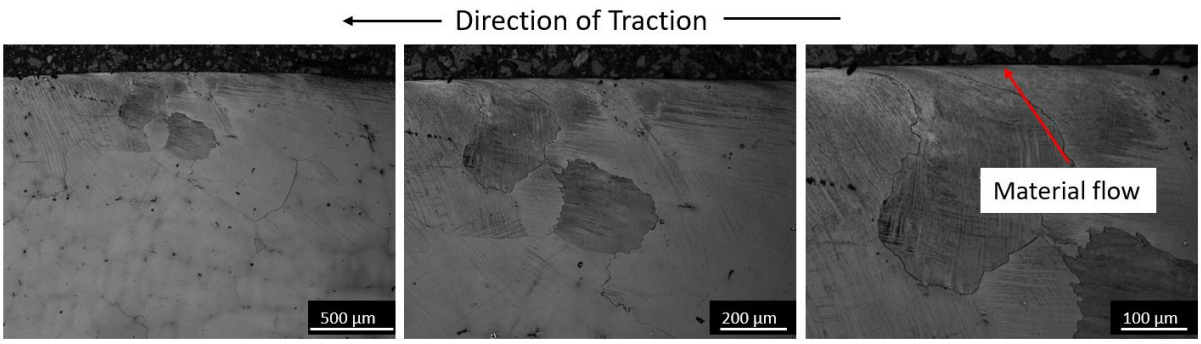

Figure 7.10: Mn 1400 MPa, 0.5 % slip microstructure images

Figure 7.11 shows the R400 sub-surface microstructure images. It shows the material flow and depth of deformation on the surface and some small, shallow cracks and flake formations on the surface. The depth of deformation is bigger than other materials in the 1400 MPa, 0.5% slip tests.

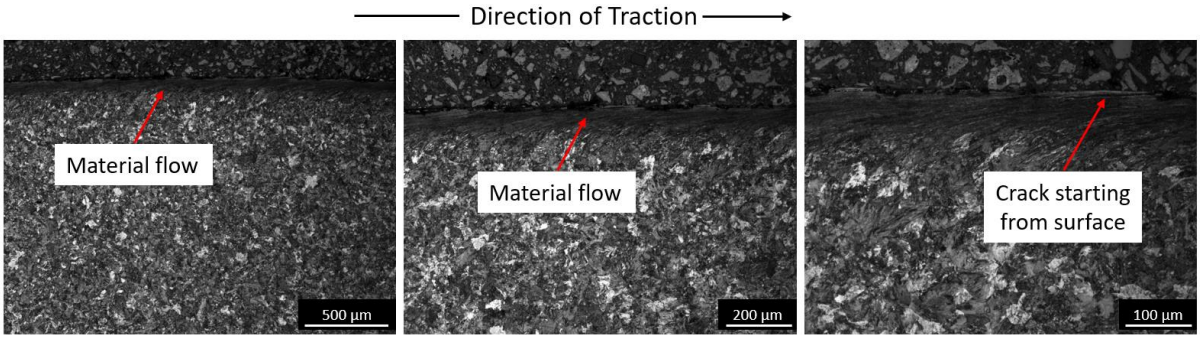

Figure 7.11: R400 1400 MPa, 0.5 % slip microstructure images

Figure 7.12 shows the MSS Clad sub-surface microstructure images. It shows the material flow and depth of deformation and flake formation on the surface. Also clad and HAZ transition images show the diffusion zone. On the surface, some intergranular shapes occurred after etching with Vilella etchant on the clad part.

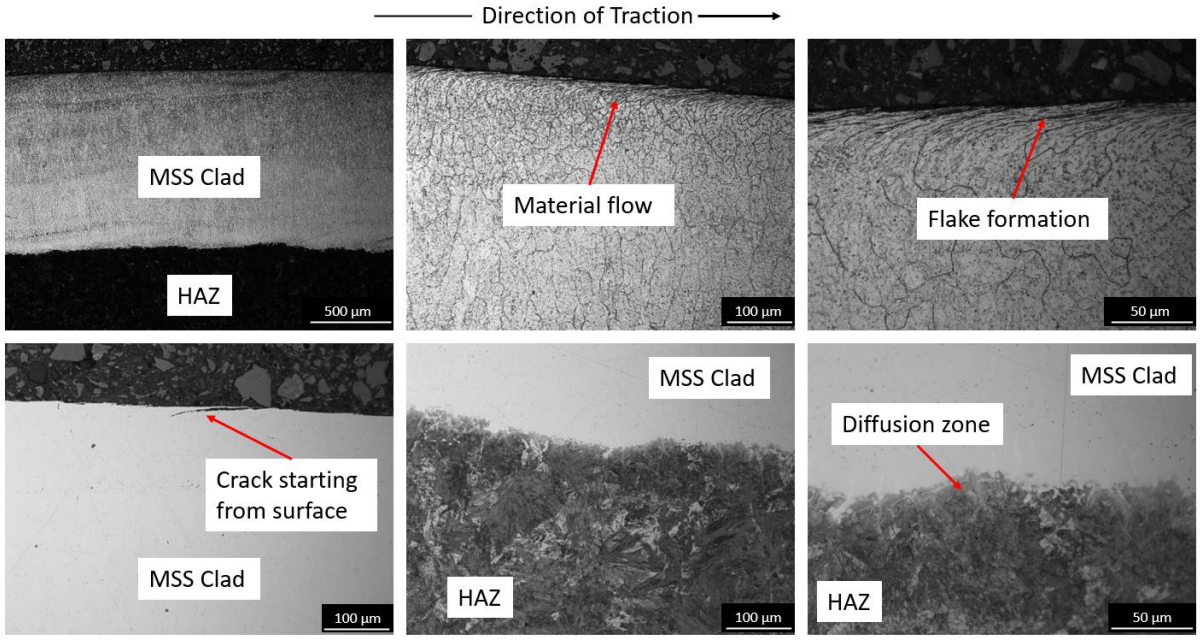

Figure 7.12: MSS Clad 1400 MPa, 0.5 % slip microstructure images

Figure 7.13 show the Cr sub-surface microstructure images of the 1800 MPa, 0.5% slip test. It shows the material flow and depth of deformation on the surface and some crack and flake formation on the surface. The deformation depth is like that in the Cr 1400 MPa test images. The deformation depth is around 75 µm in 1800 MPa and around 50 µm in 1400 MPa test. Contact stress is higher in the 1800 MPa test, but friction is lower.

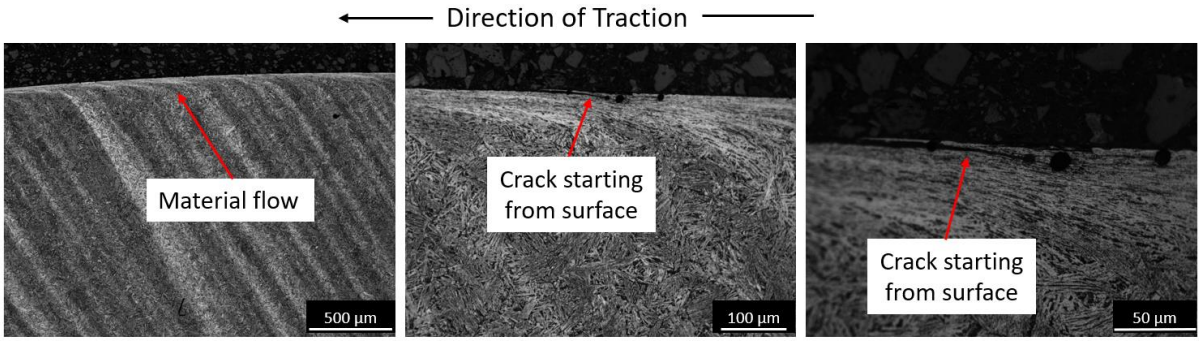

Figure 7.13: Cr 1800 MPa, 0.5 % slip microstructure images

Figure 7.14 shows the Mn sub-surface microstructure images of the 1800 MPa, 0.5% slip test. It shows the material flow and intergranular shapes on the images. Twinning mechanisms were seen in the images. Also, an unetched microscope image showed a visible crack from the surface.

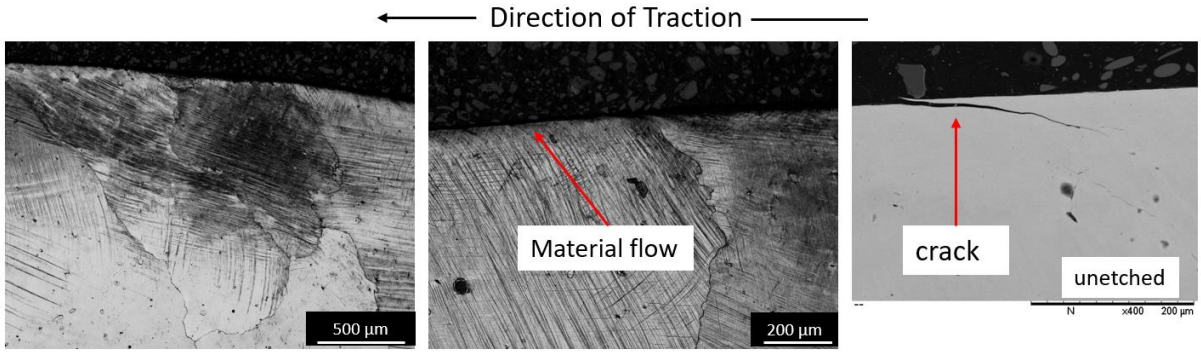

Figure 7.14: Mn 1800 MPa, 0.5 % slip microstructure images

Figure 7.15 shows the R400 sub-surface microstructure images of the 1800 MPa, 0.5% slip test. It shows the material flow and depth of deformation on the surface and some flake formation on the surface. Some shallow cracks can be seen.

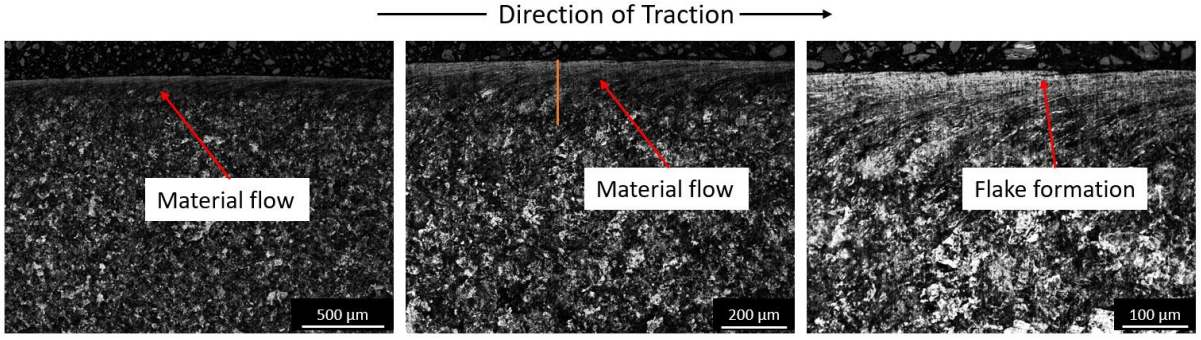

Figure 7.15: R400 1800 MPa, 0.5 % slip microstructure images

7.4.5.2 Micro Hardness and Nano Hardness Measurements of Premium Rails and MSS Clad Rail

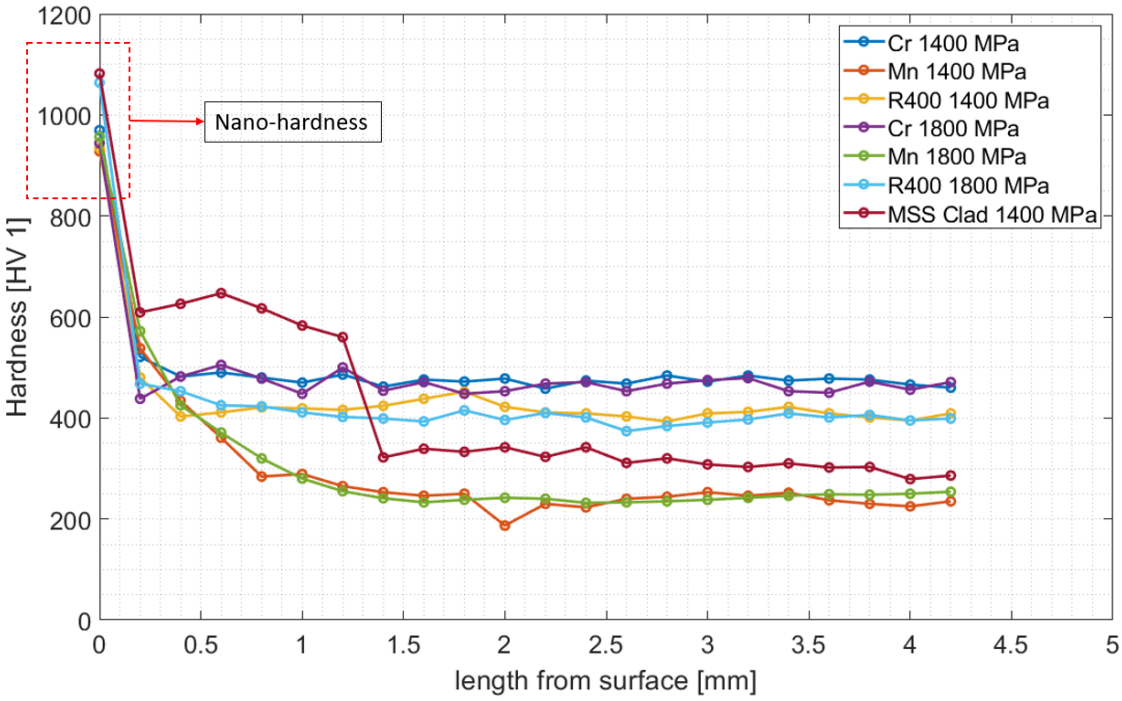

Figure 7.16: Hardness measurements of premium material discs and MSS Clad discs with nano and micro-hardness values.

Results from hardness measurements are presented in Figure 7.16. The first values of the graph on all samples show the nano-hardness value because, at the surface point, it is hard to get exact surface data due to micro-hardness tester limitations. Nano indentation gives the localized hardness however microhardness indentation gives the average hardness over the large area. Other data on graphs show micro-hardness values. Premium materials showed 3 different hardness values depending on the tests. First, Cr tests on both conditions showed the highest micro-hardness. Then R400 hardness values were followed with around 400 HV values and Mn test values showed the lowest values around 250 HV on the microhardness test. However, MSS clad showed a different trend line. The clad part showed the highest hardness among all materials with around 1080 HV on nano-hardness value. Below the clad layer, hardness values decreased to around 300 HV and then decreased gradually to the bulk material at around 260 HV values. Care must be taken with interpreting the nano-hardness value as typically values from nano-indentation are higher than the micro-hardness values by about 30% (Qian et al., 2005). They explain that the main reason for that is nano-indentations use the projected contact area at peak load, however, micro-hardness uses the residual projected area. The nano-hardness

maps and values by 10x10 indentation maps from surface points of the sectioned discs are shown in the Appendix 7.C with hardness and reduced modules values.

7.5 Discussion

7.5.1 Wear Mechanisms

Cr, R400, Mn, and MSS clad wear tests showed that materials did not deform heavily because of the high hardness, but they showed some differences between each other. Cr and R400 and MSS clad tests showed similar ratchetting wear mechanisms as evidenced by the flake formation, however Mn showed a different mechanism and features on the tests. Figure 7.10 and Figure 7.14 showed Mn microstructure of the microscope images for 1400 MPa and 1800 MPa tests respectively and that images can be seen to have similarities with twinning mechanism images from the literature shown in Figure 7.17. It can be seen that ductility and strength can increase because of the work hardening rate. As the Mn does not deform it does not exhibit any signs of ratchetting. Wear must occur due to adhesion or abrasion, which is evident in the disc surface images (see for example, Figure 7.18).

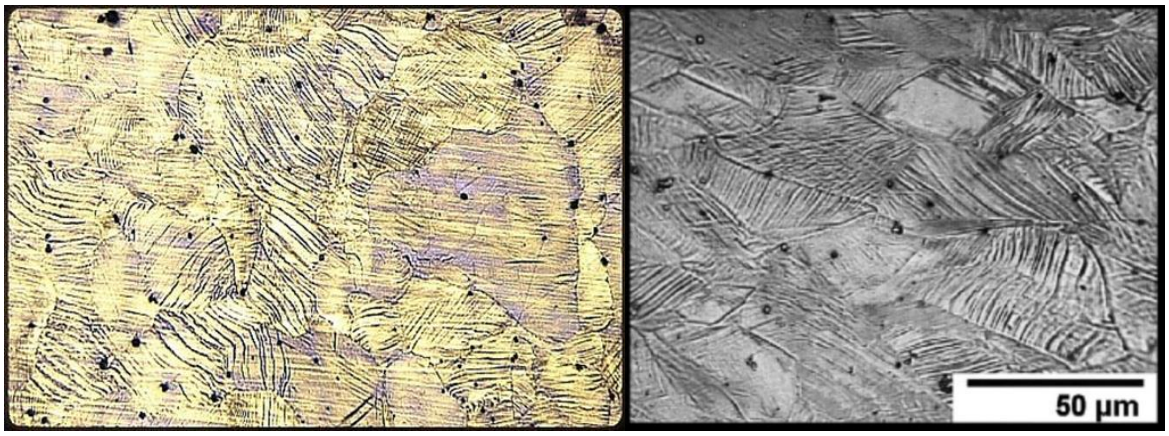

Figure 7.17: Hadfield steel SEM image and microstructure of high Mn twinning mechanism with 34% strain level microscope image [Left image from: (Langford (2023); right image from Wesselmecking et al. (2021)]

Deformation on Cr and R400 materials are similar and ratchetting occurs on those materials. Ratchetting occurs due to the passing the plastic shakedown limit and material start to fail from the contact point then cracks or wear start to occur from there.

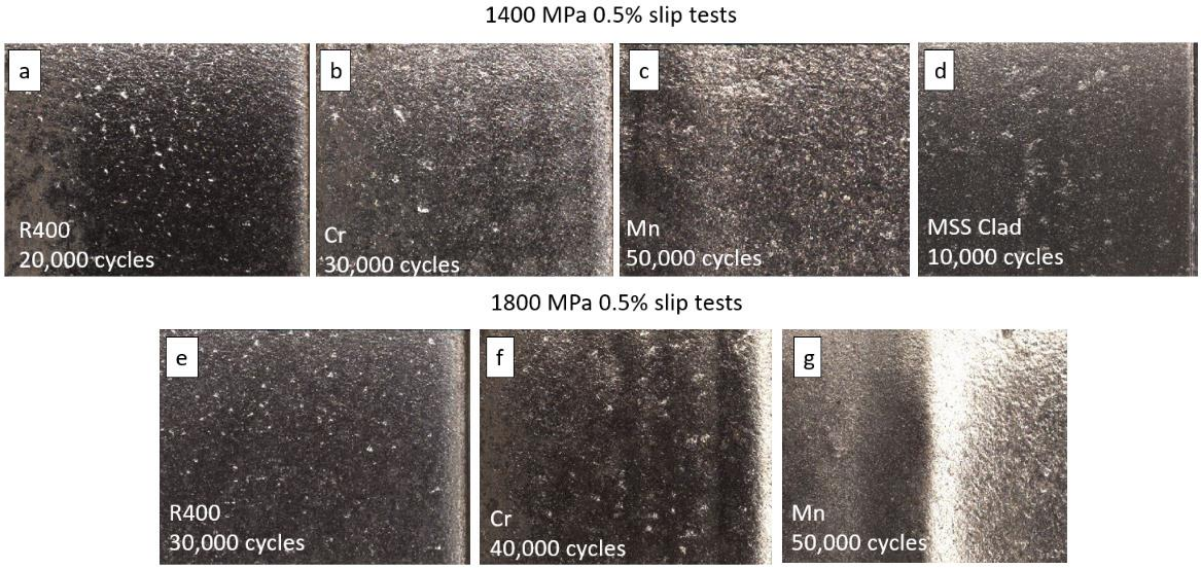

Figure 7.18: Flake formation images on premium and MSS clad wear tests with 1400 MPa, 0.5% slip and 1800 MPa, 0.5% slip test conditions.

Figure 7.18 shows the surface images of the discs and flake formations on the specimens of R400 started at 20,000 cycles in Figure 7.18 (a) 1400 MPa and 30,000 cycles in 1800 MPa tests. 1400 MPa Cr test flake formation occurred after 30,000 cycles while 1800 MPa occurred after 40,000 cycles in Figure 7.18 (b) and (f) respectively. Mn did not show flake formation due to the different wear mechanism after the 50,000 cycles both test conditions. MSS clad disc flake formation occurred after 10,000 cycles. Figure 7.19 shows the flake formation mechanism due to the strain accumulation. Disc surface flake images can be evaluated depending on the that process and after the flake formation starts, the Cr and R400 discs showed some shallow cracks at the end of the tests.

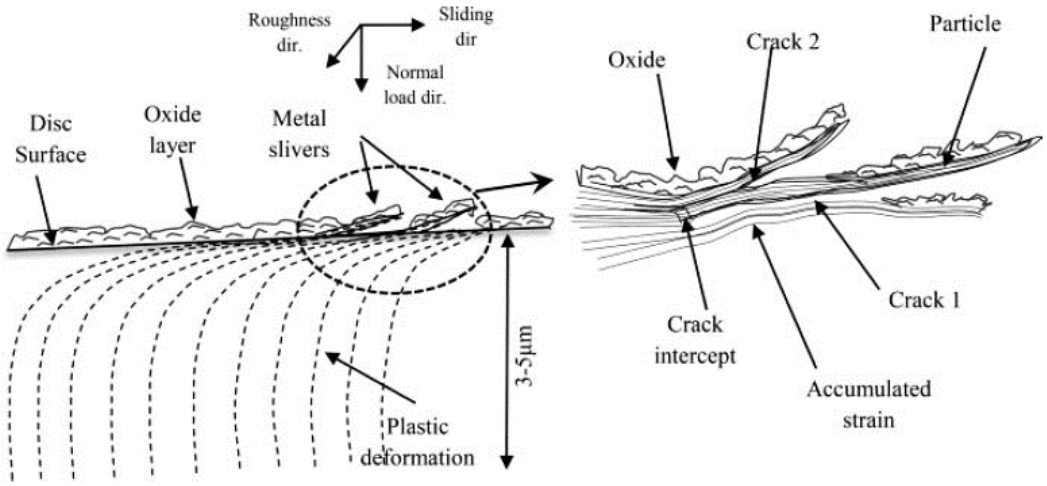

Figure 7.19: Flake formation (metal sliver) process because of strain accumulation (from Athukorala & De Pellegrin (2017))

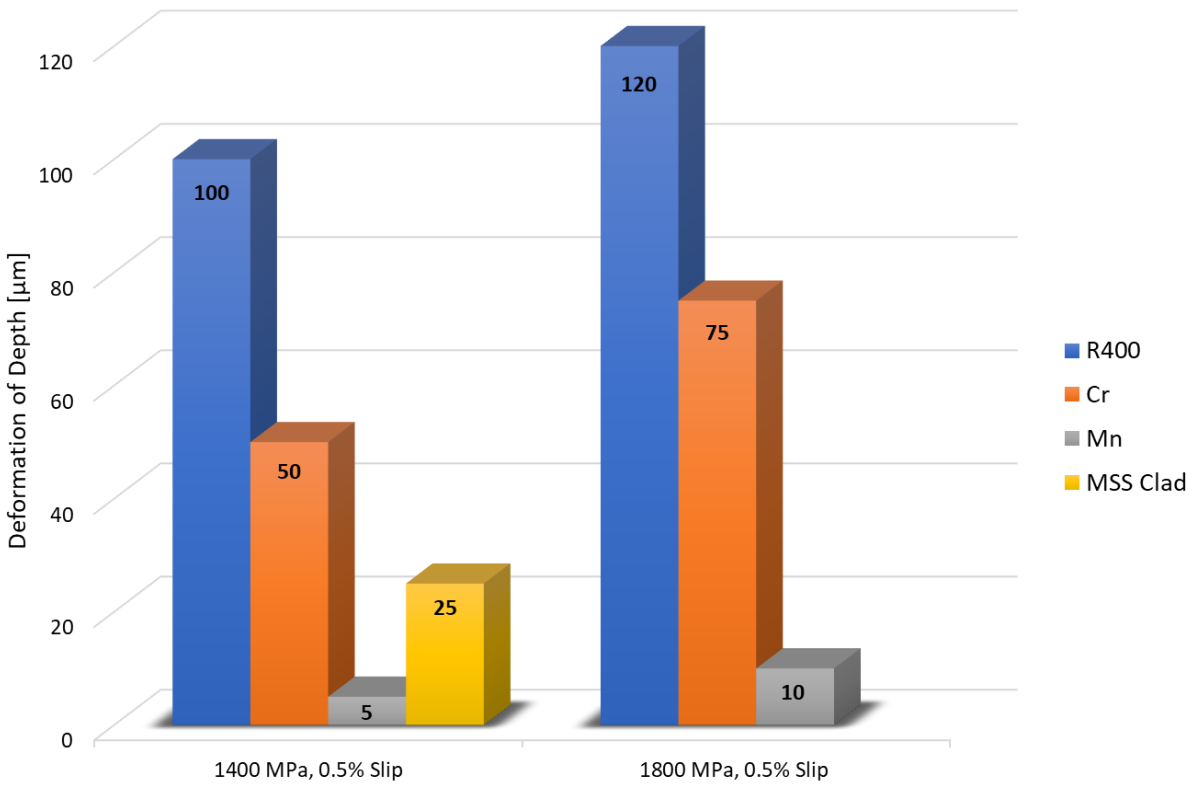

Figure 7.20: Deformation of depths after the experiments.

Deformation depths of the premium rails and MSS clad discs are shown in the Figure 7.20 after the twin-disc tests. The data is from the sub-surface images in Section 7.5.5.1. When contact force increased from 1400 MPa to 1800 MPa, deformation depths were increased for premium rails. R400 had the highest value of deformation depth in both 1400 MPa and 1800 MPa tests. Cr and Mn followed that respectively, but the MSS clad sample showed 25 µm depth in 1400 MPa tests. Figure 6.29 shows the MSS clad twin disc test depth at around 10 µm (Lu et al., 2018) and 15 µm after full-scale tests. Also, in Figure 6.29 R260 twin-disc depth of deformation is shown at 700 µm. When compared to premium rails, where R400 had the highest value, R260 is very much higher.

7.5.2 Wear Rates

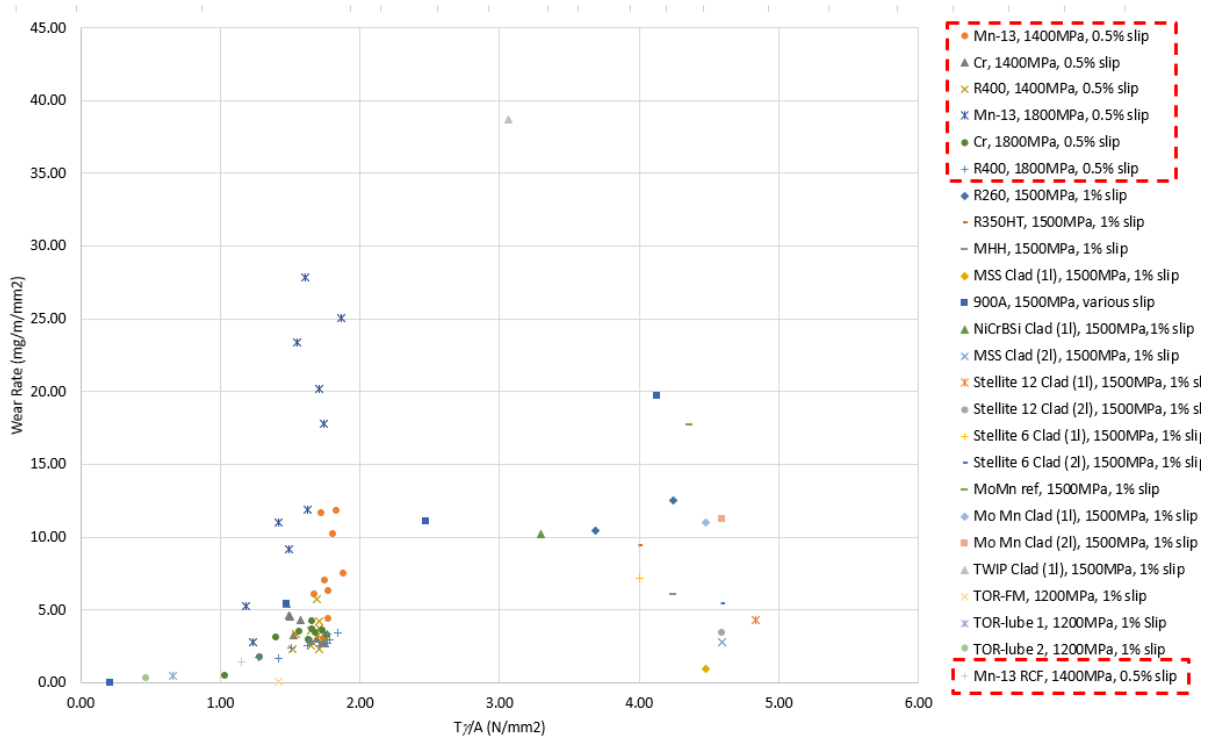

Figure 7.21: Wear rates of twin-disc specimens against Tγ/A approach

One approach that can be used to compare wear for different test scales is the Tγ method. Tγ (where T is the tractive force (friction coefficient × normal force) and γ is the slip in the contact) is an indication of energy dissipated in the interface. This can be normalised by dividing by area (A) allowing different contacts to be compared. It has been shown in the mild wear regime, that wear rate is proportional to Tγ/A (Lewis & Dwyer-Joyce, 2004). The premium rails twin disc wear rates are shown in Figure 7.21 with other materials. Mn tests showed the highest wear rates compared to most premium rail materials in these experiments. TWIP clad wear rate was the highest and close to Mn. This is also a material that hardens via a twinning rather than a deformation mechanism. The 1400 MPa Mn wear rate showed lower values than 1800 MPa Mn tests. R400 and Cr tests showed lower values and within the most common range under the 5 µg/m/mm^2. MSS Clad 1500 MPa, 1% slip data showed lowest wear rates than other 3 premium rail materials. The data is showed inside the red square were got from this research and other data were used depending on the previous research.

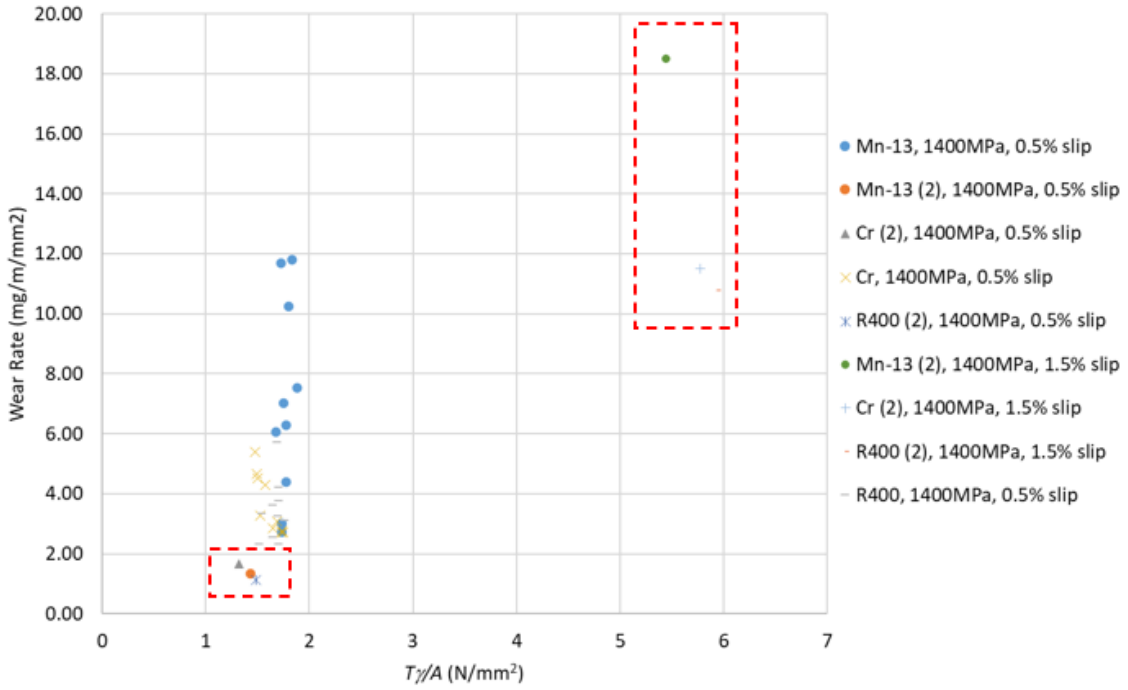

Figure 7.22: Wear rates of twin-disc premium rail specimens against Tγ/A approach

Figure 7.22 shows the wear rates of 1400 MPa tests for 0.5% slip wear and RCF and 1.5% slip values for Tγ/A comparisons. The wear tests were in the 2nd tests Mn (2), Cr (2), and R400(2) inside of the red squares over-layed parts had been done for crack initiation tests and they were shown with both 0.5 and 1.5% slip conditions and those tests continued for 40,000 cycles without stopping the test rig. The Mn wear test showed the highest wear rate, but the slip value was 1.5% slip and other specimens with 1.5% slip values showed higher values than 0.5% slip values of premium rail specimens except Mn 0.5% slip. Cr and R400 showed similar values in 1400 MPa 1.5% slip tests. That wear tests with 1400 MPa, 0.5% slip tests showed lower wear rates because on that condition. Other wear tests that had 10,000 block of cycles up to 50,000 cycles showed Mn wear rates mostly higher than R400 and Cr wear rates.

7.6 Conclusions

Twin-disc tests have been carried out of premium rails (Cr, R400, Mn) with 1400 MPa, 0.5% slip and 1800 MPa, 0.5% slip test conditions. Also, a MSS Clad rail sample was tested with 1400 MPa, 0.5 slip test condition for comparison.

Premium rails and MSS clad rail twin-disc tests showed lower wear than standard rail grades such as R260 rail. MSS clad rail showed slightly lower wear rates than the premium rail materials.

Mn showed different wear mechanisms to the other materials, and it had higher wear rates and lower hardness values than other materials. Instead of ratchetting it showed evidence of abrasion or adhesion.

MSS clad rail tests showed it is relatively more useful than premium rails due to the lower cost. MSS clad allows the use of a layer of hard material over a standard grade rail, but for premium materials the whole rail must be made of the same material so this is more costly. Cladding can also be used for field repairs which adds to its benefits.

Chapter 8

8 Tolerance of Parameters Effects on Clad Quality and Performance

The tolerance of defects caused by non-optimal laser process parameters was tested here through small-scale tests. Defects are unlikely to occur in a controlled clad application, but with the target of in-situ applications in a relatively uncontrolled environment, the tolerance of such defects must be evaluated. Twin-disc rail samples were clad with MSS laser clad coating with deliberately non-optimal parameters. Defects were created by varying laser parameters and/or powder flow rates. Non-optimal cladding can lead to a range of defects such as porosity, voids, or cracks. Cladding process parameters were shown in the Table 8.1. These parameters were used in laser cladding for creating bad quality cladding over substrate rail disc.

8.1 Test Apparatus and Test Specimens

Bad quality clad disc wear tests were assessed on a twin disc test rig as can be seen in section 3.4.1 in the Chapter 3. Experiments were carried on twin disc tests using the Sheffield University Rolling Sliding (SUROS 1) twin disc test machine. Line contact is used between twin-disc test specimens on this machine to simulate the normal load and rolling-sliding performance at the wheel/rail interface. The test specimens were shown in the section 3.4.1.1. with dimension of the SUROS test discs. Martensitic Stainless Steel (MSS) clad was used applied in 1 mm thick layer over R260 substrate rail material. When laser cladding was applying to the discs some parameters changed because of the target of the tests about bad quality clad over substrate.

8.2 Measurements

Rail discs were scanned before and after the experiments in the University of Southampton X-Ray laboratory facilities (see Fig. 3.20). After scanning the discs, twin-disc tests were then run at 1500 MPa, -1% slip for 30,000 contact cycles in blocks of 5,000 cycles. Images were taken and discs were cleaned with Acetone. After cleaning, mass was recorded along with room temperature and humidity in the SUROS 1 laboratory. After each block of cycles was complete, the test was stopped, and masses were recorded again. When all the twin-disc tests were complete, post-test X-ray scanning was conducted to observe how the defects had evolved in

the same X-Ray machine. The X-ray images were then analysed using ImageJ software. The defects and cracks were checked before and after the tests. As can be seen in table 8.1 the laser parameter and powder feed rate were changed for clad. On the table “000” values in cladding process refer to optimal parameter but starting with “+” and “-“numbers refer to higher or lower than optimal laser cladding parameters.

Two of the discs were sectioned, mounted, ground and polished. After that they were etched for microstructure analysis. SEM and optical microscopy which were then used to further analyse the defects.

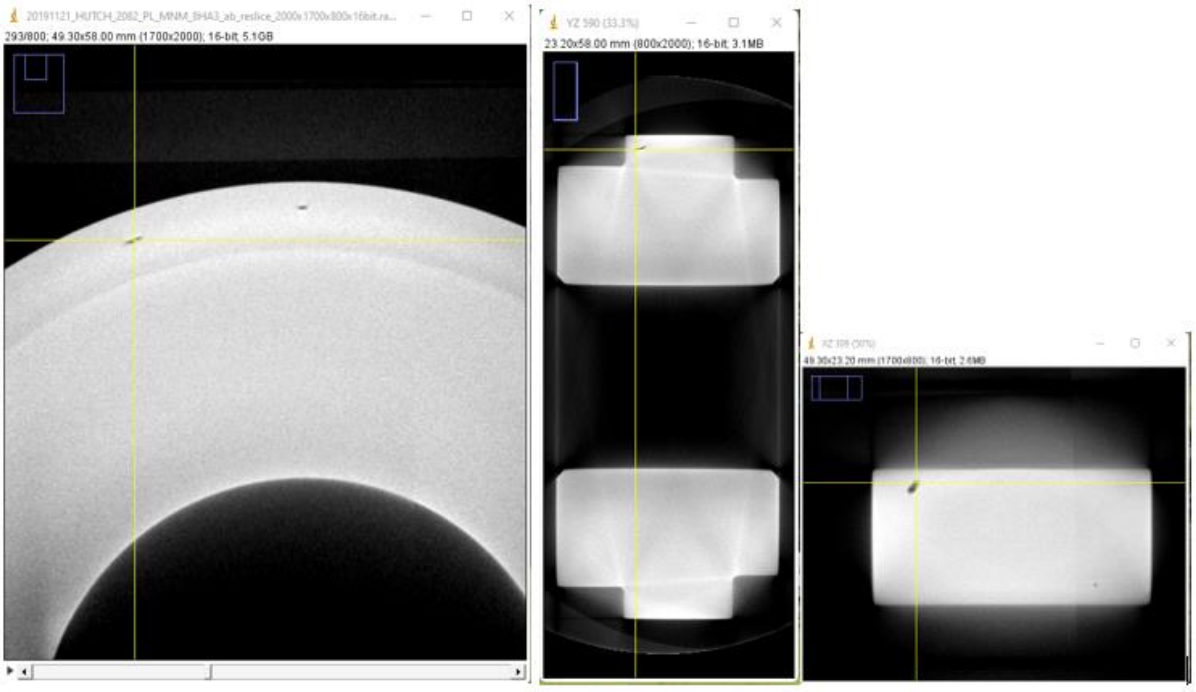

Figure 8.1: X-ray images processedby Fiji ImageJ image analysis software (ImageJ)

Figure 8.1 shows an example of the Fiji ImageJ disc section views and there can be seen XY, YZ and XZ views of the defect on the SUROS disc. For creating that images raw data were imported the software and the images analysed depending on the cracks.

8.3 Test Conditions

Table 8.1: Bad quality clad disc laser parameters and test conditions

Rail Disc	Cladding Process	Test Type and Conditions	Description
6HA-1	R260, feed +95, power -27	Wear Test [1500 MPa, 1% Slip, 400 rpm]	30,000 cycles with 5,000 block tests. All dry condition
6HA-2	R260, feed +95, power -27	RCF Tests [1500 MPa, 1% Slip, 400 rpm]	30,000 cycles with 500 dry then 29500 water lubricated test.
7B-29	R260, feed 000, power +42	Wear Test [1500 MPa, 1% Slip, 400 rpm]	30,000 cycles with 5,000 block tests. All dry condition
7B-30	R260, feed 000, power +42	Wear Test [1500 MPa, 1% Slip, 400 rpm]	30,000 cycles with 5,000 block tests. All dry condition
7B-31	R260, feed 000, power +42	RCF Test [1500 MPa, 1% Slip, 400 rpm]	30,000 cycles with 500 dry then 29500 water lubricated test.
7B-32	R260, feed 000, power +42	RCF Test [1500 MPa, 1% Slip, 400 rpm]	30,000 cycles with 500 dry then 29500 water lubricated test.
8HA-1	R260, feed 000, power +35	Wear Test [1500 MPa, 1% Slip, 400 rpm]	30,000 cycles with 5,000 block tests. All dry condition
8HA-2	R260, feed 000, power +35	Wear Test [1500 MPa, 1% Slip, 400 rpm]	30,000 cycles with 5,000 block tests. All dry condition
8HA-3	R260, feed 000, power +35	RCF Test [1500 MPa, 1% Slip, 400 rpm]	30,000 cycles with 500 dry then 29500 water lubricated test.

Table 8.1 shows the laser parameters of the discs with disc names. Cladding process changes were applied on powder feed rates and laser powers. Optimal powder feed rates were used on all discs except for 6HA-1 and 6HA-2 discs and laser power was varied on all discs to create some bad quality clad discs. Also, tests were divided as wear and RCF tests.

Wear and RCF experiments were done for finding out how these non-optimal clad coated discs perform. The defects over surface of the disc and under the surface were aimed to analyse depending on these experiments. All tests were conducted at 1500 MPa contact stress and 1% slip with 400 rpm. Wear tests were conducted with blocks of 5,000 cycles up to 30,000 cycles in dry conditions and RCF tests were conducted with 500 initial dry cycles and then up to 30,000 cycles with 1 drop of water lubrication per second.

8HA-3 and 6HA-2 disc were chosen for their different cladding processes for further microstructure analysis. Disc 8HA-3 was laser clad with a powder feed rate equal to the optimised cladding process and 35% higher laser power. It was tested under RCF conditions as described above. Disc 6HA-2 was laser clad with a powder feed rate 95% higher and 27% lower laser power than the optimised cladding process. It was tested under RCF conditions.

8.4 Results

8.4.1 Surface Evolutions after Twin Disc Experiments

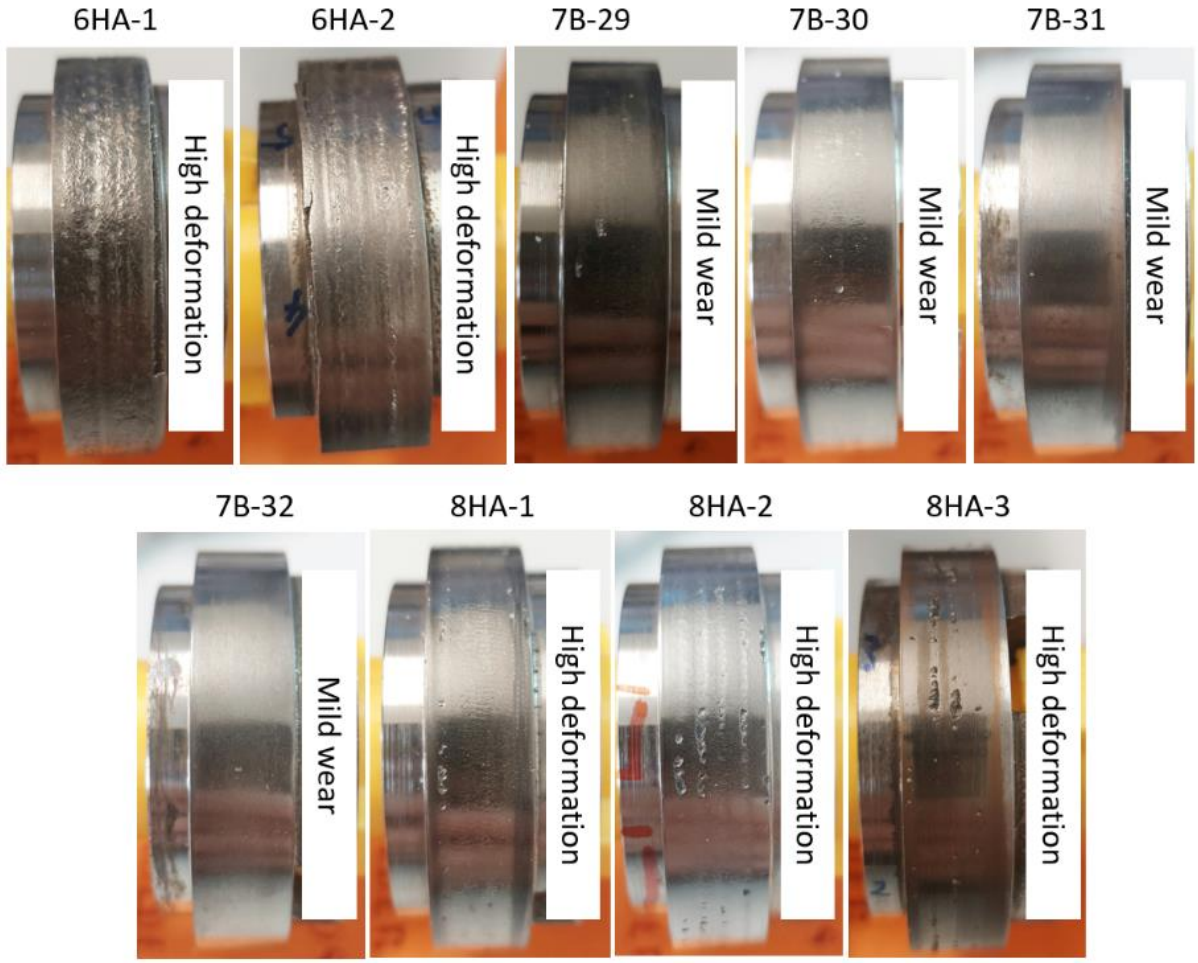

Figure 8.2: Bad quality disc surfaces after all finished twin-disc experiments

The discs are shown in Figure 8.2 after the finished twin-disc experiments. Some disc surfaces can be seen with high deformation. Surface defects and deformations were recorded again on the X-Ray scans and see how they changed before and after the tests. 6HA-2 and 8HA-3 disc chosen to section because of high and visible deformation and the clad surface as can be seen in the images as well.

There are more surface evaluation images from start of the tests to end of the tests were shown in the Appendix 8.A. 6HA1, 7B29,7B30, and 8HA1 surface images after each 5,000 block of cycles can be seen in there with Figure 3.18. The images clearly depict how surface flakes changed and behaved during the test.

8.4.2 Mass Loss

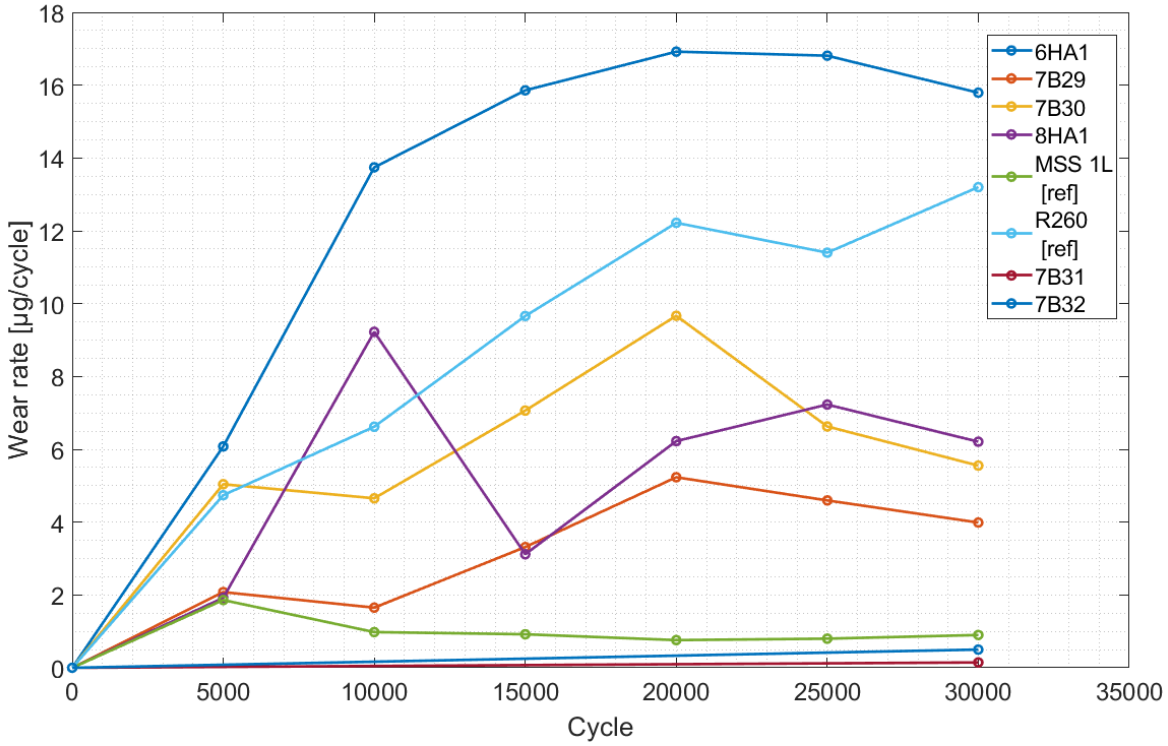

a)

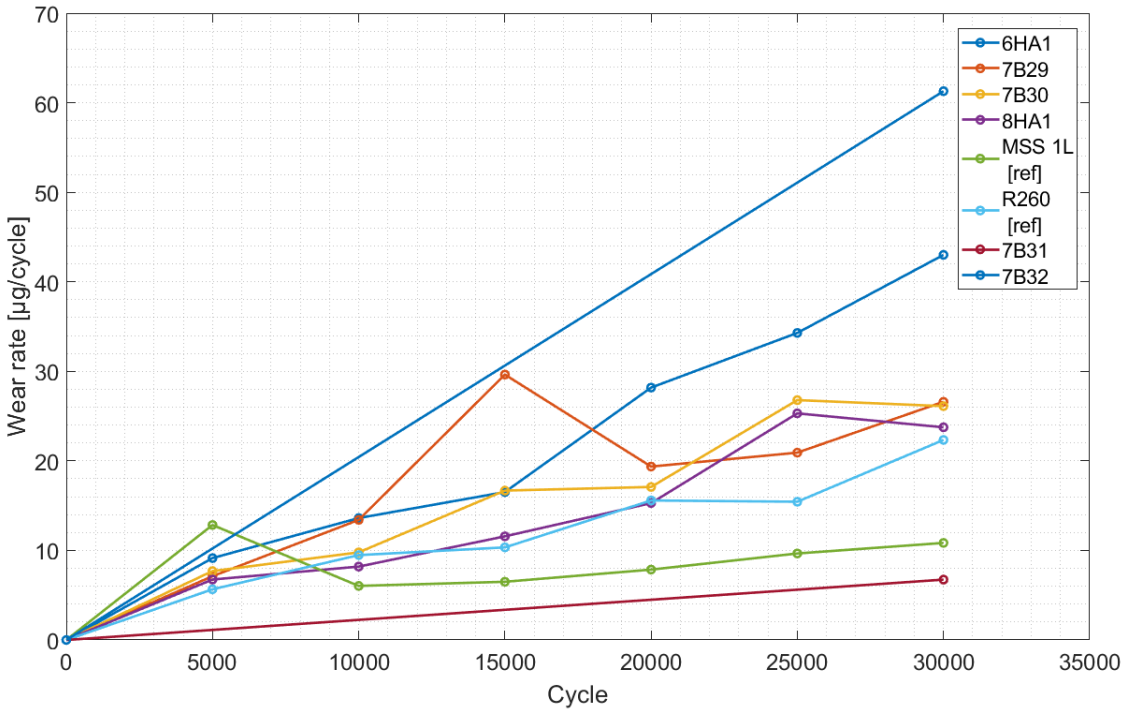

b)

Figure 8.3: Some wear and RCF tests wear rates: (a) rail disc wear rates (MSS and R260 (Lewis et al., 2016)); (b) wheel disc wear rates (MSS and R260 (Lewis et al., 2016))

Wear rates of the rail clad discs with created non optimum quality of cladding and wheel discs from wear tests are shown in Figure 8.3. Figure 8.3 (a) shows the 6HA-1 rail clad disc had the highest wear rate at 16 µg/cycle after the 30,000 cycles while the others, 7B29, 7B30 and 8HA1, showed wear rates around 4-6 µg/cycle. MSS clad wear rate showed µg/cycle at the end of the tests. Other RCF tests (7B31 and 7B32) showed lowest wear rates between 0-1 µg/cycle. Figure 8.3 (b) shows that the wheel wear rate had highest value at 62 µg/cycle on 7B32 test and then 6HA-1 wheel disc wear rate followed with 43 µg/cycle at the end of the tests, while the other wheel disc wear rates were around 24-26 µg/cycle. 6HA-1 had higher powder feed rate and low laser power and other 3 discs had optimal feed rate and high laser power. It shows that the 6HA-1 wear rate is high because of the parameter differences during the cladding period and severe wear after the experiments and less laser power usage during cladding process. 7B31 RCF test showed lowest wear rate on wheel disc with around 8 µg/cycle and MSS clad wheel wear rate followed that with around 10 µg/cycle.

8.4.3 Sub-Surface Analysis of clad discs

8.4.3.1 Subsurface Structure Images

Optimal feed rate and high laser power

The optimal powder feed rate combined with the higher laser power in disc 8HA-3 created a well bonded laser clad coating with minimal defects below the surface as seen in Figure 8.4a, but with some surface defects. After testing some material had been removed from this same region, as shown in Figure 8.4b. 7B29 and 7B30 showed similar surface behaviours with 8HA-3 because they had higher laser power and optimal powder feed rate.

Minimal wear and RCF have been seen in previous testing when the laser clad coating has been applied with optimal parameters (Tomlinson et al., 2021). The flaw from the clad surface is more severe following the application with higher laser power. Once sectioned the surface damage can be seen with the SEM images shown in Figure 8.7a and Figure 8.7b. The material at the surface has been worn away and areas of unformed powder are exposed, shown in Figure 8.5c and Figure 8.5d. Despite surface damage obtained under RCF test conditions, there is no sign of crack propagation below the surface.

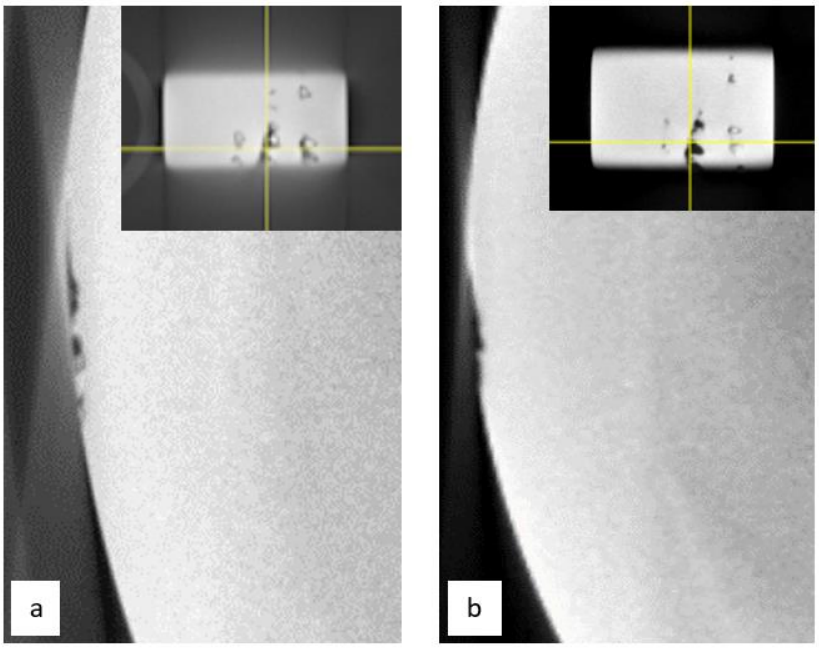

Figure 8.4: X-Ray scan images of Disc 8HA-3: (a) Pre testing; (b) Post testing

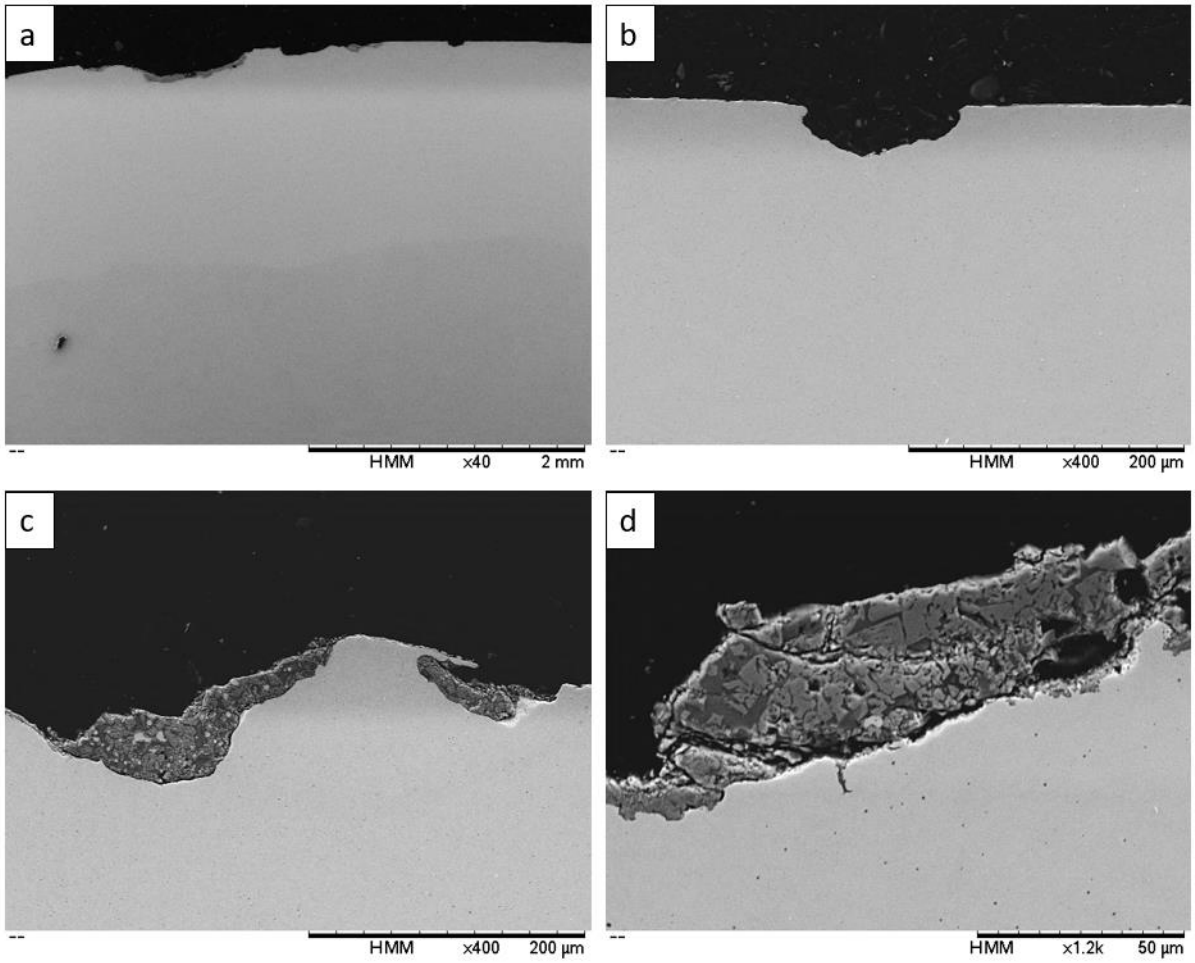

Figure 8.5: SEM images of the deliberately formed surface damage on disc 8HA-3: (a) Surface wear after testing; (b) Material removed on surface; (c) Unformed powder exposed at the surface; (d) Unformed powder.

The combination of optimal feed rate and high laser power created a coating that had minimal defects which were tolerated under the conditions tested but had much higher wear flaws at the contact surface of the disc.

High feed rate and low laser power

Disc 6AH-2, which was clad with higher powder feed rate and lower laser power, is shown in Figure 8.6 with a large amount of cracking below the surface within the laser clad coating before testing in the right-hand image of the disc. After testing there is little visible change to the extent of cracking in this position. Surface damage can be seen in the left-hand image of the disc before and after testing. The images show a dark line under the disc surface in the interface. The dark line do not continue all way through the disc surface. Those crack lines evolving depending on coming interface in the disc thickness.

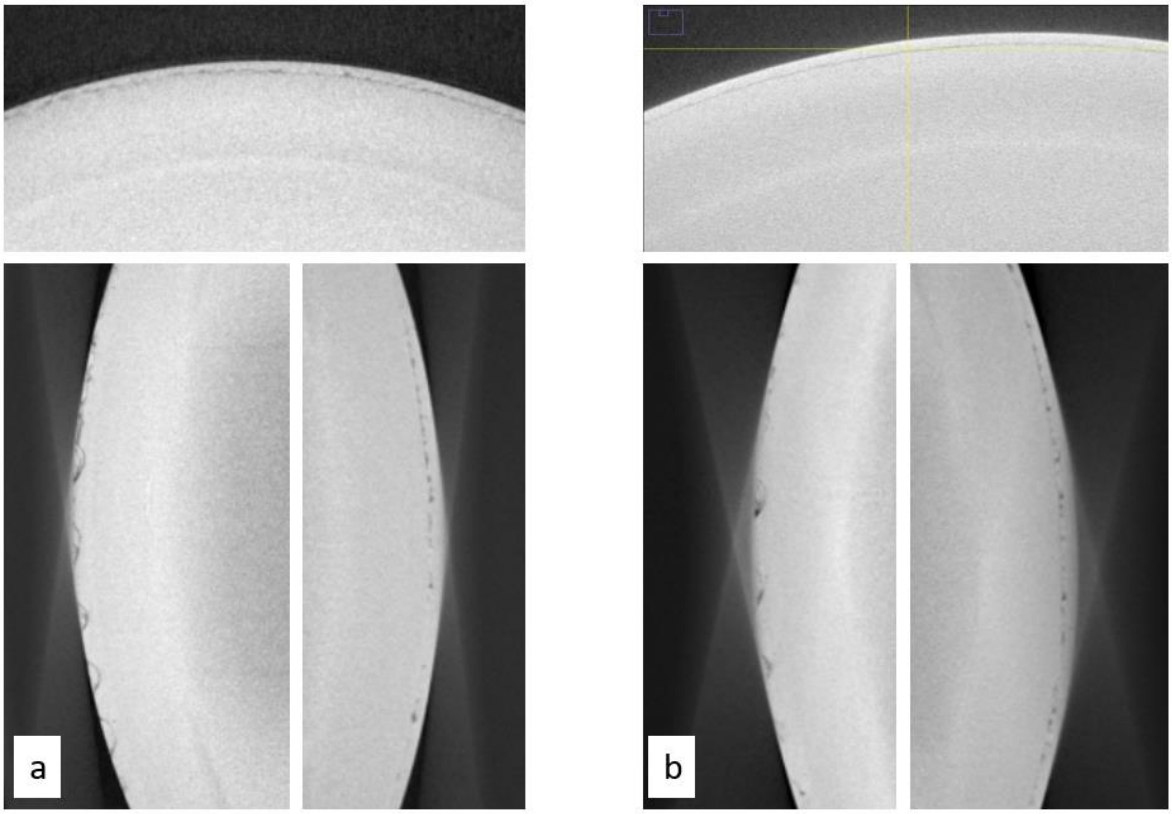

Figure 8.6: X-Ray scan images of Disc 6HA-2: (a) Pre testing. (b) Post testing

Once sectioned the SEM images revealed the cracks below the surface, shown in Figure 8.7a, which extended to a network of cracks stemming from the defects caused by the poor parameters. In Figure 8.7b, small cracks can be seen leading from the base of the large defect towards the clad coating interface with the substrate rail. On closer examination of the void

within the cracks, it can be seen that the coating remains in powder form and has not bonded, shown in Figure 8.7 c and Figure 8.7 d.

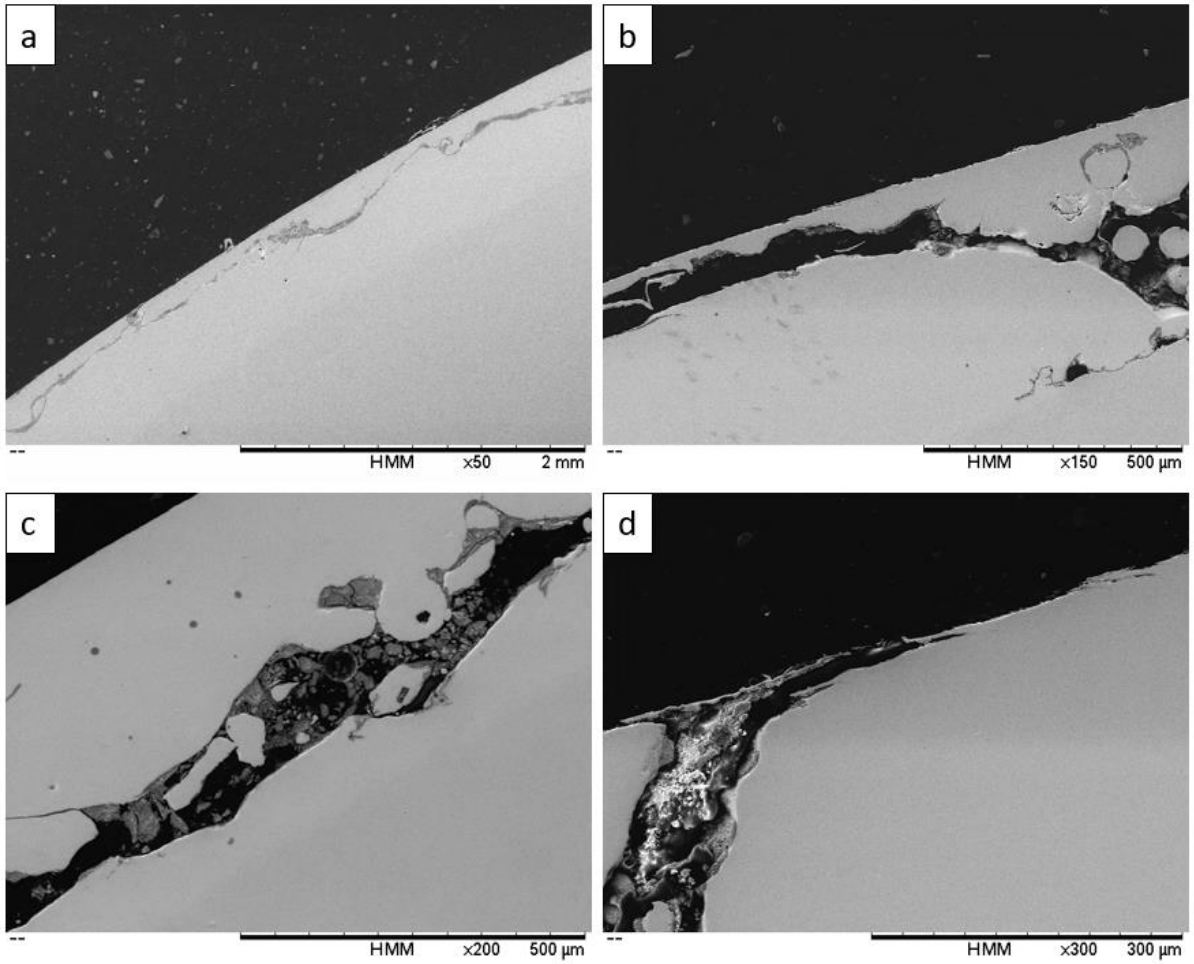

Figure 8.7: SEM images of the deliberately formed defects within disc 6HA-2: (a) Crack below the surface; (b) Cracks extending towards the material interface; (c) Unformed powder present within network of cracks below and joining the surface; (d) Unformed powder towards the surface.

Other small defects within the disc were present where the powder was once again unformed. Further magnification of one of the defects reveals unformed powder within it, shown in Figure 8.8a. Figure 8.8b shows a crevice with powder trapped within it and further cracking.

RCF cracks were seen to propagate from the surface, as shown in Figure 8.9a. Figure 8.9b shows further unformed powder at the surface from which material is seen breaking away. For context, in tests on unclad R260 conducted previously, subsurface images showed more severe cracks occurred around 30,000 cycles (Lewis et al., 2016).

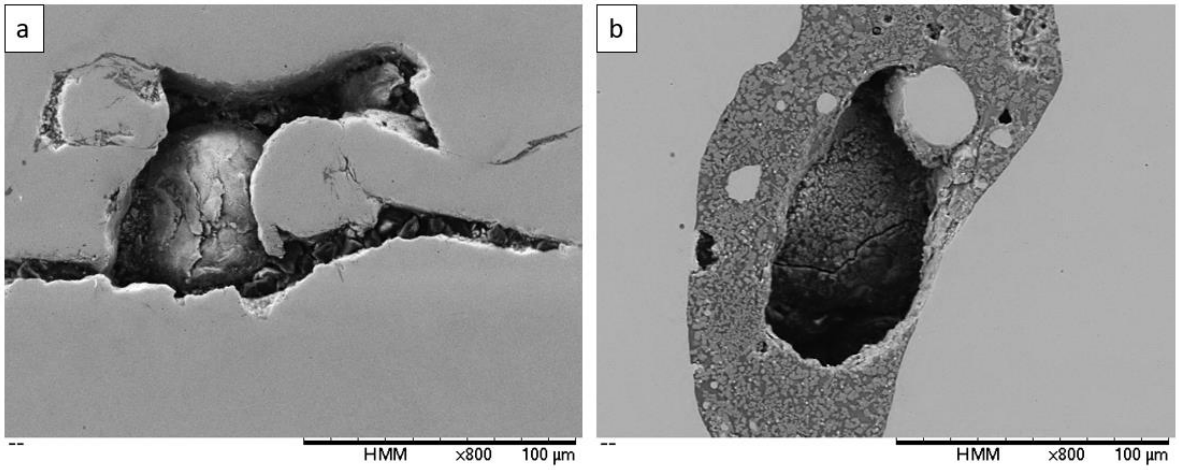

Figure 8.8: SEM images of deliberately formed defects within disc 6HA-2: (a) Powder trapped within defect; (b) Defect with cracking internally.

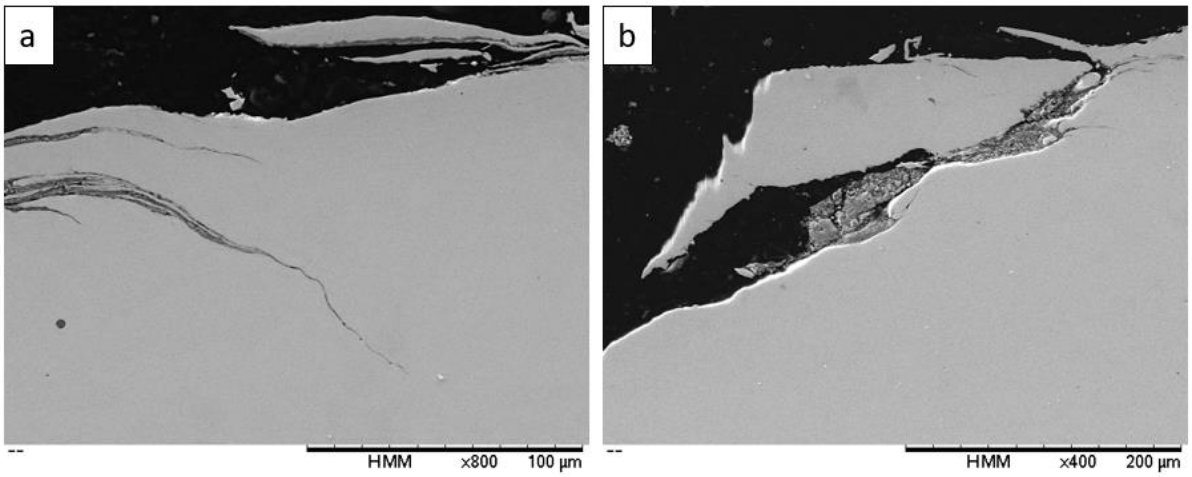

Figure 8.9: SEM images of deliberately formed surface cracks on disc 6HA-2: (a) RCF cracks propagating from the surface; (b) Surface damage with unformed powder

High feed rate and low laser power creates a laser clad coating with many defects and problems. These issues for example, cracks or holes cause the coating not good enough for testing. The coating does not stick together properly, and structural integrity cannot be achieved on disc microstructures.

8.4.3.2 Micro Hardness

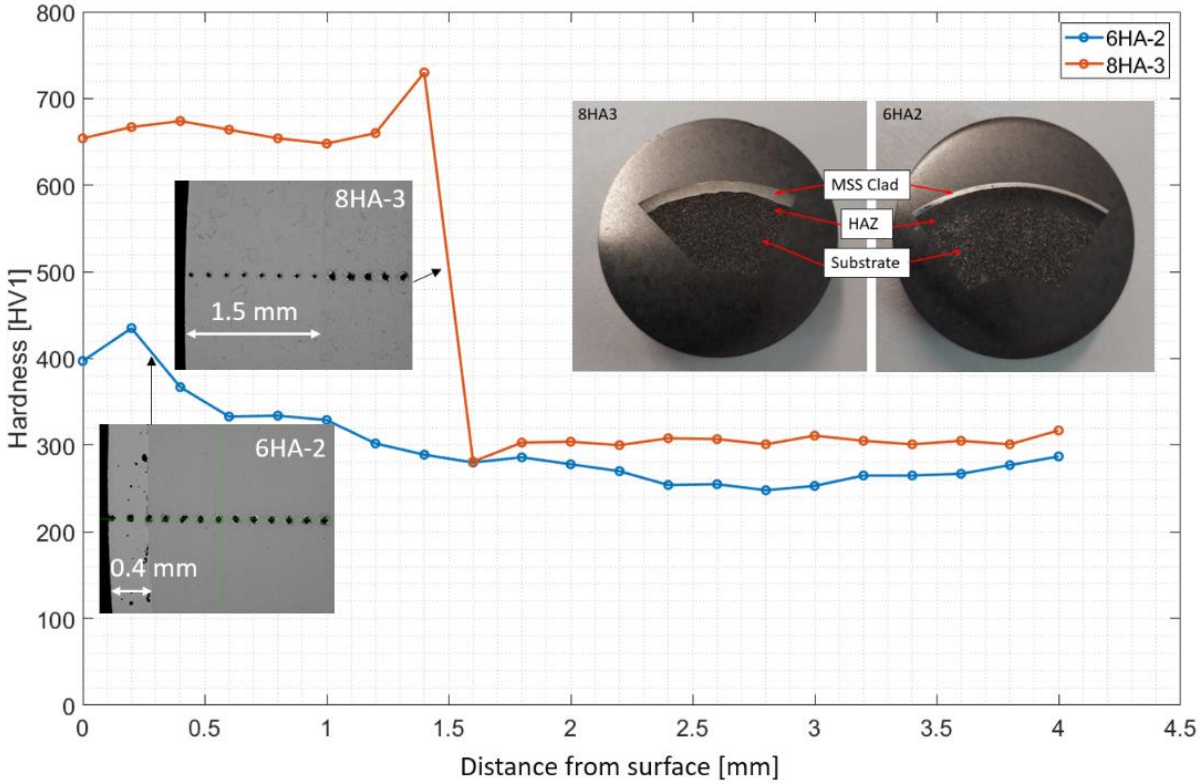

Figure 8.10: Microhardness values of 6HA-2 and 8HA-3 clad discs

Figure 8.10 shows the hardness data of the non-optimum clad rail discs from the disc surfaces to the substrate region. The 8HA-3 disc showed the highest hardness value in the clad part at around 700 HV1 while 6HA-2 was around 420 HV1. In the substrate region they were both around 280-300 HV1. The HAZ starts on the 8HA-3 disc at around 1.5 mm and for the 6HA-2 disc it starts around 0.4 mm. The HAZ hardness values range between 700HV1 to 300 HV1 on the 8HA-3 disc. The 6HA-2 HAZ shows at range between 350HV1 to 280 HV1. The clad thickness can be seen from images. 8HA3 with optimum feed rate and higher laser power created a dense clad and it caused higher hardness values than the 6HA-2 hardness values because 6HA-2 clad created higher powder feed rate with lower laser power and it created some pores on the clad part.

8.5 Discussion

On the cladding process powder feed rate and laser power had different impacts depending on the chosen parameters, as can be seen in Table 8.1.

The feed rate and laser power were both considered when testing the tolerance of laser cladding parameters. The results indicated that the feed rate had the biggest impact on the integrity of

the laser clad coating. In disc sample 6HA-2, areas of unformed clad coating powder were revealed in the cracks and defects as can be seen in Figure 8.7. The images showed that clad parts had big cracks however, there is another issue as well as the crack. There can be seen that there is unformed powder in part of the cracks which may affect bonding. Although the discs did not fail during testing, post-testing analysis shows a network of cracks, undetectable in service, which should not be tolerated.

The higher laser power with the optimal feed rate in 8HA3 disc created a clad coating which was intact down to the interface, however, excessive surface damage was seen before testing and where the surface flaws existed, material could be seen to have been removed in past-test scans. There was also further evidence of unformed powder seen in the surface flaws. 8HA3 disc had high hardness with more dense structure because of the cladding structure instead of lower dense structure 6HA-2 clad structure.

None of tests caused a large scale failure of a clad layer despite the different flaws created. Defect sizes on discs were increased as can be seen Figure 8.4 and Figure 8.6. Also, when wear rates of the tests were analysed, it could be seen that some different patterns emerged. Softer rails wore more than harder rails. This was not because of the flaws on rail, rather the properties of the clad layer formed under the different processing conditions. When compared to optimum MSS clad and R260 rail wear rates from work by Lewis et al. (2016), MSS clad wear rates showed lower values, with around 1 μg/cycle, than all wear tests, but RCF tests showed lower wear rates than that value for 7B31 and 7B32 discs. The R260 wear rate was the second highest on Figure 8.3(a). Only 6HA1 showed a higher wear rate than R260 because 6HA1 had a higher feed rate and low laser power which caused the clad layer to be relatively soft. Figure 8.9 shows 6HA2 microstructure images which are similar to 6HA1 and some unformed powders in the clad layer can be seen. This affects the wear rate during the tests and helped cause more material loss happen than in the R260 rail wear tests.

Another thing about the experiments was that there was no bending effect in the tests. There was some shear stress, but it does not affect the flaws in the same was a bending could. There should be some analysis with bending effects in the future.

8.6 Conclusions

Laser cladding is a new method to use in railway industry and it has many advantages over traditional methods. When laser cladding was used all in optimal conditions it showed good wear and RCF resistance in the last chapters. However, it can be used in non-optimal conditions

as well and the results in this chapter showed some good impacts about that. It can be seen that those clad discs structure defects stayed similar and discs did not fail under test conditions.

When changing the laser cladding parameters some defects were created in the clad layers, after running them in experiments the main outcome is that they did not fail. However it showed that it caused so high wheel wear rate. It is because of the surface defects of the rail clad discs.

Also, when pre and post-test rail defects were analysed the defects were changed a bit, but they were not such big changes, however, lower feed rate and lower laser power caused some more defects on the discs and some more pores microstructure and they affected wear losses mostly.

The optimal laser parameters are shown to be critical in the application of the laser clad coating, with feed rate being the most important factor. This must be monitored and controlled for an in-situ application to avoid networks of cracks with unformed powder.

Softer rails had higher wear rates, but it was not due to the defects by laser cladding parameters, it was because of the lower hardness of the discs.

Chapter 9

9 General Discussions and Field Test

This discussion chapter covers all the technical chapters and considers the work at a high level as detailed discussion is contained in the main chapters. This chapter shows the links between them and gives an analysis of all test scales and test materials.

9.1 Scaling Clad Tests

The experiments were conducted using small-scale and full-scale tests. The trend seen were the same when, comparing small-scale to full-scale tests. On the full-scale tests MSS clad, Stellite 6 clad and R260 non-clad pocket specimens were used in Chapter 6. MSS clad long-term experiments were conducted and they were shown in Chapter 4 with more analysis.

Wear rates of the tests were analysed with the Tγ/A approach. Figure 6.31 compares the wear rates from the small-scale twin-disc tests to the full-scale tests. It shows how wear differs between these two testing scales. Wear rates of the specimens match the same linear relationships between different scales. MSS clad wear rates showed the lowest wear rates and then Stellite 6 clad wear rates followed that. R260 wear rates showed the highest wear rates and clad specimen wear rates were compared with R260 as a reference material. MSS clad over R260 substrate rail seems the best material to improve wear and RCF resistance between those materials and long-life capacity rather than other rail clad materials depending on no more failure with the high number of cycles in the small-scale tests.

For the wear mechanisms of the materials, un-clad R260 showed higher wear and deformation than the clad layers and premium materials. Ratchetting was the main effect on R260 rail specimens and had some severe wear, but clad specimens showed there was some mild wear and almost no deformation. This work showed that small scale clad tests can give ideas about full-scale test or even field performance. Depending on the small-scale material clad selection or laser parameter selections and test performances it can give better ideas of how that materials can perform under real conditions.

The full-scale clad repair with T400 clad had many layers of the clad over R260 grade rail and it was tested to see the behaviour of many clad layers under actual loading conditions. It did

not show any big failure signs after the tests. There were some cracks through the surface layer, but these cracks were seen also before the tests as well. It did not show any crack propagation into the other layers after the test.

9.2 Clad Materials versus Premium Rail Materials

In the railway industry cost is another main issue and the need to find some alternatives to reduce that but at the same time, give better performance to overcome wear and RCF issues. R260 rails are mainly used as a rail material in the train lines, but it needs to have higher performance with increasing demand for railways and longer times use of trains without stopping the mainline traffic. Premium rails are an option for that, and they were giving good results for wear and RCF performance as can be seen in Chapter 7. Another option is laser cladding which allows coating of another harder material over R260 grade substrate material. When compared with premium rail, laser cladding is a cheaper option because premium rails are used in the full length and profile of the rail, but laser cladding is only a few milimetres over the R260 grade rail. Figure 7.21 shows the wear rates with Tγ/A approach and there it can be seen that clad material wear rates show lower values than premium rail wear rates, Laser cladding can be an alternative method for high wear and RCF resistance on the railways with lower cost than premium rails.

Premium rail experiments in small-scale tests were analysed in Chapter 7. Ratchetting is the main mechanism in the R260 rail as a wear mechanism, but other clad layers and premium materials show ratchetting is not the main mechanism for them. There might be mild abrasion occurring for the Mn premium rail specimen because there was seen some different mechanisms on the tests. It does not ratchet and harden through deformation, but by a twinning mechanism. During the experiments it was seen from surface images polishing effect happens on clad tests and it led to lower roughness values than others.

9.3 Cladding as a Repair Technology

Repair is a complex issue on railways and repair, or replacement is a huge cost for railways. When delays or waiting times occur because of railway repairs or problems it leads to extra costs. Laser cladding is considered a viable repair method for rails, and experiments have been carried out to investigate its potential. In Chapter 5, repair tests were conducted with different clad materials over R260 grade rail twin-dis specimens. Material selection and laser clad parameters are important to choose for optimum material performance. Figure 5.2 shows the repair geometries on a disc with different materials and geometries with some shallow and

some deep repairs. 3 slots for MSS, 2 slots for Stellite 6 and 1 slot for R260 clad materials were used and R260 was used as the base material on a disc for experiments. Laser cladding as a repair had some advantages with the control of heat input rather than other traditional methods.

The leading and trailing edges of the clad parts were analysed with microstructure images because after the test material flows were used to give some ideas about clad and base material bonding. It showed that R260 clad material had better performance depending on the edges of the clad geometries and allowed better material flows. The MSS clad and Stellite 6 clad showed come cracks mainly around the leading and trailing edges of the clad parts. It can be due to the high difference in hardness values between the clad and the substrate. It was shown that the hardness difference with MSS and Stellite 6 was more than R260 clad (see Figure 5.33). R260 clad hardness were higher than R260 substrate and HAZ parts because of the heat treatment. Furthermore, downward of the clad materials especially small size clad parts showed some clad part movement. Cracks generally started from trailing edges on the microstructure images on the repair specimens Also material flows examined more in that part of the clad.

Clad repair experiments showed it is useful for this purpose, but an in-situ repair can have some problems in the field. As discussed in Chapter 8 clad quality issues for example laser parameter and powder feed rates can give different results depending on the conditions. However, in the railways, there are high-value components as well such as switch blades and insulated block joints (IBJ). They can be repaired in workshop conditions for example they can have better preheating options before cladding to improve the clad quality and allow to re-use with a much longer component life.

9.4 De-Risking Cladding

Laser cladding on railways needs to be more in the environmental conditions and when clad happens some parameters can show different values. In Chapter 8, laser clad quality was analysed before and after tests with some X-ray imaging. Before the tests laser cladding process changed to use different laser cladding process parameters, they were higher feed rates than the optimum value and higher or lower powder feed rates than optimum feed rate values. MSS clad was used on R260 substrate grade rail and some defects occurred during and after the clad process in the clad layers. MSS clad discs were imaged with X-ray before the tests and tests were conducted under different conditions. After the tests, they were imaged again with the X-ray imaging system. After analysing images defects or flaws in the images showed bigger sizes

in the crack or some removals from the surface. But they did not propagate in clad layer to substrate parts.

There were 2 options analysed that are optimal feed rate and high laser power in the 8HA-3 disc and high feed rate and low laser power in the 6HA-2 disc. When microstructures were analysed it showed that feed rate has the highest impact on the clad quality and performance for integrity. 6HA-2 with a high feed rate showed some unformed powders in the clad and it showed a big crack on the layer, but that crack occurred due to the unformed powders instead of clad performance under the tests and non-bonded clad layers. It did not cause the failure of the disc under the tests. High laser power and optimal feed rate disc 8HA-3 showed better bond quality with clad and substrate, but it showed some bigger surface damage. Again, it did not fail on the tests.

Another point of the clad quality tests there was no bending effect on these tests. The bending could give some different aspects for the tests. However, bending tests were conducted on previous research for MSS clad over R260 rail substrate. After the four-point bending tests, they found that MSS clad over R260 rail did not fail within 5,000,000 cycles and it was tested 350 MPa stress range as much higher than the standard requirements for fatigue strength of about 230 MPa (Lewis et al., 2017). MSS clad has good fatigue resistance and it can be seen that it could not be a big problem for that and it can be tested with bending effect too.

9.5 Field Testing of Clad Layers

Small-scale and full-scale tests for laser clad specimens showed good results and for the usability of these materials and specimens needed to be shown in the field as well. Laser clad rails, premium rails and standard grade rails were inserted into the trainline to analyse how they behave under real rail/wheel conditions. These rails were put in track at British Steel in Scunthorpe.

The field test plans of various rails and IBJ sets is shown in Figure 9.1 (a). The plan includes 4 different types of rails. They are standard rail that is R260 grade and 3 different cladded rails. Clad materials are Stellite 6 and Martensitic stainless steel (MSS) with two different thicknesses. Stellite 6 and MSS are used for 3 mm clad, and another MSS is used for 1 mm clad thickness on standard rails. The chemical compositions of the materials are shown in the Table 9.1.

Table 9.1: Chemical compositions (%by mass) of E8 wheel, R260 rail, MSS, and Stellite 6 clad materials (Martensitic Stainless Steels; Santa et al., 2019; Stellite; HP335)

	C [%]	Mn [%]	Si [%]	Cr [%]	Ni [%]	Mo [%]	Co [%]	V [%]	W [%]	N [%]	Al [%]	S [%]	P [%]
R260	0.74	1.08	0.31	0.040	-	-	-	0.004	-	-	0.003	0.018	0.013
MSS	0.06	1.22	0.46	14.64	3.31	0.42	2.01	0.51	0.62	0.04	0.01	0.005	0.009
St. 6	1.0	<0.1	0.9	27.0	-	-	Bal	-	4	-	-	-	-
HP335	0.87-0.97	0.75-1.00	0.75-1.00	≤0.10	-	-	-	0.09-0.13	-	-	≤0.004	0.008-0.020	≤0.020

Also, left, and right rails are placed dependent on the direction of the rail. Running bands were shown in Figure 9.1. IBJs can be seen between the rails. The block joints were assembled prior to the string being welded in place in track.

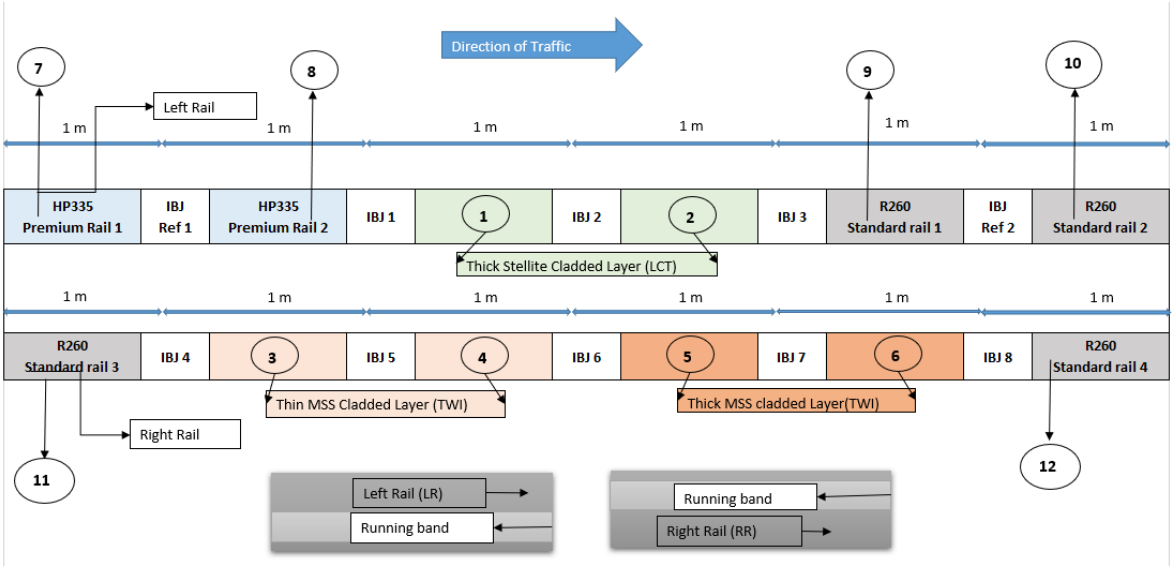

Fig. 9.1. (a)

Fig.9.1. (b)

Figure 9.1: Field test plan of rail and IBJ sets: (a) Plan of the rails and IBJ sets for assembly; (b) Assembled rails and IBJ sets.

Figure 9.1 (b) shows the assembled parts of the rails based on the plan in Figure 9.1 (a). The assembly process was done in Progress Rail, UK. There were standard R260 rails, premium rails, MSS clad and Stellite 6 clad rails. The surface of the clad rails can be seen from the images and they were put in track in that conditions.

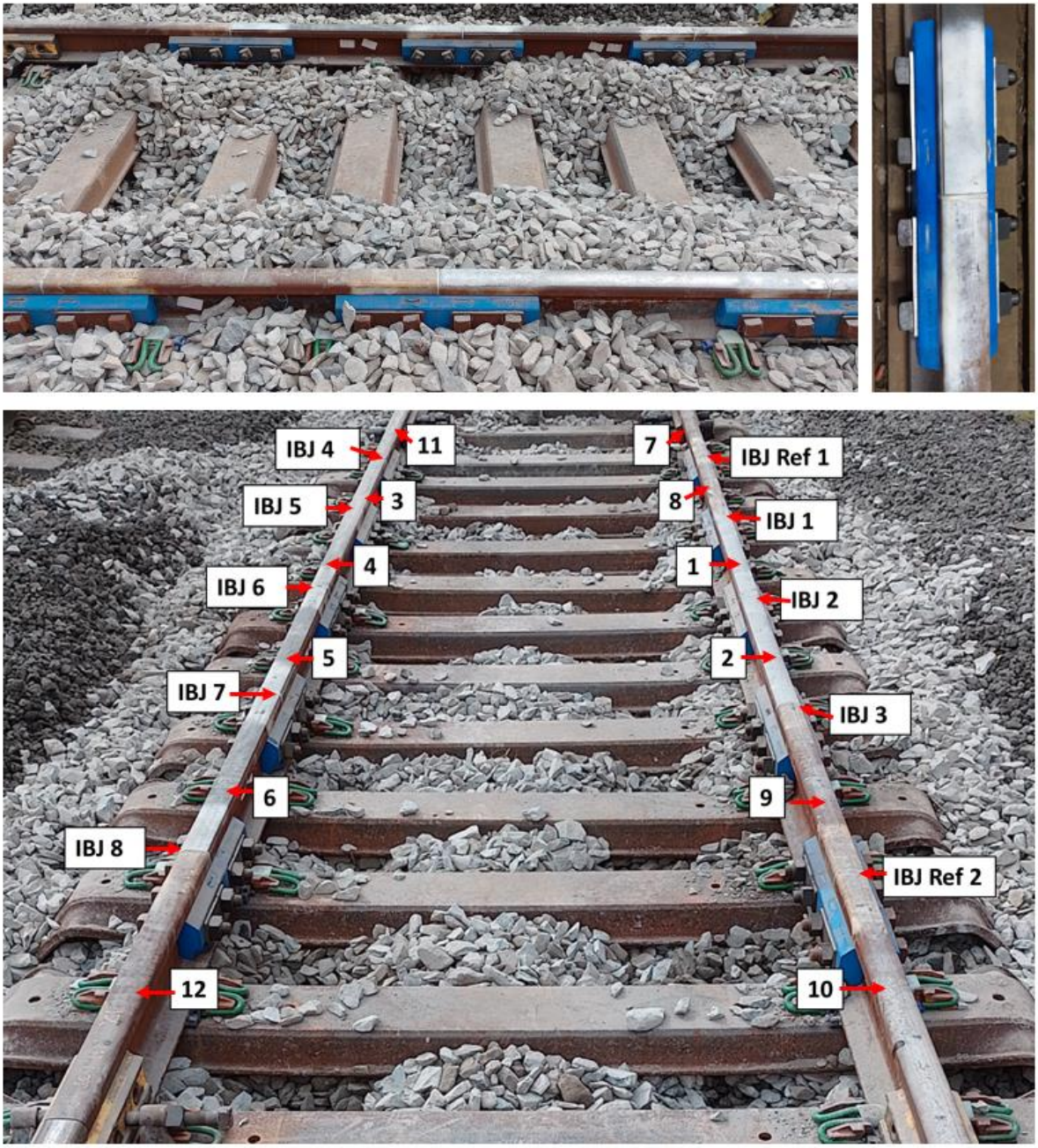

Figure 9.2: Inserted rails and IBJs into the rail track

Figure 9.2 shows the inserted rails for the field tests. The measurements of the rails are planned to be conduct over time. There can be seen IBJ parts, and all rails were fitted into the track. The measurements were planned, and these measurements included the surface roughness of rails. For the roughness measurements a replica method is used then measurements are taken using the Alicona non-contact profilometer. Photographs are taken from IBJ parts to figure out how material flow changes the plastic size between rails. Rail profile measurements are taken with a Calipri device or laser scanner to examine the changes in rail profiles. Laser scanners

also give nice images as a 3D model from the track for rail surfaces. The hardness of the rails is examined with a portable hardness tester. LIBS analyses are conducted to see chemical composition changes with traffic over the rails.

9.5.1 Roughness

Figure 9.3 shows the surface roughness Ra measurements for the lateral and longitudinal direction measurements for before the start of traffic and after the start of traffic with the 1st measurement label. The dateral direction is across the rail the longitudinal direction is along the rail. The surface features were collected by the replica method that is shown with detail in section 3.4.3.4. Those replicas analysed in the Alicona non-contact profilometer that is explained in section 3.4.3.1.

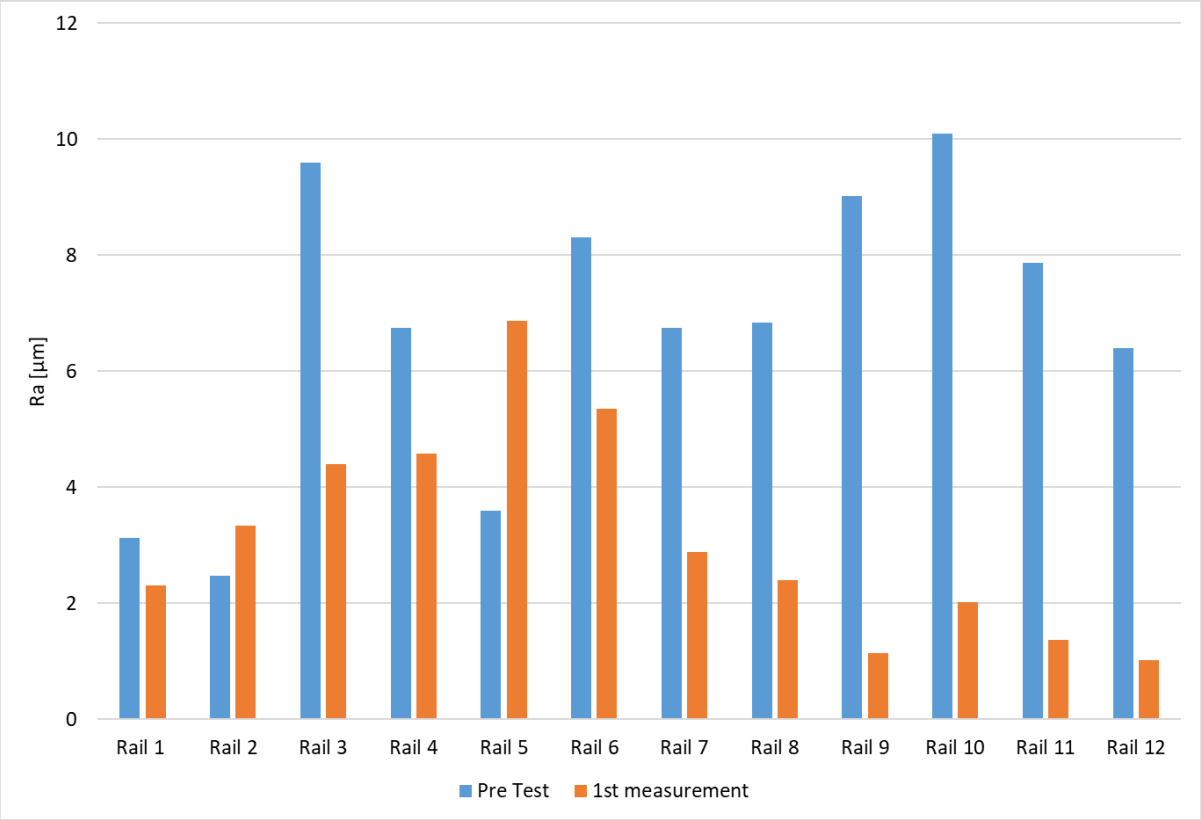

Fig.9.3. (a)

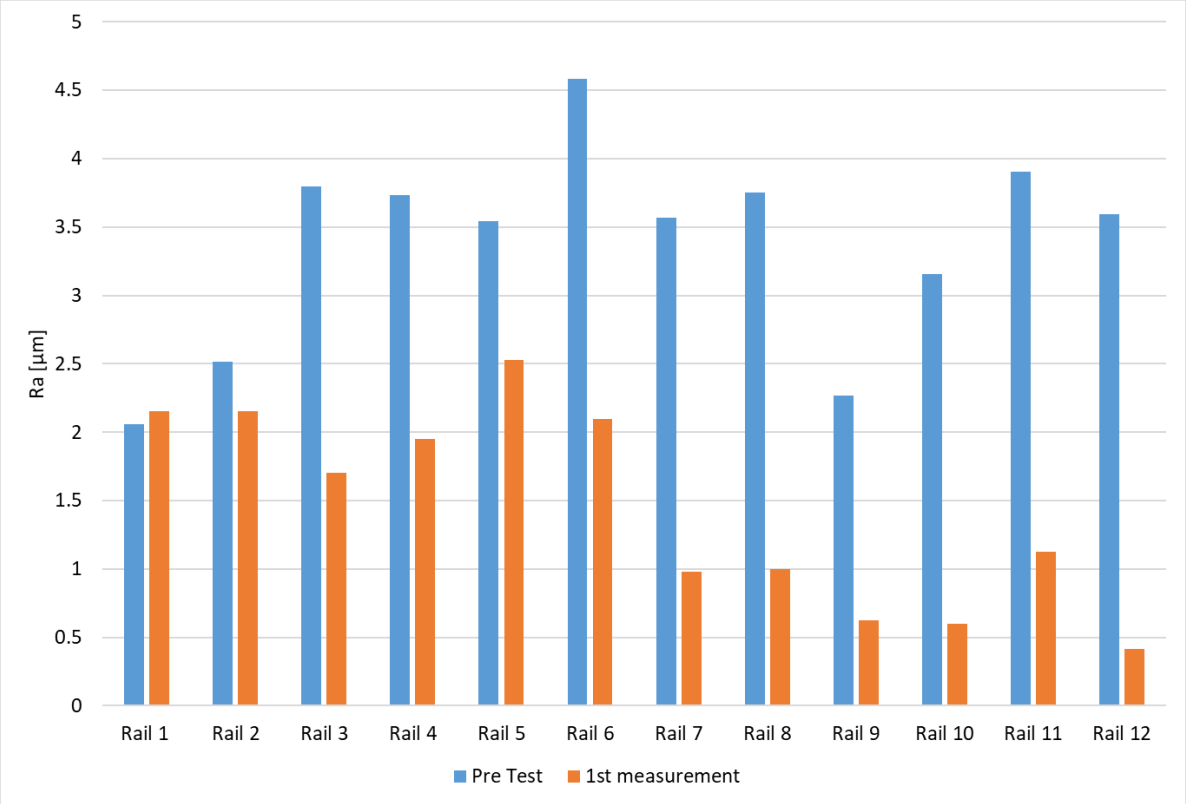

Fig. 9.3. (b)

Figure 9.3: Field track test set up surface roughness (Ra) measurements for lateral and longitudinal directions: (a) lateral; (b) longitudinal

Ra values were taken from the running band after traffic occurred on the rail. In the lateral direction in Figure 9.3 (a), surface roughness of rails was decreased except for rail 2 (Stellite 6 clad) and rail 5 (thick MSS clad) rails. R260 rails (9-10-11-12) showed the highest decrease between pre-tests and the 1st measurements. In the longitudinal direction in Figure 9.3 (b), surface roughness values decreased except rail 1 that is Stellite 6 clad rail. R260 rails (9-10-11-12) showed a big decrease from pre-test to 1st measurements with rail 7 and rail 8 premium rails.

9.5.2 Hardness

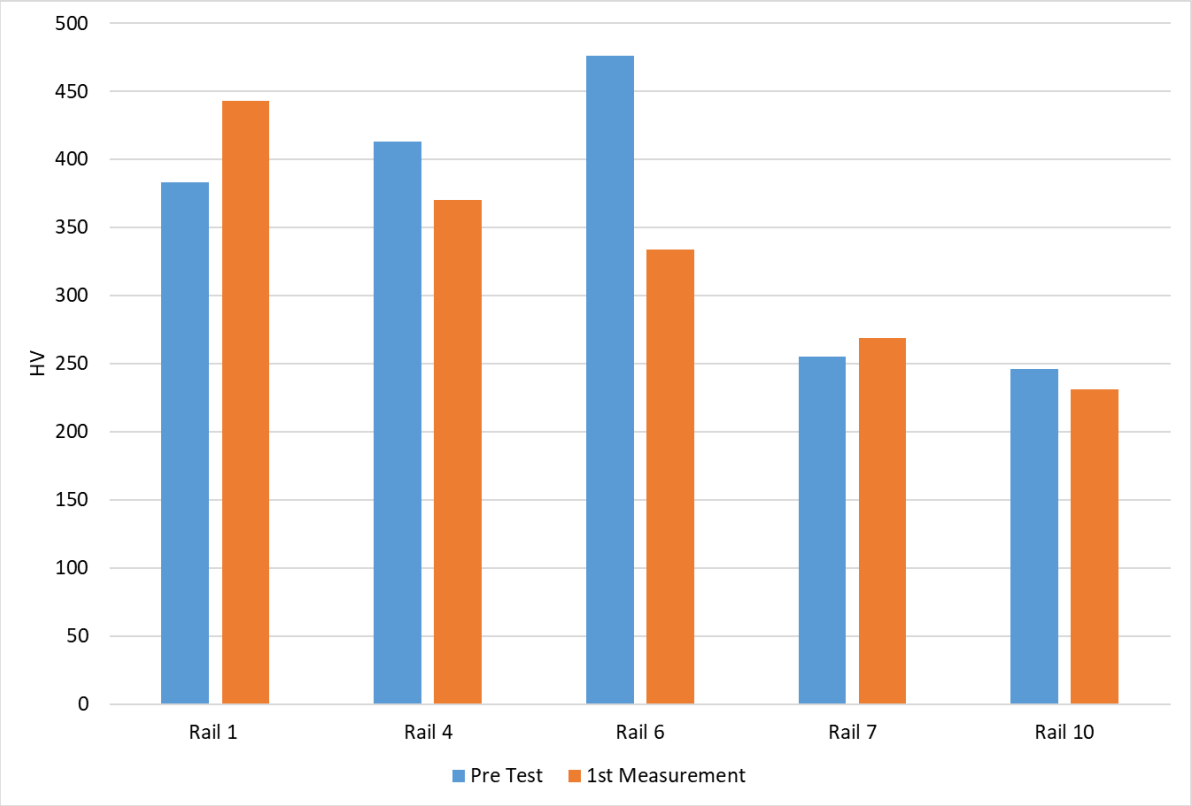

Figure 9.4: Hardness values for pre-test and after 1st measurements of rails

Figure 9.4 shows the hardness results from track that measurements were done with portable hardness tester and hardness values were got from close to the IBJ parts. The hardness values after traffic got from running band. Rail 1 (Stellite 6) showed a bit increase with rail 7 (HP 335), but other rail types showed decrease before to after traffic. Rail 6 (Thick MSS clad) showed highest decrease amount between pre and 1st measurement from 476 HV to 334 HV.

9.5.3 Surface 3D images

Figure 9.5 shows the some IBJ set surface 3D scans for before and after 1st measurements. In this figure IBJ 6,5 and 4 is showed and there can be visible how IBJ plastic part change and intend to have lipping in the middle of images. For all rails and IBJ parts will be examined with upcoming measurements and analyse as a 2D profile changes as well. Figure 9.6 shows the images after rail traffic over rails and IBJ sets. Wear band got visible over rails.

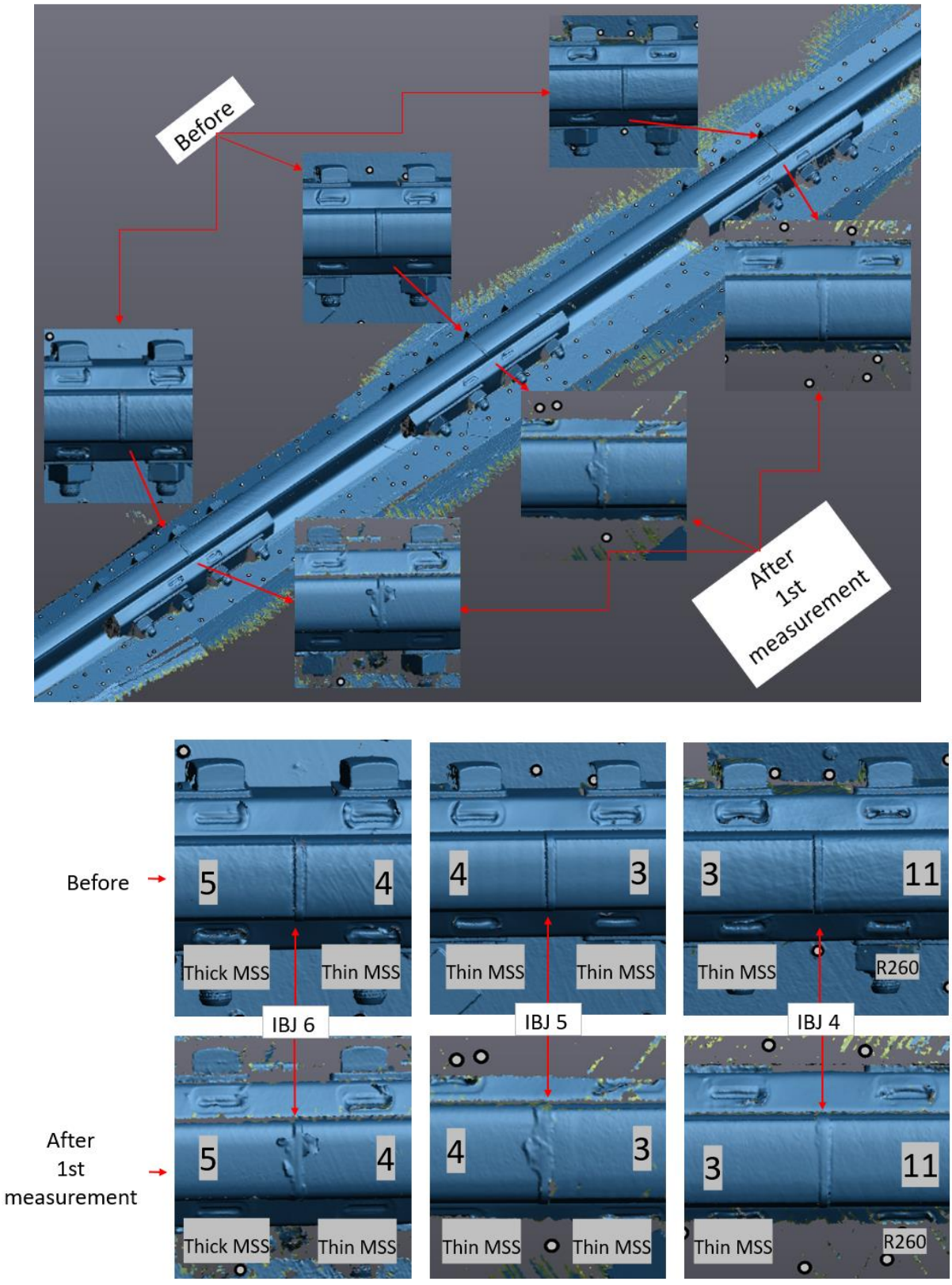

Figure 9.5: Surface 3D scan images of IBJ sets.

Figure 9.6: Some images after rail traffic over rails and IBJ components

Field tests will be conducted, and measurements will be taken with some period of time. It will show how the MSS, Stellite 6 clad, HP335 premium and R260 normal grade rails and IBJ sets performed.

Chapter 10

10 Conclusions and Future Works

10.1 Conclusions

Railways are carrying so much traffic all around the world and in the UK with this demand leading to higher speed trains and loads. The added loading on the rails means that some novel techniques or materials are needed to help prolong the life to help reduce the amount of maintenance needed (so track is more available) and maintenance costs. The two main issues for rail are wear and RCF on rails. Some new methods and materials have been used for overcoming those issues. Laser cladding is one of the novel additive manufacturing methods for solving those problems. In this thesis, laser cladding was used on small-scale rail discs, full-scale pocket specimens and full-size rails.

The experiments were conducted at different scale tests for analysing the wear and RCF performance of the laser cladding on rail specimens, premium materials, repair of the laser cladding and clad quality effects by laser clad parameters. R260 rail was used as the base material and different types of clad materials were used as clad material which were martensitic stainless steel [MSS], Stellite 6 and R260. Also, some premium rails were tested for further analysis. The premium rails were Manganese [Mn], Chromium [Cr], and R400 rails.

MSS clad was the best performing clad material from previous experiments and in Chapter 4 it was analysed at a high number of cycles to try and achieve some failure signs. The tests were continued until 420,000 cycles and the clad rail did not fail (for context R260 tested under the same regime would fail at 20-30,000 cycles). Some flake formation was seen and crack starting points from the surface, but it was very minimal. The layer still need more testing to find the failure point of the discs.

Laser cladding as a repair method showed good results. There were MSS, Stellite 6, and R260 clad materials used as clad material over the R260 rail substrate in small-scale tests. Also, T400 clad material was used over the R260 rail for a full-scale test. Small-scale repair tests showed R260 clad over R260 substrate rail was the best option instead of MSS or Stellite 6 clad materials. As a repair it showed the same materials had good bonding and material flow (e.g.

R260 on R260), but different clad materials showed some cracks on the edge of the clad parts or some differences in material flows.

On the full-scale tests, MSS clad and Stellite 6 clad pockets specimens showed good performance over un-clad R260 pocket specimens. That was expected in line with results from small-scale tests. It showed clad materials were a good option to try in field tests as well. Also, the link between small-scale and full-scale tests showed good correlations that is why in the future small-scale experiments can be used for material selection and material selection field trials.

The full-scale test of the T400 repair showed it can be used as a repair because although it had some cracks on the surface layer from the processing, those cracks did not extend to the other layers or the rail did not fail under the actual rail/wheel condition. The crack formation could be dealt with by optimising the cladding parameters.

Premium rails are another option for increased wear and RCF resistance and they were analysed to see how their performance differed from MSS clad twin disc experiments. They all showed lower wear rates than standard grade R260 rail wear rates. Mn, Cr and R400 rails were premium rails. Mn only showed some different wear mechanisms than others it had higher wear rates and lower hardness values than other premium and MSS clad materials. MSS clad showed it is a better option than premium rails because laser cladding allows harder materials over standard grade rail and that decreases the cost. If the premium rail is used cost is higher than the laser clad rails.

When laser cladding operated with optimal conditions it showed good results, but if it is used in different conditions and environments, it can give different results. Laser cladding parameters changed to create that condition affects to see how it gives results. Changed laser clad parameters showed some defects in rail clad parts. MSS clad over R260 rail substrate was used. Powder feed rate showed the most crucial factor in laser cladding because it can cause unformed powders in the clad. Optimal feed rate is important, and it must be controlled in-situ applications. The flaws did not propagate though in testing and wear rates were only higher than optimal clad layers where the processing had led to a softer layer being created.

10.2 Future Work

On this thesis it showed that laser cladding is used on different scale experiments with successfully. However, there are still some questions how to improve that and find better solutions for problems.

In the Chapter 4 MSS clad over R260 rail disc substrate showed clad disc did not fail after quite long number of cycle but still it is good to know when that clad disc will fail. It can be conducted further tests to find experimental failure cycle for small-scale test. Normal grade R260 rail twin disc sample showed damage around 15-30,000 cycles in Lewis et al. (2016) research but MSS clad test continued until 420,000 cycles and no big failure sign found that's why it need to do more experiments for that.

Repair tests were conducted in the Chapter 5. MSS, Stellite 6 and R260 materials used as clad material and R260 is used as base material on twin disc specimen. T400 used for clad material on R260 rail substrate for repair tests. Small scale tests showed R260 clad is best performed and it can be seen same clad material over same substrate material has well bonding. Other clad materials showed some more pores or cracks more in the edges of the clad parts. In the future laser clad parameters can be analysed better and try to find optimal values by manufacturers. It can be tested with only R260 clad slots over twin disc specimen for dry and water lubricated conditions. Also, for the R260 clad over R260 substrate rail it can be tested under actual load conditions as well. On the full scale T400 tests showed that did not fail under actual load condition but clad thickness was a bit higher and it can be good to have more tests for different type of shallow repairs and different slip conditions as well.

Premium rail small scale wear tests showed in Chapter 7 and they showed lower wear as MSS clad test. MSS clad showed slightly better performance than them. Mn showed different wear mechanism than others. There can be more experiments to find for different test parameters and more full-scale tests to see how premium rails perform and compare with MSS clad pocket specimens.

Laser cladding optimal parameters are so important to have good clad but when they changed how clad specimens work for seeing different conditions analysed in Chapter 8 and it showed any of the clad specimens failed during the tests. Also it can be good to have some similar tests under full-scale testing.

Full scale clad tests in Chapter 6 showed MSS clad and Stellite 6 clad had lower wear while R260 un-clad pocket specimen worn more than them. That tests conducted for 5,000 cycles and it showed that laser clad specimens can be used in the field track as well. As discussed in Discussion chapter field tests data can show some more analysis for MSS, Stellite 6 clad, HP335 premium and R260 grade standard rails. Depending on the track data it can be

conducted different test set-ups in small scale and full-scale tests and laser clad parameters or material selections in the future.

11 References

AbrasiMet 250. (n.d.).“AbrasiMet 250B Brochure.” [Online]. Available at: https://www.buehler.com/assets/Brochures/English/Sectioning/AbrasiMet250Brochure.pdf.

Athukorala, A., & De Pellegrin, D. V. (2017). Experimental Depiction of the Hypothesis of Flake-Like Wear Debris Generation in Rolling Contact Fatigue of the Rail–Wheel Contact Interface. *Tribology Transactions*, *60*(4), 581–591. https://doi.org/10.1080/10402004.2016.1188189

Ayrault, S., Chateauminois, A., Soulier, J. P., Tréheux, D., & Vannes, A. B. (1996). Deposition of a ceramic coating on a thermoplastic polymer by atmospheric plasma and laser cladding. *Surface and Coatings Technology*. https://doi.org/10.1016/0257-8972(95)02432-8

Beaty, P., Temple, B., Marshall, M. B., & Lewis, R. (2015). Experimental modelling of lipping in insulated rail joints and investigation of rail head material improvements. *Proceedings of the Institution of Mechanical Engineers, Part F: Journal of Rail and Rapid Transit*, *230*(4), 1375–1387. https://doi.org/10.1177/0954409715600740

Bhadeshia, H., & Honeycombe, R. (2006). Steels: Microstructure and Properties. In *Steels: Microstructure and Properties*. https://doi.org/10.1016/B978-0-7506-8084-4.X5000-6

Bolton, P. J., & Clayton, P. (1984). Rolling-sliding wear damage in rail and tyre steels. *Wear*. https://doi.org/10.1016/0043-1648(84)90066-8

Brunskill, H. P., Zhou, L., Lewis, R., Marshall, M. B., & Dwyer-Joyce, R. S. (2012). Dynamic characterisation of the wheel/rail contact using ultrasonic reflectometry. *9th International Conference on Contact Mechanics and Wear of Rail/Wheel Systems, CM 2012*, *January*, 98–102. https://doi.org/10.4203/ccp.104.185

Buckley-Johnstone, L., Harmon, M., Lewis, R., Hardwick, C., & Stock, R. (2019). A comparison of friction modifier performance using two laboratory test scales. *Proceedings of the Institution of Mechanical Engineers, Part F: Journal of Rail and Rapid Transit*, *233*(2), 201–210. https://doi.org/10.1177/0954409718787045

Christoforou, P. (2020). Laser Cladding for use in Extreme Tribological Interfaces.

Christoforou, P., Fletcher, D. I., & Lewis, R. (2019). Benchmarking of premium rail material wear. *Wear*, *436–437*. https://doi.org/10.1016/j.wear.2019.202990

Christoforou, P., Lewis, S., Fletcher, D. I., Pavier, M. J., Mostafavi, M., Narayanan, A., & Lewis, R. (n.d.). *Review of laser cladding tribology for high load applications Review of laser cladding tribology for high load applications*.

Chryssolouris, G., Zannis, S., Tsirbas, K., & Lalas, C. (n.d.). *An Experimental Investigation of Laser Cladding*.

Chryssolouris, G., Zannis, S., Tsirbas, K., & Lalas, C. (2002). An experimental investigation of laser cladding. *CIRP Annals - Manufacturing Technology*. https://doi.org/10.1016/S0007-8506(07)61486-3

Clare, A., Olusola, O., Folkes, J., & Farayibi, P. (2011). Laser cladding for railway repair and preventative maintenance. *30th International Congress on Applications of Lasers and Electro-Optics, ICALEO 2011*, *September 2017*, 240–249. https://doi.org/10.2351/1.4710578

Creaform3D. (n.d.). "HandySCAN BLACK 3D Laser Scanner." [Online]. Available at: https://www.creaform3d.com/en/portable-3d-scanner-handyscan-3d.

Cubus. (n.d.). "TestXpert testingsoftware, Cubus Testing software" [Online]. Available at: https://www.zwickroell.com/accessories/testxpert-testing-software/cubus-testing-software/ .

DuraScan. (n.d.). "DuraScan micro hardness tester." [Online]. Available at: http://f.jernindustri.dk/2fk3ntzke7ogxgha.pdf.

EcoMet 250. (n.d.). "BUEHLER® EcoMet®250/300 Grinder-Polisher Family & AutoMet®250/300 Power Head." [Online]. Available at: https://photos.labwrench.com/equipmentManuals/8248-3228.pdf.

Ehsan Toyserkani, Amir Khajepour, & Stephen F. Corbin. (2004). *Laser Cladding*.

Fasihi, P., Kendall, O., Abrahams, R., Mutton, P., Qiu, C., Schläfer, T., & Yan, W. (2022). Tribological Properties of Laser Cladded Alloys for Repair of Rail Components. *Materials*, *15*(21), 7466. https://doi.org/10.3390/ma15217466

Fletcher, D. I., & Beynon, J. H. (2000). Development of a Machine for Closely Controlled Rolling Contact Fatigue and Wear Testing. *Journal of Testing and Evaluation*, *28*(4), 267–275. https://doi.org/10.1520/jte12104j

Franklin, F. J., Weeda, G. J., Kapoor, A., & Hiensch, E. J. M. (2005). Rolling contact fatigue and wear behaviour of the infrastar two-material rail. *Wear*, *258*(7–8), 1048–1054. https://doi.org/10.1016/j.wear.2004.03.054

Fu, F., Zhang, Y., Chang, G., & Dai, J. (2016). Analysis on the physical mechanism of laser cladding crack and its influence factors. *Optik*, *127*(1), 200–202. https://doi.org/10.1016/j.ijleo.2015.10.043

Fu, Z. K., Ding, H. H., Wang, W. J., Liu, Q. Y., Guo, J., & Zhu, M. H. (2015). Investigation on microstructure and wear characteristic of laser cladding Fe-based alloy on wheel/rail materials. *Wear*, *330–331*, 592–599. https://doi.org/10.1016/j.wear.2015.02.053

Gao, J., Zhai, W., & Guo, Y. (2018). Wheel–rail dynamic interaction due to rail weld irregularity in high-speed railways. *Proceedings of the Institution of Mechanical Engineers, Part F: Journal of Rail and Rapid Transit*, *232*(1), 249–261. https://doi.org/10.1177/0954409716664933

Garnham, J. E., & Beynon, J. H. (1991). The early detection of rolling-sliding contact fatigue cracks. In *Wear* (Vol. 44).

Guo, H. ming, Wang, Q., Wang, W. jian, Guo, J., Liu, Q. yue, & Zhu, M. hao. (2015). Investigation on wear and damage performance of laser cladding Co-based alloy on single wheel or rail material. *Wear*, *328–329*, 329–337. https://doi.org/10.1016/j.wear.2015.03.002

Heyder, R., & Maedler, K. (2015). The influence of wheel and rail material on the wear of the respective contact partner. *CM 2015 - 10th International Conference on Contact Mechanics of Wheel / Rail Systems*.

Hitachi. (n.d.). “Hitachi Tabletop Microscope TM3030.” [Online]. Available at: https://www.hitachi-hightech.com/file/us/pdf/library/literature/TM3030_brochure_letter.pdf.

HP335. (n.d.). “HP335 Rail for combatting rolling contact fatigue and wear .” [Online]. Available at: https://britishsteel.co.uk/media/323526/british-steel-hp335-datasheet.pdf.

HP335. (2020). HP335 Rail for combatting rolling contact fatigue and wear.

Hu, Y., Zhou, L., Ding, H. H., Tan, G. X., Lewis, R., Liu, Q. Y., Guo, J., & Wang, W. J. (2020). Investigation on wear and rolling contact fatigue of wheel-rail materials under various wheel/rail hardness ratio and creepage conditions. *Tribology International*. https://doi.org/10.1016/j.triboint.2019.106091

Hysitron. (n.d.). "Hysitron TS 77 Select Nanoindenter." [Online]. Available at: https://www.bruker.com/en/products-and-solutions/test-and-measurement/nanomechanical-test-systems/hysitron-ts-77-select-nanoindenter.html.

ImageJ. (n.d.). "Image Processing and Analysis" [Online]. Available at: https://imagej.nih.gov/ij/docs/intro.html.

InfiniteFocusSL | 3D measurement system for form & finish | Alicona. (n.d.). Retrieved February 17, 2023, from https://www.alicona.com/products/infinitefocussl/

Kaierle, S., Barroi, A., Noelke, C., Hermsdorf, J., Overmeyer, L., & Haferkamp, H. (2012). Review on Laser Deposition Welding: From Micro to Macro. *Physics Procedia*. https://doi.org/10.1016/j.phpro.2012.10.046

Kendall, O., Abrahams, R., Paradowska, A., Reid, M., Qiu, C., Mutton, P., Schläfer, T., & Yan, W. (2023). Influence of multi-layer laser cladding depositions and rail curvature on residual stress in light rail components. *Engineering Failure Analysis*, *150*. https://doi.org/10.1016/j.engfailanal.2023.107330

Kendall, O., Fasihi, P., Abrahams, R., Paradowska, A., Reid, M., Lai, Q., Qiu, C., Mutton, P., Soodi, M., & Yan, W. (2022). Application of a New Alloy and Post Processing Procedures for Laser Cladding Repairs on Hypereutectoid Rail Components. *Materials*, *15*(15). https://doi.org/10.3390/ma15155447

Kendall, O., Paradowska, A., Abrahams, R., Reid, M., Qiu, C., Mutton, P., & Yan, W. (2023). Residual Stress Measurement Techniques for Metal Joints, Metallic Coatings and Components in the Railway Industry: A Review. In *Materials* (Vol. 16, Issue 1). MDPI. https://doi.org/10.3390/ma16010232

Lai, Q., Abrahams, R., Yan, W., Qiu, C., Mutton, P., Paradowska, A., Soodi, M., & Wu, X. (2019). Influences of depositing materials, processing parameters and heating conditions on material characteristics of laser-cladded hypereutectoid rails. *Journal of Materials Processing Technology*, *263*, 1–20. https://doi.org/10.1016/j.jmatprotec.2018.07.035

Langford, G., & Sc, D. (2023). *Microstructures*. 1–5.

Lewis, R., Christoforou, P., Wang, W. J., Beagles, A., Burstow, M., & Lewis, S. R. (2019). Investigation of the influence of rail hardness on the wear of rail and wheel materials under dry conditions (ICRI wear mapping project). *Wear*, *430–431*(January), 383–392. https://doi.org/10.1016/j.wear.2019.05.030

Lewis, R., & Dwyer-Joyce, R. S. (2004). Wear mechanisms and transitions in railway wheel steels. In *Part J: J. Engineering Tribology* (Vol. 218).

Lewis, R., & Olofsson, U. (2009). Basic tribology of the wheel-rail contact. In *Wheel-Rail Interface Handbook*. https://doi.org/10.1533/9781845696788.1.34

Lewis, S. R., Fretwell-Smith, S., Goodwin, P. S., Smith, L., Lewis, R., Aslam, M., Fletcher, D. I., Murray, K., & Lambert, R. (2016a). Improving rail wear and RCF performance using laser cladding. *Wear*, *366–367*, 268–278. https://doi.org/10.1016/j.wear.2016.05.011

Lewis, S. R., Fretwell-Smith, S., Goodwin, P. S., Smith, L., Lewis, R., Aslam, M., Fletcher, D. I., Murray, K., & Lambert, R. (2016b). Improving rail wear and RCF performance using laser cladding. *Wear*, *366–367*, 268–278. https://doi.org/10.1016/j.wear.2016.05.011

Lewis, S. R., Lewis, R., Evans, G., & Buckley-Johnstone, L. E. (2014). Assessment of railway curve lubricant performance using a twin-disc tester. *Wear*, *314*(1–2), 205–212. https://doi.org/10.1016/j.wear.2013.11.033

Lewis, S. R., Lewis, R., & Fletcher, D. I. (2015a). Assessment of laser cladding as an option for repairing/enhancing rails. *Wear*, *330–331*, 581–591. https://doi.org/10.1016/j.wear.2015.02.027

Lewis, S. R., Lewis, R., & Fletcher, D. I. (2015b). Assessment of laser cladding as an option for repairing/enhancing rails. *Wear*, *330–331*, 581–591. https://doi.org/10.1016/j.wear.2015.02.027

Lewis, S. R., Lewis, R., Goodwin, P. S., Fretwell-Smith, S., Fletcher, D. I., Murray, K., & Jaiswal, J. (2017a). Full-scale testing of laser clad railway track; Case study – Testing for wear, bend fatigue and insulated block joint lipping integrity. *Wear*, *376–377*, 1930–1937. https://doi.org/10.1016/j.wear.2017.02.023

Lewis, S. R., Lewis, R., Goodwin, P. S., Fretwell-Smith, S., Fletcher, D. I., Murray, K., & Jaiswal, J. (2017b). Full-scale testing of laser clad railway track; Case study – Testing for wear, bend fatigue and insulated block joint lipping integrity. *Wear*, *376–377*(February), 1930–1937. https://doi.org/10.1016/j.wear.2017.02.023

Lewis, S. R., Lewis, R., Goodwin, P. S., Fretwell-Smith, S., Fletcher, D. I., Murray, K., & Jaiswal, J. (2017c). Full-scale testing of laser clad railway track; Case study – Testing for wear, bend fatigue and insulated block joint lipping integrity. *Wear*, *376–377*(February), 1930–1937. https://doi.org/10.1016/j.wear.2017.02.023

Lu, P., Lewis, S. R., Fretwell-Smith, S., Fletcher, D. I., & Lewis, R. (2018). Laser cladding of rail; The effects of depositing material on lower rail grades. *Proceedings of the 11th International Conference on Contact Mechanics and Wear of Rail/Wheel Systems, CM 2018*, 610–617. https://doi.org/10.1016/j.wear.2019.203045

Magel, E., Mutton, P., Ekberg, A., & Kapoor, A. (2016). Rolling contact fatigue, wear and broken rail derailments. *Wear*, *366–367*, 249–257. https://doi.org/10.1016/j.wear.2016.06.009

Mandal, N. K. N., & Peach, B. (2010). An Engineering Analysis of Insulated Rail Joints: A General Perspective. *International Journal of Engineering Science and Technology*, *2*(8), 3964–3988.

Mansouri, H., & Monshi, A. (2004). Microstructure and residual stress variations in weld zone of flash-butt welded railroads. *Science and Technology of Welding and Joining*, *9*(3). https://doi.org/10.1179/136217104225012201

Markov, D. (1995). Laboratory tests for wear of rail and wheel steels. *Wear*. https://doi.org/10.1016/0043-1648(95)90184-1

Martensitic Stainless Steels. (n.d.). [Online]. Available at: https://bssa.org.uk/wp-content/uploads/2021/02/Martensitics_JB_2.pdf

Microset (n.d.) “General purpose system for small to medium replication and moulding applications.” [Online]. Available at: https://www.microset.co.uk/products/50ml-system/index.html.

Narayanan, A., Mostafavi, M., Pirling, T., Kabra, S., Lewis, R., Pavier, M. J., & Peel, M. J. (2019). Residual stress in laser cladded rail. *Tribology International*, *140*(May), 105844. https://doi.org/10.1016/j.triboint.2019.105844

Nellian, A. S., Tan, K. E., Hoh, H. J., Pang, J. H. L., Christian, I., & Chua, S. Y. (2019, February 13). Microstructure and Wear Performance Assessment of Laser Cladded Rail Steel for Service Life Extension at Sharp-Radius Curves. *2018 International Conference on Intelligent Rail Transportation, ICIRT 2018*. https://doi.org/10.1109/ICIRT.2018.8641613

Nextsense. (n.d.). “Calipri, Highly Precise Profile Measurement for Predictive Maintenance.” [Online]. Available at: https://www.nextsense-worldwide.com/en/industries/railway.html.

Niederhauser, S., & Karlsson, B. (2005). Fatigue behaviour of Co-Cr laser cladded steel plates for railway applications. *Wear*, *258*(7–8), 1156–1164. https://doi.org/10.1016/j.wear.2004.03.026

Nikon. (n.d.). “Eclipse LV150 and LV150A.” [Online]. Available at: https://www.bu.edu/photonics/files/2016/11/Nikon-LV150-Brochure.pdf.

Nishikawa, L. P., & Goldenstein, H. (2019). Divorced Eutectoid on Heat-Affected Zone of Welded Pearlitic Rails. *JOM*, *71*(2), 815–823. https://doi.org/10.1007/s11837-018-3213-5

Olofsson, U., Zhu, Y., Abbasi, S., Lewis, R., & Lewis, S. (2013). Tribology of the wheel-rail contact-aspects of wear, particle emission and adhesion. *Vehicle System Dynamics*, *51*(7), 1091–1120. https://doi.org/10.1080/00423114.2013.800215

Pawlowski, L. (1999). Thick laser coatings: A review. *Journal of Thermal Spray Technology*. https://doi.org/10.1361/105996399770350502

Qian, L., Li, M., Zhou, Z., Yang, H., & Shi, X. (2005). Comparison of nano-indentation hardness to microhardness. *Surface and Coatings Technology*, *195*(2–3), 264–271. https://doi.org/10.1016/j.surfcoat.2004.07.108

Roy, T., Paradowska, A., Abrahams, R., Law, M., Mutton, P., Soodi, M., & Yan, W. (2020). Residual stress in laser cladded heavy-haul rails investigated by neutron diffraction.

Journal of Materials Processing Technology, *278*. https://doi.org/10.1016/j.jmatprotec.2019.116511

Santa, J. F., Cuervo, P., Christoforou, P., Harmon, M., Beagles, A., Toro, A., & Lewis, R. (2019). Twin disc assessment of wear regime transitions and rolling contact fatigue in R400HT – E8 pairs. *Wear*, *432–433*(January), 102916. https://doi.org/10.1016/j.wear.2019.05.031

Schmid, F., Burstow, M., & Clark, S. (2010). *Best Practice in Wheel-rail Interface Management for Mixed Traffic Railways*. University of Birmingham Press. https://books.google.co.uk/books?id=YM0hnwEACAAJ

SciAps. (n.d.). "Handheld LIBS Analyser -SciAps Z-200+." [Online]. Available at: https://www.qesnet.com/product/handheld-libs-analyser-sciaps-z-200/.

Seo, J. W., Kim, J. –C, Kwon, S. J., & Jun, H. K. (2019). Effects of Laser Cladding for Repairing and Improving Wear of Rails. *International Journal of Precision Engineering and Manufacturing*, *20*(7), 1207–1217. https://doi.org/10.1007/s12541-019-00115-y

SF HT. (2017). "SF heat-treated range". [Online]. Available at: https://uploads-ssl.webflow.com/5db81e2f6c50c20ceba8dc08/5f478fe902f03e69a35e1e32_British%20Steel%20Stress%20Free%20Range%20Data%20Sheet.pdf

SimpliMet 1000. (n.d.). "Buehler SimpliMet 1000&3000 Automatic Mounting Press." [Online]. Available at: http://www.sjstmat.com/uploadfile/2012/0118/20120118121742618.pdf.

Singh, R., Kumar, D., Mishra, S. K., & Tiwari, S. K. (2014). Laser cladding of Stellite 6 on stainless steel to enhance solid particle erosion and cavitation resistance. *Surface and Coatings Technology*. https://doi.org/10.1016/j.surfcoat.2014.04.008

Srisungsitthisunti, P., Kaewprachum, B., Yang, Z., & Gao, G. (2022). Real-Time Quality Monitoring of Laser Cladding Process on Rail Steel by an Infrared Camera. *Metals*, *12*(5). https://doi.org/10.3390/met12050825

Stellite™, J., & Kote™, D. (n.d.). "Stellite TM 6 Alloy". [Online]. Available at: https://www.deloro.com/fileadmin/users/redakteur/006_Downloads/Data_Sheets/Deloro_MDS_Stellite6_rev00.pdf

Suh, N. P. (1977). AN OVERVIEW OF THE DEL~INA~ON THEORY OF WEAR. In *Wear* (Vol. 44). Elsevier Sequoia S.A.

Thompson, D. (2009). Railway Noise and Vibration. In *Railway Noise and Vibration*. https://doi.org/10.1016/B978-0-08-045147-3.X0023-0

Tomlinson, K., Fletcher, D., & Lewis, R. (2021). Measuring material plastic response to cyclic loading in modern rail steels from a minimal number of twin-disc tests: *Https://Doi.Org/10.1177/0954409721993615*.

Toyserkani, E., Khajepour, A., & Corbin, S. (2017). Laser Cladding - A Versatile Proactive and Reactive Technology. *New York*. https://doi.org/10.2351/1.521888

Tyfour, W. R., Beynon, J. H., & Kapoor, A. (1995). The steady state wear behaviour of pearlitic rail steel under dry rolling-sliding contact conditions. *Wear*. https://doi.org/10.1016/0043-1648(94)06533-0

University of Southampton. (n.d.). *"μ-VIS: Multidisciplinary, Multiscale, Microtomographic Volume Imaging" [Online], Available at: https://www.southampton.ac.uk/muvis/about/equipment/hutch.page*.

Vilar, R. (2001). Laser cladding. *International Journal of Powder Metallurgy (Princeton, New Jersey)*, *37*(2). https://doi.org/10.2351/1.521888

Vishnu, P. R. (2018). Solid-State Transformations in Weldments. In *Welding, Brazing, and Soldering*. https://doi.org/10.31399/asm.hb.v06.a0001341

Wang, W. J., Hu, J., Guo, J., Liu, Q. Y., & Zhu, M. H. (2014). Effect of laser cladding on wear and damage behaviors of heavy-haul wheel/rail materials. *Wear*, *311*(1–2), 130–136. https://doi.org/10.1016/j.wear.2014.01.011

Wang, X., Lei, L., & Yu, H. (2021). A review on microstructural features and mechanical properties of wheels/rails cladded by laser cladding. *Micromachines*, *12*(2), 1–16. https://doi.org/10.3390/mi12020152

Weng, F., Chen, C., & Yu, H. (2014). Research status of laser cladding on titanium and its alloys: A review. In *Materials and Design*. https://doi.org/10.1016/j.matdes.2014.01.077

Wesselmecking, S., Haupt, M., Ma, Y., Song, W., Hirt, G., & Bleck, W. (2021). Mechanism-controlled thermomechanical treatment of high manganese steels. *Materials Science and Engineering A*, *828*, 142056. https://doi.org/10.1016/j.msea.2021.142056

Williams, J. (2005). Engineering tribology. In *Engineering Tribology*. https://doi.org/10.1017/CBO9780511805905

Xiaoyan Zeng, Zengyi Tao, Beidi Zhu, Erhua Zhou, & Kun Cui. (1996). Investigation of laser cladding ceramic-metal composite coatings: processing modes and mechanisms. *Surface and Coatings Technology*. https://doi.org/10.1016/0257-8972(95)02431-x

Xie, T., Zhou, L., Ding, H., Zhu, Y., Yang, W., Xiao, Q., Wang, W., Guo, J., & Liu, Q. (2021). Investigation on the rolling contact fatigue behaviors of different laser cladding materials on the damaged rail. *Journal of Tribology*, *143*(5), 1–13. https://doi.org/10.1115/1.4050690

Xin, L., Markine, V., & Shevtsov, I. (2018). Analysis of the effect of repair welding/grinding on the performance of railway crossings using field measurements and finite element modeling. *Proceedings of the Institution of Mechanical Engineers, Part F: Journal of Rail and Rapid Transit*, *232*(3), 798–815. https://doi.org/10.1177/0954409717693960

Ya, W. (2015). *Laser Materials Interactions During a Nalyses on Clad Formation , Thermal Cycles , Residual*.

Zanzarin, S. (2015). Laser Cladding with metallic powders. *University of Trento*, *November*, 133.

Zhang, B., He, B., & Wang, H. (2022). Microstructural investigation and mechanical performance of laser cladding repaired bainite steel with AerMet100 steel. *Surface and Coatings Technology*, *440*(April), 128498. https://doi.org/10.1016/j.surfcoat.2022.128498

Zhu, D., Wang, J., & Wang, Q. J. (2015). On the Stribeck Curves for Lubricated Counterformal Contacts of Rough Surfaces. *Journal of Tribology*, *137*(2). https://doi.org/10.1115/1.4028881

Zhu, Y., Wang, W., Lewis, R., Yan, W., Lewis, S. R., & Ding, H. (2019). A review on wear between railway wheels and rails under environmental conditions. In *Journal of Tribology*

(Vol. 141, Issue 12). American Society of Mechanical Engineers (ASME). https://doi.org/10.1115/1.4044464

Zhu, Y., Yang, Y., Mu, X., Wang, W., Yao, Z., & Yang, H. (2019). Study on wear and RCF performance of repaired damage railway wheels: Assessing laser cladding to repair local defects on wheels. *Wear*. https://doi.org/10.1016/j.wear.2019.04.028

12 Appendices

12.1 Appendix for Chapter 5

12.1.1 Appendix 5.A - Clad Part Images

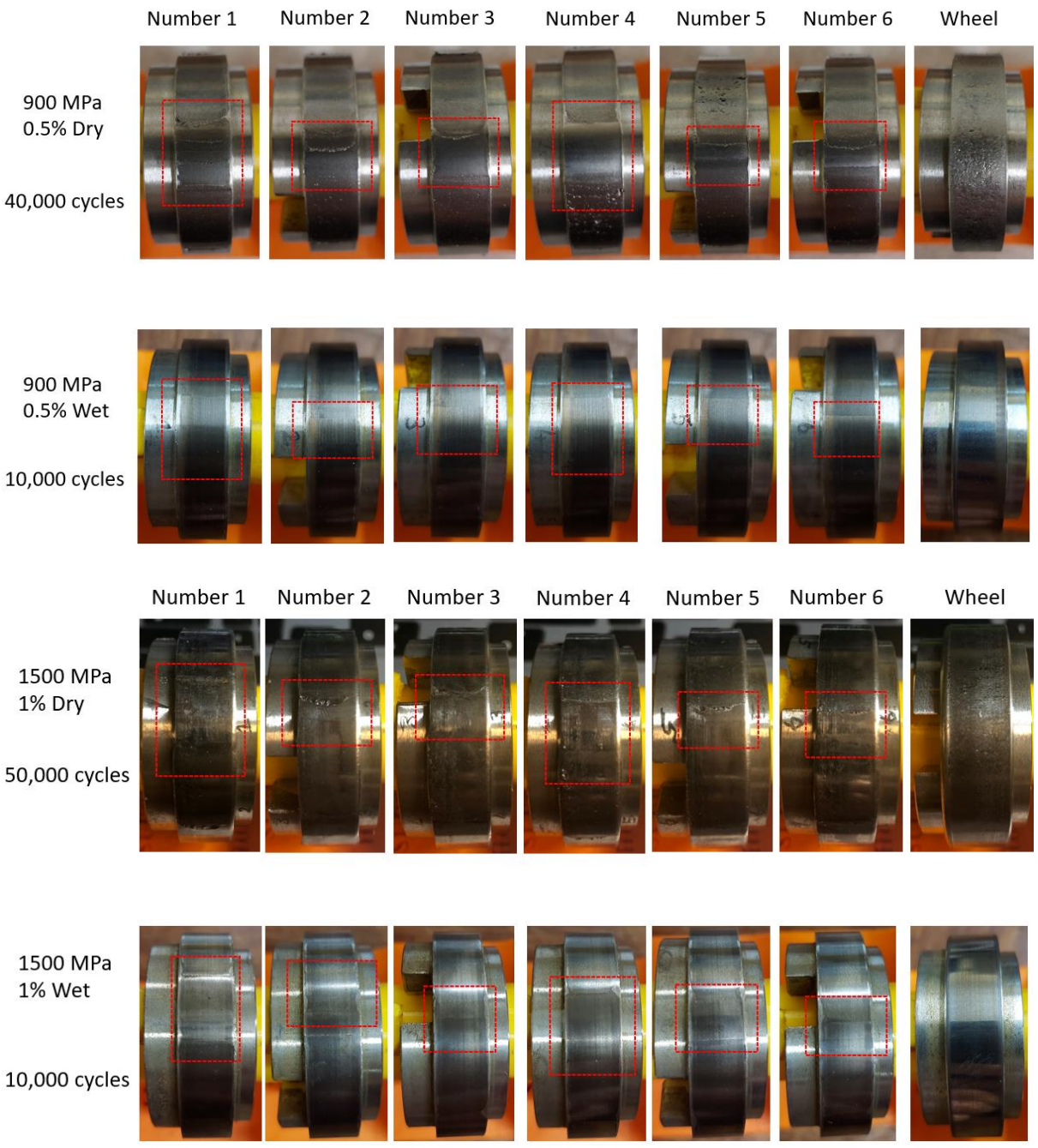

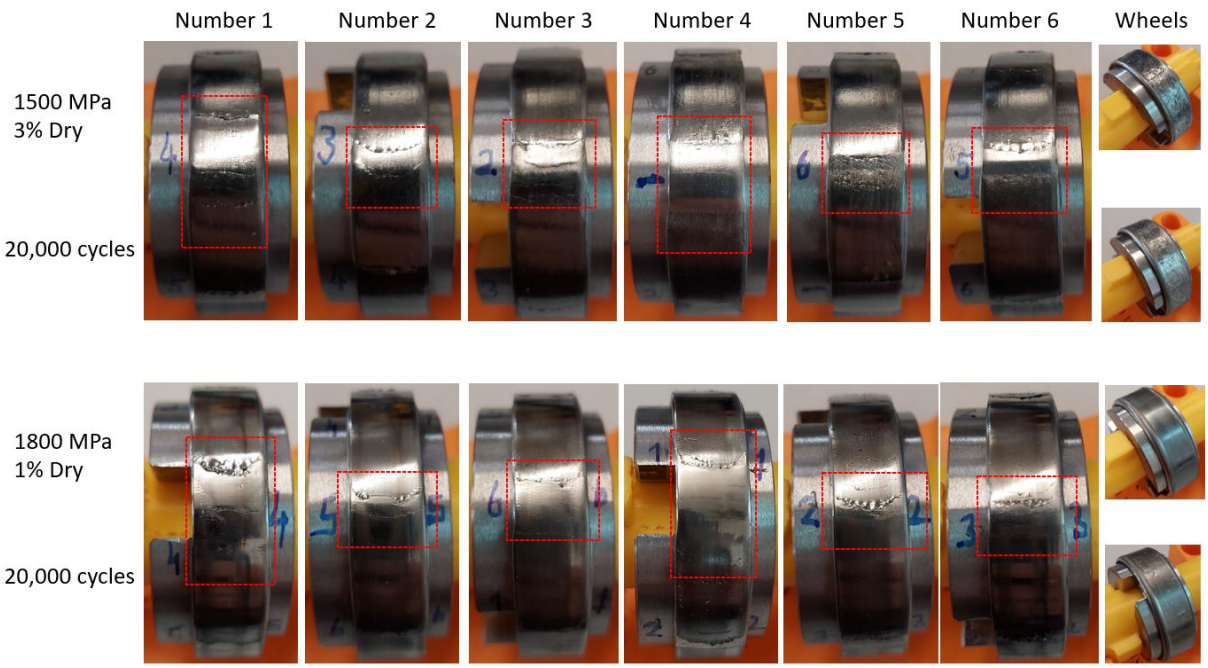

Figure 12.1: Small scale repair tests clad part images after tests

Surface Images from Alicona

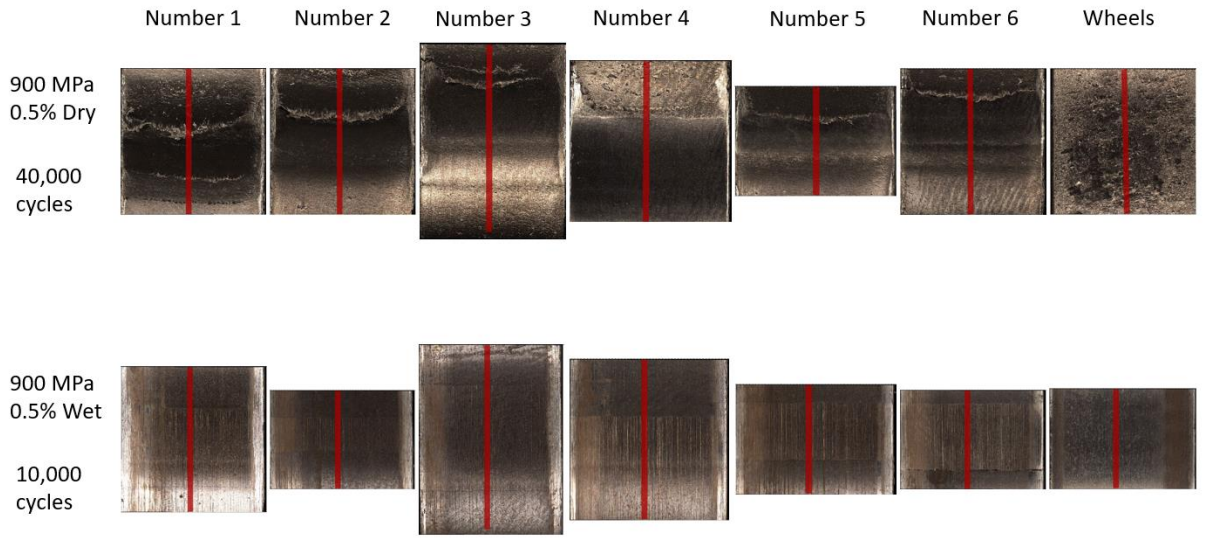

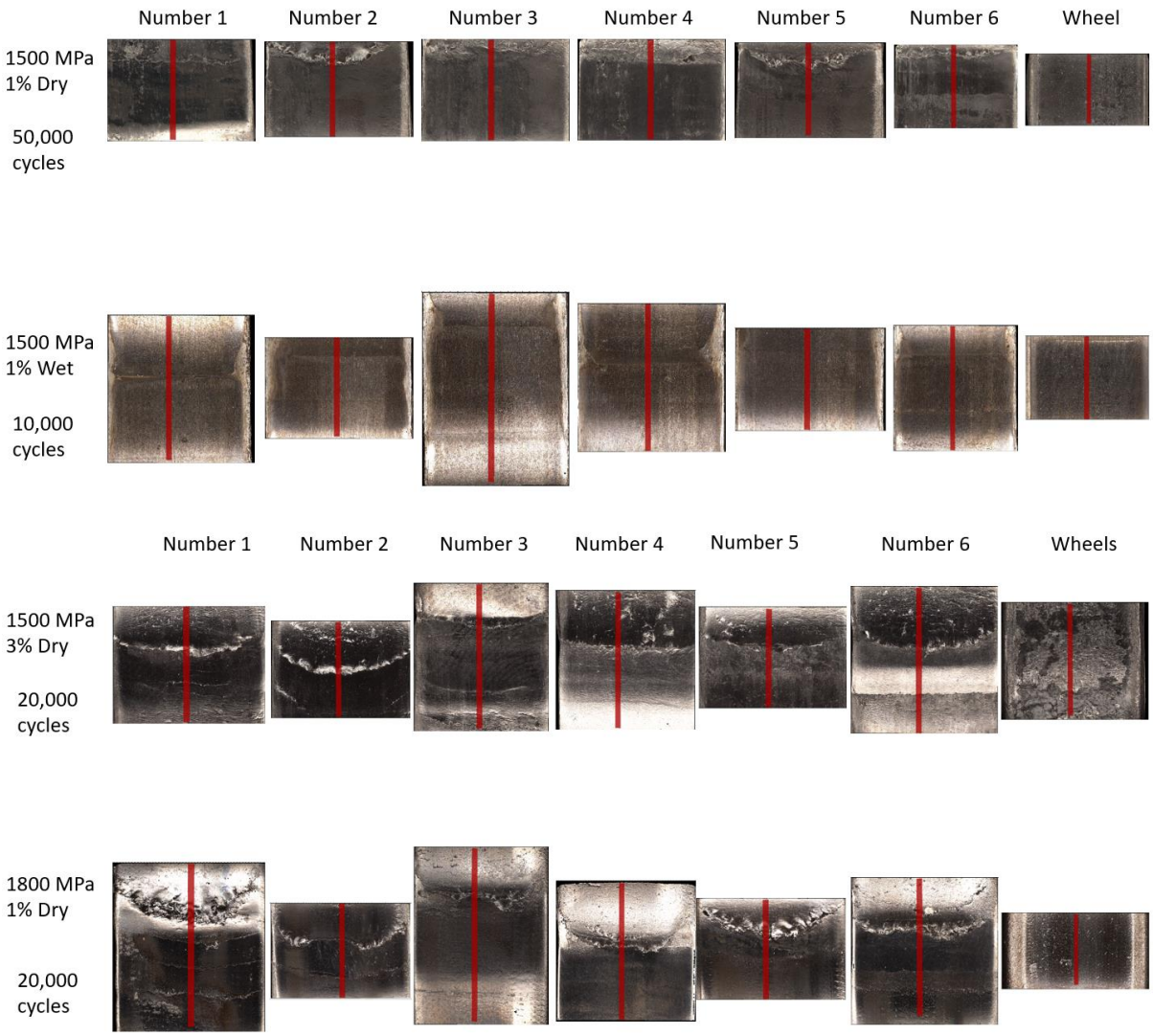

Figure 12.2: Small scale repair tests surface images from Alicona after tests

12.1.2 Appendix 5.B - Roughness Profiles

900 MPa 0.5% Slip Dry Tests

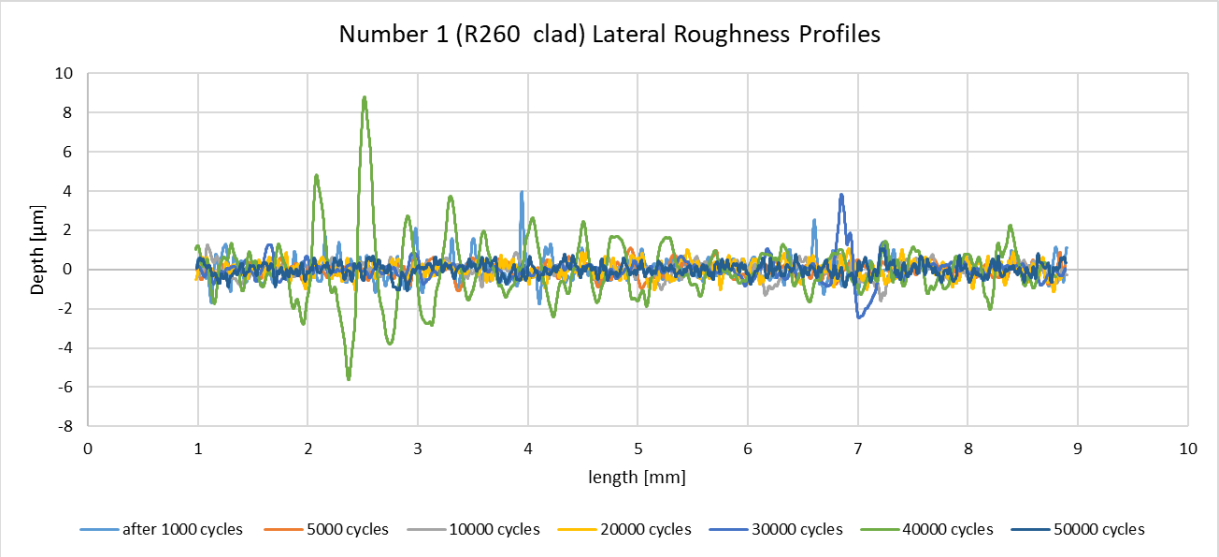

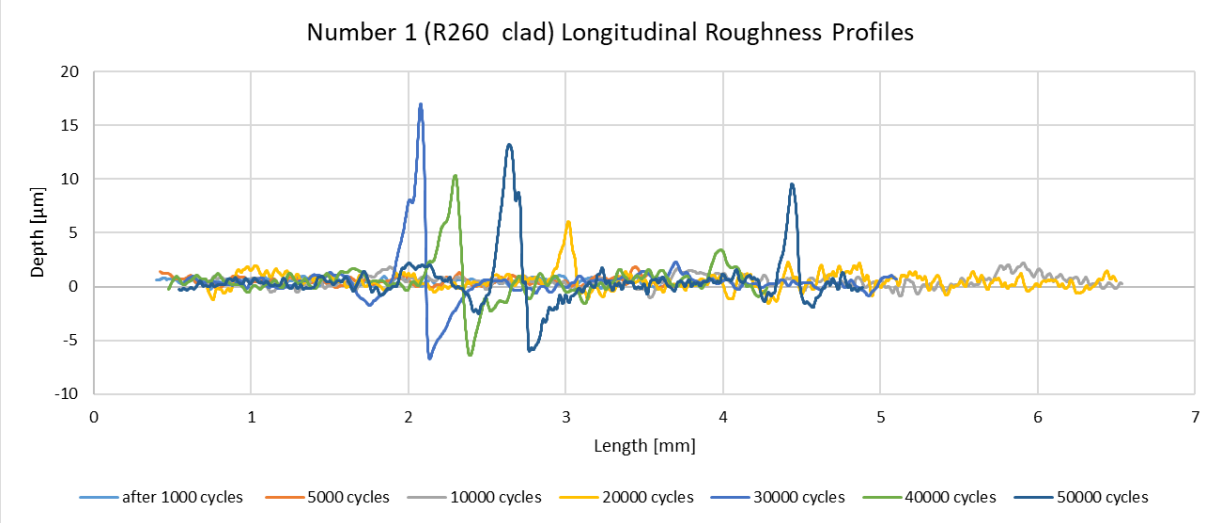

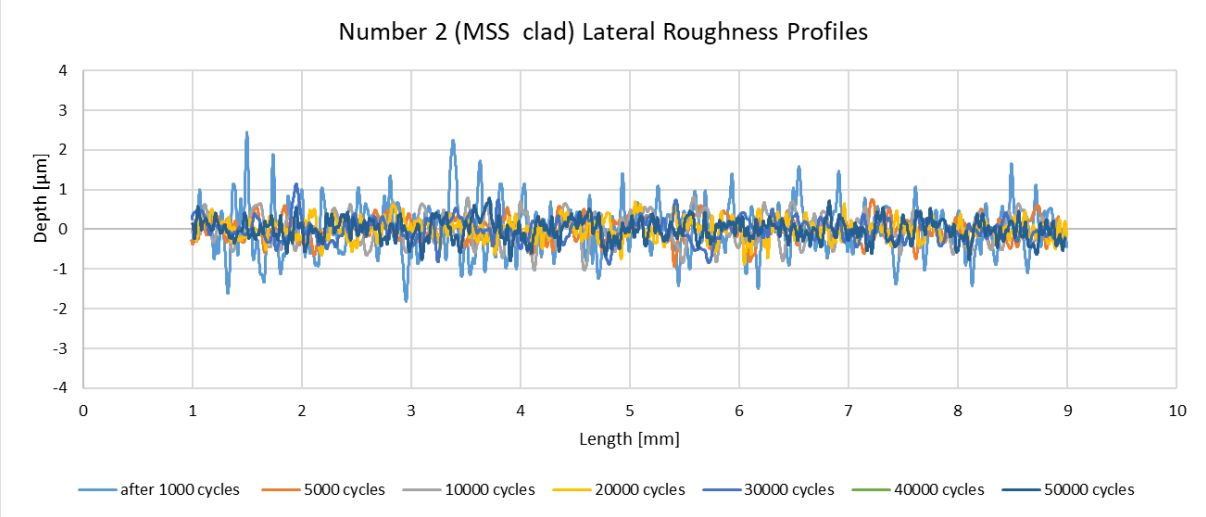

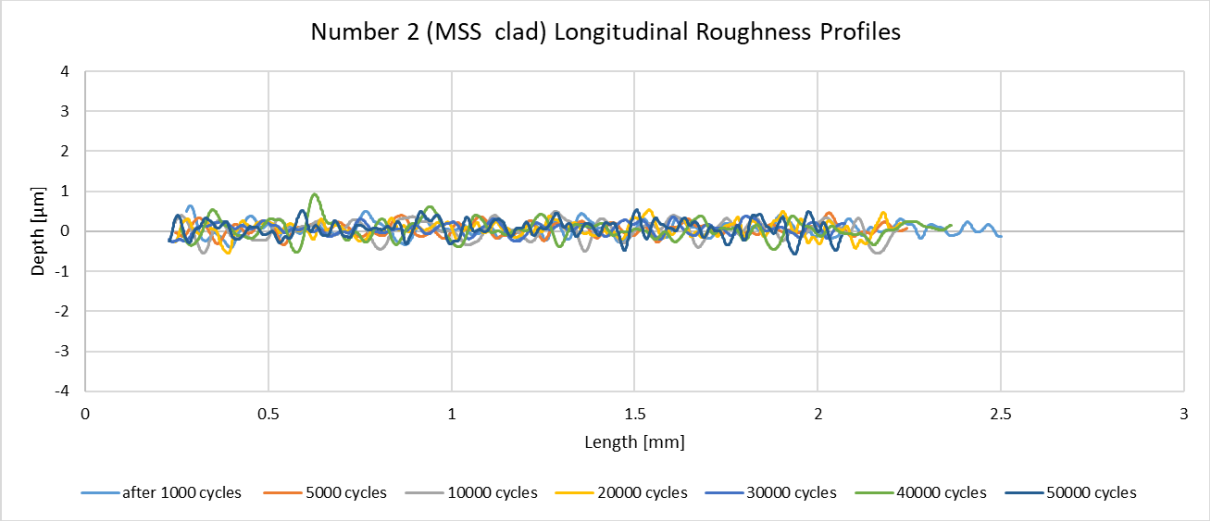
Number 2 (MSS clad) Longitudinal Roughness Profiles
Depth [µm]
Length [mm]
after 1000 cycles
5000 cycles
10000 cycles
20000 cycles
30000 cycles
40000 cycles
50000 cycles

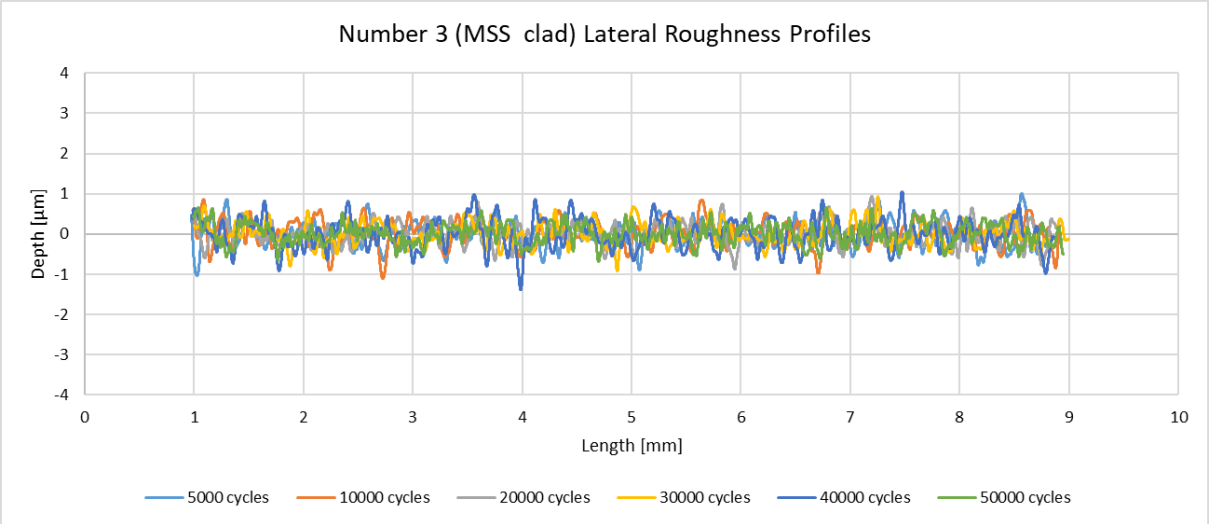
Number 3 (MSS clad) Lateral Roughness Profiles
Depth [µm]
Length [mm]
5000 cycles
10000 cycles
20000 cycles
30000 cycles
40000 cycles
50000 cycles

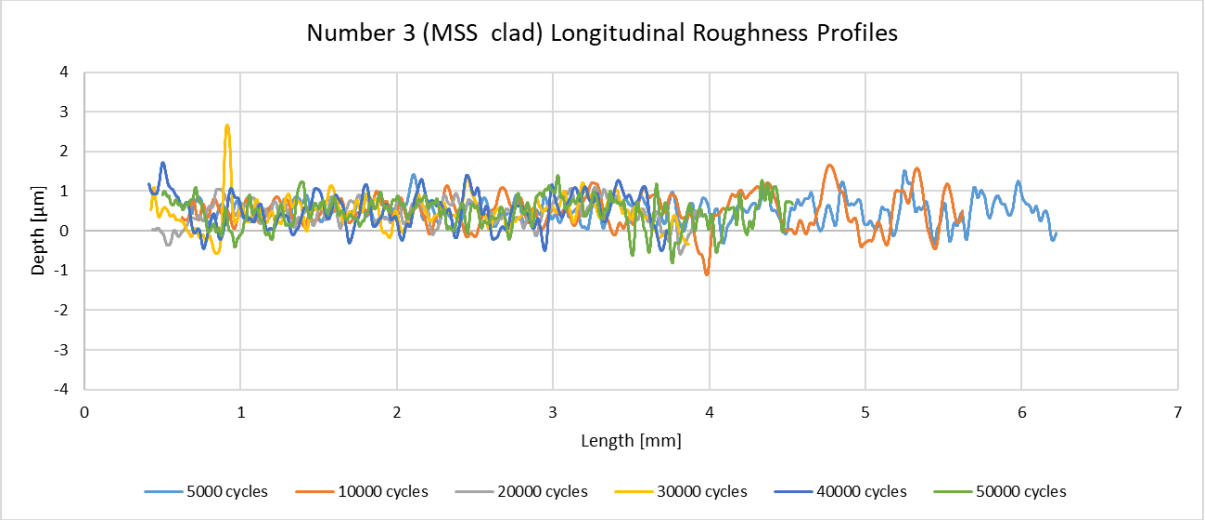
Number 3 (MSS clad) Longitudinal Roughness Profiles
Depth [µm]
Length [mm]
5000 cycles
10000 cycles
20000 cycles
30000 cycles
40000 cycles
50000 cycles

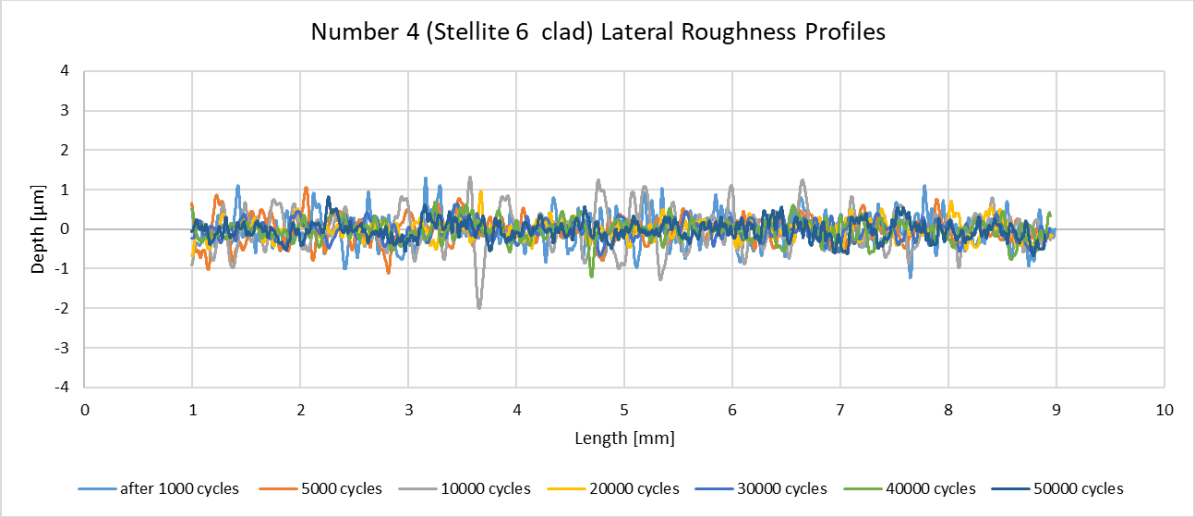
Number 4 (Stellite 6 clad) Lateral Roughness Profiles
Depth [µm]
Length [mm]
after 1000 cycles
5000 cycles
10000 cycles
20000 cycles
30000 cycles
40000 cycles
50000 cycles

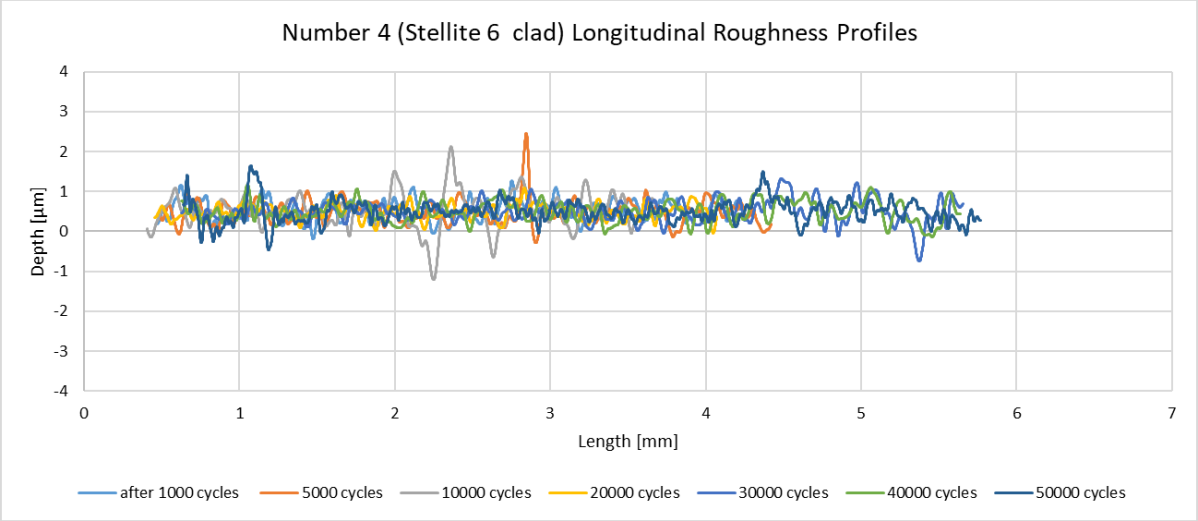
Number 4 (Stellite 6 clad) Longitudinal Roughness Profiles
Depth [µm]
Length [mm]
after 1000 cycles
5000 cycles
10000 cycles
20000 cycles
30000 cycles
40000 cycles
50000 cycles

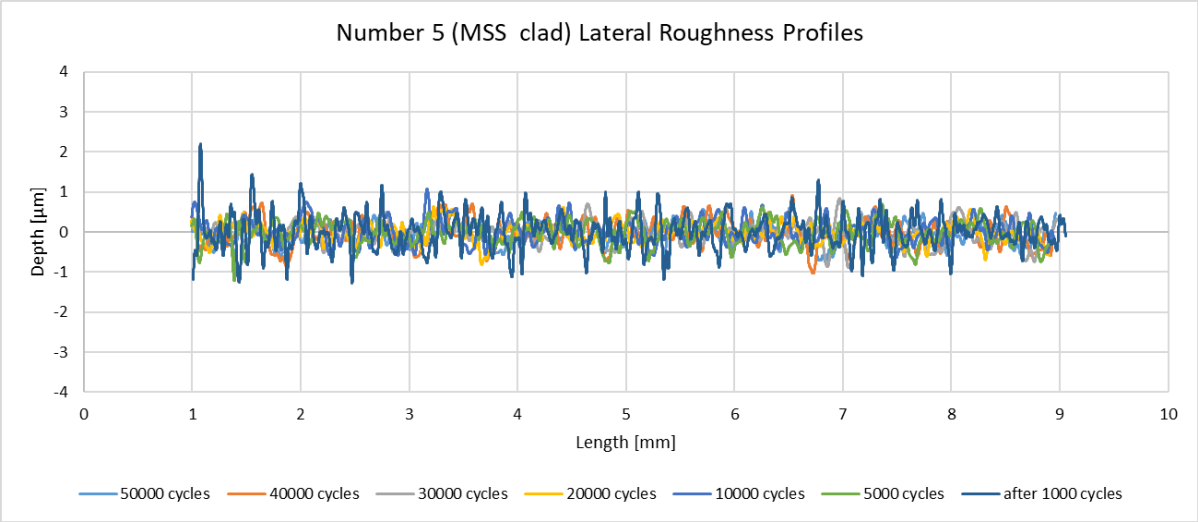
Number 5 (MSS clad) Lateral Roughness Profiles
Depth [µm]
Length [mm]
50000 cycles
40000 cycles
30000 cycles
20000 cycles
10000 cycles
5000 cycles
after 1000 cycles

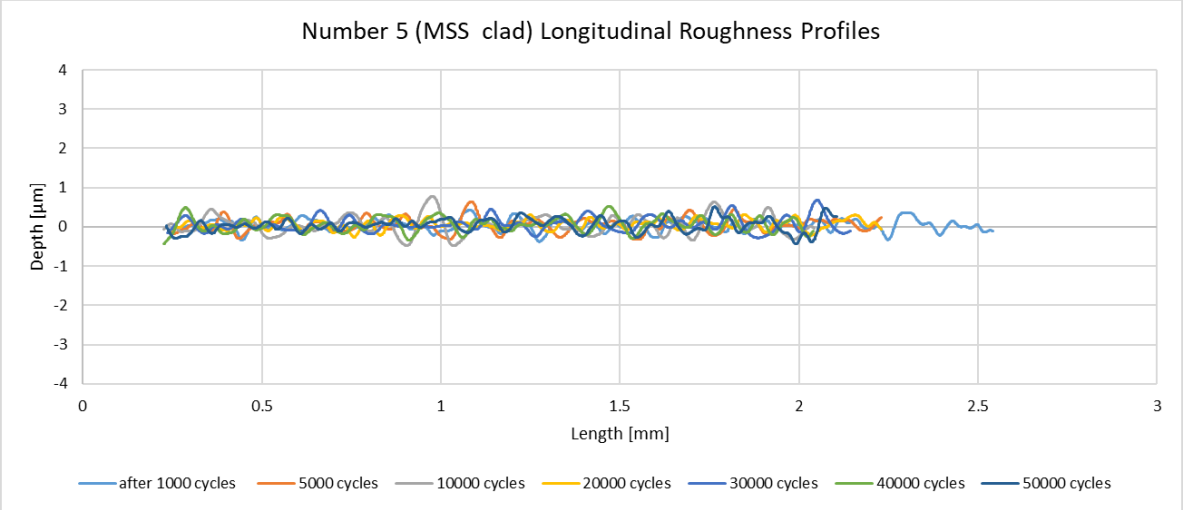
Number 5 (MSS clad) Longitudinal Roughness Profiles
Depth [µm]
Length [mm]
after 1000 cycles
5000 cycles
10000 cycles
20000 cycles
30000 cycles
40000 cycles
50000 cycles

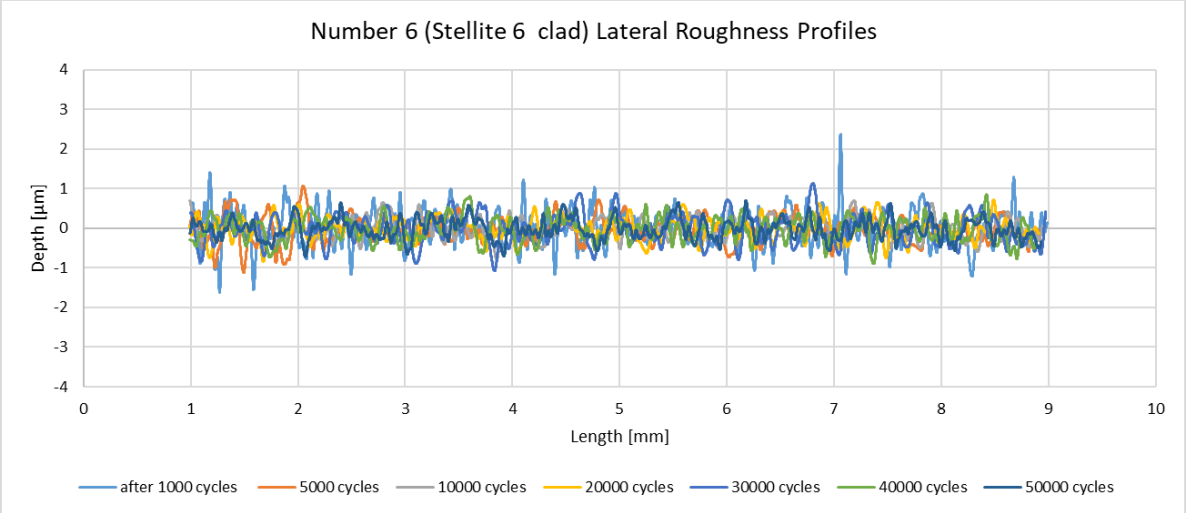
Number 6 (Stellite 6 clad) Lateral Roughness Profiles
Depth [µm]
Length [mm]
after 1000 cycles
5000 cycles
10000 cycles
20000 cycles
30000 cycles
40000 cycles
50000 cycles

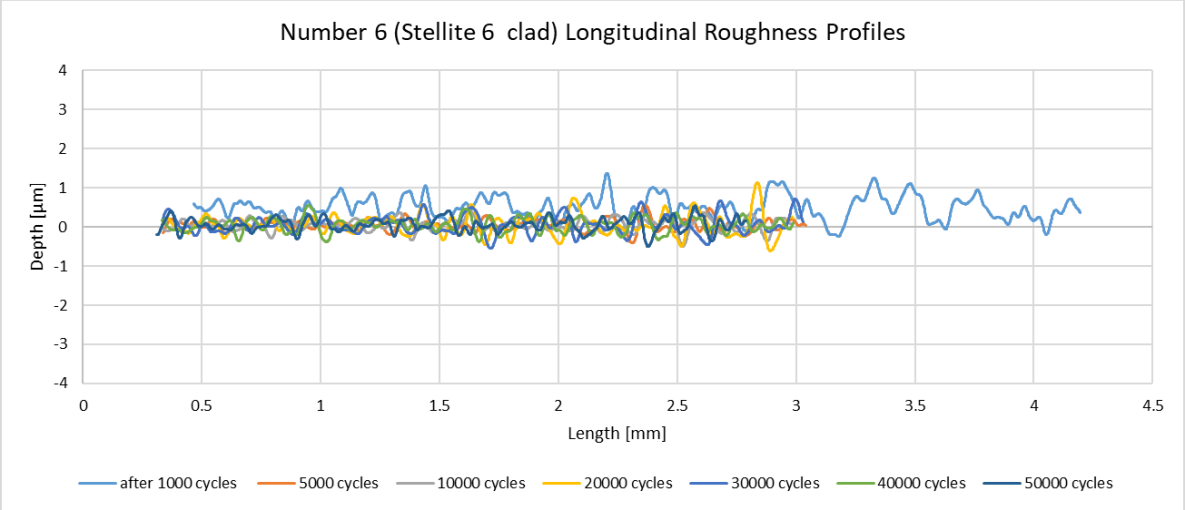
Number 6 (Stellite 6 clad) Longitudinal Roughness Profiles
Depth [µm]
Length [mm]
after 1000 cycles
5000 cycles
10000 cycles
20000 cycles
30000 cycles
40000 cycles
50000 cycles

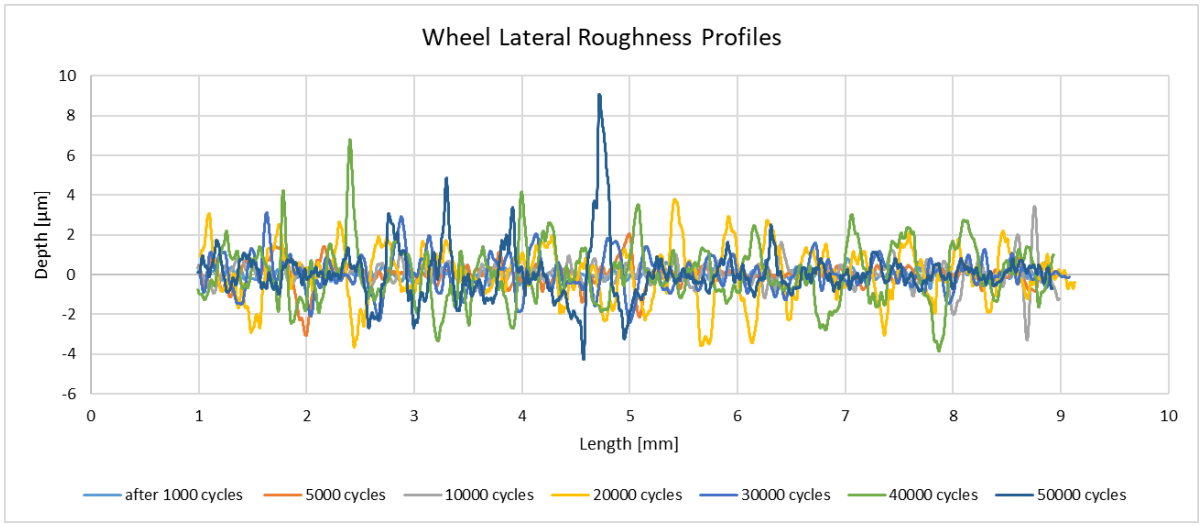

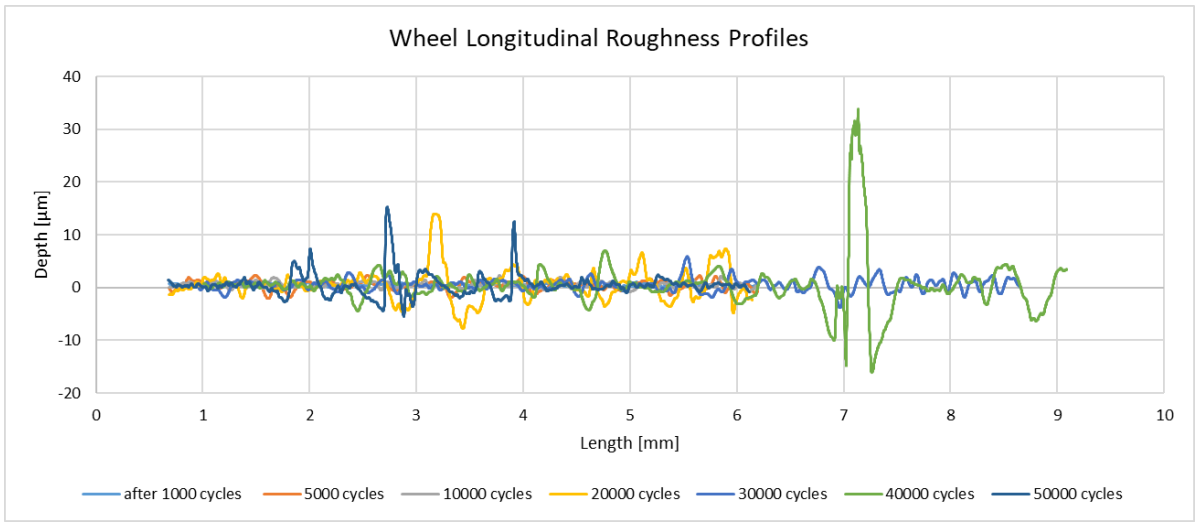

Figure 12.3: Small scale repair tests surface evolution roughness graphs from Alicona with 900 MPa, 0.5% slip, dry test condition

900 MPa 0.5% Slip Water Lubricated Tests

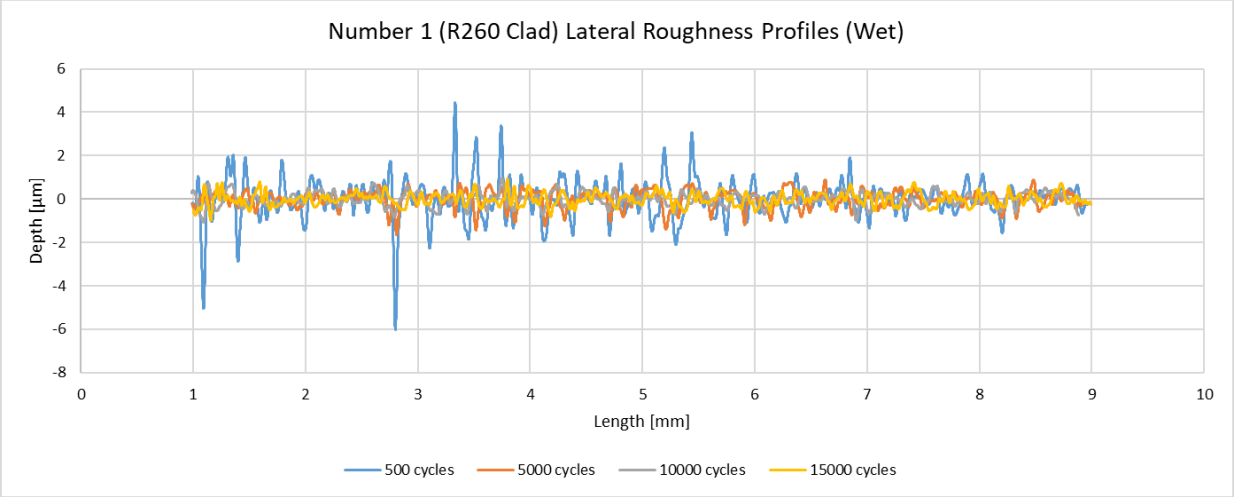

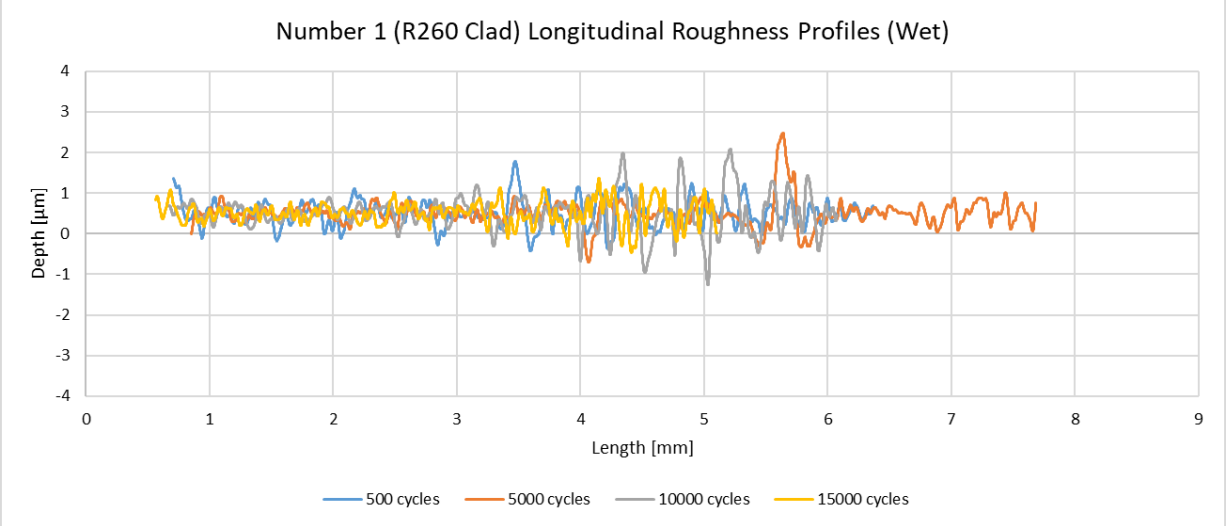

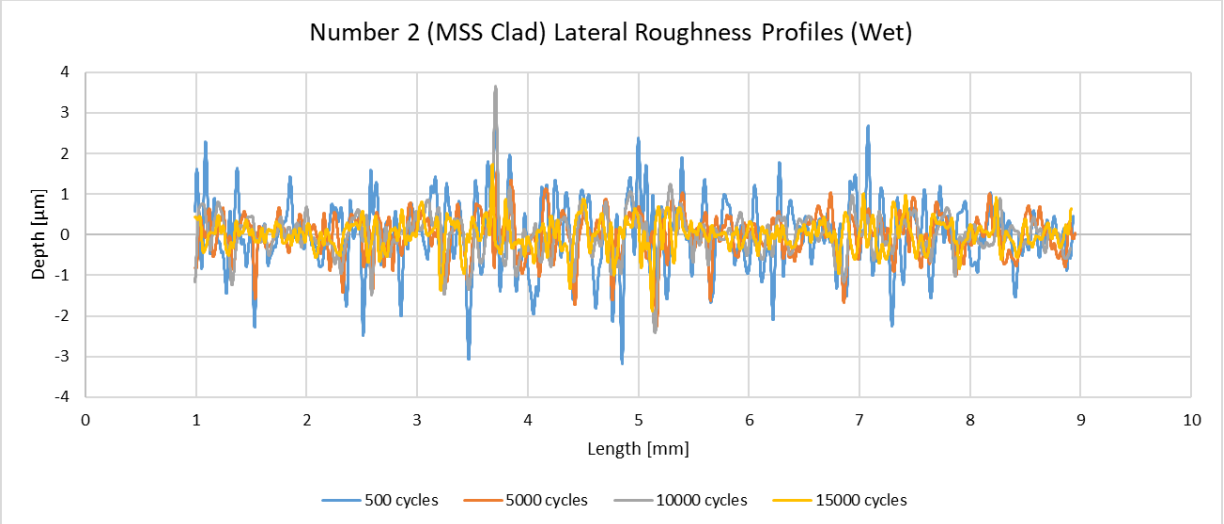

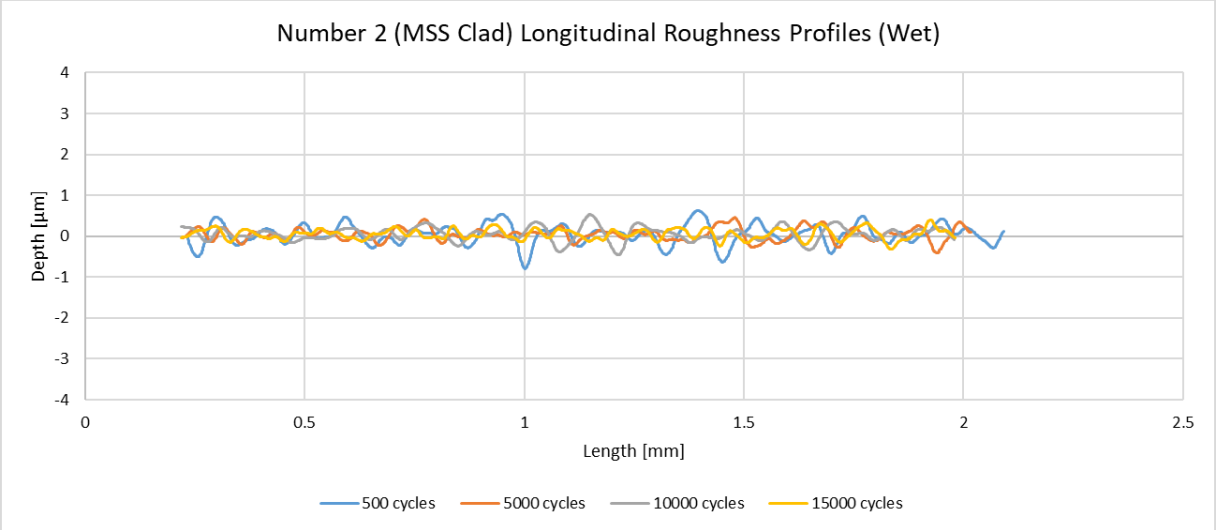
Number 2 (MSS Clad) Longitudinal Roughness Profiles (Wet)
Depth [µm]
Length [mm]
500 cycles
5000 cycles
10000 cycles
15000 cycles

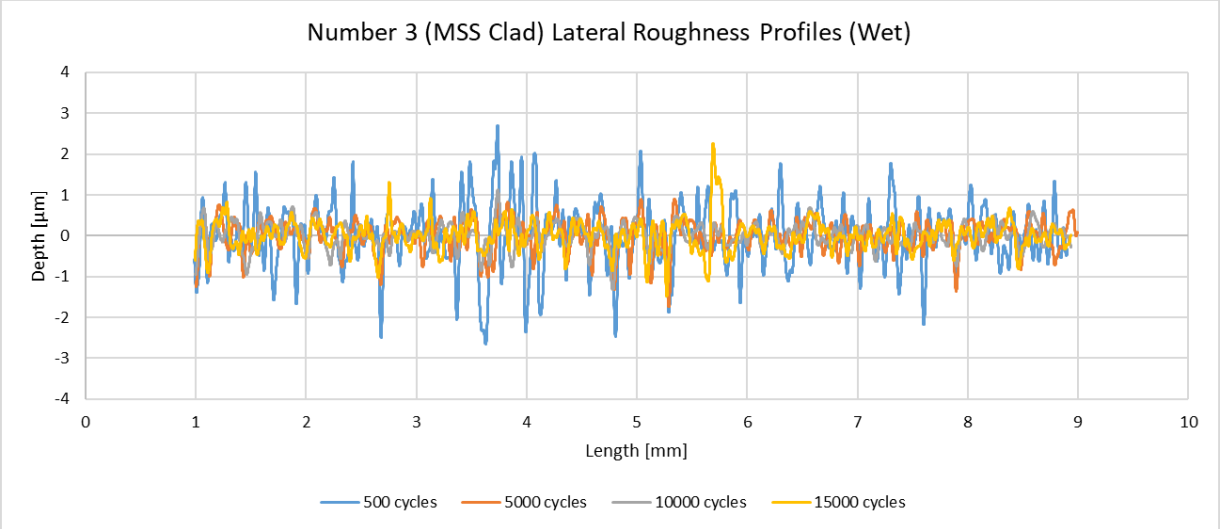
Number 3 (MSS Clad) Lateral Roughness Profiles (Wet)
Depth [µm]
Length [mm]
500 cycles
5000 cycles
10000 cycles
15000 cycles

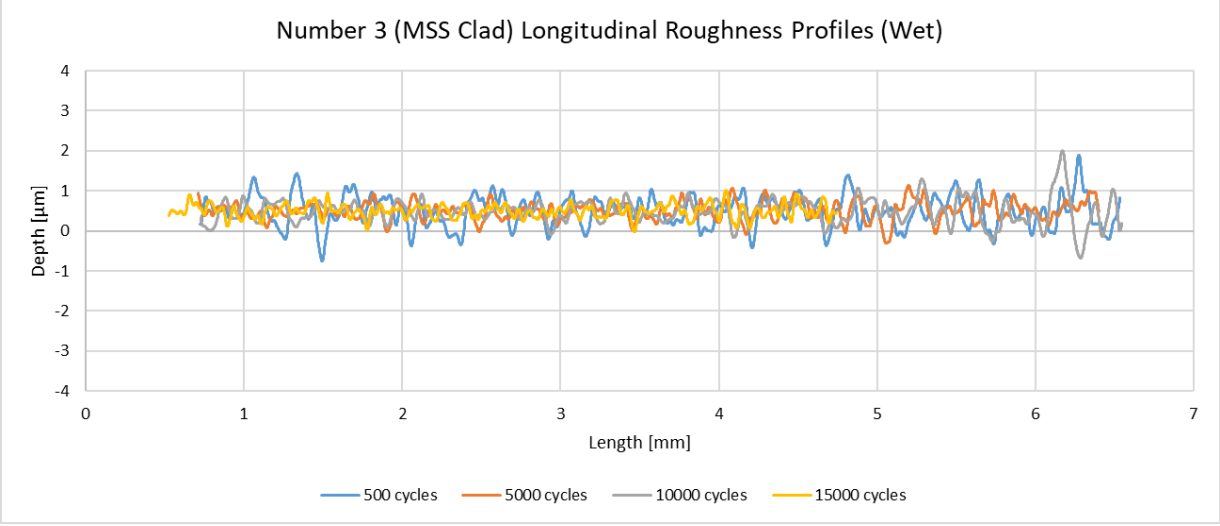
Number 3 (MSS Clad) Longitudinal Roughness Profiles (Wet)
Depth [µm]
Length [mm]
500 cycles
5000 cycles
10000 cycles
15000 cycles

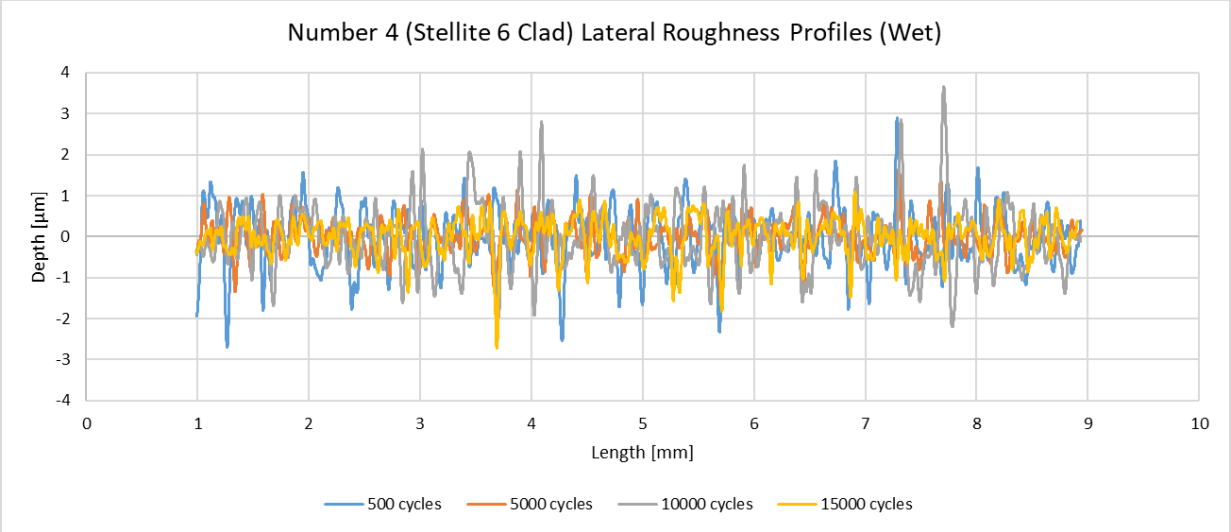
Number 4 (Stellite 6 Clad) Lateral Roughness Profiles (Wet)
Depth [µm]
Length [mm]
500 cycles
5000 cycles
10000 cycles
15000 cycles

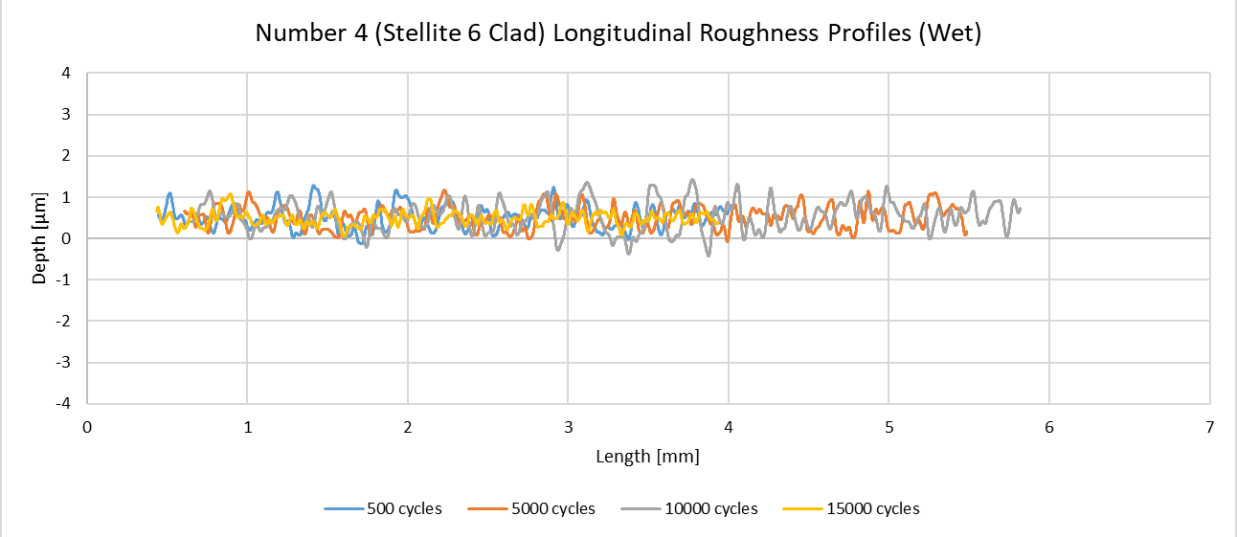
Number 4 (Stellite 6 Clad) Longitudinal Roughness Profiles (Wet)
Depth [µm]
Length [mm]
500 cycles
5000 cycles
10000 cycles
15000 cycles

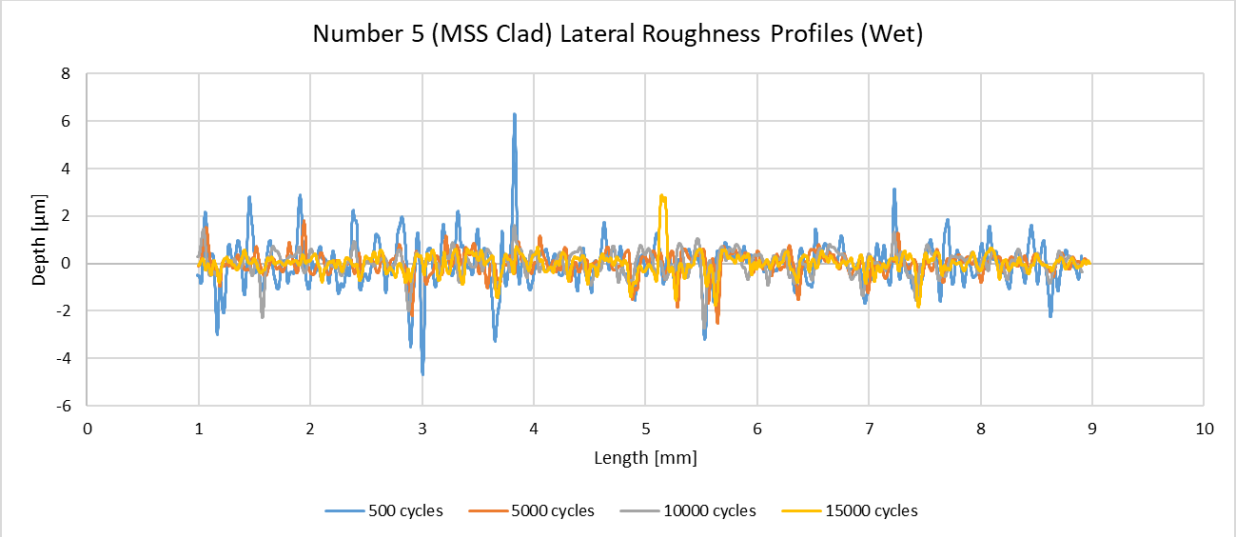
Number 5 (MSS Clad) Lateral Roughness Profiles (Wet)
Depth [µm]
Length [mm]
500 cycles
5000 cycles
10000 cycles
15000 cycles

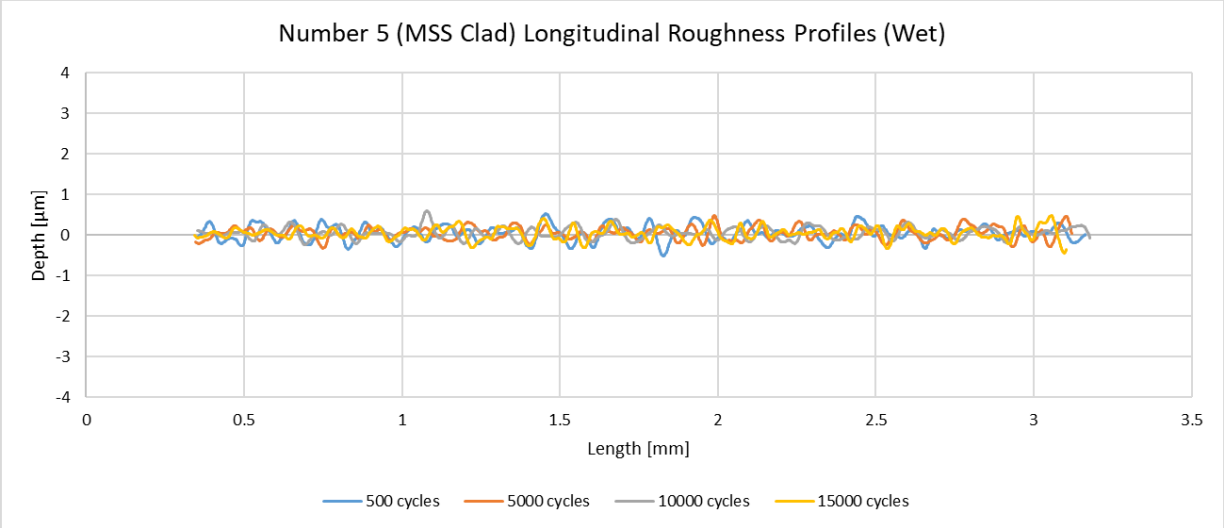
Number 5 (MSS Clad) Longitudinal Roughness Profiles (Wet)
Depth [µm]
Length [mm]
500 cycles
5000 cycles
10000 cycles
15000 cycles

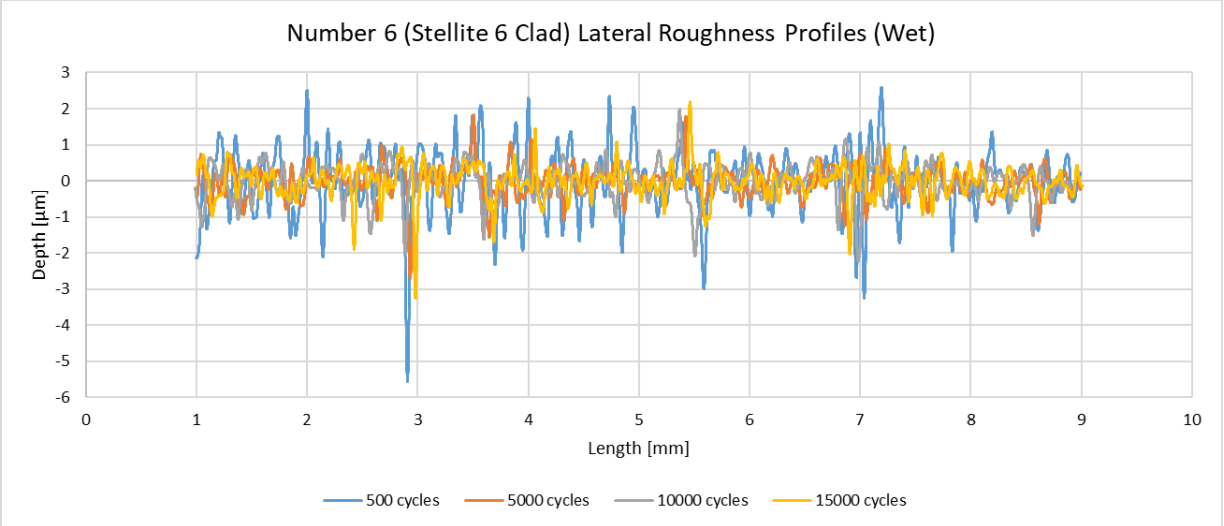
Number 6 (Stellite 6 Clad) Lateral Roughness Profiles (Wet)
Depth [µm]
Length [mm]
500 cycles
5000 cycles
10000 cycles
15000 cycles

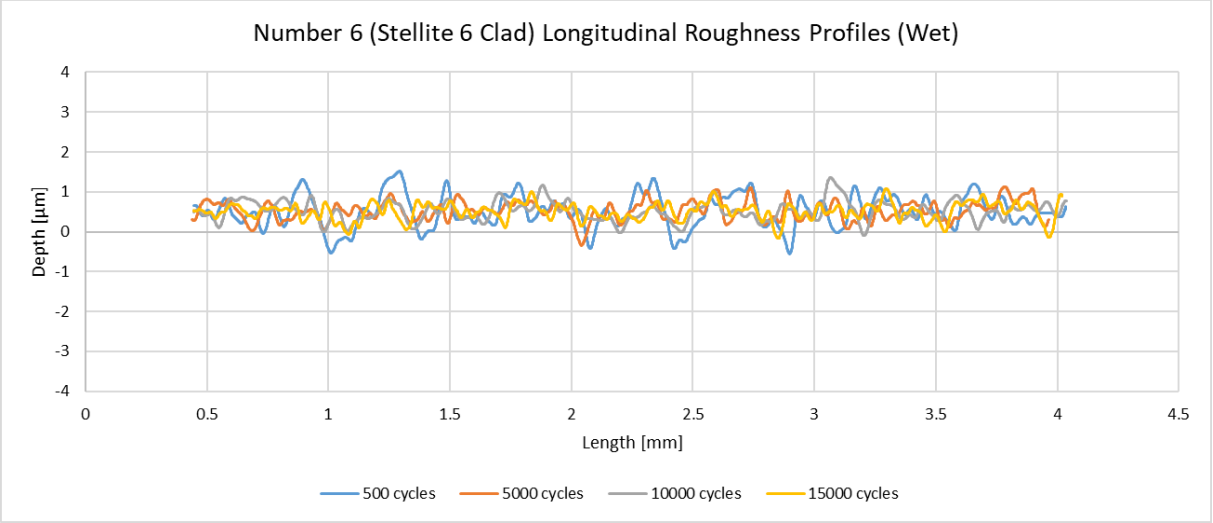
Number 6 (Stellite 6 Clad) Longitudinal Roughness Profiles (Wet)
Depth [µm]
Length [mm]
500 cycles
5000 cycles
10000 cycles
15000 cycles

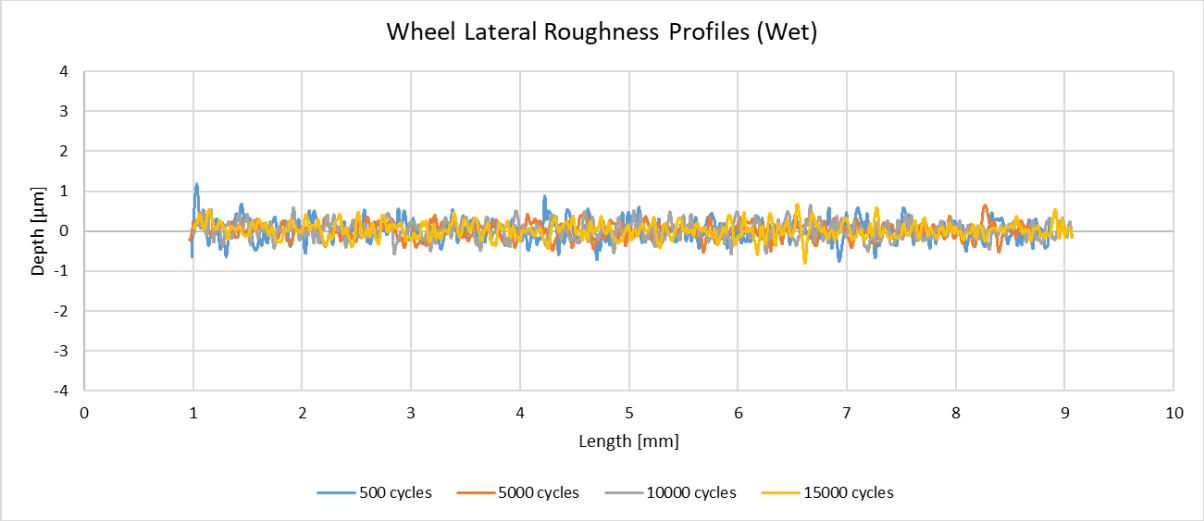

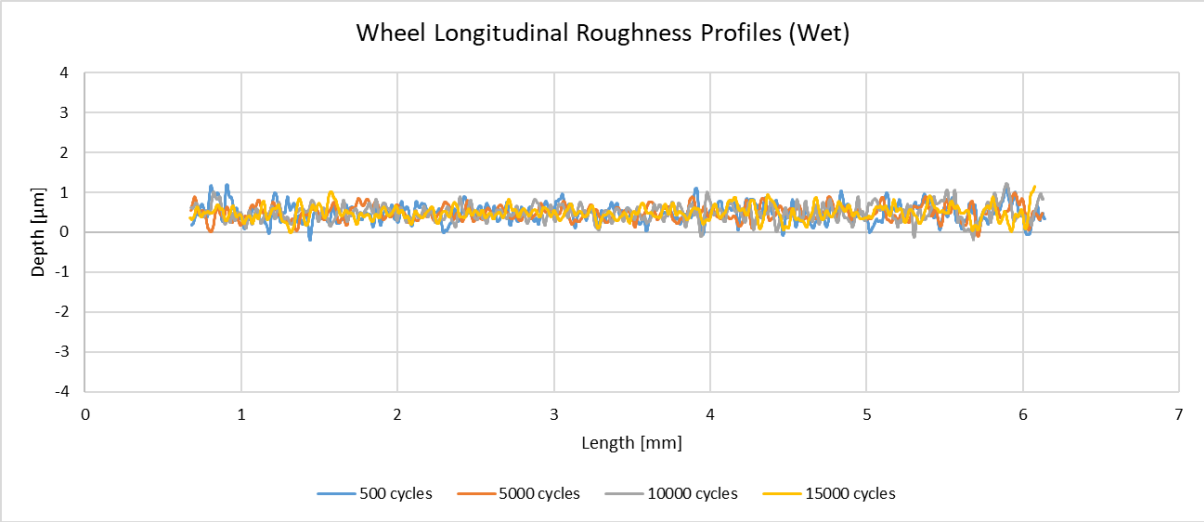

Figure 12.4: Small scale repair tests surface evolution roughness graphs from Alicona with 900 MPa, 0.5% slip, water-lubricated test condition

1500 MPa 1% Slip Dry Tests

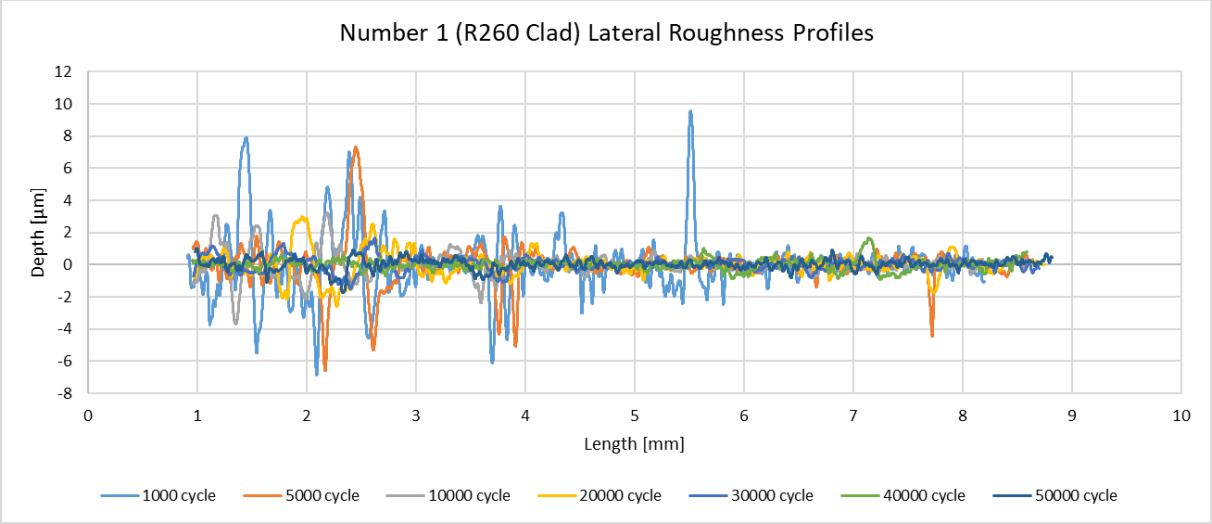

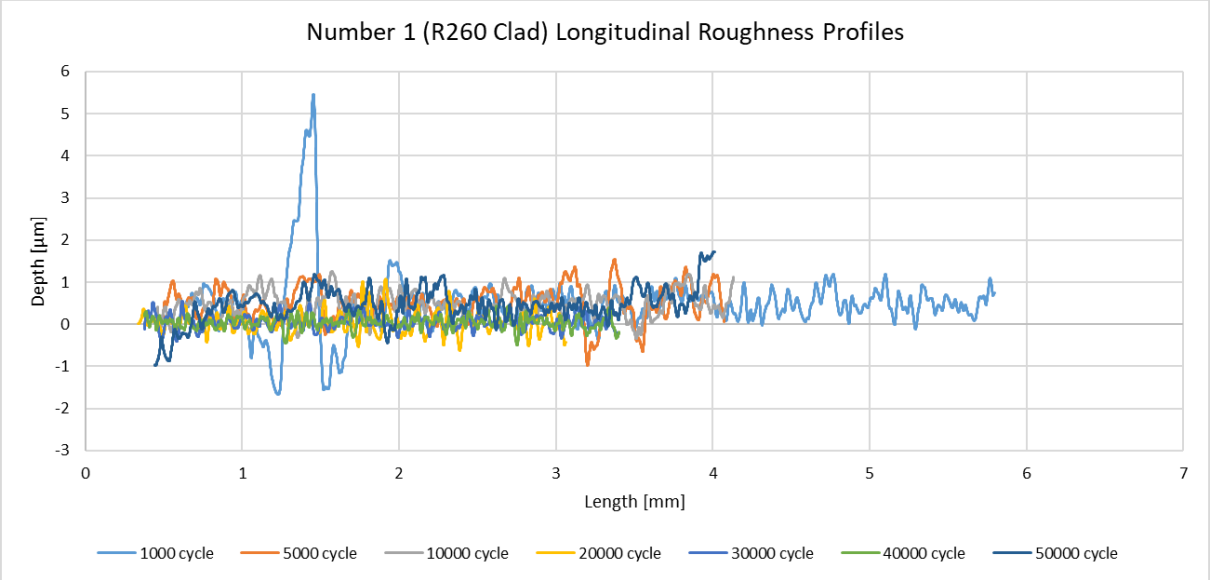

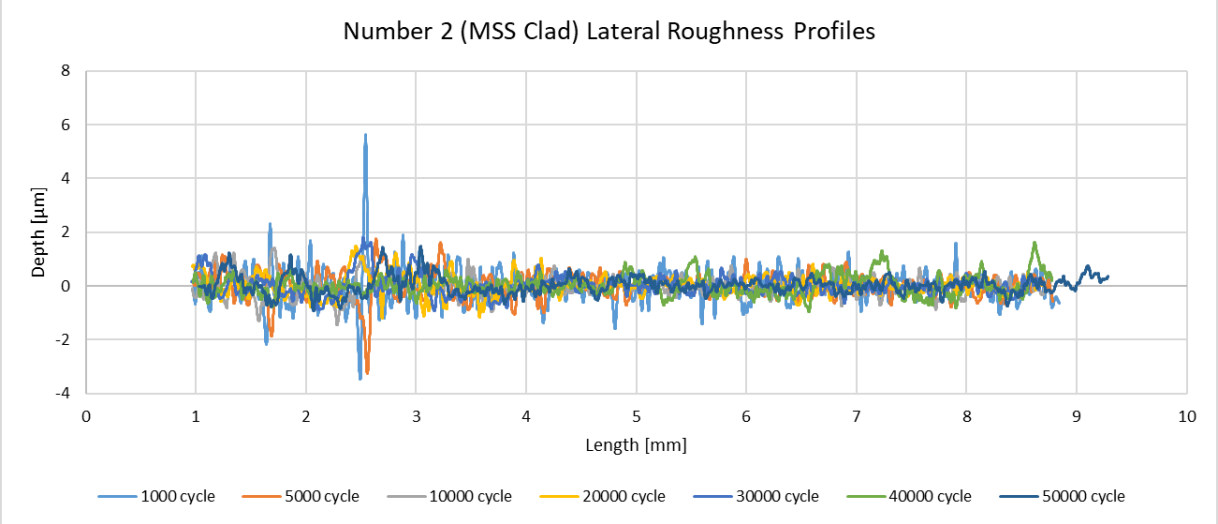

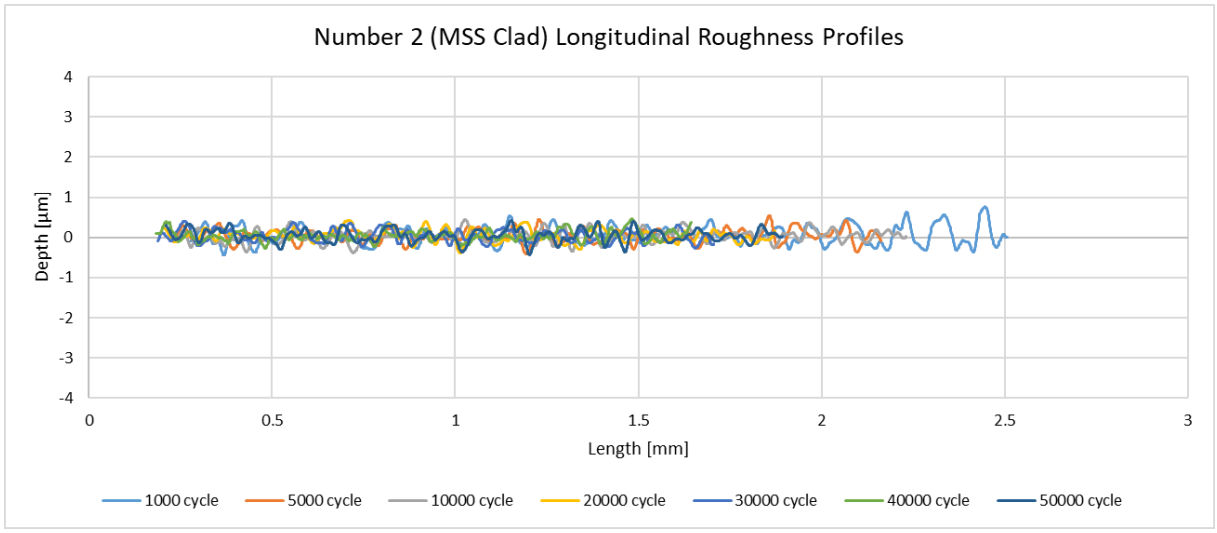
Number 2 (MSS Clad) Longitudinal Roughness Profiles
Depth [µm]
Length [mm]
1000 cycle
5000 cycle
10000 cycle
20000 cycle
30000 cycle
40000 cycle
50000 cycle

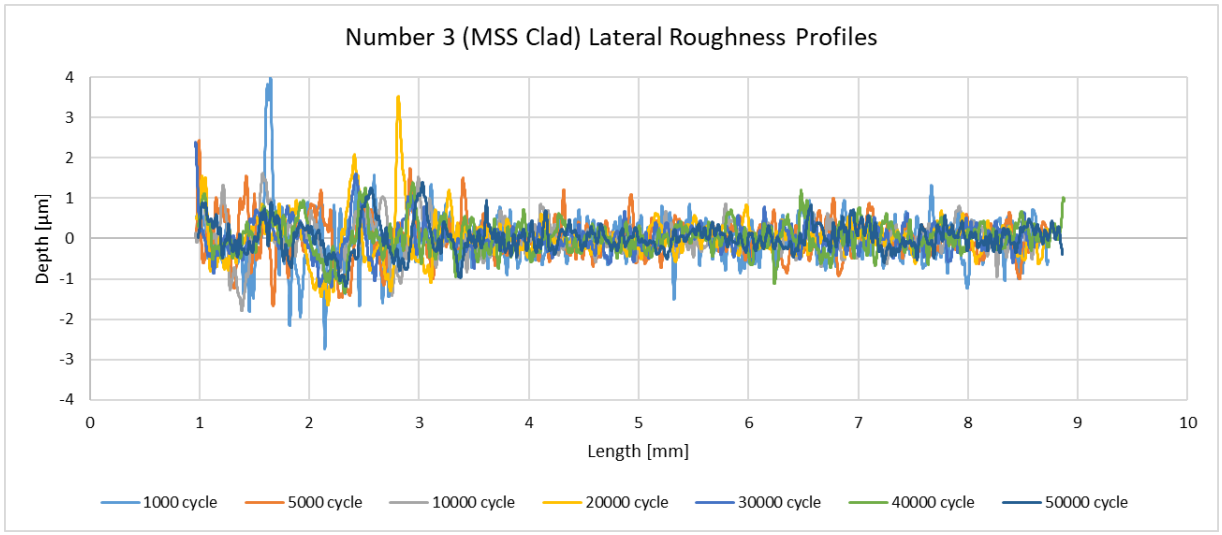
Number 3 (MSS Clad) Lateral Roughness Profiles
Depth [µm]
Length [mm]
1000 cycle
5000 cycle
10000 cycle
20000 cycle
30000 cycle
40000 cycle
50000 cycle

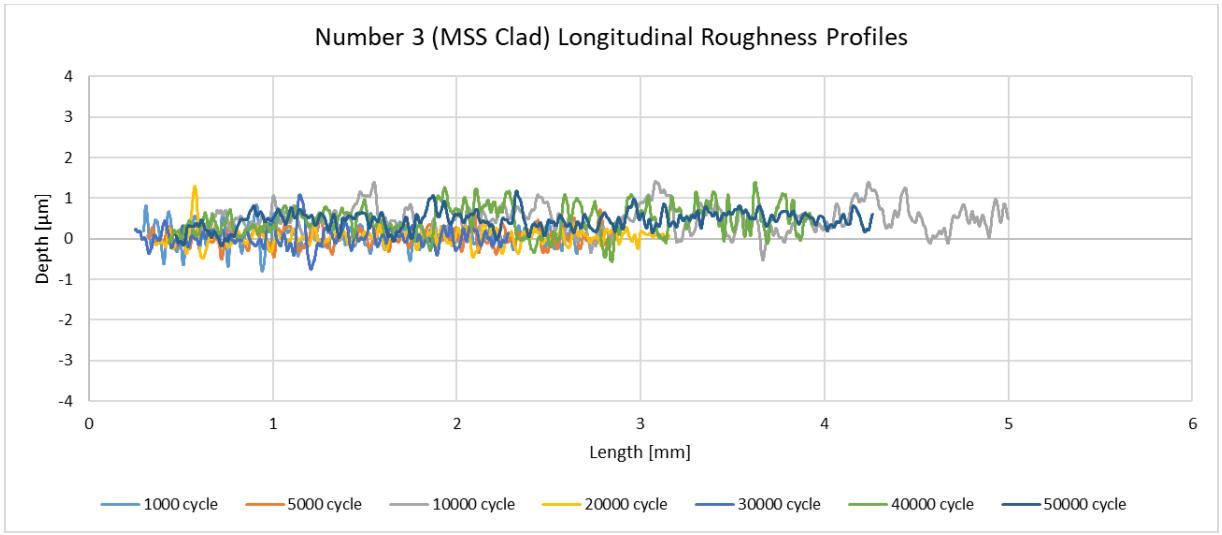
Number 3 (MSS Clad) Longitudinal Roughness Profiles
Depth [µm]
Length [mm]
1000 cycle
5000 cycle
10000 cycle
20000 cycle
30000 cycle
40000 cycle
50000 cycle

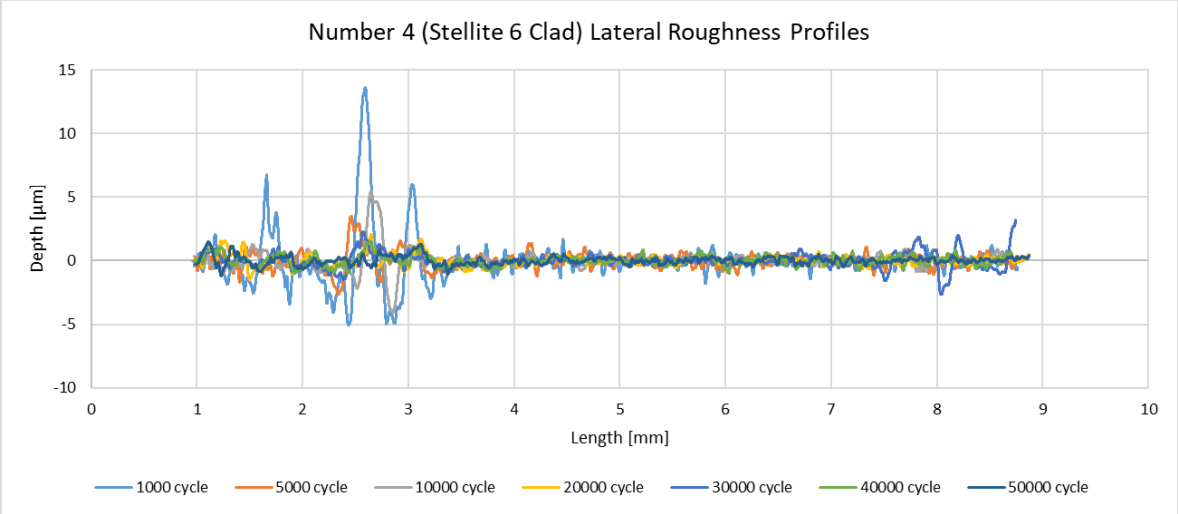
Number 4 (Stellite 6 Clad) Lateral Roughness Profiles
Depth [µm]
Length [mm]
1000 cycle
5000 cycle
10000 cycle
20000 cycle
30000 cycle
40000 cycle
50000 cycle

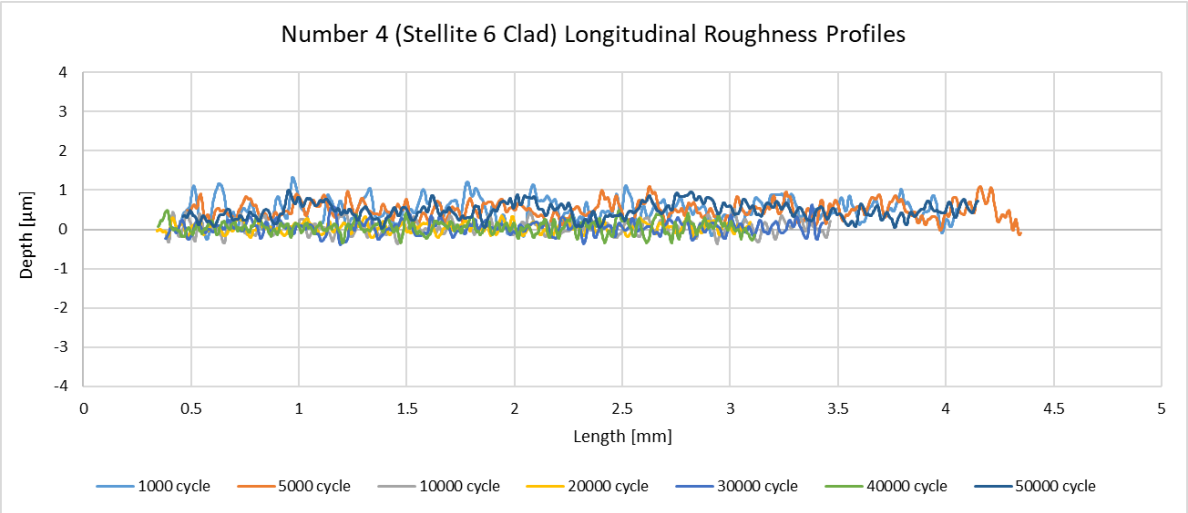
Number 4 (Stellite 6 Clad) Longitudinal Roughness Profiles
Depth [µm]
Length [mm]
1000 cycle
5000 cycle
10000 cycle
20000 cycle
30000 cycle
40000 cycle
50000 cycle

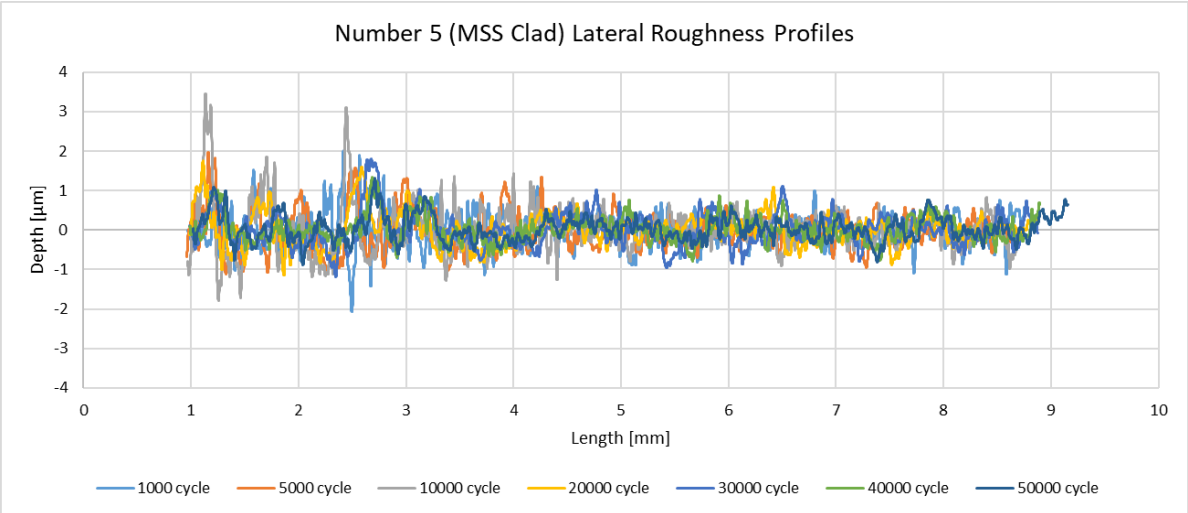
Number 5 (MSS Clad) Lateral Roughness Profiles
Depth [µm]
Length [mm]
1000 cycle
5000 cycle
10000 cycle
20000 cycle
30000 cycle
40000 cycle
50000 cycle

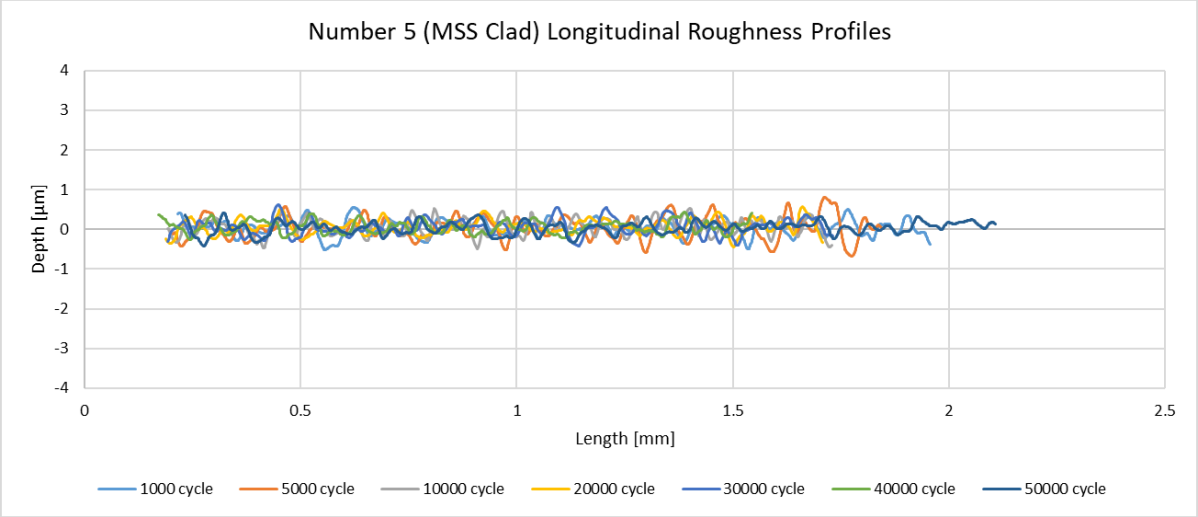
Number 5 (MSS Clad) Longitudinal Roughness Profiles
Depth [µm]
Length [mm]
1000 cycle
5000 cycle
10000 cycle
20000 cycle
30000 cycle
40000 cycle
50000 cycle

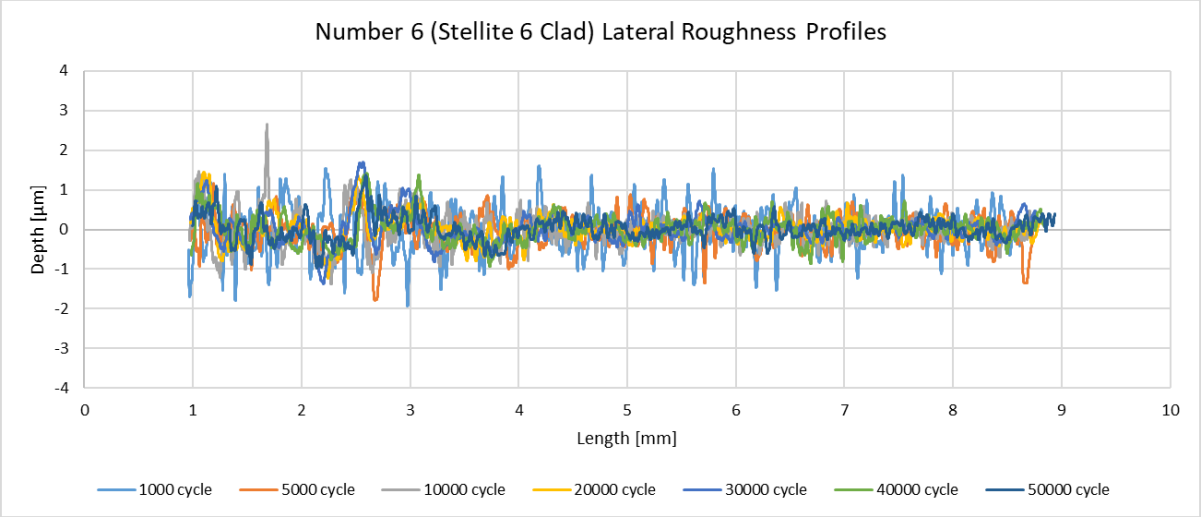
Number 6 (Stellite 6 Clad) Lateral Roughness Profiles
Depth [µm]
Length [mm]
1000 cycle
5000 cycle
10000 cycle
20000 cycle
30000 cycle
40000 cycle
50000 cycle

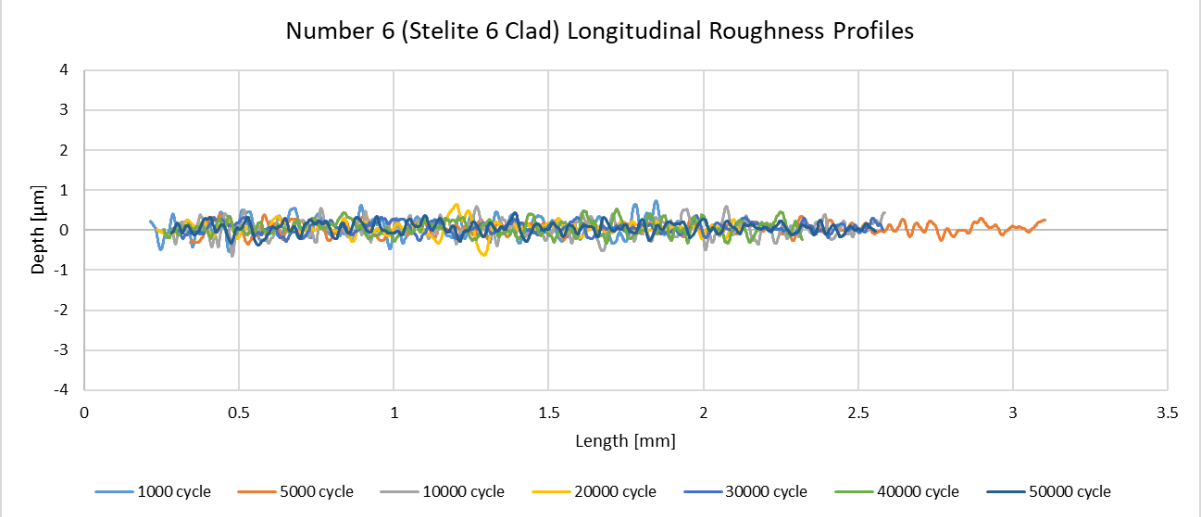
Number 6 (Stelite 6 Clad) Longitudinal Roughness Profiles
Depth [µm]
Length [mm]
1000 cycle
5000 cycle
10000 cycle
20000 cycle
30000 cycle
40000 cycle
50000 cycle

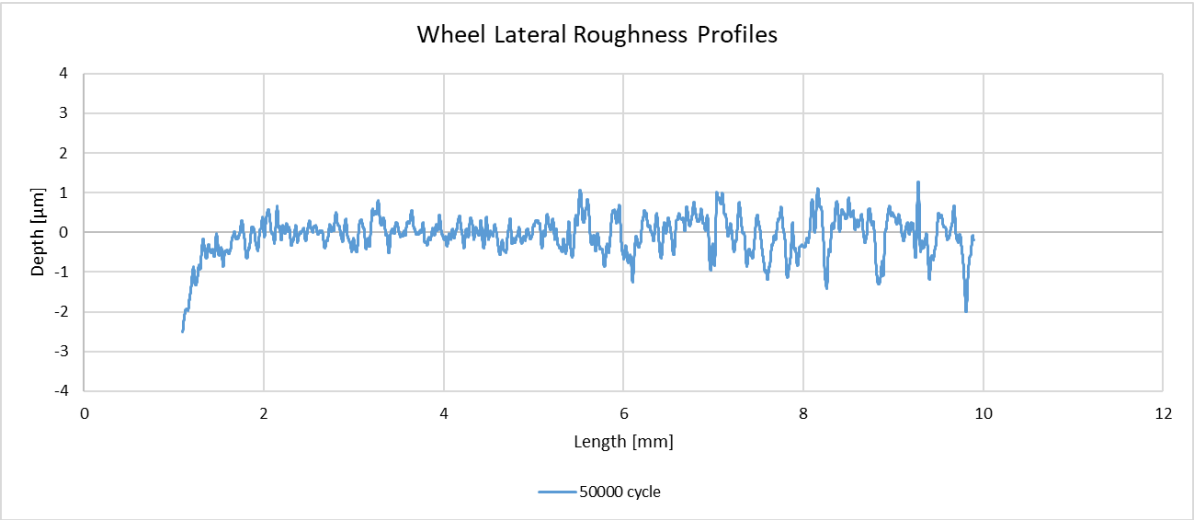

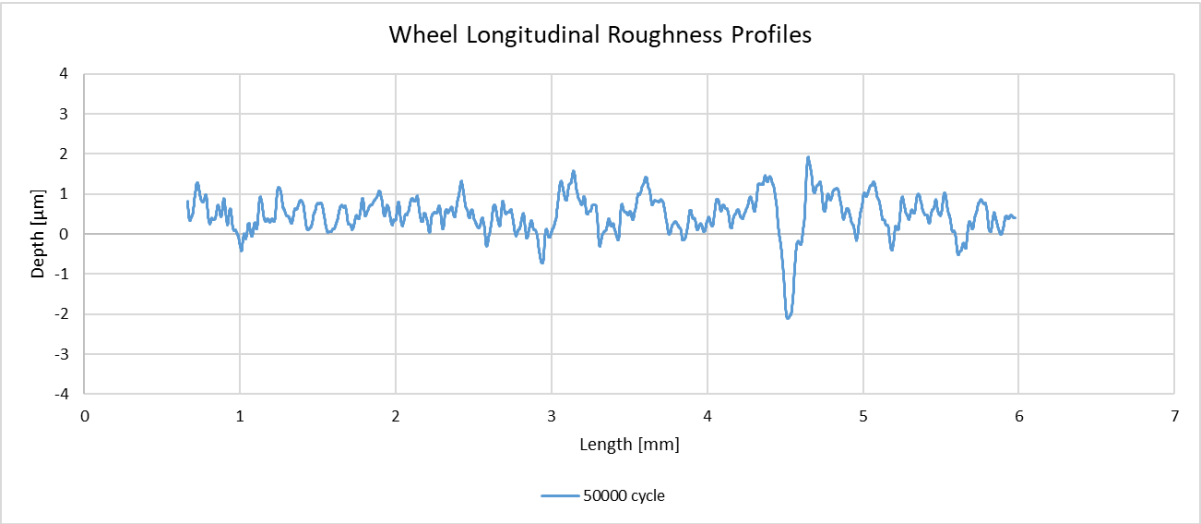

Figure 12.5: Small scale repair tests surface evolution roughness graphs from Alicona with 1500 MPa, 1% slip dry test condition

1500 MPa 1% Slip Water Lubricated Tests

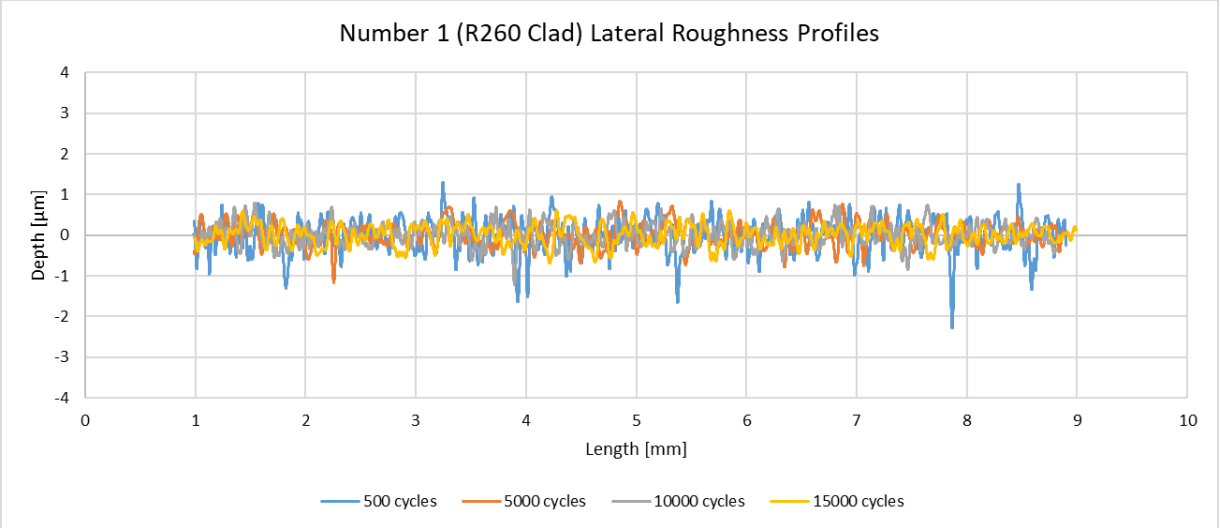

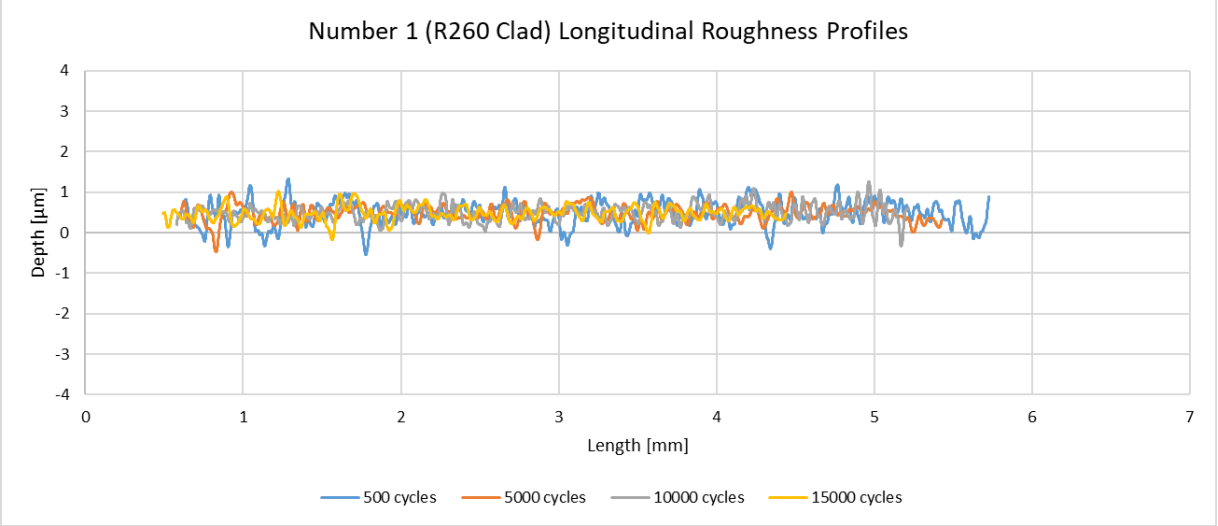

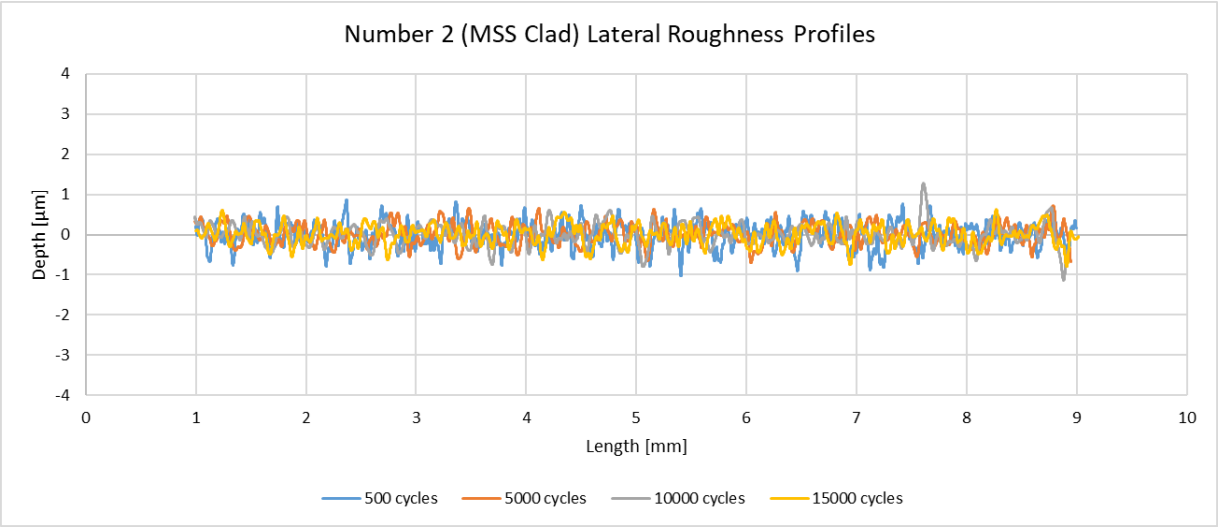

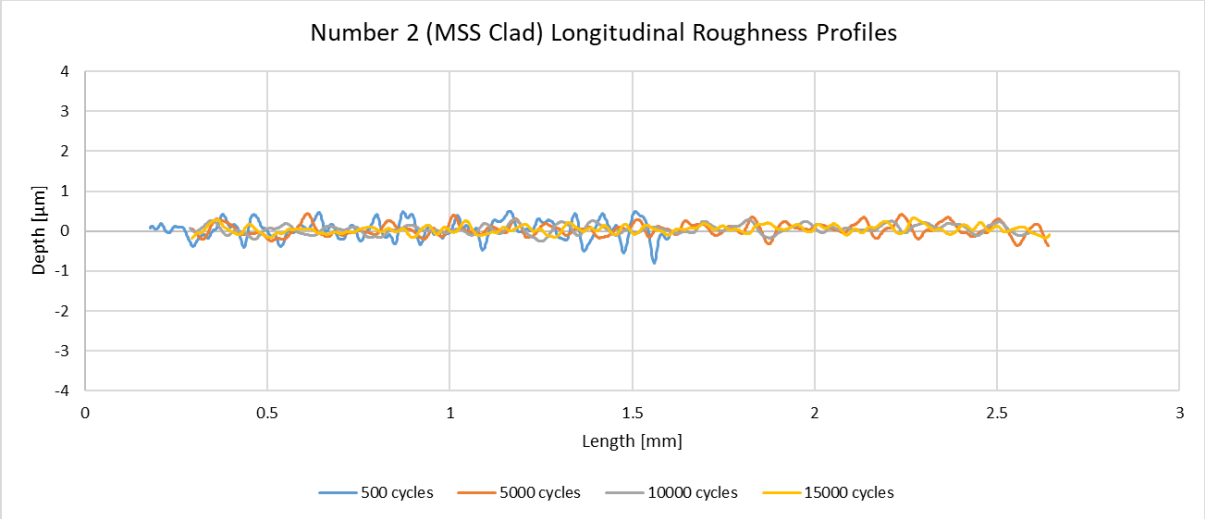
Number 2 (MSS Clad) Longitudinal Roughness Profiles
Depth [µm]
Length [mm]
500 cycles
5000 cycles
10000 cycles
15000 cycles

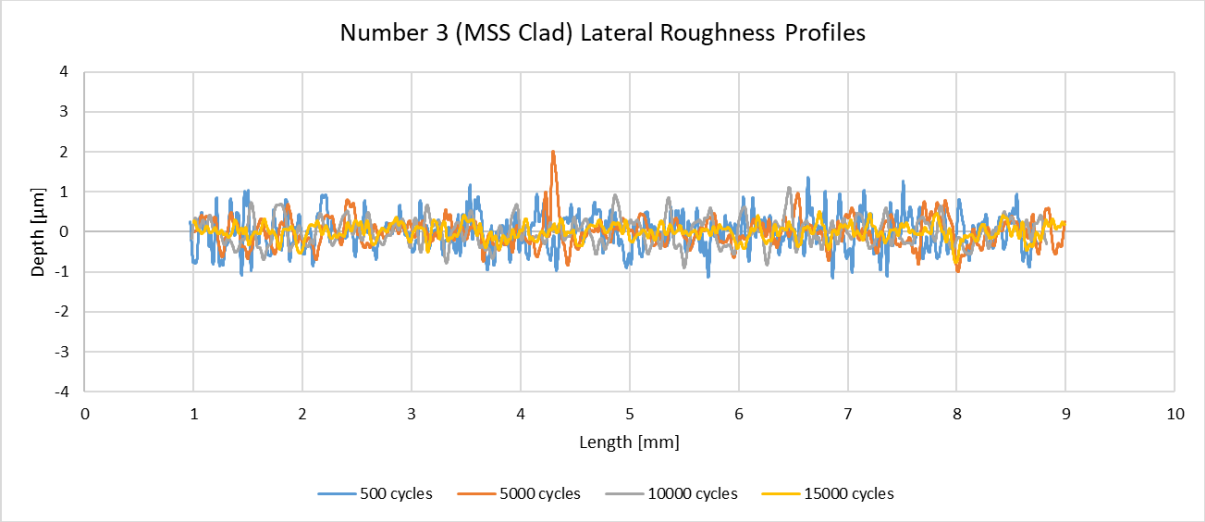
Number 3 (MSS Clad) Lateral Roughness Profiles
Depth [µm]
Length [mm]
500 cycles
5000 cycles
10000 cycles
15000 cycles

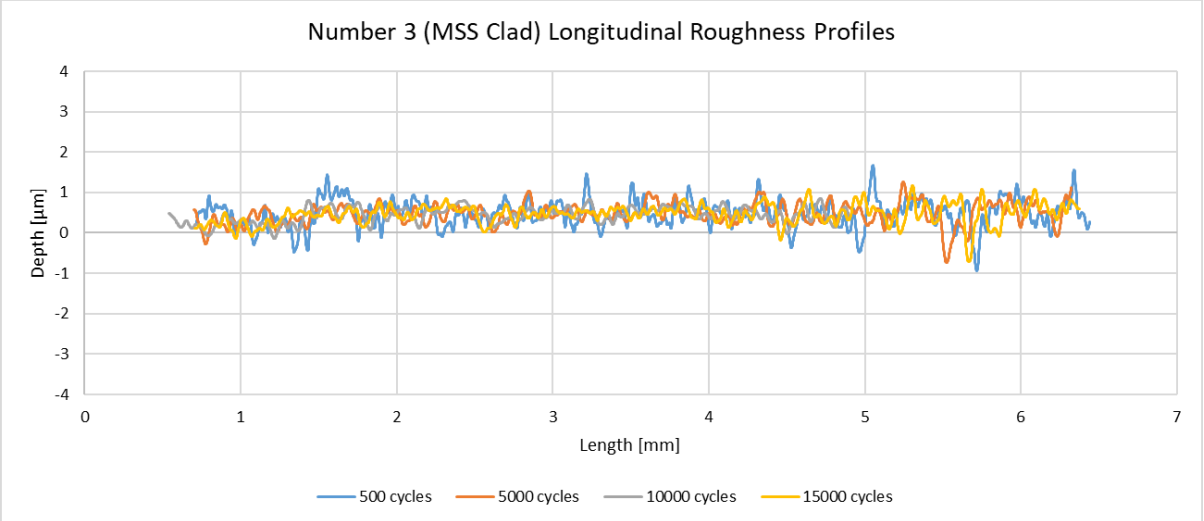
Number 3 (MSS Clad) Longitudinal Roughness Profiles
Depth [µm]
Length [mm]
500 cycles
5000 cycles
10000 cycles
15000 cycles

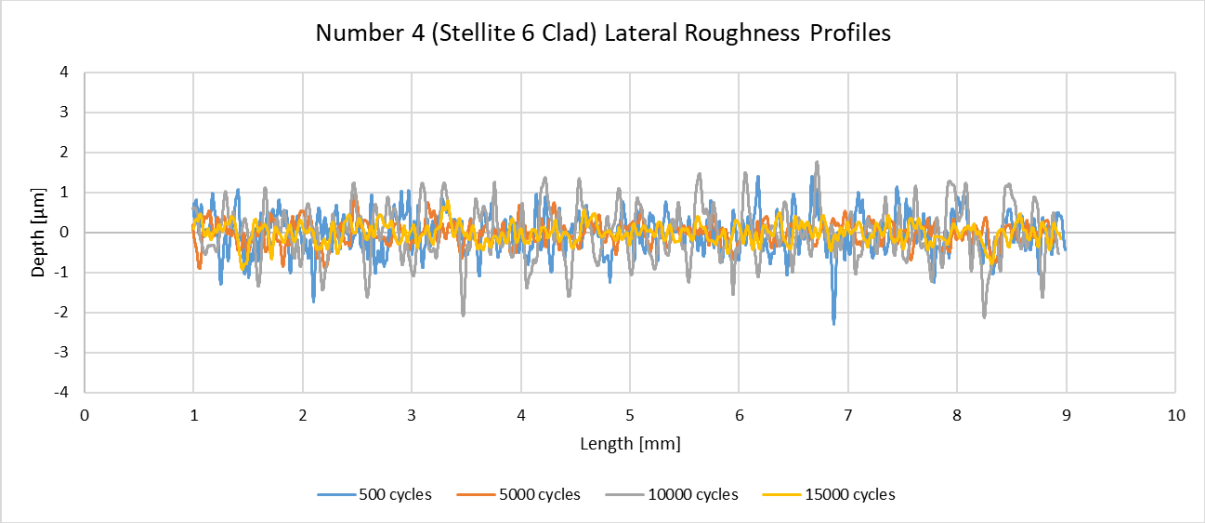
Number 4 (Stellite 6 Clad) Lateral Roughness Profiles
Depth [µm]
Length [mm]
500 cycles
5000 cycles
10000 cycles
15000 cycles

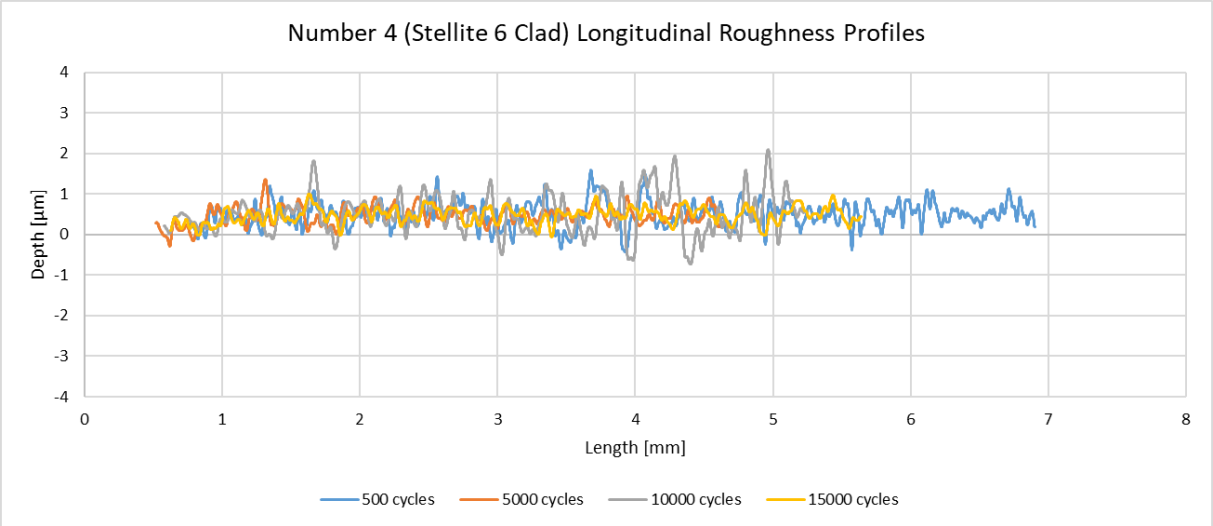
Number 4 (Stellite 6 Clad) Longitudinal Roughness Profiles
Depth [µm]
Length [mm]
500 cycles
5000 cycles
10000 cycles
15000 cycles

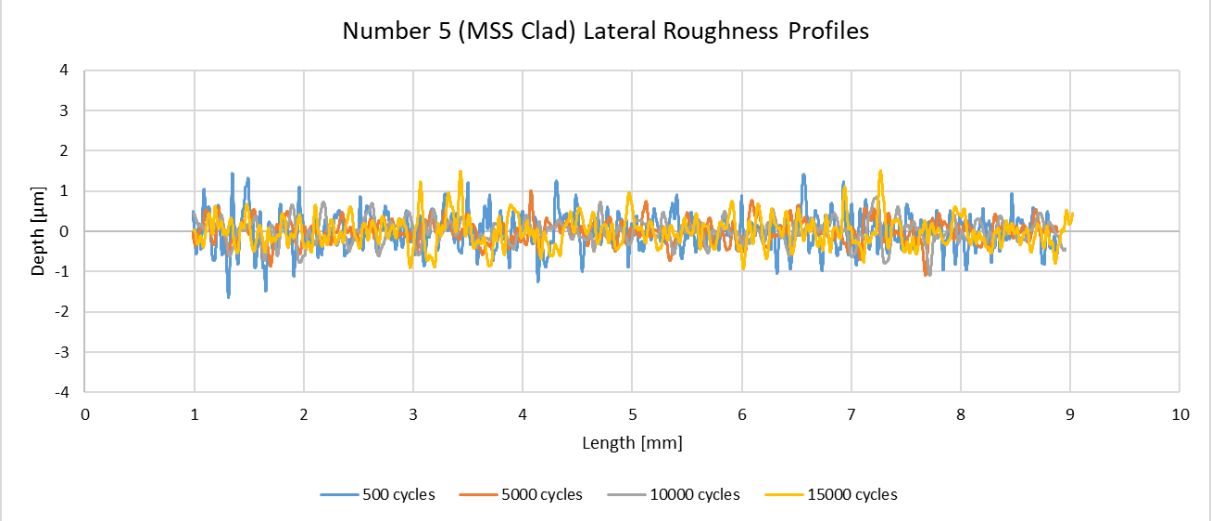
Number 5 (MSS Clad) Lateral Roughness Profiles
Depth [µm]
Length [mm]
500 cycles
5000 cycles
10000 cycles
15000 cycles

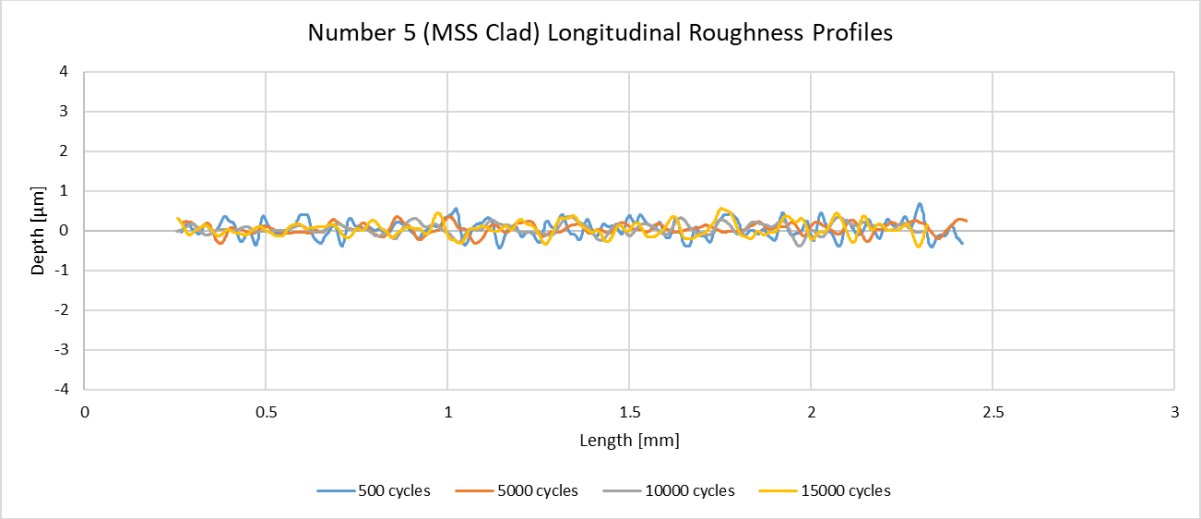
Number 5 (MSS Clad) Longitudinal Roughness Profiles
Depth [µm]
Length [mm]
500 cycles
5000 cycles
10000 cycles
15000 cycles

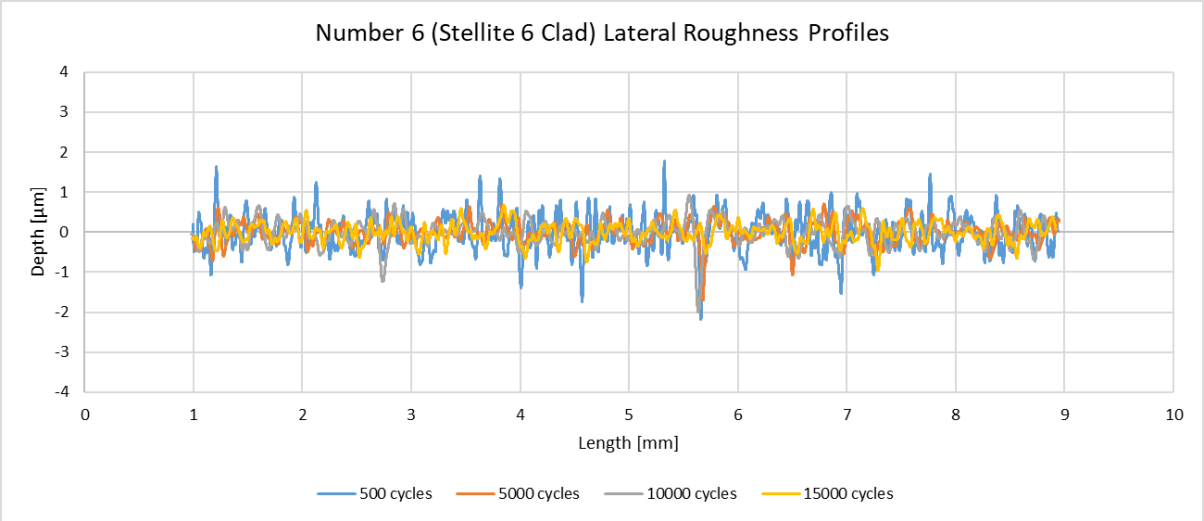
Number 6 (Stellite 6 Clad) Lateral Roughness Profiles
Depth [µm]
Length [mm]
500 cycles
5000 cycles
10000 cycles
15000 cycles

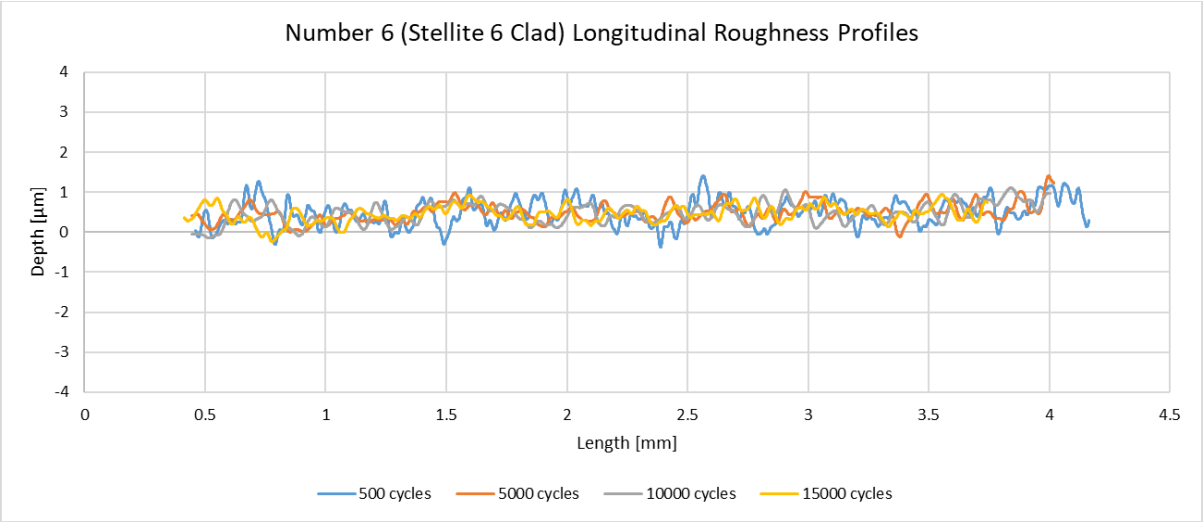
Number 6 (Stellite 6 Clad) Longitudinal Roughness Profiles
Depth [µm]
Length [mm]
500 cycles
5000 cycles
10000 cycles
15000 cycles

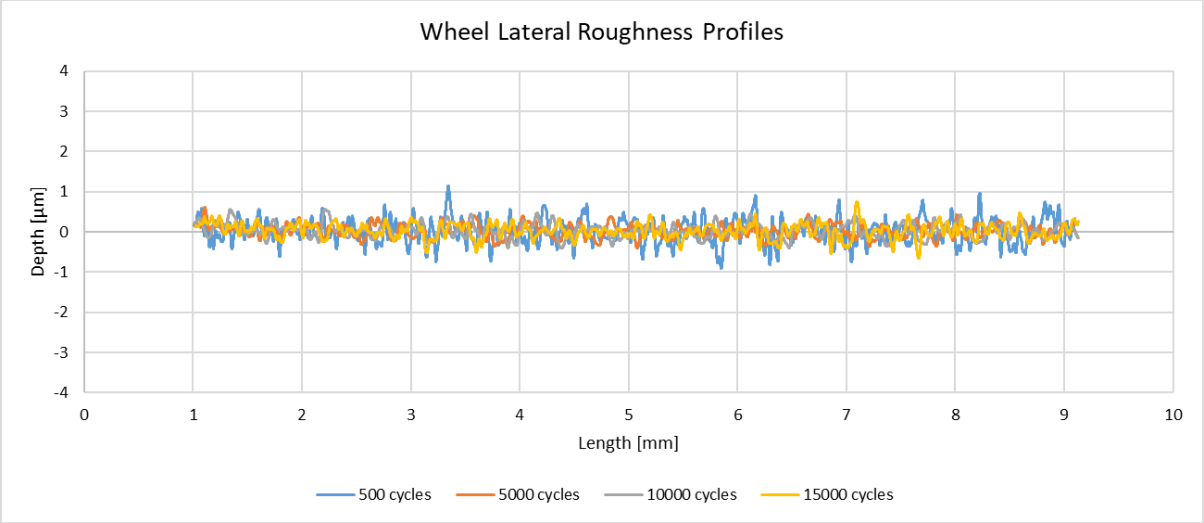

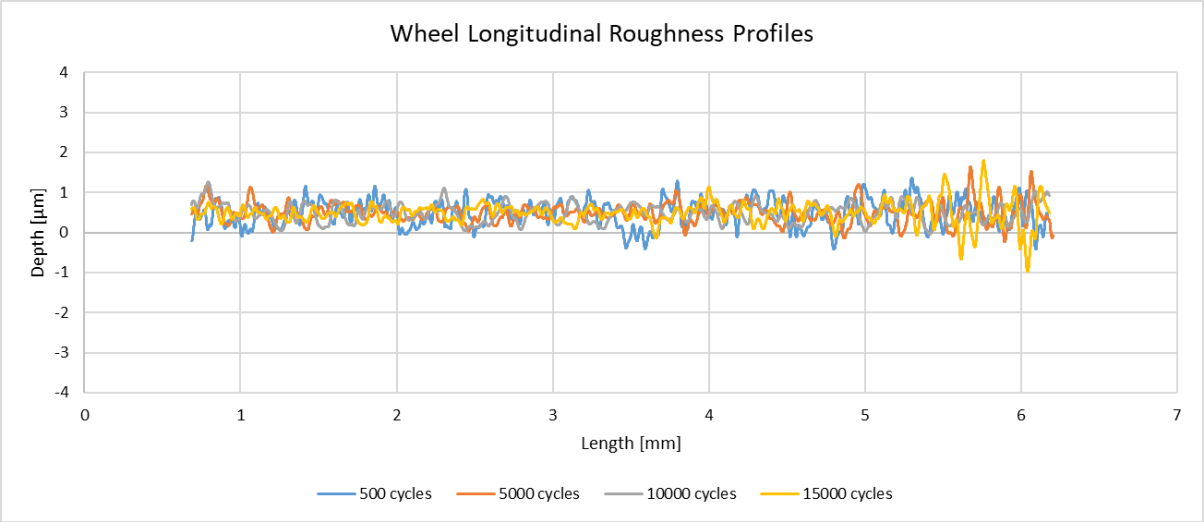

Figure 12.6: Small scale repair tests surface evolution roughness graphs from Alicona with 1500 MPa, 1% slip, water-lubricated test condition

1500 MPa 3% Slip Dry Tests

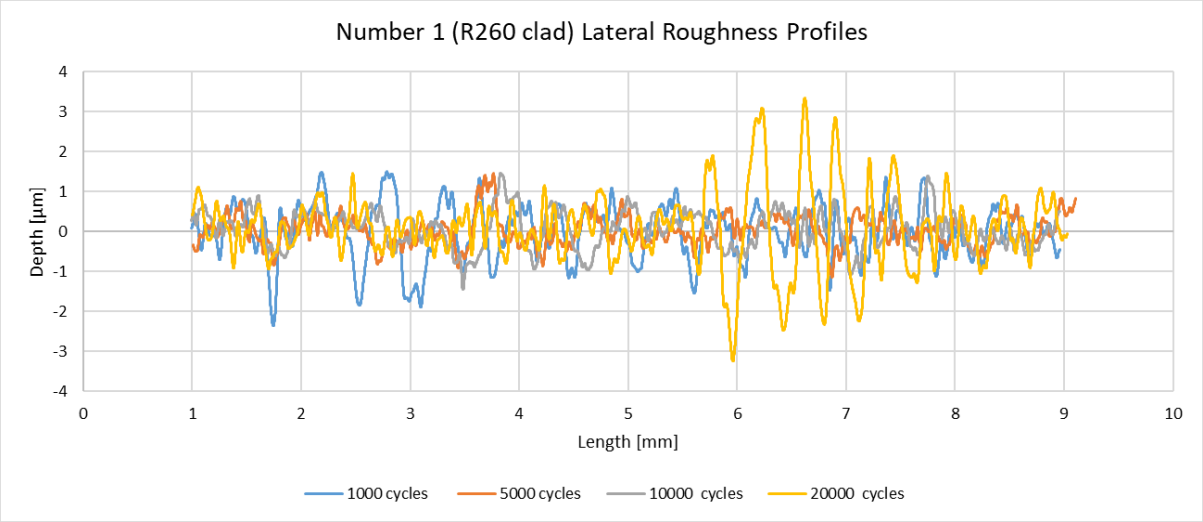

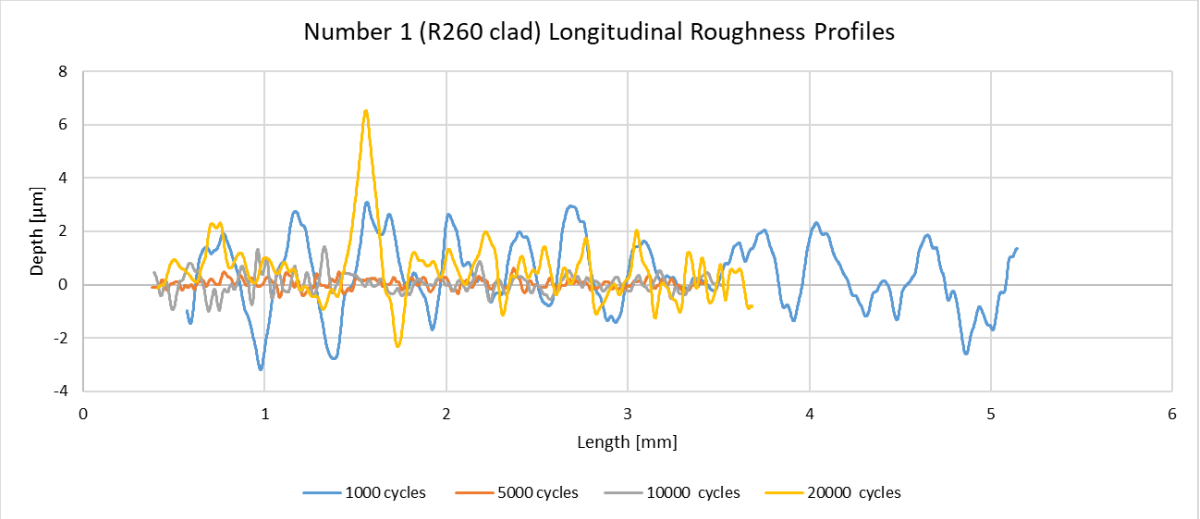

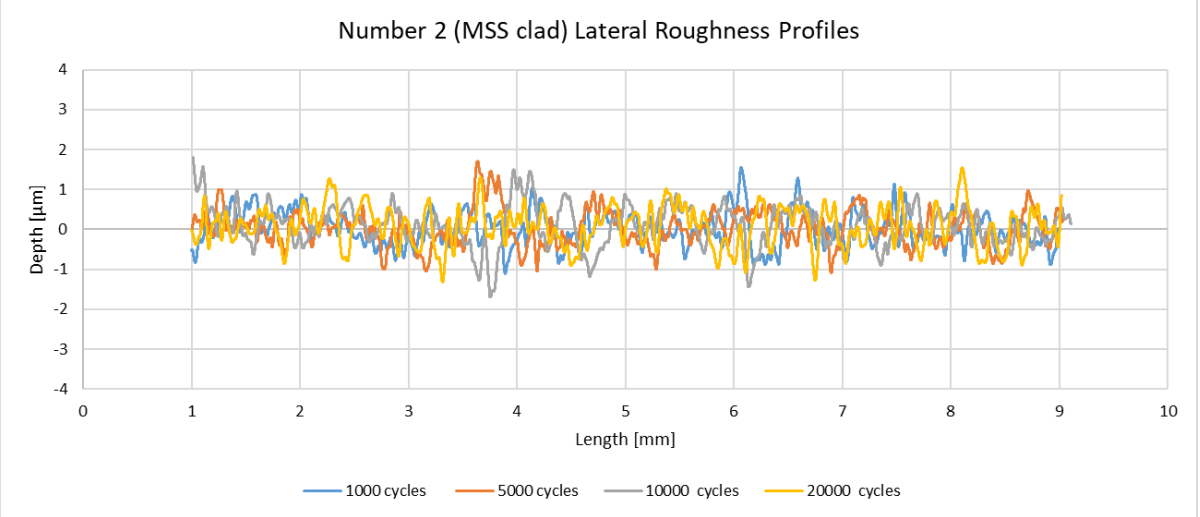

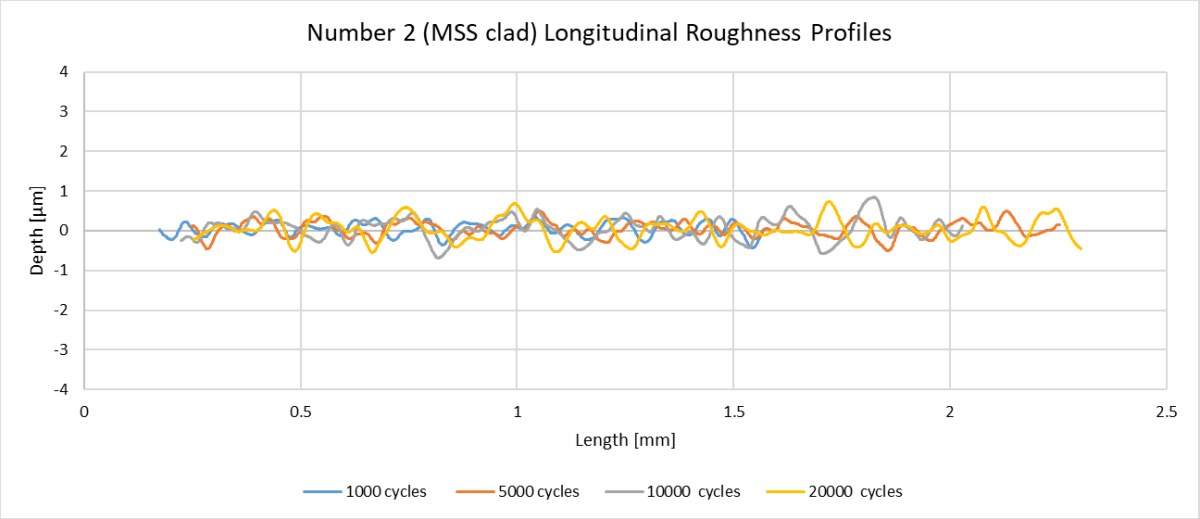
Number 2 (MSS clad) Longitudinal Roughness Profiles
Depth [µm]
Length [mm]
1000 cycles
5000 cycles
10000 cycles
20000 cycles

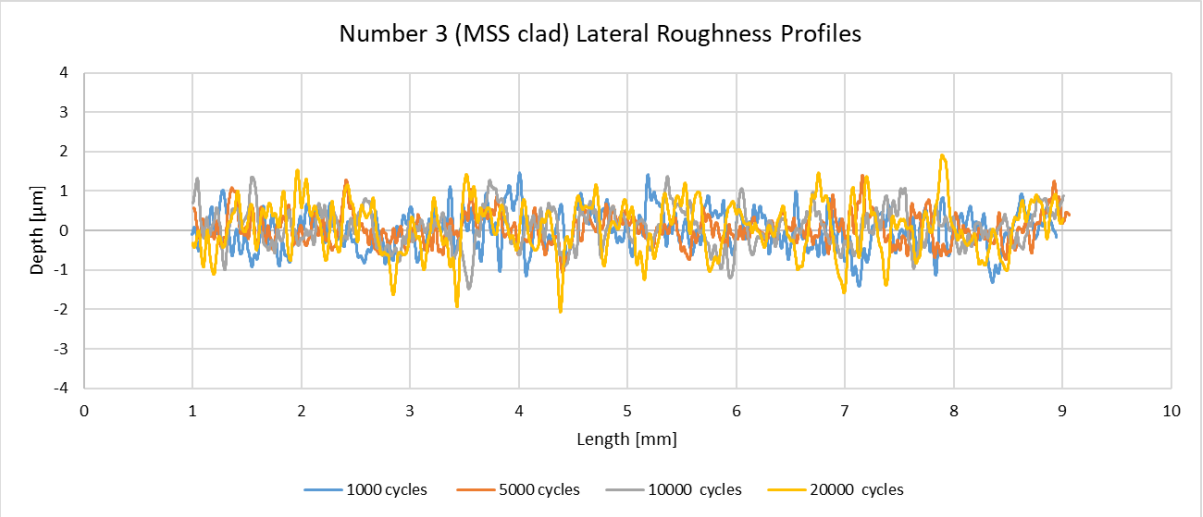
Number 3 (MSS clad) Lateral Roughness Profiles
Depth [µm]
Length [mm]
1000 cycles
5000 cycles
10000 cycles
20000 cycles

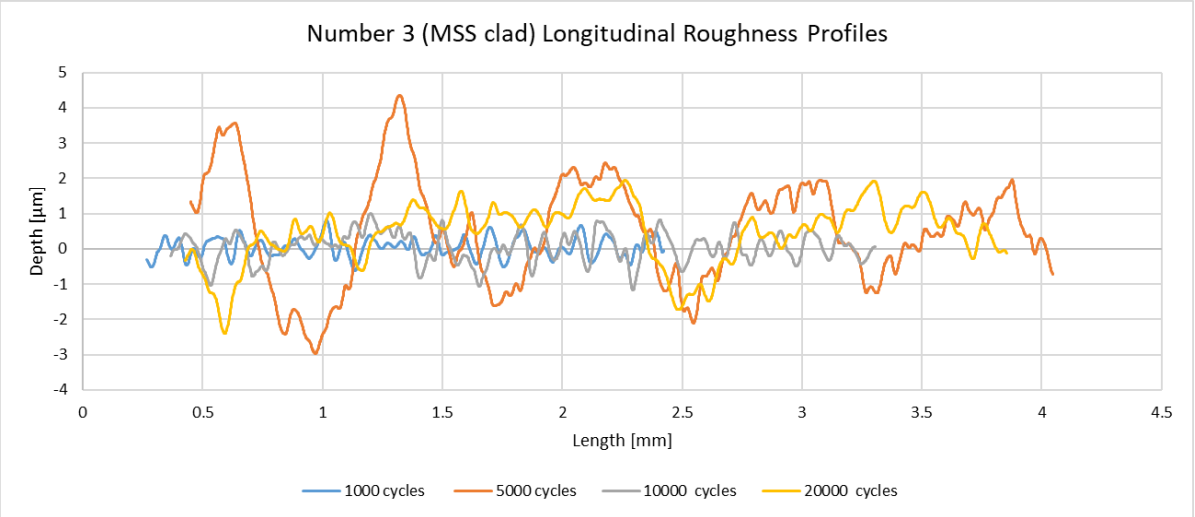
Number 3 (MSS clad) Longitudinal Roughness Profiles
Depth [µm]
Length [mm]
1000 cycles
5000 cycles
10000 cycles
20000 cycles

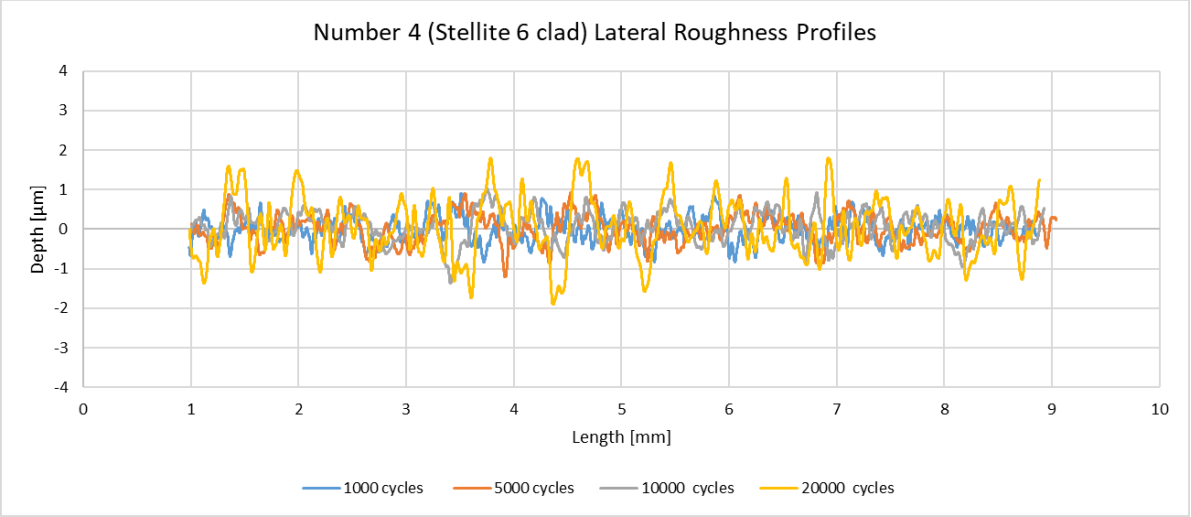
Number 4 (Stellite 6 clad) Lateral Roughness Profiles
Depth [µm]
Length [mm]
1000 cycles
5000 cycles
10000 cycles
20000 cycles

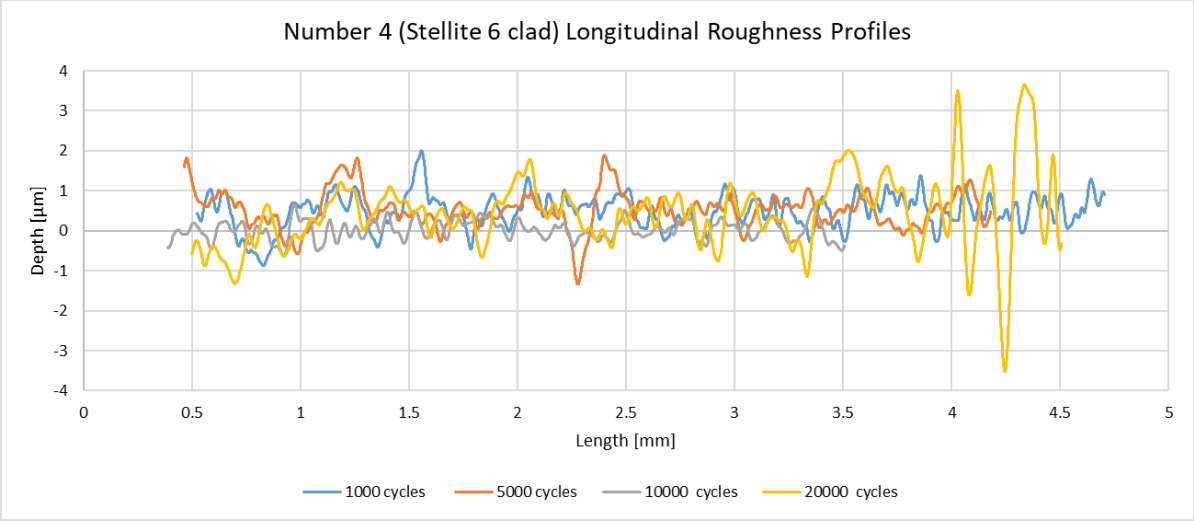
Number 4 (Stellite 6 clad) Longitudinal Roughness Profiles
Depth [µm]
Length [mm]
1000 cycles
5000 cycles
10000 cycles
20000 cycles

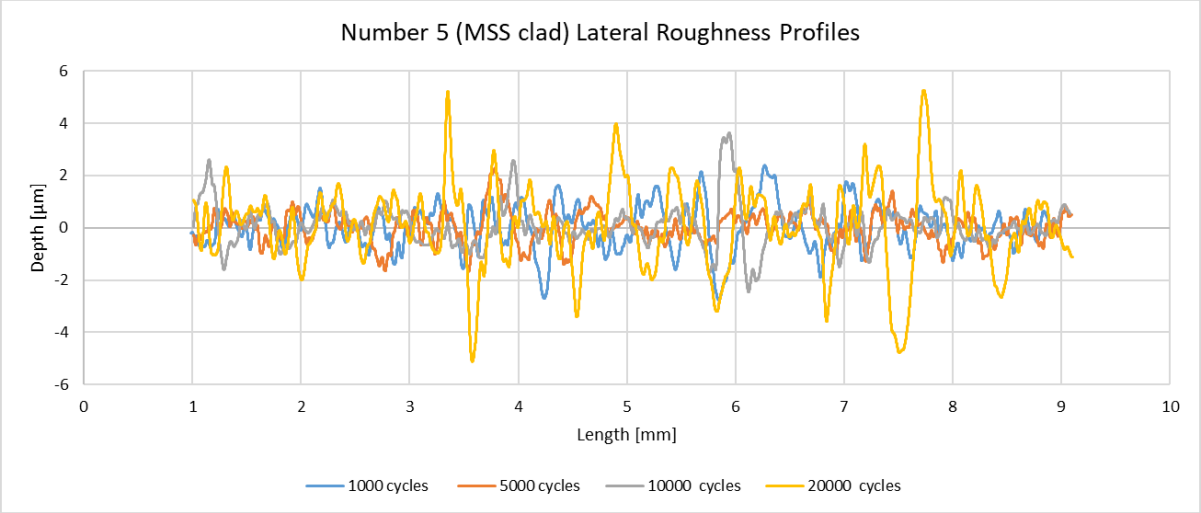
Number 5 (MSS clad) Lateral Roughness Profiles
Depth [µm]
Length [mm]
1000 cycles
5000 cycles
10000 cycles
20000 cycles

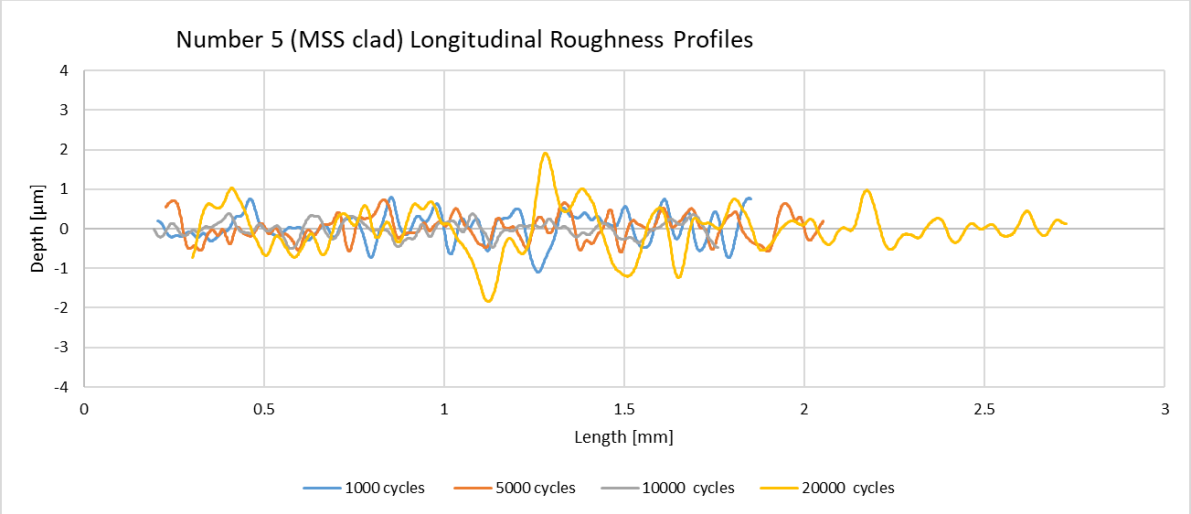
Number 5 (MSS clad) Longitudinal Roughness Profiles
Depth [µm]
Length [mm]
1000 cycles
5000 cycles
10000 cycles
20000 cycles

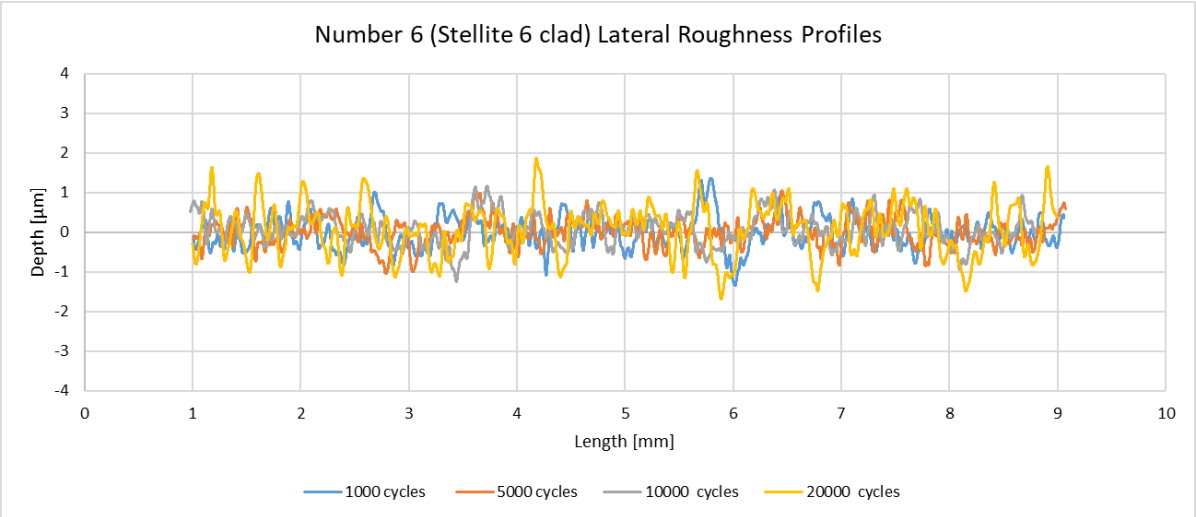
Number 6 (Stellite 6 clad) Lateral Roughness Profiles
Depth [µm]
Length [mm]
1000 cycles
5000 cycles
10000 cycles
20000 cycles

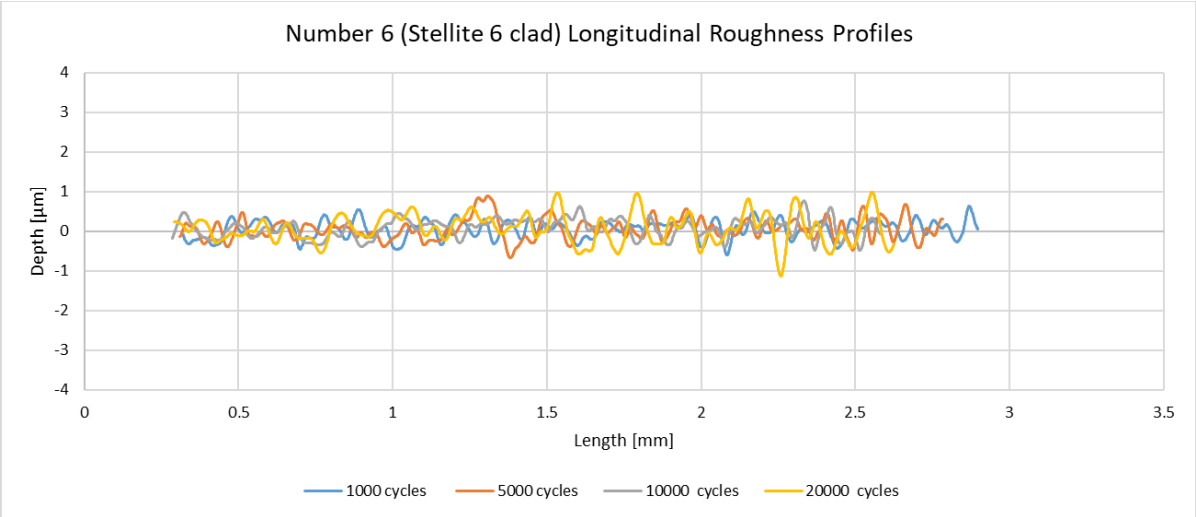
Number 6 (Stellite 6 clad) Longitudinal Roughness Profiles
Depth [µm]
Length [mm]
1000 cycles
5000 cycles
10000 cycles
20000 cycles

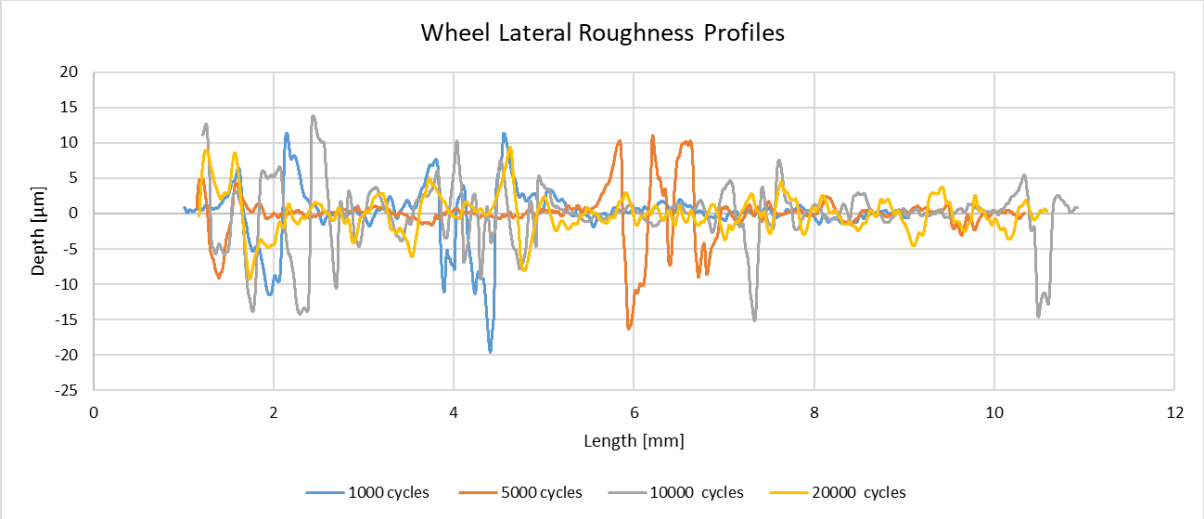

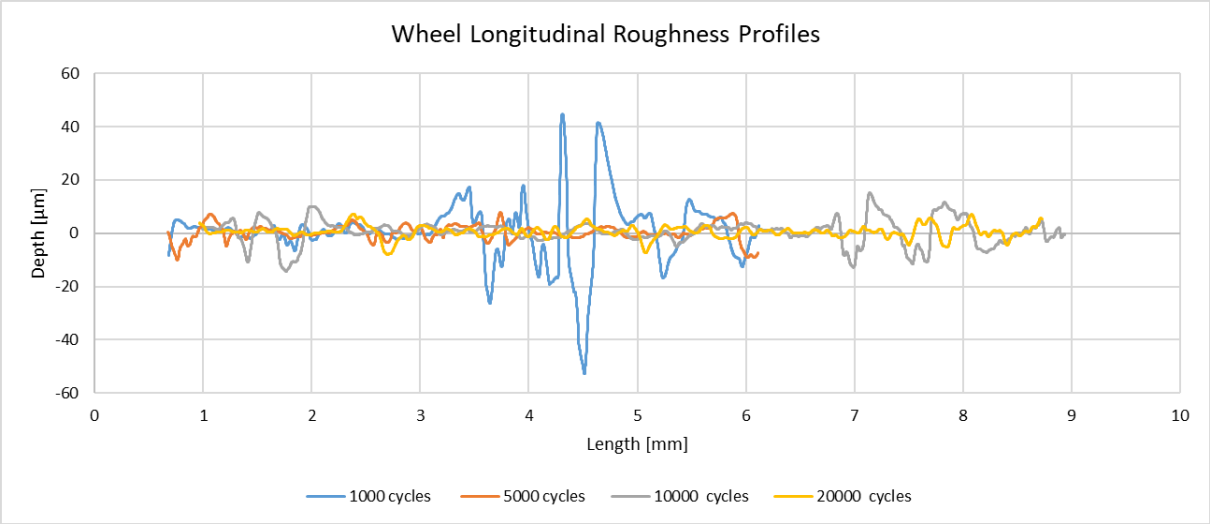

Figure 12.7: Small scale repair tests surface evolution roughness graphs from Alicona for 1500 MPa, 3% slip, dry test condition

1800 MPa 1% Slip Dry Tests

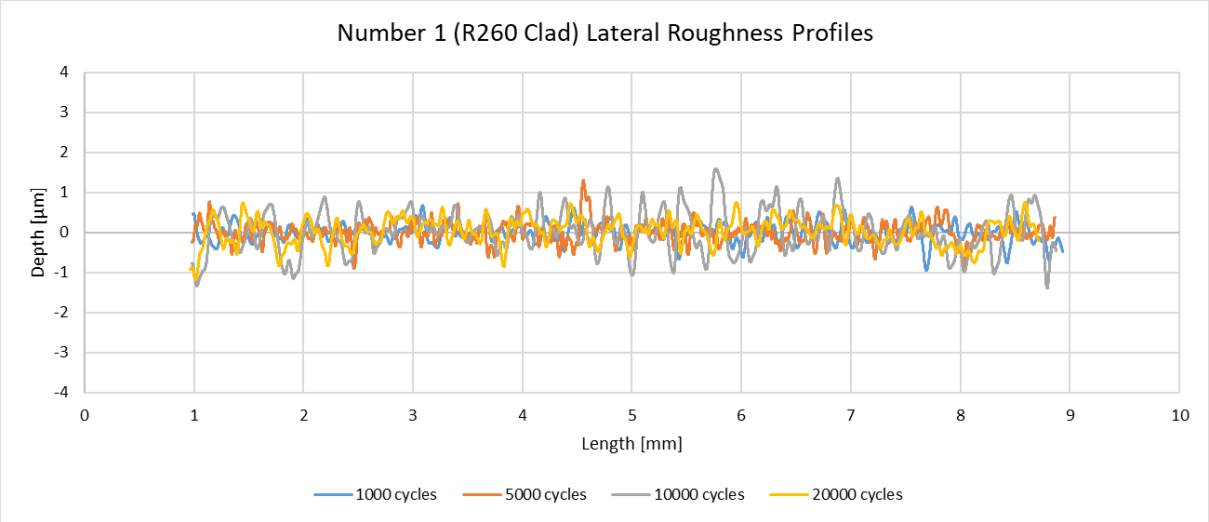

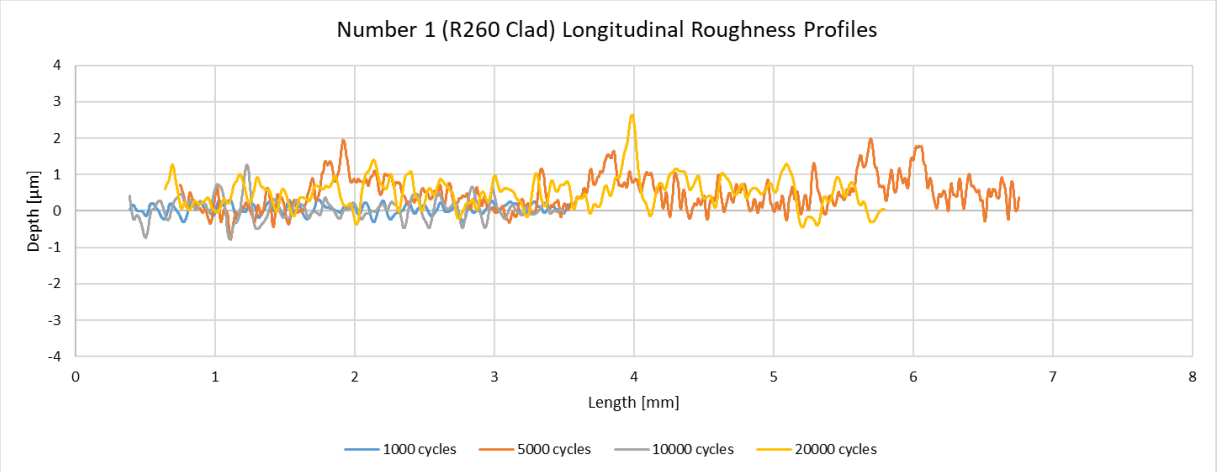

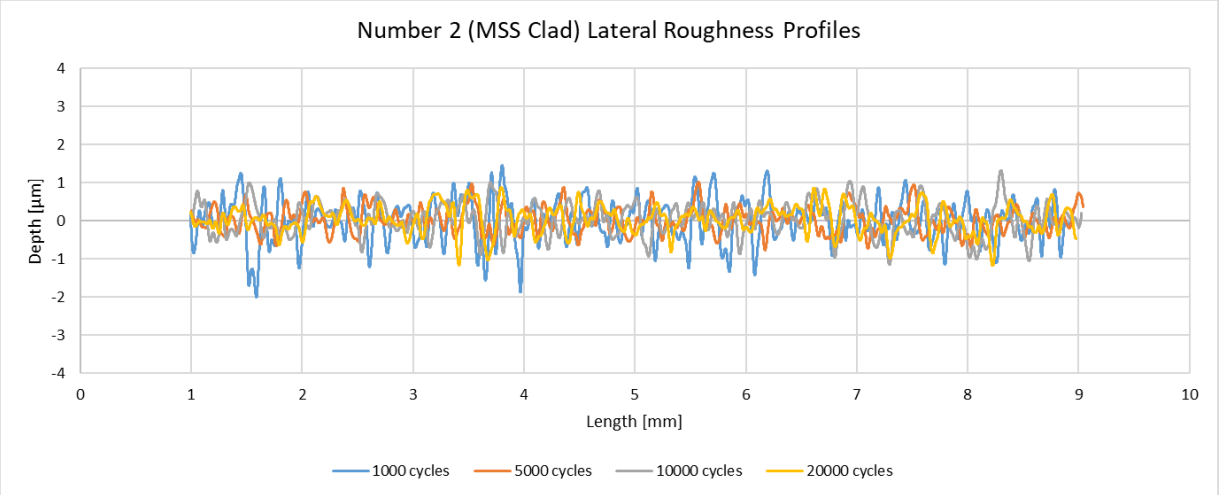

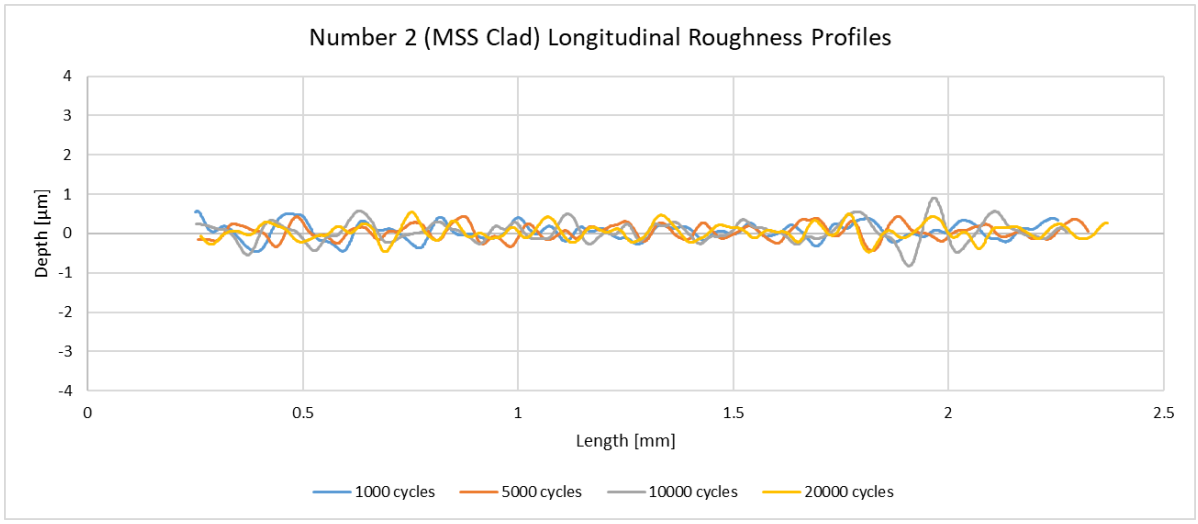
Number 2 (MSS Clad) Longitudinal Roughness Profiles
Depth [µm]
Length [mm]
1000 cycles
5000 cycles
10000 cycles
20000 cycles

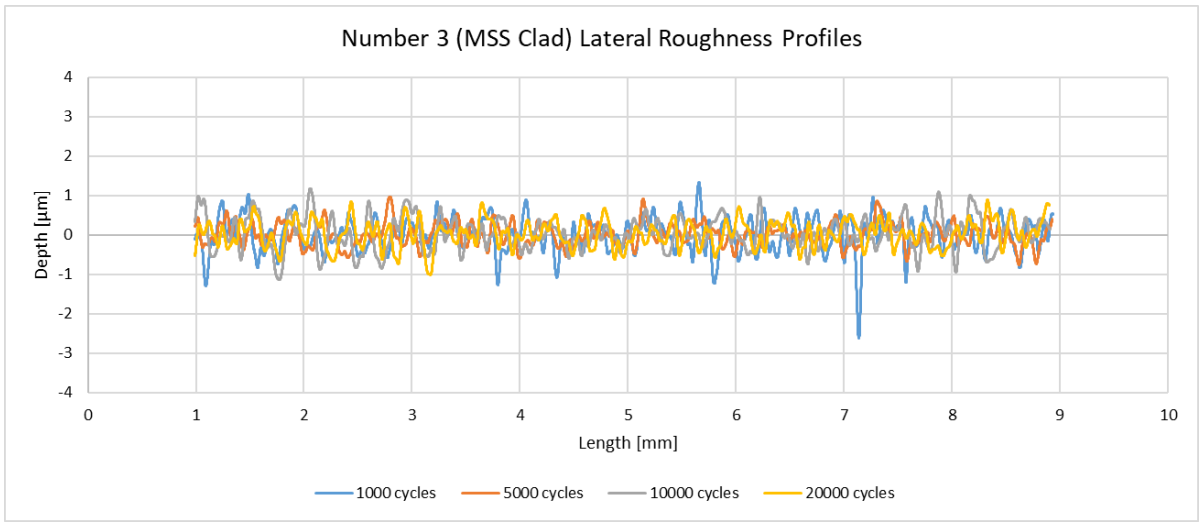
Number 3 (MSS Clad) Lateral Roughness Profiles
Depth [µm]
Length [mm]
1000 cycles
5000 cycles
10000 cycles
20000 cycles

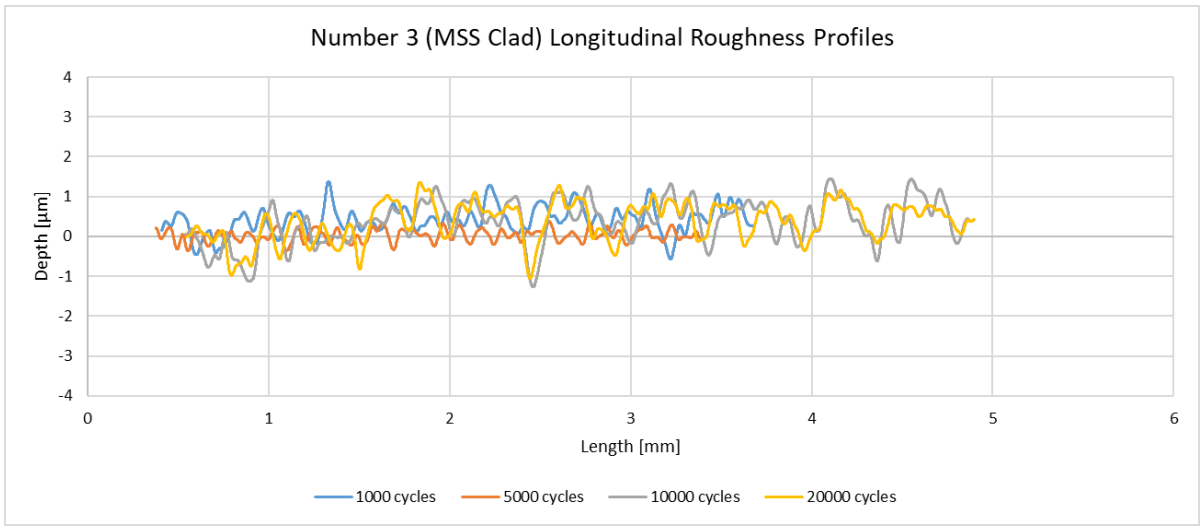
Number 3 (MSS Clad) Longitudinal Roughness Profiles
Depth [µm]
Length [mm]
1000 cycles
5000 cycles
10000 cycles
20000 cycles

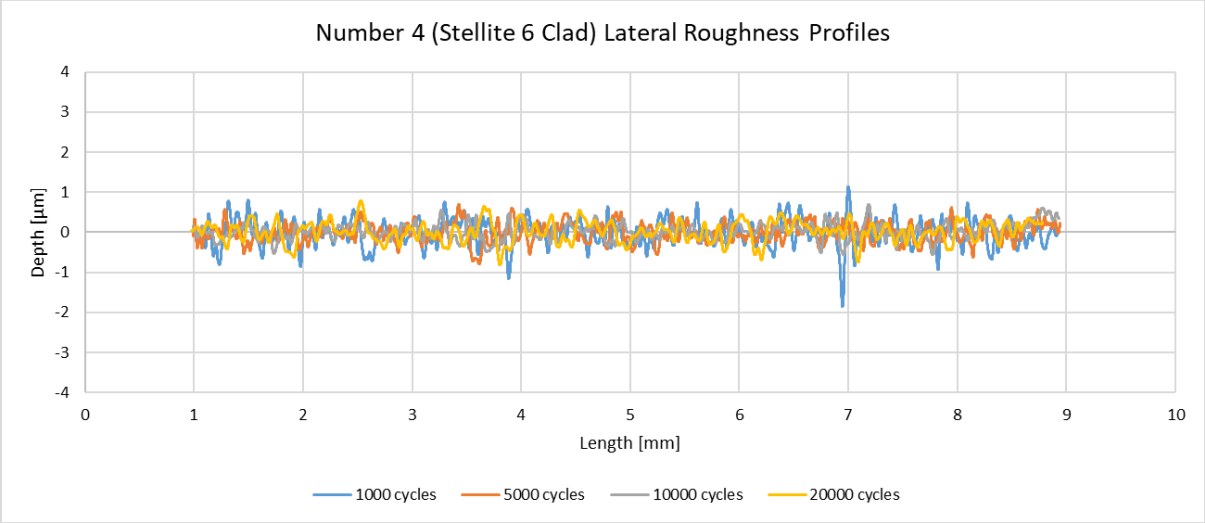
Number 4 (Stellite 6 Clad) Lateral Roughness Profiles
Depth [µm]
Length [mm]
1000 cycles
5000 cycles
10000 cycles
20000 cycles

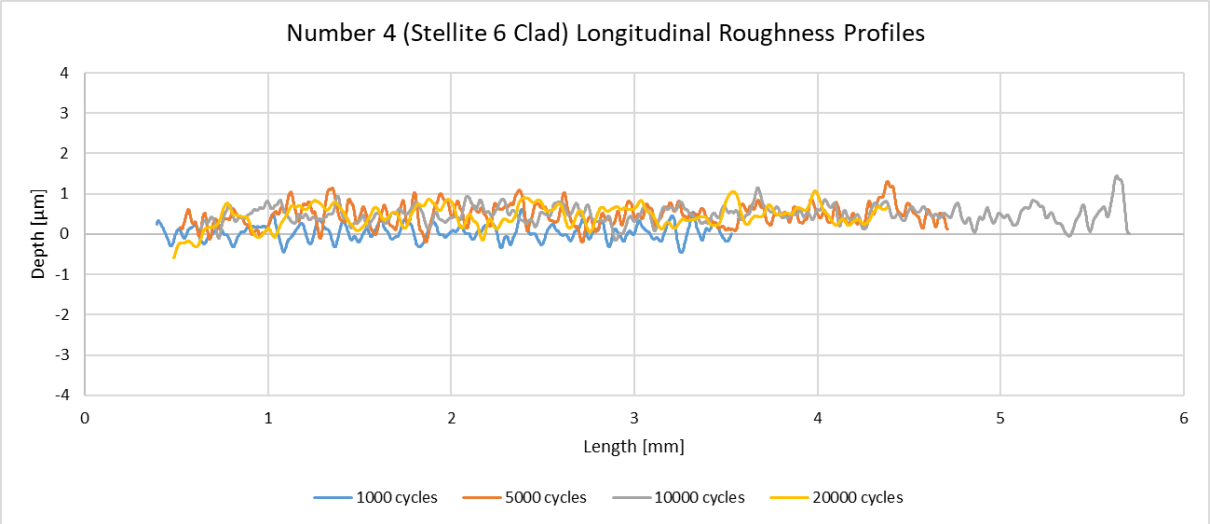
Number 4 (Stellite 6 Clad) Longitudinal Roughness Profiles
Depth [µm]
Length [mm]
1000 cycles
5000 cycles
10000 cycles
20000 cycles

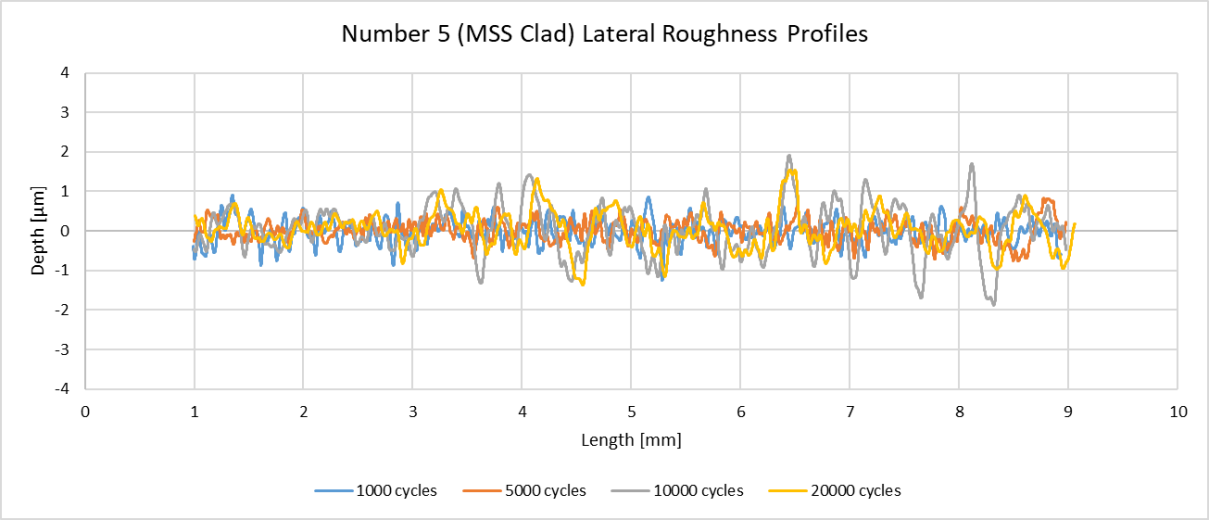
Number 5 (MSS Clad) Lateral Roughness Profiles
Depth [µm]
Length [mm]
1000 cycles
5000 cycles
10000 cycles
20000 cycles

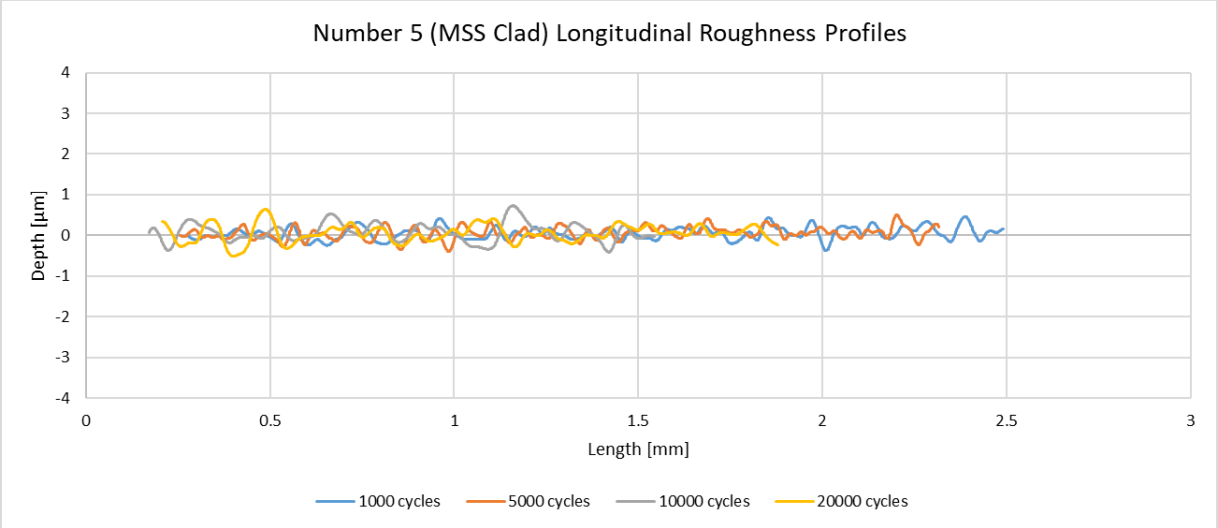
Number 5 (MSS Clad) Longitudinal Roughness Profiles
Depth [µm]
Length [mm]
1000 cycles
5000 cycles
10000 cycles
20000 cycles

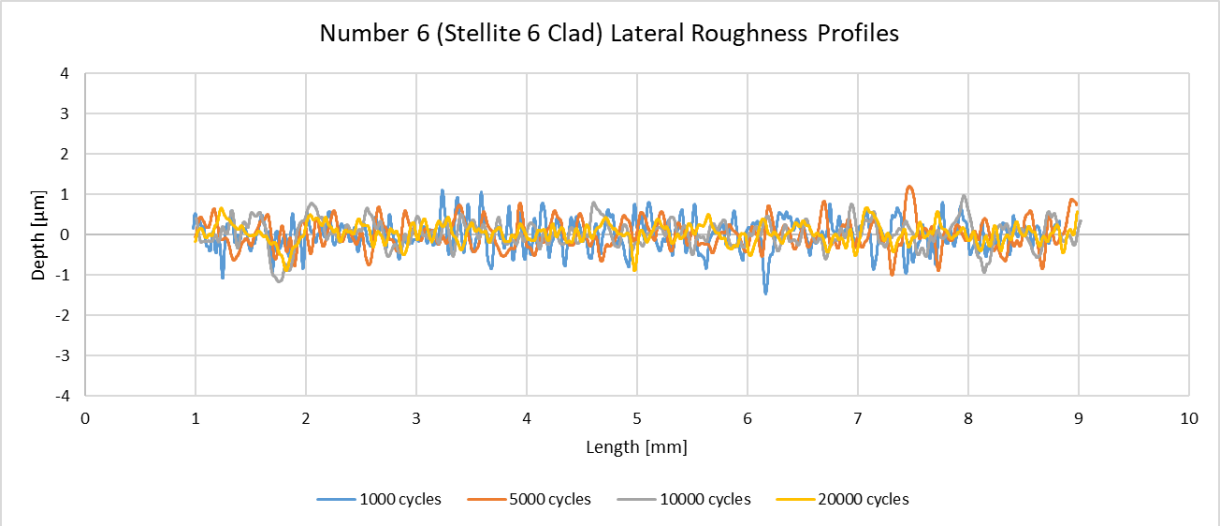
Number 6 (Stellite 6 Clad) Lateral Roughness Profiles
Depth [µm]
Length [mm]
1000 cycles
5000 cycles
10000 cycles
20000 cycles

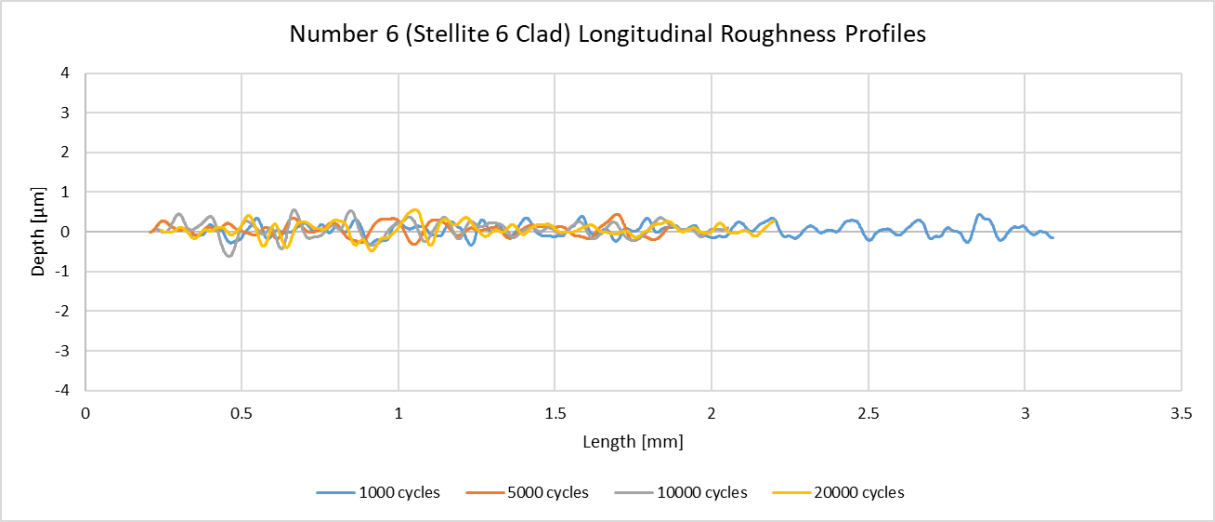
Number 6 (Stellite 6 Clad) Longitudinal Roughness Profiles
Depth [µm]
Length [mm]
1000 cycles
5000 cycles
10000 cycles
20000 cycles

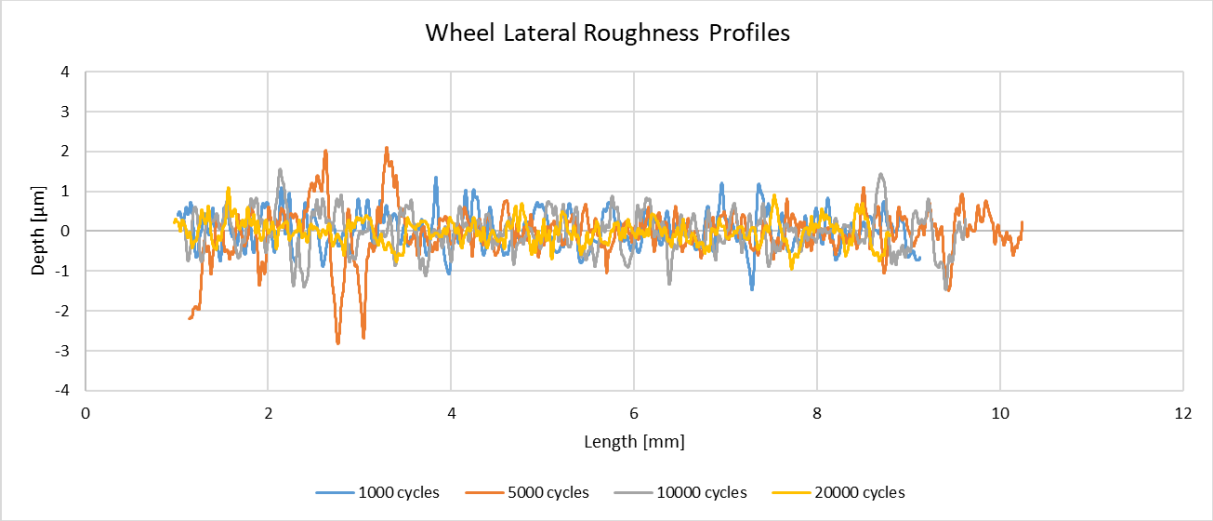

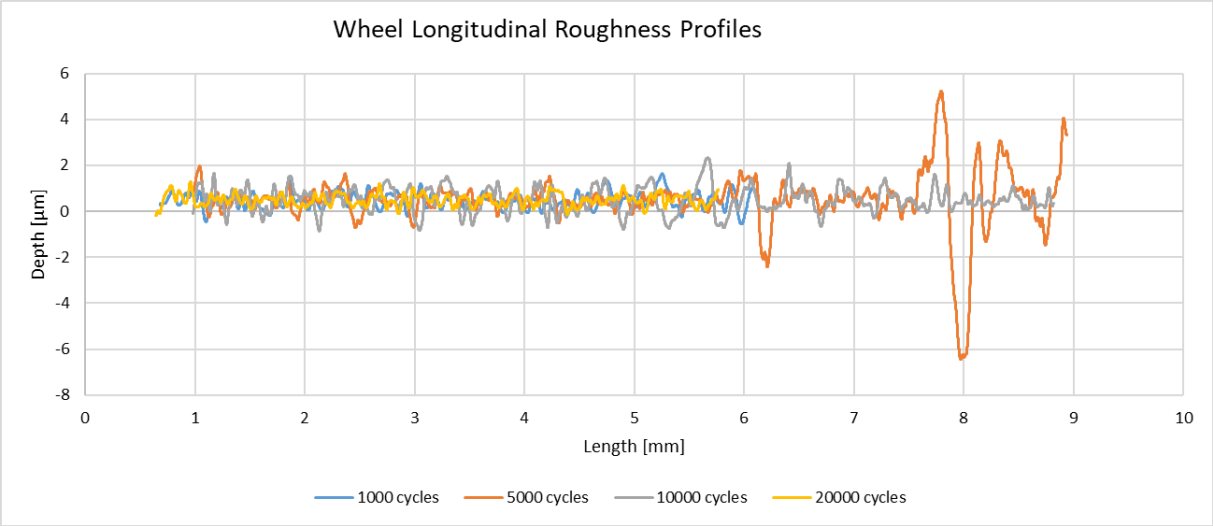

Figure 12.8: Small scale repair tests surface evolution roughness graphs from Alicona with 1800 MPa, 1% slip dry test condition

12.1.3 Appendix 5.C – Microstructure Images

R260 Clad (Number 1)

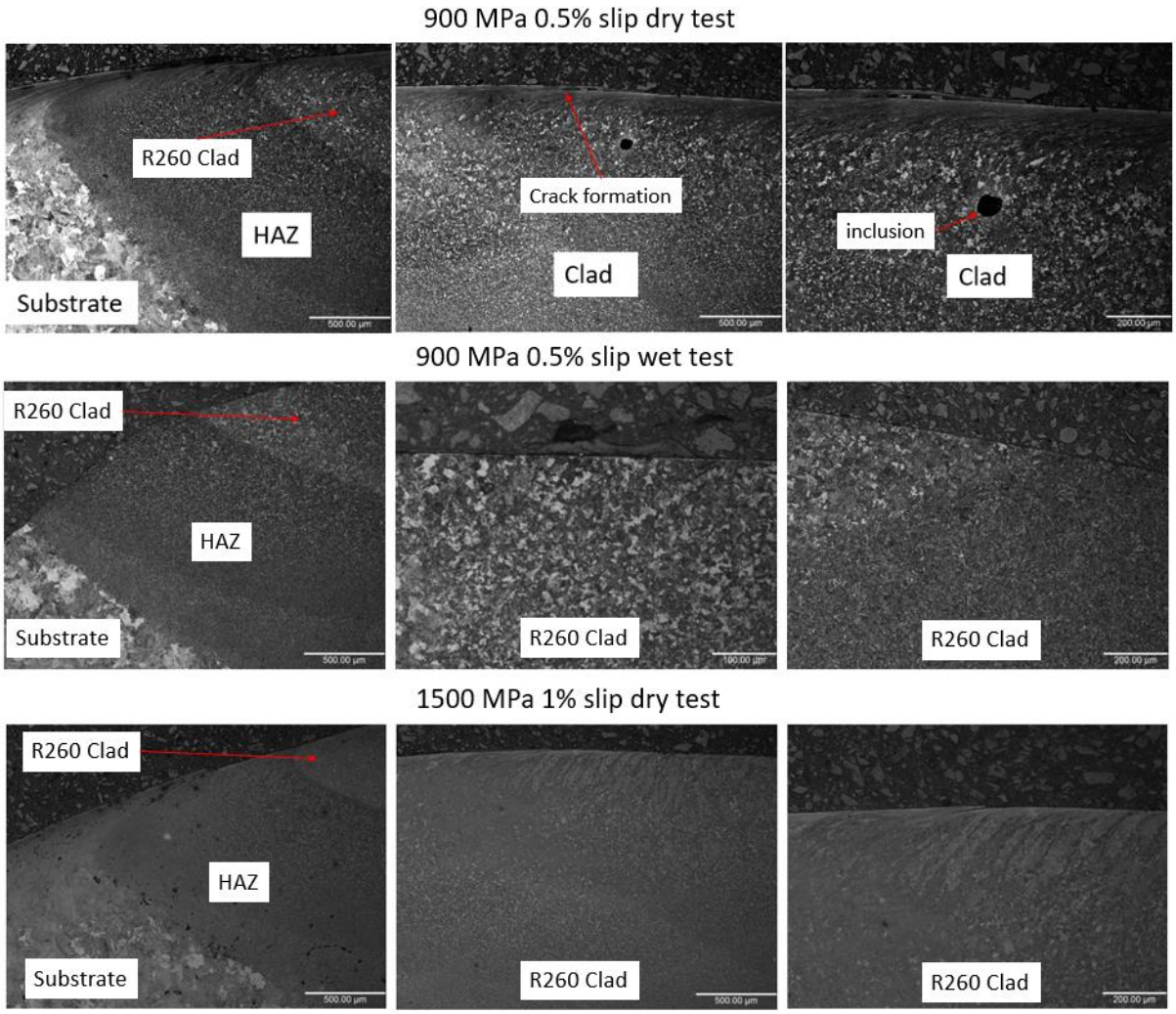

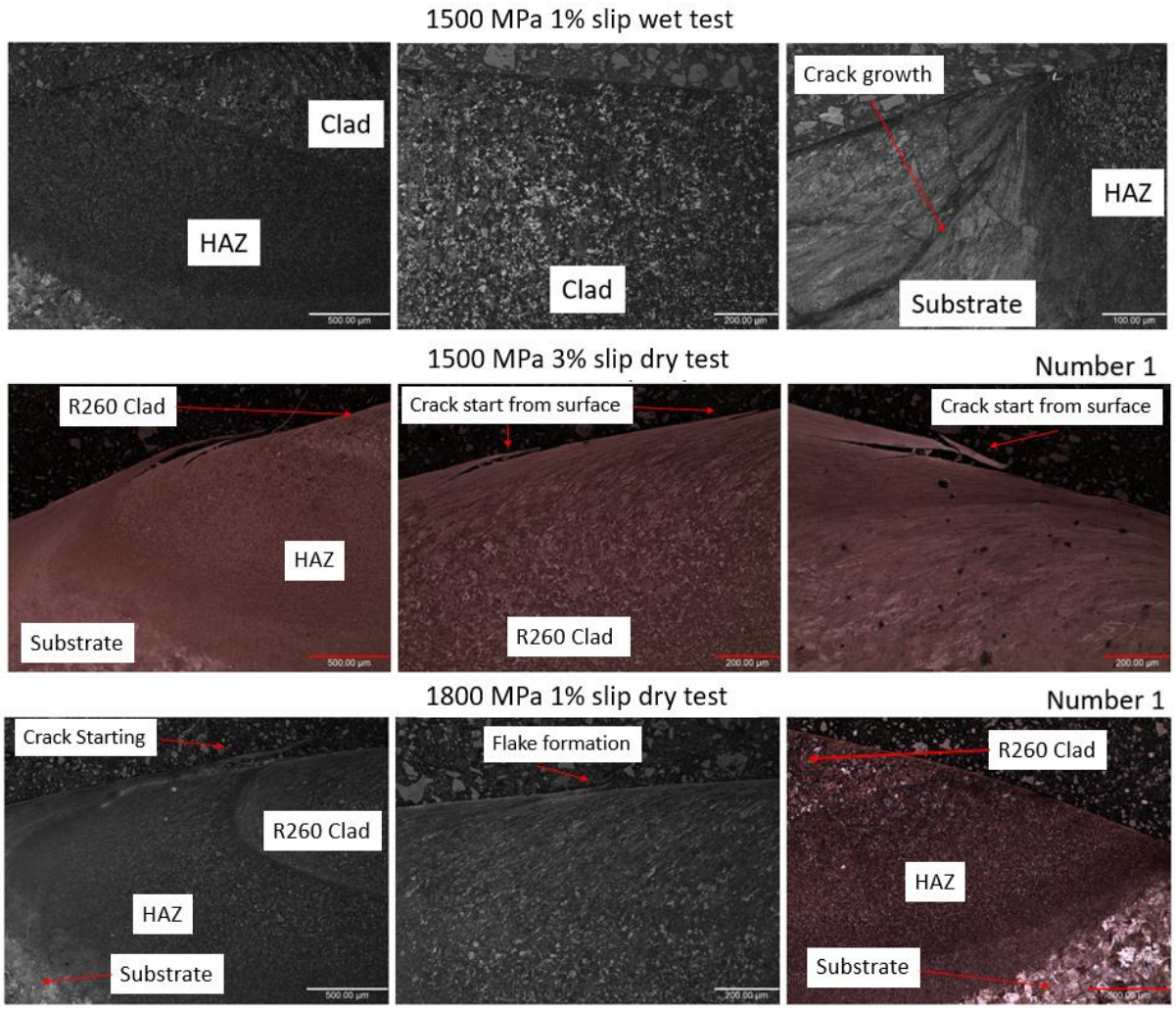

Figure 12.9: Small scale repair tests number 1 (R260 clad) microstructure images

MSS Clad (Number 2,3 and 5)

Number 2

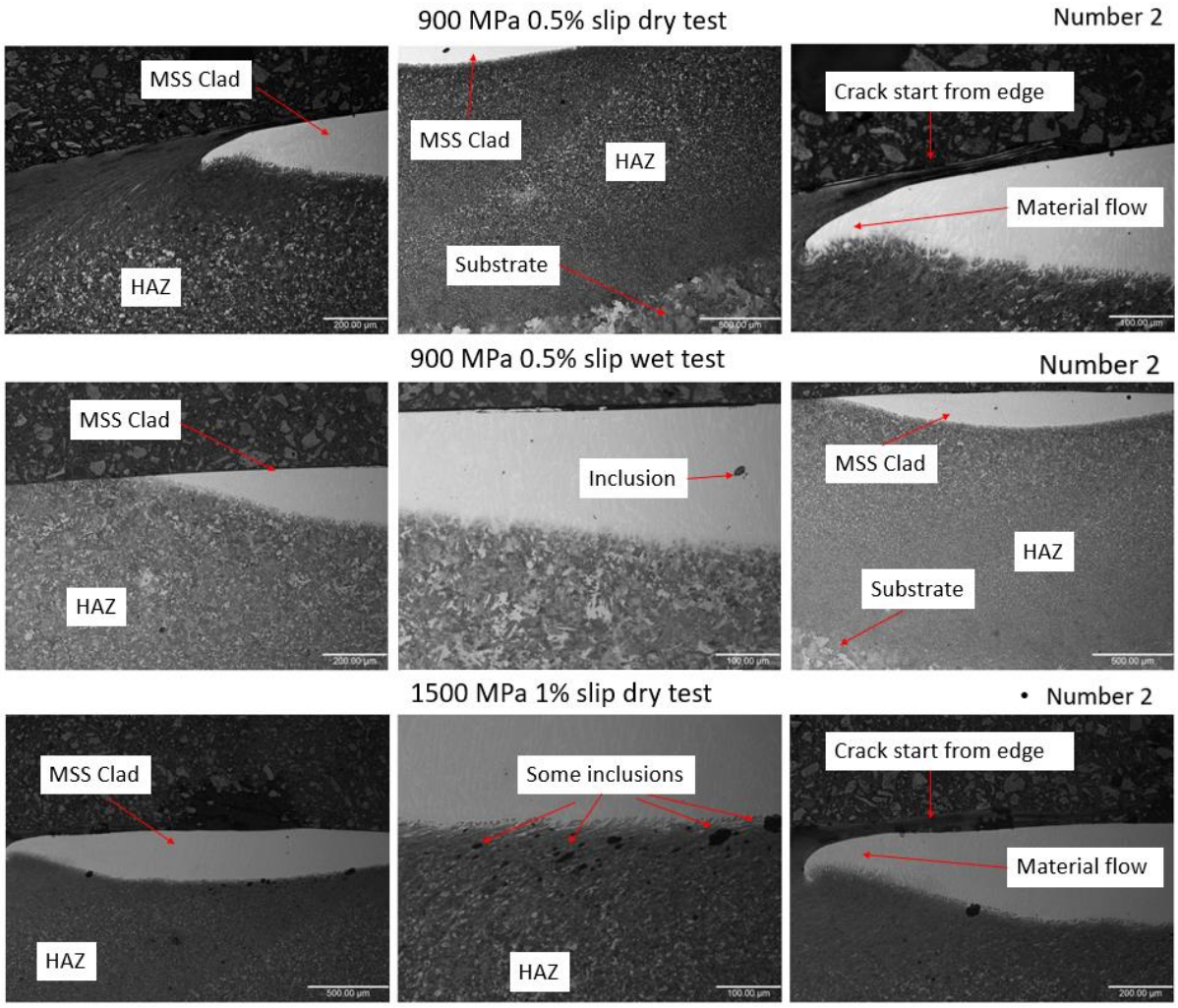

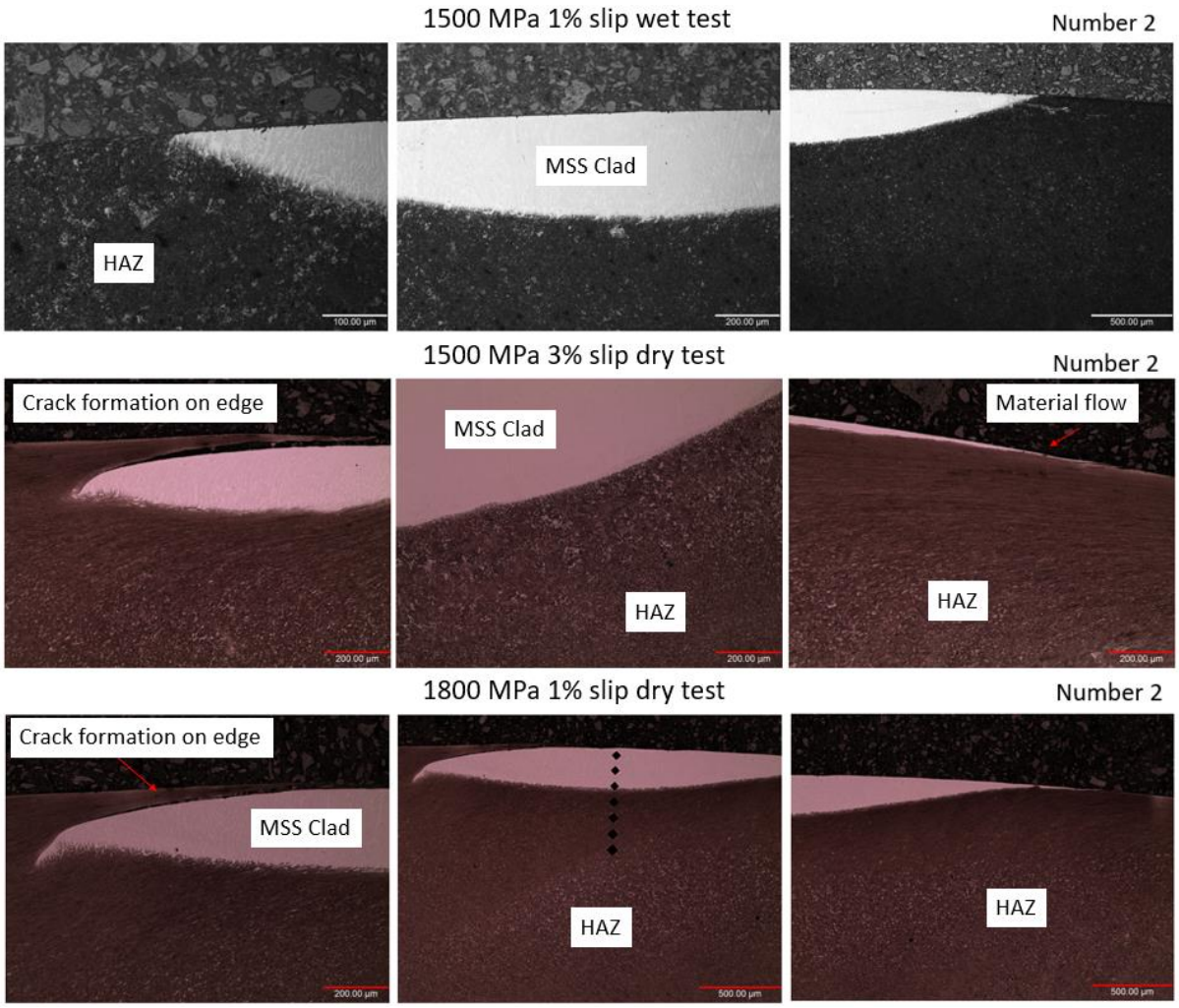

Figure 12.10: Small scale repair tests number 2 (MSS clad) microstructure images

Number 3

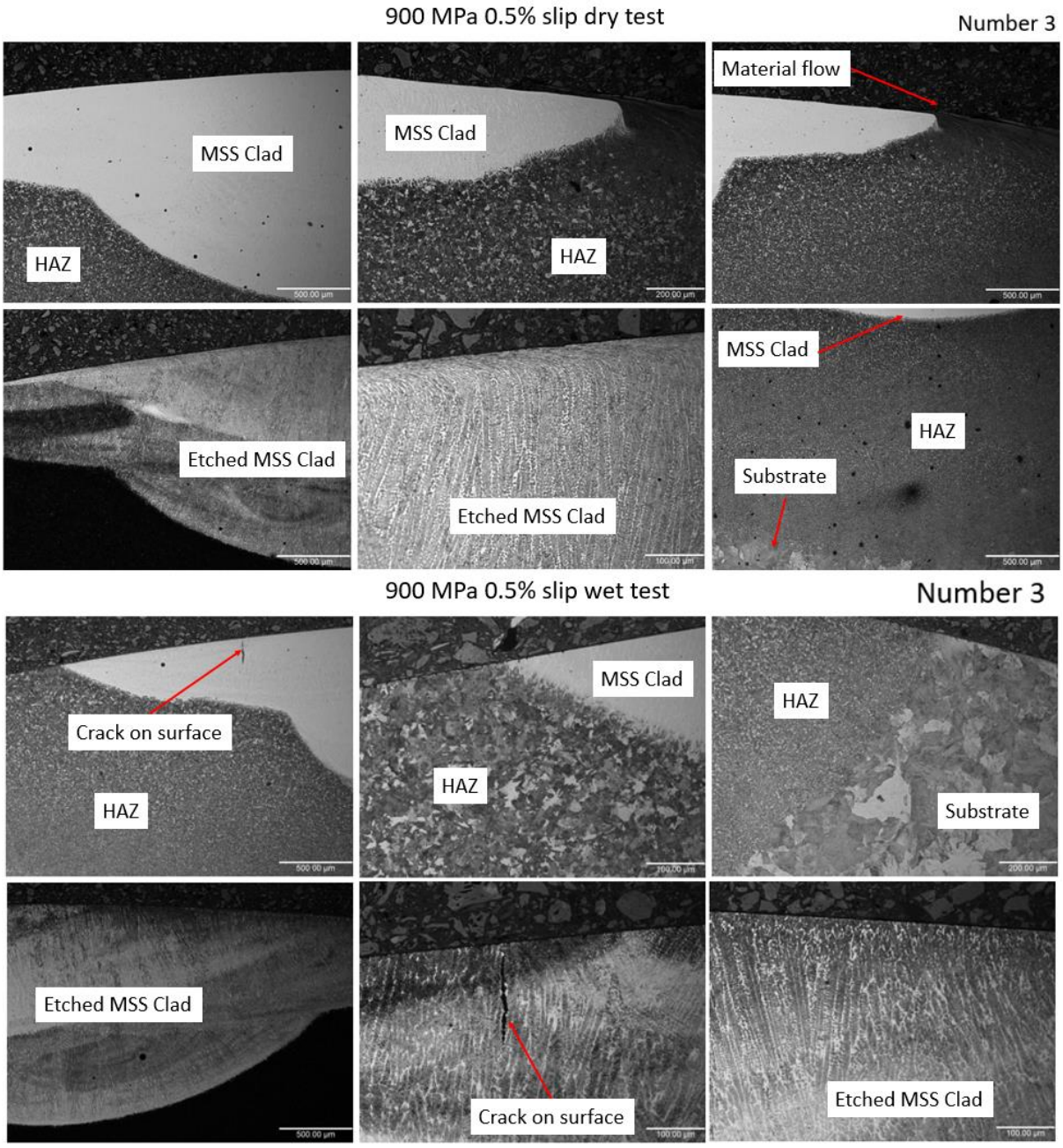
900 MPa 0.5% slip dry test
Number 3
MSS Clad
HAZ
MSS Clad
HAZ
Material flow
Etched MSS Clad
Etched MSS Clad
MSS Clad
HAZ
Substrate
900 MPa 0.5% slip wet test
Number 3
Crack on surface
HAZ
MSS Clad
HAZ
HAZ
Substrate
Etched MSS Clad
Crack on surface
Etched MSS Clad

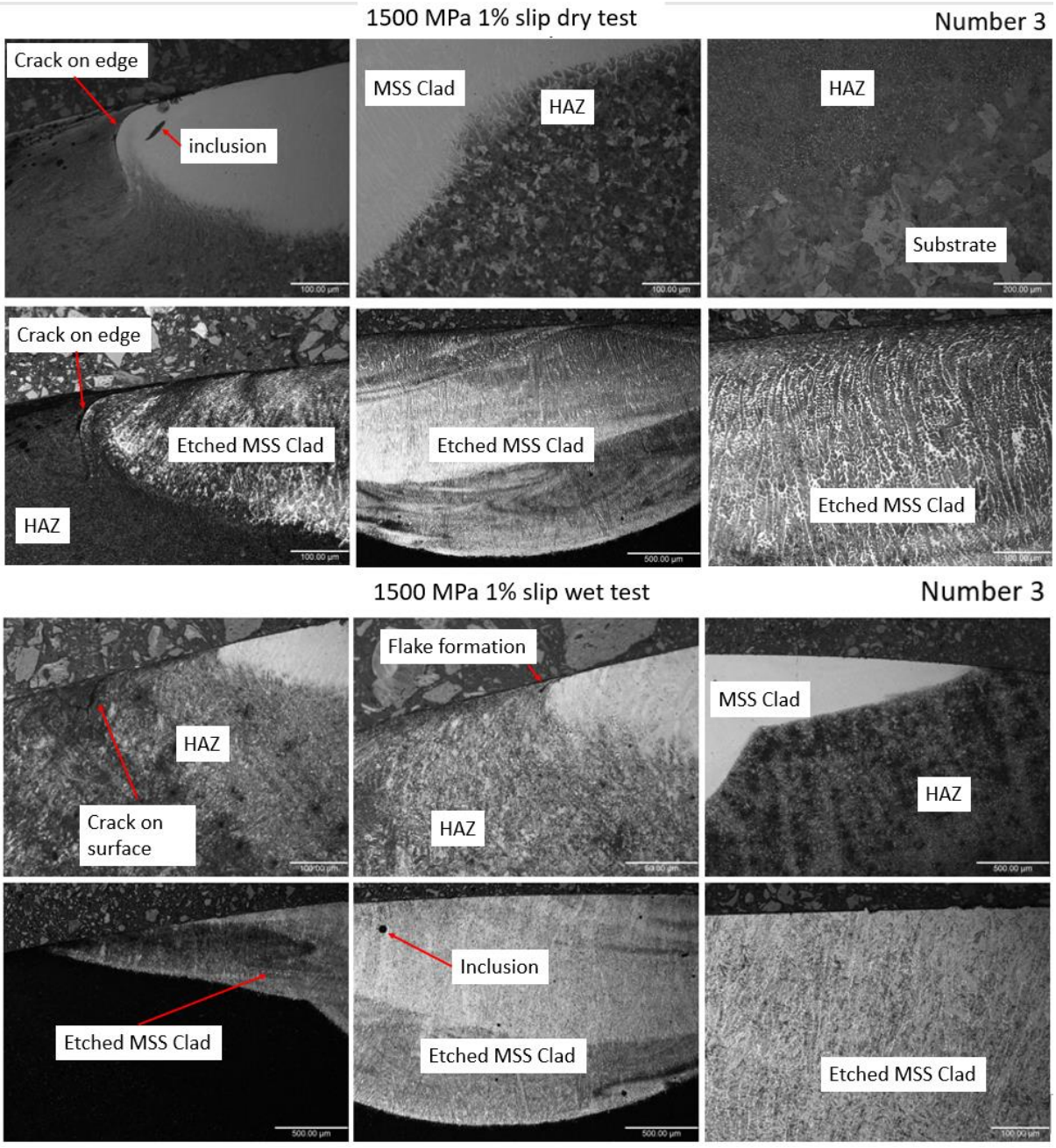
1500 MPa 1% slip dry test
Number 3
Crack on edge
inclusion
MSS Clad
HAZ
HAZ
Substrate
Crack on edge
Etched MSS Clad
HAZ
Etched MSS Clad
Etched MSS Clad
1500 MPa 1% slip wet test
Number 3
HAZ
Crack on surface
Flake formation
HAZ
MSS Clad
HAZ
Etched MSS Clad
Inclusion
Etched MSS Clad
Etched MSS Clad

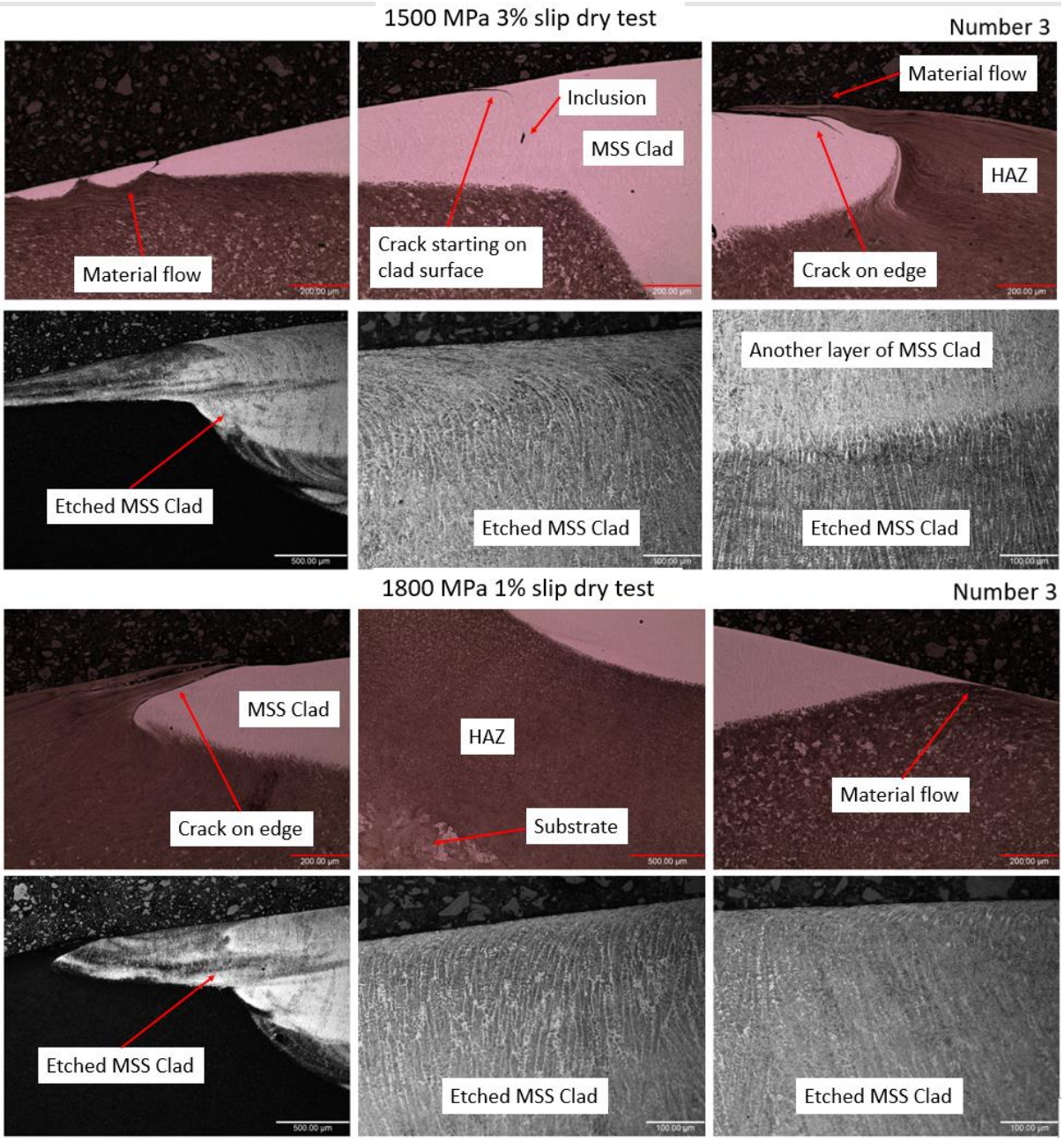

Figure 12.11: Small scale repair tests number 3 (MSS clad) microstructure images

Number 5

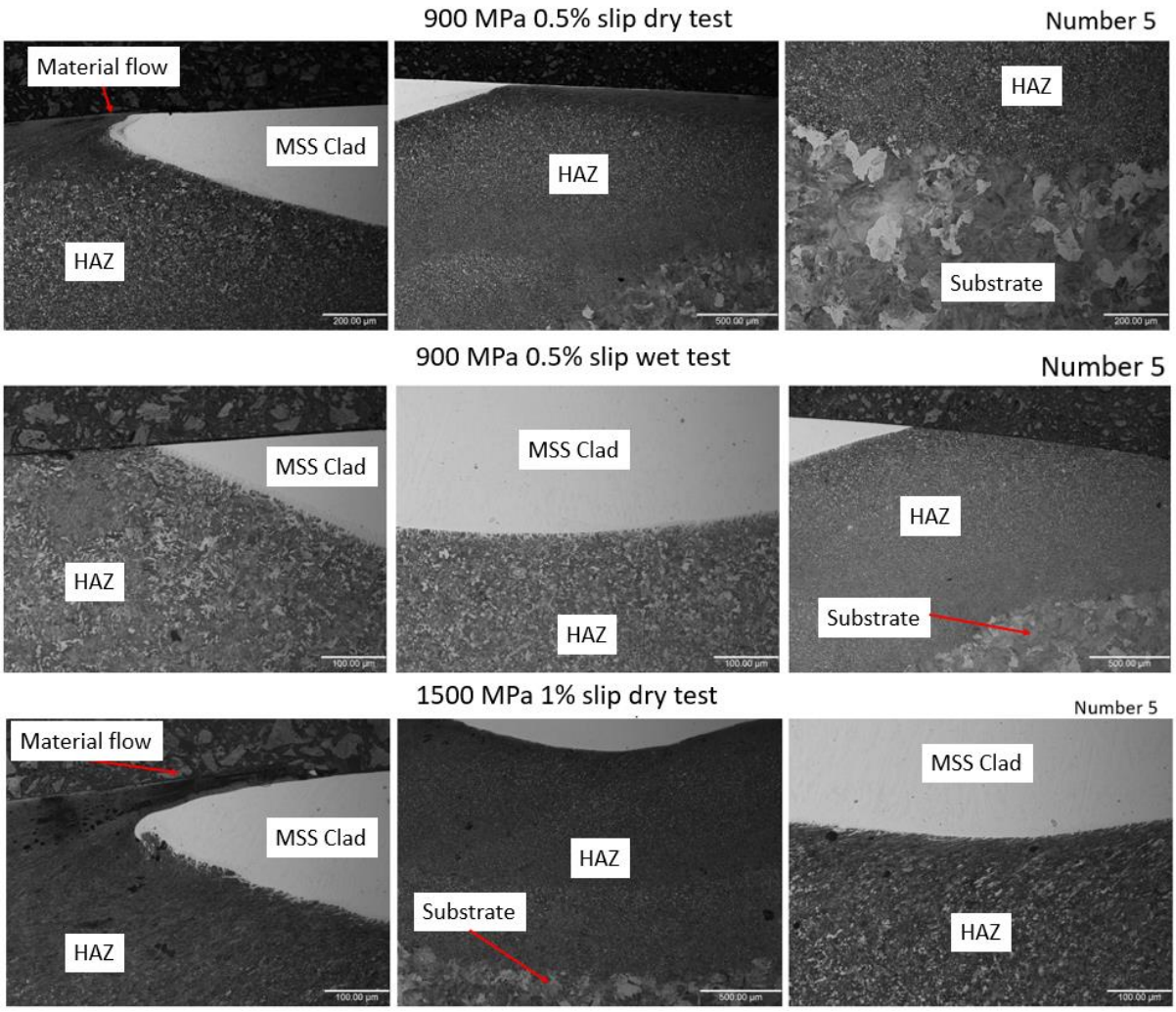
900 MPa 0.5% slip dry test
Number 5
Material flow
MSS Clad
HAZ
HAZ
HAZ
Substrate
900 MPa 0.5% slip wet test
Number 5
MSS Clad
HAZ
MSS Clad
HAZ
HAZ
Substrate
1500 MPa 1% slip dry test
Number 5
Material flow
MSS Clad
HAZ
HAZ
Substrate
MSS Clad
HAZ

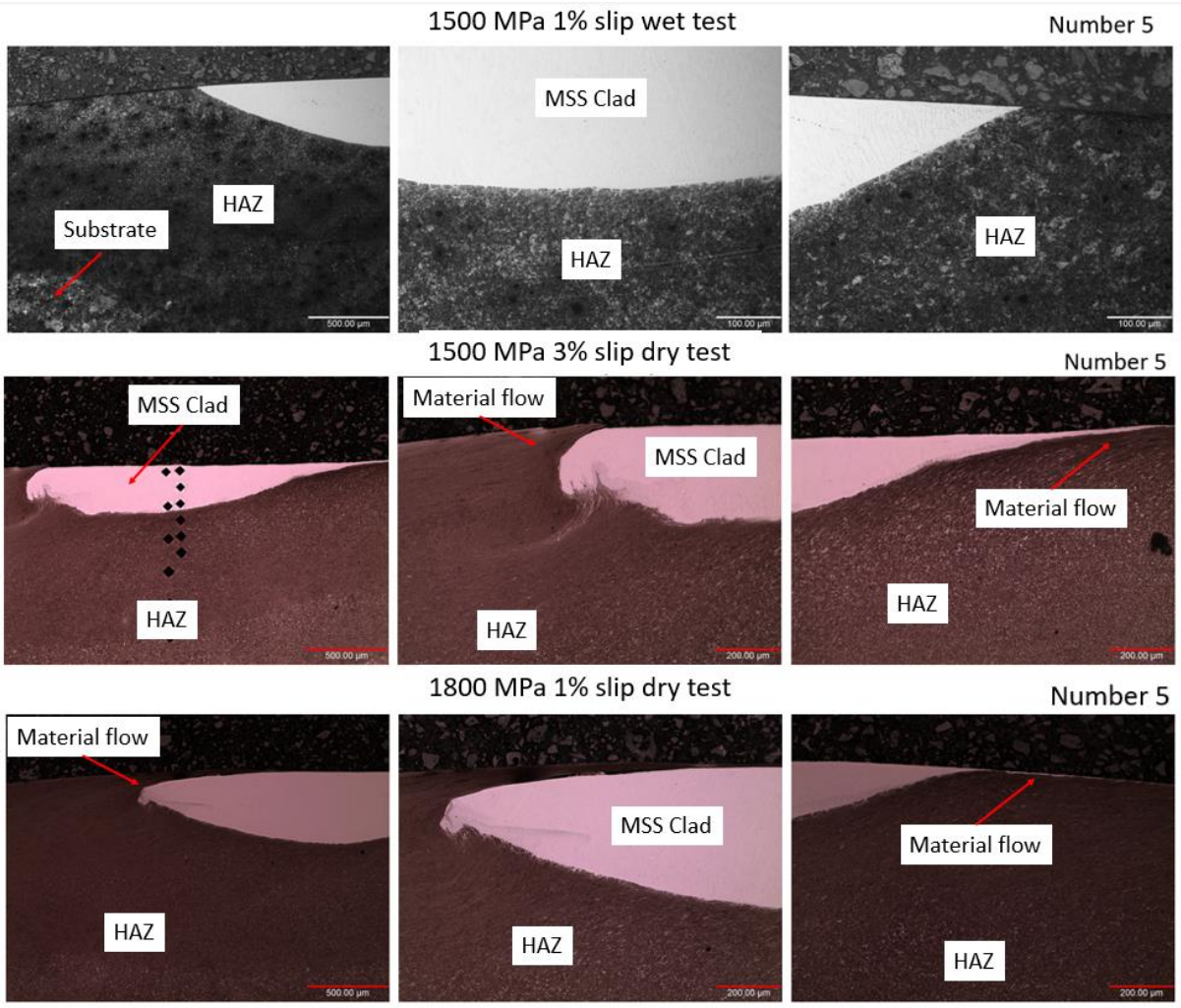

Figure 12.12: Small scale repair tests number 5 (MSS clad) microstructure images

Stellite 6 Clad (Number 4 and 6)

Number 4

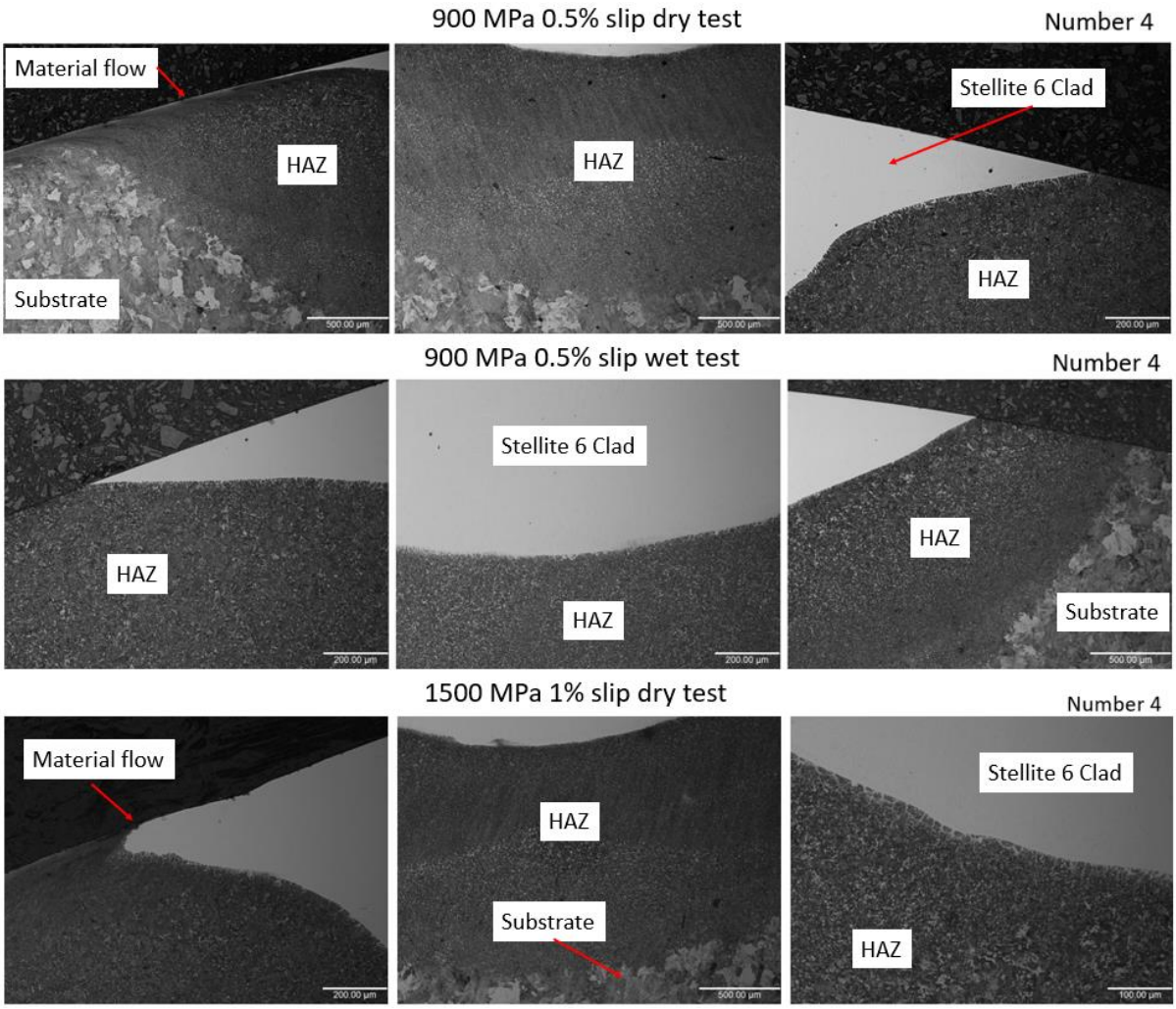

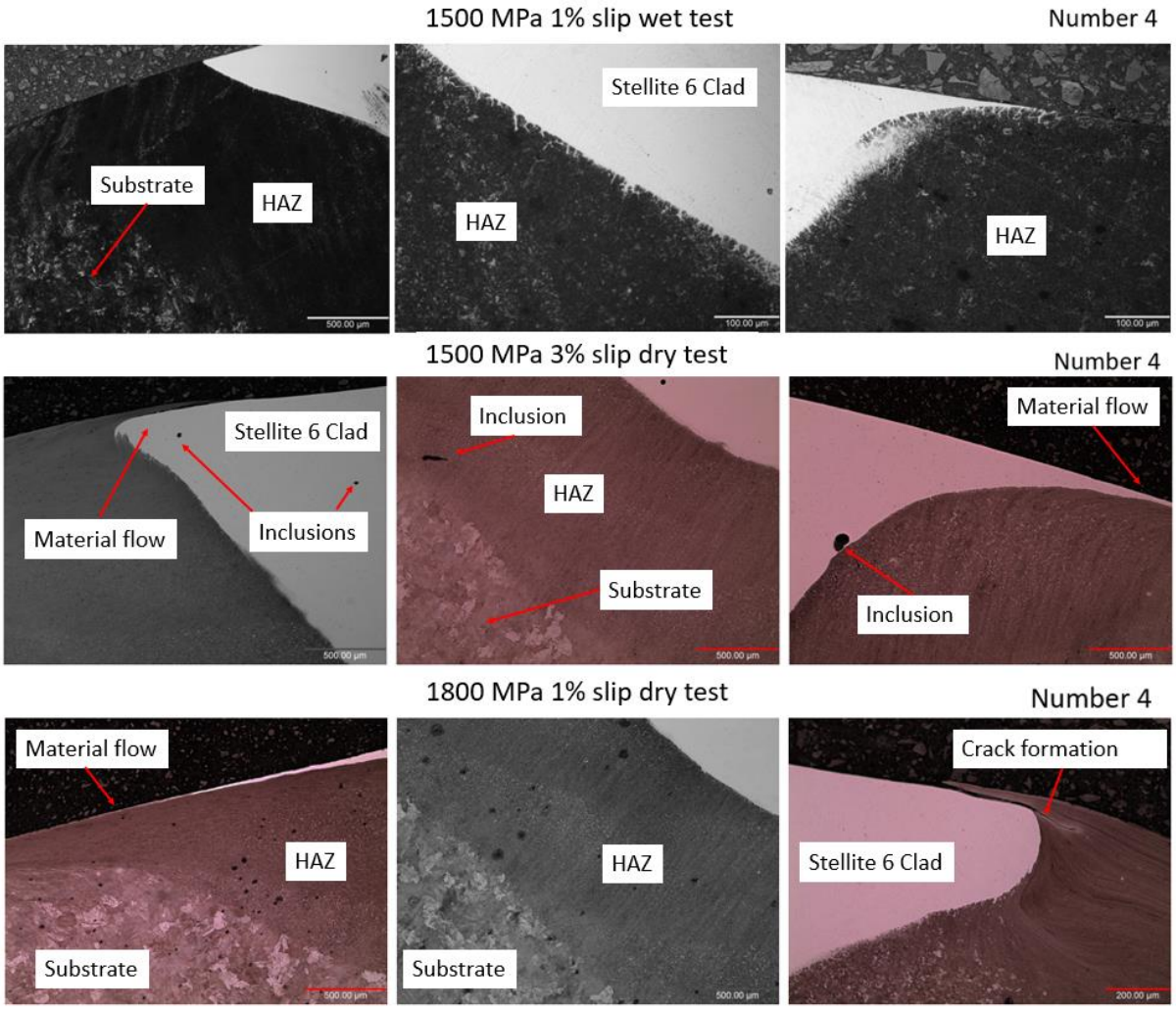

Figure 12.13: Small scale repair tests number 4 (Stellite 6 clad) microstructure images

Number 6

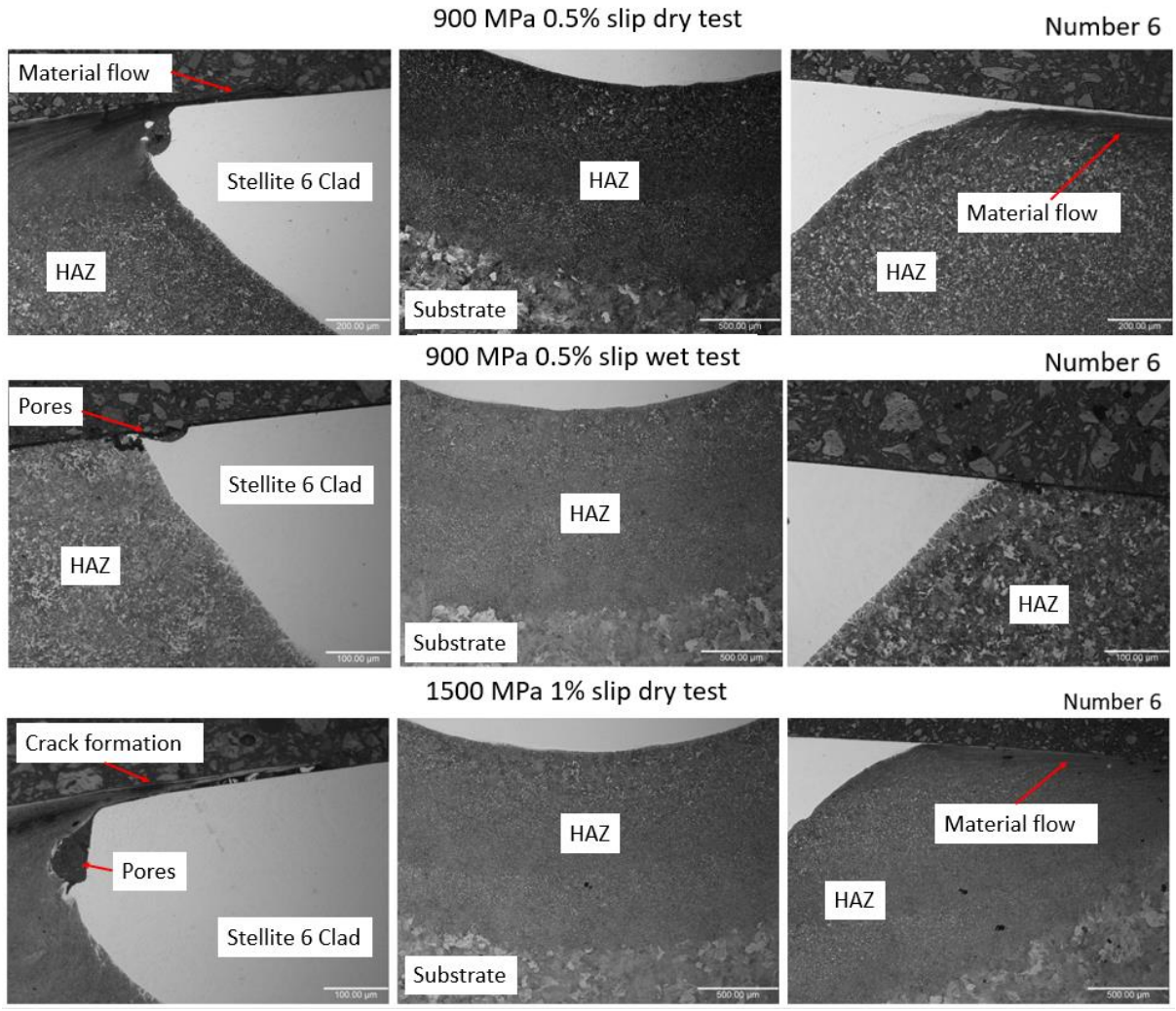
900 MPa 0.5% slip dry test
Number 6
Material flow
Stellite 6 Clad
HAZ
HAZ
Substrate
Material flow
HAZ
900 MPa 0.5% slip wet test
Number 6
Pores
Stellite 6 Clad
HAZ
HAZ
Substrate
HAZ
1500 MPa 1% slip dry test
Number 6
Crack formation
Pores
Stellite 6 Clad
HAZ
Substrate
Material flow
HAZ

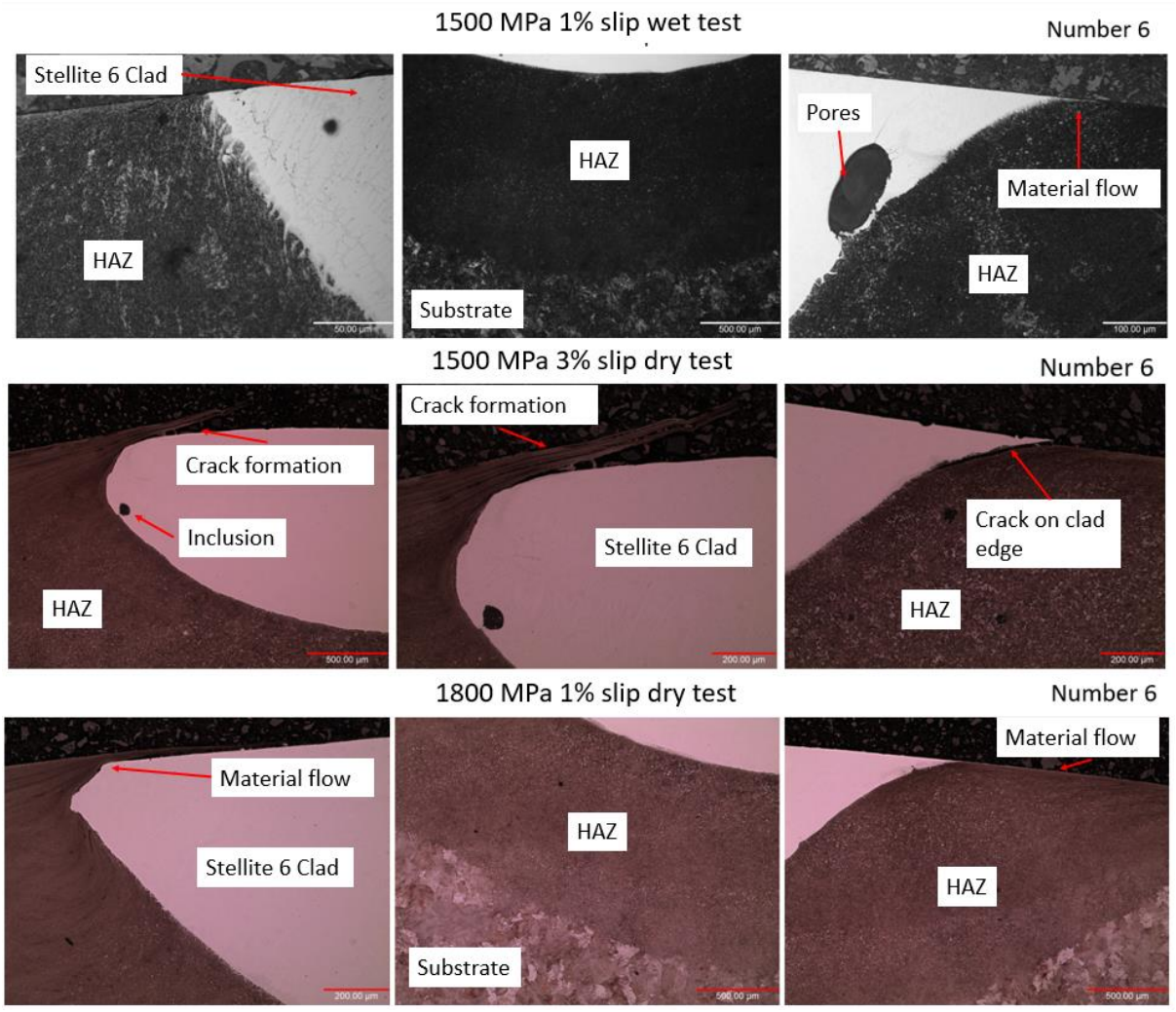

Figure 12.14: Small scale repair tests number 6 (Stellite 6 clad) microstructure images

12.2 Appendix for Chapter 7

12.2.1 Appendix 7.A – Surface Evaluations

1400 MPa 0.5% Slip Tests

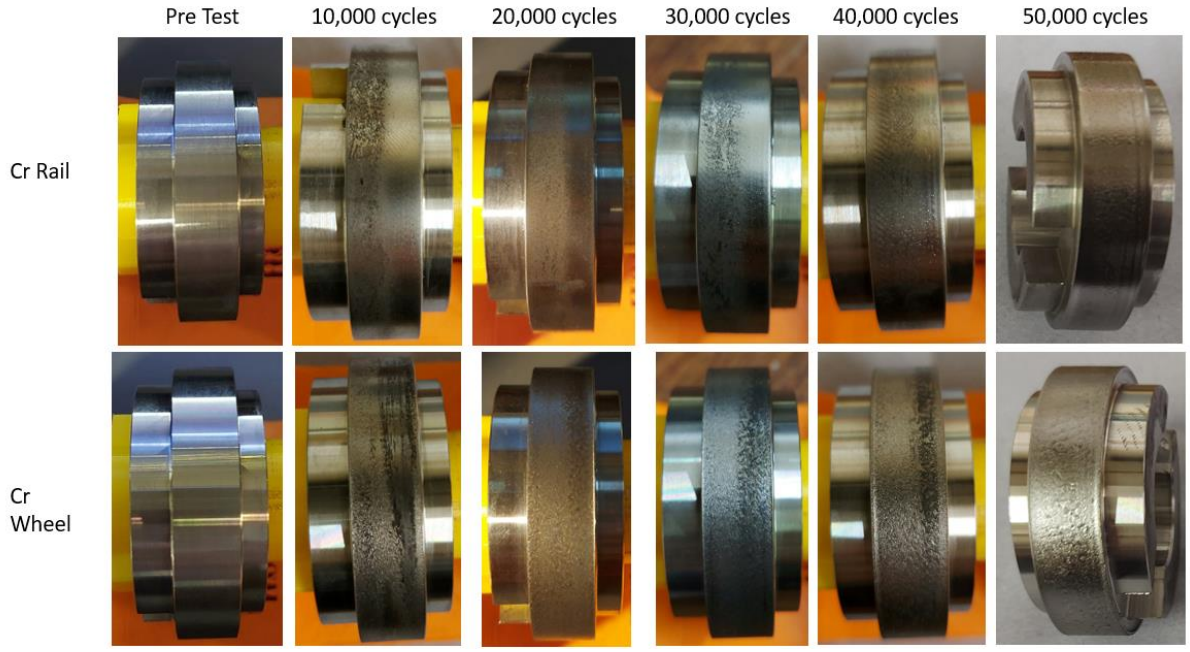

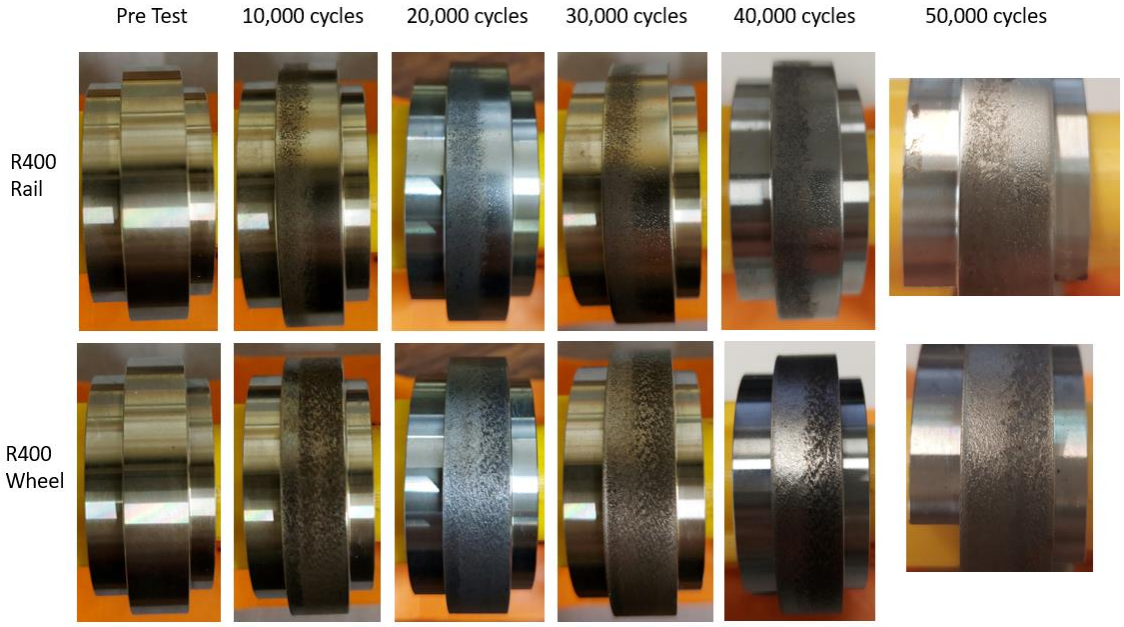

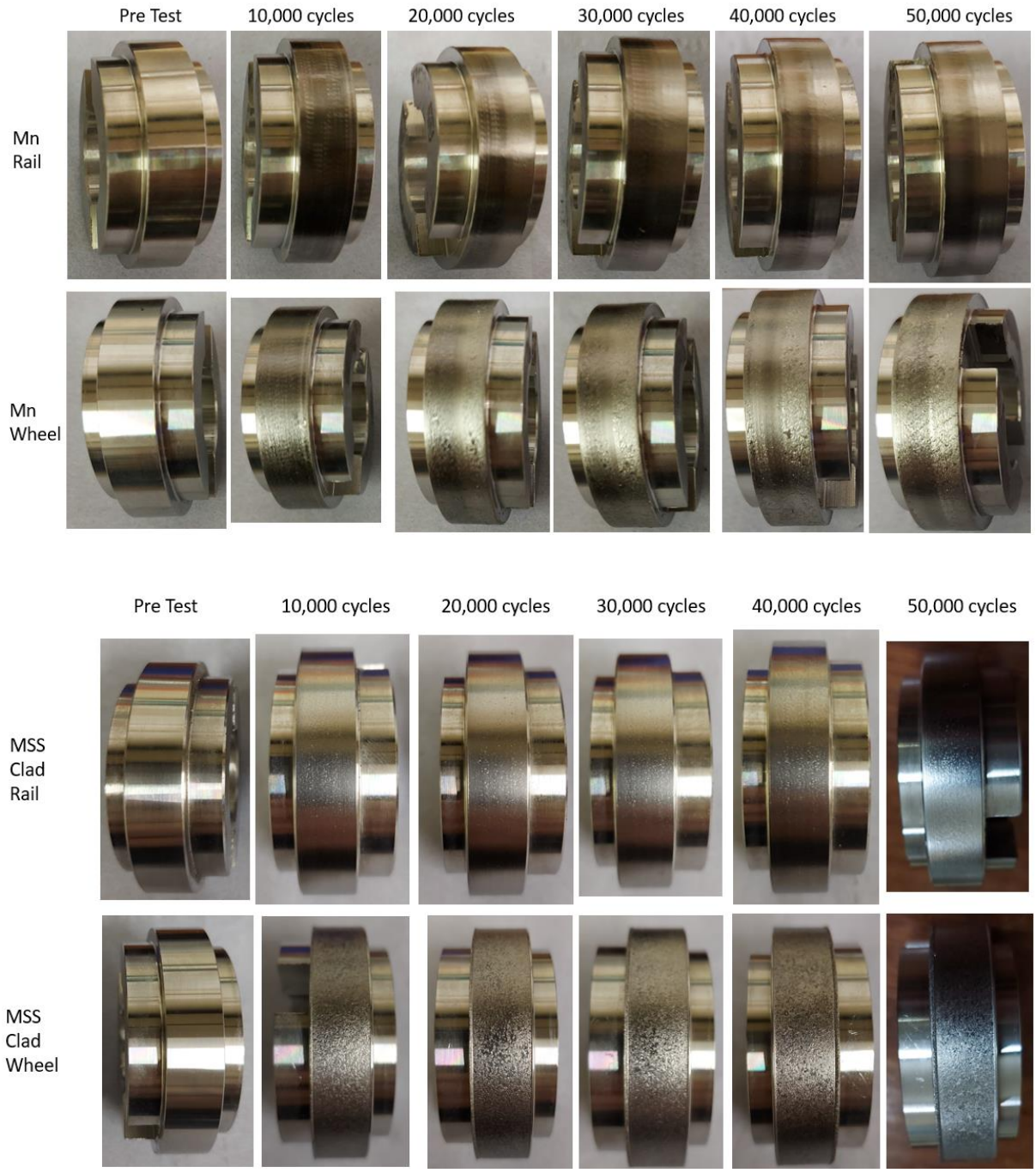

Figure 12.15: 1400 MPa, 0.5% slip test surface evaluation images of premium (Cr, R400, Mn) and MSS clad rails and ERT 7 wheels

1800 MPa 0.5% Slip Tests

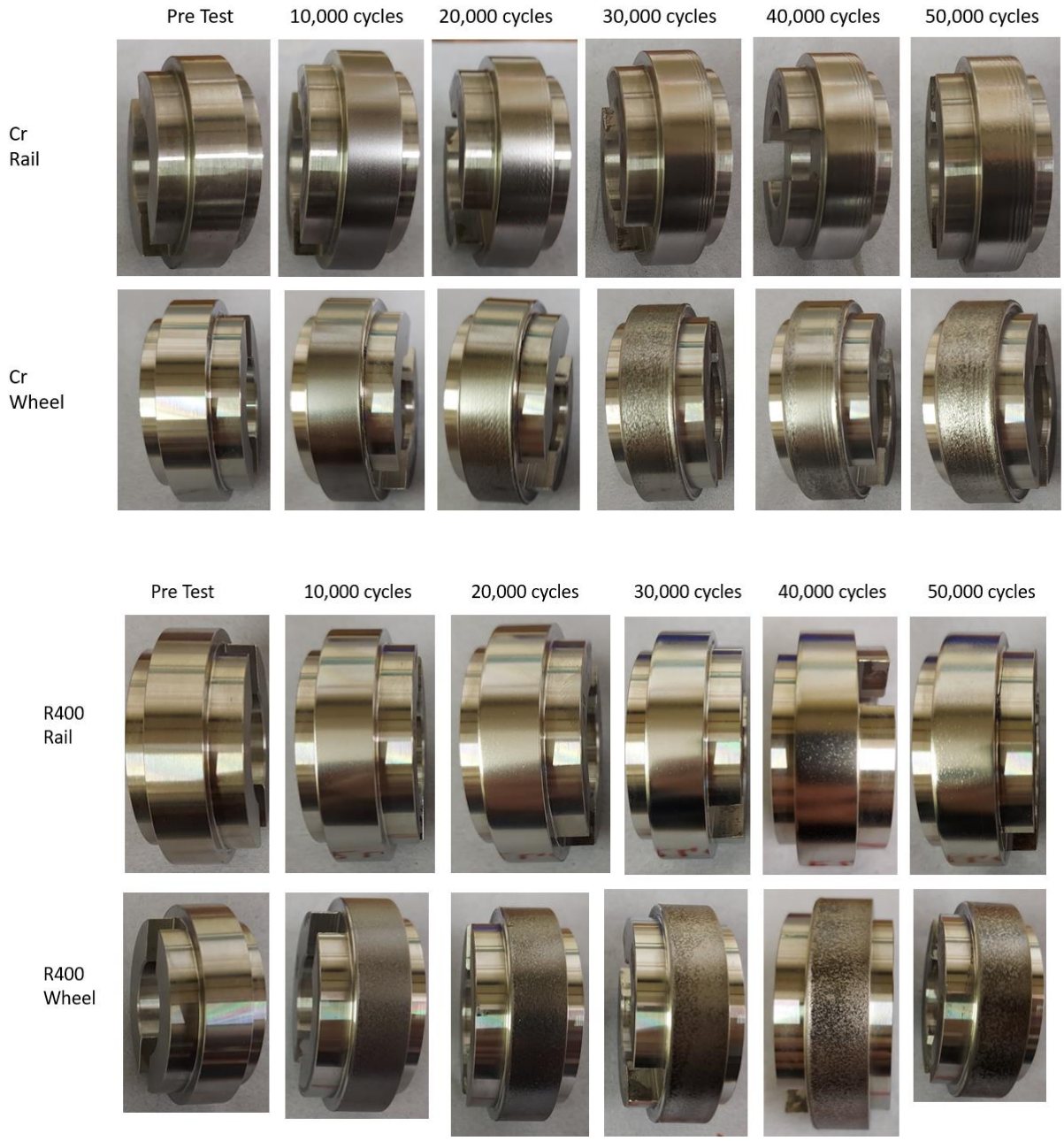

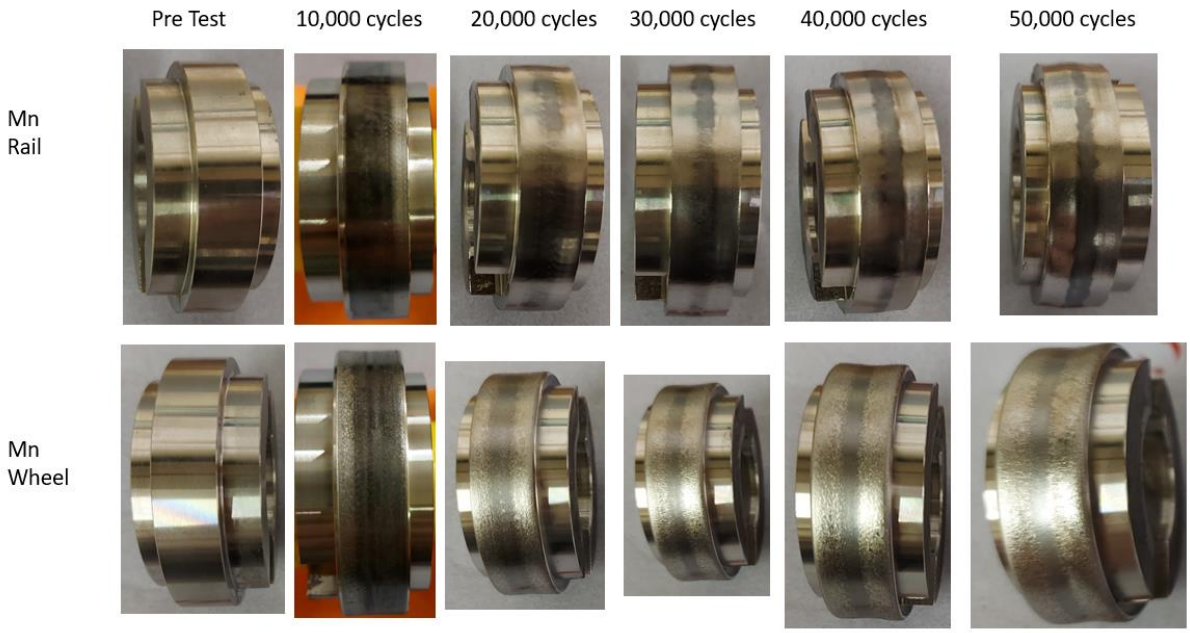

Figure 12.16: 1800 MPa, 0.5% slip test surface evaluation images of premium (Cr, R400, Mn) and MSS clad rails and ERT 7 wheels

12.2.2 Appendix 7.B – Wear Debris

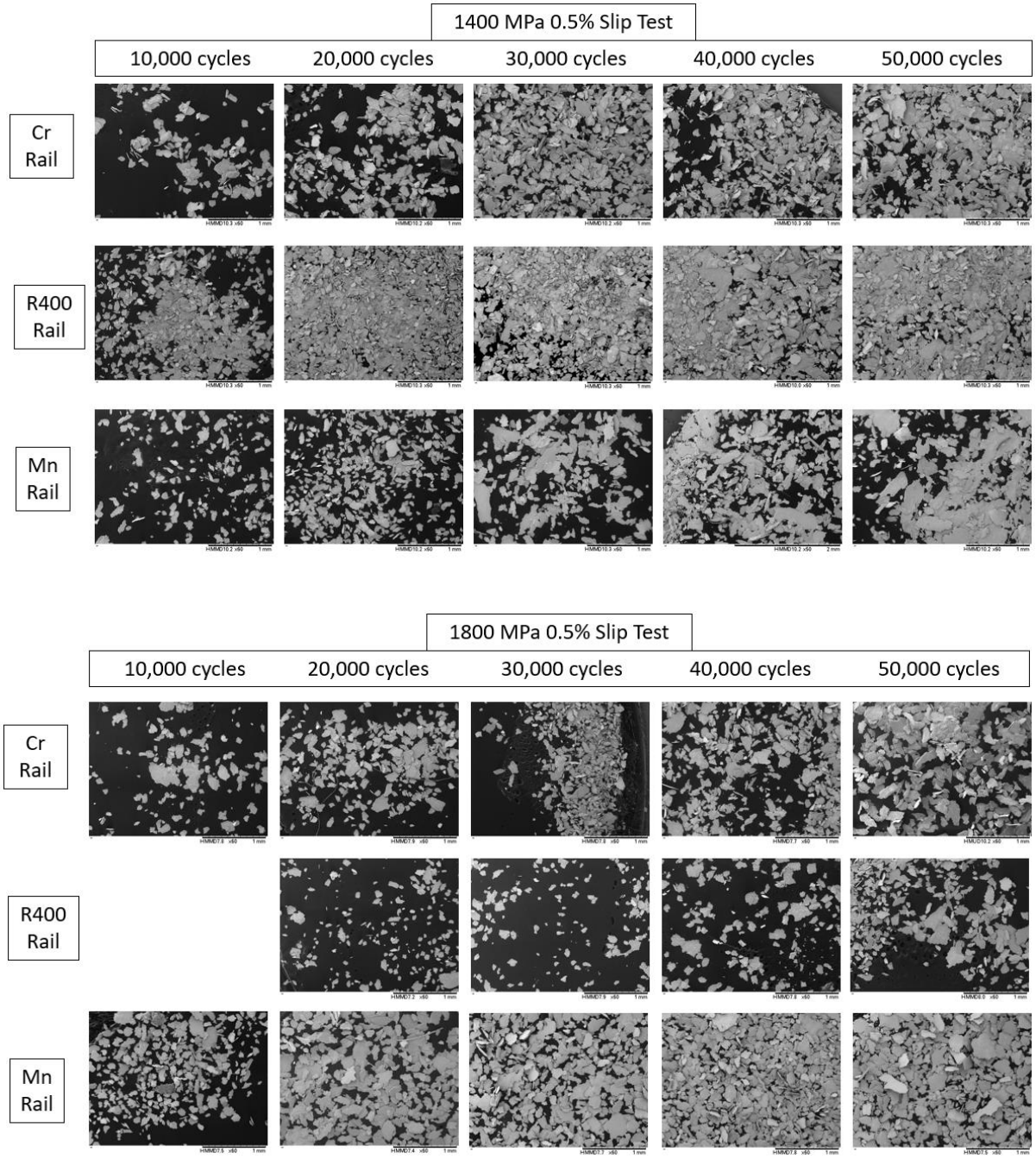

Figure 12.17: 1400 MPa, 0.5% slip and 1800 MPa, 0.5% slip tests wear debris SEM images of premium (Cr, R400, Mn) rail tests

12.2.3 Appendix 7.C – Nano Hardness Maps

Chromium (Cr)

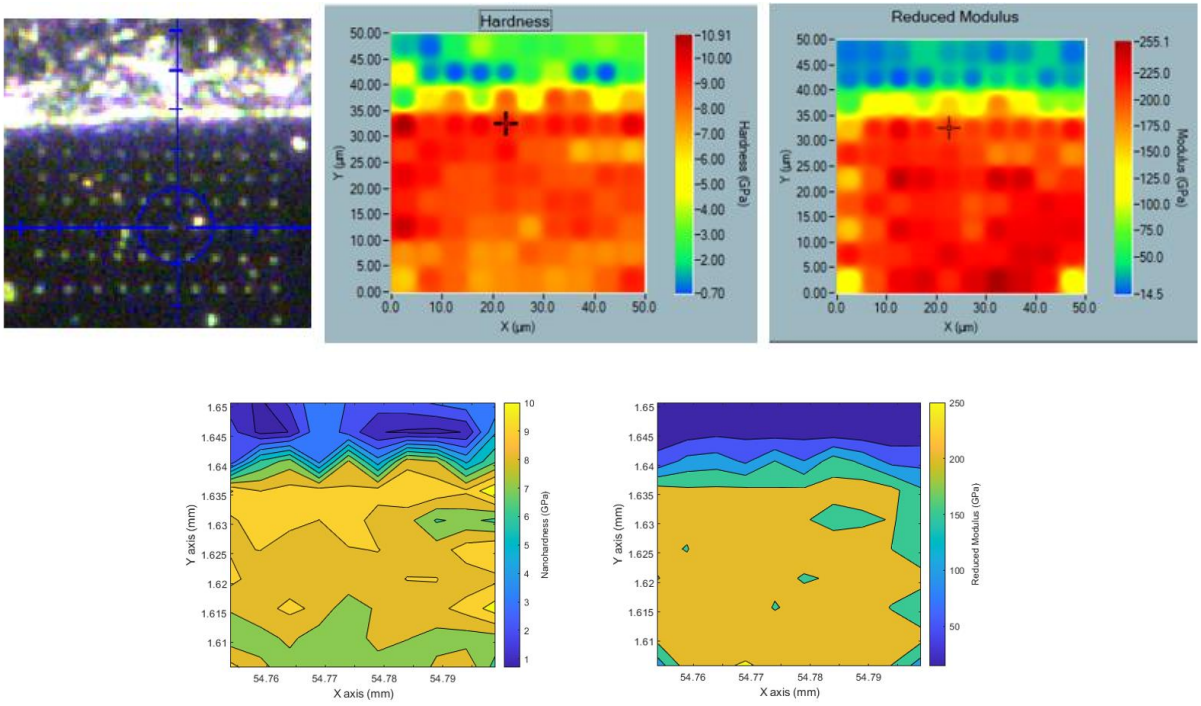

a)

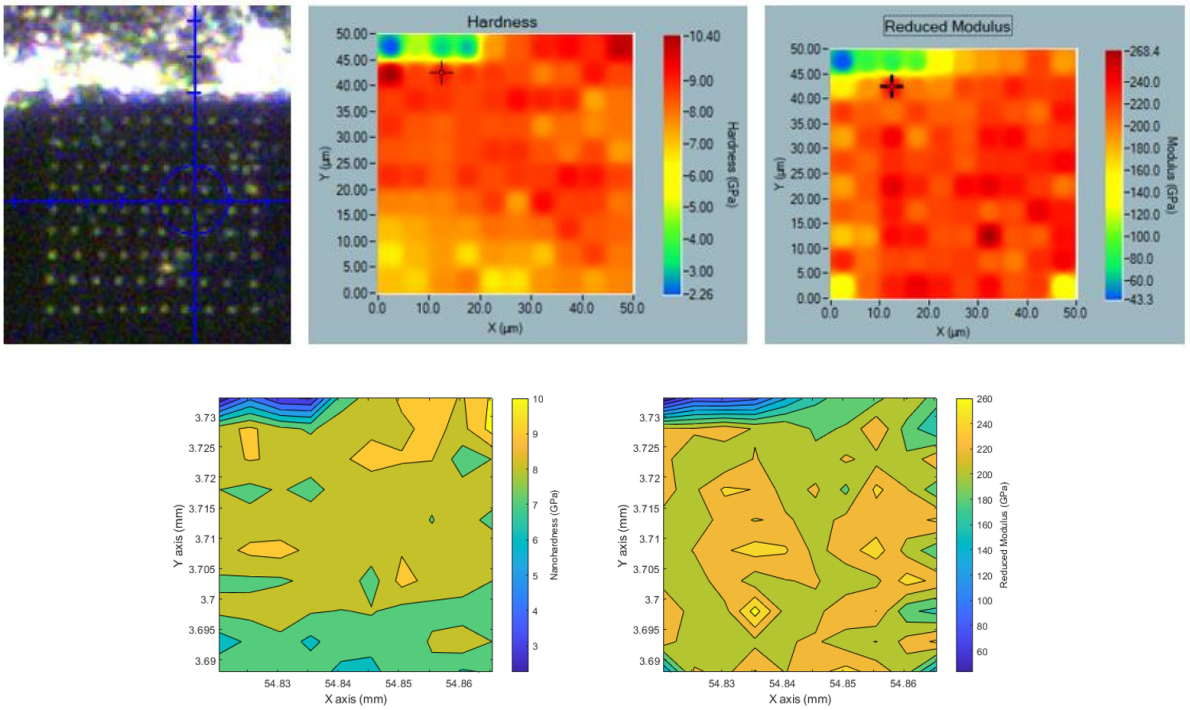

b)

Figure 12.18: Nano-indenter hardness maps of Cr material on the surface point of disc: (a) Cr test at 1400 MPa; (b) Cr test at 1800 MPa

Manganese (Mn)

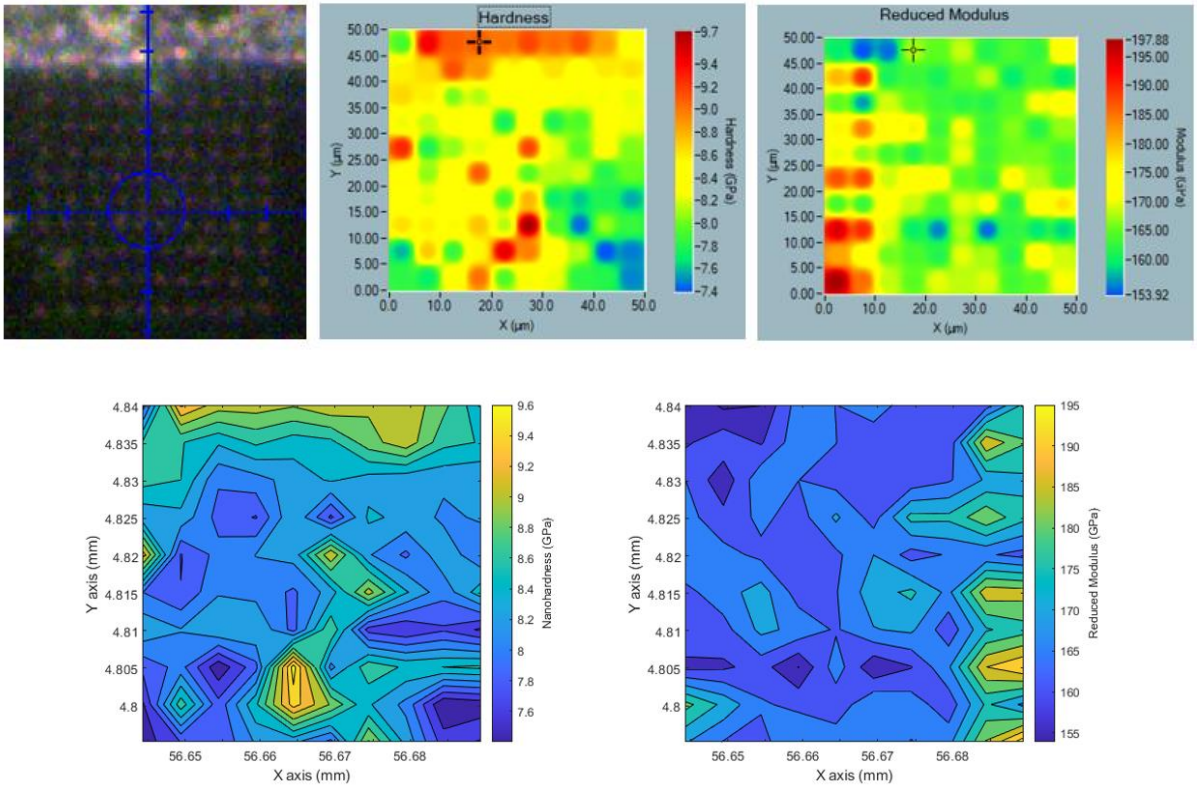

a)

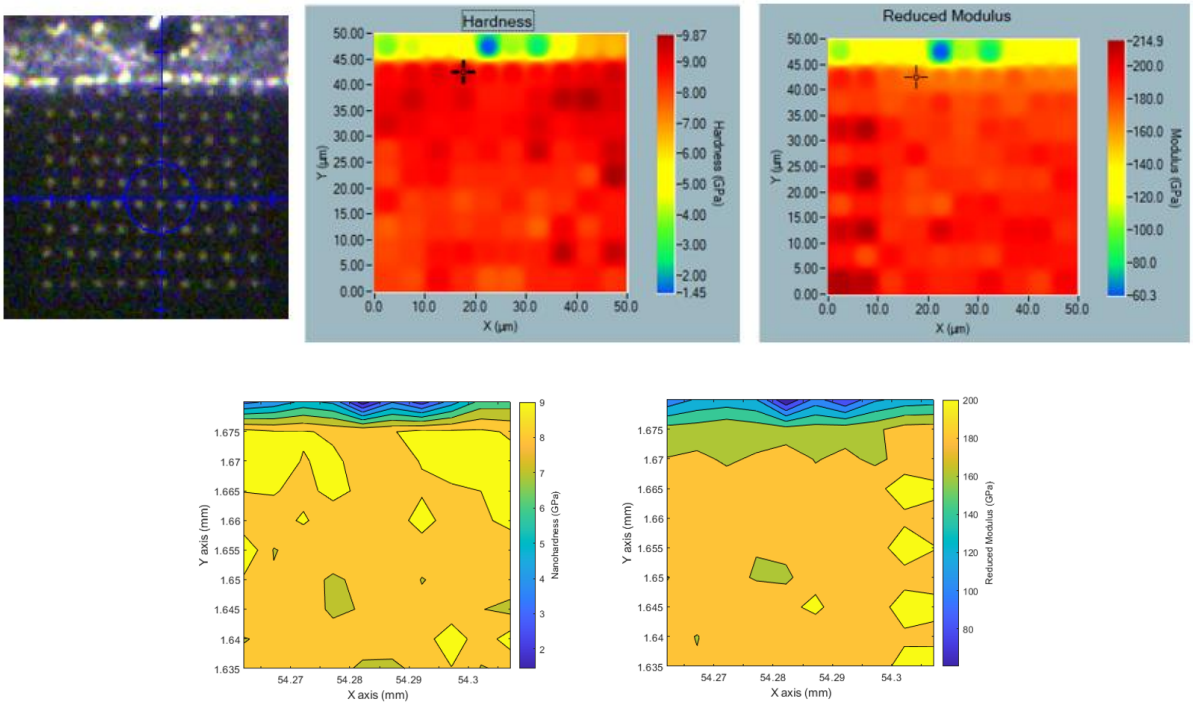

b)

Figure 12.19: Nano-indenter hardness maps of Mn material on the surface point of disc: (a) Mn test of 1400 MPa; (b) Mn test of 1800 MPa

R400

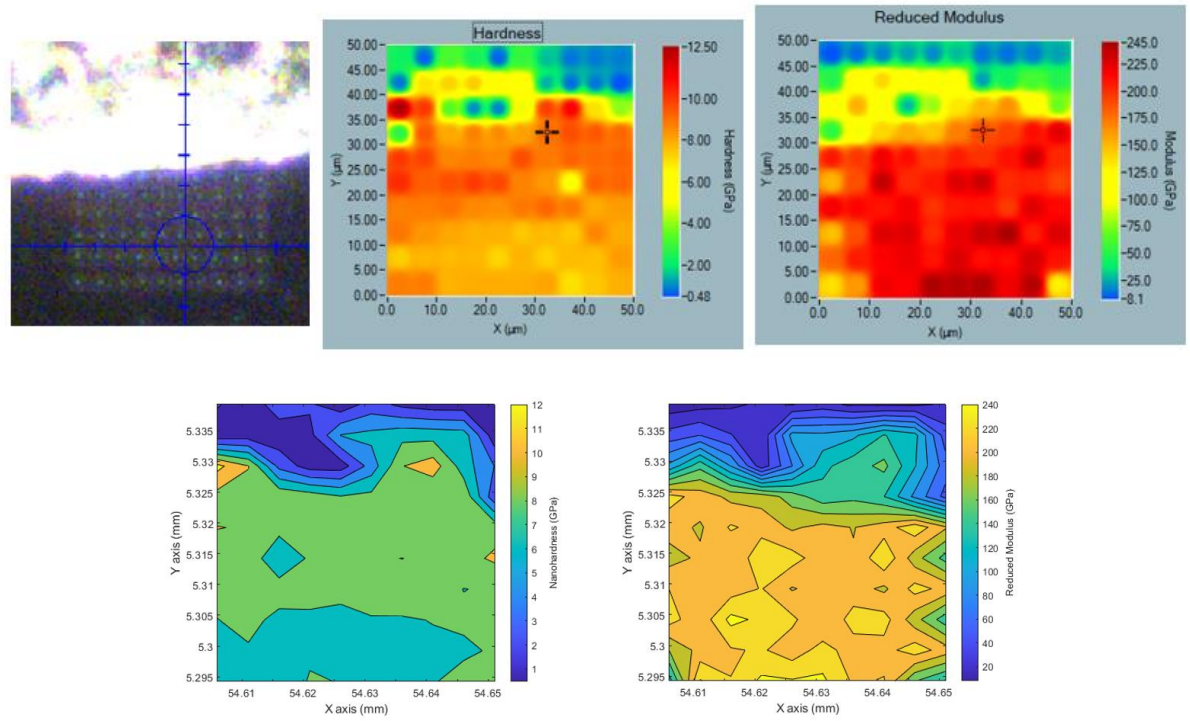

a)

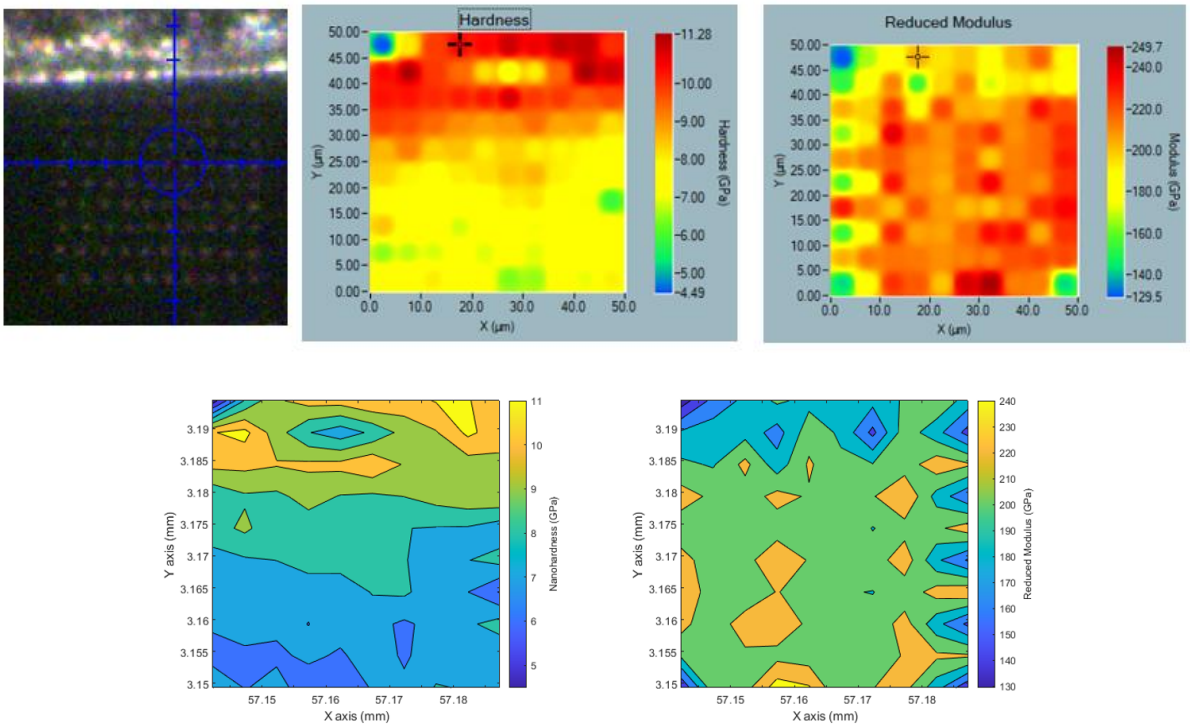

b)

Figure 12.20: Nano-indenter hardness maps of R400 material on the surface point of disc: (a) R400 test of 1400; MPa; (b) R400 test of 1800 MPa

MSS Clad

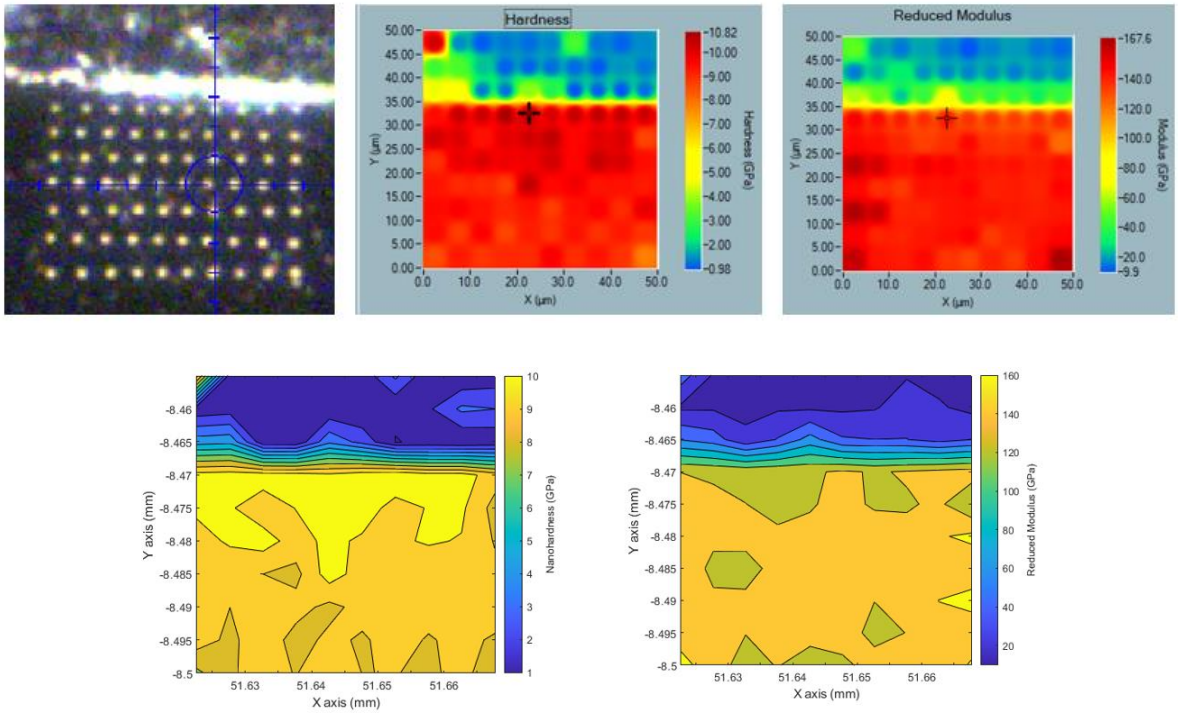

Figure 12.21: Nano-indenter hardness maps of MSS clad 1400 MPa test material on the surface point of the disc

12.3 Appendix for Chapter 8

12.3.1 Appendix 8.A – Surface Evaluations

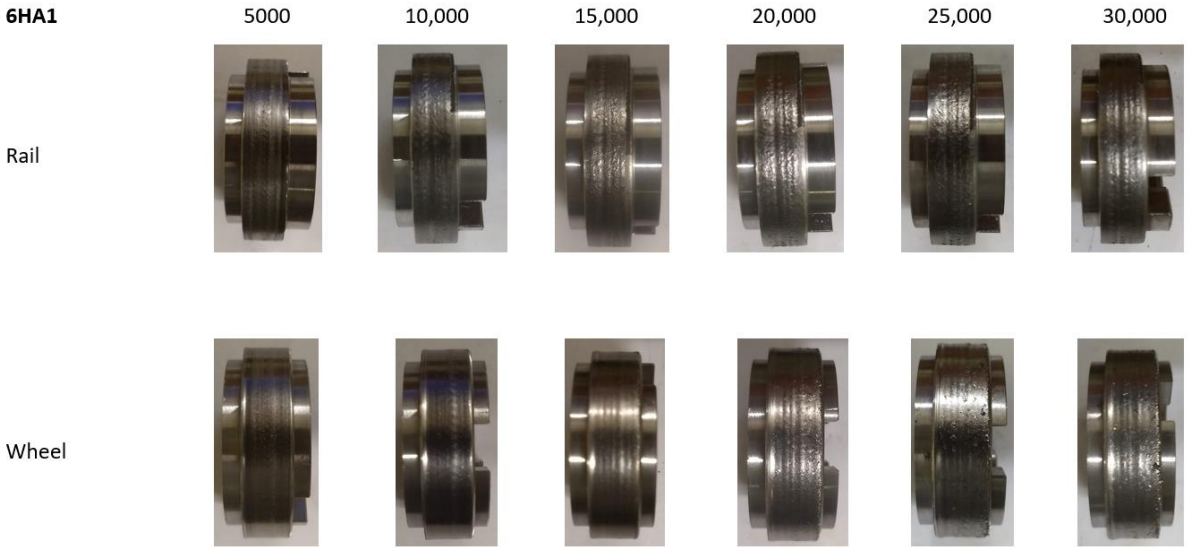

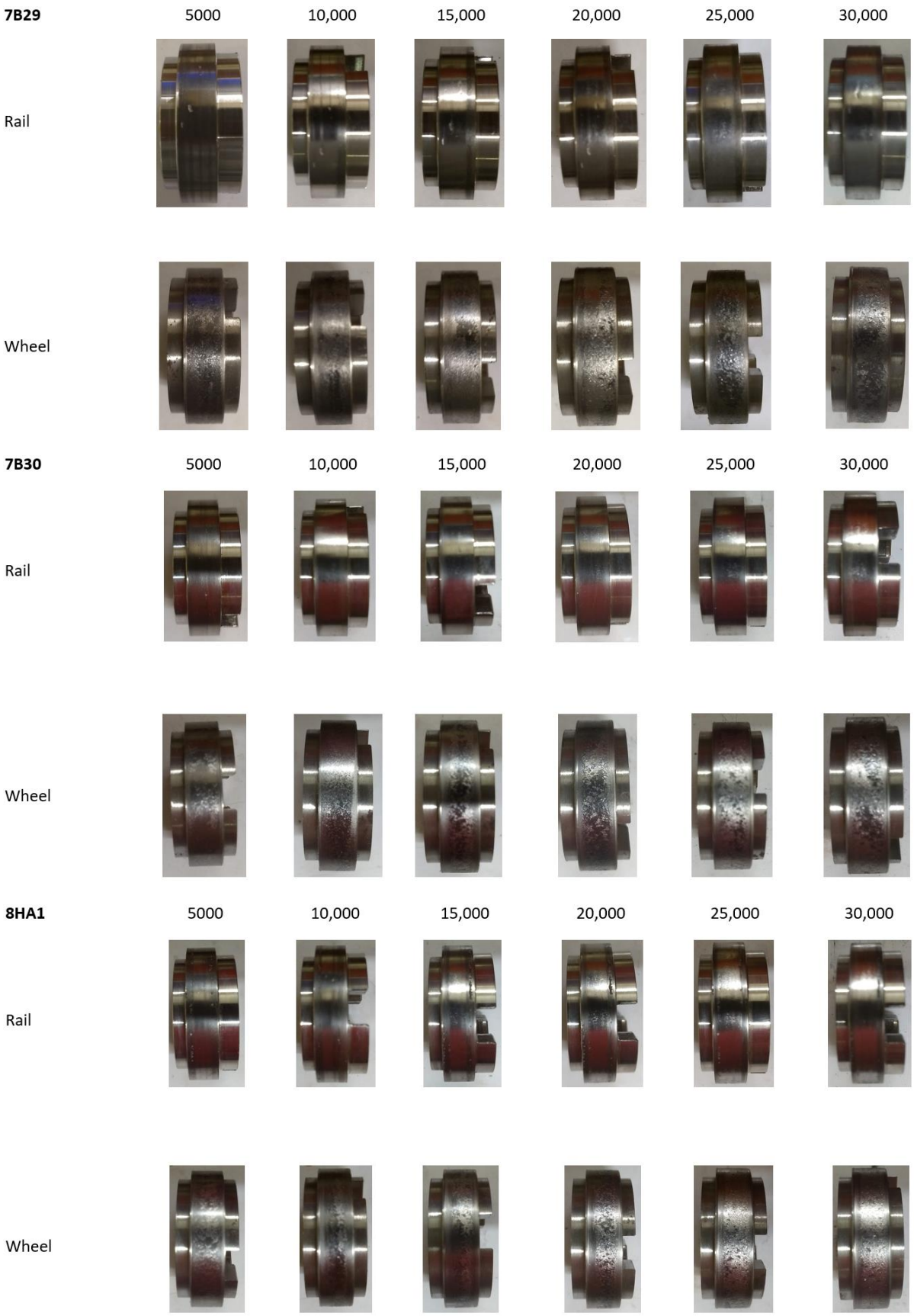

Figure 12.22: Some rail (6HA1, 7B29, 7B30, 8HA1) and wheel discs surface images during the tests